Physics of the Solid State, Vol. 44, No. 11, 2002, pp. 2013–2030. Translated from Fizika Tverdogo Tela, Vol. 44, No. 11, 2002, pp. 1921–1939.
Original Russian Text Copyright © 2002 by Agekyan.

REVIEWS

Intracenter Transitions of Iron-Group Ions in II–VI Semiconductor Matrices

V. F. Agekyan
Institute of Physics, St. Petersburg State University, St. Petersburg, Petrodvorets, 198504 Russia
e-mail: avf@VA4678.spb.edu

Received December 27, 2001

Abstract—A review is made of studies of intracenter optical transitions in 3*d* shells of iron-group divalent (magnetic) ions. Attention is focused on the emission spectra of Mn^{2+} ions in CdTe, ZnS, and ZnSe crystals. An analysis is made of the structure of intracenter absorption and luminescence and of the effect that the elemental matrix composition, magnetic-ion concentration, temperature, hydrostatic pressure, and structural phase transitions exert on the intracenter transitions. The mutual influence of two electronic excitation relaxation mechanisms, interband and intracenter, is considered. The specific features of the intracenter emission of magnetic ions embedded in two-dimensional systems and nanocrystals associated with a variation in *sp*–*d* exchange interaction and other factors are discussed. Data on the decay kinetics over the intracenter luminescence band profile are presented as a function of temperature, magnetic ion concentration, and excitation conditions. The saturation of the luminescence and the variation of its kinetic properties under strong optical excitation, which are caused by excitation migration and the cooperative effect, as well as the manifestation of a nonlinearity in intracenter absorption, are studied. *© 2002 MAIK “Nauka/Interperiodica”.*

1. INTRODUCTION

Crystals and glasses containing iron-group atoms exhibit intracenter transitions in the unfilled 3*d* shells of these atoms that manifest themselves strongly in absorption and luminescence. The intracenter emission of these ions, particularly of the divalent manganese, has a potential use, because $ZnS:Mn^{2+}$ is the most efficient electroluminescent phosphor known to date [1]. The main subject of the present review is optically excited intracenter luminescence (IL). While IL has been studied on a broad range of objects, most reports have dealt only with crystals containing Mn^{2+}. Of most interest is the investigation of the II–VI crystals, in which the relative concentration of the Mn^{2+} cations can range from a few hundredths of a percent to tens of a percent. Considered over such a broad range of concentrations, the manganese may act both as a paramagnetic impurity and an activator and as a solid-solution component capable of affecting the fundamental properties of a crystal. A large number of studies of the optical properties of II–VI solid solutions with a magnetic component and of the related quantum structures have recently been reported. These compounds make up a class of dilute magnetic semiconductors (DMS) sometimes referred to as semimagnetic semiconductors. Typically, DMSs exhibit properties basically inherent in crystalline solid solutions, such as a dependence of the fundamental parameters on the solid-solution composition, inhomogeneous broadening, electron localization associated with local compositional fluctuations, etc. If the isoelectronic impurity is a transition metal, its 3*d* shell can undergo charge transfer, thus imparting new properties to excitons bound to Cu^{2+}, Ni^{2+}, Co^{2+}, and Fe^{2+} in crystals of the wide-band-gap II–VI compounds [2, 3]. DMSs and related quantum structures exhibit specific properties associated with the large magnetic moment of the unfilled 3*d* shell, such as giant Zeeman splitting of the electronic levels, giant Faraday rotation, and the magnetic polaron effect. DMSs reveal two types of electronic excitations and of their relaxation, more specifically, the conventional semiconductor interband and the intracenter mechanisms, which can affect each other substantially. The intracenter absorption and emission of light in the 3*d* shell of a magnetic ion become manifest in crystals with a broad enough band gap. The most popular DMSs with Mn^{2+} ions are model systems for studying magnetic and magnetooptical properties and intracenter transitions. The application potential of DMSs containing various magnetic impurities lies in the area of photoinduced magnetism, laser gain media, laser shutters, electroluminescent devices, Faraday cells, and magnetosensitive low-dimensional quantum structures. Recently, electroluminescence has been studied in thin epitaxial films and composites containing a polymer and manganese-activated crystallites [4, 5]. Investigation of the properties of intracenter photoluminescence promotes our understanding of the electroluminescence processes occurring in bulk crystals and quantum structures and shows the path to their optimization. There is a variety of reviews and papers that primarily describe the band electronic states of DMSs and the effect of an internal field of magnetic ions on them (electron–ion exchange interaction), as well as the interaction of magnetic ions with one another (ion–ion exchange interaction) (see, e.g., [6–10]). The present review deals with the optical transitions occurring in the 3*d* shell of the iron-group divalent ions, mainly of Mn^{2+}, in II–VI crystals and related nanostructures. Main attention is focused on the interaction between various mechanisms of electronic-excitation relaxation, on the effect of external factors, elemental composition of the matrix, and confinement, as well as on the kinetic properties of the IL.

2. ENERGY LEVELS AND OPTICAL TRANSITIONS IN THE 3*d* SHELLS OF IRON-GROUP IONS IN THE II–VI CRYSTAL MATRICES

The properties of the 3*d* shell of an iron-group ion in a crystal and the methods to be used to calculate its electronic levels are governed by a number of factors. Among these are the electron–electron spin interaction V_{ss}, the spin–orbit interaction V_{so}, hybridization of the *d* states with *s* and *p* states of the band electrons, and the crystal field V_c. The crystal field can be written in the form

$$V_s = V_o + V_1 + V_2, \quad (1)$$

where V_o is the spherically symmetric part of the field, V_1 provides the main contribution to the lowering of the spherical field symmetry, and V_2 contains small terms of an even lower symmetry. In the systems of interest to us here, the strongest is the electron–electron interaction, which corresponds to the case of a weak crystal field. If the 3*d* shell is filled to one half or less, the weak-field complexes retain, in accordance with Hund's rule, the maximum possible total free-ion spin moment (5/2 for Mn^{2+}). In high-symmetry crystal fields, the electron–electron interaction is described by three Racah parameters, *A*, *B*, and *C*, with the first of them yielding only the general shift of the whole 3*d*-level system. The ligand crystal field acting on the cation in a zinc-blende-type lattice, to which II–VI cubic crystals belong, is tetrahedral. In this field, the *d* orbitals can be divided in two groups, with $d_{(x^2-y^2)}$, d_{z^2} belonging to the T_2 term and d_{xy}, d_{xz}, d_{yz}, to term *E*. The tetrahedral and octahedral fields acting on the magnetic ion located at the cube center are created by the ligands occupying four positions at the cube vertices and six positions at the face centers, respectively. The crystal-field splittings of the 3*d* levels in these fields are related through

$$\Delta_t = -4\Delta_o/9. \quad (2)$$

Here, the indices *t* and *o* relate to the tetrahedral and octahedral cases for which the T_1 and *E* terms are the lowest, respectively. The quantity Δ (sometimes replaced by *Dq*) is commonly used to measure the crystal field. It is due to the comparatively small value of Δ_t that the tetrahedral complexes in a II–VI matrix are classed among high-spin, weak-field complexes. In this case, the nearest neighbors (anions) forming the tetrahedron do not affect the level diagram of a single manganese atom noticeably. The tetrahedral type of the anion environment also accounts for the small change that the fields acting on the Mn^{2+} ion undergo in the transition of a II–VI crystal from the wurtzite to zinc-blende structure; indeed, the ligand field has the T_d symmetry and there is no inversion center. The level diagram for the Mn^{2+} ion in a tetrahedral field is presented in Fig. 1, with the energy reckoned from the ground state (the spin sextet $^6A_1$ with spin $S = 5/2$ and orbital number $L = 0$), which is only weakly sensitive to the field. The lowest excited states correspond to $S = 3/2$ and $L = 1, 2, 3, 4$, the ^4G term with $L = 4$ lying at the lowest energy. The ^4G term splits into four levels in a tetrahedral field. The T_1 level is the lowest, because its energy decreases considerably with increasing field, whereas the *A* and *E* levels respond very weakly to a field variation. Energy level calculations for iron-group ions in crystal matrices (the ligand field) can be found in a number of monographs and papers (see, e.g., [11, 12]).

While the positions of the 3*d*-shell levels relative to the band-state extrema are difficult to derive from optical spectra, the absence of clearly pronounced transitions from the $^6A_1$ level to the conduction band in all Mn-doped crystals of the II–VI compounds indicates that this level lies below the top of the valence band derived from the chalcogenide *p* states. Photoelectron emission spectra of $Cd_{1-x}Mn_xTe$ were studied both experimentally and theoretically in [13–18]. Two methods of photoelectron spectroscopy, integrated and angle-resolved, yielded contradictory results for the extent of hybridization of various states. These contradictions were finally removed, and it has been shown that the observation of a strong photoemission peak located a few electronvolts below the valence-band top and corresponding to the 3*d*-shell contribution to the electron density of states is not at odds with a considerable *sp*–*d* hybridization. The energy level corresponding to the removal of one 3*d* electron from Mn^{2+} lies 3.5 eV below the valence-band top, whereas that due to the addition of a sixth electron to the 3*d* shell is located 3.0–3.5 eV above the valence-band top. This paper does not consider the problems associated with charge transfer in the 3*d* shell of the iron-group atoms.

Absorption spectra corresponding to transitions in the Mn^{2+} 3*d* shell are observed in crystal matrices with a sufficiently broad band gap. Intracenter transitions with a threshold of about 2.13 eV are seen to appear in reflectance spectra of $Zn_{1-x}Mn_xTe$ already at $x = 0.02$ [19]. At comparatively high manganese concentrations, the intracenter absorption spectrum consists of bands

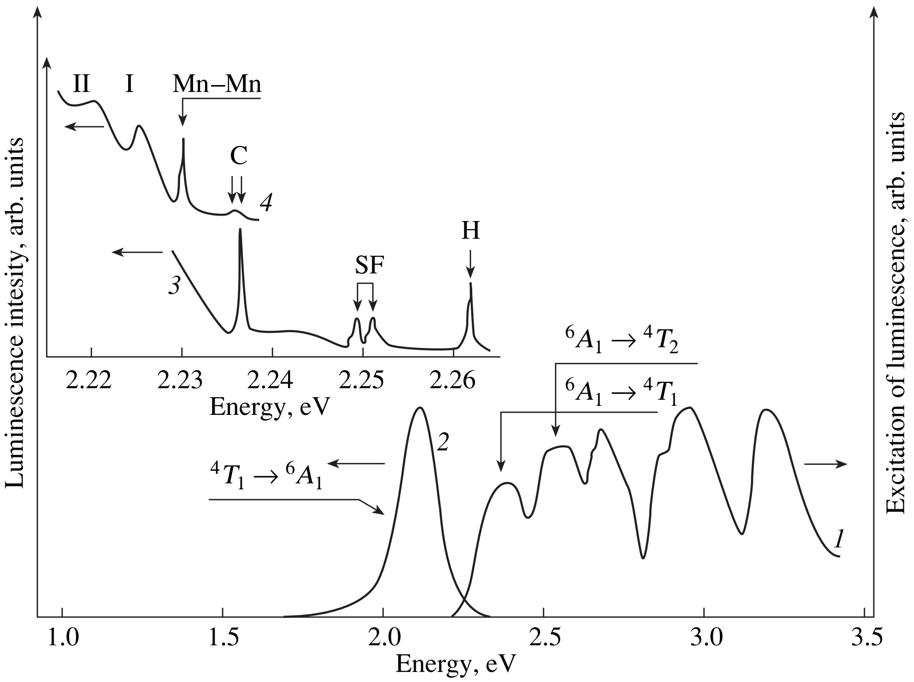

Fig. 1. (*1*) Intracenter absorption and (*2)* IL of Mn^{2+} in a $Zn_{0.96}Mn_{0.04}S$ crystal [1]. Inset presents Mn^{2+} IL spectra in ZnS doped with manganese to concentrations of (*3*) 0.01 and (*4*) 1%. The C, H, and SF lines refer to zero-phonon emission of single ions from the cubic and hexagonal crystal regions and from the region containing stacking faults, respectively. The Mn–Mn, I, and II peaks relate to emission of manganese pairs of minimum radius from a cubic region and its phonon replicas, respectively. $T = 4$ K.

about 0.1 eV wide (Fig. 1). The intracenter absorption coefficient is approximately proportional to the manganese concentration, and the band width is governed by the 3*d*-electron interaction with phonons and by inhomogeneous broadening.

The transitions between 3*d* shell levels are of the intercombination type and are forbidden in the electric-dipole approximation. The forbiddenness is partially lifted by the noncentrosymmetric crystal field components, dynamic Jahn–Teller effect, and spin–orbit coupling. The pronounced hybridization of the *d* states with the chalcogenide *p* states plays a significant part in this class of compounds. As a result, the oscillator strength of the Mn^{2+} intracenter transitions in II- to VI-type lattices is far larger than that, for instance, in MnF_2 and its analogs. The absorption coefficient at the band maxima of $Cd_{0.5}Mn_{0.5}Te$ is 10^3 cm^{-1}, which is one to two orders of magnitude smaller than the typical value of the interband absorption coefficient. In systems with a high Mn concentration, the IL band is structureless and about 120 meV wide and its maximum in $Cd_{0.5}Mn_{0.5}Te$ lies at approximately 2.0 eV, so that the Stokes losses relative to the peak of the first intracenter absorption band, $^6A_1$–$^4T_1$ (the maximum of the IL excitation spectrum), are quite large, 0.4 eV.

The intracenter absorption, IL, and IL excitation spectra have a clearly pronounced structure for low concentrations of atoms with unfilled 3*d* shells. Such spectra can be observed in wide-band-gap matrices, the best studied of them being the $ZnS:Mn^{2+}$ system. Zinc sulfide can contain regions with zinc-blende and wurtzite structure, as well as regions with stacking faults. At Mn concentrations on the order of 10^{-4}%, the IL spectrum of $ZnS:Mn^{2+}$ exhibits several narrow zero-phonon lines with energies lying in the interval 2.22–2.24 eV, the strongest of them belonging, according to [1], to the emission of Mn^{2+} ions occupying cationic sites of the cubic and hexagonal phases. The weaker lines can be assigned to Mn^{2+} positions in the regions where the ZnS lattice has stacking faults. ZnS is a polymorphic material with regular defect sequences forming the 4*H*, 6*H*, and 9*R* polytypes. In the case of irregular defects, there are inequivalent cationic positions of C_{3v} symmetry. For these reasons, the zero-phonon spectrum has a rich structure and at low Mn^{2+} concentrations and a low temperature, a system of closely spaced zero-phonon lines are observed (Fig. 1). Strong phonon replicas are seen on the low-energy side of these lines. The excitation spectrum of the IL zero-phonon lines correlates with the absorption spectrum; the former spectrum exhibits bands corresponding to transitions from the Mn^{2+} ground state $^6A_1$ to the excited states $^4T_1$, $^4T_2$, and ^4E. At low Mn concentrations, the IL decay time exceeds 1 ms and increases for the zero-phonon lines toward lower energies, from 1.15 ms for the hexagonal phase to 1.77 ms for the cubic phase. In high-quality matrices with no structural defects and at low Mn^{2+} concentrations, one succeeds in studying in consider-

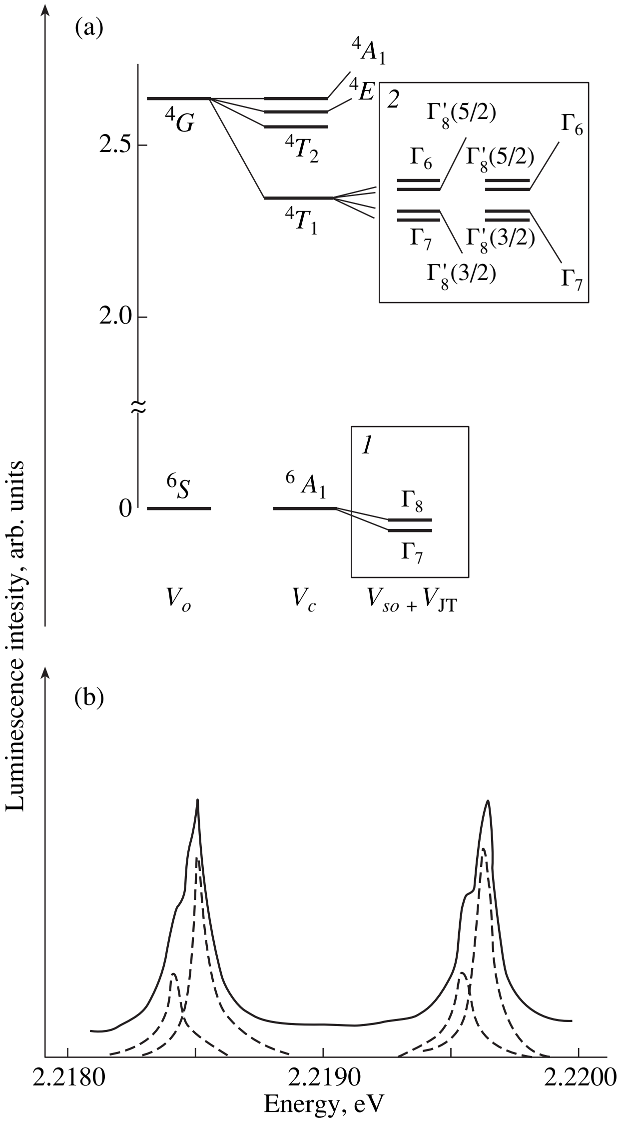

Fig. 2. Calculated energy level diagram and zero-phonon IL spectrum of Mn^{2+} in a ZnS crystal free of structural defects and having a low manganese concentration [20]. (a) Energy levels of a free ion (V_o) and of an ion in a crystal field (V_c); insets (*1*) and (*2*) show, respectively, the $^6A_1$ ground-state splitting (magnified 10^6 times) and two versions of additional splitting of the $^4T_1$ excited state (magnified 10^2 times) with inclusion of the spin–orbit (V_{so}) and Jahn–Teller (V_{JT}) interactions. (b) Fine structure of the Mn^{2+} IL spectrum in ZnS obtained at $T = 2$ K and corresponding to the four $^4T_1$ sublevels shown in inset *2*.

able detail the 3*d* level systems of single ions at low temperatures. In such $ZnS:Mn^{2+}$ crystals, the spectra of polarized excitation of the Mn^{2+} terms were investigated in [20]. The orbital-triplet fine structure is usually associated with the Jahn–Teller interaction of the 3*d* states with the ϵ-type vibrational mode. In addition to the 1-meV doublet splitting of the $^4T_1$ term, nearly degenerate states differing by 10^{-4} eV were resolved in each doublet component (Fig. 2). The doublet components derive from the Γ_6, Γ_8 and Γ_7, Γ_8 states, respectively. It has been found that the crystal field model is inadequate for determination of the multiplet splitting of terms of the $3d^5$ states.

While the covalent model provides a more accurate description of the $3d^5$ level system, it is more complicated and the determination of a number of its parameters requires experiments involving the application of a magnetic field and uniaxial strain. As follows from this model, the Mn^{2+} IL fine structure in ZnS, ZnSe, ZnTe, and CdTe is largely governed by the spin–orbit coupling of the $3d^5$ and ligand states. As the relative manganese concentration *x* is increased from 0.001 to 0.02, the IL and absorption bands shift toward higher energies at a rate of 3 meV/*x* and the spectrum becomes more complex because of the interaction between the magnetic ions. Already at an *x* value of about 0.01, $Zn_{1-x}Mn_xS$ exhibits a zero-phonon IL line of the nearest neighbor Mn–Mn pairs which is substantially stronger than the zero-phonon emission line of single Mn ions (Fig. 1). The pair line has strong replicas with the emission of LA and LO phonons. The IL excitation bands still exhibit a phonon spectrum structure at $x = 0.04$; however, at $x = 0.08$ and larger, the bands become structureless. In the 2.2-eV region, the ZnS matrix reveals bands near 1.95 and 1.6 eV in addition to the Mn^{2+} IL. While at low temperatures these bands are weak, they have the same intensity as the 2.2-eV band at 60 K and are dominant at 100–200 K. The low-energy bands should be assigned, most likely, to Mn^{2+} ions occupying interstitial positions in the crystal matrix. These bands become relatively enhanced with increasing Mn^{2+} concentration and temperature, the conditions in which energy transfer between the various manganese centers becomes efficient. The relative weakening of the 2.2-eV IL band observed to occur in a $ZnS:Mn^{2+}$ crystal heated above 60 K is accompanied by a fast decrease in the decay time as a result of the competing nonradiative mechanisms and energy transfer to lower lying states, whereas for the long-wavelength bands, this process starts at considerably higher temperatures.

Even at the limiting manganese concentrations in II–VI crystals, there is no indication of the properties of the 3*d* levels changing radically due to the nearest neighbor *d*–*d* interaction. For high Fe^{2+} and Co^{2+} concentrations, this interaction is far stronger and a transition is possible from isolated deep levels to a continuum of hybridized *d* states. As a result, as the concentration of iron or cobalt increases, the transitions involving the crystal-field-split 3*d* levels broaden and weaken in intensity.

When cobalt is doped in low concentrations into ZnSe, numerous peaks about 0.01 eV and less in width appear in the luminescence and subsequently extend over a broad spectral region from 1.7 to 2.7 eV [21]. Two bands, at 0.73 and 0.78 eV, are due to the transition from the $^4A_2(F)$ ground state of the 3*d* shell in the T_d field to the first excited state $^4T_1(F)$; the other bands involve higher excited states of the type of *G*, *D*, *H*, and *P*. The narrowness of these peaks and the absence of phonon replicas indicate a weaker interaction of Co^{2+} with lattice vibrations compared with Mn^{2+} [22]. According to [23], the strengthening of the IL bands at 1.6, 1.9, and 2.4 eV in $Zn_{1-x}Co_xSe$ with $x = 0.01–0.02$ observed at 10 K is accompanied by a weakening and disappearance of the green edge luminescence of ZnSe. At $x = 0.03$, the IL also disappears, to be replaced by a Raman continuum with a width larger than 0.5 eV, which is due to electronic transitions in a *d*-type hybridized impurity band. $Zn_{1-x}Fe_xSe$ exhibits one IL band at about 1.9 eV, which is more stable than the Co^{2+} IL band. It starts to broaden at $x = 0.2$ and decays by an order of magnitude only at $x = 0.64$, with the Raman continuum appearing at $x = 0.3$ and gaining in intensity up to the maximum concentration $x = 0.73$. Interestingly, in II–VI crystals doped with cobalt and iron, no transition from the nonconducting to metallic state occurs, despite the pronounced delocalization of the 3*d* states. This can be accounted for by the transition to the conducting state being suppressed by disorder, i.e., by the formation of a continuum of localized electronic states. One can conceive of the following model for the case of very high iron or cobalt concentrations: the Coulomb energy for the 3*d* electrons is large compared to the characteristic energy variation occurring in one electron hop, as a result of which the electronic states split into two subbands separated in energy, with one of them being completely filled and the other being empty, so that the system retains its insulating properties.

3. DEPENDENCE OF INTRACENTER LUMINESCENCE ON THE TEMPERATURE AND ELEMENTAL COMPOSITION OF CRYSTALS

The temperature dependence of the shape and width of the Mn^{2+} IL band has been studied for $Cd_{1-x}Mn_xTe$ ($0.4 < x < 0.7$) in the range 10–220 K [24]. The spectral band width was found to comply with the configurational-coordinate model up to 80 K. At higher temperatures, the experimental data are observed to deviate considerably from theoretical calculations because of the equilibrium positions of the manganese ion in the excited and ground states approaching each other with increasing temperature. This conclusion is buttressed by the considerable decrease in the Stokes losses above 80 K. The Mn^{2+} IL band in $Zn_{0.5}Mn_{0.5}Se$ shifts toward lower energies by 12 meV in the temperature interval from 4 to 45 K, after which a 40-meV shift in the opposite direction occurs within the region 45–300 K. The model based on the $^4T_1$–$^6A_1$ optical transition involving simultaneous spin flip of two electrons in the 3*d* shells of neighboring Mn^{2+} ions provides a correct description of the low-temperature behavior of the IL band and of its weak sensitivity to an external magnetic field up to 6 T [25]. The high-temperature shift toward higher energies is accounted for primarily by the lattice expansion. $Cd_{1-x}Mn_xTe$ also exhibits a shift of the Mn^{2+} IL maximum from 2.0 to 2.15 eV in the interval 77–300 K. The temperature-induced variation of the IL band width below 80 K is consistent with the configurational model; however, in the high-temperature region, one should also take into account the approach of the configurational coordinates of the Mn^{2+} ground and excited states [26]. Note that the temperature-induced shifts of the manganese absorption threshold E_t and of the Wannier exciton line E_{gx} in $Cd_{1-x}Mn_xTe$ ($x > 0.4$) are close in magnitude, while their shifts observed under hydrostatic pressure differ even in sign.

It was proposed to use the temperature-induced variation of transition energies in the 3*d* shell of the Mn^{2+} ions contained in various DMSs for determination of the temperature dependence of the lattice constant for crystals with a sufficiently wide band gap [27]. The possibility of using the IL of Mn^{2+} as a probe rests on the strong dependence of the energy of the $^4T_1$ term on the crystal field and the weak field dependence of the energy of the $^6A_1$ ground state. Optical spectroscopy has in this respect an edge over direct electronic and x-ray methods, which are difficult to employ over a broad temperature range covering the low-temperature domain. The variation of the lattice constant can also be studied by probing the band gap width E_g with exciton radiation. However, the IL has an advantage over exciton spectroscopy in its temperature stability and convenient spectral range, because measurement of the exciton spectra of wide-band-gap crystals requires the use of sophisticated techniques. This appears to be an essential point in view of the interest focused currently on II–VI crystals with a very wide band gap containing light elements (Zn, Mg, Be, Ca). Furthermore, the exciton in a solid solution is characterized by different degrees of localization at different temperatures, which makes accurate determination of E_g a difficult problem. The manganese IL in MnF_2 crystals with a different lattice structure was used to determine the crystal-field parameters and the degree of bond covalency [28]. Variations in the elemental composition also strongly affect the temperature-induced shift, which in $Cd_{1-x}Mn_xTe$, for instance, increases by a factor of more than two with *x* increasing from 0.4 to 0.7 [29]. Molecular beam epitaxy made it possible to prepare $Cd_{1-x}Mn_xTe$ films with *x* ranging from 0.6 to 1.0 and to study the temperature-induced variation of the Mn^{2+} IL at manganese concentrations inaccessible for bulk crystals [30–33]. The temperature sensitivity of the IL in MnTe is far weaker than that in $Cd_{0.3}Mn_{0.7}Te$; however, in both cases, the lowest energy of the IL maximum

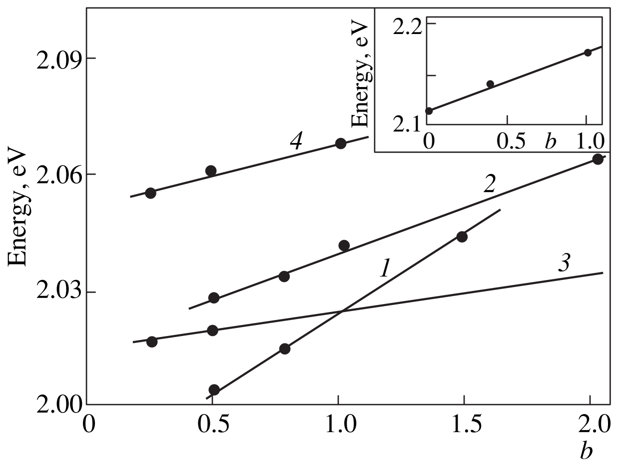

Fig. 3. Energy position of the Mn^{2+} IL profile maximum in II–VI solid solutions as a function of relative concentrations b of the cation components ($T = 77$ K). $Cd_{1-x-y}Mn_xMg_yTe$: (*1*) $b = y/(1 - x - y)$, $x = 0.375$ (Mg for Cd substitution); (*2*) $b = y/x$, $1 - x - y = 0.25$ (Mg for Mn substitution); (*3*) $b = x/(1 - x - y)$, $y = 0.25$ (Mn for Cd substitution); (*4*) $b = x/(1 - x - y)$, $y = 0.5$ (Mn for Cd substitution) [35]. Inset shows the position of the Mn^{2+} IL maximum in a $Zn_{1-x}Mg_xS$ crystal with a low manganese concentration, $b = x/(1 - x)$ (Mg for Zn substitution) [36].

corresponds to $T = 50$ K, where the interatomic distances are the smallest. Epitaxial films of other II–VI solid solutions containing iron-group elements can also be grown by molecular-beam epitaxy (MBE) within a much broader relative cation concentration range than can be done with bulk crystals.

Investigation of the spectral position of the IL in $Cd_{1-x}Mn_xTe$ [34], $Cd_{1-x-y}Mn_xMg_yTe$ [35], $Zn_{1-x}Mg_xS$: Mn^{2+} [36] and other systems performed at various x and y yielded information on the effect of the nearest cation environment on the 3*d* transition energies in Mn^{2+}. The results obtained allow qualitative interpretation based on the change that the crystal field undergoes when one cation is replaced by another and on the radii of the divalent ions, which for Cd^{2+}, Mn^{2+}, Zn^{2+}, and Mg^{2+} are 0.97, 0.80, 0.74, and 0.66 Å, respectively. As can be seen from Fig. 3, the shift rates depend strongly on the chosen pair of the substitution partners. The crystal field Dq is usually assumed to vary inversely proportional to the fifth power of the distance between the manganese ion and the anion. If one uses the variation of the lattice constant $a_0(x)$ as a basis, estimates made for x varying from 0 to 1 yield a considerably larger shift of the *d*–*d* transition bands than that observed experimentally. The reasons for this discrepancy may lie in that, first, the manganese–anion distance varies more weakly than $a_0(x)$ does (this is supported by EXAFS measurements) and, second, one should take into account not only the geometric factor but also the change in the bond covalency upon cation substitution. The concentration-induced shift varies sometimes nonmonotonically. It was shown in [37] that the Fe^{2+} IL band in $ZnS_{1-x}Se_x$, which peaks at about 1.3 eV, shifts toward lower energies up to $x = 0.3$; then, the shift reverses sign, which apparently results from the combined effect of the crystal field variation and of the degree of the *sp*–*d* hybridization.

A strong IL shift is expected to ensue from the introduction into a DMS of beryllium as a cation component (the Be^{2+} ionic radius is only 0.35 Å); beryllium has become a subject of considerable recent attention as a wide-band-gap component which would enhance the bond covalency in II–VI crystals and increase their microhardness [38]. The DMSs containing Be as one of their components are of interest (both theoretically and for application) in the form of both bulk crystals and as layers in quantum well structures [39]. The currently available data are insufficient for a quantitative description of the IL shift caused by Be introduction into various DMSs.

Table 1 presents the positions of the intracenter 3*d* absorption maxima for various group-VI elements determined for transitions to the four Mn^{2+} excited states [40].

Table 1. Energy positions of the intracenter absorption peaks in three types of DMS

DMS	Final state (transition energy from the $^6A_1$ level in eV)			
	$^4T_1(^4G)$	$^4T_2(^4G)$	$^4E(^4G)$	$^2T_2(^2I)$
$Mn_{1-x}Zn_xS$	2.33	2.40	2.60	2.75
$Mn_{1-x}Zn_xSe$	2.38	2.52	2.68	2.93
$Mn_{1-x}Zn_xTe$	2.38	2.54	2.70	2.93

We readily see that replacement of sulfur by selenium and, all the more so, by tellurium shifts the absorption bands noticeably, whereas substitution of tellurium for selenium affects them only weakly. This does not correlate well with the simple theory taking into account only the ligand crystal field (the ionic radii of S^{2-}, Se^{2-}, and Te^{2-} are 1.84, 1.91, and 2.11 Å, respectively). This disagreement can be removed, as in the case of cation substitution, if one includes the change in the bond covalency. The Racah coefficient B, which is a measure of covalency, decreases in the order S–Se–Te with weakening valence bond ionicity; this decrease corresponds to the intracenter transition bands shifting toward higher energies. The Mn^{2+} IL intensity varies little in the interval 4–60 K, but when heated to 100 K, the IL weakens by more than an order of magnitude. Note that the IL intensity in matrices with strongly differing parameters, for instance, in ZnS and CdTe, follows a similar temperature behavior, provided the Mn^{2+} concentration exceeds a few percent. This similarity is accounted for by the fact that the major factor here is the migration of intracenter excitation, a process which will be considered below.

4. EFFECT OF HYDROSTATIC PRESSURE ON INTRACENTER TRANSITIONS

The effect of hydrostatic pressure P on the energy of transitions between the 3d-shell levels of iron-group ions is connected intimately with the level shifts induced by variations in temperature or DMS elemental composition. In the final count, the problem reduces to the magnitude and symmetry of the local crystal field and the degree of sp–d hybridization. It was established that the pressure dependence of the shifts of the Wannier exciton, dE_{gx}/dP, and of the intracenter transition in the Mn^{2+} ion, dE_{Mn}/dP, in $Cd_{1-x}Mn_xTe$ measured at T = 2 K are 520 and –410 cm^{-1}/GPa, respectively [41]. At T = 40 and 77 K, the manganese level shift rates grow to –450 and –600 cm^{-1}/GPa, respectively; i.e., the temperature dependence of the shift is nonlinear. The pressure-induced shifts of the band and intracenter transitions have opposite signs, so that at certain values of P, depending on x, the threshold E_t of the intracenter transition turns out to be below the exciton transition energy even for $x < 0.4$. After the level crossing, the IL band starts to grow in intensity and the exciton emission weakens. The low-energy shift correlates with crystal-field theory for ions in that compression enhances the field and lowers the first excited level $^4T_1$ relative to the $^6A_1$ ground state; numerical calculations of the pressure-induced shifts yield, however, –160 cm^{-1}/GPa, which is considerably less than the experimental value [42]. This disagreement is most likely connected with the fact that the calculation used does not go beyond the usual crystal-field theory and does not assume strong hybridization of the Mn^{2+} 3d states with s- and d-type orbitals of other atoms. Later calculations [43] wherein the hybridization was included yielded a larger pressure-induced shift of the $^4T_1$ level. After the IL band has appeared with increasing P, interband exciton emission gradually decays and finally almost disappears. Two possible reasons were suggested for the weakening of the exciton emission with x increasing above 0.4: (i) enhanced relaxation via the Mn^{2+} 3d levels and (ii) degradation of the solid-solution quality at high x, which reduces the quantum yield of the exciton luminescence. Hydrostatic pressure experiments indicate that the first reason is more essential, because the exciton luminescence is observed to weaken under elastic strains that do not degrade the crystal quality.

The pressure-induced shifts of the Mn^{2+} IL band maxima toward lower energies measured at room temperature [42] for Zn- and Mn-based DMSs with different Group-VI elements are listed in Table 2.

Table 2. Dependence of the shift of the Mn^{2+} IL band maximum on hydrostatic pressure P measured on three DMS types with different magnetic component concentrations

DMS	x	$-dE_{Mn}/dP$ (cm^{-1}/GPa)
$Zn_{1-x}Mn_xS$	0.05	224 ± 4
	0.3	286 ± 8
	0.5	303 ± 5
$Zn_{1-x}Mn_xSe$	0.15	169 ± 16
	0.25	181 ± 16
$Zn_{1-x}Mn_xTe$	0.1	500 ± 40
	0.3	419 ± 16
	0.6	395 ± 40

An analysis produced the following results [42]. The main characteristics of the crystal field are its force Dq and two Racah coefficients, B and C, for which theory yields for the B/C ratio values ranging from four to five [43]. In the case of $Zn_{1-x}Mn_xS$, the theory can be reconciled with experiment for Dq = 500 cm^{-1} and B = 610 cm^{-1}. The magnitude of Dq scales with the distance a_0 between the Mn and S ions as a_0^{-5}, and calculations suggest that a_0 changes by 0.014 nm in the pressure interval from 0 to 10 GPa, whence dDq/dP = 18 cm^{-1}/GPa. For $ZnS:Mn^{2+}$, dB/dP = –3.5 cm^{-1}/GPa. According to [44], the dependence of intracenter transition energy on pressure can be cast as

$$\begin{aligned} dE_{Mn}/dP &= rd(Dq)/dP \\ &+ [E_{Mn} - Dqr]B - 1dB/dP, \end{aligned} \tag{3}$$

where r determines the slope of the E_{Mn}/B dependence on Dq/B in the diagrams presented in [43]. For the $^4T_1$–$^6A_1$ transition, one obtains dE_{Mn}/dP = 300 cm^{-1}/GPa, which is in accord with the experimental value (267 ± 9) cm^{-1}/GPa for $Zn_{1-x}Mn_xS$.

It was found that a hydrostatic pressure of up to 13 GPa drives a phase transition in $Zn_{1-x}Mn_xS$ ($0.01 < x < 0.1$) from the zinc-blende to rocksalt structure [45]. This transition is accompanied by a radical change in the IL spectrum, with the 2.0-eV band dying out and a new band peaking at 1.4 eV and having a considerably higher quantum yield that forms and rises in intensity (Fig. 4). These experiments permit one to estimate the change in the ligand field induced by the phase transition, as well as to use the IL as a probe to detect structural transformations. IL studies have established that temperature annealing carried out after stress removal restores the sphalerite structure practically completely.

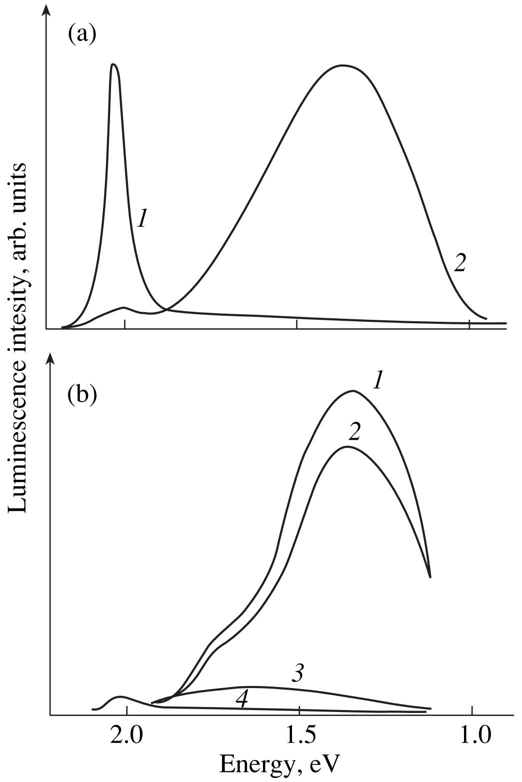

Fig. 4. Effect of hydrostatic pressure on the Mn^{2+} IL spectrum in a $\mathrm{Zn}_x\mathrm{Mg}_{1-x}\mathrm{S}$ crystal [45]. (a) IL spectra (*1*) in the original cubic crystal and (*2*) after application of a hydrostatic pressure of 13 GPa; $x = 0.07$; (b) IL after removal of hydrostatic pressure: (*1*) before annealing, (*2*, *3*, *4*) after annealing for 2 h at 200, 400, and 500°C, respectively; $x = 0.04$. The IL spectra were obtained at $T = 77$ K.

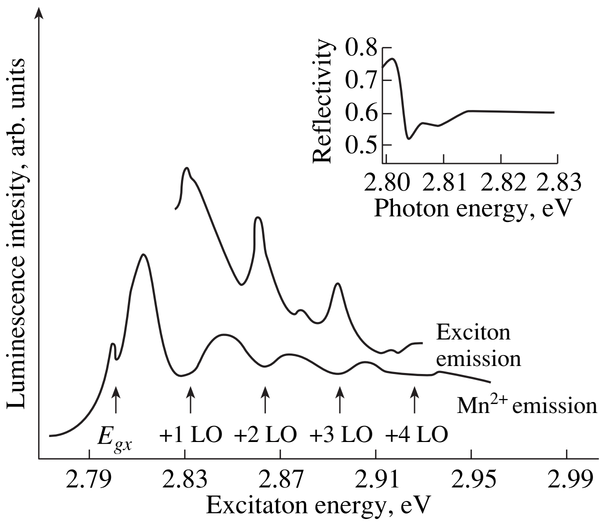

Fig. 5. Excitation spectra of the Mn^{2+} IL and exciton luminescence in a $\mathrm{Zn}_{0.95}\mathrm{Mn}_{0.05}\mathrm{Se}$ crystal obtained at $T = 4$ K [46]. Inset shows a reflectivity spectrum of a crystal with an excitonic structure near 2.803 eV. Arrows identify the position of the exciton peak E_{gx} and the positions spaced from it by an integer number of LO phonon energies.

5. COMPETITION BETWEEN THE INTRACENTER AND BAND CHANNELS OF RADIATIVE RECOMBINATION

There is ample evidence supporting the existence of a connection between the interband and intracenter electronic states, for instance, the onset of ultrafast phase relaxation of Wannier excitons in II–VI crystals following their doping by iron-group ions, the presence of a peak corresponding to the exciton energy E_{gx} in the IL excitation spectra, etc.

In the cases where the DMS band gap width E_g (more specifically, the exciton energy E_{gx}) does not exceed the threshold energy of the intracenter transition E_t, the IL is weak. Under these conditions, energy transfer from the first excited level of the 3*d* shell to band states is more likely than a radiative transition to the ground state of a magnetic ion. If $E_{gx} > E_t$, the situation changes radically and the DMS may exhibit radiative relaxation of optical excitation of two types, conventional interband and intracenter. Their relative intensity is governed by a number of factors, which we will discuss through the example of $\mathrm{Cd}_{1-x}\mathrm{Mn}_x\mathrm{Te}$ and $\mathrm{Zn}_{1-x}\mathrm{Mn}_x\mathrm{Se}$.

The band gap $E_g(x)$ in $\mathrm{Cd}_{1-x}\mathrm{Mn}_x\mathrm{Te}$ broadens with increasing Mn concentration, so that at $x = 0.4$ it reaches $E_{gx}(0.4) = E_t$. For x slightly in excess of 0.4, the peak intensities of the IL, I_{3d}, and of the Wannier exciton luminescence, I_x, are similar for the excitation intensity $I_e = 1$ W cm^{-2}. A further increase in x results in a weakening of the exciton luminescence; indeed, for $x = 0.5$, I_x is smaller than I_{3d} by two orders of magnitude and for $x = 0.6$, by three orders of magnitude for the same value of I_e [41]. As x increases, $E_{gx}(x)$ falls into the region of an ever increasing density of excited states of the Mn^{2+} 3*d* shell. The relaxation rate from these levels to lower levels of the Mn^{2+} ion is high, which leads to a weakening of radiative relaxation via the conventional semiconductor mechanisms, thus enhancing the IL.

The excitation spectra of the $\mathrm{Zn}_{0.95}\mathrm{Mn}_{0.05}\mathrm{Se}$ reveal a nonmonotonic variation of I_x and I_{3d} with increasing excitation photon energy $h\nu_e$ [46]. As seen from Fig. 5, the values

$$h\nu_e = E_{gx} + k\hbar\omega_{\mathrm{LO}} \qquad (4)$$

(where ω_{LO} is the longitudinal optical phonon frequency and $k = 0, 1, 2, \ldots$) are most favorable for the interband exciton luminescence. In this case, hot excitons relax rapidly to the lowest exciton level upon emitting an integer number of LO phonons. If, however, condition (4) for $h\nu_e$ is not upheld, the final stage of relaxation to the exciton level occurs slowly and with the emission of a large number of acoustic phonons; in other words, the probability of excitation transfer to the manganese ion levels increases. The same effect is observed at a fixed $h\nu_e$ if the crystal is placed in an external magnetic field H. Due to the giant Zeeman splitting of exciton levels, a relation similar to Eq. (4) holds for the lowest exciton Zeeman component at certain values of H and fixed $h\nu_e$.

$Zn_{0.99}Mn_{0.01}Se$ was used to study the effect that resonant excitation of one of the Zeeman splitting components of the $n = 1$ exciton exerts on the Mn^{2+} IL polarization [47]. If $h\nu_e$ and H are chosen such that the energy of the photon is equal to that of the σ^- polarized upper exciton Zeeman component, the IL band intensity in the σ^- polarization weakens and that in the σ^+ polarization is enhanced. Such a resonant excitation of one of the polarized exciton components reduces the integrated I_{3d} IL intensity, while the IL polarization exceeds 50%. This experiment can be interpreted in terms of spin-dependent exciton capture by the Mn^{2+} 3d levels under the competition of exciton and intracenter radiative recombination channels, where the selection rules for optical transitions in the 3d shell are weakened by the exchange interaction.

Evidence of a redistribution of radiative recombination between the interband and intracenter channels, depending on the relative energies of the corresponding transitions, is provided by the effect of hydrostatic pressure on the $Cd_{1-x}Mn_xTe$ luminescence, which was considered in the preceding section.

The luminescence intensity redistribution in favor of the interband exciton emission has been observed in $Cd_{0.6}Mn_{0.4}Te$ placed in a magnetic field [48]. At the level of nonselective excitation used in the experiment ($h\nu_e > E_{gx}$), the band exciton emission and the IL measured in a zero magnetic field had an approximately equal intensity, but a field $H = 5$ T enhances the exciton emission by an order of magnitude compared to the IL. While this trend can be explained as being due to a shift of the σ^+ exciton component toward lower energies with increasing H, one does not succeed in fully describing the intensity redistribution between the two emission channels in this way. The efficiency of excitation transfer from band excitons to the 3d shell is apparently affected by the spin selection rules, which gain in significance under conditions where the intracenter and exciton levels are magnetic-field-split. A later study [49] discusses the effect of the resonance between the band excitons and intracenter transitions in $Cd_{1-x}Mn_xTe$ on the efficiency of the dipole–dipole energy transfer mechanism.

Besides creating a new recombination channel, ions of the iron group are capable of acting directly on the impurity states involved in various kinds of luminescence. Doping CdTe with Fe^{2+} suppresses the donor–acceptor emission, because iron associates with the components of the donor–acceptor pairs. Increasing the iron concentration from 10^{17} to 10^{19} cm^{-3} weakens the emission of excitons bound to neutral acceptors by one and a half orders of magnitude. This is most likely associated with the acceptor concentration decreasing as a result of the Fe^{2+}–Fe^{3+} charge transfer [50].

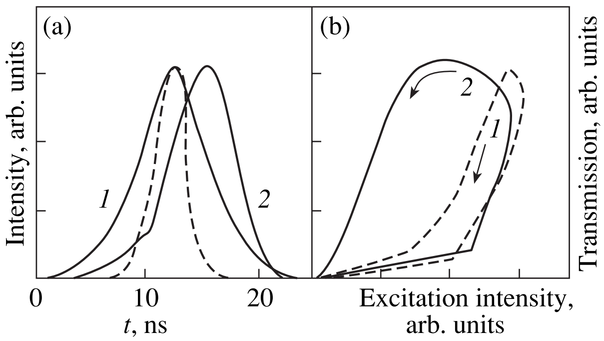

Fig. 6. Optical transmission of a 0.05-cm thick $Zn_{0.99}Mn_{0.01}Se$ crystal obtained under strong pumping by YAG : Nd^{3+} laser second-harmonic pulses into the region of the Mn^{2+} $^6A_1$–$^4T_1$ intracenter transition. $T = 280$ K [51]. (a) Shape of the laser pulse on transmission through the crystal at pulse peak intensities I_e (W cm^{-2}): (*1*) 0.5 and (*2*) 1; the dashed profile is the original laser pulse shape. (b) Optical bistability hysteresis loops describing the dependence of transmission on I_e at laser pulse peaks for cases (*1*) and (*2*) of item (a).

6. NONLINEAR ABSORPTION AND BISTABILITY

The long excited-state lifetime of the Mn^{2+} ions provides a possibility of observation of the nonlinear optical properties associated with intracenter transitions at comparatively low excitation levels. 7-ns-long YAG : Nd^{3+} laser second-harmonic pulses have been used in pump-probe experiments on $Zn_{1-x}Mn_xSe$ ($x = 0.01$) [51]. At excitation levels I_e of the order of 10^4 W cm^{-2}, intracenter absorption (the $^6A_1$–$^4T_1$ and $^6A_1$–$^4T_2$ transitions) is observed to weaken. For $I_e >$ 10^5 W cm^{-2} and at room temperature, the shape of the laser pulse becomes distorted in passing through the crystal and optical bistability simultaneously sets in (Fig. 6). The up- and down-switching times are 9 and 1.8 ns ($I_e = 10^5$ W cm^{-2}) and 6 and 0.8 ns ($I_e =$ 10^6 W cm^{-2}), respectively, the optical hysteresis loop in the latter case being three times wider. The onset of bistability is apparently accounted for by the positive feedback forming in the reflection of light inside the crystal from its polished surfaces under increasing sample transparency. The parameters of optical bistability in the region of 3d transitions in $Zn_{1-x}Mn_xSe$ should be determined by the concentration of the Mn^{2+} ions, the lifetime of their excited state with inclusion of excitation migration, the optical pumping level, and temperature. It should be pointed out that the absorption saturation and nonlinear properties in the region of intracenter transitions in iron-group ions present in II–VI crystal matrices remain inadequately understood; however, there is currently a renewed interest in this prob-

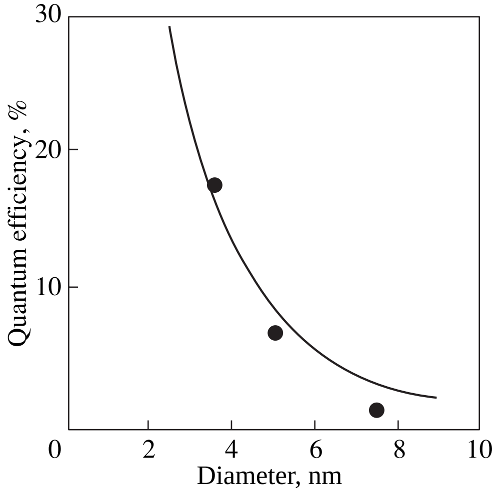

Fig. 7. IL quantum yield η of a manganese ion embedded in a ZnS nanocrystal with diameter *D*. Points are experimental data for $T = 4$ K, and the line is a plot of the fitting relation $\eta = (1 + \beta D^2)^{-1}$[55].

lem, particularly in what concerns the divalent ions of chromium.

7. INTRACENTER TRANSITIONS IN DMS-BASED NANOSTRUCTURES

Quasi-two-dimensional DMS-based quantum structures, particularly CdTe/$Cd_{1-x}Mn_xTe$, are traditionally used in optical studies. Recently, nanostructures including wide-band-gap DMSs, where intracenter transitions are observed to occur already at low concentrations of the magnetic component, have received increasing interest. Superlattices and nanocrystals doped by optically active centers have potential application. In addition, such centers can be used as probes to study the properties of nanostructures. Self-organized DMS nanocrystals 2 nm high and 20 nm in diameter have been grown on the ZnTe(100) surface [52], $Cd_{1-x}Mn_xS$ quantum wires 3.5 nm in diameter have been prepared by organometallic vapor deposition in pores of SiO_2 (MCM-4) [53], and $ZnS:Mn^{2+}$ has been embedded in a photonic crystal consisting of submicron-sized polymer spheres [54]. One can presently prepare high-quality II–VI nanocrystals containing one Mn^{2+} atom per nanocrystal. Such a nanocrystal is a model object for use in studying the single magnetic moment in a quantum dot. Studies of the optical properties, including IL, in various DMS-based nanostructures require investigation of the interaction of the 3*d* states of magnetic ions with the *s* and *p* states under the conditions of spatial confinement of the electron wave functions. Enhanced *sp*–*d* hybridization should increase the energy transfer rate from the electron–hole pairs to the 3*d* shell in interband optical excitation of DMS nanocrystals. The IL quantum yield of $ZnS:Mn^{2+}$ nanocrystals with a diameter *D* of about 3 nm (the Bohr radius of the Wannier exciton is 2.5 nm) increases with decreasing nanocrystal size and reaches as high as 18% (Fig. 7), and the luminescence decay rate is several orders of magnitude lower than that in bulk crystals (one nanocrystal contains, on the average, one Mn atom) [55].

The IL quantum yield is given by

$$\eta = \tau_R^{-1}(\tau_R^{-1} + \tau_{NR}^{-1})^{-1}, \tag{5}$$

where τ_R^{-1} and τ_{NR}^{-1} are the radiative and nonradiative recombination rates, respectively. The magnitude of τ_{NR}^{-1} is determined by the number of surface atoms in a nanocrystal per unit volume, which is proportional to D^{-1}, and τ_R^{-1} depends on the degree of zinc substitution by manganese. If a nanocrystal contains, irrespective of its size, a fixed number of Mn atoms, then $\tau_R^{-1} \sim D^{-3}$. In this case, $\eta \sim (1 + \beta D^2)^{-1}$, where the parameter β depends on the ratio τ_R/τ_{NR}. Estimates [55] show that the IL quantum efficiency in a nanocrystal with $D =$ 3 nm increases by an order of magnitude compared with a bulk crystal, which is in accord with experiment. Confinement shifts the 3*d* levels into the region of the 4*s* band states, and the recombination of 4*s* electrons with holes can take place both directly and via the 3*d* states. In this case, transitions involving 3*d* electrons become parity-allowed. Thus, two properties of nanocrystals appear to be essential: (i) fast excitation transfer from band states to the 3*d* shell of the magnetic ion as a result of the excitation being localized within one nanocrystal and (ii) an increase in τ_R^{-1} by several orders of magnitude through enhanced *sp*–*d* mixing. Otherwise, if τ_R^{-1} were to remain the same as in a bulk crystal (i.e., about 2 ms^{-1}), the fast excitation transfer to the Mn^{2+} ion and the slow radiative recombination would bring about IL saturation already at low interband optical excitation levels. Confinement produces the strongest effect on the *s*–*d* mixing of excited 3*d* states in $ZnS:Mn^{2+}$ nanocrystals, starting from $D = 2$–3 nm. These nanocrystals were employed to develop the concept of an atom under the conditions of quantum confinement [56] where the properties of an atom and its coupling with the matrix are modulated by the nanocrystal size. An analysis of $Y_2O_3:Tb^{3+}$ nanocrystals, where the luminescence efficiency is also several times higher than that in the bulk material, supports the validity of this approach.

The time interval between the interband excitation pulse and the IL intensity maximum in $ZnS:Mn^{2+}$ nanocrystals was experimentally shown to be less than 0.5 ns; in other words, excitation transfer to a magnetic ion is indeed a fast process. The crystal field acting on this ion also changes somewhat when ones crosses over from a bulk crystal to a nanocrystal, which becomes manifest in a small shift in the IL maximum; this factor cannot, however, affect the *sp*–*d* coupling noticeably.

The acceleration of excitation transfer to magnetic ions was confirmed in a number of later studies, where special measures were taken to ensure uniform manganese distribution over the nanocrystals. It was shown theoretically that the conduction band in a ZnS nanocrystal with saturated surface bonds and with a Mn^{2+} ion at its center is modified by interaction with the 3*d* states of manganese and that this interaction becomes enhanced with decreasing nanocrystal size, whereas the valence-band states remain virtually unchanged. CdS nanocrystals containing one Mn^{2+} each revealed a giant splitting of exciton spin sublevels in a zero external field [57]. This splitting permits one to estimate the giant internal field induced by the manganese ion. The magnitude of the field is evidence of an enhancement of the short-range spin–spin interaction in the case of confinement.

The authors of [58] questioned the concept of rearrangement of the *sp–d* interaction connected with confinement and assigned the fast decay of the luminescence observed to occur [55] at 2.1 eV to the superposition of the tail of the conventional ZnS impurity luminescence on the IL band. Studies of $CdS:Mn^{2+}$ nanocrystals grown in a polymer matrix revealed that the IL decays in them with $\tau_R = 1.5$ ms, which correlates with the Mn^{2+} IL kinetics in a bulk $CdS:Mn^{2+}$ crystal [59]. In all the manganese-containing nanocrystals studied, the temperature quenching of the IL is far weaker than that observed in bulk crystals. While in a bulk $CdS:Mn^{2+}$ crystal the IL intensity measured in the interval 4–100 K decreases by a factor of ten, the IL in a nanocrystal weakens only by one half in the region 4–300 K.

There are apparently sound grounds, both theoretical and experimental, to believe that the excitation localization and the enhancement of 3*d*-state hybridization with band states in DMS nanocrystals strongly affect the quantum yield and kinetics of the IL. The conflicting character of the data obtained in different studies originates most likely from technological factors. The technique used in the preparation and subsequent treatment of samples containing nanocrystals of II–VI compounds with a magnetic component strongly influence the luminescent properties. Different systems with $ZnS:Mn^{2+}$ nanocrystals having the same original manganese concentrations but grown using different techniques exhibit a strong scatter in the IL intensity. It was shown in [60] that a microemulsion containing $ZnS:Mn^{2+}$ nanocrystals subjected to hydrothermal treatment had a 60 times higher Mn^{2+} IL quantum yield than a similar material obtained in an usual aqueous reaction. The factors responsible for the enhanced IL quantum yield are the formation of nanocrystals with a perfect zinc-blende structure in the course of growth and efficient passivation of the nanocrystal surface, both during and after growth. An efficient method for uniformly distributing manganese was developed to prepare $ZnS:Mn^{2+}$ nanocrystals containing, on the average, four Mn atoms each [61], which was confirmed by ESR measurements. These systems revealed a shift in the IL maximum toward higher energies with decreasing average nanocrystal size and an increase in the IL quantum yield to 20% at room temperature and to 75% below 50 K.

Doping II–VI nanocrystals with magnetic ions suppresses the impurity–band and interimpurity emission, as well as the luminescence originating from surface states, which gain considerably in significance for small crystal sizes. $CdS:Mn^{2+}$ nanocrystals 4 nm in average size exhibit strong IL that peak at 2.12 eV but lack the surface state emission characteristic of undoped CdS nanocrystals [62]. This confirms the efficiency of excitation transfer from the band, impurity, and surface states to the 3*d* shell of magnetic ions under the conditions of spatial confinement, where defects are located close to the magnetic ion.

The strong influence of the lowered dimensionality of a system on the IL kinetics has been demonstrated in a study of a bulk zinc sulfide crystal with planes doped by manganese [63]. The IL measured from two-dimensional layers with a Mn concentration of about 10^{14} cm^{-2} has a weaker temperature dependence, and its decay at low excitation levels proceeds faster than that in the three-dimensional crystal because of the *sp–d* hybridization enhancement discussed above, as well as due to the lattice strain caused by the Mn doping. This system was found to be convenient in determining the critical distance between doped layers at which interlayer 3*d*-shell excitation transfer starts. This distance was estimated to be 9 nm [63]. This figure, equal to 30 cation separations, appears to be overevaluated, because it does not agree well with the minimum manganese concentration at which the migration of intracenter Mn^{2+} excitation sets in in uniformly doped bulk II–VI matrices.

As found in the preparation of a bulk $Zn_{1-x}Mn_xSe$ crystal ($0.15 < x < 0.25$) containing CdSe nanocrystals, manganese ions play an important part in CdSe nucleation [64]. Application of a magnetic field of up to 5 T to this system enhances exciton luminescence in the nanocrystals by an order of magnitude while suppressing the IL of the $Zn_{1-x}Mn_xSe$ matrix. The correlation between these effects, which has been established on a large number of samples, originates from a change in the efficiency of excitation transfer between the DMS and nonmagnetic nanocrystals in an external magnetic field; however, the details of this process remain unclear. Energy transfer from CdSe to $Zn_{1-x}Mn_xSe$ is a process whose selection rules depend on the values of the initial and final spin states. For this reason, the magnetic-field-induced splitting of band states and of the 3*d* levels can strongly affect the relative magnitude of the excitation transfer time and the characteristic radiative times. Remarkably, this effect is critical to nanocrystal size; more specifically, if the thickness of the CdSe interlayers of which the island nanocrystals form increases from 1.5 to 2.5 monolayers, the redistribution of the luminescence in a magnetic field disappears.

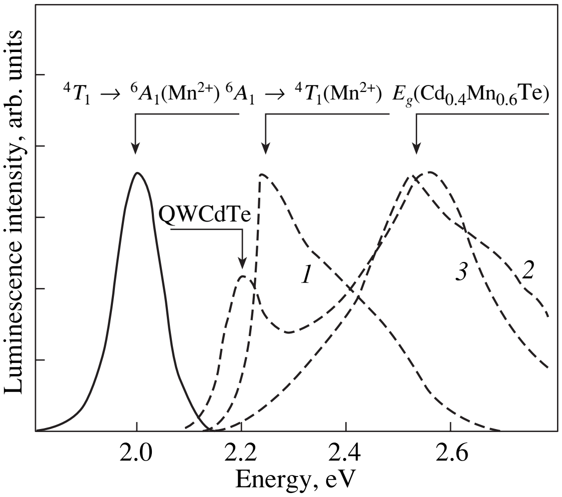

Fig. 8. Mn^{2+} IL profile (solid line) and IL excitation spectra (dashed lines) obtained on (*1*) a bulk $\mathrm{Cd}_{0.4}\mathrm{Mn}_{0.6}\mathrm{Te}$ crystal and (*2*) a quantum-well structure $\mathrm{CdTe/Cd}_{0.4}\mathrm{Mn}_{0.6}\mathrm{Te}$ [66]. Curve *3* is the exciton luminescence excitation spectrum from CdTe quantum wells. $^6A_1$–$^4T_1$ is the transition to the first excited state of the manganese ion; QWCdTe is the transition between the first levels of electrons and heavy holes in the CdTe quantum well; and $E_g(\mathrm{Cd}_{0.4}\mathrm{Mn}_{0.6}\mathrm{Te})$ is the edge of the interband transition in the barrier. $T = 4$ K.

Suppression of the energy transfer from band excitons to the Mn^{2+} 3*d* shell by a magnetic field was observed to occur in $\mathrm{Zn}_{1-x-y}\mathrm{Cd}_x\mathrm{Mn}_y\mathrm{Se/ZnSe}$ and $\mathrm{Zn}_{1-x}\mathrm{Mn}_x\mathrm{Se/ZnSe}$ epitaxial layers and in $\mathrm{Cd}_{1-x}\mathrm{Mn}_x\mathrm{Se}$ and $\mathrm{Cd}_{1-x}\mathrm{Mn}_x\mathrm{S}$ quantum wires [65]. A conclusion was drawn in [65] that the efficiency of excitation transfer in a magnetic field is determined primarily not by the degree to which the excitonic and intracenter transitions are resonant but rather by an enhancement of the role played by the spin-dependent selection rules. This is in accord with the above data on bulk $\mathrm{Cd}_{1-x}\mathrm{Mn}_x\mathrm{Te}$ crystals.

The Mn^{2+} IL at $T = 2$ K was studied in $\mathrm{CdTe/Cd}_{0.4}\mathrm{Mn}_{0.6}\mathrm{Te}$ quasi-two-dimensional quantum-well structures in [66]. Time-resolved experiments performed with a $\Delta t = 0$ delay reveal exciton emission from the CdTe quantum well with a maximum at 2.02 eV, and only the IL of barrier Mn^{2+} ions peaking at 2.0 eV is left in the spectrum for $\Delta t = 2.5$ μs. Because of the small thickness of the structure, all of the Mn-containing layers are excited, even under optical band-to-band-type pumping occurring with a high absorption coefficient. The energy is subsequently transferred from the barrier band states to the Mn^{2+} ions, thus providing a more efficient excitation of the 3*d* shells than obtained in direct intracenter excitation. For this reason, the maximum of the IL excitation spectrum lies at the fundamental edge of the barrier with E_g approximately equal to 2.6 eV rather than near the excitation threshold of the Mn^{2+} 3*d* shell at $E_t = 2.15$ eV, as is the case with bulk crystals (Fig. 8). The long-lived excitation of the barrier 3*d* shell is capable of considerably slowing down the decay of excitonic luminescence in the CdTe quantum wells because of the excitation being transferred from the barrier Mn^{2+} ions to the quantum wells. $\mathrm{CdTe/Cd}_{1-x}\mathrm{Mn}_x\mathrm{Te}$ quantum-well structures with $x = 0.5$ and 0.68 containing quantum wells from 1 to 10 nm in width were studied under a hydrostatic pressure of up to 3 GPa in [67]. The pressure-induced energy shifts obtained at 80 K constitute 640 cm^{-1}/GPa for the IL and 600 ($x = 0.5$) and 480 cm^{-1}/GPa ($x = 0.68$) for the exciton luminescence of the quantum wells. Because of the pressure-induced shifts assuming opposite signs at certain values of pressure determined by x and the quantum-well width, the exciton energy starts to transfer from quantum wells to the Mn^{2+} levels in the barriers, a process detected from the threshold enhancement of the IL.

A photonic crystal consisting of submicron-sized polymer spheres with voids filled by the $\mathrm{ZnS:Mn}^{2+}$ DMS has become a new object for optical studies [54]. In the case where the DMS IL band falls into the stop-band region of the photonic crystal, the decay kinetics over the band profile varies in an unusual manner. The $\mathrm{ZnS:Mn}^{2+}$ IL decay is the slowest at the IL band center if the latter coincides in energy with the minimum of the photonic-crystal transmission. The reason for this is the low density of photon states in the stop band, which is initiated by the strong difference in the dielectric properties between the polymer spheres making up the photonic crystal and the $\mathrm{ZnS:Mn}^{2+}$ filler. The parameters of the photonic-crystal stop band are an essential point. By properly selecting the diameter of the nanoparticles, one can control the width and energy position of the stop band and overlap, partially or completely, the IL profile, to entrap, in this way, the radiation in the photonic crystal. Moreover, by introducing defects of an appropriate type and concentration into a photonic crystal, one can also control the formation of transparency regions in the stop band. Such systems combine a high efficiency of electro- and photoluminescence with a possibility of controlling the spectral composition of the emission.

The influence of confinement on the properties of 3*d* luminescence is still not fully clear. This phenomenon, while being of interest in itself, is connected intimately with the properties of electroluminescence in nanostructures and has potential application. One can identify at least three reasons accounting for the specific features of the IL in nanostructures; these reasons are the change in the degree of *sp*–*d* hybridization, excitation transfer between the nanocrystal and the matrix (or between a quantum well and the barrier), and spatial confinement of migration.

A conclusion was drawn in [68, 69] that the 3*d* levels of transition ions correlate with the corresponding matrix levels. In particular, it was maintained that the difference between the intraion transition energies in isovalent semiconductors is equal to that between the valence-band top energies. This provides a possibility of using intracenter transitions as probes to determine the height of the heterojunction barriers for the electrons and holes separately. This point was studied on the heterostructures $Zn_{1-x}Cd_xSe$/ZnSe and $ZnS_{1-x}Se_x$/ZnSe with an Ni impurity [the $^3T_1(F)$–$^1T_2(F)$ transition] over a broad range of x, up to 0.5 [70]. While the measurements yielded good agreement with theory, the results obtained in the case of $ZnS_{1-x}Se_x$/ZnSe are at odds with the data derived from measurements of optical transitions between size quantization levels.

8. SELECTIVE EXCITATION OF Mn^{2+} INTRACENTER LUMINESCENCE

IL in $Cd_{1-x}Mn_xTe$ with $x > 0.4$ is excited by photons with $h\nu_e > 2.14$ eV. In crystals with $x = 0.5$ pumped selectively in the interval $2.14 < h\nu_e < 2.25$ eV, the IL maximum shifts, accordingly, from 1.98 to 2.005 eV [71, 72]. As $h\nu_e$ is increased further from 2.25 eV up, the IL maximum shifts again toward lower energies [72, 73]. This behavior of the IL remains unclear; one can, however, put forward several possible reasons for its occurrence. Nonmonotonic variation of the intracenter absorption coefficient within the scanned region (several absorption bands) affects the optical excitation density. Another possible reason consists in the onset of resonance conditions for excitation of the states in an inhomogeneously broadened IL profile whose energy differs from $h\nu_e$ by the LO phonon energy. A similar effect is observed for the inhomogeneously broadened bound-exciton emission band in $Cd_{0.5}Mn_{0.5}Te$ [74].

A configurational model was proposed in [72] to account for the IL spectrum obtained under selective excitation within an inhomogeneously broadened profile. In this model, the dependence of the position of the IL maximum, E_L, on $h\nu_e$ can be written as

$$dE_L/d(h\nu_e) = H_{\mathrm{in}}^2/(H_h^2 + H_{\mathrm{in}}^2), \qquad (6)$$

where H_h and H_{in} are the homogeneous and inhomogeneous broadenings. H_h, H_{in}, and the full width at half maximum of the IL profile, H, can be cast in the form

$$H^2 = H_h^2[1 + H_{\mathrm{in}}^2/(H_h^2 + H_{\mathrm{in}}^2)], \qquad (7)$$

$$H_h = H[(1+R)/(1+2R)]^{1/2}, \qquad (8)$$

$$H_{\mathrm{in}} = H_h R^{1/2}, \qquad (9)$$

where $R = H_{\mathrm{in}}^2/H_h^2$. Thus, by sweeping $h\nu_e$ and measuring the shift of the IL maximum, one can calculate the value of R. A comparison of the model with experiment suggests that for $T > 55$ K, the inhomogeneous broadening disappears [72]. It is difficult to conquer with this conclusion. If an excitation can relax during its lifetime with a lowering of energy, the inhomogeneous broadening will not be completely overcome. Moreover, under the conditions of excitation migration, inhomogeneous broadening should depend on the optical pumping level, because the lowest levels of an inhomogeneous distribution saturate with increasing excitation.

Studies of the Mn^{2+} IL in $Cd_{1-x}Mn_xTe$ show that in the interval 4–20 K, the inhomogeneous and homogeneous broadenings for $h\nu_e > 2.2$ eV are approximately equal. Within the concentration interval $0.46 < x < 0.70$, the inhomogeneous broadening varies from 70 to 85 meV, with the IL profile shape being Gaussian. There is nothing strange in there being an absence of strong concentration dependence of the inhomogeneous broadening at such high manganese concentrations. The inhomogeneous broadening should even decrease with increasing x, because the maximum disorder in a solid solution sets in usually at $x = 0.5$. The increase in H_{in} with increasing x in this interval is connected most likely with an increasing concentration of structural defects, because $x = 0.7$ is almost the highest possible concentration for bulk $Cd_{1-x}Mn_xTe$ crystals. The assumption [72] of the temperature-induced variation of H_{in} being somehow connected with magnetic phase transitions in $Cd_{1-x}Mn_xTe$ is not supported by the results of studies on the effect of temperature on the IL profile. No changes in the profile shape of the IL or in its integrated intensity have been found at the paramagnet–spin-glass and paramagnet–antiferromagnet phase transitions for x in the interval 0.4–0.7.

At liquid-helium temperatures, anti-Stokes IL is excited in crystals with $x > 0.4$ by photons with $h\nu_e < E_t$ in a two-stage process, which is suppressed as the sample is warmed up to 80 K, apparently, because of the decreasing electron lifetime in the intermediate state [71, 73]. There are grounds to believe that it is this parameter that is associated with temperature-driven magnetic phase transitions [48].

9. KINETIC PROPERTIES OF INTRACENTER LUMINESCENCE

The kinetic properties of the IL depend on many factors, most of all on the concentration of the magnetic component. Study of the concentration dependences is associated with certain difficulties. In II–VI wide-band-gap matrices, it is often difficult to dope iron-group elements in high enough concentrations, while in the comparatively narrow band-gap materials of the type of CdTe, IL is observed only for high cadmium substitutions by manganese. Combining of the data obtained on different matrices is hampered by the fact that the specific properties of a matrix affect the IL kinetics. This point can be exemplified by the observation that as the sulfur concentration in the ZnS_xSe_{1-x} matrix is increased from 0.001 to 0.3, the decay time of the Co^{2+} IL L band (2.36 eV) decreases by more than five times [75]. Partial substitution of cadmium for zinc in ZnSe brings about a similar result. These changes may be associated with the system becoming disordered in the formation of a solid solution, with changes in the 3d-state interaction with ligands and in the spin–orbit interaction. The characteristic IL decay time τ_R can be written as

$$1/\tau_R = [(\alpha\rho_p/\rho_{3d} + C) + A], \quad (10)$$

where α is determined by the sp–d hybridization, ρ_p is the valence electron LS coupling, ρ_{3d} is the LS coupling for the 3d electrons in a magnetic ion, and C and A are constants. The valence band in II–VI crystals is formed by the p electrons of the anions, and the magnitude of ρ_p varies strongly in the S–Se–Te sequence. As for ρ_{3d}, this quantity depends very little on the actual II–VI matrix for a given magnetic ion. One should also bear in mind the decrease in the spin–lattice relaxation time with increasing concentration of the magnetic component [76].

The Mn^{2+} IL kinetics in $Cd_{1-x}Mn_xTe$ can be studied only in crystals with a high manganese concentration, wherefore the relaxation dynamics of the intracenter excitation is determined largely by its migration [73, 77]. Nonradiative excitation transfer occurs due to the Coulomb interaction of electrons of the excited and nonexcited atoms [78, 79]; this interaction has a dipole–dipole, dipole–quadrupole, and quadrupole–quadrupole component. In ions in which the dipole transitions are at least partially forbidden, the nondipole components may play an important role by providing a strong dependence of the excitation transfer probability on the separation between magnetic ions. Following [73], while the IL decay curves in $Cd_{0.5}Mn_{0.5}Te$ measured at half maximum of the profile on both sides of the peak differ strongly from each other in the interval 2–60 K, they coincide at already 77 K. It is believed that the kinetics becomes the same over the IL band profile in the case where thermal energy k_BT approaches the magnitude of the average jump in energy occurring as the excitation transfers from one manganese ion to another. It was concluded that (i) the average energy change in a jump is 40 cm^{-1} and (ii) at low temperatures (migration with a decrease in energy), the excitation can transfer, on the average, over three manganese ions in the characteristic IL decay time (about 25 μs).

More comprehensive studies of the IL kinetics performed on $Cd_{0.4}Mn_{0.6}Te$ have shown that the IL profile shape measured under selective excitation near the Mn^{2+} intracenter absorption threshold ($h\nu_e = 2.175$ eV) depends strongly on temperature [80]. This dependence is determined by the efficiency of upwise excitation redistribution over the inhomogeneously broadened excitation levels of an ensemble of manganese ions in energy during the excitation lifetime. At $T = 2$ K, this process does not operate and the IL decay is exponential. At $T = 60$ K, a broad spectrum of inhomogeneously broadened states is populated and the IL decay is essentially nonexponential. Energy relaxation within a system of excited states is generally completed during the excitation lifetime. According to current models, in the case of excitation near the intracenter absorption threshold, the relaxation of excited states occurs in two stages. More specifically, it occurs due to fast relaxation by 0.2 eV in 1 ps (via the electron–phonon coupling) to the minimum of the configurational curve for the $^4T_1$ level of the Mn^{2+} photoexcited ion, followed by a slow relaxation within a few hundredths of an electronvolt over the inhomogeneously broadened $^4T_1$ levels of the manganese ion ensemble in a few tens of microseconds. When excited substantially above the intracenter absorption threshold, an intermediate process with a characteristic time of less than 0.1 μs becomes operative, which corresponds to the onset of a "preliminary" equilibrium in the system of Mn^{2+} excited ions possibly involving band states in $Cd_{1-x}Mn_xTe$ [if $h\nu_e > E_g(x)$], after which subsequent variation of the population over the inhomogeneous profile occurs only through excitation migration over the ions.

10. SATURATION OF INTRACENTER LUMINESCENCE AND ITS KINETICS UNDER STRONG OPTICAL EXCITATION

Studies of the IL kinetics are carried out in a pulsed mode assuming a sufficiently high level of optical excitation. The behavior of a system of ions with an unfilled 3d shell under strong pumping is of interest in more than one aspect. Excitation of an Mn^{2+} ion initiates an intracenter intercombination transition, with the spin of the 3d shell decreasing from 5/2 to 3/2. This affects the exchange ion–ion coupling, which is of particular significance for nearest neighbor Mn^{2+} ions. Thus, on the one hand, excitation reduces the total spin of the system of magnetic ions, while on the other, a weakening of exchange coupling between nearest neighbors destroys the magnetic order. These changes affect the paramagnetic properties of a crystal (and thus, the strength of the internal field created in an external magnetic field) in opposite ways. The decrease in the spin of 3d shells influences the carrier–ion exchange interaction and, hence, the magnetic polaron effect, the giant Zeeman splitting, and the Faraday effect. Thus, we deal here with a complex photoinduced variation of the magnetic properties of a crystal depending on the concentration of magnetic ions and of their fraction residing in the excited state. A comparison of the properties of IL under strong optical pumping with those of electroluminescence at high carrier injection levels is also of interest with respect to device applications.

Under weak optical pumping of $Cd_{1-x}Mn_xTe$ crystals with $x > 0.4$, the IL intensity I_{3d} is higher than the Wannier exciton luminescence intensity even at low temperatures and for the value most favorable for exciton emission, $x = 0.4$. However, already at excitation levels I_e on the order of a few W cm^{-2}, the IL undergoes noticeable saturation [74], so that as I_e increases, the exciton emission becomes dominant. The dependence of I_{3d} on I_e at low manganese concentrations can be studied in wide-band-gap systems (ZnS : Mn^{2+} and others). In such a system, saturation can be driven by a transition of a sizable fraction of Mn^{2+} ions to the excited state, which is favored by the long lifetime in the $^4T_1$ level. The IL saturation becomes manifest particularly strongly, however, at high manganese concentrations [74, 81], whereat excitation migration becomes a major factor. The history of the investigation of migration dates back to the cited publications [78, 79], with more comprehensive studies on the migration of excitation over the 3*d* and 4*f* shells of magnetic ions and of the role played by this migration in spectral diffusion reported in later communications (see, e.g., [82–84]).

The integrated saturation of the IL 2-eV band in $Cd_{1-x}Mn_xTe$ under excitation into the intracenter absorption region $[h\nu_e < E_g(x)]$ is presented graphically in Fig. 9 [85, 86]. The fraction of excited Mn^{2+} ions can be estimated if one knows the value of x, the intracenter absorption coefficient, the lifetime in the $^4T_1$ excited state, and the pumping parameters. Estimates show that saturation is observed to occur already at comparatively low excited-ion concentrations. Thus, the saturation occurring at high Mn^{2+} concentrations is indeed connected with the excitation migration. This conclusion is corroborated by the temperature dependence of saturation, which is far more efficient at $T > 60$ K than at 4 K at concentrations $0.45 < x < 0.75$. It should be pointed out that for $x = 0.4$, the saturation becomes enhanced with decreasing temperature, provided the excitation proceeds into the interband transition region (Fig. 10a). The reason for this lies in that for $x = 0.4$, the Wannier exciton level coincides at 80 K with the intracenter absorption threshold (where the density of electronic states of Mn^{2+} is low), whereas at 4 K, this level shifts into the region of higher densities of states, toward the maximum of the $^1A_6$–$^4T_1$ intracenter transition; this facilitates excitation transfer from band states to the manganese ions.

The quenching of IL accompanying excitation migration can be caused by relaxation on defects and by the cooperative effect (CE) [87]. While the CE (up-conversion) is usually associated with a manifestation of anti-Stokes luminescence, in our case it should be treated instead as the transfer of an additional excitation to the already excited Mn^{2+} ion, a process in which anti-Stokes luminescence cannot be observed at all. In contrast to the defect mechanism, the CE is, first, a nonlinear effect and, second, practically cannot be saturated. The Frenkel exciton concentration at a level of energy $h\nu$ at time t for a concentration x can be written in the form

$$n(t, \nu) = n(0, \nu)\exp(-t/\tau_R) f(\nu, x, t), \qquad (11)$$

where function f determines the rate of excitation transfer to other ions. Until recently, only transfer to

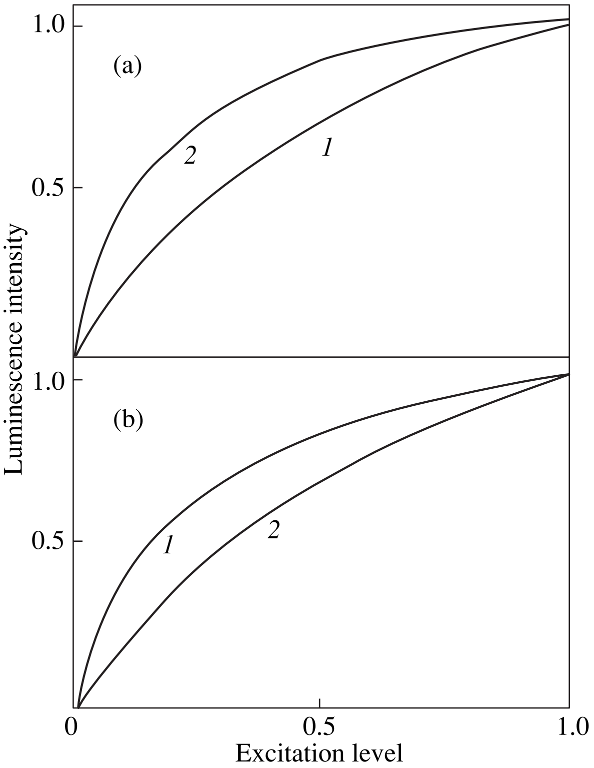

Fig. 9. Mn^{2+} IL saturation curves obtained on $Cd_{1-x}Mn_xTe$ for (a) $x = 0.7$ and (b) 0.4 at (*1*) $T = 4$ and (*2*) 77 K [85, 86]. The IL intensity is normalized against $I_e = 1$ (the value corresponding to the excitation level 4 MW cm^{-2}).

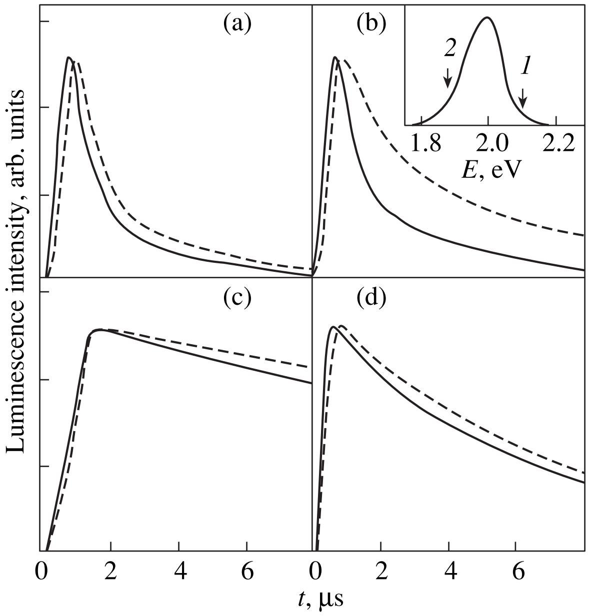

Fig. 10. Mn^{2+} IL kinetics obtained on a $Cd_{0.5}Mn_{0.5}Te$ crystal at different excitation levels I_e and temperatures [89]. (a, b) and (c, d) refer to points *1* and *2* on the IL profile (see inset), respectively; solid and dashed lines relate to the excitation levels $I_e = 4$ and 0.06 MW cm^{-2}, respectively; (a, c) $T = 4$ and (b, d) 77 K.

neighboring nonexcited ions was taken into account; in other words, the CE and the effect of the optical pumping level were left out of consideration. The CE is also disregarded in Monte Carlo simulations of the IL kinetics in $Cd_{1-x}Mn_xTe$, even under the conditions of strong pumping [88]. This effect should dominate, however, in DMSs with a not too high defect concentration. There is a substantial difference between excitation transfer to a nonexcited and to an excited ion. Relaxation involving vibrational states is a fast process, so that energy transfer to a neighboring ion occurs from the equilibrium state of the $^4T_1$ electronic level. Therefore, excitation transfer to a nonexcited ion requires that the phonon system of the crystal donate an energy corresponding to the Stokes losses of the $^6A_1$–$^4T_1$ transition. When excitation is transferred to an already excited ion, practically no energy goes into the Stokes losses, because the transition from $^4T_1$ to higher states in an acceptor ion entails a small Stokes shift. Adequate description of the IL kinetics requires analysis of at least two important points, namely, (i) estimation of the difference between the excitation transfer probabilities to a nonexcited and an excited ion and (ii) determination of the possible contribution of the CE to IL under specific experimental conditions. Because the CE and relaxation at defects are significant only under efficient migration, a strong enhancement of intracenter excitation transfer for $T > 60$ K entails as strong a decrease in the IL quantum yield; this exactly is observed in experiment.

Let us turn to the dependence of the IL kinetics in $Cd_xMn_{1-x}Te$ on the optical-pumping level. Because of the excitation being redistributed over the inhomogeneously broadened excitation levels of the ensemble of Mn^{2+} ions, the IL intensity reaches a maximum on the high-energy wing of the 2-eV band faster than it does on the low-energy one. As follows from the IL kinetics (Fig. 10), the spectral response of decay at high pumping levels I_e manifests itself strongly even at a high temperature. The variation of the IL kinetics with increasing I_e is most pronounced at a high temperature and on the high-energy wing, where the decay accelerates considerably [89]. This implies the development of a fast process associated with the CE. As follows from an analysis of the kinetics, one can isolate localized and delocalized states in a system of Mn^{2+} ions. The localized states should most probably be identified with the Mn^{2+} ions at the boundaries of manganese clusters, where the $^4T_1$ level is lower. Strong pumping saturates localized states, and, as a result, excitation migration over states lying above the mobility threshold occurs even at low temperatures. Whether the inner or interface regions in a manganese cluster correspond to localized states depends on the elemental composition of the matrix. In the case where the predominance of Mn in the nearest cation environment of Mn reduces the crystal field, the $^4T_1$ level rises at the center of the cluster and localization occurs at the boundaries (the case of $Cd_{1-x}Mn_xTe$). In the opposite case (for instance, in $Mg_{1-x}Mn_xTe$), the $^4T_1$ level is lower at the cluster center and the excitation will therein be localized at low temperatures.

The system of excited 3*d* states in a DMS with a high magnetic-ion concentration is similar in some respects to localized Wannier excitons in semiconductor solid solutions. The similarity relates to the behavior of migration with temperature, the existence of a mobility edge, the kinetics of emission migration over the inhomogeneously broadened band profile, etc. Naturally, the energy and temporal characteristics of these systems differ strongly from one another.

An interesting type of DMS is three-cation solid solutions in which two cations are nonmagnetic and one is magnetic. It has been established that the IL saturation in $Cd_{1-x}Mn_xMg_yTe$ with increasing I_e is much less pronounced than that in $Cd_{1-x}Mn_xTe$ [45]. This is accounted for by the excitation migration being suppressed by doping $Cd_{1-x}Mn_xTe$ with magnesium. Magnesium enhances the fluctuations of the local fields acting on the manganese ions, thus impeding intracenter excitation transfer. The pronounced effect exerted on the crystal field by the presence of magnesium among the ligands is corroborated by the noticeable dependence of the energy position of the $Cd_{1-x-y}Mn_xMg_yTe$ IL band on magnesium concentration (Fig. 3).

Considerable interest has been aroused recently in connection with studying the lasing effect involving 3*d* magnetic ion transitions in semiconductor matrices, which might have application potential, in particular, in medicine. Cr^{2+} ions doped into the ZnS, ZnSe, and $Cd_{1-x}Mn_xTe$ matrices (the $^5T_2$–^2E transition) in concentrations of 10^{18}–10^{19} cm^{-3} were studied as active lasing centers [90–93]. The maxima of the Cr^{2+} absorption and IL bands lie near 0.70 and 0.53 eV, respectively, and the IL band halfwidth is 0.2 eV. Under sufficiently strong selective pumping by a pulsed laser, the Cr^{2+} IL transforms to a narrow band whose energy can be swept from 0.50 to 0.45 eV depending on the actual resonator mirror characteristics. In the best $ZnSe:Cr^{2+}$ samples prepared by thermal diffusion, lasing is achieved already at 12 μJ with passive losses of 7% if the excitation is produced in the 0.7-eV region with an $YAG:Nd^{3+}$-pumped $Ba(NO_3)_2$ Raman laser [94].

11. CONCLUSION

The optical investigation of intracenter transitions in iron-group ions embedded in crystal matrices, which has been pursued over the past two decades, allows one to conclude that the properties of these transitions exhibit a rich diversity, depending on the actual type of magnetic ion and crystal matrix used, the magnetic ion concentration, the system dimensionality, excitation conditions, and temperature. Despite the numerous studies performed, the mechanism by which electronic excitation is transferred among the ions and between the crystal matrix and the 3*d* shell of a magnetic ion remains poorly understood. This makes investigation of crystal matrices containing more than one type of ion of the iron group and lanthanides an interesting field. Nevertheless, optics of the iron-group ions in bulk II–VI semiconductor matrices is fairly well known and we are presently witnessing a shift in interest to nanostructures doped by iron-group ions. The effect of confinement on the degree of *sp*–*d* hybridization and the rate of excitation transfer between the band and 3*d* states, on the magnitude of electron–phonon and electron–ion coupling, and on other characteristics of such systems will become a major area of research in the years to come. Confinement provides a possibility of purposefully controlling the characteristics of the IL, in particular, of strongly raising its quantum yield at high temperatures. Technological progress in growing nanostructures assumes precise doping of magnetic ions within one nanocrystal and their controlled arrangement over the volume or on the surface, as well as development of new composite materials with the use of DMS nanocrystals. Naturally, the performance of electroluminescent devices will also be improved by basing them on nanocrystals and quantum planes containing optically active ions, primarily Mn^{2+}. Investigation of the IL saturation in the same activated media under strong optical and injection pumping likewise deserves attention. The use of semiconductor matrices with magnetic ions as nonlinear optical media, optical shutters, and laser gain media is another promising direction in applicable fields.

ACKNOWLEDGMENTS

This study was partially supported by the Ministry of Education of the RF, grant no. E00-3.4-526.

REFERENCES

1. H. E. Gumlich, J. Lumin. **23**, 73 (1981).
2. K. A. Kikoin, V. I. Sokolov, V. N. Flerov, and V. V. Chernyaev, Zh. Éksp. Teor. Fiz. **83**, 2335 (1982) [Sov. Phys. JETP **56**, 1354 (1982)].
3. V. I. Sokolov and O. V. Dolzhenkov, Fiz. Tekh. Poluprovodn. (St. Petersburg) **32**, 455 (1998) [Semiconductors **32**, 406 (1998)].
4. M. Beale, Philos. Mag. **68**, 573 (1993).
5. X. Yang and X. Xu, Appl. Phys. Lett. **77**, 797 (2000).
6. O. Goede and W. Heimbrodt, Phys. Status Solidi B **146**, 11 (1988).
7. J. K. Furdyna, J. Appl. Phys. **64**, R29 (1988).
8. P. A. Wolff, in *Semiconductors and Semimetals*, Ed. by J. K. Furdyna and J. Kossut (Academic, London, 1988), Vol. 25.
9. H. J. Swagten, A. Twardowski, P. J. Eggenkamp, and W. J. M. de Jonge, Phys. Rev. B **46**, 188 (1992).
10. R. J. Nicholas, M. J. Lawless, H. H. Cheng, *et al.*, Semicond. Sci. Technol. **10**, 791 (1995).
11. W. Busse, H.-E. Gumlich, and D. Theiss, J. Lumin. **12/13**, 693 (1976).
12. J. N. Murrel, S. F. A. Kettle, and J. M. Tedder, *Valence Theory* (Wiley, London, 1965; Mir, Moscow, 1968).
13. P. Oelhagen, M. P. Vecchi, J. L. Treeong, and V. L. Moruzzi, Solid State Commun. **44**, 1547 (1982).
14. W. Zahorowski and E. Gilberg, Solid State Commun. **52**, 921 (1984).
15. M. Taniguchi, L. Ley, R. L. Johnson, *et al.*, Phys. Rev. B **33**, 1206 (1986).
16. A. Balzarotti, M. De Crescenzi, R. Messi, *et al.*, Phys. Rev. B **36**, 7428 (1987).
17. M. Taniguchi, A. Fujimori, M. Fujisawa, *et al.*, Solid State Commun. **62**, 431 (1987).
18. J. Mašek and B. Velicky, Phys. Status Solidi B **140**, 135 (1987).
19. A. Bonanni, K. Hingerl, H. Sitter, and D. Stifner, Phys. Status Solidi B **215**, 47 (1999).
20. D. Boulanger, R. Parrot, U. W. Pohl, *et al.*, Phys. Status Solidi B **213**, 79 (1999).
21. J. Dreyhsig, K. Klein, H.-E. Gumlich, and J. W. Allen, Solid State Commun. **85**, 19 (1993).
22. C. Chen, X. Wang, Z. Qin, *et al.*, Solid State Commun. **87**, 717 (1993).
23. C.-L. Mak, R. Sooryakumar, M. M. Steiner, and B. T. Jonker, Phys. Rev. B **48**, 11743 (1993).
24. M. M. Moriwaki, W. M. Becker, W. Gebhardt, and R. R. Galazka, Solid State Commun. **39**, 367 (1981).
25. J. F. MacKay, W. M. Becker, J. Spalek, and U. Debska, Phys. Rev. B **42**, 1743 (1990).
26. J. Watanabe, H. Arai, T. Nouchi, and J. Nakahara, J. Phys. Soc. Jpn. **61**, 2227 (1992).
27. H. Schenk, M. Wolf, G. Mackh, *et al.*, J. Appl. Phys. **79**, 8704 (1996).
28. A. Lira, A. Mendes, L. Dagdug, *et al.*, Phys. Status Solidi B **212**, 199 (1999).
29. M. M. Moriwaki, W. M. Becker, W. Gebhardt, and R. R. Galazka, Phys. Rev. B **26**, 3165 (1982).
30. S. Biernacki, M. Kutrowski, G. Karczewski, *et al.*, Semicond. Sci. Technol. **11**, 48 (1996).
31. H. Anno, T. Koyanagi, and K. Matsubara, J. Cryst. Growth **117**, 816 (1992).
32. S. M. Durbin, J. Han. O. Sungki, and M. Kobayashi, Appl. Phys. Lett. **55**, 2087 (1989).
33. T. M. Giebultowicz, P. Klosowski, N. Samarth, *et al.*, Phys. Rev. B **48**, 12817 (1993).
34. E. Muller and W. Gerhardt, Phys. Status Solidi B **137**, 259 (1986).
35. V. F. Agekyan, N. N. Vasil'ev, A. Yu. Serov, and N. G. Filosofov, Fiz. Tverd. Tela (St. Petersburg) **42**, 816 (2000) [Phys. Solid State **42**, 836 (2000)].
36. K. Ichino, H. Misasa, M. Kitagawa, *et al.*, Jpn. J. Appl. Phys. **40**, 1289 (2000).
37. T. P. Surkova, P. Kaszor, A. J. Zakrzewski, *et al.*, J. Cryst. Growth **214/215**, 576 (1999).
38. W. Paszkowicz, K. Godwod, J. Domagala, *et al.*, Solid State Commun. **107**, 735 (1998).
39. R. Fiederling, M. Keim, G. Reuscher, *et al.*, Nature **402**, 787 (1999).

40. W. Giriat, Phys. Status Solidi B **136**, K129 (1986).
41. V. F. Agekyan and F. Zung, Fiz. Tverd. Tela (Leningrad) **30**, 3150 (1988) [Sov. Phys. Solid State **30**, 1812 (1988)].
42. A. Anastassiadou, E. Liarokapis, S. Stoyanov, *et al.*, Solid State Commun. **67**, 633 (1988).
43. Y. Tanabe and S. Sugano, J. Phys. Soc. Jpn. **9**, 753 (1954).
44. S. Ves, K. Strossner, W. Gebhardt, and M. Cardona, Phys. Rev. B **33**, 4077 (1986).
45. M. Kobayashi, Y. Nakamura, S. Endo, and W. Giriat, Phys. Status Solidi B **211**, 359 (1999).
46. D. Some and A. V. Nurmikko, Phys. Rev. B **48**, 4418 (1993).
47. V. G. Abramishvili, A. V. Komarov, S. M. Ryabchenko, and Yu. G. Semenov, Solid State Commun. **78**, 1069 (1991).
48. V. F. Agekyan and F. Zung, Fiz. Tverd. Tela (Leningrad) **30**, 3444 (1988) [Sov. Phys. Solid State **30**, 1976 (1988)].
49. D. Leinen, Phys. Rev. B **55**, 6975 (1997).
50. T. P. Surkova, S. A. Permogorov, L. N. Tenichev, and V. P. Galakhov, J. Cryst. Growth **184/185**, 1128 (1998).
51. K. Dou, S. H. Huang, J. Q. Yu, *et al.*, Solid State Commun. **76**, 1165 (1990).
52. Y. Terai, Sh. Kuroda, and R. Takita, Appl. Phys. Lett. **76**, 2400 (2000).
53. L. Chen, P. L. Klar, W. Heimbrodt, *et al.*, Appl. Phys. Lett. **76**, 3531 (2000).
54. J. Zhou, Y. Zhou, S. Buddhudu, *et al.*, Appl. Phys. Lett. **76**, 3513 (2000).
55. R. N. Bhargava, D. Gallagher, X. Hong, and A. Nurmikko, Phys. Rev. Lett. **72**, 416 (1994).
56. R. N. Bhargava, J. Cryst. Growth **214/215**, 926 (2000).
57. D. M. Hoffman, B. K. Meyer, A. I. Ekimov, *et al.*, Solid State Commun. **114**, 547 (2000).
58. A. A. Bol and A. Meijerink, J. Lumin. **87/89**, 315 (2000).
59. M. Tanaka, J. Qi, and Y. Matsumoto, J. Cryst. Growth **214/215**, 410 (2000).
60. L. M. Gan, B. Liu, C. H. Chew, *et al.*, Langmuir **13**, 6427 (1997).
61. I. Yu, T. Isobe, and M. Senna, J. Phys. Chem. Solids **57**, 373 (1996).
62. S.-M. Liu, F.-Q. Liu, H.-Q. Guo, *et al.*, Solid State Commun. **115**, 615 (2000).
63. W. Park, T. C. Jones, S. Schon, *et al.*, J. Cryst. Growth **184/185**, 1123 (1998).
64. C. S. Kim, M. Kim, S. Lee, *et al.*, J. Cryst. Growth **214/215**, 395 (2000).
65. H. Falk, P. J. Klar, J. Hubner, *et al.*, in *Abstracts of Tenth International Conference on II–VI Compounds, Bremen, 2001*, Tu-09.
66. J. Nakamura, K. Takamura, and S. Yamamoto, Phys. Status Solidi B **211**, 223 (1999).
67. P. Perlin, S. Shilo, T. Sosin, *et al.*, J. Phys. Chem. Solids **56**, 415 (1995).
68. J. M. Langer and H. Heinrich, Phys. Rev. Lett. **55**, 1414 (1985).
69. J. M. Langer, C. Delerue, M. Lannoo, and H. Heinrich, Phys. Rev. B **38**, 7723 (1988).
70. T. Surkova, W. Giriat, M. Goldlewski, *et al.*, Acta Phys. Pol. **88**, 925 (1995).
71. V. F. Agekyan and F. Zung, Fiz. Tverd. Tela (Leningrad) **27**, 1216 (1985) [Sov. Phys. Solid State **27**, 732 (1985)].
72. J. Gregus, J. Watanabe, and J. Nakahara, J. Phys. Soc. Jpn. **66**, 1810 (1997).
73. E. Muller, W. Gebhardt, and V. Gerhardt, Phys. Status Solidi B **113**, 209 (1982).
74. V. F. Agekyan and F. Zung, Fiz. Tekh. Poluprovodn. (Leningrad) **18**, 1859 (1984) [Sov. Phys. Semicond. **18**, 1160 (1984)].
75. H. Born, P. Thurian, T. Surkova, *et al.*, J. Cryst. Growth **184/185**, 1132 (1998).
76. D. Scalbert, J. Chernogora, and C. Benoit a la Guillaume, Solid State Commun. **66**, 571 (1988).
77. V. F. Agekyan, Yu. V. Rud', and R. Schwabe, Fiz. Tverd. Tela (Leningrad) **29**, 1685 (1987) [Sov. Phys. Solid State **29**, 970 (1987)].
78. D. L. Dexter, Chem. Phys. **21**, 836 (1953).
79. T. H. Förster, Ann. Phys. **2**, 55 (1948).
80. L. D. Park, S. Yamamoto, J. Watanabe, *et al.*, J. Phys. Soc. Jpn. **66**, 3289 (1997).
81. M. Katiyar and A. N. Kitai, J. Lumin. **46**, 227 (1990).
82. D. L. Huber, D. S. Hamilton, and B. Barnett, Phys. Rev. B **16**, 4642 (1977).
83. D. L. Huber, Phys. Rev. B **20**, 2307 (1979).
84. V. M. Agranovich and M. D. Galanin, *Electronic Excitation Energy Transfer in Condensed Matter* (Nauka, Moscow, 1978; North-Holland, Amsterdam, 1982).
85. V. F. Agekyan, N. N. Vasil'ev, and A. Yu. Serov, Fiz. Tverd. Tela (St. Petersburg) **41**, 49 (1999) [Phys. Solid State **41**, 41 (1999)].
86. V. F. Aguekian, N. N. Vasil'ev, A. Yu. Serov, and N. G. Filosofov, J. Cryst. Growth **214/215**, 391 (2000).
87. V. V. Ovsyankin and P. P. Feofilov, Opt. Spektrosk. **37**, 262 (1973).
88. S. Yamamoto, K. Takamura, and J. Nakahara, Phys. Status Solidi B **211**, 111 (1999).
89. V. F. Agekyan, N. N. Vasil'ev, A. Yu. Serov, and N. G. Filosofov, Fiz. Tverd. Tela (St. Petersburg) **43**, 1562 (2001) [Phys. Solid State **43**, 1626 (2001)].
90. J. T. Seo, U. Hommerich, S. V. Trivedi, *et al.*, Opt. Commun. **153**, 267 (1998).
91. L. D. DeLoach, R. H. Page, G. D. Wilke, *et al.*, IEEE J. Quantum Electron. **32**, 885 (1996).
92. R. H. Page, K. I. Schlaffers, L. D. DeLoach, *et al.*, IEEE J. Quantum Electron. **33**, 609 (1997).
93. U. Hommerich, X. Wu, V. R. Davis, *et al.*, Opt. Lett. **22**, 1180 (1997).
94. A. V. Podlipensky, V. G. Shcherbitsky, N. V. Kiselev, *et al.*, Opt. Commun. **167**, 129 (1999).

Translated by G. Skrebtsov

Physics of the Solid State, Vol. 44, No. 11, 2002, pp. 2031–2033. Translated from Fizika Tverdogo Tela, Vol. 44, No. 11, 2002, pp. 1940–1942.
Original Russian Text Copyright © 2002 by Prikhod'ko, Shibanova.

METALS AND SUPERCONDUCTORS

Microwave Field Effects in HTSC Single Crystals of Bi(2212)

A. V. Prikhod'ko and N. M. Shibanova
St. Petersburg State Technical University, Politekhnicheskaya ul. 29, St. Petersburg, 195251 Russia

Received November 13, 2001

Abstract—Microwave-radiation absorption of single-phase Bi(2212) single crystals in a near-2-mm wavelength range is studied as a function of microwave field overvoltage. A characteristic plateau is detected for the electric-field orientation along superconducting planes. A possible mechanism for this behavior is considered on the basis of the concepts of percolation network and pinchlike current distributions. © *2002 MAIK "Nauka/Interperiodica".*

1. INTRODUCTION

Analysis of microwave-radiation absorption by high-temperature superconductors was found to be effective in determining the properties of intrinsic Josephson junctions. The discovered oscillatory dependence of power on the radiation absorbed for different values of a constant magnetic field is associated with the existence of such junctions [1]. An analysis of the experimental data makes it possible to single out the characteristic features of absorption. This primarily concerns the scales of mw fields which do not lead to a local loss of superconductivity. These features can be explained [2] by size quantization effects in small loops with an area on the order of hundreds of square micrometers. It follows from [2] that the frequency dependence of the absorbed power has a peak at a frequency which is a periodic function of the reciprocal amplitude of the ac magnetic field. A further increase in power leads to a more complex form of absorption. The periodicity of absorption as a function of the field vanishes in this case, and mesoscopic fluctuations start being manifested [3]. Microwave probing of HTSC single crystals revealed such features as Josephson harmonics generation and coherent conductivity peaks. In the former case, an analogue of Shapiro steps is also observed. The experiments were carried out in the range of weak microwave fields for which mesoscopic effects are not observed.

In this work, we analyze the microwave properties of Bi(2212) single crystals (in a near-2-mm wavelength range), which depend on the magnitude of the microwave field used for sample probing.

An analysis of the known features of absorption shows that, according to [2], the maximal frequency at which size-quantization effects are still observed extends approximately to a few gigahertz. It is conceivable that such effects will not be manifested at frequencies higher than the critical value. In addition, the effects of Josephson harmonics generation are observed only for multiphase samples. In this study, we analyze microwave features in a near-2-mm wavelength range, i.e., under conditions when size-quantization effects are not manifested. Samples were in the form of single-phase and multiphase single crystals which display, first, coherent conduction effects [4] and, second, weak-coupling effects [5].

2. SAMPLES AND EXPERIMENTAL TECHNIQUE

We used Bi(2212) single crystals prepared by spontaneous crystallization of melt in air. The sample size was $0.8 \times 1.7 \times 3.7$ mm. The crystal growth technology does not differ from that described in [5, 6].

Microwave experiments are made using a strongly emitting slit in a wide wall of a rectangular waveguide. We constructed an original setup for studying the profile of a standing wave in an open dielectric resonator (ODR) loaded with a sample. The effectiveness of such experiments for an analysis of superconducting properties was demonstrated in [4]. Here, we use a single-mode teflon ODR with an inner radius of 0.325 mm, outer radius of 0.470 mm, and length of 4 mm. Radial electric and azimuthal magnetic components of the electromagnetic field at the resonator end face interact with the sample surface. The resonator is pumped through a 0.1×8 mm slit. The sample was cooled to 78 K. We used a microwave oscillator (operating in a near-2-mm wavelength range) whose maximum electric power P_0 reached 4 mW (100%) and whose pulse repetition frequency was 10^3 Hz. The resonance frequency of the ODR was 143.52 GHz. Temperature measurements of the signal power were carried out at the standing-wave antinode closest to the sample, while the dependence on the normalized incident power (overvoltage) P/P_0 was measured with the sample arranged immediately above the slit. The sample orientation was specified by the mutual orientation of the electric field vector $\mathbf{E}$ in the slit and the normal $\mathbf{n}$ to the base plane of the sample.

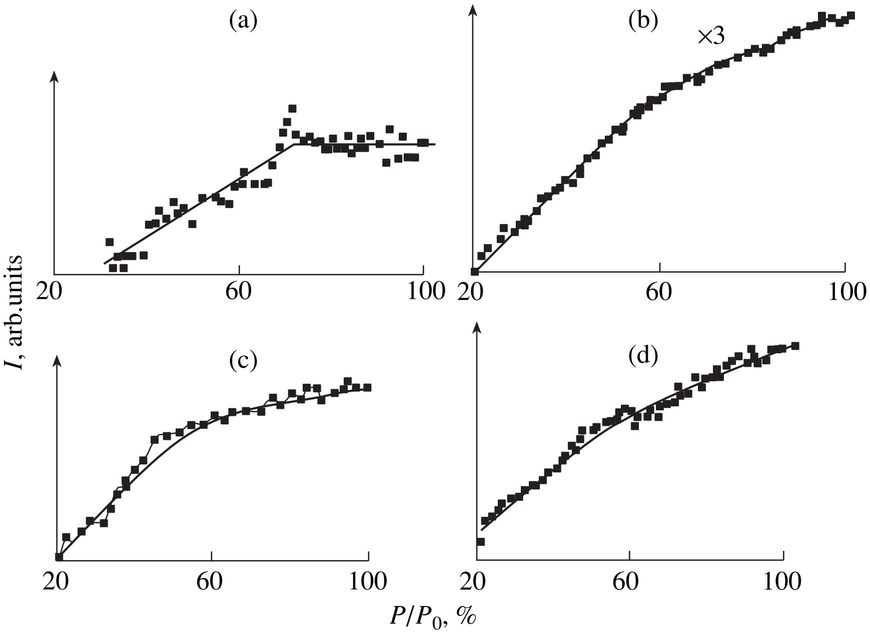

Fig. 1. Dependence of the output microwave power I on the overvoltage P/P_0 for (a, b) single-phase and (c, d) multiphase samples for the field orientation (a, c) $\mathbf{E} \perp \mathbf{n}$ and (b, d) $\mathbf{E} \parallel \mathbf{n}$.

3. EXPERIMENTAL RESULTS AND DISCUSSION

The main result is the following experimental fact: the dependence of the power on the overvoltage in a single-phase sample in fields corresponding to a 70% overvoltage displays a characteristic plateau that depends on the orientation. For a multiphase sample, a characteristic kink is detected at an overvoltage of 40%. Figure 1 shows the dependence of the output microwave power on the overvoltage for single-phase and multiphase samples oriented in different ways at liquid-nitrogen temperatures. At room temperature, the features mentioned above are not manifested; i.e., these features characterize the superconducting state. Figure 2 shows the dependence of the superconducting transition temperature T_c on the overvoltage for the field orientation $\mathbf{E} \parallel \mathbf{n}$ in a single-phase sample. This dependence indicates that the superconducting state exists over the entire range of overvoltage values (0–100%). Furthermore, the change in the form of this dependence occurs at the same value of overvoltage for which the kink in Fig. 1b is observed.

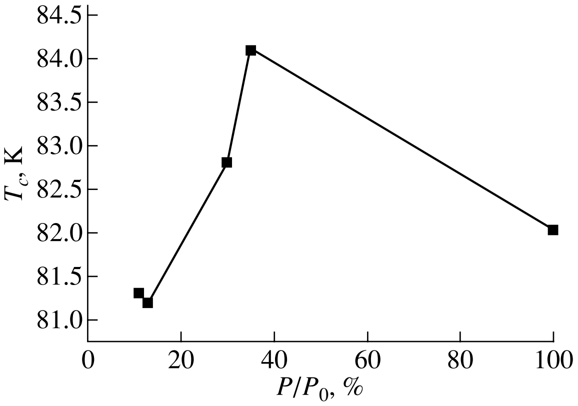

Fig. 2. Dependence of the superconducting-transition temperature T_c on overvoltage P/P_0 for a single-phase sample; the field orientation $\mathbf{E} \parallel \mathbf{n}$.

It is well known that nonlinear effects associated with the emergence of electrical instabilities can be manifested in small volumes [7]. In this case, a current pinch can be formed, which leads to a change in electrophysical parameters. For example, a study of microwave noise in the regime of current instability revealed saturation of the current noise of the low-resistivity state [8]. This effect is attributed to the pinch expansion, which is analogous to the conservation of the current density in the pinch observed earlier [7]. In accordance with Kirchhoff's law, the peculiarities of radiation must be associated with the peculiarities of absorption at the same temperature and wavelength. Actually, the absorption of microwave power in the electric-instability conditions [9] correlates with the behavior of microwave noise. It is conceivable that the decisive factor for the manifestation of the observed plateau is the emergence of electrical-instability regions in the bulk of the sample, followed by the formation of pinchlike distributions of the mw current. The centers for the emergence of such regions can be the regions of nonuniform field distribution over the volume. It is well known that, in samples of a nonellipsoidal shape, a magnetic field is distributed nonuniformly in the bulk of a sample. The nonuniform field distribution in the high-temperature superconductors measured in [10] indicates the emergence of a geometric barrier: the screening current is smaller than the critical current at the center of the sample and larger at the periphery. The geometrical barrier may determine the distribution of mw current. The beginning of the formation of a current pinch can be described in terms of the model of percolation transition [11] as follows. Under the action of mw current flowing in the bulk, a network of percolation channels forms, and a part of the conducting segments can be destroyed upon a subsequent increase in current. The onset of the destruction process suppresses the superconducting transition, which is manifested in a decrease in the superconducting-transition temperature (Fig. 2). By increasing the field, we bring the system closer to the percolation threshold, since the network of percolation channels becomes progressively coarser. As the system approaches the percolation threshold (critical concentration of conducting channels), the percolation network is ruptured completely. The effective conductivity of such a system, as well as the density of percolation channels, is determined numerically as a function of the breakdown field in [11]. In our case, the breakdown field is the mw field corresponding to the onset of electric instability in the percolation network.

4. CONCLUSION

The main result obtained in this work is the detection of the superconducting transition coexisting with electric instabilities associated with a pinchlike current distribution over the percolation network. It can be concluded that for fields strong enough for the emergence of electric instability, the physics of the processes change radically in comparison with the case of weak mw fields. In the latter case, mw fields change the structure of a percolation network, while strong fields initiate the so-called strong-field effects. The superconducting state is destroyed only for critical fields close to the percolation threshold. It should be noted that the increase in the superconducting-transition temperature may be associated with stimulation of superconducting channels with a higher transition temperature in the percolation network and requires further investigations.

ACKNOWLEDGMENTS

This study was supported by the Ministry of Industry, Science, and Technology of the Russian Federation, grant “Superconductivity.”

REFERENCES

1. V. F. Masterov, in *High-Temperature Superconductivity: Fundamental and Applied Investigations*, Ed. by A. A. Kiselev (Mashinostroenie, Leningrad, 1990), Vol. 1, p. 405.
2. V. F. Masterov and V. A. Kharchenko, Sverkhprovodimost: Fiz., Khim., Tekh. **4** (4), 629 (1991).
3. V. F. Masterov, I. L. Likholit, V. V. Potapov, and N. M. Shibanova, Supercond. Sci. Technol. **6**, 593 (1993).
4. M. N. Kotov, V. F. Masterov, V. V. Potapov, *et al.*, Int. J. Infrared Millim. Waves **14** (8), 1679 (1993).
5. A. V. Prikhod’ko and N. M. Shibanova, Fiz. Tverd. Tela (St. Petersburg) **42** (6), 992 (2000) [Phys. Solid State **42**, 1023 (2000)].
6. N. M. Shibanova, V. V. Potapov, N. M. Baranova, and G. A. Nikolaĭchuk, Sverkhprovodimost: Fiz., Khim., Tekh. **6** (3), 597 (1983).
7. S. A. Kostylev and V. A. Shkut, *Electronic Switching in Amorphous Semiconductors* (Naukova Dumka, Kiev, 1978).
8. A. V. Prikhod’ko, A. A. Chesnis, and V. A. Bareĭkis, Fiz. Tekh. Poluprovodn. (Leningrad) **15** (3), 536 (1981) [Sov. Phys. Semicond. **15**, 303 (1981)].
9. Zh. I. Alferov, A. T. Gorelenok, V. V. Mamutin, *et al.*, Fiz. Tekh. Poluprovodn. (Leningrad) **19** (11), 2004 (1985) [Sov. Phys. Semicond. **19**, 1233 (1985)].
10. E. Zeldov, Phys. Rev. Lett. **73**, 1428 (1994).
11. A. P. Vinogradov, A. V. Gol’dshteĭn, and A. K. Sarychev, Zh. Tekh. Fiz. **59** (1), 208 (1989) [Sov. Phys. Tech. Phys. **34**, 125 (1989)].

Translated by N. Wadhwa

Physics of the Solid State, Vol. 44, No. 11, 2002, pp. 2034–2038. Translated from Fizika Tverdogo Tela, Vol. 44, No. 11, 2002, pp. 1943–1947.
Original Russian Text Copyright © 2002 by Dolidze, Tsekvava.

SEMICONDUCTORS AND DIELECTRICS

On the Model of Divacancies in Germanium

N. D. Dolidze and B. E. Tsekvava
Dzhavakhishvili State University of Tbilisi, pr. Chavchavadze 3, Tbilisi, 380028 Georgia
e-mail: nugo@geo.net.ge

Received February 28, 2002

Abstract—A model of a divacancy which explains a number of experimental facts for Ge exposed to a flow of accelerated electrons at temperature $T = 77$ K is proposed. The model explains the absence of photoconduction associated with photoexcitation of infrared absorption bands at 0.44 and 0.52 eV corresponding to divacancies; the difference in the values of activation energy for divacancy energy levels determined by optical and electrical methods; and the existence of the limiting position of the Fermi level in the forbidden gap in the case of irradiation with large radiation fluxes. *© 2002 MAIK “Nauka/Interperiodica”.*

It was shown in [1] that so-called light-sensitive defects are formed in *p*-type germanium, as well as in *n*-type germanium converted into *p*-Ge as a result of irradiation with accelerated electrons (1–5 MeV). Photosensitivity is manifested only in samples possessing *p*-type conductivity after irradiation [1–6]. It is shown in [4, 6, 7] that light-sensitive defects are responsible for infrared (IR) absorption bands at 0.44 and 0.52 eV. These defects are manifested electrically (in experimental temperature dependences of the Hall coefficient) as energy levels $E_V + 0.16$ eV and $E_V + 0.08$ eV in the forbidden gap, depending on the charge state of a defect [5]. At the same time, the electrically active levels $E_V + 0.52$ eV and $E_V + 0.44$ eV have not been observed in experiments. It should also be noted that photoconduction was not observed in experiments in the case of absorption of photons with energy 0.52 and 0.44 eV. In [4, 7], these defects in germanium were called divacancies.

A similar situation (the difference between the energies of the optical absorption bands ~0.69 and ~0.32 eV and the energies of the electrically active levels $E_C - 0.39$ eV and $E_C - 0.54$ eV, respectively [8]) is observed for a divacancy in silicon [9–11]. In this case also, the absorption of photons corresponding to energies of optical absorption bands does not lead to photoconduction.

At the same time, it is well known [12, 13] that irradiation of *n*- and *p*-type germanium and silicon samples leads to a decrease in the concentration of the majority charge carriers; i.e., the Fermi level is displaced to the middle of the forbidden gap and attains a certain limiting position, which is the same for both types of conduction (the so-called limiting Fermi level) and changes insignificantly upon a further increase in the integrated radiation flux. A unified theory explaining all these experimental facts has not yet been developed.

At the present time, there exists a model of divacancy in silicon [9] (Fig. 1). The same model can also be used for germanium [7]. According to this model, at the initial stage (before Jahn–Teller distortions appear), there are two vacancies at adjacent atomic sites *c* and *c*' (dashed circles in Fig. 1) located along a spatial diagonal of the cube and six neighboring atoms (*a*, *d*, *a*', *d*', *b*, *b*') with bent bonds *a*–*d*, *a*'–*d*', and *b*–*b*'. The corresponding polyatomic nonlinear molecule possesses the D_{3d} symmetry. The group D_{3d} has four one-dimensional and two two-dimensional irreducible representations. Consequently, all electron terms of the molecule belong to one of the six irreducible representations of the group D_{3d}. Thus, in addition to nondegenerate energy levels corresponding to one-dimensional representations, there also exist doubly degenerate electron energy levels corresponding to two-dimensional irreducible representations (if we disregard spin). A degenerate electron energy level occupied by electrons is unstable to the Jahn–Teller effect. This effect leads to a distortion of the configuration of the nonlinear molecule, and its symmetry is lowered to C_{2h}; the group C_{2h} contains only three one-dimensional irreducible representations [14], and, hence, only nondegenerate electron energy

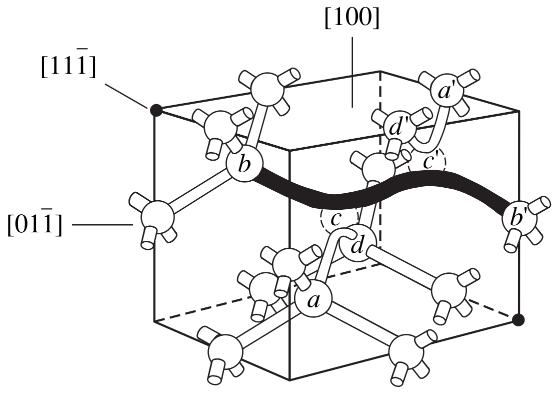

Fig. 1. 3D model of a divacancy in silicon (according to [9]).

1063-7834/02/4411-2034$22.00 © 2002 MAIK “Nauka/Interperiodica”

levels are present. The spatial model of a divacancy and its wave functions as given by the LCAO model without and with the Jahn–Teller effect included (according to [9]) are presented in Figs. 1 and 2. According to this model, a divacancy is a multiply charged center with four energy levels: the two lower levels (*1*, *2*) lie extremely close to each other in the immediate vicinity of the top of the valence band, while the other two levels (*3*, *4*) lie deep in the forbidden gap. The charge state of the divacancy is determined by the number of electrons executing the *b*–*b*' bond between the atoms. When this bond is free of electrons (levels *3*, *4* in Fig. 3), the divacancy is in the state with double positive charge. When one or two electrons (filling level *3*) execute this bond, we have a singly positively charged or neutral divacancy, respectively. This bond can accommodate one or two more electrons at level *4*. In this case, the divacancy acquires a single negative or double negative charge. This model of the divacancy used in [7, 9–11] correctly describes some experimental results but fails to explain all the above-mentioned experimental facts for germanium and silicon.

In order to solve this problem, we propose, in contrast to [7, 9–11], a model of divacancies taking into account the bending of energy bands of a semiconductor by fluctuation electric fields produced by charged defects. We assume that there is no correlation in the distribution of defects in a semiconductor and fluctuations in their concentrations are of the Gaussian type [15–17].

Let us apply the method of bent bands to our problem. It was shown in [16] that the fluctuation field of the spatial charge bending the bands is created by chemical impurities. In our case, such impurities are the initial impurities (donors) compensating radiation-induced point defects and their simple complexes, formed in *n*-Ge as a result of irradiation by an integrated flux of accelerated electrons (E = 2–6 MeV, $\Phi = 10^{16}$–5×10^{17} cm^{-2}) at temperature T = 77 K. This conclusion follows from the fact that conversion of the conduction type (overcompensation) was attained as a result of irradiation of the *n*-Ge samples under investigation with an initial concentration of conduction electrons $n \sim 10^{14}$–10^{16} cm^{-3} and that the samples displayed *p*-type conduction after irradiation. The equilibrium hole concentration in this case did not exceed ~10^{10} cm^{-3}.

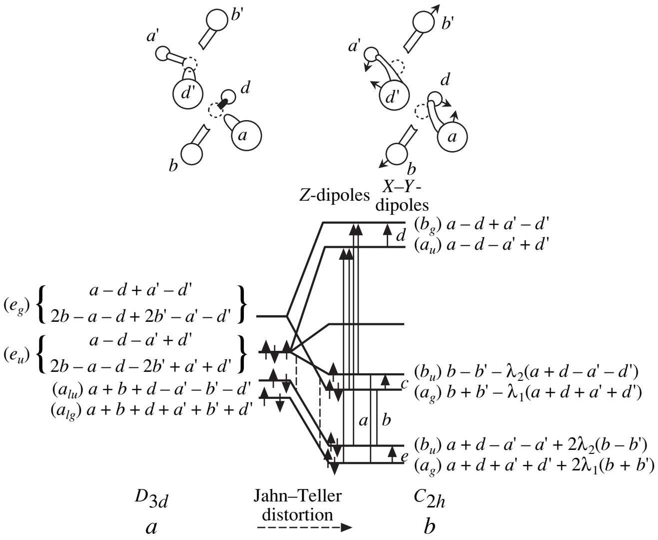

Fig. 2. Simple molecular-orbital LCAO model of the electronic structure of a divacancy (*a*) before Jahn–Teller distortion (D_{3d}) and (*b*) after the distortion C_{2h}. Solid arrows denote electrons and their spins for a singly charged positive state, while dashed arrows denote extra electrons for a singly charged negative state.

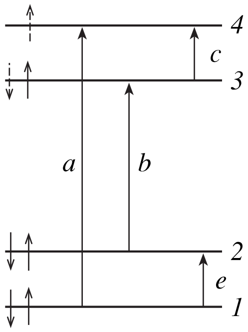

Fig. 3. Fragment of Fig. 2 showing the levels of a divacancy determining its charge state.

It should be noted that irradiation gives rise to randomly distributed charged centers (defects). In the case of a strong compensation, it is necessary to take into account Gaussian fluctuations of the concentrations of charged impurities and radiation defects, which create a fluctuating large-scale electrostatic potential. The effect of this potential on band bending and on the shift of the Fermi level toward the middle of the forbidden gap must be taken into consideration even for moderate concentrations of defects on the order of 10^{15}–10^{16} cm^{-3}. Under these conditions, the concentration of charged defects creating strong fluctuation fields is high, while screening is weak. However, a low concentration of mobile carriers and a high density of the fluctuation charge give rise to difficulties associated with the inclusion of screening [18–20].

The difficulties associated with screening in the case of a strong compensation were overcome in [16] with the help of the hypothesis that the arrangement of impurities is correlated (for shallow centers), which is determined by the crystal growth technology. In this case, a specific nonelectron mechanism of screening (mutual screening of donors and acceptors) takes place. In the case of radiation defects, such a screening model is not adequate to the actual situation. Since the experimentally determined energy spacing between the lowest and highest position of the top of the bent valence band

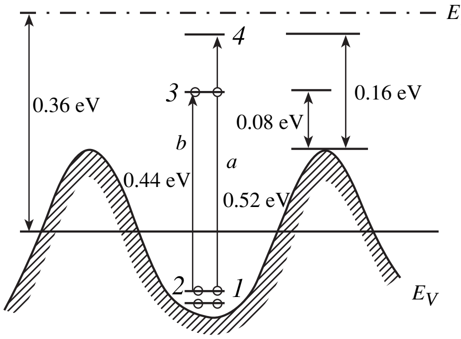

Fig. 4. Diagram explaining the difference between optically and electrically determined values of the activation energy of a divacancy in germanium: 0.52 eV is the energy of optical excitation of an electron from the lower level of the divacancy to level E_V + 0.16 eV, while 0.44 eV is the same energy corresponding to level E_V + 0.08 eV (intracenter transitions); E_i is the middle of the forbidden gap of the unexposed crystal. The curve shows the bending of the top of the valence band E_V by the fluctuation potential of charged defects, while the solid straight line corresponds to the top of the unperturbed valence band.

(potential relief) in germanium is approximately equal to 0.3 eV, the linear-screening approximation is inapplicable. The reason for this is that such a high fluctuation potential leads to a deep spatial modulation of the electron density. However, the linear-screening theory is based on linearization of the Poisson equation, which is justified only in the case of a small depth of the potential well and a weak inhomogeneity of the electron density.

We will now use the basic concepts of the theory of nonlinear screening formulated in [18–20]. In this theory, one of the main difficulties is associated with determining the form of distribution of impurities in a semiconductor. Following [18–20], we assume that there is no correlation in the distribution of defects, i.e., that the distribution is of the Poisson type and fluctuations are Gaussian (small fluctuations). In order to estimate potential-energy fluctuations, we will use the approximation of a uniformly charged sphere [20]. We assume that fluctuations have the form of homogeneous spherical defect pileups having radius R and characterized by a Poisson distribution of defects in them. We denote the average concentration of defects by N_t. Then, the average number of particles in a sphere is $N = 4\pi N_t R^3/3 \approx 4N_t R^3$ and the root-mean-square fluctuation of particles is $\Delta N = \sqrt{N} = 2\sqrt{N_t R^3}$. A typical charge of a sphere is equal to $2Ze\sqrt{N_t R^3}$ ($Z = \pm1, \pm2$), and the rms fluctuation potential energy $\gamma(R)$ of an electron is given by

$$\gamma(R) = 2Ze^2\sqrt{N_t R^3}/\varepsilon R = 2Ze^2\sqrt{N_t R}/\varepsilon, \qquad (1)$$

where ε is the permittivity of the medium and e is the electron charge. As $R \longrightarrow \infty$, we have $\gamma(R) \longrightarrow \infty$ in complete accord with the well-known result according to which the rms Coulomb energy fluctuation $[N_t\int(e^2/\varepsilon r)^2 dr]^{1/2}$ diverges at large distances. This result is physically meaningless, which indicates that screening must be taken into account in one way or another for a random distribution of Coulomb centers. In our case of large-scale fluctuations of randomly distributed charged centers, the only possible mechanism of nonlinear screening that bounds the radius of a sphere is the electron (hole) screening, in spite of the low concentration of free charge carriers. We introduce the radius of a sphere $R = R_0$ in such a way that the fluctuation charge density $\delta N = 0.5Ze\sqrt{N_t/R_0^3}$ is equal to the hole charge density. Obviously, the holes (electrons) in this volume neutralize the excess density of the negative (positive) charge of the sphere. Consequently, we have

$$p = 0.5Z\sqrt{N_t/R_0^3}, \text{ or } R_0 = \sqrt[3]{Z^2N_t/4p^2}. \qquad (2)$$

In our experiments, n-type germanium is compensated by irradiation: $N_t = N_d + N_a$ (N_d and N_a are the concentrations of radiation defects of the donor and acceptor type, respectively). Considering that compensation has been attained, we can assume that, approximately, $N_t = 2N_d$.

It follows that fluctuations of a size $R > R_0$ are neutralized completely by free carriers, while fluctuations with a size $R < R_0$ remain unscreened. Consequently, an approximate value of γ is obtained from Eqs. (1) and (2) to be

$$\gamma = \sqrt[3]{4Z^4e^6N_t^2/\varepsilon^3 p}. \qquad (3)$$

For low concentrations of holes, the potential well is found to be quite deep. The electron levels of a divacancy lie in this well (Fig. 4).

For $p = 10^{10}$ cm^{-3} and $N_d = 10^{15}$ cm^{-3} ($N_t \approx 2N_d$), estimating the amplitude γ of potential-energy oscillations for Ge from Eq. (3) gives $\gamma = 0.16$ eV. The condition for the location of the ground-state energy levels in the well, $\hbar^2/2mR_0^2 \ll \gamma$, can be written, in accordance with Eqs. (2) and (3), in the form $(p/N_t)^{5/3} \ll a^{-1}N_t^{-1/3}$, where $a = \varepsilon\hbar^2/me^2$ (m is the effective electron mass). Since $p \ll N_d$, this inequality holds with a large margin and energy levels *1* and *2* of the divacancy lie near the bottom of the well (the top of the valence band in the given part of the crystal). The energy interval between the bottom and the maximum (hump) of the potential relief (bent band) is $\Delta U = 2\gamma \approx 0.32$ eV, while the corresponding experimental value, determined with the help of optical and electrical measurements, is $\Delta U_{\text{exp}} = (0.52 - 0.16)$ eV $= (0.44 - 0.08)$ eV $= 0.36$ eV (Fig. 4). Considering that the above values of parameters are typical of our experiments, the agreement with the theoretical model can be regarded as satisfactory.

As regards the range of applicability of formulas (2) and (3), it should be noted that the characteristic scales of fluctuations (and, accordingly, the amplitude of oscillations of the potential energy $\gamma(R)$) in a compensated semiconductor with a low concentration of mobile charge carriers can become, in accordance with formulas (2) and (3), indefinitely large (e.g., can exceed the forbidden gap width). It was proved in [19], however, that if the bottom of the conduction band is lowered by $0.5E_g$ relative to its position in an unexposed crystal, it will cross the Fermi level in this region of the crystal, intrinsic carriers (electrons) will appear in a number sufficient for screening of the potential well formed, and further lowering of the bottom of the conduction band will stop. Similarly, in the crystal region with an excess of negative charge (potential well for holes), the number of holes formed upon the crossing of the Fermi level will be sufficient for preventing a further rise of the top of the valence band. Consequently, formulas (2) and (3) are inapplicable for the case of low concentrations of charge carriers when $\gamma(R) \geq 0.5E_g$. Under our experimental conditions, $\gamma(R) < 0.5E_g$, and formulas (2) and (3) hold.

Let us now apply the proposed divacancy model to explain the following experimental facts.

(1) The absence of photoconduction in the case of optical excitation of levels *3* and *4* (transitions *a*, *b* in Fig. 3). The above estimates indicate that the ground-state levels of the divacancy (*1*, *2*) lie near the bottom of the potential well. When photons with energy 0.44 or 0.52 eV are absorbed, electron transitions from these levels to levels *3* and *4* (intracenter transition) take place. In this case, electrons must perform transitions from the valence band to the lower vacant levels, *1* and *2*; i.e., holes are generated near the bottom of the well in the valence band (consequently, photoconduction must appear). However, the divacancy in the well is in an unstable charge state, and the surplus electron from the upper level instantaneously recombines with a nearest neighbor hole. Therefore, the hole disappears before it can participate in photoconduction.

(2) Difference in the values of activation energy of divacancy levels *3* and *4* (Fig. 3) determined by optical and electrical methods. The activation energies for energy levels determined from experimental temperature dependences of the Hall coefficient indicate that the Fermi level is shifted towards the middle of the forbidden gap upon an increase in temperature. In this case, electrons can occupy levels *3* and *4*; i.e., the divacancy can change its charge state. Electrons perform transitions from the hump of the bent valence band to these levels. The energy required for the excitation of such electrons corresponds to the spacing between the hump of the bent valence band and levels *3* and *4*. Figure 4 shows the diagram explaining the difference between optically and electrically determined values of activation energy of a divacancy in germanium: the optically determined value of the activation energy for level *4* (0.52 eV) corresponds to the electrically active level $E_V + 0.16$ eV, while the electrically active level for the activation energy of level *3* (0.44 eV) is $E_V + 0.08$ eV.

(3) The existence of the limiting position of the Fermi level in the forbidden gap. It was noted above that the existence of the limiting Fermi level in both types of semiconductors has been established experimentally. It has been shown that the limiting Fermi level is different for different semiconductors: it lies near the middle of the forbidden gap in silicon and is closer to the lower edge of the gap in germanium. In *n*-Ge, a conversion of the conduction type is observed. Different authors give different positions of the limiting Fermi level in the forbidden gap of germanium (from $E_V + 0.07$ eV to $E_V + 0.24$ eV) for various temperatures and types of irradiation. In [12], the limiting position of the Fermi level for *p*-Ge and for *n*-Ge converted to the *p* type by irradiation by fast electrons at $T = 77$ K was found to be $E_V + 0.07$ eV. It was assumed in [12] that an amphoteric level belonging to a complex radiation defect exists in this region. The idea of pinning of the Fermi level near an amphoteric level appears attractive, and we adhere to the same point of view. However, in contrast to [12], we proved that such an amphoteric center is a multielectron center (divacancy), whose energy level diagram is given in Fig. 4. Since $\gamma \sim 0.16$ eV, according to our estimates, the optically determined levels 0.52 and 0.44 eV must be separated by intervals ~0.16 and 0.08 eV from the hump of the bent valence band, respectively, which corresponds to a distance ~0.1 eV from the middle of the forbidden gap in the unexposed crystal. During irradiation of *n*- and *p*-Ge, divacancies (which are compensating centers in both cases) are introduced. In *p*-type samples, the divacancy formed can be in the doubly positive (no electrons on level *3*), singly positive (one electron on level *3*), or neutral (two electrons on level *3*) charge states. In the former two cases, the divacancy is a positively charged ionized center and behaves as a donor. Therefore, the Fermi level moves upwards to the middle of the forbidden gap upon irradiation of the sample (i.e., upon an increase in the divacancy concentration). When the Fermi level lies between level *3* and *4* and is separated from these levels by at least (2–3)kT, the charge state of the divacancy changes and the divacancy becomes neutral (level *3* is occupied by two electrons, while level *4* is empty). This situation comes about, because the energy interval between level *3* and *4* is $\Delta E \gg kT$, $\Delta E/kT \geq 10$ ($T = 77$ K). A further upward displacement of the Fermi level as a result of irradiation leads to a transition of the divacancy to the singly or doubly charged state (filling of level *4*), which means that the divacancy (negatively charged ionized center in this case) becomes an acceptor. As a result, the Fermi level starts moving towards the valence band again, and, after it attains the lower level, the divacancy again transforms into a donor, after which the process is repeated. The Fermi level turns out to be fixed between the two levels, which is the reason for the existence of the limiting Fermi level. The same pattern is also observed for *n*-Ge, the only difference being that the Fermi level moves, as a result of irradiation, toward the middle of the forbidden gap from the conduction band.

REFERENCES

1. A. B. Gerasimov, N. D. Dolidze, N. G. Kakhidze, *et al.*, Fiz. Tekh. Poluprovodn. (Leningrad) **1** (7), 982 (1967) [Sov. Phys. Semicond. **1**, 822 (1968)].
2. H. Saito, N. Fukuoka, H. Hattori, and J. H. Crawford, in *Radiation Effects in Semiconductors*, Ed. by F. L. Vook (Plenum, New York, 1968), p. 232.
3. T. M. Flanagan and E. E. Klontz, Phys. Rev. **167**, 789 (1968).
4. H. J. Stein, in *Radiation Damage and Defects in Semiconductors*, Ed. by J. E. Whitehouse (The Institute of Physics, London, 1973), p. 315.
5. A. R. Basman, A. B. Gerasimov, N. G. Kakhidze, *et al.*, Fiz. Tekh. Poluprovodn. (Leningrad) **7** (7), 1347 (1973) [Sov. Phys. Semicond. **7**, 903 (1973)].
6. A. B. Gerasimov, N. D. Dolidze, B. M. Konovalenko, and M. G. Mtskhvetadze, Fiz. Tekh. Poluprovodn. (Leningrad) **11** (7), 1349 (1977) [Sov. Phys. Semicond. **11**, 793 (1977)].
7. A. B. Gerasimov, N. D. Dolidze, R. M. Donina, *et al.*, Phys. Status Solidi A **70**, 23 (1982).
8. V. S. Vavilov, N. P. Kekelidze, and L. S. Smirnov, *Effects of Radiation on Semiconductors* (Nauka, Moscow, 1988).
9. G. D. Watkins and J. W. Corbet, Phys. Rev. **138**, A543 (1965).
10. L. J. Cheng, J. C. Corelli, J. W. Corbet, and G. D. Watkins, Phys. Rev. **152**, 761 (1966).
11. A. H. Kalma and J. C. Corelli, Phys. Rev. **173**, 734 (1968).
12. A. B. Gerasimov, Fiz. Tekh. Poluprovodn. (Leningrad) **12** (6), 1194 (1978) [Sov. Phys. Semicond. **12**, 709 (1978)].
13. V. S. Vavilov, *Effects of Radiation on Semiconductors* (Fizmatgiz, Moscow, 1963; Consultants Bureau, New York, 1965).
14. L. D. Landau and E. M. Lifshitz, *Course of Theoretical Physics*, Vol. 3: *Quantum Mechanics: Non-Relativistic Theory* (Nauka, Moscow, 1974; Pergamon, New York, 1977).
15. V. L. Bonch-Bruevich, Fiz. Tverd. Tela (Leningrad) **4** (9), 2660 (1962) [Sov. Phys. Solid State **4**, 1953 (1962)].
16. L. V. Keldysh and G. P. Proshko, Fiz. Tverd. Tela (Leningrad) **5** (12), 3378 (1963) [Sov. Phys. Solid State **5**, 2481 (1963)].
17. E. O. Kane, Phys. Rev. **131**, 79 (1963).
18. B. I. Shklovskiĭ and A. L. Éfros, Zh. Éksp. Teor. Fiz. **60** (2), 867 (1971) [Sov. Phys. JETP **33**, 468 (1971)].
19. B. I. Shklovskiĭ and A. L. Éfros, Zh. Éksp. Teor. Fiz. **62** (3), 1156 (1972) [Sov. Phys. JETP **35**, 610 (1972)].
20. A. L. Éfros, Usp. Fiz. Nauk **111** (3), 451 (1973) [Sov. Phys. Usp. **16**, 789 (1973)].

Translated by N. Wadhwa

Physics of the Solid State, Vol. 44, No. 11, 2002, pp. 2039–2049. From Fizika Tverdogo Tela, Vol. 44, No. 11, 2002, pp. 1948–1957.
Original English Text Copyright © 2002 by Lemanov, Sotnikov, Smirnova, Weihnacht.

Giant Dielectric Relaxation in $SrTiO_3$–$SrMg_{1/3}Nb_{2/3}O_3$ and $SrTiO_3$–$SrSc_{1/2}Ta_{1/2}O_3$ Solid Solutions[1]

V. V. Lemanov*, A. V. Sotnikov*, **, E. P. Smirnova*, and M. Weihnacht**

** Ioffe Physicotechnical Institute, Russian Academy of Sciences, Politekhnicheskaya ul. 26, St. Petersburg, 194021 Russia*

*** Leibniz Institute of Solid-State and Materials Research, Dresden, D-01069 Germany*

Received April 11, 2002

Abstract—Ceramic samples of $(1 - x)SrTiO_3$–$xSrMg_{1/3}Nb_{2/3}O_3$ and $(1 - x)SrTiO_3$–$xSrSc_{1/2}Ta_{1/2}O_3$ were prepared, and their dielectric properties were studied at $x = 0.005$–0.15 and 0.01–0.1, respectively, at frequencies 10 Hz–1 MHz and at temperatures 4.2–350 K. A giant dielectric relaxation was observed in the temperature range 150–300 K, and not so strong but well-developed relaxation was found in the temperature range 20–90 K. The activation energy U and the relaxation time τ_0 were determined to be 0.21–0.3 eV and from 10^{-11} to 10^{-12} s for the high-temperature relaxation and 0.01–0.02 eV and 10^{-8}–10^{-10} s for the low-temperature relaxation, respectively. The additional local charge compensation of the heterovalent impurities Mg^{2+} and Nb^{5+} (or Sc^{3+} and Ta^{5+}) by free charge carriers or the host ion vacancies is suggested to be the underlying physical mechanism of the relaxation phenomena. On the basis of this mechanism, the Maxwell–Wagner model and the model of reorienting dipole centers Mg^{2+} (or Sc^{3+}) associated with the oxygen vacancy are proposed to explain the high-temperature relaxation with some arguments in favor of the latter model. The polaron-like model with the Nb^{5+}–Ti^{3+} center is suggested as the origin of the low-temperature relaxation. The reasons for the absence of ferroelectric phase transitions in the solid solutions under study are also discussed. © *2002 MAIK "Nauka/Interperiodica".*

1. INTRODUCTION

Strontium titanate $SrTiO_3$ is known to be an incipient ferroelectric and a quantum paraelectric [1]. The $SrTiO_3$ crystal has a polar soft mode but never exhibits a ferroelectric phase transition down to $T = 0$ due to quantum fluctuations. At low temperatures, the dielectric constant in $SrTiO_3$ attains very high values. According to [2], $\varepsilon_a = 41900$ and $\varepsilon_c = 9380$ (4 K, 1–100 kHz). It should be noted that these remarkable values were obtained by extrapolation of the inverse susceptibility versus stress to zero stress and nobody has been able to reproduce this result directly. A more or less typical experimental value of ε_a in direct measurements is around 20000 instead of 41900, and even this value is remarkable.

The $SrTiO_3$ crystal can be considered a marginal system that is near the limit of its paraelectric phase stability. Small external perturbations such as elastic stress or impurities can destroy the stability and induce a ferroelectric phase transition. Various impurities substituted for the host ions in $SrTiO_3$ both in the *A*- and *B*-position have been studied [3, 4]. It was shown that divalent impurities substituted for Sr^{2+}, such as Ca [5], Ba [6], Pb [7], and Cd [8], induce a ferroelectric phase transition with the transition temperature T_c proportional to $(x - x_c)^{1/2}$, where the critical concentration x_c is about 0.002 and is almost the same for all these impurities, with some specific features for the case of Ba. Isovalent *B*-impurities (Zr, Sn, Ge) have a much smaller effect on the dielectric properties of $SrTiO_3$. Simultaneous replacement of the host Sr^{2+} and Ti^{4+} ions by impurity ions yields some specific effects. For example, in the $SrTiO_3$–$PbMg_{1/3}Nb_{2/3}O_3$ (PMN) solid solution, the transition to a ferroelectric phase (with relaxor properties) was observed only at $x > 0.2$ with a linear dependence of T_c on x, which was associated with random fields due to the disordered Mg^{2+} and Nb^{5+} distribution [9].

Quite a different situation takes place for heterovalent impurities. In this case, instead of induced ferroelectric phase transitions, distinct dielectric relaxation is observed. (The only exception is perhaps $SrTiO_3:Bi^{3+}$; in [10], it was claimed that the Bi impurity induces a ferroelectric phase transition with $x_c = 0.0005$.) There is a very long history of studying dielectric relaxation in $SrTiO_3$ with various heterovalent impurities, such as Bi [11–16], La [17–21], La and a wide range of other trivalent rare-earth ions [22], and Fe [23, 24].

In this paper, we studied some special cases of heterovalent substitution when the host Ti^{4+} ion is substituted by two heterovalent ions whose average charge is equal to that of the Ti^{4+} ion. As an example of such systems, the solid solutions of $SrTiO_3$ with $SrMg_{1/3}Nb_{2/3}O_3$

---

[1] This article was submitted by the authors in English.

(SMN) and with $SrSc_{1/2}Ta_{1/2}O_3$ (SST) were chosen. The $SrTiO_3$–SMN system, contrary to $SrTiO_3$–PMN, does not contain ferroelectrically active Pb^{2+} ions. A giant dielectric relaxation and no ferroelectric phase transition have been found in these solid solutions. Preliminary results of this study have been published elsewhere [25]. In the present paper, the giant relaxation in $(1 - x)SrTiO_3–xSMN$ and $(1 - x)SrTiO_3–xSST$ is studied in detail.

2. EXPERIMENTAL PROCEDURE

Ceramic samples of SMN, SST, and $(1 - x)SrTiO_3–xSMN$ and $(1 - x)SrTiO_3–xSST$ solid solutions were prepared by a standard ceramic technology. A stoichiometric mixture of strontium carbonate and of Ti, Mg, Nb, Sc, and Ta oxides of a special purity were used to prepare the appropriate compounds and solid solutions. Pure compounds of SMN and SST were synthesized through a columbite ($MgNb_2O_6$) and a wolframite ($ScTaO_4$) route, respectively, according to the reactions

$$MgO + Nb_2O_5 = MgNb_2O_6,$$

$$SrCO_3 + 1/3MgNb_2O_6 = SrMg_{1/3}Nb_{2/3}O_3 + CO_2;$$

$$Sc_2O_3\ Ta_2O_5 = 2ScTaO_4,$$

$$SrCO_3 + 1/2ScTaO_4 = SrSc_{1/2}Ta_{1/2}O_3 + CO_2.$$

The columbite and wolframite were synthesized at 1000 and 1200°C, respectively, for 20 h. After calcining the mixture at about 1200°C for several hours, the material was reground, and pellets were formed by pressing 9-mm diameter disks at 200 MPa. The final sintering was conducted at 1450°C for 1.5 h. X-ray diffraction study indicated that the samples had single-phase cubic perovskite structure for concentrations up to $x = 0.15$ in the case of SMN and more than $x = 0.2$ in the case of SST.

The symmetry of the $SrMg_{1/2}Nb_{2/3}O_3$ crystal is known [26] to be rhombohedral with the D_{3d}^3 space group with lattice parameters $a = 5.66$ and $c = 6.98$ Å. The parameter of the reduced perovskite pseudocubic unit cell is $a = 4.01$ Å. With the $SrTiO_3$ parameter $a = 3.905$ Å, one obtains a 2.7% difference in the lattice parameter between $SrTiO_3$ and SMN. At such a small difference, one might expect the possibility of obtaining the $SrTiO_3$–SMN solid solutions in the whole concentration range. However, experiment shows that there is a solubility limit, with the limiting SMN concentration lying between 0.15 and 0.20. This low solubility may be attributed to the difference in crystal structure.

The lattice parameter of the $SrTiO_3$–SMN solid solutions was measured, and it appeared that the lattice parameter follows a linear Vegard law between $a = 3.905$ ($SrTiO_3$) and 4.01 Å (SMN perovskite pseudocubic unit cell) with the slope $da/dx = 0.105$ Å.

The symmetry of the $SrSc_{1/2}Ta_{1/2}O_3$ crystal, as far as we know, has not been determined earlier, but the symmetry of the closely related compound $SrSc_{1/2}Nb_{1/2}O_3$ (SSN) is known [27] to be cubic with the O_h^5 space group; the compound has ordered perovskite structure with the doubled-unit-cell parameter $a = 8.057$ Å.

According to our measurements, the lattice parameter of SST is equal to $a = 8.054 \pm 0.003$ Å, which is very close to the SSN lattice parameter. This allows us to conclude that these compounds are isomorphic with the O_h^5 space group.

X-ray diffraction measurements demonstrated that the lattice parameter in $(1 - x)SrTiO_3–xSST$ solid solutions also follows a linear Vegard law between $a = 3.905$ ($SrTiO_3$) and 4.027 Å (SST perovskite reduced cell) with the slope $da/dx = 0.12$ Å. The lattice-parameter difference between $SrTiO_3$ and SST is 3.1%. Though this difference is a little bit higher than that between $SrTiO_3$ and SMN, this solid solution exists in a much broader range of SST concentrations due to the similarity in crystal structure.

All the samples had a density between 92 and 97% with regard to the theoretical x-ray density. Pure SMN and SST samples had a density of about 87%. The samples for dielectric measurements had a diameter of 8 mm and a thickness of 1–0.4 mm. For the measurements, the samples were coated with silver-burnt, gold-evaporated, and In–Ga-alloy electrodes. In all cases, we obtained absolutely the same (within small experimental errors) temperature and frequency dependences of the dielectric constant. The dielectric constant was measured using a Solartron SI 1260 Impedance/Gain-Phase Analyzer interfaced with a computer. The measurements were performed at frequencies between 10 Hz and 1 MHz in a temperature range between 4.2 and 300 K by cooling at a constant rate of 1 K/min. The amplitude of the ac electric field was 1 V/cm.

3. EXPERIMENTAL RESULTS AND ANALYSIS

The temperature dependence of the real part ε' of the dielectric constant for SMN and SST ceramic samples is shown in Fig. 1. For both materials, the dielectric constant as a function of temperature behaves as that of ordinary nonferroelectric dielectrics: the dielectric constant decreases with decreasing temperature with a slope of $(1/\varepsilon)d\varepsilon/dT = +0.8 \times 10^{-4}$ and $+1.0 \times 10^{-4}$ K^{-1} for SMN and SST, respectively. Similar values of $(1/\varepsilon)d\varepsilon/dT$ are characteristic of nonferroelectric oxides, alkali halides, and other conventional dielectrics. This is in great contrast with $SrTiO_3$, where the quantity $(1/\varepsilon)d\varepsilon/dT < 0$ and its absolute value in ceramics and single crystals is two and three orders of magnitude larger, respectively, as compared to $(1/\varepsilon)d\varepsilon/dT$ in SMN and SST. There is no frequency dispersion of the dielectric constant in both SMN and SST, as well as in

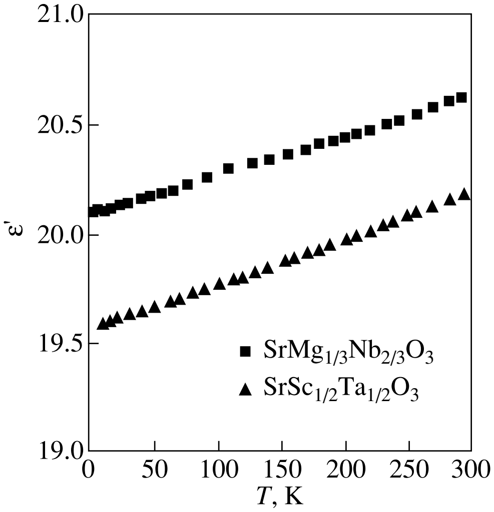

Fig. 1. Temperature dependence of the dielectric constant ε' in $SrMg_{1/3}Nb_{2/3}O_3$ and $SrSc_{1/2}Ta_{1/2}O_3$.

$SrTiO_3$, in the frequency range under study, 10 Hz–1 MHz. The situation drastically changes in the $SrTiO_3$–SMN and $SrTiO_3$–SST solid solutions. At the SMN concentration x(SMN) = 0.005, the first hints of a frequency dispersion (dielectric relaxation) appear both in the ε' and ε'' frequency spectra and in the ε' and ε'' temperature dependences. At $x = 0.01$, this relaxation becomes quite distinct (Fig. 2) and the relaxation features in this case are superimposed on the dielectric-constant temperature dependence characteristic of pure $SrTiO_3$ ceramics. It should be noted that the maximum value of the dielectric constant at 4.2 K in $SrTiO_3$ ceramic samples is usually several times less than that in single crystals; in our samples, this value is about 5000.

The relaxation strength attains a maximum at $x = 0.03$ (Fig. 3) and then decreases with increasing x. Along with this ("high-temperature") relaxation, which develops between 100 and 300 K, a low-temperature relaxation appears as x increases (Fig. 4) and the high value of the dielectric constant of $SrTiO_3$ becomes suppressed at $x \geq 0.03$. One can follow the evolution of this low-temperature relaxation in Fig. 5, where the ε'(T) dependences are shown at x between 0.05 and 0.15 at a frequency of 1 MHz.

Certainly, the dielectric relaxation reveals itself not only in the ε' and ε'' temperature dependences but also in the ε' and ε'' frequency spectra. As an example, these spectra are shown for the high-temperature relaxation at $x = 0.03$ in Fig. 6 and for the low-temperature relaxation at $x = 0.15$ in Fig. 7.

High-temperature dielectric relaxation was also observed in $(1 - x)SrTiO_3$–xSST solid solutions (Figs. 8, 9). Samples with $x = 0.01$, 0.05, and 0.1 were measured. The strongest relaxation occurs at $x = 0.05$, and the relaxation disappears at $x = 0.1$.

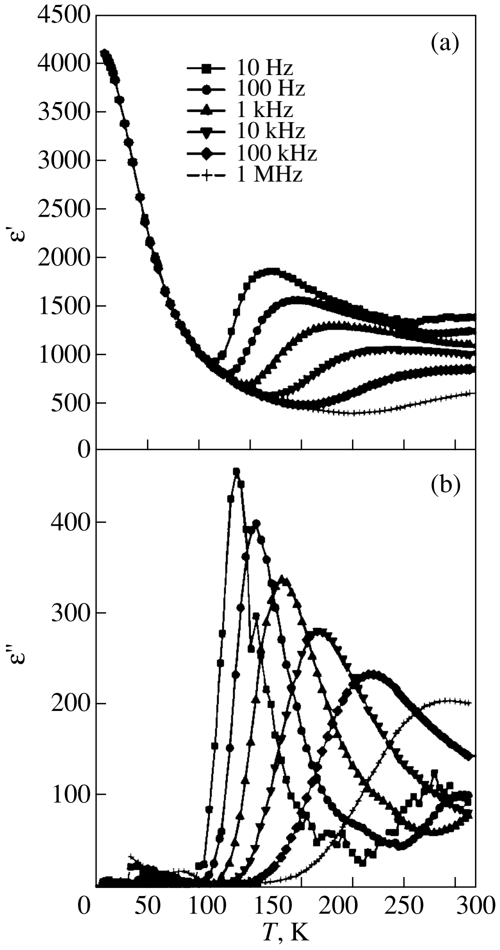

Fig. 2. Temperature dependence of (a) the real ε' and (b) imaginary ε'' parts of the dielectric constant of $(1 - x)SrTiO_3$–$xSrMg_{1/3}Nb_{2/3}O_3$ at $x = 0.01$.

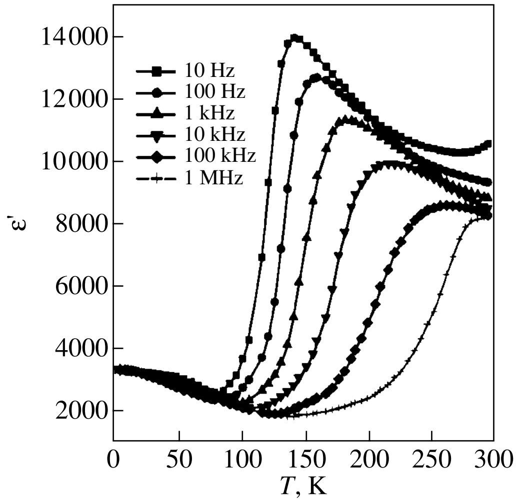

Fig. 3. Temperature dependence of ε' for $(1 - x)SrTiO_3$–$xSrMg_{1/3}Nb_{2/3}O_3$ at $x = 0.03$.

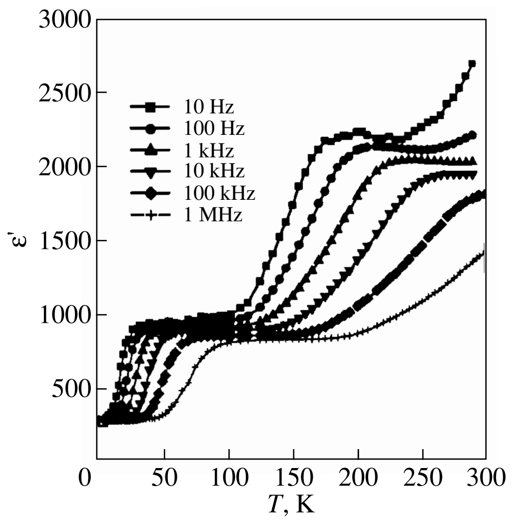

Fig. 4. Temperature dependence of ε' for $(1 - x)SrTiO_3$–$xSrMg_{1/3}Nb_{2/3}O_3$ at $x = 0.15$.

In $SrTiO_3$–SMN samples, the relaxation is much stronger than that in $SrTiO_3$–SST.

The most remarkable feature of the high-temperature relaxation in Figs. 2–4 and 6 is the very high value of the dielectric constant. At the SMN concentration x(SMN) = 0.03, the dielectric constant ε_0 attains a value of 14000 at 150 K and is roughly 1000 at 300 K. The relaxation strength $(\varepsilon_0 - \varepsilon_\infty)$ is very high and varied roughly proportional to $1/T$, as can be seen in Figs. 2 and 3.

All the temperature and frequency dependences in Figs. 2–9 look like classical textbook relaxation dependences. These dependences demonstrate a typical Debye relaxation behavior of the dielectric properties:

$$\varepsilon' = \varepsilon_\infty + \frac{(\varepsilon_0 - \varepsilon_\infty)}{1 + \omega^2\tau^2}, \qquad \varepsilon'' = \frac{(\varepsilon_0 - \varepsilon_\infty)\omega\tau}{1 + \omega^2\tau^2}. \tag{1}$$

Table 1. Activation energy U and relaxation time τ_0 for the high-temperature relaxation in $(1 - x)SrTiO_3$–$xSrMg_{1/3}Nb_{2/3}O_3$ and $(1 - x)SrTiO_3$–$xSrSc_{1/2}Ta_{1/2}O_3$

x		U, eV	τ_0, 10^{-11} s
SMN	0.01	0.23	5
	0.03	0.21	0.9
	0.05	0.23	0.3
	0.07	0.24	0.4
	0.1	0.26	0.2
	0.15	0.3	0.2
SST	0.01	0.27	1.5
	0.05	0.29	0.7

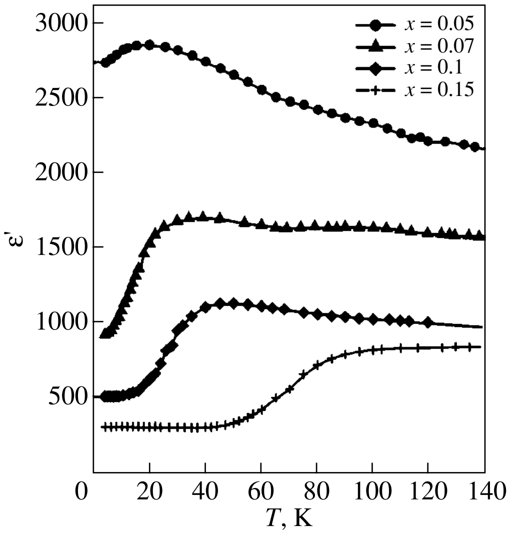

Fig. 5. Temperature dependence of ε' for $(1 - x)SrTiO_3$–$xSrMg_{1/3}Nb_{2/3}O_3$ at a frequency of 1 MHz.

From the experimental data, it follows that the relaxation time τ obeys an Arrhenius relation,

$$\tau = \tau_0 \exp(U/kT). \tag{2}$$

Fitting the experimental data to Eqs. (1) and (2), one obtains U and τ_0, which are presented in Tables 1 and 2.

In Table 1, one can see that, in general, there is a small but systematic increase in the activation energy U with increasing x. Interestingly, a similar behavior of $U(x)$ was observed in the case of $SrTiO_3$ doped with trivalent rare-earth ions [22].

A detailed analysis shows that the experimental results can be described better by a Cole–Cole complex function instead of Eq. (1):

$$\varepsilon^* = \varepsilon_\infty + \frac{(\varepsilon_0 - \varepsilon_\infty)}{1 + (i\omega\tau)^\beta}, \tag{3}$$

where $\varepsilon^* = \varepsilon' - i\varepsilon''$.

As an example, one can refer to the Cole–Cole graph at x(SMN) = 0.03 and various temperatures in Fig. 10. The best fit of the experimental data to Eq. (3) is obtained with $\beta = 0.7$.

Fitting the experimental data to Eq. (3) does not significantly change the values of U and τ_0 presented in Table 1.

Concerning the low-temperature relaxation, we should note that the experimental data can be fairly well fitted to a simple Arrhenius relation [Eq. (2)] only at temperatures $T \geq 20$ K. The best fit in the whole temperature range can be obtained using a Vogel–Fulcher relation,

$$\tau = \tau_0 \exp[U/k(T - T_g)], \tag{4}$$

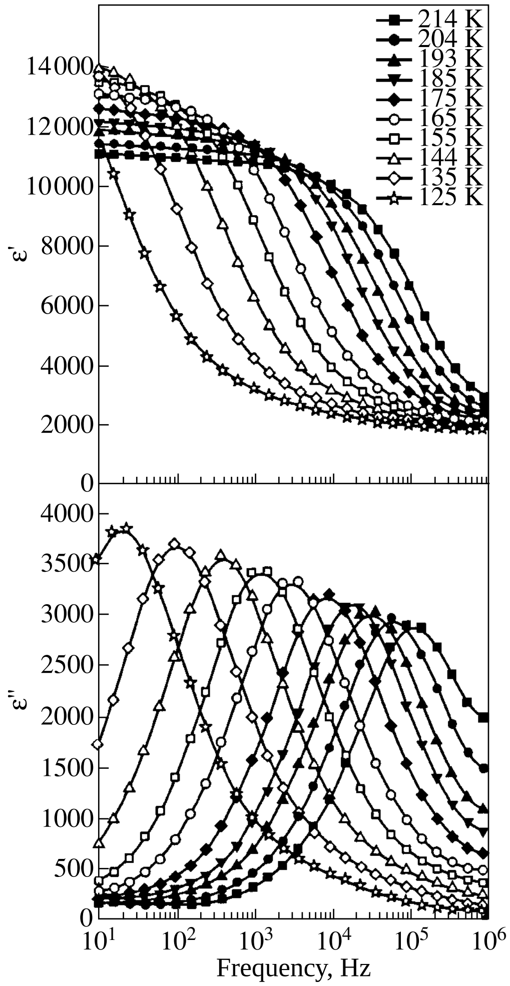

Fig. 6. Frequency spectra of ε' and ε'' for $(1 - x)SrTiO_3$–$xSrMg_{1/3}Nb_{2/3}O_3$ at $x = 0.03$. (The high-temperature relaxation at various temperatures.)

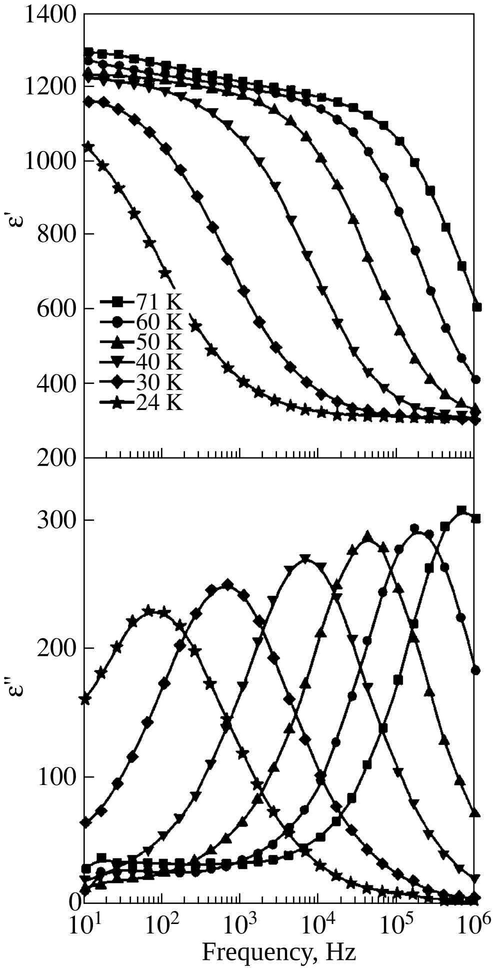

Fig. 7. Frequency spectra of ε' and ε'' for $(1 - x)SrTiO_3$–$xSrMg_{1/3}Nb_{2/3}O_3$ at $x = 0.15$. (The low-temperature relaxation at various temperatures.)

with $U \approx 0.05$ eV and $T_g < 0$. Since such values of T_g have no physical meaning, we used the Arrhenius relation with the U and τ_0 values given in Table 2.

We also tried to observe $P(E)$ hysteresis loops in our samples at low temperatures. This attempt failed, and we may conclude that there are no ferroelectric phase transitions in $SrTiO_3$–SMN and $SrTiO_3$–SST solid solutions.

4. DISCUSSION

Thus, in the $(1 - x)SrTiO_3$–xSMN and $(1 - x)SrTiO_3$–xSST solid solutions, we observed strong high-temperature (150–300 K) dielectric relaxation; much smaller low-temperature (20–90 K) relaxation was also observed in the case of $SrTiO_3$–SMN. As mentioned above, the observed high-temperature relaxation in $SrTiO_3$–SMN is characterized by a very high dielectric constant ε_0 and very high relaxation strength $(\varepsilon_0 - \varepsilon_\infty)$, which at $x = 0.03$ and a frequency of 10 Hz attain 14000 and 12000, respectively. Such a large value of ε_0 (larger than the dielectric constant at 4.2 K in nominally pure $SrTiO_3$ ceramic samples) is surprising. These values are, to our knowledge, the highest yet reported for $SrTiO_3$ with heterovalent impurities in this temperature range. In the literature, there are only two examples [16, 22] of a very high value of ε_0 and $(\varepsilon_0 - \varepsilon_\infty)$, which are close to but less than that mentioned above. One of

Table 2. Activation energy U and relaxation time τ_0 for the low-temperature relaxation in $(1 - x)SrTiO_3$–$xSrMg_{1/3}Nb_{2/3}O_3$

x	U, eV	τ_0, 10^{-9} s
0.07	0.02	0.3
0.1	0.01	0.2
0.15	0.02	15

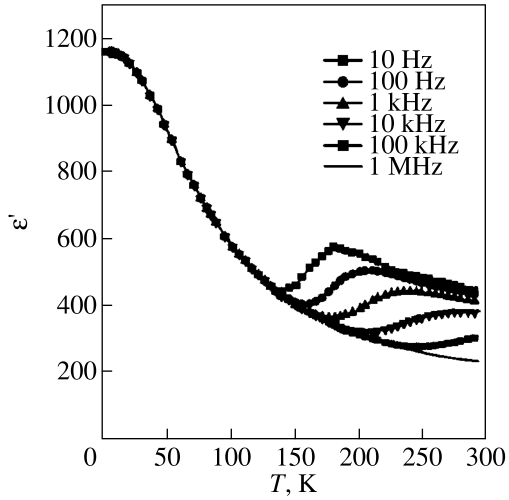

Fig. 8. Temperature dependence of ε' for $(1 - x)SrTiO_3$–$xSrSc_{1/2}Ta_{1/2}O_3$ at $x = 0.01$.

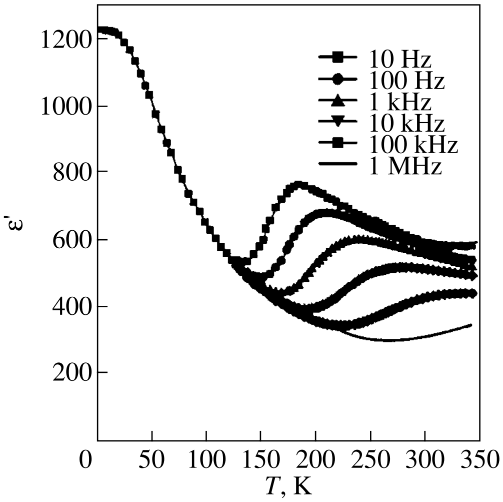

Fig. 9. Temperature dependence of ε' for $(1 - x)SrTiO_3$–$xSrSc_{1/2}Ta_{1/2}O_3$ at $x = 0.05$.

these examples is $SrTiO_3$: 2 at. % Er with $\varepsilon_0 = 10000$ and $(\varepsilon_0 - \varepsilon_\infty) = 9400$ [22].

Very strong dielectric relaxation has also been observed in another incipient ferroelectric, $KTaO_3$. In $KTaO_3$ with 2.3 at. % Nb (KTN) and 0.055 at. % Ca, dielectric relaxation was measured between about 50 and 100 K, with ε_0 being about 16000 [28]. A similar value of ε_0 in the same temperature range was found in $KTaO_3$ with 2.5% Nb and 0.1% Li (KLTN) [29]. However, in both cases [28, 29], the dielectric relaxation develops close to a ferroelectric phase transition, which certainly affects the relaxation strength strongly.

Very large values of the dielectric constant are usually observed in $SrTiO_3$ at ferroelectric phase transitions induced by impurities at an impurity concentration x near the critical concentration x_c. For example, $\varepsilon_m = 110000$ in $SrTiO_3$: Ca single crystals at $x = 0.01$ [5] and $\varepsilon_m = 170000$ in $SrTiO_3$: ^{18}O single crystals at $x = 0.37$ [30]. In ceramic samples of $Sr_{1-x}Ba_xTiO_3$, according to our measurements, $\varepsilon_m = 35000$ at $x = 0.02$. However, in the systems under study ($SrTiO_3$–SMN and $SrTiO_3$–SST), there are no ferroelectric phase transitions and the observed giant dielectric constant in them should be determined by some other mechanisms.

In discussing possible mechanisms of the giant dielectric relaxation, the first question to be answered is what positions Nb^{5+} and Mg^{2+} occupy in the $SrTiO_3$ host lattice. The Nb^{5+} ions should substitute for the Ti^{4+} host ions due to the size and charge factors. As for the Mg^{2+} ions, they can occupy, in principle, either Sr^{2+} or Ti^{4+} positions. Two experimental facts prove the latter possibility. First, the Mg^{2+} ions being added to $SrTiO_3$ alone (in the form of $MgTiO_3$) do not lead to any dielectric relaxation. Second, in the $SrTiO_3$–SMN system, as well as in $SrTiO_3$–SST, the lattice constant follows the linear Vegard law between $SrTiO_3$ and SMN (SST). Thus, we make the conclusion that the Mg^{2+} and Nb^{5+} (or Sc^{3+} and Ta^{5+}) ions substitute for the host Ti^{4+} ions in $SrTiO_3$. Though the impurity ions have a charge different from that of the host Ti^{4+} ions, they are "self-compensating;" i.e., the excess charge of two Nb^{5+} ions is compensated by the deficient charge of one Mg^{2+} ion, and their average charge is equal to the charge of the host Ti^{4+} ion. A similar situation occurs in $SrTiO_3$–SST, where the excess charge of a Ta^{5+} ion is compensated by the deficient charge of an Sc^{3+} ion.

However, at small x, when the Mg^{2+} and Nb^{5+} ions (Sc^{3+} and Ta^{5+}) are far from each other, the Mg^{2+} ion does not "know" that somewhere there are Nb^{5+} ions with compensating charge (the same is the case for the Nb^{5+} ions). Therefore, the impurity ions need some

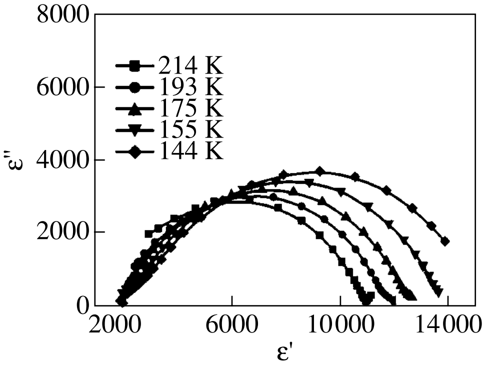

Fig. 10. Cole–Cole plot for $(1 - x)SrTiO_3$–$xSrMg_{1/3}Nb_{2/3}O_3$ at $x = 0.03$. (The high-temperature relaxation at various temperatures.)

additional local charge compensation. This hypothesis is a basic point for explanation of dielectric relaxation in the systems under study. We believe that without this hypothesis of the additional local charge compensation, it is impossible to suggest any models for the observed dielectric relaxation. The additional local charge compensation may proceed through the formation of either free charge carriers or the host ion vacancies in the following ways.

Substituting for the host Ti^{4+} ion, Nb^{5+} (and Ta^{5+}) serves as a donor and Mg^{2+} (and Sc^{3+}) acts as an acceptor. Being fully ionized, an Nb^{5+} and an Mg^{2+} provide one electron and two holes, respectively. If the electron and hole mobilities are equal, the electrical conductivity will be compensated and the sample will exhibit a high resistivity. In the opposite case, the resistivity may be relatively low.

A second possible mechanism of local charge compensation is the formation of one Sr^{2+} vacancy (V_{Sr}) per two Nb^{5+} ions and of one O^{2-} vacancy (V_O) per Mg^{2+} ion. In the case of SST, one Sr^{2+} vacancy should be formed per two Ta^{5+} ions, and one O^{2-} vacancy is formed per two Sc^{3+} ions.

These two means of local charge compensation may lead to two mechanisms of the high-temperature (150–300 K) dielectric relaxation.

High electrical conductivity may be a reason for the Maxwell–Wagner relaxation in ceramic samples, and it is well known that strong dielectric relaxation in semiconducting ceramic samples can always be attributed to the Maxwell–Wagner mechanism. This relaxation is due to the different properties of ceramic grains and grain boundaries (see [31] and references therein). In a very simplified model, the grain is considered as a resistor R with the grain boundary as an insulating layer with the capacity C in series with the resistor. A ceramic sample represents a system of such RC elements, and the relaxation time (which is the effective Maxwell relaxation time of the whole system) is given by

$$\tau = 8.8 \times 10^{-14}(\varepsilon_{\text{eff}}/\sigma), \qquad (5)$$

where the relaxation time τ is in seconds and the electrical conductivity σ is in $(\Omega\ \text{cm})^{-1}$.

The temperature dependence of conductivity $\sigma = en\mu$ is mainly determined by the temperature dependence of the charge-carrier concentration

$$n = n_0 \exp(-U/kT). \qquad (6)$$

The Maxwell–Wagner relaxation mechanism can give a very high value of ε_{eff} at $\omega\tau < 1$.

The effective dielectric constant of a ceramic sample is approximately given by [31]

$$\varepsilon_{\text{eff}} \cong (d_1/d_2)\varepsilon_2, \qquad (7)$$

where d_1 is the grain diameter, d_2 is the thickness of the grain boundary, and ε_2 is the dielectric constant of the grain boundary. With $d_1/d_2 \cong 10^2$ and $\varepsilon_2 \cong 10^2$, Eq. (7) gives $\varepsilon_{\text{eff}} \cong 10^4$.

The Maxwell–Wagner mechanism was studied in detail for $SrTiO_3$ ceramics in [31]. Ceramic samples of stoichiometric $SrTiO_3$ and those with up to 1% excess of Ti were used. It was shown that the dielectric constant reached a value of about 10^4 at 150°C at a frequency of 10^{-2} Hz and that this value of the dielectric constant was due to the Maxwell–Wagner relaxation. Temperature-dependent maxima in $\varepsilon''(\omega)$ were observed; they shifted to higher frequencies with increasing temperature. At 150°C, $\varepsilon''(\omega)$ attained a maximum value at a frequency of about 1 Hz. Assuming reasonable (though rather arbitrary) values of the parameters ($d_1 = 10$, $d_2 = 0.1$ μm, $\varepsilon_2 = 200$, carrier concentration $n_0 = 10^{18}$ cm^{-3}, mobility $\mu = 6$ cm^2/V s, activation energy $U = 0.7$ eV), the authors of [31] obtained satisfactory agreement between the experimental results and the Maxwell–Wagner model.

The value of $U = 0.7$ eV is determined by the energy levels of donors or acceptors in the band gap [31]. This energy is quite typical for $SrTiO_3$. To determine whether the relaxation in our samples that develops in the 150–300 K range can be described by the Maxwell–Wagner model, we have to set this energy equal to $U \sim 0.25$ eV. Then, using Eqs. (5)–(7) with d_1, d_2, and ε_2 taken from [31] and the charge-carrier mobility from [32], we find that the Maxwell–Wagner mechanism can satisfactorily describe the experimental results; the conductivity and carrier concentration at 150 K are $\sigma \sim 10^{-5}\ (\Omega\ \text{cm})^{-1}$, $n \sim 10^{12}$ cm^{-3}, and $n_0 \sim 5 \times 10^{20}$ cm^{-3}, and the quantities σ and n vary exponentially with temperature, following Eq. (6) with $U = 0.25$ eV. Note that at $x = 0.03$, the SMN concentration is $n \cong 5 \times 10^{20}$ cm^{-3}, which is not quite consistent with the value of n_0. Nevertheless, it is possible to conclude that the high-temperature dielectric relaxation can be associated with the Maxwell–Wagner mechanism.

However, the following experimental facts contradict the Maxwell–Wagner model of the dielectric relaxation in the temperature range 150–300 K.

According to Eq. (7), the dielectric constant is independent of temperature, whereas the experiment demonstrates a $1/T$ dependence.

At about 250 K and a frequency of 10 Hz, one observes an increase in ε' with increasing temperature, which may be the onset of an additional relaxation, which is especially distinct at $x = 0.15$ (Fig. 4). A crude estimate shows that for this relaxation, $U \geq 0.5$ eV. This relaxation can be ascribed to the Maxwell–Wagner model. Though nothing forbids the occurrence of two Maxwell–Wagner relaxations in different temperature regions (say, at $T > 300$ K and $T < 300$ K) in one sample, such an event seems to be rather accidental.

The observed dependence of the activation energy U on concentration x is difficult to explain in terms of the

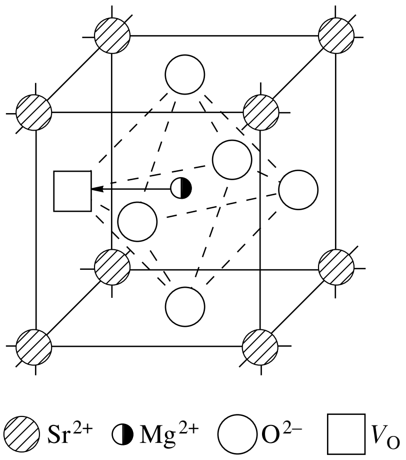

Fig. 11. Structure of the [Mg_{Ti}^{2+}–V_O] center.

Maxwell–Wagner mechanism, as has been emphasized earlier [22].

Application of a dc electric field $E = 1$ kV/cm does not change the relaxation under discussion but leads to great changes in ε'' and $\tan\delta$ at higher temperatures. At the SMN concentration $x = 0.05$, $T = 275$ K, and a frequency of 1 kHz, ε'' increases by more than an order of magnitude under the action of the dc electric field.

The Maxwell–Wagner mechanism of the dielectric relaxation in $SrTiO_3$ with rare-earth ions [16, 17, 22] in the same temperature range as discussed above has also been denied. In $SrTiO_3$:La ceramics, only relaxation at temperatures around 200°C has been found to be associated with the Maxwell–Wagner mechanism [17]. Relaxation in the range 150–300 K was ascribed to the formation of the host ion vacancies. One of the arguments against the Maxwell–Wagner mechanism for this relaxation was that the relaxation holds even in single crystals [17].

Now, we will discuss an alternative model of the giant dielectric relaxation based on the local charge compensation of impurities by the host ion vacancies as described above.

Due to electrostatic interaction, the most favorable configuration is that in which the impurity ions and related vacancies are nearest neighbors. As a result, the following impurity centers are formed:

$$[2Nb_{Ti}^{5+} - V_{Sr}] \text{ and } [Mg_{Ti}^{2+} - V_O] \text{ in } SrTiO_3\text{–SMN},$$

$$[2Ta_{Ti}^{5+} - V_{Sr}] \text{ and } [2Sc_{Ti}^{3+} - V_O] \text{ in } SrTiO_3\text{–SST}.$$

It is widely accepted that in the ABO_3 perovskites, the mobility of the oxygen vacancies is higher than that of the A ions [33]; therefore, we shall discuss below only the centers with the oxygen vacancies, namely, [Mg_{Ti}^{2+}–V_O] and [$2Sc_{Ti}^{3+}$–V_O]. The [Mg_{Ti}^{2+}–V_O] complex is shown in Fig. 11. The Mg^{2+} ion is in the center of the oxygen octahedron, in which one of six oxygen ions is absent (V_O). The Mg^{2+}–O^{2-} distance is $a/2$ (a is the lattice parameter), and the distance between the nearest neighbor O^{2-} ions is $a/\sqrt{2}$. The dipole moment $p = 2ea/2 = ea = 18.7 \times 10^{-18}$ CGSE units = 18.7 D is associated with this center. Thermally activated reorientation of this dipole moment via the vacancy jumping (or, more correctly, the oxygen ion jumping through the oxygen vacancy) is suggested as the origin of the dielectric relaxation with $U = 0.21$–0.3 eV and $\tau_0 = 10^{-11}$–10^{-12} s. These relaxation parameters seem to be quite reasonable. Indeed, in the model under discussion, $\tau_0^{-1} = \omega_0$ should be on the order of the lattice Debye frequencies. As for the activation energy, $U \sim 0.25$ eV seems to be too low, at first sight, since the activation energy for the oxygen vacancy diffusion in the perovskite is not less than 1 eV [34, 35]. However, it is well known that the activation energy for the oxygen-ion movement near a defect (as in our case) can be much lower. For example, in $KTaO_3$, where the activation energy for dc ionic conductivity is also not less than 1 eV, the activation energy for an oxygen vacancy hopping around a defect is very low: $U = 0.08$, 0.11, and 0.36 eV for the defect centers [Ca_{Ta}^{2+}–V_O], [Mn_{Ta}^{2+}–V_O], and [Co_{Ta}^{2+}–V_O], respectively (see [28] and references therein). Even for the reorientation of the Fe^{3+}–O_i^{2-} center in $KTaO_3$ with an interstitial oxygen ion O_i^{2-}, the activation energy is as low as 0.34 eV [36, 37].

One may suppose that a similar situation takes place in $SrTiO_3$; in this case, the value of $U = 0.21$–0.3 eV seems to be quite reasonable. It is important to note that an activation energy around $U = 0.25$ eV was found earlier to be characteristic of the dielectric relaxation in $SrTiO_3$ ceramics doped with Bi [11, 12], Mn [20], La [17, 20–22], and other trivalent rare-earth ions [22]. The dielectric relaxation in all these systems was ascribed to the host ion vacancies.

In the model under discussion, the relaxation strength ($\varepsilon_0 - \varepsilon_\infty$) decreases with increasing concentration x of SMN, since the Mg^{2+} and Nb^{5+} ions are progressively closer to each other and their charge self-compensation takes place instead of their compensation by the vacancies. If the observed dielectric relaxation is due to this mechanism, the relaxation strength $\varepsilon_0 - \varepsilon_\infty$ should first increase with increasing x, then reach a maximum at a certain value of x, and then decrease and completely vanish at large x. Exactly this behavior is demonstrated by the high-temperature relaxation in our samples.

Another important point is the unusually high relaxation strength $\varepsilon_0 - \varepsilon_\infty$. Let us estimate the relaxation strength in the framework of the proposed model. An electric field E induces a polarization P due to the reorientation of $[\mathrm{Mg}_{\mathrm{Ti}}^{2+}-V_{\mathrm{O}}]$ complexes with dipole moment $p = ea$ and concentration n:

$$P = (p^2 n/kT)E. \tag{8}$$

Therefore, the dielectric susceptibility is

$$\chi = p^2 n/kT. \tag{9}$$

For $x = 0.03$, assuming that all the Mg^{2+} impurity ions form $[\mathrm{Mg}_{\mathrm{Ti}}^{2+}-V_{\mathrm{O}}]$ centers, we obtain (in CGSE units) $\chi \cong 10$ and $\varepsilon \cong 4\pi\chi \cong 10^2$. This value is too small to explain the experimental results. However, the local electric field E_{loc} should be taken in Eq. (8) instead of the applied electric field E.

As a crude estimation of the local field, one can use the expression [38]

$$E_{\mathrm{loc}} = ((\varepsilon_\infty + 2)/3)E. \tag{10}$$

For the dielectric relaxation at $x = 0.03$, we have $\varepsilon_\infty \approx 2000$ (Fig. 6); i.e., the local electric field is almost three orders of magnitude larger than the applied field. As a result, one obtains $\varepsilon \approx 2.5 \times 10^4$. Certainly, this value should be considered as an upper limit and only demonstrates that the proposed model can provide a very high dielectric constant.

It is interesting to note that from experiment [37] it follows that the local electric field at the $[\mathrm{Fe}_{\mathrm{K}}^{3+}-\mathrm{O}_i]$ center in $\mathrm{KTaO_3}$:Fe is an order of magnitude larger than the applied field. This means that the local field in $\mathrm{SrTiO_3}$ is much larger than that in $\mathrm{KTaO_3}$.

Thus, we may say that the proposed model is consistent with the experimental data: the model can, in principle, give a high value of ε_0; the experimental $\varepsilon_0 \propto 1/T$ temperature dependence is described by Eq. (9); and an experimental activation energy U of about 0.25 eV is in the range of typical values of the activation energy for an oxygen vacancy jumping around an impurity ion in perovskites.

Along with the high-temperature relaxation in $\mathrm{SrTiO_3}$–SMN, a low-temperature relaxation is observed with $U \sim 0.01$–0.02 eV and $\tau_0 \sim 10^{-8}$–10^{-10} s. We believe that such an activation energy is too low for the ion movement and should be attributed to the electronic system. The following model may be suggested to explain the low-temperature relaxation.

Some part of the Nb^{5+} ions is not compensated with the Sr^{2+} vacancies but forms a new center $[\mathrm{Nb}_{\mathrm{Ti}}^{5+}-\mathrm{Ti}^{3+}]$ (Fig. 12). The Nb^{5+} ion is surrounded by six Ti^{4+} ions, and one of them is in the Ti^{3+} state; i.e., there is an electron localized on the Ti ion. This electron jumps over six Ti^{4+} ions. The distance between the Nb and Ti ions and between the Ti ions is a and $a\sqrt{2}$, respectively. The activation energy for this electron hopping can be sufficiently low. The excess electron polarizes the lattice and hops as a "polarization-dressed" electron, i.e., as a polaron. In such a case, an accepted point of view [39] is that the relaxation time τ_0 should be in the range between the characteristic lattice times ($\tau_0 = \omega_0^{-1} \cong 10^{-12}$–$10^{-13}$ s) and electronic times (10^{-14}–10^{-15} s). However, we believe that for a polaron bound to the impurity ion ($\mathrm{Nb}_{\mathrm{Ti}}^{5+}$ in our case), this relaxation time can be much longer, because it can take much time for the lattice to come to the equilibrium after the electron hopping from one Ti ion to another. Indeed, for example, in $\mathrm{TiO_2}$ reduced crystals, three relaxation processes associated with polaron hopping were observed [40] with activation energies between 10^{-3} and 10^{-2} eV and τ_0 between 10^{-8} and 10^{-6} s. Thus, our values of U and τ_0 seem to be reasonable.

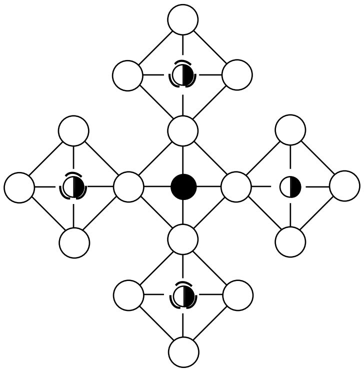

● Nb^{5+} ◑ Ti^{3+}
◒ Ti^{4+} (possible positions of Ti^{3+})

Fig. 12. Structure of $[\mathrm{Nb}_{\mathrm{Ti}}^{5+}-\mathrm{Ti}^{3+}]$ center.

Now, let us turn to the $\mathrm{SrTiO_3}$–SST solid solution. The high-temperature relaxation is also observed in this system, but the relaxation strength is much smaller than that for the $\mathrm{SrTiO_3}$–SMN. The $[2\mathrm{Sc}_{\mathrm{Ti}}^{3+}-V_{\mathrm{O}}]$ center has a rather complicated structure to provide easy movement of the oxygen vacancy. However, some small part of these centers can exist as a simple $[\mathrm{Sc}_{\mathrm{Ti}}^{3+}-V_{\mathrm{O}}]$ center. Therefore, the relaxation mechanism will be the same as for the $[\mathrm{Mg}_{\mathrm{Ti}}^{2+}-V_{\mathrm{O}}]$ centers but with a much smaller relaxation strength due to the small concentration of the $[\mathrm{Sc}_{\mathrm{Ti}}^{3+}-V_{\mathrm{O}}]$ centers.

When discussing the dielectric relaxation associated with the thermally activated movement of the host ion vacancies, one should certainly bring to mind Skanavi's relaxation model [11, 12]. This model postulates that the Sr^{2+} ion vacancies distort the neighboring oxygen octahedra and, as a result, several off-center equilibrium positions for the Ti^{4+} ion appear. The dielectric relaxation in this model is associated with thermally activated motion of the Ti^{4+} ion between these equivalent off-center positions. In $SrTiO_3$ doped with La [17], La and Mn [20], and with a wide range of the rare-earth ions [22], the observed dielectric relaxation was explained in terms of Skanavi's model. However, this purely qualitative model is difficult to accept, since it is doubtful that an asymmetric distortion of the oxygen octahedron can lead to several equivalent off-center positions for the Ti^{4+} ion. Theoretical microscopic calculations must be made to support this model. This is why we did not discuss this model as a possible reason for the dielectric relaxation. Furthermore, the authors of a recent paper [16] argue that the experimental data on the dielectric relaxation in $SrTiO_3$ are not consistent with Skanavi's model.

In conclusion, in $SrTiO_3$–$SrMg_{1/3}Nb_{2/3}O_3$ and in $SrTiO_3$–$SrSc_{1/2}Ta_{1/2}O_3$ solid solutions, the giant high-temperature (100–350 K) dielectric relaxation and a not so strong, but well-developed, low-temperature (20–90 K) relaxation were observed instead of a ferroelectric phase transition induced by impurities in the incipient ferroelectric and quantum paraelectric $SrTiO_3$. This means that not any impurity can disturb the stability of the paraelectric phase in $SrTiO_3$ and induce a ferroelectric phase transition (otherwise, one could speak about an "impurity trigger effect"). In all the incipient ferroelectric-based solid solutions studied earlier [3–9], the second-end members of the solid solutions were ferroelectrics ($BaTiO_3$, $PbTiO_3$, $CdTiO_3$, $PbMg_{1/3}$, $Nb_{2/3}O_3$ in $SrTiO_3$ and $LiTaO_3$, $KNbO_3$ in $KTaO_3$) or at least incipient ferroelectrics such as $KTaO_3$ and $CaTiO_3$ in $SrTiO_3$ [5, 41, 42]. In all these cases, a transition to the ferroelectric (or polar) phase inevitably occurred. In our case, SMN and SST are not ferroelectrics, which may be the reason for the absence of a ferroelectric phase transition in their solid solutions with $SrTiO_3$. This point of view may be supported by the data from [22], where $SrTiO_3$ doped with all the rare-earth ions except promethium was studied and no evidence of the ferroelectric state was found. This result may imply that, in the incipient ferroelectrics with impurities, the ferroelectric phase transition is not due to the impurity-trigger effect but is associated with a Vegard-type law for the $T_c(x)$ dependence at medium and large values of the concentration x of the second-end member of the incipient ferroelectric-based solid solution. At low x, the transition to the quantum ferroelectric state occurs with no ferroelectric phase transition at x values lower than the critical concentration x_c.

Returning to the dielectric relaxation in the solid solutions under study, one may conclude that both the Maxwell–Wagner mechanism and the reorienting dipole-center model can explain the main features of the high-temperature relaxation. There are some arguments in favor of the model of the reorienting dipole centers, but this conclusion is anything but final since, using only dielectric measurements, one cannot determine the structure of defect centers.

Finally, and most importantly, both models are founded on the hypothesis of the additional local charge compensation of the heterovalent *B* ions by the host ion vacancies or by free charge carriers. This scenario seems to be inevitable for explaining the dielectric relaxation in the solid solutions under study. However, in this context, more experimental proofs are desirable. Such proofs might be provided by experiments with $SrTiO_3$–SMN single crystals and/or using $SrMn_{1/2}Nb_{2/3}O_3$ instead of $SrMg_{1/3}Nb_{2/3}O_3$ to obtain the possibility of ESR study of Mn^{2+} centers. These and other more complicated experiments are now in progress.

In connection with the model of the additional local charge compensation, it is worth noting that the question of whether this charge compensation can play any role in dielectric properties of disordered relaxor ferroelectrics such as $PbMg_{1/3}Nb_{2/3}O_3$ (PMN) is not ruled out.

ACKNOWLEDGMENTS

V.V.L. would like to thank O.E. Kvyatkovskiĭ and V.K. Yarmarkin for useful discussions.

At the Ioffe Institute, this work was partly supported by the program "Physics of Solid State Nanostructures" and NWO, grant no. 16-04-1999. E.P.S. is grateful to Sächsisches Staatsministerium für Wissenschaft und Kunst for financial support.

REFERENCES

1. K. A. Müller and H. Burkhard, Phys. Rev. B **19**, 3593 (1979).
2. H. Uwe and T. Sakudo, Phys. Rev. B **13**, 271 (1976).
3. V. V. Lemanov, Fiz. Tverd. Tela (St. Petersburg) **39**, 1645 (1997) [Phys. Solid State **39**, 1468 (1997)].
4. V. V. Lemanov, Ferroelectrics **226**, 133 (1999).
5. J. G. Bednorz and K. A. Müller, Phys. Rev. Lett. **52**, 2289 (1984).
6. V. V. Lemanov, E. P. Smirnova, E. A. Tarakanov, and P. P. Syrnikov, Phys. Rev. B **54**, 3151 (1996).
7. V. V. Lemanov, E. P. Smirnova, and E. A. Tarakanov, Fiz. Tverd. Tela (St. Petersburg) **39**, 714 (1997) [Phys. Solid State **39**, 628 (1997)].
8. M. E. Guzhva, V. V. Lemanov, P. A. Markovin, and T. A. Shaplygina, Ferroelectrics **218**, 93 (1998).
9. V. V. Lemanov, A. V. Sotnikov, E. P. Smirnova, *et al.*, Fiz. Tverd. Tela (St. Petersburg) **41**, 1091 (1999) [Phys. Solid State **41**, 994 (1999)].
10. Chen Ang, Zhi Yu, P. M. Vilarinho, and J. L. Baptista, Phys. Rev. B **57**, 7403 (1998).
11. G. I. Skanavi and E. N. Matveeva, Zh. Éksp. Teor. Fiz. **30** (6), 1047 (1956) [Sov. Phys. JETP **3**, 905 (1957)].

12. G. I. Skanavi, I. M. Ksendzov, V. A. Trigubenko, and V. G. Prokhvatilov, Zh. Éksp. Teor. Fiz. **33** (2), 321 (1957) [Sov. Phys. JETP **6**, 250 (1958)].
13. Chen Ang, J. F. Scott, Zhi Yu, *et al.*, Phys. Rev. B **59**, 6661 (1999).
14. Chen Ang, Zhi Yu, J. Hemberger, *et al.*, Phys. Rev. B **59**, 6665 (1999).
15. Chen Ang, Zhi Yu, P. Lunkenheimer, *et al.*, Phys. Rev. B **59**, 6670 (1999).
16. Chen Ang, Zhi Yu, and L. E. Cross, Phys. Rev. B **62**, 228 (2000).
17. T. Y. Tien and L. E. Cross, Jpn. J. Appl. Phys. **6**, 459 (1967).
18. J. Bouwma, K. J. De Vries, and A. J. Burggraaf, Phys. Status Solidi A **35**, 281 (1976).
19. Chen Ang and Zhi Yu, J. Appl. Phys. **71**, 6025 (1992).
20. E. Iguchi and K. J. Lee, J. Mater. Sci. **28**, 5809 (1993).
21. Zhi Yu, Chen Ang, and L. E. Cross, Appl. Phys. Lett. **74**, 3044 (1999).
22. D. W. Johnson, L. E. Cross, and A. Hummel, J. Appl. Phys. **41**, 2828 (1970).
23. Chen Ang, J. R. Jurado, Zhi Yu, *et al.*, Phys. Rev. B **57**, 11858 (1998).
24. Chen Ang, Zhi Yu, Zhi Jing, *et al.*, Phys. Rev. B **61**, 3922 (2000).
25. V. V. Lemanov, E. P. Smirnova, A. V. Sotnikov, and M. Weihnacht, Appl. Phys. Lett. **77**, 4205 (2000).
26. F. S. Galasso, *Structure, Properties and Preparation of Perovskite-Type Compounds* (Pergamon, Oxford, 1969).
27. *Powder Diffraction File, Inorganic Phases* (International Center for Diffraction Data, Park Lane, Swarthmore, 1989).
28. G. A. Samara and L. A. Boatner, Phys. Rev. B **61**, 3889 (2000).
29. V. A. Trepakov, M. E. Savinov, S. Kapphan, *et al.*, Ferroelectrics **239**, 305 (2000).
30. M. Itoh and R. Wang, Appl. Phys. Lett. **76**, 221 (2000).
31. H. Neumann and G. Arlt, Ferroelectrics **69**, 179 (1986).
32. H. P. R. Frederikse and W. R. Hosler, Phys. Rev. **161**, 822 (1967).
33. A. Seuter, Philips Res. Rep. Suppl. **3**, 1 (1974).
34. G. Arlt and H. Neumann, Ferroelectrics **87**, 109 (1988).
35. I. Sakaguchi, H. Honeda, S. Hishita, *et al.*, Nucl. Instrum. Methods Phys. Res. B **94**, 411 (1994).
36. V. S. Vikhnin, A. S. Polkovnikov, H. J. Reyher, *et al.*, J. Korean Phys. Soc. **32**, S486 (1998).
37. L. S. Sochava, V. E. Bursian, and A. G. Razdobarin, Fiz. Tverd. Tela (St. Petersburg) **42**, 1595 (2000) [Phys. Solid State **42**, 1640 (2000)].
38. C. Kittel, *Introduction to Solid State Physics* (Wiley, New York, 1976; Nauka, Moscow, 1978).
39. M. Fisher, A. Lahmar, M. Maglione, *et al.*, Phys. Rev. B **49**, 12451 (1994).
40. L. A. K. Dominik and R. K. MacCrone, Phys. Rev. **163**, 756 (1967).
41. V. V. Lemanov, V. A. Trepakov, P. P. Syrnikov, *et al.*, Fiz. Tverd. Tela (St. Petersburg) **39**, 1838 (1997) [Phys. Solid State **39**, 1642 (1997)].
42. V. V. Lemanov, A. V. Sotnikov, E. P. Smirnova, *et al.*, Solid State Commun. **110**, 611 (1999).

Physics of the Solid State, Vol. 44, No. 11, 2002, pp. 2050–2054. Translated from Fizika Tverdogo Tela, Vol. 44, No. 11, 2002, pp. 1958–1962.
Original Russian Text Copyright © 2002 by Zaripov, Tarasov, Ulanov, Shakurov.

SEMICONDUCTORS AND DIELECTRICS

Jahn–Teller Chromium Ions in CdF_2 and CaF_2 Crystals: An EPR Spectroscopic Study in the Frequency Range 9.3–300 GHz

M. M. Zaripov, V. F. Tarasov, V. A. Ulanov, and G. S. Shakurov
Kazan Physicotechnical Institute, Russian Academy of Sciences, Sibirskiĭ trakt 10/7, Kazan 29, 420029 Tatarstan, Russia
e-mail: ulanov@dionis.kfti.kcn.ru

Received January 9, 2002

Abstract—The bivalent chromium impurity centers in CdF_2 and CaF_2 crystals are investigated using electron paramagnetic resonance (EPR) in the frequency range 9.3–300 GHz. It is found that Cr^{2+} ions in the lattices of these crystals occupy cation positions and form $[CrF_4F_4]^{6-}$ clusters whose magnetic properties at low temperatures are characterized by orthorhombic symmetry. The parameters of the electron Zeeman and ligand interactions of the Cr^{2+} ion with four fluorine ions in the nearest environment are determined. The initial splittings in the system of spin energy levels of the cluster are measured. © *2002 MAIK “Nauka/Interperiodica”.*

1. INTRODUCTION

The ground state of a free Cr^{2+} ion is characterized by the ^5D term. Upon incorporation into crystals of the fluorite structural family (CdF_2, CaF_2, SrF_2, and BaF_2), bivalent chromium ions occupy cation sites whose coordination polyhedron is represented by a regular cube with F^- ions in the vertices. For such a structure, according to the crystal field theory, the quintuply degenerate ground ^5D term of the chromium ion is split into the excited orbital doublet ^5E_g and the ground triplet $^5T_{2g}$. In this regard, the impurity complex $[CrF_8]^{6-}$ formed in a crystal is of considerable interest as an object exhibiting Jahn–Teller properties.

Ulrici [1] investigated the optical spectra of CdF_2 : Cr crystals and revealed transitions between the $^5T_{2g}$ and ^5E_g states. The splitting of the levels of the ground triplet $^5T_{2g}$ was estimated at 5000 cm^{-1}. This indicates considerable distortions of the crystal lattice in the vicinity of a paramagnetic impurity. The characteristic temperature dependence of the optical spectra observed in [1] suggests a Jahn–Teller nature of these distortions. It should be noted that, according to [2], the vibronic interaction of the orbital triplet $^5T_{2g}$ with e_g vibrations should lead to a tetragonal distortion of the coordination cube of the impurity ion and the interaction with t_{2g} vibrations should result in a trigonal distortion. However, the orthorhombic anisotropy is observed in the optical properties of Cr^{2+} centers [1]. Therefore, in the case under consideration, the interactions with vibrations of tetragonal and trigonal symmetries are equally efficient.

These inferences were confirmed by Jablonski *et al.* [3], who studied the electron paramagnetic resonance (EPR) spectra of CdF_2 : Cr crystals. These authors examined the ligand hyperfine structure of the EPR spectra and determined the molecular structure of the impurity paramagnetic complex [3]. It turned out that the Cr^{2+} ion is located at the center of a coordination polyhedron that is a right-angle orthorhombic prism whose vertices are occupied by eight F^- ions.

The same conclusions regarding the structure of Cr^{2+} complexes were drawn on the basis of the EPR data for crystals of CaF_2 : Cr [4, 5] and SrF_2 : Cr [6]. In our earlier work [6], we performed an EPR investigation over a wide frequency range. This made it possible to determine virtually all the spin Hamiltonian parameters with sufficient accuracy. Crystals of CdF_2 : Cr [3] and CaF_2 : Cr [4, 5] were examined at frequencies of 9.3 [3, 4] and 34 GHz [5]. For this reason, the spin Hamiltonian parameters were derived from the angular dependences of the EPR transitions $|+1\rangle \longleftrightarrow |-1\rangle$ and $|+2\rangle \longleftrightarrow |-2\rangle$. Since the transitions $|0\rangle \longleftrightarrow |-1\rangle$ and $|\pm1\rangle \longleftrightarrow |\pm2\rangle$ could not be observed at low frequencies, the majority of the parameters obtained in [3–5] were determined only approximately. For example, in [5], the splittings between the spin levels $|0\rangle$, $|\pm1\rangle$, and $|\pm2\rangle$ were evaluated from the temperature dependence of the population of the spin energy levels of the impurity complex. Note that the spin Hamiltonian parameters obtained in [3] are questionable. Their values differ severalfold from those determined in [5, 6]. This seems to be unlikely considering the similarity between the molecular structures of the complexes in these three same-type crystal matrices.

In this respect, the main purpose of the present work was to refine the data obtained in [3–5].

2. SAMPLE PREPARATION AND EXPERIMENTAL TECHNIQUE

Crystals of CdF_2 : Cr were grown by the Bridgman method in a helium atmosphere with small fluorine additives. The crucible used for a CdF_2 : Cr melt was produced from chemically pure graphite. Chromium impurities in the form of a well-dried chromium trifluoride powder were introduced into the melt. Fluorine was added to the helium atmosphere used in the crystal growth for the purpose of preparing a melt of nonstoichiometric composition with an excess fluorine content. This encouraged an increase in the equilibrium concentration of chromium ions dissolved in the melt. It turned out that the presence of excess fluorine ions in the melt was a necessary condition for the incorporation of chromium into the lattice of the growing crystal. Crystals of CaF_2 : Cr were grown under similar conditions. However, since the vapor pressure of the CaF_2 melt was substantially less than that of CdF_2 melt, the CaF_2 : Cr crystals were grown by the Czochralski method.

The grown crystals were examined by EPR spectroscopy. It was found that, depending on the growth conditions, the grown crystals contained either predominantly bivalent chromium centers (the temperature gradient in the vicinity of the crystallization front was greater than 50 K/cm, and the velocity of the crystallization front was higher than 20 mm/h) or trivalent chromium centers of trigonal symmetry (under different conditions). The latter chromium centers were described in [7].

The spectra of certain CdF_2 : Cr crystals exhibited weak EPR signals whose angular dependences indicated orthorhombic symmetry of the relevant centers. Repeated recrystallization of these samples led to the disappearance of these centers. On the other hand, the addition of oxygen in small amounts to the atmosphere used in the crystal growth resulted in an increase in the concentration of the centers under investigation. Similar oxygen-containing centers were observed in CaF_2 : Cr crystals. The parameters of the EPR spectra of these crystals coincided with those obtained for $[CrF_6O]^{6-}$ impurity complexes in [5].

In this work, we performed an EPR investigation of CdF_2 : Cr and CaF_2 : Cr samples predominantly containing $[CrF_4F_4]^{6-}$ complexes. The measurements were carried out at frequencies of 9.3 and 37 GHz (on an E-12 Varian EPR spectrometer) and in the frequency range 65–300 GHz (on a quasi-optical spectrometer described in our previous work [8]). The use of the frequency-tuned spectrometer in the submillimeter-wavelength region made it possible to determine directly all the initial splittings in the system of the spin energy levels for the Cr^{2+} impurity ion.

Since some doubts were cast upon the spin Hamiltonian parameters obtained in [3], our prime concern was the CdF_2 : Cr^{2+} crystals and the present work, for the most part, was devoted to examination of these crystals. Figure 1 displays the dependences of the frequencies of resonance electron transitions of the types $|0\rangle \longleftrightarrow |\pm1\rangle$ and $|\pm1\rangle \longleftrightarrow |\pm2\rangle$ on the external magnetic field B_0 for the CdF_2 : Cr^{2+} and CaF_2 : Cr^{2+} crystals studied in the submillimeter-wavelength region. The points are the experimental data, and the solid lines correspond to the results of calculations. The type of resonance transition is indicated near the corresponding curve in Fig. 1. To avoid overloading of the figures by too large a number of graphs, Fig. 1 shows the dependences for transitions in the system of the spin energy levels only for the structurally equivalent centers for which the Z axis is parallel to the vector $\mathbf{B}_0$ of the external constant magnetic field. In actual fact, there occur also transitions between the states of five magnetically nonequivalent centers with other orientations with respect to the vector $\mathbf{B}_0$.

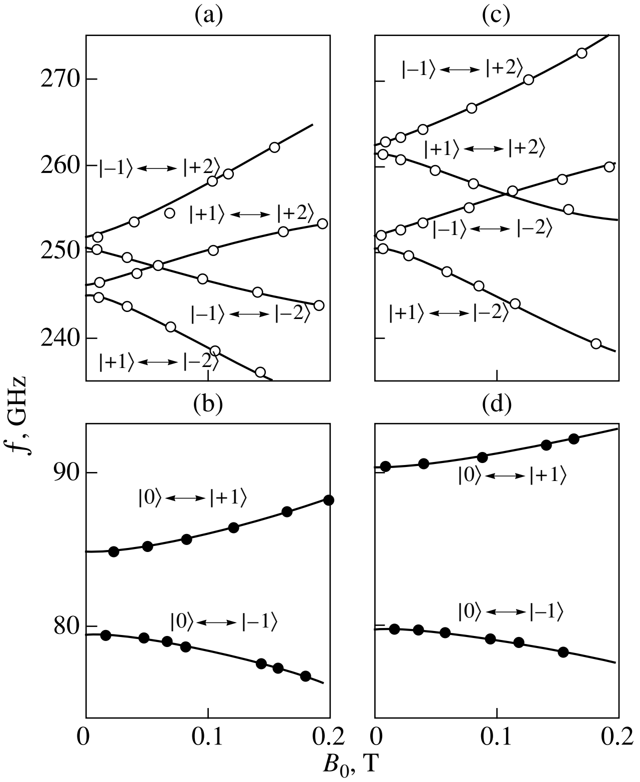

Fig. 1. Dependences of the frequencies of the resonance transitions $|0\rangle \longleftrightarrow |\pm1\rangle$ and $|\pm1\rangle \longleftrightarrow |\pm2\rangle$ on the external magnetic field B_0 for (a, b) CdF_2 : Cr^{2+} and (c, d) CaF_2 : Cr^{2+} crystals.

The angular dependences of the resonance external magnetic field measured upon rotation of the vector $\mathbf{B}_0$ in the (110) plane of the crystal at T = 4.2 K and f = 37 GHz are plotted in Fig. 2. The dependences shown in this figure correspond to transitions within the pairs of the spin levels $|\pm1\rangle$ and $|\pm2\rangle$ and between the levels

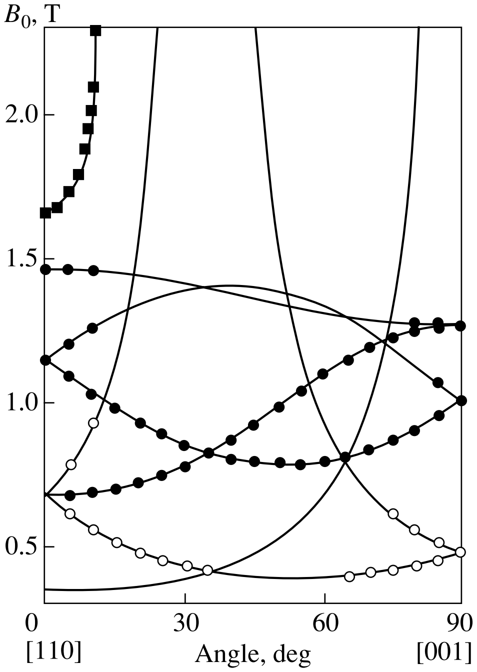

Fig. 2. Angular dependences of the resonance external magnetic field upon rotation of the vector $\mathbf{B}_0$ in the (110) plane of the $CdF_2 : Cr^{2+}$ crystal (T = 4.2 K, f = 37 GHz) for the electron transitions $|+1\rangle \longleftrightarrow |-1\rangle$ (closed circles), $|+2\rangle \longleftrightarrow |-2\rangle$ (open circles), and $|0\rangle \longleftrightarrow |-1\rangle$ (closed squares).

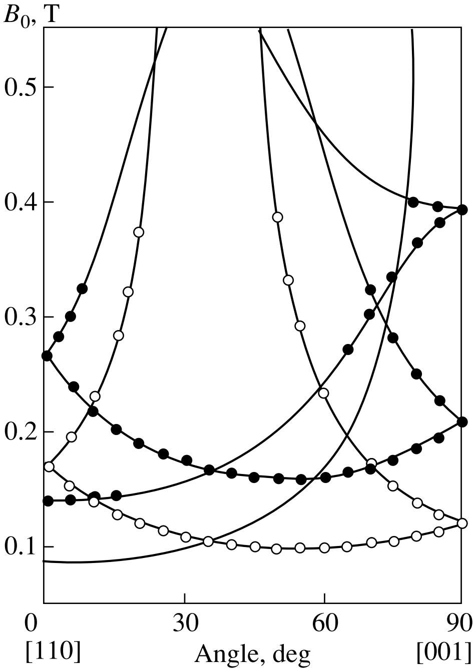

Fig. 3. Angular dependences of the resonance external magnetic field upon rotation of the vector $\mathbf{B}_0$ in the (110) plane of the $CdF_2 : Cr^{2+}$ crystal (T = 4.2 K, f = 9.3 GHz) for the electron transitions $|+1\rangle \longleftrightarrow |-1\rangle$ (closed circles) and $|+2\rangle \longleftrightarrow |-2\rangle$ (open circles).

$|0\rangle$ and $|-1\rangle$. The transitions $|-1\rangle \longleftrightarrow |+1\rangle$ are observed for all six magnetically nonequivalent centers. The transitions $|0\rangle \longleftrightarrow |-1\rangle$ occur only for one group of these centers, in which the vector $\mathbf{B}_0$ is oriented at small angles (≤12°–15°) with respect to the Z axis. This can be explained by the fact that the states $|0\rangle$ and $|\pm1\rangle$ are characterized by a considerable energy splitting, which is determined primarily by the parameter b_2^0 of the initial splitting (because $3b_2^0 \gg \beta_e g B_0 \sim 6b_2^2$).

In the case when the magnetic vector $\mathbf{B}_f$ of the electromagnetic field in the spectrometer cavity is oriented perpendicularly to the quantization axis of spin moments of the centers under investigation, the transitions $|2\rangle \longleftrightarrow |+2\rangle$ are forbidden. However, the vector $\mathbf{B}_f$ during rotation of the vector $\mathbf{B}_0$ in the (110) crystal plane has a nonzero component along the quantization axes of five (out of six) groups of the magnetically nonequivalent centers. Therefore, the possibility appeared of recording the resonance lines corresponding to these transitions. In reality, this could be done only for the four groups of these centers for which the angle between the Z axis and the vector $\mathbf{B}_0$ did not exceed 50°–60°.

For certain orientations of the vector $\mathbf{B}_0$ of the external magnetic field with respect to the principal axes of the $CdF_2 : Cr^{2+}$ and $CaF_2 : Cr^{2+}$ crystals, the EPR spectra exhibited a ligand hyperfine structure. The best resolution was achieved for the transitions $|+2\rangle \longleftrightarrow |-2\rangle$. For the transitions $|+1\rangle \longleftrightarrow |-1\rangle$, the ligand hyperfine structure was revealed only in the $CdF_2 : Cr^{2+}$ samples with the orientation $\mathbf{B}_0 \parallel Y$. For the transition $|0\rangle \longleftrightarrow |-1\rangle$, a partly resolved ligand hyperfine structure was observed in the $CdF_2 : Cr^{2+}$ samples at the orientation $\mathbf{B}_0 \parallel Z$. In the majority of cases, the ligand hyperfine structure was represented by five resonance lines with relative intensities approximately equal to the ratio 1 : 4 : 6 : 4 : 1. Moreover, the dependence of the line width of the ligand hyperfine quintet on the direction of the vector $\mathbf{B}_0$ was observed for the transitions $|+2\rangle \longleftrightarrow |-2\rangle$ in both matrix crystals.

The angular dependences of the resonance external magnetic field upon rotation of the vector $\mathbf{B}_0$ in the (110) plane at T = 4.2 K and f = 9.3 GHz are depicted in Fig. 3. It can be seen that the line attributed to the transitions $|+1\rangle \longleftrightarrow |-1\rangle$ should be observed at the orientation $\mathbf{B}_0 \parallel \langle 001\rangle$ in a magnetic field of ≈0.4 T. In [3], this line was erroneously assigned to the transition $|+2\rangle \longleftrightarrow |-1\rangle$.

3. RESULTS AND DISCUSSION

The theoretical positions of the resonance lines in Figs. 1–3 were determined from the equality between the corresponding differences of the eigenvalues of the spin Hamiltonian

$$H = \beta_e B_0 gS + b_2^0 O_2^0 + b_2^2 O_2^2 + b_4^0 O_4^0 + b_4^2 O_4^2 + b_4^4 O_4^4 \tag{1}$$

and the energy of electromagnetic-field quanta in the spectrometer cavity. Here, the spin Hamiltonian parameters are as follows: b_2^0 = –27700 ± 50 MHz, $|(b_2^2 - 4b_4^2)|$ = 900 ± 30 MHz, $b_4^0 \approx 5$ MHz, $|b_4^4|$ = 45 ± 5 MHz, $g_x = 1.978 \pm 0.005$, $g_y = 1.995 \pm 0.005$, and $g_z = 1.946 \pm 0.005$ for the CdF_2 crystal and b_2^0 = –28 400 ± 100 MHz, $|(b_2^2 - 4b_4^2)|$ = 1800 ± 50 MHz, $b_4^0 \approx 3$ MHz, $|b_4^4|$ = 25 ± 10 MHz, $g_x = 1.97 \pm 0.01$, $g_y = 1.98 \pm 0.01$, and $g_z = 1.94 \pm 0.01$ for the CaF_2 crystal.

The spin Hamiltonian (1) is represented in a coordinate system whose axes are oriented with respect to the principal axes of the crystal as follows: $X \parallel \langle 001\rangle$, $Y \parallel \langle 1\text{–}10\rangle$, and $Z \parallel \langle 110\rangle$. The choice of the Z axis was governed by the requirement for a maximum magnitude of the coefficient b_2^0 of the spin operator O_2^0 in Hamiltonian (1). The Hamiltonians of the other five centers can be obtained through transformation of the cubic symmetry group.

In the course of calculations, some doubts were cast on the possibility of uniquely determining all eight parameters of the spin Hamiltonian (1). In order to elucidate this problem, we constructed a system of approximate linear equations in which the parameters b_2^0, b_2^2, b_4^0, b_4^2, b_4^4, g_x, g_y, and g_z were unknown; i.e., we used the least-squares method to the first order in the perturbation theory. For this purpose, the matrix of the spin Hamiltonian (1) was determined using the eigenfunctions of the truncated Hamiltonian

$$H^{(0)} = \beta_e B_0 g^{(0)} S + (b_2^{(0)})^{(0)} O_2^0 + (b_2^2)^{(0)} O_2^2, \tag{2}$$

where $(b_2^{(0)})^{(0)}$ and $(b_2^2)^{(0)}$ are the approximate values of the parameters b_2^0 and b_2^2, respectively. These approximate parameters can be obtained, for example, from the splittings of the spin energy levels at $B_0 = 0$ (Fig. 1). Then, the approximate components $g_i^{(0)}$ ($i = x, y, z$) of the tensor g can be found from the EPR spectra measured at a frequency of 37 GHz. Thereafter, for a necessary set of experimental points in the angular dependences of the resonance external magnetic field B_0, we write the initial approximate equalities determining the coefficients of the system of simultaneous equations in the least-squares method. In the approximate equalities, the corresponding differences between the diagonal matrix elements of the spin Hamiltonian (1), which is represented with the use of the eigenfunctions of the spin Hamiltonian (2), are taken to be equal to the photon energy of electromagnetic oscillations at the resonance frequency.

It turned out that the determinant of the matrix of the coefficients is close to zero. This indicates that the occurrence of unavoidable experimental errors prevents unique determination of the parameters of the spin Hamiltonian (1). In particular, it is found that, in the matrix, the column of the coefficients of the unknown b_2^2 linearly depends on the column of the coefficients of the unknown b_4^2. This linear dependence can be approximated using the quantity $(b_2^2 - 4b_4^2)$. Furthermore, it is revealed that, when the set of experimental points is limited to those corresponding to the transitions $|+1\rangle \longleftrightarrow |-1\rangle$ and $|+2\rangle \longleftrightarrow |-2\rangle$, the solutions of the system of equations become extremely sensitive to experimental errors. Actually, these calculations make it possible to determine a number of important parameters of the spin Hamiltonian (1), namely, b_2^0, $(b_2^2 - 4b_4^2)$, g_x, g_y, and g_z, with a satisfactory accuracy. However, the other parameters can be obtained with a considerably lower accuracy.

Analysis of the splittings in the ligand hyperfine structure of the EPR spectra enabled us to derive the parameters of the Hamiltonian of the ligand hyperfine interaction between the electron magnetic moment of the studied center and the nuclear magnetic moments of fluorine ions in the nearest environment of the chromium impurity ion. In the case under consideration, this Hamiltonian has the form

$$H_{shfi} = \sum_i S A^{F(i)} I^{F(i)}, \tag{3}$$

where S is the electron spin moment operator, $A^{F(i)}$ is the tensor for the ligand hyperfine interaction with $F^-(i)$ ions, and $I^{F(i)}$ is the nuclear spin moment operator for $F^-(i)$ ions. In order to describe the ligand hyperfine splittings in the EPR spectrum, Hamiltonian (3) should be considered simultaneously with the nuclear Zeeman interaction Hamiltonian [representing the interaction of the external magnetic field with the nuclear magnetic moment of the $F^-(i)$ ion]; that is,

$$H_{NZ} = -\sum_i g_N \beta_N B_0 I^{F(i)}, \tag{4}$$

where g_N and β_N are the g factor and the nuclear magneton of this ion, respectively.

As follows from the experimental data, each center interacts only with four equivalent fluorine ions. These ions are located in the same plane as the Cr^{2+} impurity ion. This plane coincides with the XOY coordinate plane and is aligned parallel to one out of the six (110) planes in the crystal. The ligand hyperfine interaction with four fluorine ions each is described by the symmetry group C_s, and the symmetry of the paramagnetic complex, as a whole, corresponds to the D_{2h} group. This inference is confirmed by the angular dependences of the resonance magnetic field B_0 measured at frequencies of 9.3 and 37 GHz and in the submillimeter-wavelength region. It is known (see, for example, [5]) that, in the case of large initial splittings of the spin energy levels, the ligand hyperfine splitting of the EPR lines for the electron transition $|+2\rangle \longleftrightarrow |-2\rangle$ is predominantly determined by three components (A_{ZX}, A_{ZY}, and A_{ZZ}) of the tensor $A^{\mathrm{F}(i)}$ and very weakly depends on the direction of the external magnetic field. If the ligands are located in the XOY plane, we have $A_{ZY} = A_{ZX} = 0$ and the measured splittings in the ligand hyperfine structure of the EPR spectra permit us to determine only one component of the tensor $A^{\mathrm{F}(i)}$ [i.e., the component A_{ZZ}, which corresponds to the perpendicular component $A_\perp$ of the same tensor $A^{\mathrm{F}(i)}$ represented in a local coordinate system with the Z' axis aligned along the Cr^{2+}–$\mathrm{F}^-(i)$ bond]. An examination of the ligand splittings in the EPR spectra recorded at frequencies of 9.3 and 37 GHz for the transition $|+2\rangle \longleftrightarrow |-2\rangle$ demonstrates that nearly identical ligand hyperfine splittings of the nuclear energy levels are observed under all experimental conditions. The splitting of the electron level $|M\rangle$ can be determined from the approximate relationship

$$\delta E_M \cong \{(\langle S_Z\rangle^2 A_\perp^2 + f_L^2) - 2A_\perp f_L \langle S_Z\rangle_M \cos\alpha\}^{-1/2}. \quad (5)$$

Here, $\langle S_Z\rangle_M$ is the mean of the electron operator S_Z in the state $|M\rangle$ that corresponds to either of two electron levels between which the resonance transition occurs ($M = +2$ or -2), $f_L = g_N\beta_N B_0$ (resonance) is the Larmor precession frequency of fluorine ions in the external magnetic field, α is the angle between the Z axis and the vector of the external magnetic field, and $A_\perp\langle S_Z\rangle_M \gg f_L$.

Relationship (5) holds with a high accuracy in a weak external magnetic field (the EPR spectra measured at a frequency of 9.3 GHz). Moreover, according to calculations, this relationship in our case can also be used for analyzing the ligand hyperfine structure of the EPR spectra measured at a frequency of 37 GHz. The calculations performed using relationship (5) give the components $|A_\perp| = 40 \pm 4$ MHz for $\mathrm{CdF_2 : Cr^{2+}}$ crystals and 42 ± 5 MHz for $\mathrm{CaF_2 : Cr^{2+}}$ crystals (the latter value coincides with the result obtained in [5]). The ligand hyperfine interaction tensor component $A'_{ZZ} \approx A_\parallel$ (the prime indicates the local coordinate system) for $\mathrm{CdF_2 : Cr^{2+}}$ crystals was determined from the ligand hyperfine structure of the EPR spectrum for the electron transition $|+1\rangle \longleftrightarrow |-1\rangle$ at the orientation $\mathbf{B}_0 \parallel Y$. It was found that $|A_\parallel| = 20 \pm 8$ MHz. A similar tensor component for $\mathrm{CaF_2 : Cr^{2+}}$ crystals cannot be obtained because the ligand hyperfine structure of the EPR spectrum is observed only for the transition $|+2\rangle \longleftrightarrow |-2\rangle$.

As regards the interaction with the other four nearest ligands, its influence on the EPR spectra manifests itself in an angular dependence of the line width in the ligand hyperfine structure of the EPR spectra for the electron transitions $|+2\rangle \longleftrightarrow |-2\rangle$.

4. CONCLUSIONS

Thus, the results of the above investigation allow us to make the inference that the models of the studied centers in $\mathrm{CdF_2}$ and $\mathrm{CaF_2}$ crystals are consistent with the model of a bivalent chromium impurity complex in the $\mathrm{SrF_2}$ crystal [6]. The hyperfine structure parameters determined from analyzing the EPR spectra of $\mathrm{CdF_2}$ crystals in the present work and in [3] differ significantly. This can be explained by the misinterpretation of the EPR spectra in [3], most likely, as a result of a lack of necessary experimental data.

REFERENCES

1. W. Ulrici, Phys. Status Solidi B **84**, K155 (1977).
2. I. B. Bersuker and V. Z. Polinger, *Vibronic Interactions in Molecules and Crystals* (Nauka, Moscow, 1983; Springer-Verlag, New York, 1989).
3. R. Jablonski, M. Domanska, and B. Krukowska-Fulde, Mater. Res. Bull. **8**, 749 (1973).
4. J. M. Baker, W. Hayes, and D. A. Jones, Proc. Phys. Soc. London **73**, 942 (1959).
5. P. V. Oliete, V. M. Orera, and P. J. Alonso, Phys. Rev. B **53** (6), 3047 (1996).
6. M. M. Zaripov, V. F. Tarasov, V. A. Ulanov, *et al.*, Fiz. Tverd. Tela (St. Petersburg) **37** (3), 806 (1995) [Phys. Solid State **37**, 437 (1995)].
7. R. Alcala, P. J. Alonso, V. M. Orera, and H. V. den Hartog, Phys. Rev. B **32** (6), 4158 (1985).
8. V. F. Tarasov and G. S. Shakurov, Appl. Magn. Reson. **2** (3), 571 (1991).

Translated by O. Borovik-Romanova

Physics of the Solid State, Vol. 44, No. 11, 2002, pp. 2055–2062. Translated from Fizika Tverdogo Tela, Vol. 44, No. 11, 2002, pp. 1963–1969.
Original Russian Text Copyright © 2002 by Novikov, Wojciechowski.

Frequency Dependences of Dielectric Properties of Metal–Insulator Composites

V. V. Novikov* and K. W. Wojciechowski**
** Odessa State Polytechnical University, Odessa, 65044 Ukraine*
e-mail: novikov@Te.Net.Ua
*** Institute of Molecular Physics, Polish Academy of Sciences, Poznan, 60-179 Poland*

Received March 11, 2002

Abstract—Based on the fractal model of an inhomogeneous medium with a chaotic structure and the iteration method of averaging, frequency dependences of the dielectric properties of metal–insulator composites were determined. In the low-frequency limit, the considered methods of the investigation of two-component media were shown to permit one to obtain detailed information on the metal–insulator transition. *© 2002 MAIK “Nauka/Interperiodica”.*

1. INTRODUCTION

Theoretical investigations of the dielectric properties of inhomogeneous media stem from works published as far back as the 1870s–1930s [1–3]. Based on these works, the method of an effective medium was developed [4], which in essence represents the replacement of an inhomogeneous medium consisting of two composites with conductivities σ_1 and σ_2 by a continuous medium with an effective conductivity σ. Note that such an approximation is only applicable for the case where the length of the electromagnetic wave interacting with the medium is much greater than the sizes of inhomogeneities and the spacings between them.

The effective-medium method has been sufficiently widely used for the description of physical properties of inhomogeneous media [4]; however, it did not permit one to predict the behavior of the system upon the metal–insulator transition near the percolation threshold [5–9]. For the case where the ratio of the conductivities of the phases σ_2/σ_1 tends to zero, scaling dependences were obtained in terms of the percolation theory for the effective dc conductivity σ (see [5, 6]), which reflect the behavior of the conductivity near the geometrical phase transition (near the metal–insulator transition) when the disconnected region of the conducting phase passes into a connected region:

$$\sigma \sim \Delta p^{-s}, \quad \Delta p = p - p_c < 0, \qquad (1)$$

$$\sigma \sim \Delta p^{T}, \quad \Delta p > 0, \qquad (2)$$

where $T = s \approx 1.1$ for two-dimensional systems ($d = 2$) and $T \approx 1.6$, $s \approx 1$ for three-dimensional systems ($d = 3$); p_c is the percolation threshold. If we assume that for local regions the strength of the electric field $\mathbf{E}(\mathbf{r}, t)$ changes upon the propagation of the electromagnetic field periodically with a frequency ω as

$$\mathbf{E}(\mathbf{r}, t) = \mathbf{E}_0(\mathbf{r}, \omega)\exp(i\omega t), \qquad (3)$$

then Ohm’s law may be written in the form [10]

$$\mathbf{j}(\mathbf{r}, \omega) = \sigma^*(\mathbf{r}, \omega)\mathbf{E}(\mathbf{r}, \omega), \qquad (4)$$

where $\mathbf{j}(\mathbf{r}, \omega)$ is the current density and $\sigma^*(\mathbf{r}, \omega)$ is the complex coefficient of conductivity:

$$\sigma^*(\mathbf{r}, \omega) = \sigma(\mathbf{r}, \omega) + i\omega\varepsilon(\mathbf{r}, \omega). \qquad (5)$$

For an inhomogeneous medium with a chaotic structure, the dielectric constant $\varepsilon(\mathbf{r}, \omega)$ and the conductivity $\sigma(\mathbf{r}, \omega)$ are random (stochastic) functions of the coordinates $\mathbf{r}$.

Note that from Eq. (5) we can determine the scaling expressions for the conductivity of a lattice of resistors of finite dimensions l, which were first obtained in [11, 12]:

$$\sigma = \sigma_1\xi^{-t/\nu}G_+(\sigma_1/\sigma_2\xi^{(t+s)/\nu}, \xi/l), \quad \Delta p > 0, \qquad (6)$$

$$\sigma = \sigma_2\xi^{s/\nu}G_-(\sigma_2/\sigma_1\xi^{(t+s)/\nu}, \xi/l), \quad \Delta p < 0, \qquad (7)$$

where $G_+(x, y)$ and $G_-(x, y)$ are the functions of two variables that describe the frequency and scale dependences of the conductivity of the function above and below the percolation threshold.

In recent years, great attention has been paid to an analysis of the dependences of the properties of metal–insulator composites on frequency [11–31], which is related to the difficulties in the description of the anomalous behavior of dielectric properties in the low-frequency limit. The nature of the anomalous behavior of frequency dependences of dielectric properties can be clarified if we consider a model medium consisting of

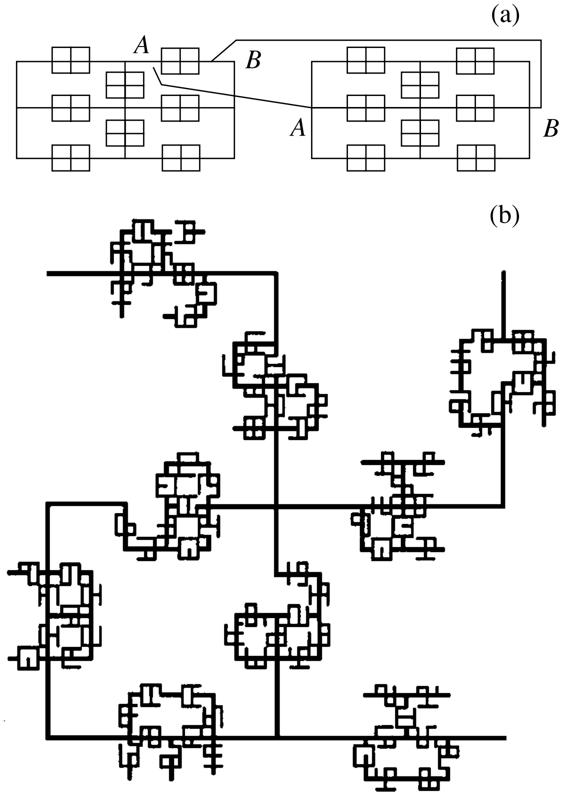

Fig. 1. Obtaining the $\Omega_n(l_0, p_0)$ set for $l_0 = 2$ at the fourth iteration step ($k = 4$): (a) $p_0 = 1$ and (b) $p_0 = 0.75$ (schematic).

small spherical metallic particles described by the Drude dielectric function

$$\varepsilon_1(\omega) = 1 - \frac{\omega_{p1}^2}{\omega(\omega + i/\tau_1)} \tag{8}$$

and embedded into an insulating matrix with a dielectric constant equal to unity ($\varepsilon_2 = 1$). In Eq. (8), ω_{p1} is the plasma frequency and τ_1 is the relaxation time of the metallic phase.

If such a medium is subjected to the action of an electric field (3), then, with allowance for the fact that the solution to the electrostatic problem for a spherical inclusion in a homogeneous medium yields for the electric field E_1 inside a spherical metallic particle a dependence of the form

$$E_1 = 3E_0/(\varepsilon_1 + 2), \tag{9}$$

we obtain that the electric field E_1 tends to infinity at frequencies close to

$$\omega \cong \omega_{p1}/\sqrt{3}. \tag{10}$$

At such frequencies, the applied field is in resonance with the mode of the small metallic particle; as a result, a strong absorption appears at this frequency; i.e., the imaginary part of the effective dielectric constant of the medium strongly increases in the vicinity of the frequency $\omega_p/\sqrt{3}$ [11, 12].

For inhomogeneous media such as a metal–insulator composite with a chaotic structure, the behavior becomes even more complex.

In the majority of numerical calculations of the anomalous frequency behavior of the metal–insulator composites (in particular, near the percolation threshold p_c) under the action of an alternating current, lattice (discrete) models have been used, which were studied in terms of the transfer-matrix method [11, 12] and using the Frank–Lobb algorithm [13]. The numerical calculations and the theoretical analysis of the properties of metal–insulator composites performed in [11–31] led to significant progress in the understanding of this phenomenon, but the dielectric properties of metal–insulator composites with fractal structures virtually have not been considered in the literature.

Below, we report the results of calculations of the dielectric properties of metal–insulator composites with a chaotic hierarchic self-similar structure on the basis of a fractal model in the entire concentration range of inhomogeneities at various frequencies of an external field. In the work, the iteration method of averaging was employed [24, 32–36].

2. MODEL

Simulation of a chaotic structure of an inhomogeneous medium was performed on the basis of a lattice with a random distribution of its parameters. The sites of the lattice simulated microinhomogeneities (components of the system) in space, and the bonds between the sites simulated their contacts with neighbors [32, 35, 36].

The basic set of bonds Ω was obtained with the help of an iteration process in which at the first step ($k = 0$), there is a finite lattice in $d = 3$ space with a probability p_0 that the bond between neighboring nodes of the lattice is unbroken (is "painted" a definite color). Bonds of the same color possess the same properties. At the next step ($k = 1, 2, \ldots, n$), each bond in the lattice is replaced by the lattice obtained at the previous step (Fig. 1). The iteration process is terminated when the properties of the lattice stop being dependent on the number of the iteration k. The set of bonds $\Omega_n(l_0, p_0)$ obtained using the iteration procedure depends on the size of the initial lattice l_0 and on the probability p_0.

The probability of forming a set of bonds of the same color connecting two opposite faces of the lattice $Y(l_0, p_0)$ was calculated as the ratio of the number of connecting sets (CS) to the number of all possible configurations of bonds of the same color (σ_1^*) at a given p_0 and l_0 [32].

At the first iteration step, the length of the lattice edge is equal to $l_1 = l_0^2$ and the density of bonds of the same color, e.g., black (σ_1^*), is equal to $p_1 = Y(l_0, p_0)$. At the next iteration steps, the length of the lattice edge is $l_2 = l_1^2$ and the density of black bonds is

$$p_2 = Y(l_1, p_1), \ldots, p_k = Y(l_{k-1}, p_{k-1}).$$

Here, $p_k = Y(l_{k-1}, p_{k-1})$ is the density of CSs at the kth iteration step.

The growth of the chaotic fractal set $\Omega_n(l_0, p_0)$ is terminated at the nth step at the fixed point 0 or 1 for the function $p_n = Y(l_{n-1}, p_{n-1})$:

$$p_n = \begin{cases} 1, & p_0 > p_c \\ 0, & p_0 < p_c. \end{cases}$$

The functions $Y(l_0, p_0)$ for various rectangular lattices were calculated using the Monte Carlo method in [32].

The unstable critical point p_c (percolation threshold) was determined from the equality $p_c = Y(l_0, p_c)$.

Then, the probability function p_k for the event that the set of bonds at the kth iteration step is a CS was determined using the formula [37]

$$\begin{aligned} p_k = {} & p_{k-1}^2(4 + 8p_{k-1} - 14p_{k-1}^2 - 40p_{k-1}^3 \\ & + 16p_{k-1}^4 + 288p_{k-1}^5 - 655p_{k-1}^6 \\ & + 672p_{k-1}^7 - 376p_{k-1}^8 + 112p_{k-1}^9 - 14p_{k-1}^{10}), \end{aligned} \tag{11}$$

which agrees satisfactorily with numerical calculations [32].

The percolation threshold p_c, according to [11], is equal to 0.2084626828…; i.e., the nonconnecting set (NCS) passes into the connecting set (CS) at $p_c \approx 0.208462$.

Each kth bond in the set $\Omega_n(l_0, p_0)$ possesses a complex resistance (impedance) $Z_k(\omega)$ which consists of an active resistance R_k, an inductance L_k, and a capacitance C_k:

$$Z_k^{-1}(\omega) = (R_k + i\omega L_k)^{-1} + i\omega C_k. \tag{12}$$

In what follows, each bond will be characterized by the complex conductivity σ_k^* with allowance for the fact that the equality

$$\sigma_k^* = Z_k^{-1}(\omega) \tag{13}$$

is fulfilled.

Consider a two-phase system with a distribution function

$$P_0(\sigma^*) = (1 - p_0)\delta(\sigma^* - \sigma_2^{*(0)}) + p_0\delta(\sigma^* - \sigma_1^{*(0)}), \tag{14}$$

where $\delta(x)$ is the Dirac delta function, p_0 is the probability that a given local region possesses the property $\sigma_1^{*(0)} = \sigma_1^*$, and $1 - p_0$ is the probability that this region possesses the property $\sigma_2^{*(0)} = \sigma_2^*$.

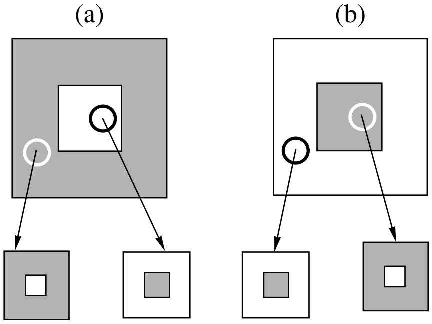

Fig. 2. Simulation of (a) a connecting set (CS) and (b) a nonconnecting set (NCS) (schematic).

In this case, after k iteration steps, the density function takes on the form

$$P_k(\sigma^*) = (1 - p_k)\delta(\sigma^* - \sigma_2^{*(k)}) + p_k\delta(\sigma^* - \sigma_1^{*(k)}). \tag{15}$$

In what follows, we will distinguish two types of sets of bond configurations: connecting sets (CSs) and nonconnecting sets (NCSs).

To determine the dielectric properties of the CSs and NCSs, we used a cell of the cube-in-cube type (Fig. 2); i.e., at each step of the iteration process of the calculation of the properties, the structures of the CSs and NCSs were simulated by a cube-in-cube cell as follows: CS, a continuous body of a well conducting phase including a cube of a poorly conducting phase (Fig. 2a); NCS, a continuous body of a poorly conducting phase including a cube of a well conducting phase (Fig. 2b).

The dc conductivity of the cube-in-cube cell (Fig. 2) was determined in [7, 38]. The results obtained in [7, 38] for a cell in which a cube with a conductivity σ_2 is in the center of a cube with a conductivity σ_1 can be written in the form

$$\sigma = \frac{\sigma_1}{2}(\psi_1 + \psi_2), \tag{16}$$

where

$$\psi_1 = \frac{\sigma_1 + (\sigma_2 - \sigma_1)(1 - p)^{2/3}}{\sigma_1 + (\sigma_2 - \sigma_1)(1 - p)^{2/3}[1 - (1 - p)^{1/3}]}, \tag{17}$$

$$\psi_2 = \frac{\sigma_2 + (\sigma_1 - \sigma_2)(1 - p)^{1/3}[1 - (1 - p)^{2/3}]}{\sigma_2 + (\sigma_1 - \sigma_2)(1 - p)^{1/3}}. \tag{18}$$

Here, p is the volume concentration of the phase with a conductivity σ_1.

According to Eqs. (4) and (5), the problem of the determination of the effective characteristics of a medium in a quasi-stationary approximation differs from the static case only in the replacement of the conductivity σ (dc conductivity) by the complex conductivity σ^*.

With allowance for Eqs. (16)–(18), the complex conductivity of CSs at the kth step of the calculations was determined using the formulas

$$\sigma_c^{*(k)} = \frac{\sigma_c^{*(k-1)}}{2}(\psi_1^{(k-1)} + \psi_2^{(k-1)}), \qquad (19)$$

where

$$\psi_1^{(k-1)} = \frac{\sigma_c^{*(k-1)} + (\sigma_n^{*(k-1)} - \sigma_c^{*(k-1)})(1-p_{k-1})^{2/3}}{\sigma_c^{*(k-1)} + (\sigma_n^{*(k-1)} - \sigma_c^{*(k-1)})(1-p_{k-1})^{2/3}[1-(1-p_{k-1})^{1/3}]}, \qquad (20)$$

$$\psi_2^{(k-1)} = \frac{\sigma_c^{*(k-1)} + (\sigma_c^{*(k-1)} - \sigma_n^{*(k-1)})(1-p_{k-1})^{1/3}[1-(1-p_{k-1})^{2/3}]}{\sigma_n^{*(k-1)} + (\sigma_c^{*(k-1)} - \sigma_n^{*(k-1)})(1-p_{k-1})^{1/3}}, \qquad (21)$$

$\sigma_c^{*(0)} = \sigma_1^*$, $\sigma_n^{*(0)} = \sigma_2^*$, and $p_0 = p$. The magnitudes of p_k were determined using formula (11).

In Eqs. (19)–(21), the subscripts n and c denote that a given quantity refers to the NCS and CS, respectively, and the index k indicates the order number of the iteration step.

To determine the complex conductivity of an NCS $\sigma_n^{*(k)}$, it is necessary to replace the indices in Eqs. (19)–(21) as follows: $n \longleftrightarrow c$, $1 \longleftrightarrow 2$, and $(1-p) \longleftrightarrow p$.

3. CALCULATION RESULTS

The calculations were performed for a two-phase (two-component) medium.

The calculations of the dielectric properties of inhomogeneous media at various frequencies and concentrations of the phases using Eqs. (11) and (19)–(21) showed that the iteration process converges; i.e.,

$$\lim_{k\to\infty} \sigma_c^{*(k)} = \lim_{k\to\infty} \sigma_n^{*(k)} = \sigma^*. \qquad (22)$$

The complex local conductivity for the metallic phase with allowance for the Drude dielectric function (8) was determined as

$$\sigma_1^*(\omega) = \sigma_1 + i\omega\left(\varepsilon_1 - \frac{1}{x^2+\gamma^2}\right), \qquad (23)$$

where

$$x = \omega/\omega_p, \quad \gamma = 1/\omega_p\tau_1.$$

The complex local conductivity of the insulating phase was determined as

$$\sigma_2^*(\omega) = \sigma_2 + i\omega\varepsilon_2. \qquad (24)$$

It was assumed in the calculations that

$$\varepsilon_1 = 1; \quad \varepsilon_2 = 10; \quad \gamma = \frac{1}{30}; \quad \omega_p\tau_1 = 30;$$

$$\sigma_2/\sigma_1 = 10^{-2}; \quad \tau_1 = 1; \quad 0.001 \le \omega/\omega_p \le 1.5.$$

Figures 3 and 4 display the dependences of the effective dielectric constant $\varepsilon = \mathrm{Im}(\sigma^*)/\omega$ and the effective conductivity $\sigma = \mathrm{Re}(\sigma^*)$ on the concentration of the metallic phase p and the relative frequency ω/ω_p. The zeros of the effective dielectric constant ε determine the plasma frequencies of the system, i.e., the metal–insulator transition.

It follows from the calculations (Figs. 3, 4) that at low frequencies, a divergence arises in the effective dielectric constant and in the effective conductivity (a sharp increase in losses). This is explained by the fact that in this case, in the system, finite clusters of the metallic phase arise which are separated by thin insulating interlayers. Such structures form a hierarchic self-similar chaotic capacitance net which generates a system of resonance frequencies.

In addition, the frequency dependences of the effective properties are affected by the configurations of the finite clusters [39]. This may be illustrated by the consideration of a pair of inclusions that have the shape of a circle with the associated set of discrete frequencies:

$$\begin{aligned} \omega_{1m}^2 &= \omega_p^2 \tanh(m\xi_0), \\ \omega_{2m}^2 &= \omega_p^2 \coth(m\xi_0), \quad m = 1, 2, \ldots, \end{aligned} \qquad (25)$$

where

$$\xi_0 = \ln\left|\frac{\rho + (\rho^2 - 4R)^{1/2}}{2R}\right|,$$

ρ is the spacing between the centers of the circles, and R is the radius of the circles.

Thus, if such regions are formed in a composite, they create circuits with resonance frequencies.

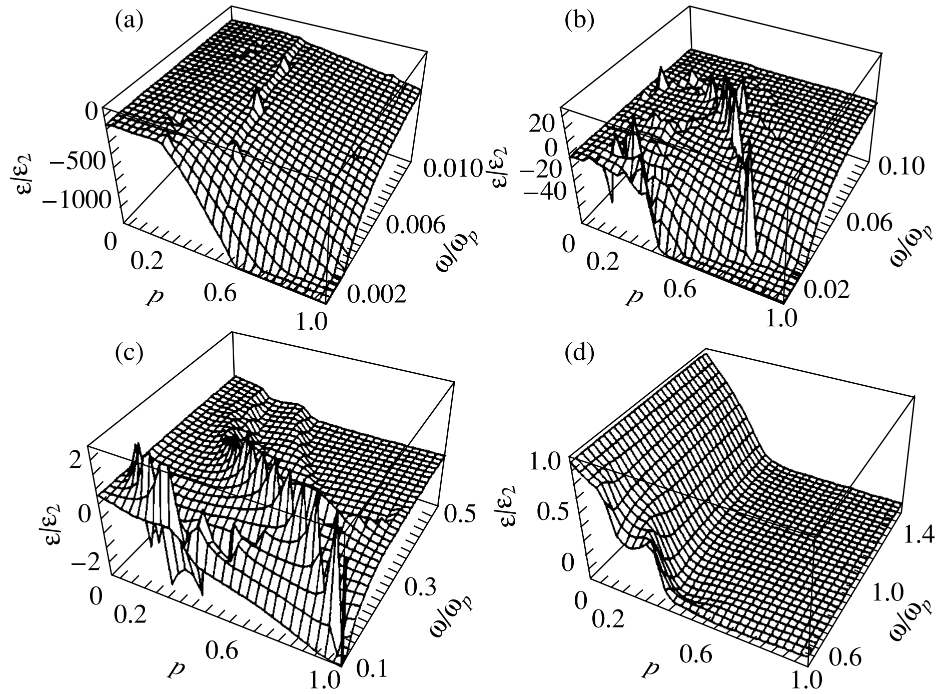

Fig. 3. Variation of the dielectric constant $\varepsilon/\varepsilon_2$ of a metal–insulator composite as a function of the concentration of the metallic phase p and the frequency ω/ω_p.

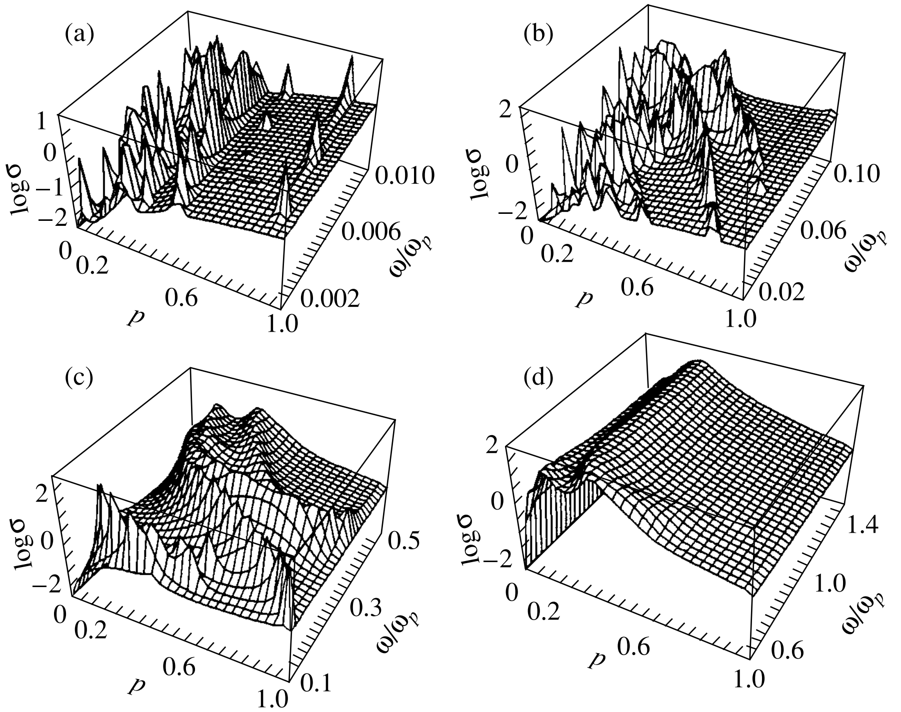

Fig. 4. Variation of the logarithm of the conductivity $\log\sigma$ of a metal–insulator composite as a function of the concentration of the metallic phase p and the frequency ω/ω_p.

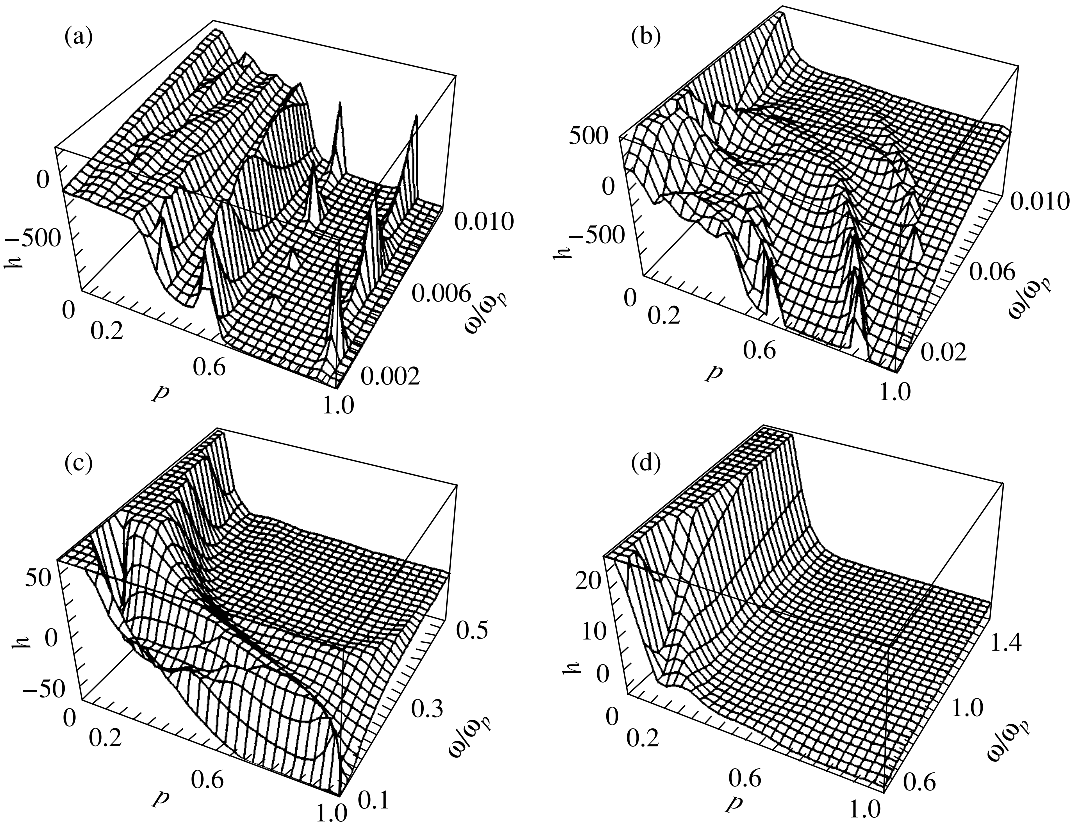

Fig. 5. Variation of the ratio of the capacitance conductivity to the active conductivity $h = |\varepsilon\omega/\sigma|$ of a metal–insulator composite as a function of the concentration of the metallic phase p and the frequency ω/ω_p.

It also follows from Eq. (25) that, at $\rho \longrightarrow 2R$, we have $\xi_0 \longrightarrow 0$ and frequencies (25) form a quasi-continuous spectrum [39].

It was shown in [11, 12] that ring-shaped structures (ring clusters) generate double peaks in the frequency dependence of the conductivity. Such ring structures in the system at hand are located chaotically, hierarchically, in a self-similar way, and also lead to the appearance of peaks in the conductivity.

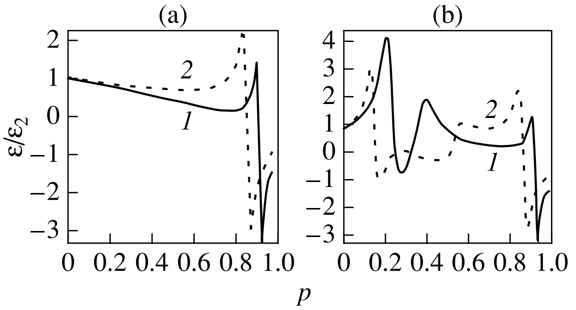

Fig. 6. Variation of the dielectric constant $\varepsilon/\varepsilon_2$ of a metal–insulator colloid solution as a function of the metallic phase (silver) p: (a) calculation based on the Lorentz model; (b) calculation based on the fractal model; (*1*) $\omega/\omega_p = 0.25$ and (*2*) $\omega/\omega_p = 0.3$.

Figure 5 displays the dependences of the modulus of the ratio of the capacitance conductivity to the active conductivity $h = |\varepsilon\omega/\sigma|$ on p and ω/ω_p. Calculations show that the displacement current in the region of small frequencies ($\omega/\omega_p < 1$) behaves nonmonotonically. In the range of high frequencies ($\omega/\omega_p > 1$) and at concentrations of the metallic phase below the percolation threshold ($p < p_c$), the displacement current exceeds the current through the active conductors ($h \gg 1$) and the surface of the dielectric properties becomes smooth. At $p > p_c$, the current through the active conductors exceeds the displacement current ($h \ll 1$).

Now, we discuss one of the possible applications of the above model concepts of the dielectric properties of fractal systems.

The optical properties of colloid systems have not yet been explained in terms of the classical theory (e.g., in terms of the Mie theory [40–42]). In the framework of this theory, the change in the color of sols was assumed to be due to the appearance of metallic (silver) particles of various sizes in the solution; the change in the color was ascribed to the dependence of the resonance (plasma) frequency on the particle radius. However, the experimental investigations showed that the spectral dependences of colloid solutions do not correlate with the statistical particle-size distribution function; i.e., the role of the particle size seems to be insignificant [43]. The appearance of a long-wavelength wing in the spectrum of the colloid solution can be explained by the aggregation of particles into fractal structures.

Indeed, a small silver particle has a frequency of plasma vibrations with a wavelength $\lambda = 2\pi c/\omega_p =$ 140 nm. To explain the presence of a peak at 650 nm, the classical (Lorentz) theory [40–42] requires the presence in the colloid solution of silver with a volume concentration of $p \cong 0.86$ (Fig. 6a), whereas the experiment yields p values that are much smaller [44], which agrees with our calculations (Fig. 6b). Thus, the shift of the peak in colloid solutions toward the region of small concentrations of metal can be explained by the formation of fractal structures in these solutions.

We indicate some other objects that have fractal structures. For example, using sputtering regimes that correspond to the model of diffusional aggregation [5], thin films consisting of metallic fractal clusters can be obtained. Fractal structures are also characteristic of percolation clusters near the percolation threshold, as well as some binary solutions and polymer solutions. The dielectric properties of all these objects can be predicted using the above-considered fractal model.

4. CONCLUSION

Thus, calculations of the dependences of the conductivity and the dielectric constant of chaotic hierarchic self-similar structures of metal–insulator composites were performed on the basis of a fractal model in the entire range of concentrations of inhomogeneities at various frequencies of an external field. The metal–insulator transition was shown to occur not only near the percolation threshold. It was also shown that the transition depends on the concentration of the metallic phase and the frequency of the external field.

REFERENCES

1. J. C. Maxwell, *A Treatise on Electricity and Magnetism* (Clarendon, Oxford, 1873); J. C. Maxwell, *A Treatise on Electricity and Magnetism* (Dover, New York, 1973).
2. J. C. Maxwell-Garnett, Philos. Trans. R. Soc. London **203**, 385 (1904).
3. D. A. G. Bruggeman, Ann. Phys. **24**, 636 (1935).
4. R. Landauer, in *Proceedings of the 1st Conference on the Electrical Transport and Optical Properties of Inhomogeneous Media*, Ohio State University, 1997, edited by J. C. Garland and D. B. Tanner; R. Landauer, AIP Conf. Proc. **40**, 2 (1978).
5. D. Stauffer, *Introduction to the Percolation Theory* (Taylor and Francis, London, 1985).
6. M. Sahimi, *Applications of Percolation Theory* (Taylor and Francis, London, 1994).
7. V. P. Privalko and V. V. Novikov, *The Science of Heterogeneous Polymers: Structure and Thermophysical Properties* (Wiley, Chichester, 1995).
8. I. Webman and J. Jortner, Phys. Rev. B **11** (8), 2885 (1975).
9. I. Webman and J. Jortner, Phys. Rev. B **13** (2), 713 (1976).
10. L. D. Landau, E. M. Lifshitz, and L. P. Pitaevskii, *Course of Theoretical Physics*, Vol. 8: *Electrodynamics of Continuous Media* (Nauka, Moscow, 1982; Pergamon, New York, 1984).
11. X. Zeng, P. Hui, and D. Stroud, Phys. Rev. B **39** (2), 1063 (1989).
12. X. C. Zeng, P. M. Hui, D. J. Bergman, and J. D. Stroud, Phys. Rev. B **39** (18), 13224 (1989).
13. D. J. Frank and C. J. Lobb, Phys. Rev. B **37** (1), 302 (1988).
14. J. Abel and A. A. Kornyshev, Phys. Rev. B **54** (9), 6276 (1996).
15. D. Bergman and Y. Imry, Phys. Rev. Lett. **39** (19), 1222 (1977).
16. A. Bug, G. Grest, M. Cohen, and I. Webman, J. Phys. A **19** (1), 323 (1986).
17. A. Bug, G. Grest, M. Cohen, and I. Webman, Phys. Rev. B **36** (7), 3675 (1987).
18. T. W. Noh and P. H. Song, Phys. Rev. B **46** (7), 4212 (1992).
19. T. B. Schroder and J. C. Dyre, Phys. Rev. Lett. **84** (2), 310 (2000).
20. X. L. Lei and J. Qzhang, J. Phys. C **19**, L73 (1986).
21. R. Koss and D. Stroud, Phys. Rev. B **35** (17), 9004 (1987).
22. D. Stroud and P. Hui, *The Physics and Chemistry of Small Clusters* (Plenum, New York, 1987), pp. 547–565.
23. A. Jonscher, *Dielectric Relaxation in Solids* (Chalsea Dielectric Press, London, 1983).
24. V. V. Novikov, O. P. Poznansky, and V. P. Privalko, Sci. Eng. Compos. Mater. **4** (1), 49 (1995).
25. V. Raicu, Phys. Rev. E **60** (4), 4677 (1999).
26. V. E. Dubrov, M. E. Levinshteĭn, and M. S. Shur, Zh. Éksp. Teor. Fiz. **70** (5), 2014 (1976) [Sov. Phys. JETP **43**, 1050 (1976)].
27. Y. Yagil, P. Gadenne, C. Julin, and G. Deutscher, Phys. Rev. B **46** (4), 2503 (1992).
28. F. Brouers, Phys. Rev. B **47** (2), 666 (1993).
29. A. K. Sarychev, D. J. Bergman, and J. Yagil, Phys. Rev. B **51** (8), 5366 (1995).
30. F. Brouers, S. Blacher, A. N. Lagrkov, *et al.*, Phys. Rev. B **55** (19), 13234 (1997).
31. V. M. Shalaev and A. K. Sarychev, Phys. Rev. B **57** (20), 13265 (1998).
32. V. V. Novikov and V. P. Belov, Zh. Éksp. Teor. Fiz. **106** (3), 780 (1994) [JETP **79**, 428 (1994)].
33. V. V. Novikov, Teplofiz. Vys. Temp. **34** (5), 688 (1996).
34. V. V. Novikov, Phys. Met. Metallogr. **83** (4), 349 (1997).

35. V. V. Novikov and K. W. Wojciechowski, Fiz. Tverd. Tela (St. Petersburg) **41** (12), 2147 (1999) [Phys. Solid State **41**, 1970 (1999)].
36. V. V. Novikov, K. W. Wojciechowski, V. P. Privalko, and D. V. Belov, Phys. Rev. E **63**, 036120 (2001).
37. J. Bernasconi, Phys. Rev. B **18** (5), 2185 (1978).
38. S. R. Coriell and J. L. Jackson, J. Appl. Phys. **39** (10), 4733 (1968).
39. B. Ya. Balagurov, Zh. Éksp. Teor. Fiz. **88** (15), 1664 (1985) [Sov. Phys. JETP **61**, 991 (1985)].
40. H. C. van de Hulst, *Light Scattering by Small Particles* (Wiley, New York, 1957; Inostrannaya Literatura, Moscow, 1961).
41. C. F. Bohren and D. R. Huffman, *Absorption and Scattering of Light by Small Particles* (Wiley, New York, 1983; Mir, Moscow, 1986).
42. Yu. I. Petrov, *Clusters and Small Particles* (Nauka, Moscow, 1986).
43. S. H. Heard, F. Griezer, G. G. Barrachough, and J. V. Sanders, J. Colloid Interface Sci. **93** (3), 545 (1983).
44. V. I. Emel’yanov and I. I. Koroteev, Usp. Fiz. Nauk **135** (2), 345 (1981) [Sov. Phys. Usp. **24**, 864 (1981)].

Translated by S. Gorin

Physics of the Solid State, Vol. 44, No. 11, 2002, pp. 2063–2066. Translated from Fizika Tverdogo Tela, Vol. 44, No. 11, 2002, pp. 1970–1973.
Original Russian Text Copyright © 2002 by Zaĭnullina, Leonidov, Kozhevnikov.

DEFECTS, DISLOCATIONS, AND PHYSICS OF STRENGTH

Specific Features of the Formation of Oxygen Defects in the $SrFeO_{2.5}$ Ferrate with a Brownmillerite Structure

V. M. Zaĭnullina, I. A. Leonidov, and V. L. Kozhevnikov
Institute of Solid-State Chemistry, Ural Division, Russian Academy of Sciences,
Pervomaĭskaya ul. 91, Yekaterinburg, 620219 Russia
e-mail: Veronika@ihim.uran.ru

Received December 4, 2001

Abstract—The electronic structure and chemical bonding in the $Sr_2Fe_2O_5$ strontium ferrate are investigated in the framework of the *ab initio* linear-muffin-tin-orbital tight-binding representation and extended Hükcel calculations. Models of defect formation (oxygen vacancies and anti-Frenkel defects) in the brownmillerite structure are considered. A model of ion transfer in strontium ferrate is proposed reasoning from the results of the calculations. *© 2002 MAIK “Nauka/Interperiodica”.*

1. INTRODUCTION

Oxide compounds with a brownmillerite structure of the general formula $A_2B_2O_5$ have attracted considerable attention, because they are promising materials for use in designing high-temperature electrochemical devices [1, 2]. In particular, strontium ferrate exhibits high characteristics of ion transfer. Recently [3], we revealed that the oxygen ion conductivity in $Sr_2Fe_2O_5$ reaches 0.1 S/cm in the temperature range 850–900°C.

The structure of the $Sr_2Fe_2O_5$ ferrate can be considered a derivative of the $SrFeO_3$ perovskite structure in which 1/6 of the oxygen sites are empty. The orthorhombic unit cell of this compound is shown in Fig. 1. The unit cell consists of alternating layers of $Fe(1)O_6$ octahedra and $Fe(2)O_4$ tetrahedra, whereas oxygen vacancies are ordered in the [101] direction. As a rule, ordering of oxygen vacancies leads to suppression of ion transfer [4]. In this respect, it is of interest to elucidate the mechanism of the disordering of the $Sr_2Fe_2O_5$ structure that is favorable to electrical conduction through oxygen ions. In the present work, the use of the *ab initio* linear-muffin-tin-orbital tight-binding (TB-LMTO) method [5] in combination with extended Hückel calculations [6] made it possible for the first time to investigate the electron energy spectrum, chemical bonding, and the energy of formation of anti-Frenkel defects in strontium ferrate. The mechanism of ion transfer in $Sr_2Fe_2O_5$ was proposed from analyzing the results of quantum-chemical calculations.

2. CALCULATION TECHNIQUE

In order to calculate the electronic structure and the total energy, we used one of the most time-efficient and sufficiently exact methods in the electron density functional theory, namely, the linear-muffin-tin-orbital tight-binding method. The theoretical concepts of this approach were thoroughly described in [5, 7]. Here, we dwell on some computational details that affect the accuracy of the results obtained, especially for the total energy of the crystal.

The Bloch functions for the studied crystal are constructed using a basis set of atomic orbitals, including the valence 5*s* and 4*d* orbitals of strontium atoms; the 4*s*, 4*p*, and 3*d* orbitals of iron atoms; and the 2*p* orbitals of oxygen atoms. The Sr 5*p* orbitals are not included in

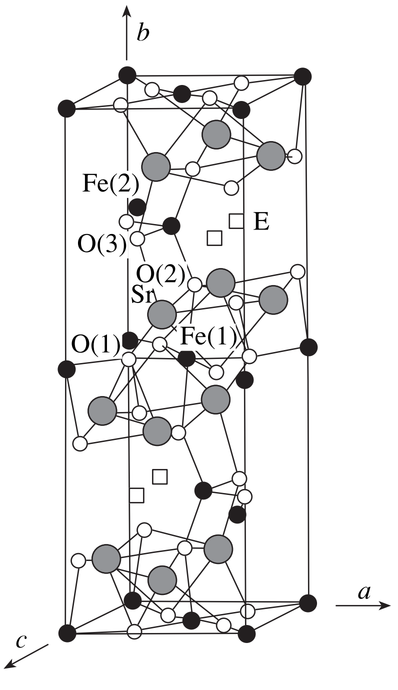

Fig. 1. Supercell of strontium ferrate.

Table 1. Atomic parameters used in the extended Hükcel calculations: the ionization potentials of valence orbitals H_{ii}, the exponents ξ_i, and the weight coefficients C_i of exponents in the expressions for atomic orbitals of the Slater type

Atom	Orbital	H_{ii}, eV	$\xi_1(C_1)$ $\xi_2(C_2)$
O	2*s*	32.30	2.275
	2*p*	14.80	2.275
Fe	4*s*	9.10	1.90 (1.00)
	4*p*	5.32	1.90 (1.00)
	3*d*	12.60	5.35 (0.5505)
			2.00 (0.6260)
Sr	5*s*	6.62	1.214 (1.00)
	5*p*	3.92	1.214 (1.00)

the basis set of the Bloch functions used to construct the Hamiltonian matrices with the use of the down-folding method [8], which is based on the Löwdin perturbation theory [9]. The calculations are performed with a supercell of composition $Sr_8Fe_8O_{20}E_4$, where E are empty interstitial spheres.

Since the TB-LMTO method is developed and offers the most exact results for close-packed lattices, in our calculations, interstices are filled by empty spheres with a basis set of *s* orbitals (extraspheres [5, 7]); the *p* and *d* states of extraspheres are taken into account only within the down-folding approach.

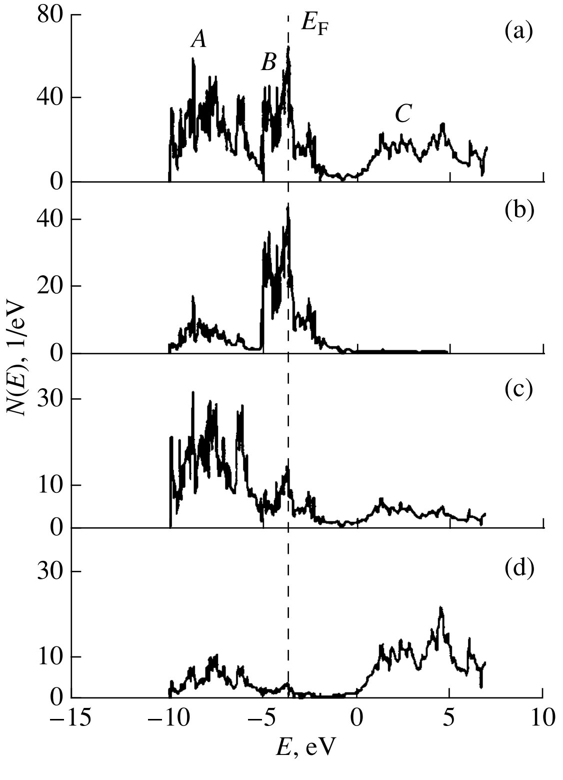

Fig. 2. Densities of states $N(E)$ for a perfect crystal of $SrFeO_{2.5}$: (a) the total density of states and (b) Fe 3*d*, (c) O 2*p*, and (d) Sr 5*s* and Sr 5*p* partial densities of states.

The calculations are performed using 256 *k* vectors in the Brillouin zone (75 *k* vectors per irreducible part of the Brillouin zone). The radii of atomic spheres are determined from the condition of filling the defect-free crystal volume with these spheres according to the procedure described in [10]. The accuracy in the determination of the energies of defect formation depends on the appropriate choice of the radii of the extraspheres and real atoms, which interchange sites with one another to form a defect. We assume that the oxygen atom occupying an extrasphere site takes on the extrasphere radius and vice versa; at the same time, the radii of atoms and extraspheres that are not involved in the defect formation remain unchanged. This procedure of choosing the atomic radii was detailed and approved for alkaline-earth fluorides and zirconium oxides in our earlier work [11]. The lattice parameters for the $Sr_2Fe_2O_5$ crystal are taken from [12].

The characteristics of the chemical bonding in the ferrate under investigation were analyzed in the framework of semiempirical extended Hükcel calculations [6, 13]. The standard parameters used in the extended Hükcel calculations are tabulated in [14] and presented in Table 1.

3. RESULTS AND DISCUSSION

Figure 2 shows the total and partial densities of states for $Sr_2Fe_2O_5$, which were obtained in the framework of *ab initio* LMTO calculations. The broad band *A* in the energy range from –9.87 to –5.27 eV corresponds to a hybrid O 2*p*–Fe 3*d* band with an admixture of Sr 5*s* and Sr 5*p* states. The high-energy band *B* in the energy range from –5.27 to –0.75 eV consists predominantly of Fe 3*d* orbitals with an admixture of O 2*p* states. The metallic band *C*, which is composed of Sr 5*s* and Sr 5*p* states, is located at even higher energies. The Fermi level corresponds to a maximum of the *B* band. The absence of the band gap at the Fermi level is a consequence of incomplete inclusion of correlation effects in the calculation. Note that the correlation effects are responsible for the splitting of the *B* band and the transition of the ferrate to a Mott–Hubbard insulator. This assumption is confirmed by the fact that a band gap of ~1.4 eV appears in the electronic spectrum in the course of simulation of the electronic structure of $Ba_2In_2O_5$ with a similar crystal lattice. This band gap is underestimated with respect to the experimental value of 2.7 eV [15]. It should be noted that traditional *ab initio* calculations (TB-LMTO [5], full-potential LMTO [16], and Hartree–Fock [17] methods) give sufficiently exact values of the total crystal energy and the energy of formation of point defects [18, 19]. More correct calculation procedures of the electronic band structure and the total energy of Mott–Hubbard insulators must take

Table 2. Populations of overlap of crystal orbitals, the total energies E_{tot} of the crystal lattice with one oxygen vacancy per supercell, the total populations of overlap of crystal orbitals for different-type oxygen atoms, and the energies of formation of anti-Frenkel defects E_{AFD} in the $SrFeO_{2.5}$ crystal

		Type of oxygen atom		
		O(1)	O(2)	O(3)
Populations of overlap of crystal orbitals	Fe(1)–O	0.274–0.254	0.163	–
	Fe(2)–O	–	0.422	0.465–0.292
	Sr–O	0.050–0.022	0.079–0.043	0.156
E_{tot}, Ry		–74011.00176	–74010.8814	–74010.9569
Total populations of overlap of crystal orbitals		0.674	0.767	0.915
E_{AFD}, Ry (eV)		0.225 (3.067)	0.264 (3.597)	–

into account nonlocal exchange-correlated interactions and their dependence on the energy of skeletal states of the crystals. However, these methods are still under development (see, for example, [20]).

Apart from analyzing the electronic spectrum of strontium ferrate, we investigated chemical interactions in the $Sr_2Fe_2O_5$ structure in the framework of the semiempirical Hückel method. The results of the calculations of chemical bonding are given in Table 2. The strongest covalent interactions are observed between the Fe(2) and O(3) atoms (the bond order is equal to 0.466) in layers formed by the FeO_4 tetrahedra. The Fe–O(1) bonds, which involve oxygen atoms located in the equatorial plane of the FeO_6 octahedra, prove to be somewhat weaker. Small populations of the overlap of the crystal orbitals (0.022) correspond to a substantial contribution of the ionic component and a small contribution of the covalent component of the Sr–O(1) chemical bond. Therefore, the structure of strontium ferrate is characterized by a rigid framework consisting of iron–oxygen octahedra and tetrahedra with strong Fe–O covalent bonds. The strontium atoms are more weakly bonded to the nearest oxygen environment, and the Sr–O interactions exhibit a mixed ionic–covalent nature.

In order to elucidate the mechanism of ion transfer in the brownmillerite structure, we simulated the defect-containing phases of the strontium ferrate. All the calculations of the total energy for crystals with one oxygen vacancy or one anti-Frenkel defect per computational supercell were carried out in the framework of the *ab initio* TB-LMTO representation. We considered three possible variants of the arrangement of a particular oxygen vacancy in the brownmillerite structure, namely, at the O(1), O(2), and O(3) sites. The configuration with an oxygen vacancy in the $Fe(1)O(1)_4$ equatorial plane of the $Fe(1)O(2)_2O(1)_4$ octahedra, which form perovskite-like structural units, turned out to be the most energetically favorable (Table 2). The formation of an oxygen vacancy in the O(2) apical position of these octahedra is less probable. The independent band calculations within the extended Hückel approximation confirm the preferential formation of oxygen vacancies in the equatorial plane of the $Fe(1)O(2)_2O(1)_4$ oxygen octahedron. The total population of the overlap of crystal orbitals for different types of oxygen atoms characterizes the covalent contribution to the chemical bond and appears to be minimum for the O(1) atom (Table 2). The results obtained allow us to assume that the ion migration in ferrate occurs through vacant oxygen sites in the equatorial plane of the FeO_6 octahedra.

The above assumption is confirmed by the calculated energies of formation of anti-Frenkel defects in the $Sr_2Fe_2O_5$ crystal. The lowest energy of formation of anti-Frenkel defects corresponds to a transition of the O(1) atom to a tetrahedral interstice (E) (Table 2). The transition of the O(2) atom to the nearest tetrahedral vacancy is less energetically favorable. Analysis of the calculated data demonstrates that the formation of anti-Frenkel defects proceeds through the direct interstitial mechanism. As a result, the interstitial oxygen atom occupies a tetrahedral position and the oxygen vacancy is located in the equatorial plane of the oxygen octahedron. The lower bonding energy of the equatorial oxygen atoms suggests that the dominant mechanism of ion migration in the ferrate is the positional exchange of oxygen ions and oxygen vacancies in the equatorial plane of FeO_6 octahedra forming perovskite-like structural units of the $Sr_2Fe_2O_5$ structure.

Moreover, we evaluated the degree of interaction between oxygen vacancies in the case when their concentration increases to two vacancies per computational supercell of the studied ferrate. The results obtained indicate a preferential arrangement of vacancies in the form of V_O–Fe–V_O chains in the equatorial plane of the perovskite-like structural unit. The formation of these associates leads to an effective elimination of vacancies from the ion transfer even at sufficiently high temperatures. This explains the decrease in the ion conduction in ferrate at extremely low oxygen pressures in the gas phase [3].

ACKNOWLEDGMENTS

We would like to thank V.P. Zhukov for his participation in discussions of the results.

This work was supported in part by the Russian Foundation for Basic Research, project RFBR-Ural 01-03-96519.

REFERENCES

1. J. B. Goodenough, J. E. Ruiz-Diaz, and Y. S. Zhen, Solid State Ionics **44**, 21 (1990).
2. M. Schwartz, J. White, and A. Sammels, Int. Patent Application PCT. WO 97/41060 (1997).
3. V. L. Kozhevnikov, I. A. Leonidov, M. V. Patrakeev, *et al.*, J. Solid State Chem. **158**, 320 (2000).
4. H. J. M. Bouwmeester and A. J. Burggraaf, in *Fundamentals of Inorganic Science and Technology Series*, Ed. by A. J. Burggraaf and L. Cot (Elsevier, Amsterdam, 1996), Issue 4.
5. O.-K. Andersen and O. Jepsen, Phys. Rev. Lett. **53**, 2571 (1984).
6. M.-H. Whangbo and R. Hoffmann, J. Am. Chem. Soc. **100**, 6093 (1978).
7. O.-K. Andersen, Phys. Rev. B **34** (8), 5253 (1986).
8. W. R. L. Lambrecht and O.-K. Andersen, Phys. Rev. B **34** (4), 2439 (1986).
9. P. O. Löwdin, J. Chem. Phys. **19** (11), 1396 (1951).
10. G. Krier, O. Jepsen, A. Burkhardt, and O.-K. Andersen, *The TB-LMTO-ASA Program* (MPI für Festkorperforschung, Stuttgart, 1996).
11. N. M. Zainullina, V. P. Zhukov, and V. M. Zhukovsky, Phys. Status Solidi B **210**, 145 (1998).
12. B. C. Greaves, A. J. Jacobson, B. C. Tofield, and B. E. Fender, Acta Crystallogr. B **31**, 641 (1975).
13. R. Hoffmann, *Manuals for Extended Hückel Calculations* (Cornell Univ. Press, Ithaca, 1989).
14. S. Alvarez, *Tables of Parameters for Extended Hückel Calculations* (Universitat de Barcelona, Barcelona, 1989).
15. G. B. Zhang and D. M. Smyth, Solid State Ionics **82**, 161 (1995).
16. M. Methfessel, Phys. Rev. B **38** (2), 1537 (1988).
17. C. Pisani, R. Dovesi, and C. Roetti, in *Lecture Notes in Chemistry* (Springer-Verlag, Berlin, 1988), Vol. 48.
18. H. M. Polatoglou, M. Methfessel, and M. Scheffler, Phys. Rev. B **48** (3), 1877 (1993).
19. T. Brudevoll, E. A. Kotomin, and N. E. Christensen, Phys. Rev. B **53** (12), 7731 (1996).
20. B. Holm and F. Aryasetiawan, Phys. Rev. B **62** (8), 4858 (2000).

Translated by N. Korovin

Physics of the Solid State, Vol. 44, No. 11, 2002, pp. 2067–2071. Translated from Fizika Tverdogo Tela, Vol. 44, No. 11, 2002, pp. 1974–1978.
Original Russian Text Copyright © 2002 by Lisitsyn, Yakovlev.

DEFECTS, DISLOCATIONS, AND PHYSICS OF STRENGTH

Relaxation Kinetics of Primary Pairs of Radiation Defects in Ionic Crystals

V. M. Lisitsyn and A. N. Yakovlev
Tomsk Polytechnical University, Tomsk, 634034 Russia
e-mail: yackov@list2.epd.tpu.edu.ru

Received October 23, 2001; in final form, January 8, 2002

Abstract—The relaxation kinetics of primary pairs of radiation defects in ionic crystals with a face-centered lattice is investigated using the Monte Carlo method. The dependence of the relaxation kinetics of an *F*–*H* pair on the parameters of the interaction potential between the components of the pair is studied. The obtained kinetic dependences are analyzed to determine the factors responsible for the relaxation processes. *© 2002 MAIK "Nauka/Interperiodica".*

1. INTRODUCTION

The action of ionizing radiation on ionic crystals results in the creation of electron excitations decaying into pairs of Frenkel defects [1]. The decay occurs over time periods of the order of several or tens of picoseconds [2, 3]. The primary Frenkel pairs (*F* and *H* pairs) formed in this way remain stationary up to 0.1–10 ns. Subsequent motion of the mobile component (*H* center) of a pair leads, as a result of a series of consecutive thermally activated jumps, either to the annihilation of the pair or to spatial separation of its components. In this case, the number of pairs decreases with time and the movable component is transformed into a stable hole center. A model of relaxation of primary defects with time, taking into account the sample temperature, was proposed in [4, 5]. This model was confirmed experimentally and developed in [6, 7].

This study aims at analyzing the primary processes of relaxation of defect pairs created during the decay of electron excitations by using methods of computer simulation and determination of the dependence of the kinetics on the form of the interaction potential and on the initial mutual distribution of pair components.

2. COMPUTATIONAL METHOD

We calculated the motion of a mobile component (*H* center) of a pair in the field of the stationary component (*F* center) in the face-centered lattice of an alkali halide metal. We specified the initial position of the *H* center at one of the lattice sites nearest to the *F* center. Using the Monte Carlo method [8], we then determined the probabilities of the transition of the *H* center from the given state to any other state possible for its arrangement as a result of a series of consecutive jumps as a function of the interaction potential between the components of the defect pair. The *H* center moves over the anionic sublattice as a result of thermally activated jumps. The origin of the coordinate system is taken to be at the *F* center, which corresponds to the zeroth state. Each state corresponds to a coordination shell around the *F* center in which the *H* center can be arranged as it moves away from the *F* center. The *H* center is in the field of the *F* center, which is taken into account in the model by introducing the interaction potential between the *H* and *F* centers and, therefore, by a difference in the barrier height for the motion of the *H* center towards the *F* center and away from it. The fall of the *H* center to the zeroth state means its annihilation with the *F* center and the vanishing of the pair. In the case when the *H* center is beyond the twelfth shell of its possible arrangement around the *F* center, the *H* center is assumed to be transformed into a center that is stable under the experimental conditions and cannot be annihilated during its subsequent motion. This corresponds to the actual situation upon irradiation: at temperatures higher than the delocalization temperature, an *H* center is transformed into a stable V_k center after several jumps over the lattice. We calculated the probability of survival of the *H* center (and, accordingly, of the *F*–*H* pair) by a given instant of its migration as a function of the crystal temperature. Any *H* center was regarded as having survived irrespective of its location (inside or outside the twelve shells around the *F* center).

We assumed that, in the course of decay of electron excitations, the initial mutual arrangement of the components of pairs is created in the form of a compact function with a maximum in the first shell around the *F* center, which is taken as the starting point for calculations.

The effect of the stationary defect on the motion of the mobile defect was presented by the superposition of the periodic potential of the crystal lattice and the interaction potential of the form $E(r) = -a\exp(-br)$. The periodic variation of the potential during migration of the *H* center is associated with the fact that the *H* center,

Table 1. Starting probabilities of arrangement of an *H* center in different shells around the *F* center used in the calculations (initial distribution function, IDF)

No.	First shell	Second shell	Third shell
1	1	0	0
2	0.5	0.5	0
3	0	1	0
4	0	0	1

when moving from a lattice site to a neighboring site, must pass through the constriction formed by cations in a plane perpendicular to the direction of motion of the *H* center. The form of the interaction potential is unknown. However, its representation in exponential form ensures the possibility of wide variation of its form, which is determined by the type of interaction (electrostatic, elastic, etc.).

The transition of an *H* center to a state more distant from the *F* center indicates spatial separation of the pair components. We calculated the migration of an *H* center in the bulk of a crystal containing 1000 anionic lattice sites.

At present, neither the form of the interaction potential of the components of a primary pair nor the form of the function describing their initial mutual distribution is known. It is known, however, that the components of a genetically connected primary pair of defects interact with each other. This leads to the assumption that the components of a pair created during the decay of an electron excitation are in the nearest shells of their possible arrangement. To establish the dependence of the relaxation kinetics on the starting state, the initial mutual distribution of the pair components was specified as follows. We assumed that the *H* center is in the first, second, or third shell of its possible arrangement around the *F* center. These shells correspond to location of the *H* center at sites with coordinates equivalent to ⟨110⟩, ⟨200⟩, and ⟨211⟩ relative to the *F* center. Table 1 gives the probabilities of distribution of the *H* center over the shells of its possible location around the *F* center. The values 1 and 0.5 in the table indicate the starting probability of the location of the *H* center in the corresponding shell. The starting probability of the location of the *H* center indicates the initial distribution function for primary pairs formed as a result of the decay of electron excitations.

The parameters of the interaction potential were chosen such that the *H* center could be in a metastable state even at a site nearest to the *F* center. This means that we presumed the existence of a barrier for a jump of the *H* center towards the *F* center from the site nearest to the *F* center. The forms of the potential relief for the migrating *H* center in the vicinity of the *F* center are presented in Fig. 1. The values of the parameters of the interaction potential were set in the intervals $a = 0.1$–0.25 and $b = 0.5$–2.0. Calculations were made for the same sample temperature, 100 K. In this case, an *H* center with an activation energy for its motion equal to 0.04 eV is mobile.

3. RESULTS OF CALCULATION

Typical relaxation kinetics curves calculated for various initial states of mutual distribution of pair components are presented in Fig. 2. All the curves have three clearly manifested segments on which the probability of pair survival decreases with time (the first segment corresponds to the time interval 10^{-12}–10^{-8} s, the second to 10^{-8}–10^{-7} s, and the third to a time longer than 10^{-7} s). The first segment corresponds to 1–3 single jumps of the *H* center. The probability decrease on this segment is significant if the *H* center starts from the sites closest to the *F* center. As the distance between the starting point of the *H* center and the *F* center increases, the role of the first stage in the decrease becomes much smaller. For example, the results of calculations presented in Fig. 2 (curves *4*) show that in the case when the *H* center starts from the third shell, the contribution of the first stage is insignificant. The contribution of the first stage to the kinetics of decay depends not only on the initial mutual arrangement of the pair components

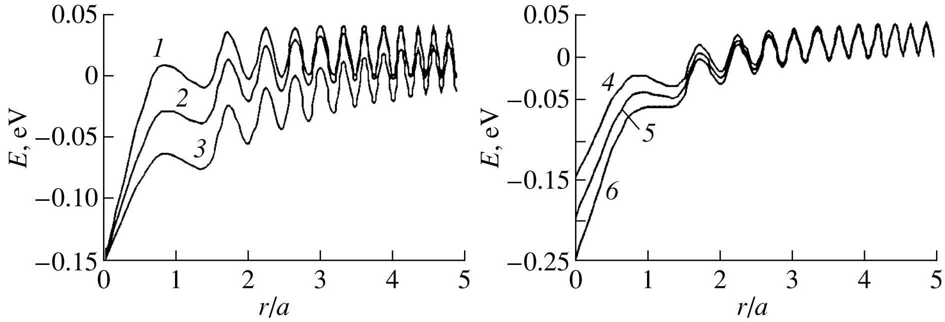

Fig. 1. Interaction potential reliefs for the components of a pair of defects for different values of the model parameters. Curves *1*–*3* correspond to $b = 2.0$, 1.0, and 0.5, respectively, and $a = 0.15$; curves *4*–*6* correspond to $a = 0.15$, 0.2, and 0.25, respectively, and $b = 1$.

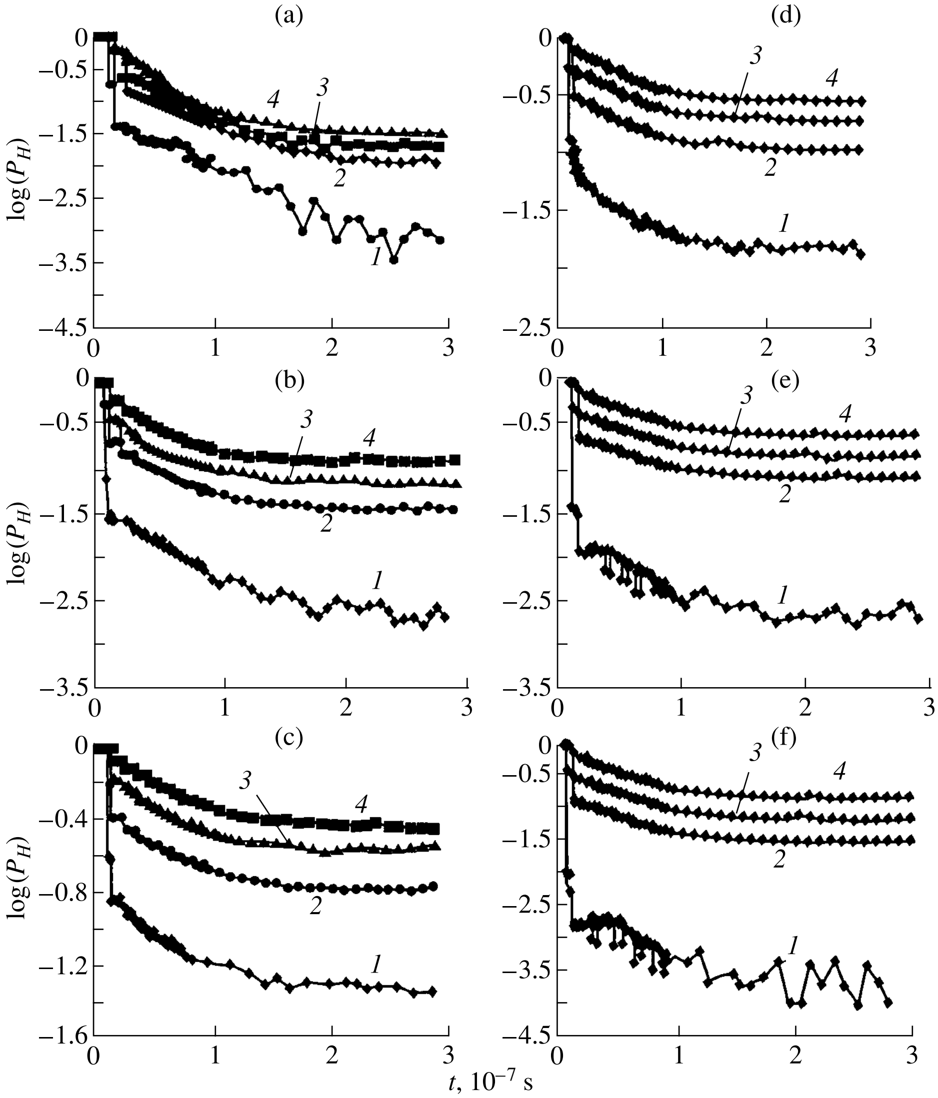

Fig. 2. Relaxation kinetics curves of *F*–*H* pairs for different initial distributions of pair components in the nearest three coordination shells for the following values of interaction potential parameters: (a) $a = 0.15$, $b = 0.5$; (b) $a = 0.15$, $b = 1.0$; (c) $a = 0.15$, $b = 2.0$; (d) $a = 0.15$, $b = 1.5$; (e) $a = 0.2$, $b = 1.5$; and (f) $a = 0.25$, $b = 1.5$. $E_a = 0.04$ eV. Numbers *1* to *4* correspond to serial numbers of the IDF from Table 1.

but also on the parameters of the interaction potential (Fig. 2). As the interaction potential (parameter *a*) increases, the fraction of pairs annihilating during the first jumps of the *H* center increases sharply. A dependence on the rigidity of the interaction potential (parameter *b*) can also be seen.

The decay at the second stage is most interesting. At this stage, the main decrease in the concentration of pairs with time from the beginning of motion of the mobile component is observed for all the ranges of the parameters of the interaction potential and for all starting mutual arrangements of the pair components. The length of the second segment corresponds to the time required for performing from three to several dozens of jumps of the *H* center.

The results of our calculations show that the defect relaxation on the second segment is described satisfactorily in semilogarithmic coordinates by a linear function with the characteristic relaxation time τ_2. Table 2 contains the calculated values of τ_2 for the second stage of Frenkel defect relaxation. At this stage, the characteristic relaxation time slightly decreases with increasing interaction parameter *a* and exhibits a noticeable dependence on the interaction parameter *b*: the relaxation time increases with *b*.

The results presented in Table 2 show that τ_2 weakly depends on the starting arrangement of the *H* center relative to the *F* center and is independent of the starting state in the case when the interaction potential is extended (the value of *b* is small). For any other ver-

Table 2. Dependence of the characteristic relaxation time for an *F*–*H* pair (s) on the parameters of interaction potential for different starting states (see Table 1)

Potential parameters		Starting state			
a	*b*	1	2	3	4
0.15	0.5	1.1×10^{-7}	1×10^{-7}	1×10^{-7}	1×10^{-7}
0.15	1	1.25×10^{-7}	1.43×10^{-7}	1.43×10^{-7}	1.43×10^{-7}
0.15	2	2.5×10^{-7}	3.3×10^{-7}	3.3×10^{-7}	3.3×10^{-7}
0.15	1.5	1.67×10^{-7}	2.5×10^{-7}	2.5×10^{-7}	2.5×10^{-7}
0.2	1.5	1.43×10^{-7}	2×10^{-7}	2×10^{-7}	2×10^{-7}
0.25	1.5	1.43×10^{-7}	2×10^{-7}	2×10^{-7}	1.67×10^{-7}

sions of interaction potentials, τ_2 is independent of the starting state for any initial states except the first; the relaxation time τ_2 upon a start from the first state is shorter than that for starts from all other states (but not by more than 30%).

The last, third, segment, on which the number of pairs remains unchanged with time, corresponds to the case where all of the mobile components of pairs escape from the rated volume and transform into stable hole color centers. The results of investigations of the third relaxation stage are presented in Table 3 in the form of a dependence of the fraction of preserved pairs on the parameters of the interaction potential and on the starting mutual arrangement of the components of the pairs. It follows from the results of calculations presented in the table that the survival probability for a pair depends on the initial mutual arrangement of the pair components. The shorter the distance between the pair components in the initial state, the higher the probability of their annihilation; in other words, the longer the distance between the starting *H* center and the *F* center, the larger the fraction of surviving (accumulated, long-lived) pairs by the beginning of the third stage. As the interaction potential (parameter *a*) increases and, especially, as the rigidity of the interaction potential (parameter *b*) decreases, the fraction of preserved pairs decreases.

Table 3. Dependence of the probability of survival of an *F*–*H* pair after completion of the relaxation process on the parameters of interaction potential for different starting states (see Table 1)

Potential parameters		Starting state			
a	*b*	1	2	3	4
0.15	0.5	0.03	0.09	0.12	0.17
0.15	1	0.06	0.22	0.28	0.38
0.15	2	0.26	0.45	0.58	0.64
0.15	1.5	0.14	0.35	0.45	0.55
0.2	1.5	0.06	0.3	0.39	0.5
0.25	1.5	0.02	0.28	0.34	0.45

4. DISCUSSION

In this study, we used computer simulation methods for analyzing the relaxation kinetics of correlated interacting Frenkel pairs. The calculations were made for different starting arrangements of correlated pair components relative to each other, i.e., for situations with different extents of correlation of pairs. The degree of correlation in our calculations varied from extremely high, when the components of a pair were at nearest neighbor sites, to that corresponding to the location of the *H* center in the third shell around the *F* center.

Of the two stages of the decay of correlated pairs due to annihilation during thermally activated motion of the mobile component of a pair, the second stage is more interesting. Obviously, this stage can be observed experimentally as the shortest stage. In fact, it follows from the results of calculations that the maximum decrease is observed in the second stage in most versions of the interaction potential and starting states that we used. The first stage of the calculated relaxation kinetics is of too short a duration and is noticeable only when the first state is predominantly the starting state.

The results of calculations showed that the relaxation kinetics depends on the starting state only slightly (Table 2). This means that from the relaxation kinetics we can only judge whether or not a pair is correlated; i.e., kinetic curves provide no information on the degree of correlation and, in particular, on the type of starting state.

The experimental results on the decay kinetics of *F*–*H* centers in alkali halide crystals available at present [5, 7] show that at least two stages of defect relaxation exist after the application of a short radiation pulse in the nanosecond and microsecond time ranges. The first (nanosecond) stage is correctly described by monomolecular kinetics, while subsequent stages are described by bimolecular kinetics. The ratios of decay rates and of the decreases in the pair concentration at the two (monomolecular and bimolecular) stages depend on the temperature of the sample during irradiation. In the temperature range from liquid-nitrogen to room temperature, the initial concentration of primary defects induced by the radiation pulse depends on temperature only slightly. However, the ratio of concentrations of correlated and uncorrelated pairs changes significantly in favor of the latter pairs.

The ratio of concentrations of correlated and uncorrelated pairs created by a radiation pulse also depends on the energy of the exciting pulse. The fraction of uncorrelated pairs increases with the excitation power.

Thus, in the range of short times following excitation by a nanosecond radiation pulse, the relaxation of primary defects has several stages. The shortest stage is associated with annihilation of correlated pairs. Uncorrelated pairs of defects have a longer lifetime and are, hence, referred to as long-lived. The relation between the relaxation stages associated with correlated and uncorrelated pairs is determined by the experimental conditions.

The results of experimental investigation at the initial stages of breakdown of *F*–*H* pairs formed in alkali halide crystals as a result of the decay of electron excitations are described in [6]. The experimentally measured relaxation curves for *F* centers in the nanosecond time interval exhibit two clearly manifested stages: a short stage, in time intervals from tens to hundreds of nanoseconds, and a long stage, for which no noticeable time variation is observed in these time intervals [6]. At the first relaxation stage, at least half of the created pairs of centers decay at 80 K.

A comparison of the results of theoretical and experimental investigations of the initial stages of the breakdown of *F*–*H* pairs leads to the following conclusions. The second relaxation stage on the theoretical curves obviously corresponds to the shortest experimentally observed relaxation stage [6]. The results of calculations show that only correlated and uncorrelated pairs can be distinguished in the relaxation kinetics of the components of *F*–*H* pairs during thermally activated migration of the *H* centers. The degree of correlation is manifested too weakly in the kinetics. Consequently, we can conclude that only one (the shortest) relaxation stage observed in the experiments is associated with correlated pairs. Any subsequent stage is not the result of annihilation of correlated pairs.

The concepts of short- and long-lived pairs are often encountered in the description and analysis of the results of investigations. Such pairs are often referred to as unstable and stable, respectively. The division into two groups is carried out arbitrarily. In connection with this, we can propose the following division of pair components into short- and long-lived centers. Short-lived pairs should be regarded as correlated and long-lived pairs as uncorrelated, irrespective of their origin. Uncorrelated pairs can be formed both due to primary processes of decay of electron excitations and as a result of separation of the correlated pairs formed. There can be several long-lived stages. Relaxation can result from reactions between uncorrelated pairs, as well as from a combination of reactions involving secondary affects.

5. CONCLUSIONS

The theoretical analysis carried out in this paper proved that experimentally measured relaxation kinetics curves for primary pairs created as a result of a radiation pulse can provide information on the presence of correlated and uncorrelated pairs and on the ratio of their concentrations. However, the relaxation kinetics curves give no information on the degree of correlation and, in particular, on the function of the initial mutual arrangement of the components of primary pairs.

ACKNOWLEDGMENTS

This study was supported by the Russian Foundation for Basic Research, project no. 01-2-18035.

REFERENCES

1. Ch. B. Lushchik and A. Ch. Lushchik, *Decay of Electron Excitations with Defect Formation in Solids* (Nauka, Moscow, 1989).
2. T. Sugiyama, H. Fujiwara, T. Suzuki, and K. Tanimura, Phys. Rev. B **54** (21), 15109 (1996).
3. H. Fujiwara, T. Suzuki, and K. Tanimura, J. Phys.: Condens. Matter **9**, 923 (1997).
4. V. M. Lisitsyn, Izv. Vyssh. Uchebn. Zaved., Fiz., No. 2, 86 (1979).
5. P. V. Bochkanov, V. I. Korepanov, and V. M. Lisitsyn, Izv. Vyssh. Uchebn. Zaved., Fiz., No. 3, 16 (1989).
6. V. M. Lisitsyn, V. I. Korepanov, and V. Yu. Yakovlev, Izv. Vyssh. Uchebn. Zaved., Fiz., No. 11, 5 (1996).
7. V. M. Lisitsyn, L. A. Lisitsyna, and E. P. Chinkov, Izv. Vyssh. Uchebn. Zaved., Fiz., No. 3, 13 (1995).
8. I. M. Sobol’, *Numerical Monte Carlo Methods* (Nauka, Moscow, 1973), pp. 7–9.

Translated by N. Wadhwa

Physics of the Solid State, Vol. 44, No. 11, 2002, pp. 2072–2079. Translated from Fizika Tverdogo Tela, Vol. 44, No. 11, 2002, pp. 1979–1986.
Original Russian Text Copyright © 2002 by Malygin.

DEFECTS, DISLOCATIONS, AND PHYSICS OF STRENGTH

Kinetic Mechanism of the Formation of Fragmented Dislocation Structures upon Large Plastic Deformations

G. A. Malygin

Ioffe Physicotechnical Institute, Russian Academy of Sciences,
ul. Politekhnicheskaya 26, St. Petersburg, 194021 Russia
e-mail: malygin.ga@pop.ioffe.rssi.ru

Received January 22, 2002; in final form, January 29, 2002

Abstract—The mechanism of formation of fragmented (banded, block) dislocation structures (FDSs) in crystals subjected to large plastic deformations are discussed. The theoretical analysis is based on the kinetic equations for the density of geometrically necessary dislocations (GNDs). The equations include the processes of multiplication, immobilization, annihilation, and diffusion of GNDs. The formation of an FDS is considered a synergetic process of self-organization of GNDs obeying the principle of similitude of dislocation structures at various degrees of plastic deformation. Conditions for the formation of the structures at hand have been determined, as well as their parameters and the dependence of these parameters on the degree of deformation. The theoretical results are compared with the available experimental data. *© 2002 MAIK "Nauka/Interperiodica".*

1. INTRODUCTION

Experiments show that after large plastic deformations ($\gamma > 0.5$–10), a fragmented dislocation structure (FDS) is formed in crystalline materials [1–14]. Such a structure is also called a banded or block dislocation structure according to the shape of the fragments that are formed after large deformation. The formation of such a structure is determined by the amount of deformation and is independent of the way in which this deformation has been reached, i.e., irrespective of whether it is formed in the neck of a tensile sample [2] as a result of twisting [4], drawing [1], rolling [3], or multiple extrusion through a knee-shaped die (equal-channel angular pressing technique [11]).

The formation of an FDS is accompanied by the appearance of strong crystallographic misorientations in the crystal, since the boundaries of fragments contain a large density of like dislocations (of the same sign). As the degree of deformation increases, the fragment dimensions decrease from several microns to several hundreds of nanometers and the misorientation of the lattice between neighboring fragments changes from fractions of a degree of arc to several tens of degrees. Straining to large degrees of plastic deformation is at present one of the most efficient techniques for the production of fine-crystalline (nanostructured) materials.

The formation of an FDS begins at the third stage of the strain-hardening process and continues at the fourth and fifth stages. At the second and third stages of strain hardening, a cellular dislocation structure is known to be formed in the crystal. Its formation is related to the formation and accumulation in the crystal of statistically random dislocations (SRDs) as a result of their generation at dislocation sources and subsequent multiplication. As to FDSs, there are good grounds to assume that geometrically necessary dislocations (GNDs) take part in their formation [12–14]. These dislocations are formed as a response of the crystal to its elastic bending (twisting) due to the nonuniformity of plastic deformation and the related geometrical distortions in the shape of the crystal or its local regions [15]. Thus, the geometrically necessary dislocations differ from the statistically random dislocations in their origin.

The concentration of GNDs in fragment boundaries decreases the energy of a dislocation ensemble as a result of a decrease in the energy of dislocation interactions [16, 17]. However, this cause alone cannot lead to the formation of an FDS. Experiments show that GNDs can be distributed in the crystal randomly. Such a distribution is observed if dislocations, during their motion, suffer strong friction from the side of the Peierls crystal relief or, in the case of alloys, friction due to a high concentration of impurities or disperse inclusions in the lattice. In this case, continuous rather than localized misorientations arise in the crystal [5, 14]. A similar situation takes place when a cellular dislocation structure is formed: such a structure has not been observed in strongly doped and dispersion-hardened alloy [6, 18].

Thus, the formation of an FDS has geometrical (disclinational [2]), energetical [16], and kinetic aspects. The last aspect was considered in [12, 13, 19]. It follows from these works that the FDSs, like cellular dislocation structures, obey the principle of similitude of dislocation structures. According to this principle, the dislocation structure changes in a self-similar way with increasing plastic deformation; i.e., it retains the relationship between its parameters during its evolution.

The self-similar character of the evolution of FDSs indicates that their formation is due to the process of self-organization of dislocations.

This paper is aimed at a theoretical analysis of the kinetic mechanism of formation of FDSs on the basis of equations that describe the evolution of the density of GNDs at large plastic deformations. In Section 2, the corresponding kinetic equations are formulated. Section 3 is devoted to an analysis and solution of these equations. In Section 4, a comparison of the theoretical results with available experimental data on the evolution of parameters of fragmented structures with increasing deformation is performed.

2. EQUATION OF THE EVOLUTION OF THE DENSITY OF GEOMETRICALLY NECESSARY DISLOCATIONS

What is the mechanism of generation of GNDs and the size (scale) of the regions of bend–twist that lead to the formation of these dislocations upon large plastic deformations in the crystal? Since the formation of fragmented structures is independent of the loading conditions, it is obvious that it is due to internal causes. According to Ashby [15], the density of GNDs is determined by the relationship $\rho = \gamma/bl$, where γ is the degree of plastic deformation and l is the size of the region of bending (it determines the radius of the lattice curvature $R = l/\gamma$). The radius of curvature R is linked with the dislocation density as $\rho = 1/bR$, wherefrom we immediately obtain the Ashby relation.

A cellular dislocation structure is related to a nonuniformity of plastic deformation of the crystal on a scale of l_3 (the size of a dislocation cell) due to a nonuniform distribution of dislocations, i.e., their high density in the cell boundaries and a small density in the bulk of the cells. Therefore, at the second and third stages of the strain-hardening curve, the size of the region of bending is on the order of several l_3, i.e., is on the order of the length of slip lines in the cellular dislocation structure. At the fourth and fifth stages of the strain-hardening curve, the size of the slip lines can apparently be much greater than the size of fragments l_4, since the GNDs are pileups of like dislocations.

In their kinetic properties, the geometrically necessary dislocations do not differ from the statistically random dislocations. Therefore, the evolution of their ensemble should be described by a kinetic equation of the same type as in the case of SRDs; i.e., it should include the processes of multiplication, immobilization, annihilation, and diffusion of dislocations [20, 21]. As was said above, the main feature of GNDs is that these are dislocations that are not compensated in the Burgers-vector sign. Therefore, they form their own mesostructure in the crystal, which differs from the mesostructure of statistically random dislocations compensated in the Burgers-vector sign. Experiments show that the fragment boundaries lie in the slip planes of dislocations [7, 22], as in the case of cell boundaries in cellular dislocation structures [23]. This means that the walls of the fragments are formed as a result of dislocation slip and contain dislocations of various slip systems.

According to the Ashby relation, the rate of generation of GNDs is $\dot{\rho} = (1/bl)\dot{\gamma}$, where $\dot{\gamma} = b\rho u$ is the rate of plastic deformation and u is the dislocation velocity. With the above in mind, we can write equations of evolution of the densities of GNDs of different signs (ρ_+ and ρ_-) that are analogous in their structure to the equation of evolution of the density of SRDs [20, 21]:

$$\frac{\partial\rho_\pm}{\partial t} + \nabla \mathbf{J}_\pm = \left(\frac{1}{l} - \frac{1}{\lambda_i}\right)u\rho_\pm + \delta_f\frac{1}{2}(\sqrt{\rho_+} + \sqrt{\rho_-})u\rho_\pm - h_a u\rho_+\rho_-, \tag{1a}$$

where $\mathbf{J}_\pm$ are the fluxes of unlike dislocations and t is the time. The first term on the right-hand side describes the rate of generation of dislocations caused by the nonuniformities of plastic deformation with characteristic dimensions of order l; the second term describes the immobilization of dislocations by obstacles; the third term is responsible for the multiplication of dislocations on the dislocation forest; and the fourth term allows for dislocation annihilation. The coefficients λ_l^{-1}, δ_f and h_a determine the intensity of the corresponding processes. When writing Eq. (1a), we assumed that there occurs multiple slip in the crystal and that the dislocation densities in intersecting slip planes differ only insignificantly.

Assuming that, in the process of deformation at the fourth and fifth strain-hardening stages, the relationship between the unlike dislocations remains constant ($\rho_- = \beta\rho_+$, where $\beta < 1$), we obtain, instead of Eq. (1a), the equation of evolution of the density of dislocations of one sign (ρ_+)

$$\frac{\partial\rho_+}{\partial t} + \nabla \mathbf{J}_+ = \left(\frac{1}{l} - \frac{1}{\lambda_i}\right)u\rho_+ + \delta_4 u\rho_+^{3/2} - \delta_5 u\rho_+^2, \tag{1b}$$

where $\delta_4 = (1 + \sqrt{\beta})\delta_f/2$ and $\delta_5 = \beta h_a$. In what follows, we omit the plus sign at ρ and $\mathbf{J}$ for the time being.

According to [21], the appearance of spatially nonuniform drift- and diffusion-related dislocation fluxes $\mathbf{J}$ in the crystal can be caused by the nonuniform multiplication of dislocations by double cross slip of screw dislocations:

$$J_x = u\rho + D_1\frac{\partial\rho}{\partial x} + D_2\frac{\partial^3\rho}{\partial x^3}, \tag{2}$$

where $D_1 = \delta_1(M - 1)(h_c^2/\lambda_s)u$ and $D_2 = \delta_2(M - 1)(h_c^4/\lambda_s)u$ are the diffusion coefficients for dislocations of the first and second orders, respectively; $\delta_1 \approx \delta_2 \approx 1$

are numerical parameters; $M = -\partial \ln u/\partial \ln \rho > 1$ is the coefficient of dislocation-related strain hardening; λ_s is the free path of screw dislocations between the events of double cross slip; and h_c is the characteristic distance for the escape of a dislocation segment into a parallel slip plane upon double cross slip of screw dislocations. Since $M = V\tau_\mu/2kT \gg 1$, the diffusion fluxes (2) change their sign due to local strain hardening of the crystal in the regions of an enhanced dislocation density. (Here, $V = b^2\rho^{-1/2}$ is the activation volume upon multiple slip; $\tau_\mu = \alpha\mu b\rho^{1/2}$, the dislocation-induced strain-hardening of the crystal; α, the coefficient of dislocation interaction; μ, the shear modulus; k, the Boltzmann constant; and T, the temperature.)

Substituting Eq. (2) into Eq. (1b), we can investigate the spatial stability of the dislocation distribution determined using this equation. Let us denote, for brevity, the right-hand side of Eq. (1b) by $u\Phi(\rho)$. Equation $\Phi(\rho) = 0$ has three roots, namely,

$$\begin{gathered} \rho_{1,2}^{1/2} = \left(\frac{\delta_4}{2\delta_5}\right)[1 \pm (1-\eta)^{1/2}], \\ \rho_3 = 0, \quad \eta = 4(\beta_i - 1)\frac{\delta_5}{\delta_4^2 l}, \end{gathered} \tag{3}$$

where $\beta_i = l/\lambda_i > 1$ is the coefficient of immobilization of dislocations. Near the critical values ρ_1, ρ_2, and ρ_3, the stability of the dislocation density toward fluctuations of the form $\delta(x, t) \sim \exp(\omega t + iqx)$ is determined by the equation $\omega(q) = \omega_i(q) + i\omega_2(q)$, where

$$\omega_1(q) = u\frac{\partial\Phi}{\partial\rho}\bigg|_{\rho_{1,2,3}} + D_1q^2 - D_2q^4, \quad \omega_2 = uq. \tag{4}$$

The condition $\partial\omega_1/\partial q = 0$ yields critical values of the wave vectors $q_{1,2,3}$ and increments $\omega_1(q_{1,2,3})$:

$$\begin{gathered} q_{1,2,3} = \left(\frac{D_1}{2D_2}\right)^{1/2} = 1/\sqrt{2}h_c, \\ \omega_1(q_{1,2,3}) = u\left(\frac{\partial\Phi}{\partial\rho}\bigg|_{\rho_{1,2,3}} + \frac{M-1}{4\lambda_s}\right). \end{gathered} \tag{5}$$

At $0 < \eta \ll 1$, it follows from Eq. (3) that $\rho_1 \approx (\delta_4/\delta_5)^2$ and $\rho_2 \approx [(\beta_i - 1)/\delta_4 l]^2$. An analysis shows that at the critical points ρ_2 and ρ_3 under the condition $(M - 1)l/(\beta_i - 1)\lambda_s > 1$, the increments $\omega_1(q_{2,3}) > 0$ are positive and, consequently, the dislocation density is unstable toward fluctuations of size $\lambda_c = 2\pi\sqrt{2}\,h_c$. At the critical point $\rho_1 > \rho_2$, the dislocation density is stable to such fluctuations if $(M - 1)\delta_5 < 2\delta_4^2\lambda_s$. In addition, since $\omega_2(q_{1,2}) \neq 0$, the critical fluctuations are convectively unstable.

3. FRAGMENTED DISLOCATION STRUCTURES

The above linear analysis shows that the distribution of GNDs in the crystal is unstable to spatial fluctuations of the dislocation density near the critical value of the density ρ_2. What is the subsequent evolution of the fluctuations of dislocation density and of the ensemble of GNDs on the whole? To answer this question, we should solve nonlinear equation (1b), in which the dislocation flux **J** in the general case depends on the integral of the dislocation density [21]. Since this is an unsolvable problem, we consider, as the first approximation, the solution to Eq. (1b) using Eq. (2) for the dislocation flux and restricting ourselves to the first diffusion term in it.

As a result, we obtain the equation

$$\begin{gathered} \frac{\partial\rho}{\partial t} + u\frac{\partial\rho}{\partial x} + \lambda_D u\frac{\partial^2\rho}{\partial x^2} \\ = -(\beta_i - 1)\frac{u}{l}\rho + \delta_4 u\rho^{3/2} - \delta_5 u\rho^2, \end{gathered} \tag{6}$$

where $\lambda_D = (M - 1)h_c^2/\lambda_s$. Taking into account the convective instability of density fluctuations, we seek the solution to Eq. (6) in the form $\rho(z, t)$, where $z = x - Ut$ and U is a constant velocity. Taking into account that $\partial\rho/\partial t = \partial'\rho/\partial' t - U\partial\rho/\partial z$, we have, instead of Eq. (6), the equation

$$\begin{gathered} \frac{\partial'\rho}{\partial' t} + (u - U)\frac{\partial\rho}{\partial z} + \lambda_D u\frac{\partial^2\rho}{\partial z^2} \\ = -(\beta_i - 1)\frac{u}{l}\rho + \delta_4 u\rho^{3/2} - \delta_5 u\rho^2. \end{gathered} \tag{7}$$

Assuming then that $U = u$, we transform Eq. (7) by taking into account that $\partial'\rho/\partial' t = (\partial\rho/\partial\gamma)\dot{\gamma}$, where $\dot{\gamma} = b\rho u$. As a result, we obtain for the density of GNDs $\rho(z, \gamma)$ an equation of the form

$$\rho\frac{\partial\rho}{\partial\gamma} + \frac{\lambda_D}{b}\frac{\partial^2\rho}{\partial z^2} = -(\beta_i - 1)k_3\rho + k_4\rho^{3/2} - k_5\rho^2, \tag{8}$$

where $k_3 = 1/bl$, $k_4 = \delta_4/b$, and $k_5 = \delta_5/b$. Equation (8) describes the spatial evolution of the dislocation density of GNDs depending on the degree of deformation γ.

To find this density, we write Eq. (8) in the dimensionless form

$$\Psi\frac{\partial\Psi}{\partial\Gamma} + \frac{\partial^2\Psi}{\partial Z^2} = \Psi[-\Psi_0 + (1 + \Psi_0)\Psi^{1/2} - \Psi] \tag{9a}$$

by introducing the following designations:

$$\Psi = \frac{\rho}{\rho_1}, \quad \Gamma = k_5\gamma, \quad Z = \frac{z}{\Lambda_0},$$
$$\Lambda_0 = \left(\frac{\lambda_D}{bk_5\rho_1}\right)^{1/2}, \quad \Psi_0 = \left(\frac{\rho_2}{\rho_1}\right)^{1/2} = \frac{1-\sqrt{1-\eta}}{1+\sqrt{1-\eta}}. \tag{9b}$$

We seek the solution to Eq. (9a) in a self-similar form $\Psi(Z_1, \Gamma) = \nu^2(\Gamma)\psi(Z_1)$, where $Z_1 = Z\nu^{1/2}(\Gamma)$. As a result, we obtain

$$2\frac{\partial\nu}{\partial\Gamma} + \nu$$
$$= \frac{1}{\psi^2}\left[-\frac{\partial^2\psi}{\partial Z_1^2} + \psi[-\Psi_0\nu^{-1} + (1+\Psi_0)\psi^{1/2}]\right] \tag{10}$$

from which we see that the variables $\nu(\Gamma)$ and $\psi(Z_1)$ are not completely separated. To separate the variables, we should assume that $\Psi_0 = \psi_0\nu$. This means that in Eq. (9b) we have $\eta \ll 1$ and that $l = l_5/\nu$, $\beta_i = l/\lambda_i =$ const, and $\psi_0 = (\beta_i - 1)\delta_5/\delta_4^2 l_5$, where l_5 is the length of slip lines at the fifth stage of strain-hardening. The coefficient $\beta_i > 1$ has in this case the meaning of the coefficient of transparency of the fragment boundaries for GNDs. Then, equating the left-hand and right-hand sides of Eq. (10) to unity, we obtain an equation for ν, the solution to which has the form

$$\nu(\Gamma) = 1 - \exp[1 - (1/2)\Gamma]. \tag{11}$$

For the function $\psi(Z_1)$, we have the equation

$$\frac{\partial^2\psi}{\partial Z_1^2} = \psi[-\psi_0 + (1+\psi_0\nu)\psi^{1/2} - \psi]. \tag{12}$$

Since $\psi_0\nu \ll 1$, this equation describes a stationary distribution of GNDs in the crystal.

Integrating Eq. (12) under the conditions

$$\Delta = \frac{16}{25}(1+\psi_0\nu)^2 - \frac{8}{3}\psi_0 > 0, \quad \psi_0 > 0 \tag{13}$$

leads to a tabulated integral and a solution to Eq. (9a), which, after simple transformations, may be written in the following compact form (now, we restore the plus sign at ρ):

$$\rho_+(z, \gamma) = \frac{\overset{+}{\rho}_{\max}(\gamma)}{\left[1 + (f_0 - 1)\sin^2\left(\pi\frac{z+z_0}{\Lambda(\gamma)}\right)\right]^2}, \tag{14a}$$

where z_0 is the integration constant and

$$\overset{+}{\rho}_{\max}(\gamma) = \frac{4\psi_0^2\rho_1\nu^2(\gamma)}{\left[\frac{4}{5}(1+\psi_0\nu) - \sqrt{\Delta}\right]^2},$$
$$\Lambda(\gamma) = \Lambda_\infty/\nu^{1/2}(\gamma),$$
$$\Lambda_\infty = 4\pi\left[\frac{(M-1)l_5}{(\beta_i - 1)\lambda_5}\right]^{1/2} h_c, \tag{14b}$$
$$f_0 = \left[\frac{\rho_{\max}(\gamma)}{\rho_{\min}(\gamma)}\right]^{1/2} \approx \psi_0^{-1}.$$

It follows from relations (13) that the stationary ($\nu = 1$) fragmented structure is formed if $0 < \psi_0 < 2/3$. Equation (14a) describes a spatially periodic dislocation structure with fragment dimensions Λ and with a dislocation density in the fragment boundaries and in the bulk of fragments equal (at $\psi_0 \ll 1$) to

$$\overset{+}{\rho}_{\max}(\gamma) = \rho_\infty\left[1 - \exp\left(-\frac{1}{2}k_5\gamma\right)\right]^2,$$
$$\overset{+}{\rho}_{\min}(\gamma) \approx \psi_0^2\overset{+}{\rho}_{\max}(\gamma), \quad \rho_\infty = (6/5)^2\rho_1, \tag{14c}$$

respectively.

Taking into account (see Section 2) that the density of dislocations with the opposite sign of the Burgers vector is $\rho_-(z, \gamma) = \beta\rho_+(z + z_-, \gamma)$, we have the following expression for the distribution of the total density of GNDs:

$$\rho(z, \gamma) = \rho_+(z, \gamma) - \beta\rho_+(z + z_-, \gamma), \tag{15}$$

where $z_- = (1/2)\Lambda$. Figures 1a and 1b show the distribution of the density of GNDs in the crystal according to Eq. (15) under deformations $\Gamma = k_5\gamma \longrightarrow \infty$ and $\psi_0 = 4 \times 10^{-2}$ and $f_0 = 25$ in the cases where $\beta = 0$ and $\beta \neq 0$ ($\beta = 0.5$).

Since the density of GNDs and the angle of lattice rotation (misorientation between fragments) θ are related as $\rho = b^{-1}\partial\theta/\partial z$, the distribution of the rotation angles $\theta(z, \gamma)$ corresponding to the density of GND given by (15) is described by the integral

$$\theta(z, \gamma) = b\int_0^z \rho(z, \gamma)dz. \tag{16a}$$

Figures 1c and 1d display the distribution of rotation angles corresponding to the distribution of the density of GNDs given in Figs. 1a and 1b. It is seen that the fragment boundaries, in which most GNDs are concen-

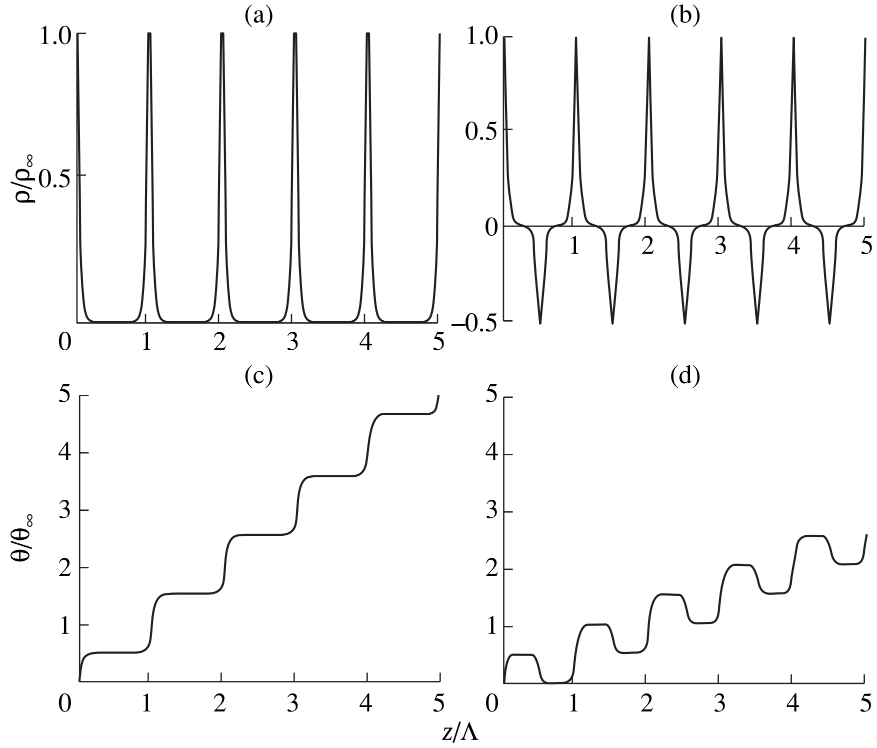

Fig. 1. Distributions of (a, b) the density of geometrically necessary dislocations (GNDs) ρ and (c, d) misorientation angles θ in the fragmented dislocation structure according to Eqs. (15) and (16a) at $\gamma \longrightarrow \infty$ with (a, c) $\beta = 0$ and (b, d) $\beta = 0.5$.

trated, lead to misorientations of the fragment lattices by the angles

$$\theta_+(\gamma) = \frac{f_0+1}{2f_0^{3/2}} b\Lambda(\gamma)\overset{+}{\rho}_{\max}(\gamma) = \theta_\infty \nu^{3/2}(\gamma),$$

$$\theta_-(\gamma) = \beta\theta_+(\gamma), \quad \theta_\infty = \frac{f_0+1}{2f_0^{3/2}} b\Lambda_\infty\rho_\infty, \qquad (16b)$$

where $\nu(\gamma)$ is determined by Eq. (11). Experiments show that in the fragmented structures, fragments with misorientations of both the same sign (Fig. 1c) and with alternating signs (Fig. 1d) can occur [7].

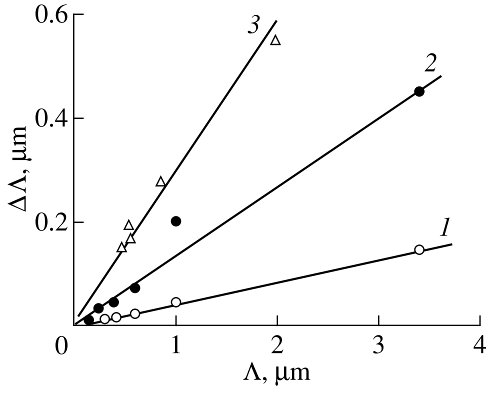

Fig. 2. Correlation between the width of fragment boundaries $\Delta\Lambda$ and fragment size Λ in (*1*, *2*) fragmented and (*3*) cellular dislocation structures in Ni [2, 12].

4. COMPARISON WITH EXPERIMENT

It was found while treating data for Ni [12] that a correlation exists between the width (thickness) of fragment boundaries $\Delta\Lambda(\gamma)$ and the dimensions of the fragments $\Lambda(\gamma)$. This correlation is illustrated in Fig. 2 (straight lines *1*, *2*). Line *1* refers to the narrowest boundaries ($\Delta\Lambda(\gamma)/\Lambda(\gamma) = 0.04$); line *2*, to the widest boundaries ($\Delta\Lambda/\Lambda = 0.13$). Assuming that in Eq. (14a) the boundary width $\Delta\Lambda_{1/2}$ corresponds to a dislocation density $\rho^+(z, \gamma) = (1/2)\overset{+}{\rho}_{\max}(\gamma)$, we find that

$$\frac{\Delta\Lambda_{1/2}(\gamma)}{\Lambda(\gamma)} = \frac{2}{\pi}\arcsin\left(\frac{\sqrt{2}-1}{f_0-1}\right)^{1/2} \approx 0.43\psi_0^{1/2}. \qquad (17)$$

At the average width of the boundaries in Fig. 2 equal to $\Delta\Lambda/\Lambda = 0.085$, we obtain, according to Eq. (17), that $\psi_0 = 4 \times 10^{-2}$. Line *3* in Fig. 2 illustrates the correlation between the width of cell boundaries and cell dimensions in the cellular dislocation structure of nickel (processing of the data from [2]). It is seen that, as compared to fragment boundaries, the cell boundaries are much wider ($\Delta\Lambda/\Lambda = 0.32$).

The ratio $\Delta\Lambda/\Lambda$ is independent of the degree of deformation; this means that the evolution of the FDSs at the fourth and fifth stages of strain hardening occurs in a self-similar manner, with the retaining of a constant relation between the FDS parameters, as in the case of a cellular dislocation structure at the second and third stages of strain hardening [21]. To illustrate this, Fig. 3 displays the results of treatment of the data of [12] on the misorientation angles of the fragments (line *1*) and the cells (line *3*) in the fragmented and cellular dislocation structures of nickel, respectively. It is seen that the product of the average angles of misorientation by the average dimension of the fragments or the cells $\bar{\theta}(\gamma)\bar{\Lambda}(\gamma)/b$ remains constant in the process of the formation and evolution of the corresponding structures, which indicates a correlated, synergistic character of dislocation processes occurring in the crystal at all stages of plastic deformation. The fact that this correlation has a regular rather than accidental character is also confirmed by the results of treatment of the data on the evolution of the parameters of the fragmented dislocation structure in α-Fe [1] depending on the amount of deformation (line *2* in Fig. 3).

According to the above-developed theory (Eqs. (14b), (16a)), the product $\theta(\gamma)\Lambda(\gamma)/b = (\theta_\infty\Lambda_\infty/b)\nu(\gamma)$ does not remain constant in the process of evolution of a fragmented dislocation structure. The cause of this is likely that the initial kinetic equation for the density of GNDs (Eq. (1b)) has an excessively deterministic character and does not take into account the statistically random mechanism of the fragment formation, which, as was established in [12, 13], leads to a distribution of fragments in size and misorientation angle of the type

$$P(\Lambda) \sim (\Lambda/\bar{\Lambda}(\gamma))^2 \exp[-3\Lambda/\bar{\Lambda}(\gamma)]. \qquad (18)$$

For the product $\bar{\theta}(\gamma)\bar{\Lambda}(\gamma)/b$ to remain constant, it is necessary that the average size and the misorientation angle of fragments change as $\bar{\Lambda}(\gamma) = \bar{\Lambda}_\infty/\nu(\gamma)$ and $\bar{\theta}(\gamma) = \bar{\theta}_\infty\nu(\gamma)$.

The experiment confirms such dependences. Straight line *1* in Fig. 4 demonstrates a dependence $\bar{\Lambda}(\varepsilon) = \bar{\Lambda}_\infty[1 - \exp(-(1/2)mk_5\varepsilon)]^{-1}$ for nickel [12] in the theoretical coordinates $\log[1 - \bar{\Lambda}_\infty/\bar{\Lambda}(\varepsilon)] - \varepsilon$, where $\varepsilon = \gamma/m$, m is the Taylor factor, and $\bar{\Lambda}_\infty = 0.1$ μm. For comparison, Fig. 4 also demonstrates an analogous dependence for the average size of dislocation cells in nickel [2] (line *2*, $\Lambda_\infty = 0.21$ μm). At $m = 3$, we find, from the slope of line *1*, the effective coefficient of annihilation of dislocations at the fifth stage of strain-hardening $k_5 = 0.2$; the slope of line *2* yields the coefficient of dislocation annihilation at the third stage $k_a = h_a/b = 2.5$. Thus, the ratio between the densities of dislocations of different signs in nickel is $\beta = k_5/k_a = 0.08$. This value is close to the value found in [19] for copper ($\beta = 0.1$, according to [24]).

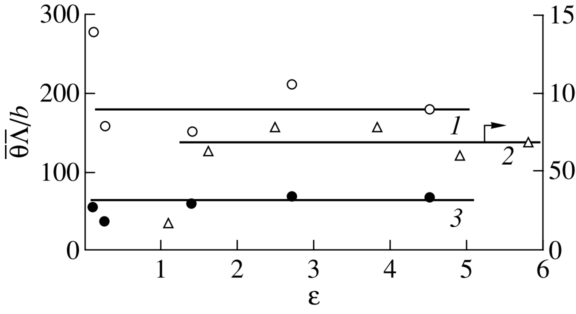

Fig. 3. The independence of the product of the average misorientation angle $\bar{\theta}$ and the average fragment size $\bar{\Lambda}$ from the amount of deformation ε in (*1*, *2*) fragmented and (*3*) misoriented cellular dislocation structures; (*1*, *3*) Ni [12] and (*2*) α-Fe [1].

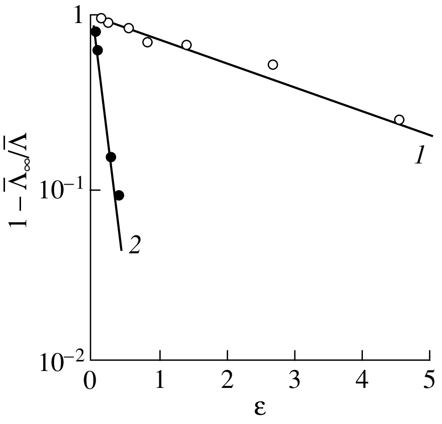

Fig. 4. Variation of the average size of (*1*) fragments [12] and (*2*) cells [2] in Ni as a function of the amount of deformation ε in semi-logarithmic coordinates $\log(1 - \bar{\Lambda}_\infty/\Lambda(\varepsilon)) - \varepsilon$.

It follows from the above experimental and theoretical results that, as in the case of cellular dislocation structures [25], the average density of dislocations $\rho(\gamma)$ and the flow stress $\tau(\gamma)$ at the fourth and fifth stages of crystal strengthening may be described by the relations

$$\rho(\gamma) = (1+\beta)[f_G\overset{+}{\rho}_{\max}(\gamma) + (1-f_G)\overset{+}{\rho}_{\min}(\gamma)] \approx f_G(1+\beta)\overset{+}{\rho}_{\max}(\gamma), \qquad (19a)$$

$$\tau = \alpha\mu b\rho^{1/2} = \tau_5\left[1 - \exp\left(-\frac{1}{2}k_5\gamma\right)\right], \qquad (19b)$$

where $f_G = \Delta\Lambda/\Lambda \approx 0.43\psi_0^{1/2}$ is the volume fraction occupied by fragment boundaries, $\tau_5 = \alpha_* f_G^{1/2} b\mu\rho_\infty^{1/2}$, and $\alpha_* = \alpha(1+\beta)^{1/2}$. The density of dislocations in the

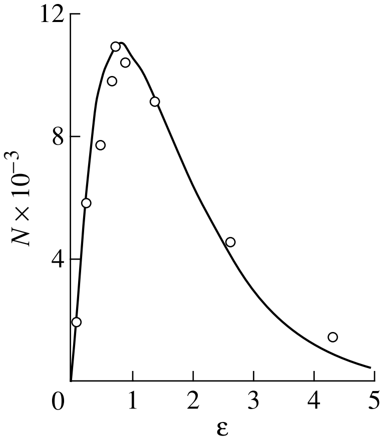

Fig. 5. Variation of the number of fragments N in the transverse section of a nickel sample with the amount of deformation ε [12]. The curve corresponds to a calculation according to Eq. (23).

boundaries $\rho^+_{\max}(\gamma)$ is determined by Eq. (15). An analysis of the curves of strain hardening in copper at the fourth and fifth stages confirms the above relations [19].

Thus, in accordance with the principle of similitude of dislocation structures, we have the following relationships between the parameters of a fragmented dislocation structure:

$$\bar\Lambda(\gamma) = K_1\frac{\mu b}{\tau(\gamma)} = K_2\rho^{-1/2} = \frac{\bar\Lambda_\infty}{1-\exp[-(1/2)k_5\gamma]}, \quad (20a)$$

$$\bar\theta(\gamma) = K_3 b\rho^{1/2} = \bar\theta_\infty[1-\exp(-(1/2)k_5\gamma)], \quad (20b)$$

$$\frac{\bar\theta(\gamma)\bar\Lambda(\gamma)}{b} = K_2K_3, \quad \tau(\gamma) = K_4\mu\theta(\gamma). \quad (20c)$$

Here, K_1, K_2, and K_3 are coefficients that are independent of deformation but depend on the relative volume of fragment boundaries in the volume of the crystal f_G and, consequently, on the magnitude of kinetic coefficients that determine the intensity of the processes of multiplication, immobilization, and diffusion of dislocations in Eqs. (1b) and (6).

Assuming that the average dislocation density is $\rho = 1/\bar\Lambda h$, where $h = \rho_{\max}^{-1/2} = f_G^{1/2}\rho^{-1/2}$ is the separation between dislocations in fragment boundaries, we find that

$$K_2 = f_G^{-1/2}, \quad K_1 = \alpha_* f_G^{-1/2}, \quad K_4 = \alpha_*/K_3. \quad (21)$$

It follows from Eqs. (16b), (17), and (19) that at $f_0 \approx \psi_0^{-1} \gg 1$, the average angle of misorientation between the fragments is $\bar\theta \approx b\bar\Lambda\rho$ and, consequently, $K_3 = K_2 = f_G^{-1/2}$. According to Eq. (20c) and to the data given in Fig. 3 (line *1*), we have for nickel $K_2K_3 = f_G^{-1} = 183$, $K_2 = K_3 = 13.5$, and $f_G = 5.4\times10^{-3}$. Assuming that $\alpha_* = 0.5$, we obtain the following estimates for the other scale coefficients: $K_1 \approx 7$ and $K_4 = 3.7\times10^{-2}$. Note for comparison that in the case of a misoriented cellular dislocation structure in nickel (line *3* in Fig. 3), we have $K_2K_3 = f_S^{-1} = 64$ and $K_2 = K_3 = 8$.

In a similar way, in the case of α-Fe (line *2* in Fig. 3), we find that $K_2K_3 = f_S^{-1} = 70$ and $K_2 = K_3 = 8.4$. It follows from the relation $\sigma = A/\Lambda$ between the flow stress σ and the size of fragments Λ in iron (see [26]) that at $m = 3$ and $A = 120$ MPa μm, the coefficient K_1 in (20a) is equal to 2. The estimation of this coefficient according to Eq. (21) yields a twice as large value at $\alpha_* = 0.5$. It was also found in [1] that in α-Fe at mean misorientation angles and fragment sizes, a relation $\bar\theta/\bar\Lambda = B\varepsilon^2$ is held, where $B = 50$ mm^{-1}. It follows from Eqs. (20a) and (20b) that

$$\bar\theta/\bar\Lambda = b\rho = (\bar\theta_\infty/\bar\Lambda_\infty)\left[1-\exp\left(-\frac{1}{2}mk_5\varepsilon\right)\right]^2. \quad (22)$$

Therefore, according to Eq. (22), we have $\bar\theta/\bar\Lambda \sim \varepsilon^2$ at the fourth stage of the strain-hardening curve (at $\varepsilon \ll 2/mk_5$), which is in agreement with the results of [1].

The kinetic mechanism of formation of fragmented dislocation structures permits us to clarify the paradox related to the evolution of the sizes and shapes of fragments at large plastic deformations, namely, the violation of the Taylor–Polanyi (TP) law in a fragmented dislocation structure [26]. According to this law, upon the deformation of a polycrystalline aggregate, the grain sizes d with increasing plastic deformation ε should increase in the direction of the dislocation slip and decrease in the transverse direction: $d = d_0\exp(-\varepsilon)$, where d_0 is the initial grain size. For example, at $d_0 = 100$ μm and $\varepsilon = 10$, we have $d \approx 10^{-4}d_0 = 10^{-2}$ μm. However, experiments show that in a strongly misoriented dislocation structure that arises instead of the initial polycrystalline structure, the fragment size, after deformations to $\varepsilon > 1$, changes only a little and lies in the range of 0.1–0.5 μm irrespective of the initial grain size, even upon the deformation of single-crystal samples.

Upon drawing or rolling, the transverse dimensions of the samples subjected to deformation decrease by a factor of a few tens or even hundreds. In this case, because of the violation of the Taylor–Polanyi law, a second paradox arises; namely, at deformations $\varepsilon > 1$, the number of dislocation fragments in the transverse section of the sample begins decreasing with increasing degree of plastic deformation. Figure 5 illustrates this according to the data of [12] for nickel. The experimental points show the change in the number of fragments

$N(\varepsilon) = H(\varepsilon)/\bar{\Lambda}(\varepsilon)$ in the transverse section of a planar sample with initial thickness H_0. Since the sample thickness changes with increasing degree of deformation as $H(\varepsilon) = H_0\exp(-\varepsilon)$, we have, with allowance for the dependence of $\bar{\Lambda}$ on ε (Eq. (20a)),

$$N(\varepsilon) = N_0\left[1 - \exp\left(-\frac{1}{2}mk_5\varepsilon\right)\right]\exp(-\varepsilon), \qquad (23)$$

where $N_0 = H_0/\bar{\Lambda}_\infty$. The curve in Fig. 5 demonstrates this dependence for $N_0 = 6.6 \times 10^4$ and $mk_5 = 1.06$. It is seen that at deformations $\varepsilon < 0.8$, the number of fragments in the section increases because of the decrease in their dimensions, whereas at large deformations, this number decreases because of the thinning of the sample at an approximately constant size of the fragments $\bar{\Lambda}_\infty$.

A question that arises is where do the fragments disappear to from the section. According to [12], their disappearance is related to the coalescence of low-angle boundaries of fragments with the formation of high-angle boundaries, as well as to the annihilation of boundaries of opposite signs. Although such processes can take place if the fragment sizes and misorientations obey a distribution of type (18), upon deformation, the number of “medium” fragments in the section of the deformed sample decreases according to Fig. 5 and the law of similitude of fragmented structures (Fig. 3). Therefore, the only way in which the number of fragments can decrease in the section is through the escape of fragment boundaries to outside the sample, i.e., their annihilation with the surface, as in the case of individual dislocations emerging onto the surface of the sample.

This means that the fragment boundaries are mobile, as follows from the solution (14a) to Eqs. (1) and (6), rather than static, as may be supposed based on electron-microscopic investigations of samples unloaded after deformation. Since the formation of fragments is a dynamic process of self-organization of dislocations caused by internal factors, the emergence of fragment boundaries onto the surface of the crystal does not disturb this dynamic process until the fragment dimensions become comparable with the sample thickness. The dynamic, synergetic character of the process of formation of FDSs explains why the Taylor–Polanyi law is violated for such structures.

In conclusion, we note that the analysis of experimental data on the basis of equations of dislocation kinetics makes it possible to consider the processes of deformation strengthening [19, 21] and the formation of dislocation structures [21] at all five stages of the curves of deformation strengthening of crystals from common positions.

REFERENCES

1. G. Langford and M. Cohen, Metall. Trans. A **6** (4), 901 (1975).
2. A. S. Rubtsov and V. V. Rybin, Fiz. Met. Metalloved. **44** (3), 618 (1977).
3. A. S. Malin and M. Hatherly, Met. Sci. **13** (8), 463 (1979).
4. D. A. Hughes and W. D. Nix, Mater. Sci. Eng., A **122** (2), 153 (1989).
5. N. A. Koneva and É. V. Kozlov, Izv. Vyssh. Uchebn. Zaved., Fiz. **33** (2), 89 (1990).
6. D. A. Hughes, Acta Metall. Mater. **41** (5), 1421 (1993).
7. J. H. Driver, D. J. Jensen, and N. Hansen, Acta Metall. Mater. **42** (9), 3105 (1994).
8. N. Hansen and D. A. Hughes, Phys. Status Solidi A **149** (1), 155 (1995).
9. D. A. Hughes, Q. Liu, D. C. Chrzan, and N. Hansen, Acta Mater. **45** (1), 105 (1997).
10. N. Hansen and D. J. Jensen, Philos. Trans. R. Soc. London, Ser. A **357**, 1447 (1999).
11. Y. Iwahashi, Z. Horita, M. Nemoto, and T. G. Langdon, Acta Mater. **46** (9), 3317 (1998).
12. D. A. Hughes and N. Hansen, Acta Mater. **48** (11), 2985 (2000).
13. A. Godfrey and D. A. Hughes, Acta Mater. **48** (8), 1897 (2000).
14. A. N. Tyumentsev, M. V. Tret’yak, Yu. P. Pinzhin, and A. D. Korotaev, Fiz. Met. Metalloved. **90** (5), 44 (2000) [Phys. Met. Metallogr. **90** (5), 461 (2000)].
15. M. F. Ashby, Philos. Mag. **21** (170), 399 (1970).
16. N. Hansen and D. Kuhlmann-Wilsdorf, Mater. Sci. Eng. **81** (1/2), 141 (1986).
17. G. A. Malygin, Fiz. Tverd. Tela (St. Petersburg) **44** (7), 1249 (2002) [Phys. Solid State **44**, 1305 (2002)].
18. M. A. Lewis and J. W. Martin, Acta Metall. **11** (11), 1207 (1963).
19. G. A. Malygin, Fiz. Tverd. Tela (St. Petersburg) **43** (10), 1832 (2001) [Phys. Solid State **43**, 1909 (2001)].
20. G. A. Malygin, Fiz. Tverd. Tela (Leningrad) **31** (7), 43 (1989) [Sov. Phys. Solid State **31**, 1123 (1989)].
21. G. A. Malygin, Usp. Fiz. Nauk **169** (9), 979 (1999) [Phys. Usp. **42** (9), 887 (1999)].
22. J. Kim, I. Kim, and D.-H. Shin, Scr. Mater. **45** (4), 421 (2001).
23. L. Kawasaki, J. Phys. Soc. Jpn. **36** (1), 142 (1974).
24. M. Zehetbauer and V. Seumer, Acta Metall. Mater. **41** (2), 577 (1993).
25. H. A. Mughrabi, Mater. Sci. Eng. **85** (1), 15 (1987).
26. G. Langford and M. Cohen, Trans. Am. Soc. Met. **62** (3), 623 (1969).

Translated by S. Gorin

Physics of the Solid State, Vol. 44, No. 11, 2002, pp. 2080–2082. Translated from Fizika Tverdogo Tela, Vol. 44, No. 11, 2002, pp. 1987–1989.
Original Russian Text Copyright © 2002 by Gruzdkov, Petrov, Smirnov.

DEFECTS, DISLOCATIONS, AND PHYSICS OF STRENGTH

An Invariant Form of the Dynamic Criterion for Yield of Metals

A. A. Gruzdkov, Yu. V. Petrov, and V. I. Smirnov
St. Petersburg State University, Universitetskaya nab. 7/9, St. Petersburg, 191119 Russia
e-mail: dyn@unicorn.math.spbu.edu

Received December 28, 2001

Abstract—The known dynamic criteria for yield of metals are generalized to the case of any stressed–strained state and an arbitrary loading duration. The criteria for uniaxial tension and simple shear are a special case. The dependences of the yield point on the strain rate are calculated using the proposed criterion and are compared with the experimental data. *© 2002 MAIK “Nauka/Interperiodica”.*

For slow uniaxial tension or compression, it is generally assumed that the material transforms into a plastic state under a critical load (yield point). In this case, the yield criterion can be written in the form

$$\sigma(t) \le \sigma_Y, \tag{1}$$

where σ_Y is the yield point for a slow uniaxial tension.

The classical generalizations of criterion (1) to the case of an arbitrary stressed state are the Mises yield criterion and Tresca yield criterion. The latter criterion turns out to be more adequate for the majority of materials and satisfies the condition

$$T_k(t) \le \frac{\sigma_Y}{\sqrt{3}}, \tag{2}$$

where

$$T_k = \frac{1}{\sqrt{6}}\sqrt{(\sigma_x - \sigma_y)^2 + (\sigma_y - \sigma_z)^2 + (\sigma_z - \sigma_x)^2 + 6(\sigma_{xy}^2 + \sigma_{yz}^2 + \sigma_{zx}^2)}$$
$$= \frac{1}{\sqrt{6}}\sqrt{(\sigma_1 - \sigma_2)^2 + (\sigma_2 - \sigma_1)^2 + (\sigma_3 - \sigma_1)^2}$$

is the intensity of shear stresses (σ_1, σ_2, and σ_3 are the principal stresses). This criterion makes it possible, first, to analyze the complex stressed state and, second, to compare the results of testing with the use of different schemes (for example, testing for bending and tension). For a stressed state, criterion (2) transforms into criterion (1). For a simple shear, criterion (2) transforms into the condition

$$\tau(t) \le \tau_Y, \tag{3}$$

where τ is the shear stress and $\tau_Y = \sigma_Y/\sqrt{3}$ is the shear yield point.

It is well known that, under the conditions of instantaneous loads, criteria (1) and (2) cease to describe adequately the behavior of the material. Traditional attempts to introduce corrections to these criteria by substituting a strain rate function for the statistical yield point have a number of material disadvantages. First, the invariance is lost; i.e., in this case, we can deal only with a certain type of testing (for example, testing under loading at a constant rate). This hampers comparison with the results obtained using other load schemes. Second, in many cases, the strain rate cannot be considered to be constant even approximately. This is particularly true in regard to pulsed (impact) load and tests for yield delay under a permanent load applied instantly. Finally, the construction of the experimental diagram $\sigma_Y(\dot{\varepsilon})$ presents considerable technical difficulties, especially if account is taken of the strong effects of temperature, structural features of the material (for example, grain size), etc.

The problem of constructing a dynamic yield criterion is associated with the experimental determination of a certain invariant characteristic of the process that must be independent of the type of action. Suvorova [1] analyzed the results of numerous experimental investigations and proved that, for high-rate loading, the dependence of the yield stress (σ_*) on the time of transition to a plastic state (t_*) is well approximated by a

1063-7834/02/4411-2080$22.00 © 2002 MAIK “Nauka/Interperiodica”

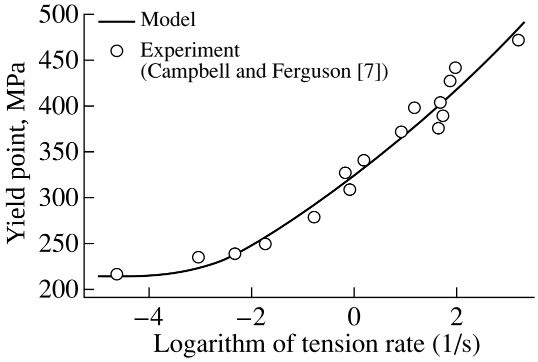

Fig. 1. Dependence of the yield point on the logarithm of the tension rate. The curve represents the results of our calculations, and the points are the experimental data taken from [7].

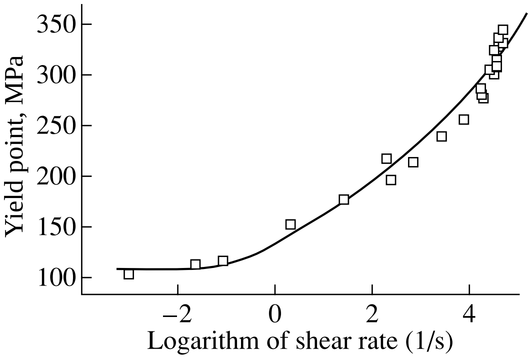

Fig. 2. Dependence of the yield point on the logarithm of the shear rate. The curve represents the results of our calculations, and the points are the experimental data taken from [7].

straight line in logarithmic coordinates, i.e., by the relationship

$$\alpha \log \sigma_* + \log t_* = \text{const}.$$

We considered variants of the generalization of this relationship to the case of an arbitrary law of variation in the stress with time. Analysis demonstrates that the best qualitative agreement with the experimental data on instantaneous loads is achieved with the criterion proposed by Campbell [2]:

$$\int_0^t \left(\frac{\sigma(s)}{\sigma_0}\right)^\alpha ds \le C \quad (C = \text{const}). \tag{4}$$

Here, σ is the current stress, σ_0 is the yield point at absolute zero temperature, and α is the dimensionless parameter. The time t^* of transition to the plastic state corresponds to the shortest time t at which relationship (4) transforms into an equality. The advantage of this criterion is its applicability to arbitrary variations in the stress with time. The disadvantages of this criterion are its applicability only to uniaxial tension or compression and only to very short-term loading. In actual fact, criterion (4) is contradictory to criterion (1) and, starting with a certain loading duration, leads to considerably underestimated threshold values of the yield stress as compared to the experimental data. The change-over to the quasi-static case becomes impossible in terms of the limiting condition (4). As a consequence, the position of the dynamic branch in the time dependence of the yield remains uncertain. For uniaxial tension, these disadvantages can be eliminated under the condition proposed in [3–5], that is,

$$\int_{t-t_{\text{inc}}}^t \left(\frac{\sigma(s)}{\sigma_Y}\right)^\alpha ds \le t_{\text{inc}}. \tag{5}$$

Here, t_{inc} is the incubation time, which characterizes the rate of structural transformation in the material. Since the transition to a plastic state is associated with the development of the dislocation structure, it is reasonable to assume that this quantity is related to the time characteristics of the dislocation motion; i.e., t_{inc} is inversely proportional to the dislocation velocity V. The dislocation velocity V can be represented using the expression proposed by Gilman [6]; that is,

$$V = V_0 \exp\left(-\frac{\Delta G}{kT}\right).$$

Here, ΔG is the activation free energy, k is the Boltzmann constant, and T is the absolute temperature. Consequently, the relationship for the incubation time can be written in the following form:

$$t_{\text{inc}} = \gamma \exp\left(\frac{\Delta G}{kT}\right). \tag{6}$$

Criterion (5) agrees well with the experimental data over a wide range of strain rates and temperatures [4]. In order to generalize criterion (5) to the case of any complex stressed–strained state, we can represent it in the form

$$\int_{t-t_{\text{inc}}}^t \left(\frac{\sqrt{3}T_k(s)}{\sigma_Y}\right)^\alpha ds \le t_{\text{inc}}. \tag{7}$$

Now, we consider two special cases. Let t_0 be the characteristic time of loading. It is easy to verify that, for uniaxial load, criterion (7) coincides with condition (5). For a slowly varying load, the limiting transition $t_{\text{inc}}/t_0 \longrightarrow 0$ satisfies the static criterion (1). Figure 1 depicts the calculated dependence of the yield point on the tension rate ($\alpha = 17$, $t_{\text{inc}} = 0.1$ s, and $\sigma_Y = 215$ MPa) upon uniaxial loading at a constant rate in comparison with the experimental data taken from [7].

For simple shear, we have $\sigma_1 = \tau$, $\sigma_2 = 0$, and $\sigma_3 = -\tau$; consequently, we obtain $T_k(t) = \tau(t)$. As a result, inequality (7) takes the form

$$\int_{t-t_{\mathrm{inc}}}^{t}\left(\frac{\tau(s)}{\tau_Y}\right)^{\alpha}ds \le t_{\mathrm{inc}}.$$

The change-over to the static case leads to criterion (3). Figure 2 presents the calculated dependence of the yield point on the shear rate ($\alpha = 11$, $t_{\mathrm{inc}} = 5 \times 10^{-4}$ s, and $\tau_Y = 110$ MPa) and the experimental data taken from [7]. As can be seen from Figs. 1 and 2, the proposed model is in good agreement with the experiment.

ACKNOWLEDGMENTS

This work was supported by the Russian Foundation for Basic Research (project no. 99-01-00718 and project TsKP 00-01-05020) and the Federal Program "Integration."

REFERENCES

1. Yu. V. Suvorova, Prikl. Mekh. Tekh. Fiz., No. 3, 55 (1968).
2. J. D. Campbell, Acta Metall. **1** (6), 64 (1953).
3. A. A. Gruzdkov and Yu. V. Petrov, in *Proceedings of the 1st All-Union Conference "Technological Problems of Strength of Load-Carrying Structures," Zaporozhye, 1991*, Vol. 1, Part 2, p. 287.
4. A. A. Gruzdkov and Yu. V. Petrov, Dokl. Akad. Nauk **364** (6), 786 (1999) [Dokl. Phys. **44**, 114 (1999)].
5. N. V. Morozov and Yu. V. Petrov, *Problems of Fracture Dynamics of Solids* (St. Petersburg Univ., St. Petersburg, 1997).
6. M. A. Meyers, *Dynamic Behavior of Materials* (Wiley, New York, 1994), Chap. 13, p. 323.
7. J. D. Campbell and W. G. Ferguson, Philos. Mag. **21** (169), 63 (1970).

Translated by N. Korovin

Physics of the Solid State, Vol. 44, No. 11, 2002, pp. 2083–2086. Translated from Fizika Tverdogo Tela, Vol. 44, No. 11, 2002, pp. 1990–1993.
Original Russian Text Copyright © 2002 by Zakrevskiĭ, Pakhotin, Shul'diner.

DEFECTS, DISLOCATIONS, AND PHYSICS OF STRENGTH

On the Possible Effect of a Magnetic Field on the Breaking of Mechanically Loaded Covalent Chemical Bonds

V. A. Zakrevskiĭ, V. A. Pakhotin, and A. V. Shul'diner
Ioffe Physicotechnical Institute, Russian Academy of Sciences, St. Petersburg, 194021 Russia
e-mail: V.Zakrevsky@pop.ioffe.rssi.ru

Received February 8, 2002; in final form, February 15, 2002

Abstract—It was established using the EPR method that a magnetic field ($B = 0.6$ T) does not affect the process of the appearance of free radicals that are formed as a result of the breaking of covalent chemical bonds in macromolecules of mechanically loaded fibers of polycaproamide. On this basis, as well as on the basis of some other data, doubts were cast on the possibility of using the assumption (frequently discussed in the literature) on the influence of a magnetic field on the rate of transformation of defect complexes due to singlet–triplet transitions upon the fluctuational lengthening of covalent bonds in such complexes for explaining some manifestations of the magnetoplastic effect in ionic crystals. *© 2002 MAIK "Nauka/Interperiodica".*

Al'shits *et al.* [1, 2] revealed an increase in the mobility of individual dislocations under the effect of a relatively weak dc magnetic field ($B < 1$ T) in alkali-halide crystals (AHCs). Later, it turned out that the magnetic field also affects the macroplastic properties of these crystals. A decrease in the yield stress in a magnetic field was observed [3, 4], as well as an increase in the rate of straining after switching-on a field [5–7] and a decrease in the microhardness of AHCs in a magnetic field [8].

The change in the plastic properties of crystals in a magnetic field was called the magnetoplastic effect (MPE). In recent years, several dozen works were devoted to the MPE. The main results of these investigations were generalized in a comprehensive review [9] containing a complete list of papers related to studying the MPE. Based on the data obtained in those works, a conclusion was derived on the occurrence in ionic crystals of magnetosensitive reactions in the subsystem of structural defects, namely, of reactions between paramagnetic centers (PMCs) at dislocations and point defects. Thus, a hypothesis was suggested on the electron nature of the MPE.

According to [9–11], a magnetic field acts not only on the process of interaction of dislocations with obstacles but also on the structure of the dislocations themselves, as well as on the structure of point defects and their complexes. A conclusion was made on the important role of short-range exchange forces (formation and opening of covalent chemical bonds between PMCs) in the formation of plastic properties of crystals.

Because of the lack of data on the structure of PMCs, the discussion of the mechanism of the effect of a magnetic field on the dislocation plasticity of crystals has frequently been performed in a general form, without consideration of reactions with the participation of concrete centers, proceeding from only the general concepts of spin-dependent free-radical reactions. However, works have appeared recently [11–13] in which concrete transformations in the systems of point defects were considered. To be more precise, a scheme of magnetosensitive reactions in complexes of point defects containing several impurity ions was suggested. In particular, the effect of a magnetic field on the transformations in trimers of impurity–vacancy dipoles was studied. The heart of the scheme is as follows. Various types of trimers differ from one another in binding energy and the spacing between impurity ions (bond lengths). Changes in the structure of impurity complexes may affect the plasticity of crystals. The magnetic field may affect the spin-dependent stages of the transition of the complexes into more stable configurations with changes in the separation between impurity ions. It is assumed that a magnetic field may accelerate the transition of a complex of defects from the configuration in which the spacing between the impurity ions is minimum and, consequently, the contribution of exchange forces to the interaction is large into a configuration in which the separation between impurities is enhanced as compared to the initial one. Thus, it is assumed that in the initial configuration, there exists a covalent bond between some impurity ions in the paramagnetic state, i.e., possessing unpaired electrons.

A transformation of a defect complex, as was noted in [12, 13], is a thermoactivational process. It may be supposed that it also can occur in a field of mechanical forces [11]. At sufficiently large thermofluctuational increments in the lengths of the covalent interatomic ("interion") bonds in a magnetic field, singlet–triplet (S–T) transitions occur, which are accompanied by an increase in the interion spacings. The complexes loosened due to the presence of broken covalent bonds then

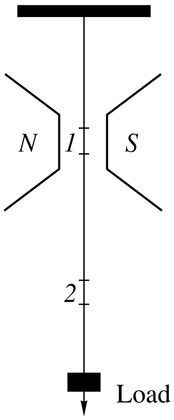

Fig. 1. Schematic of the loading of a polymer fiber. Horizontal bars mark fiber segments (*1* and *2*) in which free radicals were registered.

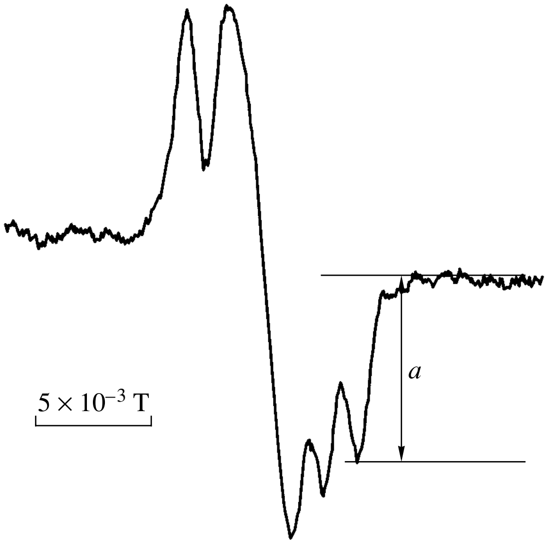

Fig. 2. An EPR spectrum of free radicals formed in a loaded fiber of nylon-6.

suffer a sufficiently fast rearrangement due to a facilitated motion of dipoles.

It was of interest to experimentally test the validity of the basic assumption on the acceleration of the thermofluctuational breaking of stressed covalent chemical bonds under the effect of a magnetic field. To detect the events of the breaking of covalent bonds in loaded materials, the EPR method has long been successfully applied. Suitable objects for studying the processes of breaking of interatomic chemical bonds in mechanically loaded materials are high-strength polymer fibers, in which high concentrations of rather stable (long-lived) free macroradicals that can reliably be registered using the EPR method can be accumulated upon tension [14, 15].

In this work, we used monofibers of polycaproamide (nylon-6) 0.8 mm in diameter. The EPR spectra were recorded after applying a mechanical load to the fiber. The load decreases the energy of activation for bond breaking and accelerates the thermofluctuational breaking of bonds. The concentrations of free macroradicals (concentrations of broken bonds) formed in the fiber under the effect of a dc magnetic field with an induction $B = 0.6$ T and without a magnetic field were compared.

The scheme of the experiment is illustrated in Fig. 1. A piece of a fiber was loaded with a force of 27 kg (a stress of 54 kg/mm^2). Part of the fiber was located between the poles of a dc magnet, i.e., in a magnetic field, and part of the fiber was outside the field. After holding under a load for 2 min, the fiber was unloaded and placed in a cylindrical resonator of a V4500-10A EPR spectrometer operating in the *Q* range. Then, the spectra of the fiber segments *1* and *2* marked by horizontal bars in Fig. 1 were recorded sequentially (during loading, segment *1* was located in the magnetic field; segment *2* was outside the magnetic field). The tensile tests and the recording of the spectra were performed at room temperature. The time of recording a spectrum was 2.5 min; therefore, the time between two successive recordings of spectra (with allowance for the time necessary for the translation of the fiber along the resonator axis when selecting a proper position of a segment) was 3 min and the time between two sequential recordings of spectra from the same segment (*1* or *2*) was 6 min. Twelve spectra were recorded for each sample (six spectra from each of the selected segments). All the spectra had the same shape, shown in Fig. 2.

The spectra mainly belong to secondary middle macroradicals –NH–CH–CH$_2$– (I) that are formed as a result of interaction of active primary end macroradicals with neighboring macromolecules [16]. The concentration of the radicals was about 10^{17} cm^{-3}. Since in the center of the spectrum there is a weak singlet belonging to free radicals that are more stable than radicals of type I, we selected the amplitude of the high-field line of the hyperfine structure of the spectrum (*a* in Fig. 2) as a measure of the concentration of radicals. The dependence of the amplitude of this line on the time of recording of the spectrum (reckoned from the moment of the beginning of the recording of the first spectrum) is shown in Fig. 3. The decrease in the concentration of free radicals in time is caused by their recombination. It is seen that the points corresponding to both segments fall well on the same curve. This means that the number of radicals formed under a load in the segment located in a magnetic field is equal to the number of radicals that arise in the segment that did not suffer the field effect. Therefore, the magnetic field does not affect the process of the breaking of covalent bonds.

This fact indicates that the scheme of transformation of defect complexes suggested in [11–13] is insufficiently substantiated. Note one more obvious circumstance concerning the main supposition of the authors of those works: the mixing of spin states (*S*–*T* conversion) upon thermofluctuational excitations of the bonds. To realize transitions between the spin states of a pair of paramagnetic particles, it is necessary that the exchange energy (spin contribution to the energy of interaction of the particles) be comparable with the energy of transitions stimulated by the magnetic field; i.e., the difference between the energies of the singlet and triplet states should be approximately 10^{-6} eV. This is possible only at very large bond lengthenings.

The estimates can be made using one of the known potentials, e.g., the Morse potential, to characterize the interatomic interaction:

$$U = D\{\exp[-2b(r-r_0)] - 2\exp[-b(r-r_0)]\},$$

where D is the energy of dissociation of the bond, $b = 2F/D$, F is the maximum force of interatomic interaction, and r_0 is the equilibrium interatomic separation.

At $r \gg r_0$, we have $U \sim -2D\exp(-br)$. Assuming $D = 1$ eV, $U = -2 \times 10^{-6}$ eV, and $b = 2 \times 10^7$ cm^{-1}, we obtain $r = 7.0$ nm. This is a formal estimate, since it makes no sense to speak of chemical bonding when $|U| \ll kT$. Nevertheless, it is clear that the above-considered bond lengthenings in crystals are unrealistic.

Note also that the expected times of *S*–*T* transitions, which are, according to [12, 13], 10^{-9} to 10^{-8} s, exceed the lifetime of a fluctuationally extended bond (equal to 10^{-13} s, according to [17]) by several orders of magnitude.

Thus, the scheme of transformation of complexes (trimers) of defects that was discussed in the literature apparently cannot be regarded as a basis for explaining the spin origin of the magnetoplastic effect (MPE). In this connection, we consider this problem in some more detail.

As was noted above, the MPE is attributed to the occurrence of spin-dependent reactions between paramagnetic centers (PMCs). Therefore, the problems of substantiating the presence of PMCs in alkali-halide crystals (AHCs) subjected to no preliminary actions (e.g., to ionizing radiations), as well as of clarifying the structure of the centers possessing unpaired electrons and determining the minimum concentration of PMCs sufficient for the observation of the MPE against the background of “nonmagnetic” defects, seems to be very important. In our opinion, these problems have been given insufficient attention. However, these are by no means simple problems. Indeed, there are no reliable data on the behavior of PMCs at dislocations in AHCs in the literature. The attempts to record EPR signals upon severe deformation and fracture of AHCs were unsuccessful [18]. The references to [19] sometimes occurring in the literature are somewhat unconvincing, since this work contains no data on PMCs at dislocations in unirradiated crystals. Moreover, in view of the results obtained in [20–22], the conclusions made in [19] apparently require corrections.

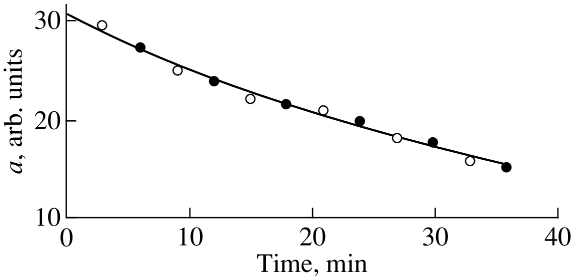

Fig. 3. Time dependence of the amplitude of the EPR spectra. Open circles correspond to segment *1* ($B \neq 0$); solid circles, to segment *2* ($B = 0$).

The paramagnetism of point defects is frequently attributed to the presence of calcium as an impurity in AHCs (e.g., in NaCl crystals that are widely used as a suitable object for the investigation of various properties of ionic crystals) [9]. The Ca^{++} ions enter into the composition of impurity–vacancy dipoles, in which vacancies compensate their charge. There are no data on the observation of EPR signals from paramagnetic Ca^{+} ions in AHCs even at a high concentration of the impurity [23], which appears to be due to the small magnitude of the second ionization potential of calcium, for which reason the impurity calcium is present in AHCs in the form of double-charged ions.

The assumption on the presence in the complexes of dimers of single-charged ions participating in the formation of covalent bonds seems insufficiently grounded, in particular, since, with the change of the charged state of the impurity (e.g., with the appearance of a single-charged instead of a double-charged calcium ion), the reason for which the impurity ion can hold a vacancy disappears; the reason for the formation of a dipole also disappears. In addition, the separation between the cations, e.g., in NaCl, exceeds 0.4 nm. At the same time, it is known that the lengths of even weak covalent bonds do not exceed 0.25 nm. At large distances, the unpaired electrons form the so-called radical pairs, which have a characteristic doublet EPR spectrum. Naturally, the possibility of a sharp (approximately twofold) change in the interatomic separation (upon the formation of a covalent bond) requires special substantiation.

Finally, when discussing the nature of the MPE, we should take into account that there are data on the absence of the effect of impurity paramagnetic Mn^{++} ions on the plasticity of AHCs in a magnetic field [24] and on the insensitivity of MPE to the presence of *F* centers in the crystal [25].

From the above-said, we conclude that the scheme of transformation of defect complexes in alkali-halide crystals that was discussed earlier in the literature cannot be considered to be well grounded. To clarify the mechanism of the magnetoplastic effect and, above all, to determine the concrete type of spin-dependent reactions in the system of defects in ionic crystals, further investigations are necessary.

ACKNOWLEDGMENTS

We are grateful to É.E. Tomashevskiĭ for the opportunity to perform experiments on the investigation of electron paramagnetic resonance of free radicals in fibers subjected to tension.

REFERENCES

1. V. I. Al'shits, E. V. Darinskaya, T. M. Perekalina, and A. A. Urusovskaya, Fiz. Tverd. Tela (Leningrad) **29** (2), 467 (1987) [Sov. Phys. Solid State **29**, 265 (1987)].
2. V. I. Al'shits, E. V. Darinskaya, and E. A. Petrzhik, Fiz. Tverd. Tela (Leningrad) **33** (10), 3001 (1991) [Sov. Phys. Solid State **33**, 1694 (1991)].
3. Yu. I. Golovin and R. B. Morgunov, Izv. Ross. Akad. Nauk, Ser. Khim., No. 4, 739 (1997).
4. A. A. Urusovskaya, V. I. Al'shits, A. E. Smirnov, and N. N. Bekkauér, Pis'ma Zh. Éksp. Teor. Fiz. **65** (6), 470 (1997) [JETP Lett. **65**, 497 (1997)].
5. Yu. I. Golovin and R. B. Morgunov, Fiz. Tverd. Tela (St. Petersburg) **37** (7), 2118 (1995) [Phys. Solid State **37**, 1152 (1995)].
6. Yu. I. Golovin, R. B. Morgunov, S. V. Zhulikov, and A. M. Karyakin, Izv. Ross. Akad. Nauk, Ser. Fiz. **60** (9), 173 (1996).
7. Yu. I. Golovin, R. B. Morgunov, and S. V. Zhulikov, Fiz. Tverd. Tela (St. Petersburg) **39** (3), 495 (1997) [Phys. Solid State **39**, 430 (1997)].
8. Yu. I. Golovin, R. B. Morgunov, D. V. Lopatin, and A. A. Baskakov, Phys. Status Solidi A **160** (2), R3 (1997).
9. Yu. I. Golovin and R. B. Morgunov, Materialovedenie, No. 3, 2 (2000); No. 4, 2 (2000); No. 5, 2 (2000); No. 6, 2 (2000).
10. Yu. I. Golovin and R. B. Morgunov, Zh. Éksp. Teor. Fiz. **115** (2), 605 (1999) [JETP **88**, 332 (1999)].
11. Yu. I. Golovin and R. B. Morgunov, Izv. Ross. Akad. Nauk, Ser. Fiz. **61** (5), 850 (1997).
12. Yu. I. Golovin, R. B. Morgunov, V. E. Ivanov, and A. A. Dmitrievskiĭ, Zh. Éksp. Teor. Fiz. **117** (6), 1080 (2000) [JETP **90**, 939 (2000)].
13. R. B. Morgunov, Author's Abstract of Doctoral Dissertation (Voronezh. Gos. Tekhn. Univ., Voronezh, 2000).
14. S. N. Zhurkov, A. Ya. Savostin, and É. E. Tomashevskiĭ, Dokl. Akad. Nauk SSSR **159** (2), 303 (1964) [Sov. Phys. Dokl. **9**, 986 (1965)].
15. B. Ya. Levin, A. V. Savitskiĭ, A. Ya. Savostin, and É. E. Tomashevskiĭ, Vysokomol. Soedin., Ser. A **13** (4), 947 (1971).
16. V. A. Zakrevskiĭ, V. V. Baptizmanskiĭ, and É. E. Tomashevskiĭ, Fiz. Tverd. Tela (Leningrad) **10** (6), 1699 (1968) [Sov. Phys. Solid State **10**, 1341 (1968)].
17. A. I. Slutsker, A. I. Mikhaĭlin, and I. A. Slutsker, Usp. Fiz. Nauk **164** (4), 357 (1994) [Phys. Usp. **37**, 335 (1994)].
18. V. V. Boldyrev, V. A. Zakrevskiĭ, and F. Kh. Urakaev, Izv. Akad. Nauk SSSR, Neorg. Mater. **15** (12), 2154 (1979).
19. S. Z. Shmurak and F. D. Senchukov, Fiz. Tverd. Tela (Leningrad) **15** (10), 2976 (1973) [Sov. Phys. Solid State **15**, 1985 (1973)].
20. A. A. Kusov, M. I. Klinger, and V. A. Zakrevskiĭ, Fiz. Tverd. Tela (Leningrad) **31** (7), 67 (1989) [Sov. Phys. Solid State **31**, 1136 (1989)].
21. A. V. Shuldiner and V. A. Zakrevskii, Radiat. Prot. Dosim. **65** (1–4), 113 (1996).
22. V. A. Zakrevskiĭ and A. V. Shul'diner, Fiz. Tverd. Tela (St. Petersburg) **42** (2), 263 (2000) [Phys. Solid State **42**, 270 (2000)].
23. C. Hoentzsch and J. M. Spaeth, Phys. Status Solidi B **88** (2), 581 (1978).
24. Yu. I. Golovin and R. B. Morgunov, Pis'ma Zh. Éksp. Teor. Fiz. **61** (7), 583 (1995) [JETP Lett. **61**, 596 (1995)].
25. Yu. I. Golovin and R. B. Morgunov, Fiz. Tverd. Tela (St. Petersburg) **35** (9), 2582 (1993) [Phys. Solid State **35**, 1280 (1993)].

Translated by S. Gorin

Physics of the Solid State, Vol. 44, No. 11, 2002, pp. 2087–2090. Translated from Fizika Tverdogo Tela, Vol. 44, No. 11, 2002, pp. 1994–1997.
Original Russian Text Copyright © 2002 by Melnichuk, Malanushenko.

MAGNETISM AND FERROELECTRICITY

Effect of Irradiation with Ne^+ Ions on the Transformations of Domain Structures of a Uniaxial Magnetic Film in an AC Magnetic Field

I. A. Melnichuk and E. L. Malanushenko
Donetsk National University, Universitetskaya ul. 24, Donetsk, 83055 Ukraine
e-mail: magnet@dongu.donetsk.ua

Received November 2, 2001

Abstract—Effects of irradiation with Ne^+ ions on the transformations of domain structures (DSs) that occur in a uniaxial magnetic film under the action of an ac magnetic field are investigated. Transitions of a DS from an amorphous state into a hexagonal lattice and a labyrinthine structure are considered. The irradiation is found to lead to a change in the amplitudes of the ac field at which phase transformations of the DS occur. The effect of the magnitude of the ac field on the number of domains in a block with a hexagonal lattice has been studied. It is shown that the process of annealing of defects in a DS consisting of blocks with a hexagonal lattice can be described by the equation of a first-order reaction. The irradiation-induced change in the energy of activation for the annealing of defects in the DS has been found. *© 2002 MAIK “Nauka/Interperiodica”*.

1. INTRODUCTION

In recent years, large attention has been paid to the investigation of phase transformations of domain structures (DSs) in thin magnetic films. The interest in the investigation of DSs in the presence of a low-frequency ac magnetic field is, on the one hand, due to the specific features of new dynamic stable domain configurations [1, 2] and, on the other hand, to the effect of an ac magnetic field on the phase transformations in DSs, which are described using the concept of an effective temperature related to the ac magnetic field [3–5].

The experimental investigations of the transformations of DSs in an ac magnetic field show that the use of the effective temperature makes it possible to qualitatively correctly describe such features of the behavior of DSs in ac magnetic fields as the times of relaxation of DSs in ac magnetic fields toward the equilibrium state [6] and the changes in the average spacings between the bends in stripe domains [7]. In addition, the velocity distribution for the segments of domain walls (DWs) that move in an ac field is Maxwellian, which indicates a sufficient “chaotization” in the system of DWs [8].

The effective temperature is defined through the average kinetic energy of domains [4] or domain walls [5]; therefore, the presence of defects, which contribute to the pinning or retardation of DWs, affects the conditions of phase transformations in the DSs. To break away a DS from the site of pinning and to overcome friction forces, the ac field must do additional work; therefore, the introduction of additional defects into the sample increases the amplitudes of the ac field at which phase transformations occur in DSs. The study of transformations in DSs in samples with various concentrations of defects makes it possible to test the validity of the application of the concept of effective temperature for describing the behavior of DSs in an ac magnetic field.

This work was aimed at the study of the effect of irradiation with accelerated particles on the conditions of the transition from an amorphous domain structure (ADS) of bubble domains into the states of the hexagonal lattice (HL) and labyrinthine domain structure (LDS) and also at describing the ADS–HL transition.

2. EXPERIMENTAL

Domain structures were observed on a magnetooptical device using the Faraday effect. The investigations were performed on a uniaxial epitaxial film of $(YEuTmCa)_3(FeGe)_5O_{12}$ with a thickness $h = 2.9$ μm and a saturation magnetization $4\pi M = 250$ G. This sample was chosen for two reasons. First, the DSs in such films are easily observable, and the technology of their growth permits one to obtain samples of quite varying degrees of perfection. Second, the main features of the effect of irradiation on the magnetic and structural properties of iron garnet films have been very well studied (see, e.g., [9]). To introduce additional defects into the sample, it was irradiated with Ne^+ ions (60 keV) to a dose of 0.8×10^{14} cm^{-2}. This dose is smaller than the dose 2×10^{14} cm^{-2} necessary for the formation of anisotropy of the easy-plane type over the whole thickness of the irradiated layer; therefore, the properties of the DWs are mainly affected by radiation defects. Under given irradiation conditions, the depth of pene-

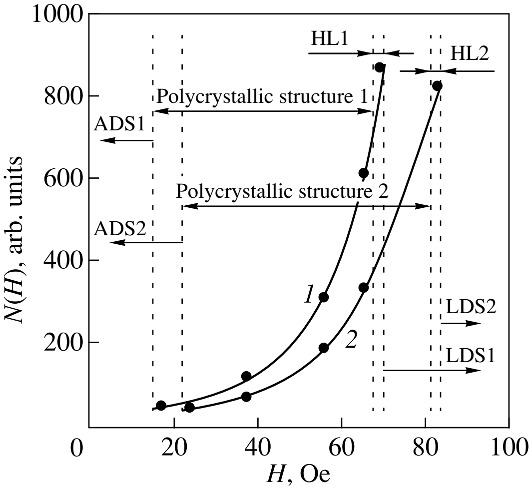

Fig. 1. Variation of the number of domains in an HL block as a function of the amplitude of the ac magnetic field: (*1*) unirradiated sample; (*2*) irradiated sample; ADS, amorphous domain structure; LDS, labyrinthine domain structure; and HL, hexagonal lattice.

tration of Ne^+ ions into the sample is about 0.1 μm; consequently, for this thickness of the film, all the defects are localized near its surface.

An ADS was obtained by converting the sample from a saturated state into a single-domain state by decreasing the external magnetic field applied parallel to the film plane. The ADS–HL–LDS transitions were realized by applying an ac magnetic field H oriented along the normal to the sample surface ($H = H_0 \sin \omega t$, where $\omega/2\pi = 300$ Hz and $H_0 = 0$–80 Oe). The application of an ac magnetic field led to transformations of the DS, which manifested themselves in changes in the domain size and in domain displacements. In a certain time, the changes were stopped and the DS passed into a stable state (for a given magnitude of H_0). The transformations of the DS were considered to be completed after the termination of domain displacements. Further, to diminish the diffuse character of the DWs in the DS images, the amplitude of the ac magnetic field was decreased to zero.

The intermediate state of the DS between ADS and HL represents a polycrystalline structure (PS). This structure consists of blocks of HL separated by defects and regions of an ADS. To quantitatively describe the DS in this state, we used the average number of domains that compose a single block with a hexagonal packing (N). Other quantities to be measured were the critical fields of the transitions ADS–PS (field H_1) and HL–LDS (field H_2). Note that while the field of the HL–LDS transition can easily be determined from the fact of the formation of stripe domains in the DS, no strict criterion for distinguishing between the ADS and PS exists. In this work, as in [10], the magnitude of H_1 was determined based on the formation of HL nuclei in the DS. As a nucleus of the HL, a block with a hexagonal packing containing no less than 30 domains was considered. This criterion is very close to that used in [11]; in addition, it is precisely 30 domains that are required to construct the second coordination shell of the HL in bubble domains with allowance for the fact that its unit cell contains two domains. Since no HL blocks with a domain number $N \geq 30$ were observed in the ADS, we used the formation of blocks with this number of domains as a criterion for the transition of the ADS into a polycrystalline structure. At $H_1 < H_0 < H_2$, the DS represented a set of HL blocks with $N \geq 30$.

3. RESULTS AND DISCUSSION

Figure 1 displays the dependence of N on H_0. As is seen, the average number of domains in an HL block grows with increasing H_0, and irradiation leads to a shift of this dependence along the H_0 axis toward larger amplitudes of the ac field. The fields of existence of the ADS, PS, HL, and LDS for the irradiated and unirradiated samples are separated in Fig. 1 by dashed vertical lines. It is seen that the irradiation of the sample increases H_1 by 25% and H_2 by 17%. The changes are large, since the phase transition at $H = H_2$ is observed very clearly and occurs in a rather narrow range of fields. In addition, the criterion for the determination of H_1 used in this case also permits us to reliably determine the field for the transition from the ADS to the PS. The errors in the measurements of critical fields are no more than 3%. Since the effective temperature of the DS is unambiguously related to the amplitude of the ac field [4, 5], an increase in the critical fields upon irradiation may be interpreted as being due to the influence of irradiation on the effective temperature of phase transformations in the DS.

An analysis of the ADS–HL transition for the irradiated and unirradiated samples was performed using the effective temperature with allowance for the $N(H_0)$ dependences shown in Fig. 1. This transition has many common features with the process of crystallization of solids; therefore, the analysis of the effect of an ac magnetic field on the behavior of the DS was based on the model of defect annealing in the crystal lattice of a solid. According to [12, 13], the process of defect elimination may be described by the following equation:

$$dc/dt = -Kc^n, \quad K = K_0 \exp(U_0/kT), \qquad (1)$$

where c is the concentration of defects, n is the order of the reaction, K_0 is a constant, U_0 is the activation energy, k is the Boltzmann constant, and T is the temperature. The order of the reaction is determined by the mechanism of defect elimination [12, 13]. According to [14], the main mechanism of elimination of defects in DSs in the range $H_1 < H_0 < H_2$ is connected with their migration to sinks or with the annihilation of close paired defects. Therefore, the process of defect elimination was described using the equation of a first-order reaction. It is seen that Eq. (1) qualitatively correctly reflects the behavior of the $N(H_0)$ dependence shown in Fig. 1.

In order to obtain a quantitative correspondence of the $N(H_0)$ dependence to Eq. (1), it is necessary to use the dependence of the effective temperature on the amplitude of the ac field and unambiguously relate the number of domains in an HL block to the concentration of defects in the DS. According to [4, 5], the effective temperature may be determined as $T_{\mathrm{eff}} = \alpha H_0^2$, where α is a constant depending on the parameters of the sample.

The analytical relation between the concentration of defects in the DS and the number of domains in an HL block was obtained under the assumption that the number of domains remained constant with increasing amplitude of the ac magnetic field and that at $H_0 > H_1$, all the defects were localized at the boundaries of these blocks. The width of the interface between the blocks of the HL was assumed to be equal to one unit cell of this lattice.

The relative concentration of defects was determined as follows: $C(N) = N_d/(N_d + N)$, where N_d is the number of domains in the cells localized at the block boundaries and N is the total number of domains in an HL block. On the assumption that the block has a hexagonal symmetry, we obtained $C(N) = 4/(4 + \sqrt{N})$. This relation permits comparison of the measured $N(H_0)$ dependence with the $C(N)$ dependence calculated using Eq. (1).

Note that, in accordance with the model used, the number of defects in the lattice exponentially depends on time. Therefore, the defect concentration decreases sharply with increasing time of residence of the DS in an ac field. Such a behavior corresponds to the way of estimation of the moment of termination of the transformations of the DS in an ac field assumed in the model.

To compare the experimental values of $N(H_0)$ with calculated values of $C(H_0)$, it is convenient to use the function $Q(H_0) = \ln\ln(C(H_0)^{-1})$. Then, in accordance with Eq. (1) and the definition of the effective temperature, we obtain

$$Q(H_0) = A - U_0/k\alpha H_0^2, \tag{2}$$

where A is a constant that is independent of the magnetic field. Therefore, if the experimental $N(H_0)$ dependence corresponds to the model under consideration, then the magnitude of Q linearly depends on H_0^{-2} and the magnitude of the activation energy determines the slope of this dependence.

The $Q(H_0^{-2})$ dependences for the irradiated and unirradiated sample are given in Fig. 2. We emphasize that, in accordance with the results of [14], the mechanism of annihilation of paired defects is realized in the middle of the interval of variation of the fields H_0. It is for this reason that in Fig. 2, we chose only these values of the amplitude of the ac field. As is seen from Fig. 2, both dependences are linear; note that irradiation led to a change in the slope of the $Q(H_0^{-2})$ dependence. This means that the model of the annealing of defects in a DS upon transition from the amorphous state into an HL is described by the equation of a first-order reaction.

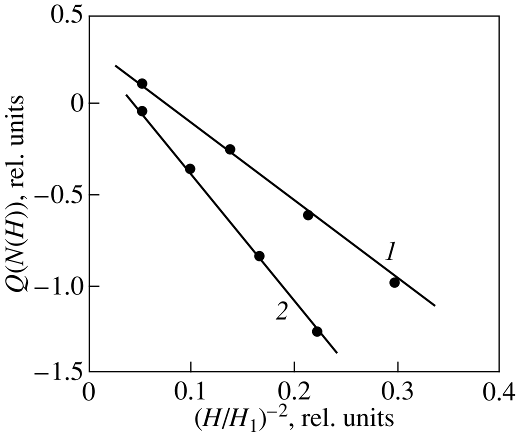

Fig. 2. $Q(N(H))$ dependence plotted for (*1*) unirradiated and (*2*) irradiated samples. Points correspond to experimental values of $N(H)$; solid lines, to calculated values of $N(H)$.

The slope of the straight line $Q(H_0^{-2})$ in the dependence on H yields the energy of activation for the process of defect annealing. A comparison of the $Q(H_0^{-2})$ dependences for the irradiated and unirradiated samples shows that an irradiation with ions not only leads to a change in the first and second critical fields but also changes the entire process of crystallization of the DS on the whole, which manifests itself in a change in the activation energy, which, in turn, causes a change in the slope of the $Q(H_0^{-2})$ dependence. The comparison shows that in this case, the irradiation led to an increase in the activation energy of the process by 50%. Note that the changes that occurred in the sample are related to the appearance of additional defects as a result of irradiation with Ne ions.

4. CONCLUSION

Thus, in this work, we showed that irradiation affects the magnitudes of the critical fields for the ADS–HL–LDS transitions. It was found that $N(H_0)$ increases with increasing H_0, while the irradiation leads to a shift of this dependence along the H axis toward larger amplitudes of the ac magnetic field. It is shown that the change in $N(H_0)$ may be described in terms of the model of annealing of DS defects with the use of an equation of the first-order reaction. In this case, the irradiation leads to an increase in the energy of activation for the process of annealing of structural defects of the DS. The effective temperature related to the ac field can be used for the description of the ADS–HL transition.

ACKNOWLEDGMENTS

This work was supported by the Ministry of Education and Science of the Ukraine.

REFERENCES

1. G. S. Kandaurova and A. É. Sviderskiĭ, Zh. Éksp. Teor. Fiz. **97** (25), 1218 (1990) [Sov. Phys. JETP **70**, 684 (1990)].
2. I. E. Dikshteĭn, F. V. Lisovskiĭ, and E. G. Mansvetova, Zh. Éksp. Teor. Fiz. **100** (5), 1606 (1991) [Sov. Phys. JETP **73**, 888 (1991)].
3. K. L. Babcock and R. M. Westervelt, Phys. Rev. Lett. **64**, 2168 (1990).
4. V. A. Zablotskii and Yu. A. Mamalui, J. Phys.: Condens. Matter **7**, 5271 (1995).
5. E. S. Denisova, Physica B (Amsterdam) **253** (3–4), 250 (1998).
6. V. A. Zablotskii, Yu. A. Mamalui, and E. N. Soika, in *Proceedings of the 7th International Conference on Ferrites, Bordeux, France, 1996*, p. 274.
7. Yu. I. Gorobets and I. A. Melnichuk, in *Proceedings of the XVII International School-Workshop "Novel Magnetic Materials for Microelectronics," Moscow, 2000*, p. 494.
8. D. A. Chumakov and I. A. Melnichuk, in *Abstract of the 8th European Magnetic Materials and Applications Conference (EMMA), Kiev, 2000*, p. 279.
9. *Bubble-Based Elements and Devices: Reference Book*, Ed. by N. N. Evtikhiev and B. N. Naumov (Radio i Svyaz', Moscow, 1987).
10. Yu. I. Gorobets, E. L. Malanushenko, and I. A. Melnichuk, in *Abstracts of the Euro-Asian Symposium "Trends in Magnetism" (EASTMAG), Ekaterinburg, 2001*, Vol. 17, p. 336.
11. Yu. I. Gorobets, I. A. Melnichuk, and I. V. Komissarov, Vestn. Donetsk. Univ., Ser. A: Estestv. Nauki, No. 2, 98 (1999).
12. L. Pranyavichyus and Yu. Dudonis, *Modification of Solid Properties by Ion Beams* (Mokslas, Vilnius, 1980).
13. A. N. Goland, in *Atomic Structure and Mechanical Properties of Metals* (*Proceedings of the International School of Physics "Enrico Fermi,"* Course LXI, Ed. by G. Gaglioti) (North-Holland, New York, 1976), pp. 1–119.
14. Yu. I. Gorobets and I. A. Melnichuk, in *Proceedings of the XVII International School-Workshop "Novel Magnetic Materials for Microelectronics," Moscow, 2000*, p. 491.

Translated by S. Gorin

Physics of the Solid State, Vol. 44, No. 11, 2002, pp. 2091–2094. Translated from Fizika Tverdogo Tela, Vol. 44, No. 11, 2002, pp. 1998–2000.
Original Russian Text Copyright © 2002 by Guanghua, Eremin, Kolmakova, Lagutin, Levitin.

MAGNETISM AND FERROELECTRICITY

Magnetic Properties of the $HoMn_2Ge_2$ Intermetallic Compound

Guo Guanghua*, M. V. Eremin, N. P. Kolmakova**,**
A. S. Lagutin*, and R. Z. Levitin***
** Moscow State University, Vorob'evy gory, Moscow, 119899 Russia*
*** Bryansk State Technical University, Bryansk, 241035 Russia*
**** Institute of Molecular Physics, Russian Research Centre Kurchatov Institute,*
pl. Akademika Kurchatova 1, Moscow, 123182 Russia
e-mail: npk@bitmcnit.bryansk.su

Received December 11, 2001

Abstract—The magnetic properties of a tetragonal intermetallic compound, namely, $HoMn_2Ge_2$, are investigated experimentally and theoretically. The experimental temperature dependences of the initial magnetic susceptibility and the lattice parameters are obtained in alternating and static magnetic fields. The magnetization curves are measured in strong magnetic fields up to 50 T. The parameters of the crystal field and Ho–Mn and Mn–Mn exchange interactions are determined, and the temperature dependence of the magnetic field of the phase transition from an antiferromagnetic phase to a ferromagnetic phase in a magnetic field aligned along the tetragonal axis is calculated. *© 2002 MAIK "Nauka/Interperiodica".*

1. Crystals of intermetallic compounds of the general formula RMn_2Ge_2 (R is a rare-earth element) have a tetragonal structure of the $ThCr_2Si_2$ type (space group $I4/mmm$) that consists of a set of –R–Ge–Mn–Ge–R– layers aligned perpendicularly to the c axis. As is known, RMn_2Ge_2 intermetallic compounds are ideal natural superlattices. Over the last two decades, the physical (including magnetic) properties of RMn_2Ge_2 have been intensively investigated, especially, as regards the numerous phase transitions revealed in these compounds. In RMn_2Ge_2 intermetallic compounds with heavy rare-earth elements, the magnetic moments of manganese are ordered in layers due to Mn–Mn exchange interactions (these interactions appeared to be the strongest of the interactions involved). It is found that Mn–Mn and R–Mn interactions exhibit antiferromagnetic nature. At $T < T_N \approx 460$ K (where T_N is the Néel temperature), the manganese subsystem is antiferromagnetically ordered, whereas the rare-earth subsystem is disordered. In the $HoMn_2Ge_2$ compound, unlike the intermetallic compound with other rare-earth elements (R = Gd, Tb, or Dy), the rare-earth subsystem remains disordered to very low temperatures [1]. Szutula and Leciejewicz [2] demonstrated that this phenomenon is associated with the weak R–Mn exchange interaction. According to neutron diffraction data [1], the magnetic moments of holmium at temperatures below $T_N^{Ho} = 2.5$ K are characterized by a superposition of two sinusoidally modulated magnetic structures with different wave vectors. The manganese subsystem whose magnetic moments are collinear with respect to the tetragonal axis remains antiferromagnetically ordered down to 1.3 K [1]. Kirste *et al.* [3] investigated the magnetic phase transitions in RMn_2Ge_2 intermetallic compounds in ultrastrong magnetic fields and revealed that, at the liquid-helium temperature, the holmium-containing compound undergoes a first-order phase transition from an antiferromagnetic phase to a ferromagnetic phase in a magnetic field of approximately 90 T. In the present work, we discussed the magnetic properties of the $HoMn_2Ge_2$ intermetallic compound reasoning from the aforementioned findings and the results of our measurements of the initial magnetic susceptibility, lattice parameters, and magnetization curves in magnetic fields up to 50 T. Moreover, we determined the parameters of the main interactions revealed in this compound.

2. Polycrystalline samples of the $HoMn_2Ge_2$ intermetallic compound were prepared by melting the initial components (with a purity of 99.9%) in an induction furnace under quasi-levitation conditions in an argon atmosphere. In order to achieve a better homogenization, the samples were remelted three times and were then annealed at a temperature of 750°C in a dynamic vacuum for 170 h. The phase homogeneity of the prepared samples was checked using x-ray diffraction analysis. The initial magnetic susceptibility was measured both in an alternating magnetic field (in the temperature range from 4.2 to 270 K) and in a static magnetic field (in the temperature range from 300 to 500 K). The temperature dependence of the lattice parameters was measured using the x-ray diffraction technique on a Geigerflex diffractometer (Japan) in the temperature range from 10 to 800 K. Figure 1 shows the temperature dependences of the initial magnetic susceptibility and the lattice parameters of the $HoMn_2Ge_2$ compound. It can be seen from Fig. 1 that, at $T_N \approx 460$ K,

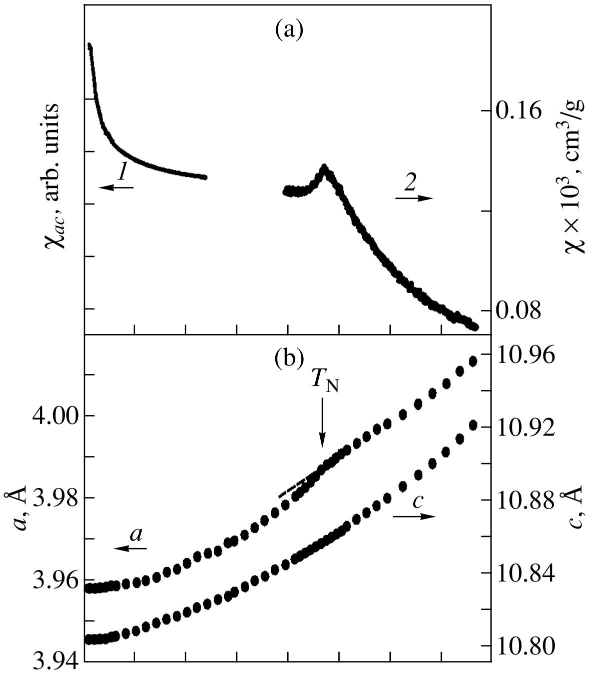

Fig. 1. Temperature dependences of (a) the initial magnetic susceptibility in (*1*) an alternating magnetic field and (*2*) a static magnetic field and (b) the lattice parameters of the $HoMn_2Ge_2$ compound.

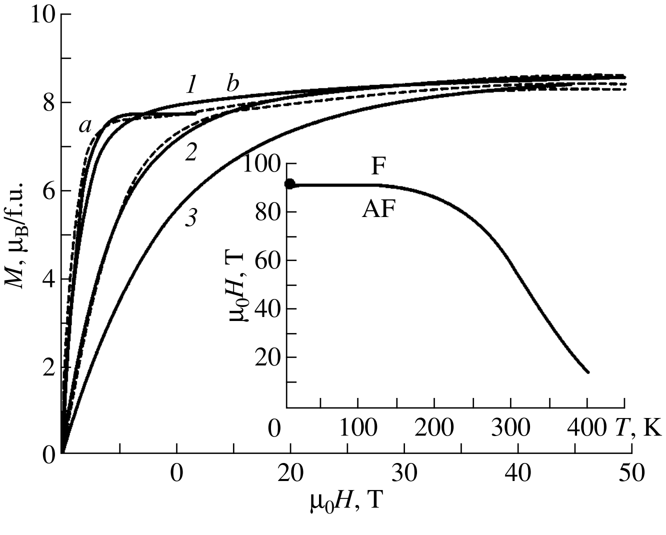

Fig. 2. Experimental (solid lines) and calculated (dashed lines) curves of the magnetization at temperatures of (*1*) 8, (*2*) 27.5, and (*3*) 49 K. The inset shows the *H*–*T* phase diagram for the transition from the antiferromagnetic (AF) phase to the ferromagnetic (F) phase in a magnetic field directed along the tetragonal axis. The closed circle indicates the experimentally determined field of the phase transition at $T = 5$ K [3]. For explanation of curves *a* and *b*, see the text.

the manganese subsystem undergoes a transition from the paramagnetic state to the antiferromagnetic state and the temperature dependence of the lattice parameter $a(T)$ exhibits a negative anomaly. At low temperatures, the magnetic susceptibility increases drastically. This can be associated with the appearance of precursors of magnetic ordering in the holmium subsystem.

The magnetization of $HoMn_2Ge_2$ was measured on a pulsed induction magnetometer [4] in the temperature range from 8 to 50 K in strong pulsed magnetic fields up to 50 T with a pulse duration of 26 ms. The magnetization measurements were performed with powders whose particles could rotate in a magnetic field. At $T =$ 8 K, the magnetization was also measured on a vibrating-coil magnetometer in magnetic fields up to 12 T. Figure 2 depicts the magnetization curves of the $HoMn_2Ge_2$ compound. As can be seen from this figure, the results of magnetization measurements carried out using the two techniques are in good agreement (cf. curves *a* and *b*). The magnetization of $HoMn_2Ge_2$ in strong magnetic fields is approximately equal to 8 μ_B/f.u. This value is less than that for a free ion (10 μ_B/f.u.) and indicates a considerable effect of the crystal field.

3. As was noted above, at temperatures below $T_N^{Ho} =$ 2.5 K, the holmium subsystem of the $HoMn_2Ge_2$ intermetallic compound is in the paramagnetic state, whereas the manganese subsystem is antiferromagnetically ordered and jumpwise transforms into the ferromagnetic state in a critical magnetic field oriented along the tetragonal axis. Let us now consider the magnetic properties of this compound in a magnetic field aligned parallel to the tetragonal axis with allowance made for the smallest (but sufficiently large for describing the experimental data) number of exchange interactions in the molecular field approximation. For the manganese subsystem, we take into account both the exchange interactions in a layer (the exchange parameter λ_{22}^0) and the exchange interactions between adjacent layers (the parameter λ_{22}). The Ho–Ho exchange interaction is disregarded, because, in this case, it is relatively weak [1] and is of no significance in the temperature range under investigation. The effect produced by all the layers involved in the manganese subsystem on the rare-earth subsystem is summed and can be described by the parameter λ_{12} (see [5]). In these calculations, we also take into account the known dependence of the parameter λ_{22} (characterizing the Mn–Mn exchange interactions in adjacent layers) on the interatomic distance in the layer, i.e., the lattice parameter *a* [6]; this dependence leads to the temperature dependence of the exchange parameter and can be represented by the relationship

$$\lambda_{22} = \rho(a - a_c), \tag{1}$$

where a_c = 4.045 Å for $R\mathrm{Mn_2Ge_2}$ intermetallic compounds.

The effective Hamiltonian for an $\mathrm{Ho^{3+}}$ ion subjected to a tetragonal crystal field in a magnetic field directed along the tetragonal axis (the z axis) has the form

$$H = \sum_{n,\,m} B_n^m O_n^m - g_J \mu_B J_z (H + H_z^{(\mathrm{Ho})}), \qquad n = 2, 4, 6; \quad m = 0.4, \tag{2}$$

where B_n^m stands for the crystal field parameters, O_n^m are the equivalent operators, g_J is the Landé splitting factor ($g_J = 5/4$), and J_z is the z component of the angular momentum operator for the $\mathrm{Ho^{3+}}$ ion. The molecular field of the manganese subsystem can be represented by the relationship $H_z^{(\mathrm{Ho})} = \lambda_{12}(m_{1z} + m_{2z})$, $m_{kz} = \mu_B g \langle S_{kz} \rangle$, where k = 1 and 2, g is the Landé splitting factor for manganese, and S_{kz} is the z component of the operator of the kth spin moment for manganese.

The thermodynamic potential of the system in a magnetic field along the tetragonal axis per formula unit is determined by the expression

$$\Phi = -k_B T \ln Z + \frac{1}{2} M_z H_z^{(\mathrm{Ho})} - k_B T \sum_{k=1}^{2} \ln \frac{\sinh[(2S+1)x_k/2]}{\sinh(x_k/2)} + \frac{1}{2} \sum_{k=1}^{2} m_k H_{mk}. \tag{3}$$

The partition function Z for the holmium magnetic moment was determined using numerical diagonalization of Hamiltonian (2), $M_z = \mu_B g_J \langle J_z \rangle$, and $x_k = \mu_B g H_k^{(\mathrm{Mn})}/k_B T$, where $H_k^{(\mathrm{Mn})} = H\cos\varphi_k + H_{mk}$, $H_{mk} = \sum_{n = k,\, k \pm 1} \lambda_{22}^{(n)} m_n \cos(\varphi_n - \varphi_k) + \lambda_{12} M_z \cos\varphi_k$, φ_k is the polar angle of the kth magnetic moment of manganese (in our case, $\varphi_k = 0$ or π), and $\lambda_{22}^{(n)}$ are the parameters of the Mn–Mn exchange interaction between atoms of the kth and nth layers. The second and fourth terms in expression (3) are conventional correcting terms in the molecular field theory.

Thus, we calculated the magnetization curves $M(H)$ and the H–T phase diagram for the magnetic field of the first-order phase transition from the antiferromagnetic state to the ferromagnetic state in the manganese subsystem in a magnetic field directed along the tetragonal axis. The lattice parameters of the $\mathrm{HoMn_2Ge_2}$ compound were determined by comparing the calculated and experimental data.

4. The experimental magnetization curves for the $\mathrm{HoMn_2Ge_2}$ compound at three temperatures (solid lines in Fig. 2) indicate that the crystal field substantially affects the magnetic moment of the holmium subsystem. In this case, the holmium subsystem resides in the paramagnetic state, because, in the temperature range under investigation, the molecular fields acting on each holmium layer from the two adjacent layers cancel each other. The magnetization curves were used to determine the crystal field parameters. For lack of reliable spectroscopic information, we restricted our consideration to the case of three parameters (the sixth-order parameters B_6^0 and B_6^4 were taken to be equal to zero, as was done by Venturini *et al.* [7] in their determination of the crystal field parameters from the temperature dependences of the hyperfine field and the quadrupole interaction in the case of $\mathrm{DyMn_2Ge_2}$). The fitting was performed with the crystal field parameters of $\mathrm{DyMn_2Ge_2}$, which were taken as the initial values. These parameters were refined using available magnetic data in our recent work [5]. The best fitting of the magnetization curves (Fig. 2) was achieved with the following parameters (in $\mathrm{cm^{-1}}$): $B_2^0 = 169$, $B_4^0 = -72$, and $B_4^4 = -556$. These parameters differ significantly from those determined with the use of only the parameter B_4^0 for $\mathrm{DyMn_2Ge_2}$.

5. The parameters of Mn–Mn and Ho–Mn exchange interactions (λ_{22} and λ_{12}, respectively) were obtained using the experimentally determined field of the transition from the antiferromagnetic phase to the ferromagnetic phase in a magnetic field directed along the tetragonal axis: $H_{\mathrm{AF}\to\mathrm{F}} = 91$ T at $T = 5$ K [3]. At low temperatures, from the expansion of the thermodynamic potential (3) (see also [5]), we obtain

$$H_{\mathrm{AF}\to\mathrm{F}} = -\lambda_{12} M - \lambda_{22} m. \tag{4}$$

The magnetic moment M for holmium, according to our experimental data, is taken to be equal to $8.3\mu_B$ (Fig. 2), and the magnetic moment m for manganese in the antiferromagnetic phase is assumed to be $2.3\mu_B$. The latter value was found in [1] by averaging the magnetic moments over a series of $R\mathrm{Mn_2Ge_2}$ compounds (R = Tb, Ho, Er, and Tm). The exchange parameters λ_{12} and λ_{22} were determined from their linear combination (4) using two methods. In the first method, the exchange parameter λ_{12} for $\mathrm{HoMn_2Ge_2}$ was calculated from the parameter λ_{12} for $\mathrm{DyMn_2Ge_2}$ [5] with the use of the relevant Landé factors; then, the parameter λ_{22} was obtained from expression (4). In the second method, the exchange parameter λ_{22} for $\mathrm{HoMn_2Ge_2}$ was calculated from the parameter λ_{22} for $\mathrm{DyMn_2Ge_2}$ [5] with the use of formula (1) (for the lattice parameter a_{Dy}, we used our data obtained earlier in [5]); then, the parameter λ_{12} was determined from expression (4). It is worth noting that both methods lead to close values of the exchange parameters: $\lambda_{12} = -4.5 \pm 0.5\mathrm{T}/\mu_B$ and $\lambda_{22} = -23 \pm 2\mathrm{T}/\mu_B$. A similar calculation of the exchange parameters for $\mathrm{HoMn_2Ge_2}$ from the parameters for $\mathrm{GdMn_2Ge_2}$, which were determined in [8], gives a larger spread of the results obtained. This can be explained by the fact that, compared to dysprosium, gadolinium is more distant from holmium in the row of rare-earth elements in the periodic table.

The temperature dependence of the critical field $H_{AF \to F}$ of the transition from the antiferromagnetic phase to the ferromagnetic phase was calculated using the thermodynamic potential (3), which accounts for the temperature and field dependences of all the characteristics of the system under consideration. Moreover, we took into account the temperature dependence of the Mn–Mn interlayer exchange parameter λ_{22} according to formula (1) with the use of the measured temperature dependence of the lattice parameter $a(T)$ (Fig. 1b). The parameter λ_{22}^0 characterizing Mn–Mn exchange interactions in a layer was found from the temperature T_N = 460 K and the known parameter λ_{22}: $\lambda_{22}^0 = 2.1 \times 10^3 T/\mu_B$. The calculated phase diagram is depicted in the inset to Fig. 2.

ACKNOWLEDGMENTS

This work was supported in part by the Russian Foundation for Basic Research, project no. 99-02-17358.

REFERENCES

1. G. Venturini, B. Malaman, and E. Ressouche, J. Alloys Compd. **240** (1), 139 (1996).
2. A. Szutula and J. Leciejewicz, in *Handbook on the Physics and Chemistry of Rare Earths*, Ed. by K. A. Gschneidner, Jr. and L. Eyring (Elsevier, Amsterdam, 1989), Vol. 12, p. 133.
3. A. Kirste, R. Z. Levitin, M. von Ortenberg, *et al.*, Fiz. Tverd. Tela (St. Petersburg) **43** (9), 1661 (2001) [Phys. Solid State **43**, 1731 (2001)].
4. A. S. Lagutin, J. Vanacken, N. Harrison, and F. Herlach, Rev. Sci. Instrum. **66** (8), 4267 (1995).
5. Guo Guanghua, M. V. Eremin, A. Kirste, *et al.*, Zh. Éksp. Teor. Fiz. **120** (10), 910 (2001) [JETP **93**, 796 (2001)].
6. C. Kittel, Phys. Rev. **120** (2), 335 (1960).
7. G. Venturini, B. Malaman, K. Tomala, *et al.*, Phys. Rev. B **46** (1), 207 (1992).
8. A. Yu. Sokolov, Guo Guanghua, S. A. Granovskiĭ, *et al.*, Zh. Éksp. Teor. Fiz. **116** (4), 1346 (1999) [JETP **89**, 723 (1999)].

Translated by O. Borovik-Romanova

Physics of the Solid State, Vol. 44, No. 11, 2002, pp. 2095–2097. Translated from Fizika Tverdogo Tela, Vol. 44, No. 11, 2002, pp. 2001–2003.
Original Russian Text Copyright © 2002 by Granovskiĭ, Sato, Aoki, Yurasov.

MAGNETISM AND FERROELECTRICITY

Tunneling Thermopower in Magnetic Granular Alloys

A. Granovskiĭ*, H. Sato, Y. Aoki**, and A. Yurasov***
** Moscow State University, Vorob'evy gory, Moscow, 119899 Russia*
e-mail: granov@magn.ru
*** Department of Physics, Tokyo Metropolitan University, Tokyo, 192-0397 Japan*

Received December 25, 2001

Abstract—The nature of the field dependence of thermopower in the Co–Al–O and Fe–Al–O magnetic granular alloys with tunneling conduction is shown to be related to tunneling thermopower. The tunneling thermopower is small and depends approximately linearly on temperature and squared magnetization, and its field dependence is described by a relation of the type $S(H)/T = a + b\rho(0)/\rho(H)$, where ρ is the alloy electrical resistivity and the parameters a and b are field-independent. *© 2002 MAIK "Nauka/Interperiodica".*

Recently, Sato *et al.* [1, 2] found that thermopower S in the Co–Al–O and Fe–Al–O magnetic granular alloys of the metal–insulator type with tunneling magnetoresistance (TMR) is negative and considerably smaller than that in bulk Co and Fe and that its field dependence is described by the relation

$$\frac{S(H)}{T} = a + b\frac{\rho(0)}{\rho(H)}, \qquad (1)$$

where a and b are field-independent and ρ is the electrical resistivity. A relation of the type of Eq. (1), found earlier to hold for metallic multilayers and granular alloys with giant magnetoresistance (see, e.g., [3]), has been shown to be due to the fact that both $\rho(H)$ and $S(H)$ are governed in these metallic systems by spin-dependent scattering in the grain volume and from interfaces. In granular metal–insulator alloys, however, the magnetoresistance is connected with electron tunneling transport through the insulating spacer between adjacent grains; therefore, Eq. (1) requires adequate substantiation. Moreover, one can readily show that the effective-medium theory developed for metal–insulator composites fails to account for this relation [4].

We present here a calculation of tunneling thermopower S^{tun} in granular metal–insulator alloys and show that the thermopower in these systems near the percolation threshold is primarily of tunneling nature and can be approximated by Eq. (1). As far as we know, tunneling thermopower has not yet been discussed in the literature.

Near the percolation threshold, it can be assumed that the conducting channel in the metal–insulator system is made up of series-connected elements of two types, more specifically, of metallic grains and tunneling barriers. Let each of these elements be characterized by the values of their thermopower (S^{met}, S^{tun}) and thermal resistance (W^{met}, W^{tun}). Following the obvious Kohler rule [5], we can present the thermopower of such a conductor in the form

$$S = \frac{S^{\text{met}}W^{\text{met}} + S^{\text{tun}}W^{\text{tun}}}{W^{\text{met}} + W^{\text{tun}}}. \qquad (2)$$

Kohler's rule is a consequence of a temperature gradient distribution in the inhomogeneous system. If all the elements of the conductor are metallic and obey the Wiedemann–Franz law, Eq. (2) reduces to the well-known Nordheim–Gorter rule [5]. In the case under consideration, Eq. (2) is a rough approximation, because it is assumed at the very beginning that all the elements of the electrical circuit are identical. In a more consistent analysis, one should take into account the difference in the height of the tunneling barriers and perform an averaging over the optimum electron transport trajectories, as is done, for instance, in the theory of magnetoresistance [6]. However, this would be beyond the scope of the present communication, which deals primarily with calculation of S^{tun}.

Because the thermal resistance of the insulating spacer W^{tun} is of the order of that of the insulator and is certainly larger than W^{met}, we have

$$S \approx S^{\text{tun}} + S^{\text{met}}\frac{W^{\text{met}}}{W^{\text{tun}}} = S^{\text{tun}} + S^{\text{met}}\frac{\gamma^{\text{tun}}}{\gamma^{\text{met}}}, \qquad (3)$$

where γ^{tun} and γ^{met} are the thermal conductivities of the insulator and the metal, respectively.

The tunneling process does not involve a change in the electron energy; therefore, S^{tun} can be calculated using Mott's relation:

$$S^{\text{tun}} = \frac{-\pi^2 k_B^2}{3\,|e|}T\left[\frac{1}{G(E)}\frac{\partial G(E)}{\partial E}\right]_{E_F}, \qquad (4)$$

where $G(E)$ is the tunneling conductance. In terms of the TMR theory, the tunneling conductance can be written in the form [7]

$$G(E) = G_0[1 + P^2(E)m^2]e^{-2\sqrt{2\kappa(E)C/k_BT}}, \tag{5}$$

where G_0 = const, C = const, m is the relative magnetization,

$$P(E) = \frac{D_\uparrow(E) - D_\downarrow(E)}{D_\uparrow(E) + D_\downarrow(E)}, \tag{6}$$

$D_\sigma(E)$ ($\sigma = \uparrow, \downarrow$) is the local density of states at the tunneling junction interfaces for the corresponding energy E,

$$\kappa = \sqrt{2m_{\text{eff}}(V - E)/\hbar^2}, \tag{7}$$

m_{eff} is the effective mass of a tunneling electron, and V is the height of the barrier. In accordance with Eq. (5), the temperature dependence of the conductance is

$$G \sim e^{-(T_0/T)^{1/2}}, \quad T_0 = \sqrt{\frac{8kc}{k_B}}, \tag{8}$$

which is in good agreement with experiment [6]. Equation (5) also quite well describes the dependence of TMR on m^2 and the weak temperature dependence of the TMR. We note that Eqs. (5) and (8) are valid within a fairly broad but limited temperature interval $T_{\min} < T < T_{\max}$ [6] and although these equations were derived using the approximation of Sheng *et al.* [8] for conductance averaging over intergrain distances, relations of the same kind can be obtained based on general considerations concerning the character of grain distribution with respect to size [6]. For high temperatures, the $T^{1/2}$ law in Eq. (8) fails and is replaced by a relation describing an activated behavior. We shall restrict ourselves to the region where Eq. (8) holds, because the high-temperature case is not realized in ferromagnetic systems even if the Curie temperature is high.

After substituting Eq. (5) into Mott's relation (4) and performing some straightforward calculations, we obtain

$$S^{\text{tun}} = \frac{-\pi^2}{3}\frac{k_B^2}{|e|}T\left[\frac{\left(2P\frac{\partial P}{\partial E}\right)_{E_F}m^2}{1 + P^2m^2} + \frac{m_{\text{eff}}}{2\hbar^2\kappa^2}\left(\frac{T_0}{T}\right)^{1/2}\right]. \tag{9}$$

It follows from Eq. (5) that

$$\frac{\Delta\rho}{\rho} = \frac{G^{-1}(0) - G^{-1}(H)}{G^{-1}(0)} = 1 - \frac{\rho(H)}{\rho(0)} = \frac{P^2m^2}{1 + P^2m^2}, \tag{10}$$

$$\frac{\rho(0)}{\rho(H)} = 1 + P^2m^2. \tag{11}$$

According to Eq. (11), $m^2 = \frac{1}{P^2}\left(\frac{\rho(0)}{\rho(H)} - 1\right)$; Eq. (9) can now be recast in the form of Eq. (1), where

$$a = \frac{-\pi^2}{3}\frac{k_B^2}{|e|}\left[\left(\frac{T_0}{T}\right)^{1/2}\frac{m_{\text{eff}}}{2\hbar^2\kappa} - \frac{2\left(\frac{1}{P}\frac{\partial P}{\partial E}\right)_{E_F}}{1 + P^2m^2}\right], \tag{12}$$

$$b = \frac{-\pi^2}{3}\frac{k_B^2}{|e|}\left[\frac{2\left(\frac{1}{P}\frac{\partial P}{\partial E}\right)_{E_F}}{1 + P^2m^2}\right]. \tag{13}$$

Equations (9), (12), and (13) sum up the main result of our study. Because, in all the systems studied, the TMR does not exceed 9% [1, 3] and the spin polarization is $P \sim 0.3$ [7, 9], one can limit oneself without any loss of generality to a linear approximation in P. Furthermore, the second term in brackets in Eq. (9) is small compared to the first one and should be taken into account only in the case of paramagnetic alloys. Indeed, because $\kappa \geq k_{\text{F}}$ (where k_{F} is the Fermi wave vector [7]) and near the percolation threshold $T_0 \approx 10$ K [6], the second term in Eq. (9) is certainly smaller than $1/4E_F$. However, the quantity

$$\frac{\partial P}{\partial E} = \frac{1}{2}\left[\frac{1}{D_\uparrow}\frac{\partial D_\uparrow}{\partial E} - \frac{1}{D_\downarrow}\frac{\partial D_\downarrow}{\partial E}\right]_{E_F} \tag{14}$$

may be considerably larger than P/E_F for transition metals if the *sp*–*d* hybridization is included. As we shall see below, a comparison with experiment shows that the neglect of the second term in Eq. (9) is indeed justified, particularly in the temperature interval 77–300 K. In this case, Eqs. (9), (12), and (13) become simplified:

$$S^{\text{tun}} = \frac{-\pi^2}{3}\frac{k_B^2}{|e|}T\left[\left(2P\frac{\partial P}{\partial E}\right)_{E_F}\right]m^2, \tag{15}$$

$$b = -a = \frac{-\pi^2}{3}\frac{k_B^2}{|e|}\left[\left(\frac{2}{P}\frac{\partial P}{\partial E}\right)_{E_F}\right]. \tag{16}$$

For the Fe–Al–O system, these relations show good agreement with the experimental data $b_{\text{exp}} = (0.08 \pm 0.01)$ μV/K^2 and $a_{\text{exp}} = -(0.09 \pm 0.01)$ μV/K^2 [10]. Indeed, $b_{\text{exp}} \approx -a_{\text{exp}}$ and both parameters are practically temperature-independent. Moreover, it is commonly accepted that tunneling is dominated by *sp*-like electrons and that their relatively large polarization ($P \approx 0.3$) is related to *sp*–*d* hybridization. For the free-electron model $D_{\uparrow(\downarrow)} = A_{\uparrow(\downarrow)}(E \mp \Delta)^{1/2}$, where Δ is the subband spin splitting, or for the case of a semielliptical curve of density of states with a nearly half-filled subband with spin $\sigma = \uparrow$, which corresponds to Fe, we have $\frac{\partial P}{\partial E} < 0$. Because $P > 0$, we have $\frac{1}{P}\frac{\partial P}{\partial E} < 0$ and $b > 0$, which is in agreement with experiment. We can reasonably assume, for a rough estimate, that $\frac{1}{D_\uparrow}\frac{\partial D_\uparrow}{\partial E} - \frac{1}{D_\downarrow}\frac{\partial D_\downarrow}{\partial E} = -\frac{1}{\omega}$, where ω is the band half-width or the Fermi energy. Then, for $\omega = 1$ eV [7], we obtain from Eq. (16) that $b_{\text{calc}} = 0.08$ μV/K^2.

While S for the Co–Al–O system is of the same order of magnitude, here, in contrast to Fe–Al–O, we have $b_{\text{exp}} < 0$ and $a_{\text{exp}} > 0$, with $|b_{\text{exp}}| \neq |a_{\text{exp}}|$, with the parameter a being temperature-dependent [10]. This can be readily understood if we assume that $P\frac{\partial P}{\partial E} > 0$ and take into account the second term in Eq. (3). That the second term in Eq. (3) must be retained follows clearly from the fact that the room-temperature thermopower in Co is –30 μV/K, which is substantially larger in magnitude than S^{tun}; because $\frac{\gamma^{\text{tun}}}{\gamma^{\text{met}}} \geq \frac{1}{5}$, one cannot neglect the metallic contribution to the thermopower in the system in question when comparing theory with experiment. We believe that in order to isolate S^{tun} from experimental data, one should make use of the correlation $S^{\text{tun}} \sim m^2$, which follows from Eq. (15). The situation with the sign of the quantity $P\frac{\partial P}{\partial E}$ is more complex. As already mentioned, this quantity must be negative for nearly free electrons $\left(P > 0, \frac{\partial P}{\partial E} < 0\right)$. If we take, for an estimate, the total density of states for Co, we will obtain $P < 0$, $\frac{\partial P}{\partial E} < 0$, and, in accordance with experiment, $P\frac{\partial P}{\partial E} > 0$. It is usually accepted, however, that d-like electrons are not involved in tunneling and, therefore, $P > 0$ for all systems, while for sp–d hybridized states, the sign of $\frac{\partial P}{\partial E}$ depends substantially on the subband filling. Moreover, the local density of states near interfaces may differ considerably from that of the grain material. Using experimental data on tunneling thermopower for the determination of $\frac{\partial P}{\partial E}$ of the electrons taking part in tunneling appears to be a promising approach.

It should be pointed out that, because tunneling thermopower is associated neither with scattering processes, including interband s–d transitions, nor with phonon or magnon drag, this thermopower is substantially simpler and, in this sense, more informative than conventional thermopower. In addition, tunneling thermopower should be taken into account when describing thermoelectric phenomena in composites in terms of the percolation theory [4]. Alongside elastic tunneling processes, phonon- or magnon-assisted tunneling may take place. Since Mott's relation is invalid for description of the corresponding contribution to thermopower, this problem requires additional analysis.

Thus, the nature of the field dependence of the thermopower in Co–Al–O and Fe–Al–O magnetic granular alloys is related to the tunneling thermopower. The tunneling thermopower is small and depends approximately linearly on temperature, and its field dependence is described by Eq. (1).

REFERENCES

1. H. Sato, Y. Kabayashi, K. Hashimoto, *et al.*, J. Magn. Soc. Jpn. **23**, 73 (1999).
2. H. Sato, Y. Kabayashi, K. Hashimoto, *et al.*, J. Phys. Soc. Jpn. **67**, 2193 (1998).
3. J. Shi, K. Pettet, E. Kita, *et al.*, Phys. Rev. B **54**, 15273 (1996).
4. O. Levy and D. Bergman, Mater. Res. Soc. Symp. Proc. **195**, 206 (1990).
5. R. O. Barnard, *Termoelectricity in Metals and Alloys* (Taylor and Francis, London, 1972), p. 259.
6. E. Z. Meĭlikhov, Zh. Éksp. Teor. Fiz. **115**, 1484 (1999) [JETP **88**, 819 (1999)].
7. J. Inoue and S. Maekawa, Phys. Rev. B **53**, R11927 (1996).
8. P. Sheng, B. Abeles, and Y. Arie, Phys. Rev. Lett. **31**, 44 (1973).
9. R. Meservey and P. M. Tedrow, Phys. Rep. **283**, 173 (1994).
10. H. Sato, Y. Aoki, S. Mitany, H. Fujimory, and K. Takanashi, private communication.

Translated by G. Skrebtsov

Physics of the Solid State, Vol. 44, No. 11, 2002, pp. 2098–2103. Translated from Fizika Tverdogo Tela, Vol. 44, No. 11, 2002, pp. 2004–2009.
Original Russian Text Copyright © 2002 by Morosov, Sigov.

Unidirectional Anisotropy in a Ferromagnet–Antiferromagnet System

A. I. Morosov and A. S. Sigov
Moscow State Institute of Radioengineering, Electronics, and Automation,
pr. Vernadskogo 78, Moscow, 119454 Russia
e-mail: mor-alexandr@yandex.ru

Received December 25, 2001

Abstract—The unidirectional anisotropy arising in a ferromagnetic film on an antiferromagnetic substrate due to the proximity effect is investigated. Consideration is given to the smooth and rough film–substrate interfaces. The conditions of the formation of a domain wall in the film and the passage of the wall into the substrate in the course of magnetization reversal are determined. The parameters of the static spin vortices formed in the vicinity of the rough interface are studied as functions of the magnetic field strength. *© 2002 MAIK “Nauka/Interperiodica”.*

1. INTRODUCTION

Unidirectional anisotropy (the exchange bias) manifests itself in a shift of the magnetization curve of a ferromagnetic film deposited on the surface of an antiferromagnet, for example, NiFe/FeMn, NiFe/CoO, Ni/NiO, Fe/FeF$_2$, or Fe/Cr. The effect of unidirectional anisotropy has been investigated in many works (see, for example, review [1]).

In this work, we examined the case when, in the antiferromagnet, the atomic plane aligned parallel to the ferromagnet–antiferromagnet interface involves uncompensated spins. The origin of unidirectional anisotropy in the case of a compensated surface of antiferromagnets was explained by Koon [2].

Earlier [3], we considered the limiting case when the exchange stiffness of the film is appreciably larger than that of the substrate. In the present work, we analyzed the situation when the exchange stiffness of the film is substantially smaller than that of the substrate. The smooth film–substrate interface is considered in Section 2. The “thickness–roughness” magnetic phase diagram in the absence of an external magnetic field is presented in Section 3. The magnetization reversal in single-domain and polydomain phases is treated in Sections 4 and 5, respectively.

2. AN ATOMICALLY SMOOTH INTERFACE

For an atomically smooth interface, the exchange interaction between spins of the upper atomic layer of the substrate and the lower atomic layer of the film has the same sign over the entire interface. It is assumed that the magnetization and antiferromagnetic vectors lie in the plane parallel to the interface and are characterized by the angle θ_i ($i = f$ and af) formed by the order parameter with the preferred axis in this plane. In the mean-field approximation, the film–substrate interaction can be described by the relationship

$$W_{f,af} = -\frac{J_{f,af}S_fS_{af}}{b^2}\int\cos(\theta_f-\theta_{af})d\sigma, \tag{1}$$

where S_f and S_{af} are the mean spins of the film and the substrate, respectively; $J_{f,af}$ is the exchange integral (the integration is performed over the interface); and b is a lattice constant that is nearly identical for both materials.

Irrespective of the sign of the integral $J_{f,af}$, interaction (1) leads to a shift of the magnetization curve of the film from the position symmetric with respect to the sign of the external field. In order to estimate this shift, it is necessary to determine the equilibrium magnetization curve from the condition for the minimum of the total energy W of the system; that is,

$$W = W_{f,af} + \int d^3\mathbf{r}(w_{ex}^f + w_{an}^f + w_Z^f) + \int d^3\mathbf{r}(w_{ex}^{af} + w_{an}^{af}). \tag{2}$$

Here, the first and second integrals are taken over the volumes of the film and the substrate, respectively;

$$w_{ex} = A_iS_i^2(\nabla\theta_i)^2 \tag{3}$$

is the excess exchange energy due to the order parameter inhomogeneity (where A_i is the exchange stiffness);

$$w_{an} = -K\cos 4\theta_i \tag{4}$$

is the anisotropy energy in the layer plane; and

$$w_Z^f = -MB_0\cos(\theta_f-\varphi) \tag{5}$$

is the Zeeman energy (where M is the film magnetization and B_0 is the induction of an external magnetic field which is aligned parallel to the film plane and forms the angle φ with the preferred axis).

In this case, we disregard the sublattice angularity (by virtue of the smallness of B_0) and the corresponding Zeeman energy of the antiferromagnet. For definiteness, we assume that $J_{f,\,af} > 0$ and $\theta_{af} = 0$ deep into the substrate. As a result, the magnetization curve at $\varphi = 0$ is shifted toward the negative-field range.

Malozemoff [4] and Mauri *et al.* [5] obtained an estimate of the corresponding shift in the form

$$B_{af}^0 \sim \frac{(A_{af}K_{af})^{1/2}S_{af}^2}{Ma}, \qquad (6)$$

where a is the film thickness. This result was obtained from simple considerations: the magnetization reversal of the film brings about the formation of a domain wall with the surface energy $(A_{af}K_{af})^{1/2}S_{af}^2$ in the substrate, and the Zeeman energy gain should compensate for the expenditure of energy to form the wall.

This estimate for B_{af}^0 is valid for the large exchange stiffness of the film when the energy $(A_fK_f)^{1/2}S_f^2$ of the domain wall in the film is higher than that of the domain wall in the substrate. Otherwise, the above estimate turns out to be erroneous.

Before preceding to the case of a lower energy of the domain wall in the ferromagnet, it should be noted that, in a magnetic field, the characteristic width $\Delta_f(B_0)$ of the 180° domain wall is governed not by the competition between the exchange interaction and anisotropy energies but by the competition between the exchange interaction energy and the sum of the anisotropy and Zeeman energies [6]; that is,

$$\Delta_f(B_0) = \pi\left(\frac{A_fS_f^2}{K_fS_f^2 + 2MB_0}\right)^{1/2}. \qquad (7)$$

It is easy to see that the Zeeman energy in the vicinity of the Curie point of the ferromagnet makes the dominant contribution ($M \propto S_f$).

Let the external magnetic field be applied antiparallel to the direction of the film magnetization in the absence of the field. Now, we determine the magnetic induction B_f at which the 180° domain wall aligned parallel to the film–substrate interface is formed in the film in the vicinity of the interface (Fig. 1a) under the assumption that $B_f \ll B_{af}^0$, i.e., that the substrate remains virtually homogeneous. For this purpose, we equate the domain wall energy and the Zeeman energy gain. Taking into account that the domain wall can arise in the film only at $\Delta_f(B_0) < a$, we obtain

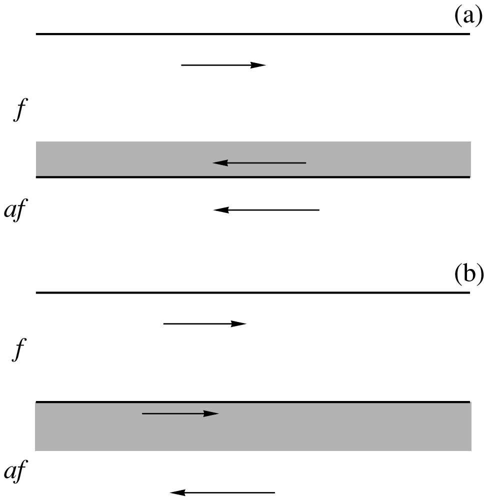

Fig. 1. Domain walls (gray regions) in (a) the film and (b) the substrate in the vicinity of the interface. Arrows indicate the directions of the magnetization and antiferromagnetic vectors.

$$B_f \approx \begin{cases} (A_fK_f)^{1/2}S_f^2/Ma, & \text{at } a \gg \Delta_f(0) \\ \dfrac{A_fS_f^2}{Ma^2}, & \text{at } a \ll \Delta_f(0), \end{cases} \qquad (8)$$

$$\approx \frac{A_fS_f^2}{Ma\min(a, \Delta_f(0))}.$$

As the magnetic field increases to $B_0 \approx B_{af}$, the domain wall becomes thinner; i.e., it is "pressed" to the interface. The value of B_{af} can be found from the condition for the equality of the domain wall energies in the ferromagnet and the antiferromagnet; that is,

$$B_{af} \approx \frac{A_{af}K_{af}S_{af}^4}{A_fS_f^2M}. \qquad (9)$$

At $B_0 \approx B_{af}$, the domain wall begins to move into the substrate. At $B_0 \gg B_{af}$, the film becomes homogeneously magnetized and a 180° domain wall arises in the antiferromagnet in the vicinity of the film boundary (Fig. 1b). Certainly, this state is metastable, because, for the domain wall, it is likely to disappear after passing across the whole width of the substrate.

For very thin films (when $B_f > B_{af}^0$), the 180° domain wall is formed immediately in the antiferromagnetic substrate. The dependences of the magnetic fields B_f and B_{af} on the film thickness are plotted in Fig. 2.

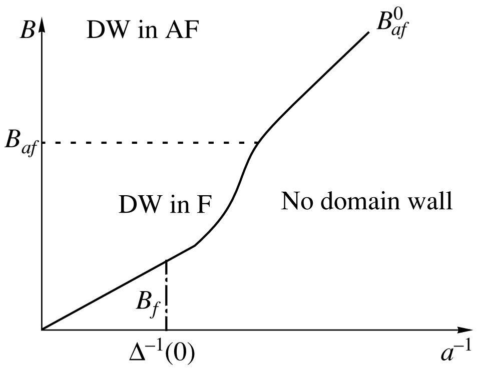

Fig. 2. "Thickness–field" phase diagram in the case of a smooth interface. The solid line shows the dependence of the bias field on the film thickness.

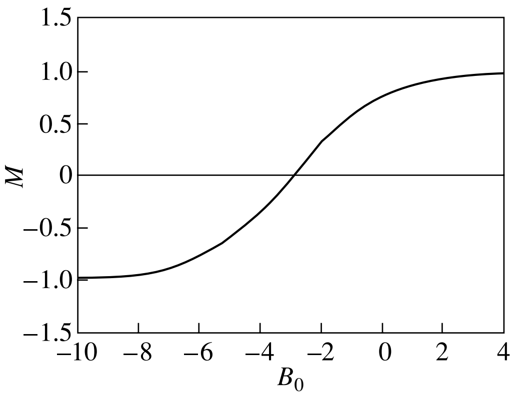

Fig. 3. Magnetization curve in the case of a smooth film–substrate interface. The magnetic field strength is given in arbitrary units, and the magnetic moment is expressed in terms of the saturation moment.

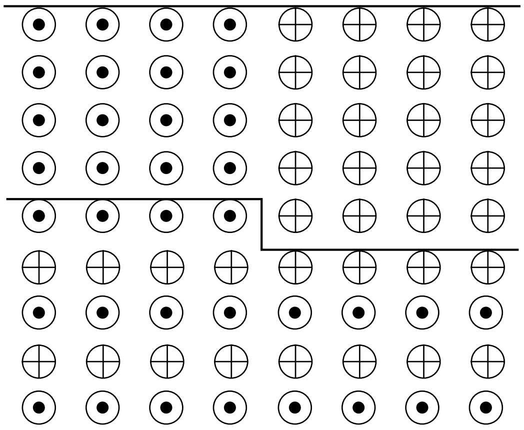

Fig. 4. A transverse domain wall due to frustration in the film.

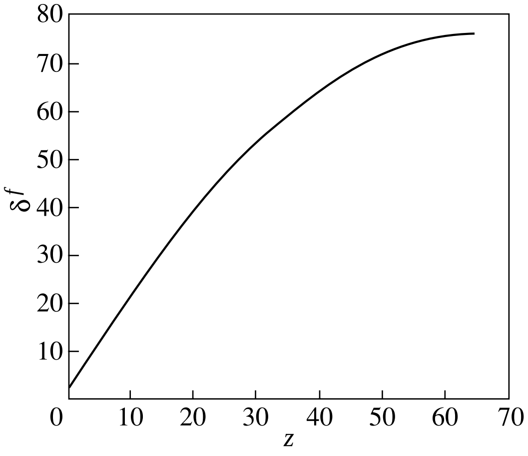

Fig. 5. Dependence of the thickness of the "unusual" domain wall on the distance to the interface. The distances are expressed in terms of a lattice constant (a = 64).

Thus, the magnetization curve is shifted by min(B_f, B^0_{af}) from the symmetric position toward the negative-field range. The corresponding magnetization curve is depicted in Fig. 3. The above analysis can easily be extended to the case of magnetic fields applied at arbitrary angles φ to the film magnetization.

3. PHASE DIAGRAM IN THE CASE OF A ROUGH INTERFACE

Apparently, the real interface is not perfectly smooth and involves atomic steps that change the substrate thickness by one atomic layer. On different sides of the step, spins of the upper atomic layer of the antiferromagnet have opposite orientations. As a result, regardless of the sign of the exchange integral $J_{f,af}$ for spins of the film and the substrate, the presence of steps at the interface leads to frustrations. In our previous work [7], the phase diagram of the magnetic film on the antiferromagnetic substrate with a large exchange stiffness was considered in the framework of the continuum model.

In the absence of a magnetic field, an individual step is responsible for the formation of a 180° domain wall of a new type—a domain wall induced by the frustration. This wall coincides with the step edge and penetrates throughout the film; i.e., the wall plane is perpendicular to the film surface (Fig. 4). On different sides of the step, spins of the ferromagnet are parallel to spins of the upper layer of the antiferromagnet. The width δ^f_0 of this domain wall in the vicinity of the film–substrate interface depends on the parameter η defined by the formula

$$\eta = J_{f,af}S_{af}a/J_fS_fb. \qquad (10)$$

If $\eta \gg 1$, the width δ_0^f is given by the expression

$$\delta_0^f \approx b(J_{f,af}S_{af} + J_fS_f)/J_{f,af}S_{af}. \qquad (11)$$

An increase in the distance from the interface results in an almost proportional increase in the domain wall width (Fig. 5). The characteristic wall width is estimated as $\delta^f \approx a$. For a typical film thickness a ~10 Å, this width is considerably less than the width of conventional domain walls [see expression (7)]. At $\eta \ll 1$, the increase in the width of the domain wall can be ignored and the wall width can be represented as

$$\delta^f \approx a/\sqrt{\eta}. \qquad (12)$$

The above relationships hold at $a < \Delta_f(0)$. At $a > \Delta_f(0)$, the domain wall width increases to $\Delta_f(0)$ and then remains unchanged.

When the distance R between the step edges is larger than $\max(\delta_0^f, a)$, the film breaks down into domains with opposite magnetization directions. Distortions of the order parameter in the substrate appear to be insignificant.

For a relatively thick film ($a \gg R \gg \delta_0^f$), the film in the bulk is in a single-domain state and static spin vortices arise in the film in the vicinity of the interface (Fig. 6). If the exchange stiffness of the film is relatively large, the vortices are formed in the substrate. Each vortex is bounded by the step edges and diverges in the direction away from the edges. At $\Delta_f(B_0) > R$, the vortex size in the direction perpendicular to the interface is equal to R in order of magnitude. At $\Delta_f(B_0) < R$, a domain wall aligned parallel to the interface is formed in the film and the transverse size of the vortex is equal to $\Delta_f(B_0)$.

As was noted above, the steps separate the interface into regions of two types with the total surface areas σ_1 and σ_2. The interfacial energy is minimum at $\theta_f = \theta_{af}$ in regions of the former type and at $\theta_f = \pi - \theta_{af}$ in regions of the latter type. Now, we assume that the magnetization of the ferromagnetic film makes an angle ψ with the antiferromagnetic order parameter deep into the substrate. In this case, the angle θ_f varies from zero to ψ in vertices in the former regions and from ψ to π in vertices in the latter regions.

As in the case of a large exchange stiffness of the film [1, 8], it can be shown, by analogy with the "magnetic proximity" model proposed by Slonczewski [9], that the energy of the system can be represented by the relationship

$$W = C_1\psi^2 + C_2(\pi - \psi)^2, \qquad (13)$$

where

$$C_j \equiv C\sigma_j \approx \frac{J_fS_f^2\sigma_j}{Rb} \qquad (14)$$

at $\Delta_f(B_0) > R$ and $C_j = (A_fK_f)^{1/2}S_f^2\sigma_j$ at $\Delta_f(B_0) < R$. If $\sigma_1 = \sigma_2$, the angle $\psi = \frac{\pi}{2}$ corresponds to the minimum energy of the system in a zero magnetic field.

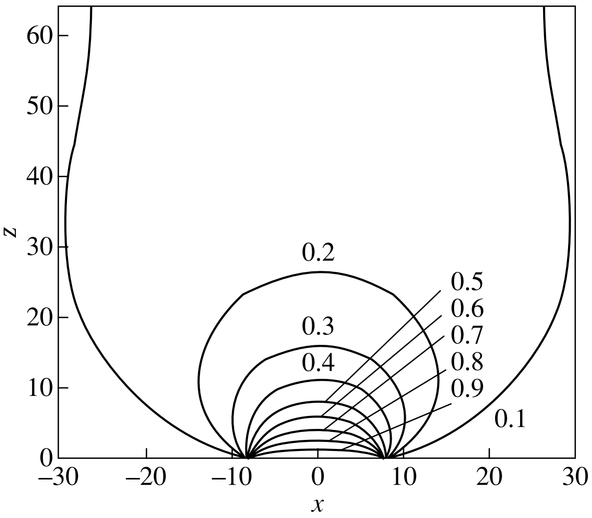

Fig. 6. Static spin vortex in the film in the vicinity of the film–substrate interface ($z = 0$) at $a \gg R$. Numbers near the isolines of θ_f are the values of θ_f in units of π. Steps are located at the points $x = \pm 8$ and $z = 0$. The distances are expressed in terms of a lattice constant.

At $R \ll \delta_0^f$, the system is characterized by weak distortions of the order parameter. Below, we will consider the behavior of each phase in an external magnetic field.

4. THE SINGLE-DOMAIN PHASE IN A MAGNETIC FIELD

The application of the magnetic field results in rotation of the film magnetization and in the formation of the domain wall first in the film and then in the substrate. The magnetization reversal and unidirectional anisotropy in the single-domain phase are similar to those observed in the case of the smooth interface. The differences are as follows.

(i) In the absence of the field, the film magnetization is perpendicular rather than parallel to the antiferromagnetic order parameter.

(ii) In the field range corresponding to $\Delta_f(B_0) < R$, the vortex shape changes: the vortex size in the direction perpendicular to the interface becomes equal to $\Delta_f(B_0)$ in order of magnitude and decreases with an increase in the field. The vortices take an elongated shape (Fig. 7a) and are then displaced into the substrate

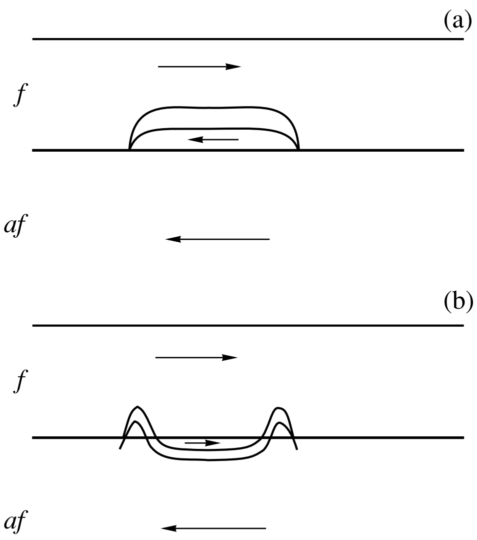

Fig. 7. Vortices in the film–substrate system in the magnetic fields (a) $B_0 < \tilde{B}_{af}$ and (b) $B_0 > \tilde{B}_{af}$. The isolines of the order parameter are shown.

by the magnetic field (Fig. 7b). This field is defined by the expression

$$\tilde{B}_{af} \approx \frac{A_{af}^2 S_{af}^4}{M A_f S_f^2 [\min(R, \Delta_{af})]^2}, \tag{15}$$

where $\Delta_{af} = \pi(A_{af}/K_{af})^{1/2}$.

However, even at $B_0 > \tilde{B}_{af}$, in the region of radius $\Delta_f(B_0)$ which is adjacent to the step edge, the distortions of the order parameter occur in the film rather than in the substrate (Fig. 7b). Qualitatively, we can make the inference that the magnetic field displaces the distortions from the region in which the Zeeman energy exceeds the difference between the energies of inhomogeneities in the antiferromagnet and the ferromagnet.

5. THE POLYDOMAIN PHASE IN A MAGNETIC FIELD

In the polydomain phase, the unidirectional anisotropy can be observed in the case when the magnetic field is applied perpendicularly to the magnetization direction in domains and the domain walls with a particular sense of rotation of magnetization are predominant [3]. These 180° domain walls disappear with an increase in the magnetic field strength for one of the two directions of the magnetic field and transform into 360° domain walls for the reverse direction of the field.

The characteristic change in the wall energy in the saturation field is of the order of the energy. Therefore, the shift of the magnetization curve can be determined as

$$B^* \approx \frac{(A_f K_f)^{1/2} S_f^2}{MR} \frac{\Delta n}{n}, \tag{16}$$

where Δn is the excess concentration of particular walls and n is the total wall concentration. When the field is applied parallel to the domain magnetization, the magnetization curve is not shifted.

Let us now analyze the magnetization reversal. If the domain size is larger than Δ_{af}, the surface can be treated as virtually smooth; i.e., we can consider the magnetization reversal of an individual domain in the same manner as for the smooth interface. In this case, the region in the vicinity of the domain walls makes an insignificant contribution. The characteristic magnetization field is of the order of $\min(B_f, B_{af}^0)$.

In the case when $R \ll \Delta_{af}$ and the magnetic field is applied normally to the domain magnetization, the magnetization reversal of domains in the field $B_0 < \tilde{B}_{af}$ occurs in much the same manner as in the case of the smooth interface. At $B_f < \tilde{B}_{af}$, the magnetization vector in the domain in the magnetic field $B_0 \sim B_f$ begins to rotate and a spin vortex arises in the film in the vicinity of the interface. The transverse size of this vortex decreases with an increase in the field. At $B_0 > \tilde{B}_{af}$, a set of static vortices (similar to that in the single-domain phase) appears in the antiferromagnetic substrate. Since the film magnetization in a strong external field is orthogonal to the order parameter deep into the antiferromagnetic substrate, no domain walls are formed. At $B_f > \tilde{B}_{af}$, the vortices appear immediately in the substrate. The characteristic magnetization field is equal to $\min(B_f, \tilde{B}_{af})$.

The magnetic field applied parallel to the magnetization in ferromagnetic domains leads to a magnetization similar to that considered above, except that the 90° domain wall is formed in the substrate in the magnetic field defined as

$$B_{dw} \approx \begin{cases} B_{af}, \text{ at } B_f < B_{af} \\ \min(B_f, B_{af}^0 \Delta_{af}/R), \quad \text{at } B_f > B_{af}. \end{cases} \tag{17}$$

The reason for the formation of this wall is the same as in the case when the film magnetization in the single-domain phase in the absence of the magnetic field is orthogonal to the order parameter deep into the substrate: the formation of the wall results in a decrease in the energy of the system of vortices.

Actually, in the absence of the domain wall, no vortices are formed in domains whose magnetization is parallel to the external field. At the same time, a 180° vortex arises in the magnetic field $B_0 \approx \min(B_f, B_{af}^0 \Delta_{af}/R)$ in domains with initial antiparallel orientations of the magnetization and the field. In the presence of the domain wall, 90° vortices appear in domains of both types. Note that, in different-type domains, the magnetization (or the antiferromagnetic order parameter) has an opposite sense of rotation. Since the vortex energy is proportional to the rotation angle squared, the energy of vortices decreases in the presence of the domain wall. The difference between the energies of the states with a domain wall and without it should exceed the energy of formation of the domain wall.

6. CONCLUSIONS

Thus, the main inferences made in the present work can be summarized as follows.

(1) The unidirectional anisotropy and the characteristic magnetization field of the ferromagnetic film on the antiferromagnetic substrate depend on the film thickness and the degree of roughness of the film–substrate interface.

(2) The presence of atomic steps (changing the antiferromagnet thickness by one monoatomic layer) in the interface leads to frustrations in the ferromagnet–antiferromagnet system. In thin films, the frustrations are responsible for the formation of domain walls of the new type that separate the film surface into domains. In thicker films, static spin vortices arise in the vicinity of the interface, whereas the magnetization in the bulk of the film remains unchanged.

(3) In single-domain films, the formation of domain walls in the course of magnetization reversal depends on the film thickness. In thin films, the domain wall is immediately formed in the antiferromagnetic substrate. In thick films, the domain wall initially arises in the film in the vicinity of the interface with the substrate. As the field increases, the wall becomes sharper and then moves into the antiferromagnetic substrate.

(4) Similar behavior is observed for the static spin vortices arising in polydomain films during their magnetization reversal.

ACKNOWLEDGMENTS

This work was supported by the Russian Foundation for Basic Research, project no. 00-02-17162.

REFERENCES

1. J. Nogues and I. K. Schuller, J. Magn. Magn. Mater. **192** (2), 203 (1999).
2. N. C. Koon, Phys. Rev. Lett. **78** (25), 4865 (1997).
3. V. D. Levchenko, A. I. Morozov, and A. S. Sigov, Fiz. Tverd. Tela (St. Petersburg) **44** (1), 128 (2002) [Phys. Solid State **44**, 133 (2002)].
4. A. P. Malozemoff, Phys. Rev. B **35** (7), 3679 (1987).
5. D. Mauri, H. C. Siegmann, P. S. Bagus, and E. Kag, J. Appl. Phys. **62** (7), 3047 (1987).
6. S. Mangin, G. Marchal, and B. Barbara, Phys. Rev. Lett. **82** (21), 4336 (1999).
7. V. D. Levchenko, A. I. Morozov, A. S. Sigov, and Yu. S. Sigov, Zh. Éksp. Teor. Fiz. **114** (11), 1817 (1998) [JETP **87**, 985 (1998)].
8. V. D. Levchenko, A. I. Morosov, and A. S. Sigov, Pis'ma Zh. Éksp. Teor. Fiz. **71** (9), 544 (2000) [JETP Lett. **71**, 373 (2000)].
9. J. C. Slonczewski, J. Magn. Magn. Mater. **150** (1), 13 (1995).

Translated by O. Borovik-Romanova

Physics of the Solid State, Vol. 44, No. 11, 2002, pp. 2104–2106. Translated from Fizika Tverdogo Tela, Vol. 44, No. 11, 2002, pp. 2010–2012.
Original Russian Text Copyright © 2002 by Platonov, Tatsenko, Plis, Popov, Zvezdin, Barbara.

MAGNETISM AND FERROELECTRICITY

Magnetic Susceptibility of the V_{15} Nanocluster in Megagauss Magnetic Fields

V. V. Platonov*, O. M. Tatsenko*, V. I. Plis, A. I. Popov**,**
A. K. Zvezdin*, and B. Barbara******

** Russian Federal Nuclear Center, Institute of Experimental Physics, Sarov, Nizhni Novgorod oblast, 607188 Russia*
*** Moscow State Institute of Electronic Engineering Technical University, Zelenograd, Moscow oblast, 103498 Russia*
e-mail: aip_2001@mail.ru
**** Institute of General Physics, Russian Academy of Sciences, ul. Vavilova 38, Moscow, 117942 Russia*
***** Laboratoire de Magn. Lois Néel, CNRS, Grenoble, 38042 France*

Received January 8, 2002

Abstract—The low-temperature behavior of the magnetic susceptibility of the V_{15} low-spin cluster in ultrastrong magnetic fields of up to 550 T was studied. Ultrastrong magnetic fields were generated by an MK-1 magnetic explosion generator. Anomalies in the susceptibility were found to exist in fields $B_1 = 200$ T and $B_2 = 350$ T. It is concluded that these anomalies indicate the initial phase of a field-induced transformation of the cluster magnetic structure from quasi-ferrimagnetic to ferromagnetic. This transformation occurs by discrete quantum jumps at low temperatures. The experimental data are compared with theory. © *2002 MAIK "Nauka/Interperiodica".*

1. INTRODUCTION

Considerable interest is presently focused on magnetic nanoclusters containing *d* or *f* ions (Mn_{12}Ac, Fe_6, Fe_8, Fe_{10}, Fe_{17}, V_{12}, etc.) [1–11], most of which are giant-spin organometallic molecules. These clusters are mesoscopic objects whose behavior reveals, in addition to specific quantum features typical of individual atoms, classical characteristics inherent in bulk single crystals. The clusters form molecular crystals in which they retain their individuality, because the coupling between the clusters is fairly weak. The unique properties of such systems are molecular bistability [12] and macroscopic quantum tunneling of magnetization [5, 8, 12, 13]. These phenomena are of undeniable interest for understanding the fundamental problems of magnetism. Until recently, only integer-spin clusters, such as Mn_{12}Ac ($S = 10$ in the ground state), Fe_8 ($S = 10$ in the ground state), and Mn_6R_6 ($S = 12$ in the ground state), were studied. A deeper insight into the physics of magnetic nanoclusters can be gained, however, by studying clusters with a half-integer spin, to which the V_{15} magnetic cluster belongs.

Moreover, one should know the exchange interactions between the magnetic ions contained in a cluster. The most direct method of studying these interactions is based on measurements of the total magnetization curve in megagauss magnetic fields. This is the object of the present study, which deals with the behavior of the magnetic susceptibility of the V_{15} cluster in ultrastrong magnetic fields.

2. EXPERIMENT

We measured the magnetic susceptibility of a polycrystal formed of polyoxyvanadate V_{15} molecules ($K_6[V^{IV}_{15}As_6O_{42}(H_2O)] \cdot 8H_2O$). These crystals possess trigonal symmetry (space group *R*3 with $a = 14.029$ Å, $\alpha = 79.26°$, $V = 2632$ Å^3 [11, 14]). The unit cell contains two V_{15} clusters. The V_{15} cluster consists of 15 V^{IV} ions, each having a spin $S = 1/2$. The V^{IV} ions occupy the vertices of two plane hexagons and of a triangle located between them. The cluster structure is shown schematically in Fig. 1. Each hexagon of the cluster

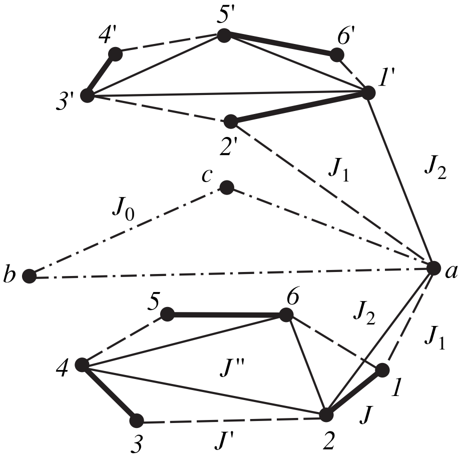

Fig. 1. Schematic structure of the V_{15} cluster and exchange interactions between vanadium ions.

contains three pairs of strongly coupled spins ($J \approx -800$ K); the spin of each ion belonging to the triangle is coupled to two pairs of spins, with one pair belonging to the upper hexagon and the other to the lower hexagon ($J' \approx J_1 \approx -150$ K, $J'' \approx J_2 \approx -300$ K). The exchange interaction between the spins located at the vertices of the triangle is very weak ($J_0 \approx -2.5$ K [15]). The magnetic (dipole) interaction between the spins of the neighboring clusters is negligible (a few millikelvins). The ground-state cluster spin is $S = 1/2$. This value of the spin results from antiferromagnetic interactions between the V^{IV} ions [14]; therefore, such a cluster can be treated on the molecular level as a multisublattice ferrimagnet. An external magnetic field induces transformation of the magnetic structure from quasi-ferrimagnetic with spin $S = 3/2$ to ferromagnetic with $S = 15/2$. According to [16], this transformation should take place in ultrastrong magnetic fields and proceed via three quantum jumps at low temperatures.

The magnetic susceptibility measurements were conducted at liquid- helium temperature in fields of up to 550 T. Magnetic fields were produced by an MK-1 magnetic explosion generator [17]. The generator was employed in its single-stage version (without intermediate internal stages) to produce a smooth magnetic-field pulse and to increase the usable volume. Several samples (from four to eight) could be studied in one experiment. The original magnetic field ($B \approx 16$ T) was generated in a thin-walled multilayered multiple-coil solenoid by a capacitor battery discharge ($W = 2$ MJ). The magnetic flux trapped inside the conducting cylinder was compressed by the products of explosion to a diameter of 20 mm. The magnetic-field compression time was about 16 μs. At the maximum magnetic field, the usable volume was a cylinder of approximately 20 mm in diameter and about 100 mm in length. The samples and magnetic-field sensors were disposed on a plate of fiberglass laminate and immersed in liquid helium in a continuous-flow cryostat. The magnetic field was measured with a set of single-turn induction sensors varying from 0.6 to 14.0 mm in diameter wound with PÉTV-2 wire. The signals were fed to Tektronix 784 and Tektronix 744 four-channel oscillographs having a resolution of 2 ns/T.

The magnetic susceptibility was measured with a compensation pickup, which represented two oppositely connected, well-compensated induction coils. The PÉTV-2 wire, 71 μm in diameter, was laid in spiral grooves 2 mm in diameter cut in two caprolon blocks, with 9 turns in each. The degree of coil compensation was checked in a high-frequency magnet. The total coil areas NS (where S is the area of one turn) differed by no more than 2%. A hole 1.6 mm in diameter and intended for placing the sample to be studied was drilled in one of the blocks. When one of the coils contains a sample, the signal is proportional to the derivative of the sample magnetic moment, $U(B) \propto dM/dt + KdB/dt$. The coefficient K depends on the accuracy with which the coils are compensated. An ideal coil compensation is impossible to achieve, particularly if the rate of magnetic field variation is as high as $dB/dt \approx 10^6$ T/s. However, if the rate of magnetic field variation dB/dt is a smooth function of time, the jumps observed on the $U(B)$ curve can originate only from a change in the sample magnetic moment.

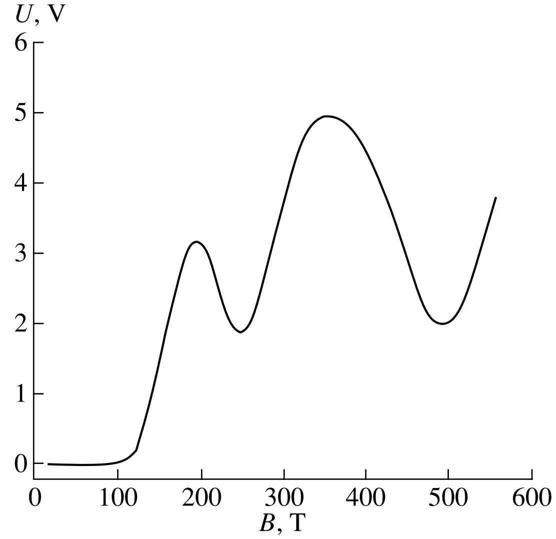

Fig. 2. Inductive sensor plotted signal of differential magnetic susceptibility dM/dt vs. magnetic field.

Figure 2 presents an oscillogram of the signal obtained from the inductive sensor of the differential magnetic susceptibility dM/dt. At fields of ~200 and 350 T, one can see signal jumps, which may be due to changes in the sample magnetic moment produced by the V_{15} cluster undergoing discrete quantum transitions in the spin structure.

3. DISCUSSION OF RESULTS

The theoretical study of the spin structure rearrangement in a V_{15} cluster conducted in [16] yielded analytical relations describing the behavior of the cluster magnetization upon variation of the magnetic-field induction B and of temperature T. The expression given in [16] for the magnetic moment of a cluster can be cast in the form

$$M(B) = 4\mu_B \frac{\sum_{S=0}^{3} S(3S - S^2 + 2)\exp\left(-\frac{E(S, B)}{kT}\right)}{\sum_{S=0}^{3} (3S - S^2 + 2)\exp\left(-\frac{E(S, B)}{kT}\right)} + 3\mu_B, \quad (1)$$

where

$$E(S, B) = -S\left[\tilde{J} - \frac{2-S}{4}(J' + 2J'') + 2\mu_B B\right],$$
$$\tilde{J} = J - \frac{1}{4}(J_1 + J_2), \qquad (2)$$

with J, J_1, J', J_2, and J'' being exchange integrals between the $\mathrm{V^{IV}}$ ions (Fig. 1).

Equation (1) allows one to derive the following relation for the magnetic susceptibility:

$$\chi(B, T) = (\partial M(B, T)/\partial B)_T$$
$$= \frac{8\mu_B^2}{kT}\left\{\frac{\sum\limits_{S=0}^{3} S^2(3S - S^2 + 2)\exp\left(-\frac{E(S, B)}{kT}\right)}{\sum\limits_{S=0}^{3}(3S - S^2 + 2)\exp\left(-\frac{E(S, B)}{kT}\right)} - \left(\frac{M(B, T)}{2\mu_B} - \frac{3}{4}\right)^2\right\}. \qquad (3)$$

It follows from Eq. (2) that in the fields

$$B_1 = \frac{1}{2\mu_B}\left(-\tilde{J} + \frac{J' + 2J''}{4}\right),$$
$$B_2 = -\frac{1}{2\mu_B}\left(\tilde{J} + \frac{J' + 2J''}{4}\right), \qquad (4)$$
$$B_3 = -\frac{1}{2\mu_B}\left(\tilde{J} + \frac{3}{4}(J' + 2J'')\right),$$

the crossing of the lower energy levels of the cluster occurs. This should initiate sharp anomalies at B_1, B_2, and B_3 (at low temperatures) in the magnetization (1) and in the magnetic susceptibility $\chi(B, T)$ (3). Accepting, as a rough estimate, the values $J = -800$ K, $J' \approx J_1 \approx -150$ K, and $J'' \approx J_2 \approx -300$ K for the exchange integrals [14], we obtain from Eq. (4) for B_1, B_2, and B_3 the values 371, 650, and 929 T, respectively. The anomalies revealed experimentally in the differential magnetic susceptibility occur in fields $B_1 = 200$ T and $B_2 = 350$ T (Fig. 2), which is in obvious disagreement with the theoretical figures. The observed anomalies in magnetic susceptibility correspond to the following values of the exchange integrals: $J = -490$ K, $J' = J_1 = -80$ K, and $J'' = J_2 = -161$ K. It should be pointed out that the procedure used in comparing the theoretical data with experimental results does not allow an unambiguous choice of the exchange parameters. To determine the values of J, J', J_1, J'', and J_2, we used the relations $J' \approx J_1$ and $J'' \approx J_2$ [14].

4. CONCLUSION

Thus, we have studied, both experimentally (in fields of up to 550 T) and theoretically, the spin structure rearrangement induced by megagauss-scale magnetic fields in the $\mathrm{V_{15}}$ magnetic nanocluster. It was shown that the transition from the quasi-ferrimagnetic to the quasi-ferromagnetic structure of the $\mathrm{V^{IV}}$ spins occurs at low temperatures through three quantum jumps. The experimental data were compared with theory. It was established that the values of the exchange integrals given in [14] do not allow quantitative description of the experimentally observed initial stage of the spin structure rearrangement of the $\mathrm{V_{15}}$ cluster. A set of exchange parameters was proposed that permits one to reconcile quantitatively the theoretical results with experiment. Observation of a complete picture of quantum jumps in the $\mathrm{V_{15}}$ spin structure would require fields of up to 10^3 T.

REFERENCES

1. D. Gattecshi, A. Canecshi, L. Pardi, and R. Sessoli, Science **265**, 1054 (1994).
2. R. Sessoli, D. Gattecshi, A. Canecshi, and H. A. Novak, Nature **356**, 141 (1993).
3. J. R. Friedman, M. P. Sarachik, J. Tejada, and R. Ziolo, Phys. Rev. Lett. **76**, 3830 (1996).
4. L. Thomas, F. Lionti, R. Ballou, *et al.*, Nature **383**, 145 (1996).
5. V. V. Dobrovitski and A. K. Zvezdin, Europhys. Lett. **38**, 377 (1997).
6. D. Gattecshi, L. Pardi, A. L. Barra, *et al.*, Nature **354**, 465 (1991).
7. A. Canecshi, D. Gattecshi, and R. Sessoli, J. Am. Chem. Soc. **113**, 5872 (1991).
8. L. Gunther, Europhys. Lett. **39**, 1 (1997).
9. A. K. Zvezdin and A. I. Popov, Zh. Éksp. Teor. Fiz. **109**, 2115 (1996) [JETP **82**, 1140 (1996)].
10. A. L. Barra, P. Debrunner, D. Gattecshi, *et al.*, Europhys. Lett. **35**, 133 (1996).
11. A. Muller and J. Doring, Angew. Chem. Int. Ed. Engl. **27**, 1721 (1991).
12. O. Kahn and C. Jay Martinez, Science **279**, 44 (1998).
13. A. K. Zvezdin, V. V. Dobrovitski, B. N. Harmon, and M. I. Katsnelson, Phys. Rev. B **58**, 14733 (1998).
14. D. Gattecshi, L. Pardi, A. L. Barra, and A. Muller, Mol. Eng. **3**, 157 (1993).
15. I. Chiorescu, W. Wernsdorfer, A. Muller, *et al.*, Phys. Rev. Lett. **84**, 3454 (2000).
16. A. K. Zvezdin, V. I. Plis, A. I. Popov, and B. Barbara, Fiz. Tverd. Tela (St. Petersburg) **43** (1), 177 (2001) [Phys. Solid State **43**, 185 (2001)].
17. A. I. Pavlovskiĭ and R. Z. Lyudaev, in *Problems of Modern Experimental Science and Technology*, Ed. by A. P. Aleksandrov (Nauka, Leningrad, 1984), p. 206.

Translated by G. Skrebtsov

Physics of the Solid State, Vol. 44, No. 11, 2002, pp. 2107–2111. Translated from Fizika Tverdogo Tela, Vol. 44, No. 11, 2002, pp. 2013–2017.
Original Russian Text Copyright © 2002 by Levitin, Zvezdin, Ortenberg, Platonov, Plis, Popov, Puhlmann, Tatsenko.

MAGNETISM AND FERROELECTRICITY

Faraday Effect in $Tb_3Ga_5O_{12}$ in a Rapidly Increasing Ultrastrong Magnetic Field

R. Z. Levitin*, A. K. Zvezdin, M. von Ortenberg***, V. V. Platonov****, V. I. Plis*****, A. I. Popov*****, N. Puhlmann***, and O. M. Tatsenko******
** Moscow State University, Vorob’evy gory, Moscow, 119899 Russia*
*** Institute of General Physics, Russian Academy of Sciences, ul. Vavilova 38, Moscow, 117942 Russia*
**** Institute of Physics, Humboldt University, Berlin, D-10115 Germany*
***** Russian Federal Nuclear Center, Arzamas-16, Sarov, Nizhni Novgorod oblast, 607189 Russia*
****** Moscow State Institute of Electronic Engineering (Technical University),*
Zelenograd, Moscow oblast, 103498 Russia

Received January 8, 2002

Abstract—The Faraday effect is measured in paramagnetic terbium gallate garnet $Tb_3Ga_5O_{12}$ at a wavelength $\lambda = 0.63$ μm at 6 K in pulsed magnetic fields up to 75 T increasing at a rate of 10^7 T/s for field orientation along the crystallographic direction ⟨110⟩. The experimental data are compared with the results of theoretical calculations taking into account the crystal fields acting on the Tb^{3+} ion and various contributions to the Faraday rotation. Since the measurements in pulsed fields are carried out in the adiabatic regime, the dependence of the sample temperature on the magnetic field acting during a current pulse is obtained from the comparison of the experimental dependence of Faraday rotation with the theoretically calculated dependences of the Faraday effect under isothermal conditions at various temperatures. *© 2002 MAIK “Nauka/Interperiodica”.*

1. INTRODUCTION

At present, the magnitude of experimentally attainable static magnetic fields reaches 50 T, while fields with a higher induction (which are usually referred to as ultrastrong) are generated only in the pulse regime [1].

Experiments in ultrastrong magnetic fields attract considerable attention, since the substances investigated in them are in extreme conditions (huge Zeeman splittings for the spin and orbital degrees of freedom, quantum limit in semiconductors and semimetals, “rupture” of exchange coupling in magnetically ordered materials and nanoclusters). In such experiments, magnetic transformations that cannot occur in other conditions take place.

Although the methods of generation of pulsed magnetic fields in the range 50–100 T have been developed to perfection, the measuring technique for such fields is far from perfect. In particular, the entropy redistribution among the magnetic subsystem, crystal lattice, and thermostat and, hence, the temperature conditions for pulsed magnetization remain unclear, since the rate of variation of the field in experiments with ultrastrong fields is very high (10^7–10^8 T/s). This work is devoted to this methodologically important and physically interesting problem. It is expedient to choose for such experiments a material whose properties and energy spectrum of the magnetic subsystem are well known. We chose terbium gallate $Tb_3Ga_5O_{12}$ with the garnet structure for our investigation. The “tracing” of the magnetic subsystem (and of the sample temperature) is carried out using the Faraday effect, whose features in rare-earth compounds with the garnet structure have been studied extensively [2–4]. An important argument in favor of the Faraday effect is that the measuring unit is outside the magnetic field in this method, which makes it possible to minimize electric stray currents induced in ultrastrong pulsed magnetic fields.

Crystals with garnet structure possess cubic symmetry. Their crystallographic structure is rather complex and is described by the space group O_h^{10} [5–7]. The unit cell of the garnet contains 160 atoms. Rare-earth ions in the garnet structure are located in six inequivalent dodecahedral positions with orthorhombic symmetry of their surroundings (point group D_2) with different orientations of local axes. The orientation of local axes for all six inequivalent sites can be obtained by rotating the crystallographic system of coordinates through an angle $\pm\pi/4$ relative to the axes [100], [010], and [001] (Table 1).

The low symmetry of the crystal surroundings of the rare-earth ion R^{3+} in the garnet structure leads to the maximum possible removal of degeneracy of its ground multiplet. For the non-Kramers ion Tb^{3+}, the low-energy part of the spectrum consists of quasi-doublets: the ground state is a quasi-doublet with a gap of 2.5 cm^{-1}, the first excited quasi-doublet lies 34 cm^{-1} above the ground one, the third is separated from the latter by 43 cm^{-1}, and so on [8]. The exchange interaction energy in rare-earth gallate garnets is lower than the energy of

Table 1. Orientation of local symmetry axes for six inequivalent dodecahedral positions of rare-earth ions in rare-earth garnets

Unit vector	1	2	3	4	5	6
$\mathbf{e}_x$	[001]	[001]	[100]	[100]	[010]	[010]
$\mathbf{e}_y$	$[1\bar{1}0]$	[110]	$[01\bar{1}]$	[011]	$[\bar{1}01]$	[101]
$\mathbf{e}_z$	[110]	$[\bar{1}10]$	[011]	$[0\bar{1}1]$	[101]	$[10\bar{1}]$

Table 2. Crystal-field parameters for terbium gallate garnet [10] (in cm^{-1})

B_{20}	B_{22}	B_{40}	B_{42}	B_{44}	B_{60}	B_{62}	B_{64}	B_{66}
–81	169	–2163	249	945	677	–155	1045	–4

the crystal field (the Néel temperature of terbium gallate is $T_N = 0.25$ K [9], which corresponds to approximately 0.17 cm^{-1}); consequently, we can disregard the exchange interaction in an analysis of experimental results at liquid-helium temperatures.

The parameters of the crystal field acting on a Tb^{3+} ion in gallate garnet have been determined by various methods [10, 11]. In our opinion, the set of parameters given in [10] (Table 2) is most adequate. This set of parameters makes it possible to describe quantitatively the crossing of energy levels in the spectrum of the Tb^{3+} ion, which is observed experimentally in $Tb_3Ga_5O_{12}$, in a field parallel to direction $\langle 110 \rangle$, as well as magnetization curves along this direction in fields up to 15 T [10]. One of our tasks was to verify the applicability of the above crystal-field parameters for describing the properties of the terbium gallate garnet in stronger fields (up to 75 T).

It should be noted that magnetization was measured in [10] in static fields and, hence, under isothermal conditions. In the pulsed magnetic fields used in our experiments, the measurements were made in the adiabatic regime. It was demonstrated for the first time in [12] that, by comparing the experimental results obtained under adiabatic conditions with the (experimental and theoretical) results obtained in the isothermal regime, it is possible to determine the magnetocaloric effect. This was a second problem solved in this study. It should be noted that, apart from its scientific value, an analysis of the magnetocaloric effect is important for applications, since rare-earth paramagnetic garnets are regarded as promising materials for low-temperature magnetic refrigerators [13].

2. THEORY

2.1. Faraday Effect

The angle of rotation in the light-polarization plane in $Tb_3Ga_5O_{12}$ contains two contributions,

$$\alpha_F = \alpha(\mathrm{Tb}) + \alpha_D, \tag{1}$$

where α(Tb) is the contribution from paramagnetic Tb^{3+} ions and α_D is the contribution from the matrix formed by diamagnetic gallium and oxygen ions. The term α_D is independent of temperature and proportional to the magnetic field B,

$$\alpha_D = VB. \tag{2}$$

As the Verdet constant V of the matrix, in the first approximation, we can take the Verdet constant of yttrium gallate garnet $V(YGG) = 0.043$ min/(cm Oe) [14].

In the visible and ultraviolet regions, the contribution of rare-earth ions to Faraday rotation is mainly determined by the allowed electric-dipole *f–d* transitions, except in narrow spectral regions in the vicinity of the resonance frequencies of forbidden *f–f* transitions. In general, the quantity α(Tb) contains three terms: the paramagnetic contribution, the contribution of mixing, and the diamagnetic contribution [2–4, 15]. The diamagnetic contribution is linear in the magnetic field B, is significant only in a narrow spectral region in the vicinity of resonance frequencies of optical transitions, and is reduced to a renormalization of constant V in Eq. (2). According to [3], the paramagnetic contribution and the contribution of mixing have the form

$$\alpha(\mathrm{Tb}) = A\left(M_0 - \frac{g_{J_0}}{2 - g_{J_0}} M_{VV}\right), \tag{3}$$

where M_0 is the magnetization associated with the splitting of the energy levels of the ground multiplet $^7F_6$, M_{VV} is the Van Vleck correction to magnetization [3, 4] associated with admixing of the first excited multiplet $^7F_5$ of the Tb^{3+} ion to the ground multiplet, $g_{J_0} = 3/2$ is the Landé factor of the ground multiplet of this ion, and A is a constant depending on the frequency of incident radiation and the oscillator strength for allowed *f–d* transitions. In order to calculate $M_0(B)$ and $M_{VV}(B)$ and thus calculate $\alpha_F(B)$, we must determine the electron structure of Tb^{3+} ions formed under the action of the ionic surroundings (described by the crystal-field

Hamiltonian) and the magnetic field. The actual Hamiltonian of the problem is [6]

$$\hat{H} = \hat{H}_{\mathrm{cr}} + \hat{H}_Z, \tag{4}$$

where

$$\hat{H}_{\mathrm{cr}} = \sum_{kqi} B_{kq}(C_q^k(i) + C_{-q}^k(i)); \tag{5}$$

C_q^k are irreducible tensor operators [16]; $k = 2, 4, 6$; $q \le k$; and summation over i is carried out over all $4f$ electrons of the Tb^{3+} ion. In Eq. (4), H_Z is the interaction Hamiltonian of the ion with the magnetic field:

$$\hat{H}_Z = \mu_{\mathrm{B}}(\mathbf{L} + 2\mathbf{S})\mathbf{B}. \tag{6}$$

It was mentioned above that in our calculations we used the set of crystal field parameters from [10] (Table 2).

Using this algorithm, we calculated the energy levels E_n and determined the eigenfunctions of Tb^{3+} ions in a wide range of magnetic fields parallel to the $\langle 110\rangle$ axis, taking into account inequivalent positions occupied by Tb^{3+} ions in the garnet structure (Table 1). It was found that, as indicated in [10], the lower energy levels of the Tb^{3+} ion located in position 1 cross in a field $B \approx 9.5$ T. Then, we calculated the magnetizations $M_0(B)$ and $M_{VV}(B)$ in $\mathrm{Tb_3Ga_5O_{12}}$ as a function of the magnetic field at various temperatures ($6 \le T \le 41$ K). It should be noted that, according to calculations, the value of $M_{VV}(B)$ turned out to be quite small (it amounts to 1% of $M_0(B)$ in fields on the order of 100 T) and can be disregarded in the first approximation. The contribution of terbium to the Faraday effect is calculated using Eq. (3) (in relative units) for various temperatures under isothermal conditions.

2.2. Magnetocaloric Effect

Since we measured Faraday rotation under adiabatic conditions, it is necessary to take into account in calculations the magnetocaloric effect, i.e., the change in the sample temperature as a result of magnetization. The change in temperature upon adiabatic magnetization can be calculated by solving the equation of the adiabat (see, e.g., [17])[1]:

$$S_M(T_0, 0) + S_P(T_0) = S_M(T, B) + S_P(T), \tag{7}$$

where $S_P = \int_{T_0}^{T} \frac{C_V dT}{T}$ is the phonon contribution to the entropy; C_V is the molar heat capacity, which can be approximated at low temperatures by the expression

$$C_V = \frac{12}{5} R\pi^4 n(T/\Theta_D)^3, \tag{8}$$

where $n = 20$ is the number of atoms in a $\mathrm{Tb_3Ga_5O_{12}}$ molecule; R is the universal gas constant; and Θ_D is the Debye temperature, whose exact value for $\mathrm{Tb_3Ga_5O_{12}}$ is not known to us at the moment; however, a comparison of the available data on the Debye temperature for aluminate garnets [18] makes it possible to estimate it as $\Theta_D \approx 500$ K. It should be noted that the approximation of the heat capacity by Eq. (8) is rather rough, especially for crystals with a complex crystallographic structure as in rare-earth garnets. This follows, for example, from the results obtained in [19], where it is shown that the Debye temperature of gadolinium gallate garnet depends strongly on the temperature at which it is measured.

Entropy S_M (per $\mathrm{Tb_3Ga_5O_{12}}$ molecule) in Eq. (7) is given by

$$S_M = -\frac{1}{2}\sum_{m=1}^{6}\sum_{n} Z_m^{-1}\exp\left(-\frac{E_n(m)}{T}\right) \times \ln\left[Z_m^{-1}\exp\left(-\frac{E_n(m)}{T}\right)\right], \tag{9}$$

where $Z_m = \sum_n \exp\left(-\frac{E_n(m)}{T}\right)$ is the magnetic contribution to entropy, which is averaged over inequivalent positions (index m). The solution of Eq. (7) gives the magnetocaloric effect, viz., the field dependence of $T(B)$.

The theoretical formulas derived in this section were used for an analysis of experimental data (see below).

3. EXPERIMENTAL TECHNIQUE AND SAMPLES

We measured the Faraday effect in $\mathrm{Tb_3Ga_5O_{12}}$ for the initial sample temperature 6 K. Measurements were made at a wavelength of 0.63 μm lying in the transparency window, far away from the absorption lines of rare-earth ions, and were carried out according to the conventional intensity scheme using a gas laser. A pulsed magnetic field up to 75 T was generated by discharging a capacitor bank through a one-turn solenoid. Cooling to low temperatures was carried out in a gas-flow helium cryostat, so that the sample was in helium vapor during measurements. The pulse duration was 6 μs. Earlier [12], it was proved theoretically and experimentally that, for such a cooling regime, magnetization is an adiabatic process if the rate of increase in the field exceeds about 100 T/s. Since the rate of variation of the magnetic field in our case was much higher (more than 10^7 T/s), we can state that measurements were made under adiabatic conditions.

---

[1] Here, we assume that entropy is transferred from the magnetic subsystem to the lattice quite rapidly, so that the magnetic subsystem and the lattice can be described by the same temperature.

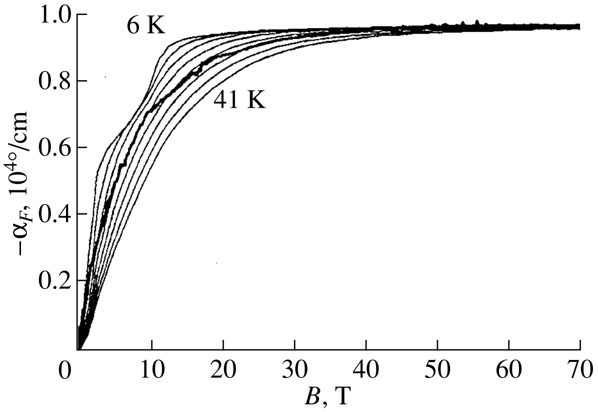

Fig. 1. Dependence of the Faraday effect in $Tb_3Ga_5O_{12}$ on the magnetic field. Thick curve describes the experimental $\alpha_F(B)$ dependence under adiabatic conditions at the initial temperature of 6 K of the sample; thin curves are the experimental $\alpha_F(B)$ dependences under isothermal conditions, obtained at temperatures varying from 6 to 41 K with a step of 5 K.

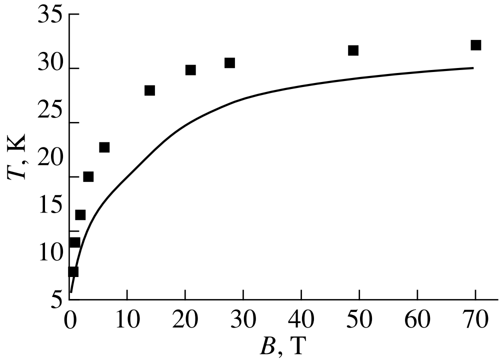

Fig. 2. Magnetocaloric effect *T*(*B*) in $Tb_3Ga_5O_{12}$. Dark squares correspond to experimental results, and the solid curve is calculated theoretically.

A terbium gallate garnet $Tb_3Ga_5O_{12}$ single crystal was grown from solution in melt. A plate having a thickness of 0.64 mm and oriented perpendicular to the crystallographic direction ⟨110⟩ was cut from this crystal.

4. EXPERIMENTAL RESULTS AND DISCUSSION

Figure 1 shows the experimental field dependence of the Faraday effect in $Tb_3Ga_5O_{12}$ in a pulsed field for the initial sample temperature 6 K. It can be seen that Faraday rotation attains saturation in comparatively weak fields $B \approx 40$ T. It should be noted that no features associated with crossing of energy levels of the Tb^{3+} ion in a magnetic field are observed on the experimental curves. Figure 1 also shows the theoretical dependences of the Faraday effect in the terbium gallate garnet under isothermal conditions at low temperatures. For plotting these curves in absolute units, we made use of the fact that, according to calculations, the magnetization M_0 of the terbium sublattice in strong fields ($B \geq 50$ T) and at low temperatures ($T \leq 50$ K) is virtually independent of temperature; i.e., the adiabatic and isothermal magnetizations coincide under these conditions. This allowed us to determine constant *A* in Eq. (3) for the Faraday effect from a comparison of theoretical results obtained for isothermal conditions with the experimental data for adiabatic magnetization in the region of strong fields ($B = 70$ T); the result is $A = 1500$ deg/(μ_B cm).

It can be seen from Fig. 1 that the experimental adiabat of the Faraday effect intersects the theoretically calculated isothermal $\alpha_F(B)$ dependences. At the intersection points, the sample temperature in the adiabatic regime is equal to the temperature of the corresponding isothermal dependence. Thus, a comparison of the experimental adiabatic curve of Faraday rotation of the polarization plane of incident light with the $\alpha_F(B)$ isotherms makes it possible to determine directly the magnetocaloric effect, i.e., the dependence of the sample temperature on the magnetic field under adiabatic conditions.

Figure 2 shows the *T*(*B*) dependence for terbium gallate garnet determined in this way. It can be seen that the increase in temperature as a result of adiabatic magnetization in a field of 75 T attains a value of 35 K. Figure 2 also shows a theoretical dependence calculated on the basis of Eqs. (7)–(9) using the value $\Theta_D = 500$ K for the Debye temperature. It can be seen that the experimental and theoretical *T*(*B*) dependences are of the same type and the calculated and experimental values of magnetocaloric effect are close, although the experimental effect is slightly stronger (by 3–4 K). The reason for this discrepancy has not been found as yet. According to estimates, the temperature variation as a result of adiabatic magnetization depends on the Debye temperature only slightly; its variation within 20–30% does not remove the discrepancy between theory and experiment. This discrepancy is probably due to the non-Debye character of the phonon spectrum in garnets (see above).

In Fig. 3, the theoretical adiabat of the Faraday effect calculated by using the magnetocaloric effect determined from the solution to Eq. (7) is compared with the experimental $\alpha_F(B)$ dependence measured at the initial temperature of 6 K. It can be seen that the agreement between the experimental and theoretical curves is quite small, which confirms the correctness of the model and the adequacy of the values of the parameters of the crystal field indicated above. We note that other sets of crystal-field parameters available in the literature [11] provide a poorer description of the experimental results.

It should be noted that, in all probability, the small variations of the crystal-field parameters used by us

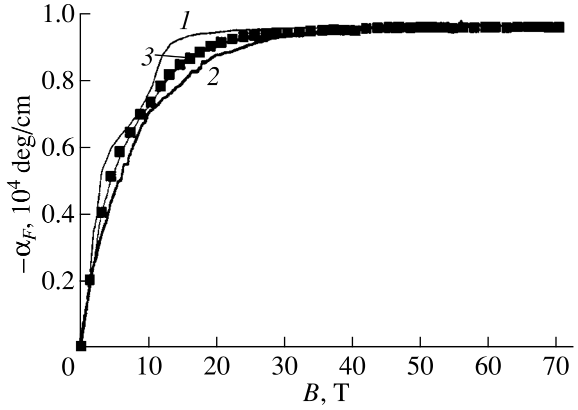

Fig. 3. (*1*) Calculated $\alpha_F(B)$ isotherm at 6 K and (*2*, *3*) $\alpha_F(B)$ adiabat for the initial sample temperature of 6 K (curve *2* corresponds to experiment, and curve *3* is calculated theoretically).

here will provide an even better agreement between the experimental and theoretical results.

Figure 3 also shows the theoretically calculated isotherm of the Faraday effect at 6 K. It clearly displays a feature near 9.5 T associated with a crossing of energy levels. The absence of this feature in adiabatic measurements can be explained by the elevation of temperature due to the magnetocaloric effect, leading to a blurring of this feature.

5. CONCLUSION

Thus, using the parameters of the crystal field acting on Tb^{3+} ions in $Tb_3Ga_5O_{12}$ taken from [10] (Table 2), we have described both the behavior of magnetization of terbium gallate garnet in weak magnetic fields under isothermal conditions and the field dependence of the Faraday effect in strong magnetic fields under adiabatic conditions, as well as the dependence of the sample temperature on the magnetic field during the action of a pulse.

ACKNOWLEDGMENTS

This study was supported by the Russian Foundation for Basic Research, project no. 00-02-17240.

REFERENCES

1. F. Herlach, *Strong and Ultrastrong Magnetic Fields and Their Applications* (Springer, Berlin, 1985).
2. U. V. Valiev, A. K. Zvezdin, G. S. Krinchik, *et al.*, Zh. Éksp. Teor. Fiz. **79**, 235 (1980) [Sov. Phys. JETP **52**, 119 (1980)].
3. U. V. Valiev, A. K. Zvezdin, G. S. Krinchik, *et al.*, Zh. Éksp. Teor. Fiz. **85**, 311 (1983) [Sov. Phys. JETP **58**, 181 (1983)].
4. A. K. Zvezdin and V. A. Kotov, *Modern Magnetooptics and Magnetooptical Materials* (Institute of Physics Publ., Bristol, 1997).
5. S. Krupicka, *Physik der Ferrite und der verwandten magnetischen Oxide* (Academia, Prague, 1973; Mir, Moscow, 1976), Vol. 2.
6. A. K. Zvezdin, V. M. Matveev, A. A. Mukhin, and A. I. Popov, *Rare-Earth Ions in Magnetic-Ordered Crystals* (Nauka, Moscow, 1985).
7. Yu. A. Izyumov, V. E. Naĭsh, and R. P. Ozerov, *Neutron Diffraction Analysis of Magnetics* (Atomizdat, Moscow, 1981).
8. J. A. Koningstein and C. J. Kaue-Maguire, Can. J. Chem. **52**, 3445 (1974).
9. F. Harbus and H. E. Stanly, Phys. Rev. **88**, 1156 (1973).
10. M. Guillot, A. Marchand, V. Nekvasil, and F. Tcheou, J. Phys. C **18**, 3547 (1985).
11. V. Nekvasil and I. Veltruski, J. Magn. Magn. Mater. **86**, 315 (1990).
12. R. Z. Levitin, V. V. Snegirev, A. V. Kopylov, *et al.*, J. Magn. Magn. Mater. **170**, 223 (1997).
13. M. D. Kuz'min and A. M. Tishin, Cryogenics **32**, 545 (1992).
14. U. V. Valiev, A. A. Klochkov, A. I. Popov, and B. Yu. Sokolov, Opt. Spektrosk. **66**, 613 (1989) [Opt. Spectrosc. **66**, 359 (1989)].
15. R. Serber, Phys. Rev. **41**, 489 (1932).
16. B. G. Wybourne, *Spectroscopic Properties of Rare Earth* (Wiley, New York, 1965).
17. K. P. Belov, A. K. Zvezdin, A. M. Kadomtseva, and R. Z. Levitin, *Orientational Phase Transitions* (Nauka, Moscow, 1979).
18. B. Nagaian, M. Pam Babu, and D. B. Sirdeshmukh, Indian J. Pure Appl. Phys. **17**, 838 (1979).
19. Wen Dai, E. Gmelin, and R. Kremer, J. Phys. D **21**, 628 (1988).

Translated by N. Wadhwa

Physics of the Solid State, Vol. 44, No. 11, 2002, pp. 2112–2115. Translated from Fizika Tverdogo Tela, Vol. 44, No. 11, 2002, pp. 2018–2021.
Original Russian Text Copyright © 2002 by Bokov, Volkov, Petrichenko.

MAGNETISM AND FERROELECTRICITY

High-Drive-Field Domain Wall Dynamics in Low-Damping Garnet Films

V. A. Bokov, V. V. Volkov, and N. L. Petrichenko

Ioffe Physicotechnical Institute, Russian Academy of Sciences,
Politekhnicheskaya ul. 26, St. Petersburg, 194021 Russia

Received January 22, 2002

Abstract—Domain wall (DW) dynamics in a low-damping YBiFeGa film with perpendicular magnetic anisotropy was studied under FMR conditions. Measurements were carried out under radial expansion of magnetic bubbles in high pulsed drive fields and in an in-plane dc magnetic field. A high-speed image recording technique was employed. The pattern of the dependence of DW velocity on drive field for the parts of the DW oriented parallel and perpendicular to the in-plane field was established. In all cases, this dependence contains a saturation region in which the DW velocity increases noticeably with increasing in-plane field. The experimental data obtained do not agree with theory. A possible explanation for this discrepancy is proposed. The onset of spatially periodic distortions in a moving DW is discussed. © *2002 MAIK “Nauka/Interperiodica”.*

While domain wall (DW) dynamics in ferrite-garnet films with perpendicular magnetic anisotropy has been extensively studied, the results reported relate primarily to weak drive fields H_g not in excess of the saturation magnetization $4\pi M$. Only a limited number of studies have dealt with stronger fields ($H_g > 4\pi M$), and the results of these studies are contradictory. It is reported in [1], for instance, that in this region the character of DW motion changes, the saturated velocity behavior being replaced by a regime in which the DW velocity V increases substantially with the field H_g. In [2, 3], no velocity saturation was observed, whereas in [4–6] it was seen. Several communications have discussed the effect of a dc in-plane field H_p on DW motion in high drive fields. According to [7], when the field H_p is weak ($\sim 4\pi M$) and parallel to the film plane, the relation $V(H_g)$ has a region with positive differential mobility followed by another region at higher H_g that exhibits negative differential mobility. As H_p increases, the mobility in the second region reverses sign to become positive. At the same time, according to [5, 6], as the in-plane field increases, the velocity saturation in weak fields H_p disappears and the DW velocity increases monotonically with increasing drive field. The data on the $V(H_p)$ behavior in high fields H_g are also contradictory. For instance, the findings reported in [7] fit Eq. (12) from a theoretical analysis made in [8]. However, the data reported in [5, 6] agree neither with that relation nor with the expression derived on the basis of a simple model in [9]. Domain wall motion is frequently observed to entail the so-called widening effect, i.e., formation of a broad diffuse boundary and generation of microdomains in front of the moving DW [4–6, 10]. These phenomena are sometimes preceded by the onset of spatially periodic DW shape distortions [1, 7, 10]. While there is no lack of conjectures concerning the origin of these effects [1, 7, 11–14], the problem remains basically unsolved. In view of the disagreements among the results obtained in various studies and the fairly limited amount of available experimental data, it appeared reasonable to study the dynamic behavior of a DW in a low-damping film under high drive fields. It is believed that in such fields, the effects specific for this field region should be most clearly expressed.

Our measurements were performed on a (111)-oriented film of the YBiFeGa system with the following characteristics: the film thickness $h = 4.6$ µm, $4\pi M = 156$ G, the field of uniaxial anisotropy was 6200 Oe, the Bloch wall width parameter $\Delta = 2 \times 10^{-6}$ cm, the effective gyromagnetic ratio $\gamma = 1.67 \times 10^{7}$ Oe^{-1} s^{-1}, the Gilbert damping parameter $\alpha = 0.002$, and the bubble domain static collapse field was 34 Oe. A high-speed video recording technique was used, with a rhodamine 6G dye laser (pumped by a nitrogen laser) providing single light pulses ~5 ns long. The image obtained was stored in digital video memory and could be displayed on a monitor screen for processing. The spatial resolution was ~0.4 µm. A bubble was stabilized by a dc bias field H_b and expanded by applying a pulsed uniform field H directed opposite to H_b. The DW was displaced by an effective drive field:

$$H_g = H - H_b + H_e,$$

where the last term takes into account the fact that the effective field due to the DW curvature and the effective demagnetization field normal to the film plane depend on the bubble radius. This term in H_g was found using the well-known relations from the theory of bubble stability (see, e.g., [15]). The lowest value of the drive field in our measurements was 60 Oe, because below this value of H_g, the bubble shape underwent irreproducible distortions. The dc in-plane magnetic field H_p applied to the film could be varied. For $H_p < 145$ Oe, the maximum value of H_g was 970 Oe. In a stronger field H_p, the walls of the expanding bubble approached the neighboring domains; to avoid their interaction, measurements under these conditions were conducted in lower drive fields. The translation of parts of the bubble wall parallel and perpendicular to the in-plane field was measured experimentally as a function of time during the drive field pulse. For this purpose, the laser illumination pulse was delayed with respect to the instant of the field pulse application by an amount varied from 0.3 to 0.7 μs. The measurements were made repeatedly for each delay time. To exclude the effect of the initial DW displacement phase, the minimum delay was always 0.3 μs. The data thus obtained were used to find the DW velocity and its dependence on the drive field H_g for various values of H_p.

Figure 1 exemplifies typical $V(H_g)$ dependences obtained for the in-plane field H_p equal to 0, 200, and 360 Oe. At $H_p = 0$, the DW velocity is seen to reach saturation at $V_s = 4.5$ m/s. This velocity agrees well with the value of 4.2 m/s calculated for the film under study from the empirical relation $V_s = M\Delta\gamma(1 + 7.5\alpha)$ [16, 17]; this agreement lends additional support to the theoretical model developed in [18, 19], which is in accord with this relation and according to which the saturation regime corresponds to the state of chaos. The analysis performed in [18, 19] was applicable to low fields $H_g < 4\pi M$. As follows from our data, the state of chaos can also set in in high drive fields.

For $H_p \leq 110$ Oe, the experiment reveals only the velocity saturation region throughout the H_g variation range studied. When $H_p > 145$ Oe and is oriented perpendicular to the DW plane, one can see an interval of $V(H_g)$, preceding the velocity saturation region, where the DW velocity increases with the field H_g (Fig. 1). If the field H_p is parallel to the DW plane, such an interval appears for $H_p > 250$ Oe. Thus, the initial part of the $V(H_g)$ relation ($H_g \leq 220$ Oe) is characterized by velocity anisotropy. As already mentioned, the measurements were conducted in drive fields $H_g \geq 60$ Oe; for this reason, the region of linear DW translation and a maximum in the DW velocity are not observed, because, even in high H_p fields, the maximum occurs for $H_g < 5$ Oe in low-damping films [20]. It is believed that, after the steady-state motion breaks down, the DW structure contains a horizontal Bloch line (HBL) and undergoes periodic transformations, with the wall velocity increasing with the field H_g (see [21, Fig. 1] and [22, Fig. 1]). It is apparently this region of increase in velocity that becomes manifest in the corresponding curves in Fig. 1. The parts of the DW oriented perpendicular and parallel to the in-plane field should differ in structure. In the former case, the DW should contain a region of the Néel wall type whose size increases with H_p [23]. The HBLs in such DWs will apparently have different twist angles and move differently; this is what initiates an anisotropy in the DW velocity.

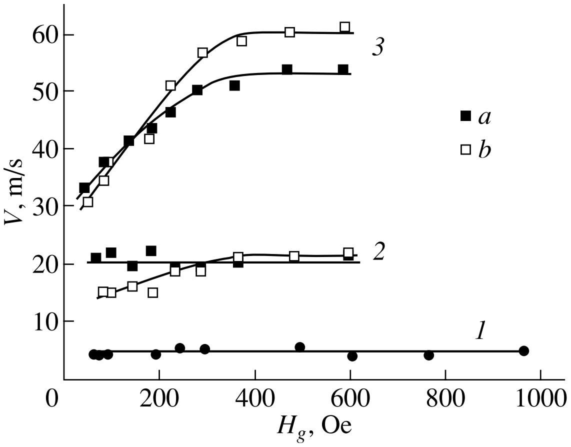

Fig. 1. Domain wall velocity plotted vs. drive field for different values of the in-plane field H_p: (*1*) 0, (*2*) 200, and (*3*) 360 Oe. (*a*, *b*) The wall is parallel and perpendicular to the field H_p, respectively.

The $V(H_g)$ relations obtained by us differ from those observed in [7]. In our case, regions with negative differential mobility that transform into those exhibiting positive mobility were not seen. The reason for these discrepancies is unclear; the films studied had similar parameters, except the uniaxial-anisotropy field (in our sample, this field was ~60% higher). The difference from the results reported in [5] is as difficult to explain. It is possible that the measurements in [5] were carried out in fields H_g that were not high enough, and thus the velocity saturation region was not reached.

The data plotted in Fig. 1 were used to derive the dependence of the saturation velocity on the in-plane field for DWs oriented differently relative to this field (Fig. 2). The saturation regime is known to set in when the average DW velocity reaches a certain critical value and does not vary thereafter. The $V_s(H_p)$ relation is likely to reflect the dependence of this critical velocity on the in-plane field. This field should stabilize the DW spin structure. Therefore, Fig. 2 suggests that, starting with a certain value of H_p, the DW structure with a Néel-type region observed in walls oriented perpendicular to the in-plane field is more stable. In this wall, chaos arises at a higher DW velocity. The theory developed in [8] permits the conclusion that the velocity saturation effect is caused by a change in the relaxation mechanisms with increasing DW velocity and yields the following expression relating the saturation velocity and the in-plane field:

$$V_s = \frac{\pi}{2}\Delta\gamma H_p. \tag{1}$$

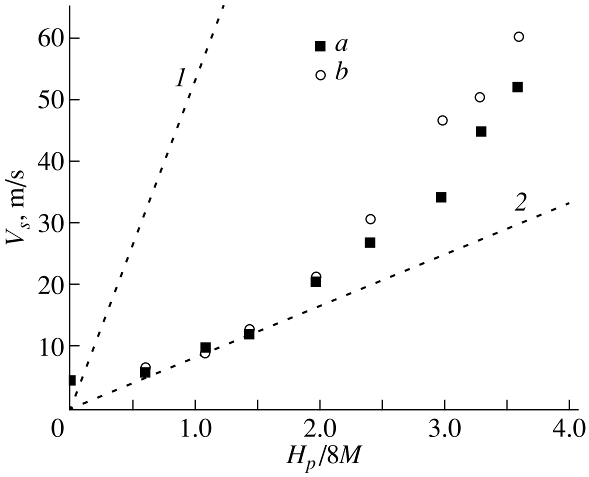

Fig. 2. Domain wall saturation velocity plotted vs. in-plane field. (*a*, *b*) The wall is parallel and perpendicular to the field H_p, respectively. Curve *1* is a plot of Eq. (1), and curve *2* is a plot of Eq. (2).

Another relation was obtained in [9] from an analysis of a simple model of wall motion and has the form

$$V_s = \frac{\Delta\gamma}{4}H_p. \tag{2}$$

Equations (1) and (2) are plotted in Fig. 2. The obvious disagreement with the experimental data is accounted for by the fact that the velocity saturation regime is due to a mechanism different from the ones treated in the communications cited above.

Throughout the ranges of the fields H_g and H_p studied here, the wall parallel to the in-plane field did not exhibit the spatially periodic distortions reported in [7, 10] for this DW orientation. At the same time, as in [7, 10], such distortions formed on the wall perpendicular to the in-plane field. When this field was 110 Oe, the distortions appeared when the wall moved in a drive field $H_g \geq 300$ Oe. As H_p increases, the value of the drive field above which DW distortions arise decreases; for $H_p = 360$ Oe, the corresponding value of H_g is ~100 Oe. Distortions arise at drive field values below the velocity saturation region, at least for $H_p > 240$ Oe. The width of the DW region where spatially periodic distortions are observed is comparatively small. For $H_p = 360$ Oe, this width was ~3 μm 0.7 μs after application of a field $H_g = 590$ Oe; at this instant, the domain size in the direction collinear with the in-plane field was 115 μm. The spatially periodic DW distortions may be one more reason for the above-mentioned anisotropy in the wall velocity.

Formation of a broad diffuse DW in a field H_p normal to its plane was reported in [5]; this observation found theoretical interpretation [13] within a concept assuming random wall motion in high drive fields. We did not observe such a DW widening, and, as shown by our data, the formation of spatially periodic distortions is not related to a crossover to the velocity saturation regime.

Thus, our analysis of the behavior of a low-damping ferrite-garnet film under FMR conditions in high drive fields has established the character of the dependence of the DW velocity on the drive field for domain walls oriented parallel and perpendicular to the in-plane field. It was shown that velocity saturation is reached in all cases, and the dependence of the saturation velocity on the in-plane field was found. On the whole, the results obtained find interpretation in terms of a concept by which the DW velocity saturation corresponds to the state of chaos. When the in-plane field is perpendicular to the wall, spatially periodic distortions arise on the DW; this phenomenon is not related in any way to the velocity saturation.

ACKNOWLEDGMENTS

This work was supported by the Russian Foundation for Basic Research, project no. 00-02-16945.

REFERENCES

1. V. G. Kleparski, I. Pinter, and G. J. Zimmer, IEEE Trans. Magn. **17** (6), 2775 (1981).
2. R. V. Telesnin, S. M. Zimacheva, and V. V. Randoshkin, Fiz. Tverd. Tela (Leningrad) **19** (3), 907 (1977) [Sov. Phys. Solid State **19**, 528 (1977)].
3. V. V. Randoshkin, Tr. Inst. Obshch. Fiz. Ross. Akad. Nauk **35**, 49 (1992).
4. L. P. Ivanov, A. S. Logginov, and G. A. Nepokoĭchitskiĭ, Zh. Éksp. Teor. Fiz. **84** (3), 1006 (1983) [Sov. Phys. JETP **57**, 583 (1983)].
5. K. Vural and F. B. Humphrey, J. Appl. Phys. **50** (5), 3583 (1979).
6. T. Suzuki, L. Gal, and S. Maekawa, Jpn. J. Appl. Phys. **19** (4), 627 (1980).
7. V. V. Randoshkin and M. V. Logunov, Fiz. Tverd. Tela (St. Petersburg) **36** (12), 3498 (1994) [Phys. Solid State **36**, 1858 (1994)].
8. B. A. Ivanov and N. E. Kulagin, Zh. Éksp. Teor. Fiz. **112** (3), 953 (1997) [JETP **85**, 516 (1997)].
9. F. H. de Leeuw, IEEE Trans. Magn. **9** (4), 609 (1973).
10. M. V. Logunov and V. V. Randoshkin, Tr. Inst. Obshch. Fiz. Ross. Akad. Nauk **35**, 107 (1992).
11. V. V. Randoshkin, Fiz. Tverd. Tela (St. Petersburg) **37** (3), 652 (1995) [Phys. Solid State **37**, 355 (1995)].
12. A. S. Logginov, G. A. Nepokoĭchitskiĭ, and T. B. Rozanova, Zh. Tekh. Fiz. **60** (7), 186 (1990) [Sov. Phys. Tech. Phys. **35**, 861 (1990)].
13. R. A. Kosinski, Phys. Rev. B **50** (10), 6751 (1994).
14. P. A. Polyakov, Pis'ma Zh. Éksp. Teor. Fiz. **60** (5), 336 (1994) [JETP Lett. **60**, 343 (1994)].

15. V. V. Randoshkin, Prib. Tekh. Éksp., No. 2, 155 (1995).
16. V. V. Volkov, V. A. Bokov, and V. I. Karpovich, Fiz. Tverd. Tela (Leningrad) **24** (8), 2318 (1982) [Sov. Phys. Solid State **24**, 1315 (1982)].
17. V. A. Bokov, V. V. Volkov, and N. L. Petrichenko, Phys. Met. Metallogr. **92** (S1), 1 (2001).
18. E. E. Kotova and V. M. Chetverikov, Fiz. Tverd. Tela (Leningrad) **32** (4), 1269 (1990) [Sov. Phys. Solid State **32**, 748 (1990)].
19. A. Sukiennicki and R. A. Kosinski, J. Magn. Magn. Mater. **129**, 213 (1994).
20. V. A. Bokov, V. V. Volkov, N. L. Petrichenko, and M. Maryshko, Fiz. Tverd. Tela (St. Petersburg) **39** (7), 1253 (1997) [Phys. Solid State **39**, 1112 (1997)].
21. G. N. Patterson, R. C. Giles, and F. B. Humphrey, IEEE Trans. Magn. **27**, 5498 (1991).
22. V. A. Bokov and V. V. Volkov, Fiz. Tverd. Tela (St. Petersburg) **39** (4), 660 (1997) [Phys. Solid State **39**, 577 (1997)].
23. R. A. Kosinski and J. Engemann, J. Magn. Magn. Mater. **50**, 229 (1985).

Translated by G. Skrebtsov

Physics of the Solid State, Vol. 44, No. 11, 2002, pp. 2116–2123. Translated from Fizika Tverdogo Tela, Vol. 44, No. 11, 2002, pp. 2022–2028.
Original Russian Text Copyright © 2002 by Buchel'nikov, Bychkov, Nikishin, Palmer, Lim, Edwards.

MAGNETISM AND FERROELECTRICITY

Electromagnetic–Acoustic Transformation in an Erbium Single Crystal

V. D. Buchel'nikov*, I. V. Bychkov*, Yu. A. Nikishin*, S. B. Palmer, C. M. Lim**, and C. Edwards****
** Chelyabinsk State University, Chelyabinsk, 454021 Russia*
*** University of Warwick, Coventry CV4 7AL, United Kingdom*
e-mail: buche@csu.ru
e-mail: phrah@warwick.ac.uk

Received February 1, 2002

Abstract—The temperature dependences of the electromagnetic–acoustic transformation (EMAT) efficiency and the velocity of transverse sound for the erbium rare-earth metal with three complex magnetic structures are experimentally investigated at different external constant magnetic fields. An intensive generation and anomalies in the velocity of transverse sound are revealed in the temperature range of the magnetic phase transitions. It is found that an increase in the magnetic field leads to an increase in the sound generation efficiency and a decrease in the anomalies in the velocity of sound. The relationships for the efficiency of transverse-sound generation through the magnetoelastic mechanism are theoretically derived for two magnetic structures of erbium. It is demonstrated that an increase in the EMAT efficiency in the phase transition range is associated with the specific features in the static and dynamic magnetic susceptibilities of erbium. *© 2002 MAIK "Nauka/Interperiodica".*

1. INTRODUCTION

Magnetic ordering of some magnets, among them rare-earth metals, exhibit a complex nature. As a rule, all rare-earth metals undergo a number of phase transitions between different magnetic structures with a decrease in the temperature. In particular, the erbium rare-earth metal in the absence of magnetic fields undergoes the following sequence of spontaneous phase transitions [1–4]. At temperatures $T > T_{\mathrm{N1}} = 87$ K, erbium is a paramagnet. In the temperature range $T_{\mathrm{N1}} > T > T_{\mathrm{N2}} = 54$ K, erbium has a magnetic structure which is referred to as the longitudinal spin wave structure. This structure is characterized by oscillations of the longitudinal magnetization projection onto the anisotropy axis. In this case, the transverse magnetization components are equal to zero. The transverse and longitudinal magnetization projections onto the hexagonal axis **c** oscillate in the structure observed in the temperature range $T_{\mathrm{N2}} > T > T_{\mathrm{C}} = 18$ K. This magnetic structure is termed the complex spiral (or cycloidal) structure. With a decrease in the temperature in this phase, the wave vector of a cycloid decreases and passes through a series of commensurate and incommensurate values [15]. At $T < T_{\mathrm{C}}$, erbium has a structure of the ferromagnetic spiral type.

The complex magnetic structure of erbium is retained in the external magnetic field **H** aligned along the hexagonal axis up to $H = 26$–28 kOe [3, 4]. An increase in the magnetic field results in an increase in the temperature range of existence of the ferromagnetic spiral phase and a decrease in the temperature ranges of existence of the longitudinal spin wave and cycloidal phases. An increase in the magnetic field in the cycloidal phase is attended by stabilization of the commensurate structures, which possess a net magnetization along the hexagonal axis [3]. At $H > 16$ kOe, the cycloidal phase is characterized by only one commensurate structure with a wave number of 2/7 (in terms of a reciprocal lattice constant along the **c** axis) [3]. By contrast, the number of commensurate and incommensurate structures increases in the ferromagnetic spiral phase [3, 4].

The occurrence of several magnetic phase transitions and different long-period magnetic structures in erbium and other rare-earth metals leads to the fact that the behavior of different physical characteristics of these metals can essentially differ from the behavior of similar characteristics in magnets with a simpler magnetic structure. In particular, it is of interest to investigate experimentally and theoretically the electromagnetic–acoustic transformation (EMAT) in rare-earth metals, because all changes in the magnetic structure of these materials should affect the sound generation efficiency [6].

The electromagnetic–acoustic transformation in rare-earth metals with a modulated magnetic structure has been investigated in a number of works (see, for example, review [6]). Andrianov *et al.* [7, 8] experimentally studied the electromagnetic excitation of sound in ferromagnetic and modulated phases of terbium and dysprosium. The electromagnetic–acoustic transformation in ferromagnetic phases of modulated magnets was theoretically analyzed in [6, 8]. However, the efficiency of the electromagnetic–acoustic transformation in modulated phases of rare-earth metals was theoretically treated in only one work [9], which dealt with this process in a modulated phase of the simple spiral type.

In the present work, we experimentally investigated the electromagnetic–acoustic transformation in an erbium single crystal. The efficiency of the electromagnetic–acoustic transformation through the magnetoelastic mechanism was theoretically calculated for the longitudinal spin wave and ferromagnetic spiral modulated phases. The results of theoretical calculations were compared with experimental data.

2. EXPERIMENTAL TECHNIQUE

The EMAT efficiency and the velocity of generated sound were investigated using a Matec DSP-8000 automated ultrasonic measuring system [10, 11], which was adapted for measurements according to the standard echo pulse noncontact sound generation technique described, for example, in review [6]. A cylindrical single-crystal sample 2.8 mm long and 4.5 mm in diameter was placed in a pancake coil. The hexagonal axis **c** of the sample coincided with the cylinder axis. The coil with the sample was placed in a constant magnetic field whose vector **H** was perpendicular to the coil plane and parallel to the hexagonal axis **c** of the sample. In this geometry, the transverse sound with the wave vector **k** aligned parallel to the **c** axis was generated in the sample [6]. Electromagnetic field pulses with an amplitude of 200 V, a width of 0.6–0.8 μs, and a carrier frequency of 10 MHz were applied to the coil. These pulses excited a sequence of decaying acoustic signals in the sample. Since the electromagnetic pulse-repetition frequency was equal to 1 kHz, the whole sequence of generated acoustic signals fell in this range. The ultrasound pulses at the frequency of the incident electromagnetic wave were generated at both cylinder ends, propagated along the cylinder axis, and recorded at the opposite cylinder end by the same coil. Echo signals following at intervals $t = h/S$ (where h is the cylinder length and S is the velocity of ultrasound) arrived from the coil at the Matec DSP-8000 precision instrument. The propagation time of the signal through the sample was determined from the third and fourth echo signals, and the amplitude of the generated signal was measured from the third echo signal [10]. The error in the measurement of the velocity of sound with the use of the Matec DSP-8000 instrument did not exceed 0.1%. Analysis of the echo signal shape showed that the ultrasonic attenuation in the sample was relatively small and had no noticeable effect on the EMAT efficiency [10]. In this case, the recorded signal amplitude under the above experimental conditions was proportional to the EMAT efficiency squared [6, 10].

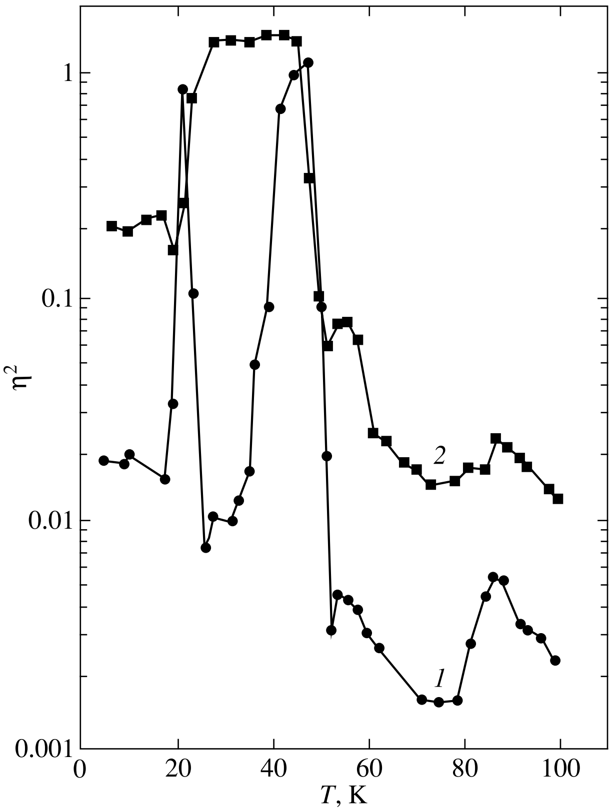

Fig. 1. Experimental temperature dependences of the EMAT signal amplitude for the erbium single crystal in the magnetic field **H** || **c** at H = (*1*) 10 and (*2*) 20 kOe. The signal amplitude is given in arbitrary units.

The temperature dependences of the EMAT signal amplitude at two constant magnetic fields are displayed in Fig. 1. It can be seen that, at H = 10 kOe, the dependence of the EMAT signal amplitude in the temperature ranges of the paramagnet –longitudinal spin wave, longitudinal spin wave–cycloid, and cycloid–ferromagnetic spiral phase transitions exhibits pronounced peaks in the sound generation. At H = 20 kOe, the generation efficiency also increases in these temperature ranges. Note that the generation efficiency in the cycloidal phase is characterized by a plateau and exceeds the generation efficiency in other phases. The generation efficiency in all the phases increases with an increase in the magnetic field. The temperature dependences of the velocity of generated transverse sound at three magnetic fields are plotted in Fig. 2. As is seen from this figure, the anomalies in the velocity of sound are observed in the above temperature ranges. The anomalies are smoothed as the magnetic field increases. The velocity of transverse sound most strongly decreases in the cycloidal phase at the magnetic field H = 10 kOe. In this case, the velocity of sound changes by 15–20%. It should be noted that such a considerable change in the velocity of ultrasound in the range of magnetic phase transitions has never been observed in other rare-earth metals.

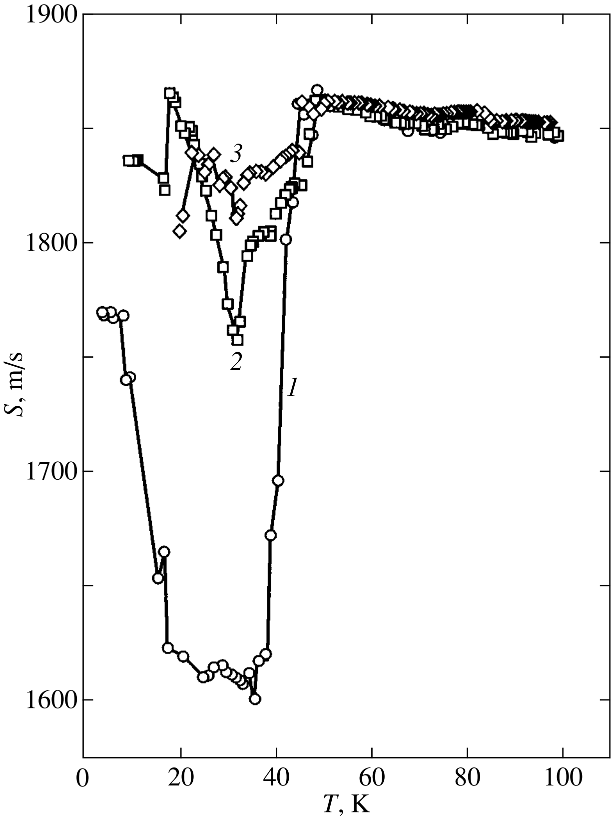

Fig. 2. Experimental temperature dependences of the velocity of transverse sound for the erbium single crystal in the magnetic field **H** || **c** at *H* = (*1*) 10, (*2*) 15, and (*3*) 20 kOe.

3. THEORY

3.1. The free energy and the ground state. Rare-earth metals have a hexagonal crystal structure. The free energy of such a magnet can be described by the phenomenological relationship [1, 9, 12]

$$W = \frac{1}{V}\int F dV,$$

where

$$\begin{aligned} F &= \frac{1}{2}a\mathbf{M}^2 + \frac{1}{4}b\mathbf{M}^4 - \frac{1}{2}\beta_1 M_z^2 - \frac{1}{4}\beta_2 M_z^4 \\ &+ \frac{1}{2}\beta_6(M_+^6 + M_-^6) + \frac{1}{2}\alpha_\perp\left[\left(\frac{\partial\mathbf{M}}{\partial x}\right)^2 + \left(\frac{\partial\mathbf{M}}{\partial y}\right)^2\right] \\ &+ \frac{1}{2}\alpha_\parallel\left(\frac{\partial\mathbf{M}}{\partial z}\right)^2 + \frac{1}{2}\gamma\left(\frac{\partial^2\mathbf{M}}{\partial x_i^2}\right)^2 - \mathbf{M}(\mathbf{H} + \mathbf{h}) \\ &+ \gamma_{ik}\mathbf{M}^2 U_{ik} + \gamma_{iklm}M_i M_k U_{lm} + c_{iklm}U_{ik}U_{lm}. \end{aligned} \tag{1}$$

Here, **M** is the magnetization; $M_\pm = M_x \pm iM_y$ are its circular components; *a* and *b* are the homogeneous exchange constants; α and γ are the inhomogeneous exchange constants; β stands for the anisotropy constants, **H** and **h** are the strengths of constant and alternating magnetic fields, respectively; γ_{ik} and γ_{iklm} are the exchange and relativistic magnetostriction tensors, respectively; U_{ij} is the strain tensor, and c_{iklm} is the elastic constant tensor.

Let us determine the ground state of a crystal without regard for the anisotropy in the basal plane ($\beta_6 = 0$) provided the external magnetic field is aligned along the hexagonal axis: **H** || **c** || **z**. For this purpose, it is necessary to solve a set of equations that involves the Euler equations for the magnetic subsystem and the equilibrium equations for the elastic subsystem under the Saint Venant strain compatibility conditions [12].

We will separately consider the ground states for the longitudinal spin wave and ferromagnetic spiral phases.

In the case of a longitudinal spin wave structure, the equilibrium components of the magnetization vector can be written in the form [1]

$$M_\pm = 0, \quad M_z = \sum_{n=-\infty}^{n=+\infty} M_n^z e^{iqnz}, \tag{2}$$

where $2\pi/q$ is the period of the structure along the **z** axis.

The equilibrium strain tensor, which is obtained by solving the equilibrium equations for the elastic medium under the Saint Venant compatibility conditions with due regard for relationships (2) in the approximation $qd \gg 1$ (i.e., in the case when the period of the structure is considerably less than the magnet thickness *d*), is given in the Appendix [formulas (A1)].

In order to determine the equilibrium values of M_n^z and *q*, formulas (2) and (A1) should be substituted into relationship (1) for the free energy, which should then be minimized with respect to M_n^z and *q*. Analysis of the set of equations derived by minimizing the free energy of the system demonstrates that $M_n^z = M_{-n}^z$. Hence, hereafter, we will treat only the components M_n^z with $n = 0, 1, 2, 3, \ldots$. We will also restrict our consideration to weak magnetic fields. In this case, it is sufficient to retain the terms with $n = 0, 1, 2$, and 3 ($M_1 \gg M_0, M_2$, and M_3) in expression (2) [1]. To a first approximation in the small parameter $\tilde{b}_i/L(q)$, we obtain the following relationships for the components M_0, M_1, M_2, and M_3:

$$\begin{gathered} M_0^z = H/L(0), \quad M_1^z = -L(q)/3\tilde{b}, \\ M_2^z = -\frac{3\tilde{b}_1 M_0^z}{L(2q)}(M_1^z)^2, \\ M_3^z = -\frac{\tilde{b}_1}{L(3q)}(M_1^z)^3, \quad q = q_0. \end{gathered} \tag{3}$$

Here, $L(q) = a - \beta_1 + \alpha_{\|}q^2 + \gamma q^4$ is the eigenvalue of the differential operator

$$\hat{L} = a - \beta_1 - \alpha_{\|}\frac{\partial^2}{\partial z^2} + \gamma\frac{\partial^4}{\partial z^4}, \quad q_0^2 = -\frac{\alpha_{\|}}{2\gamma},$$

$$\tilde{b} = b - \frac{2\tilde{\gamma}_3^2}{c_{33}} + \frac{8(c_{33}\tilde{\gamma}_1 - c_{13}\tilde{\gamma}_3)^2}{3c_{33}\Delta}, \quad \tilde{b}_1 = b - \frac{2\tilde{\gamma}_3^2}{c_{33}}.$$

The ground state of the magnet in the ferromagnetic spiral phase can be determined under the assumption that the energy W is minimum when the magnetization has the form

$$M_0^+ = M_0 e^{iqz}\sin\theta, \quad M_0^- = M_0 e^{-iqz}\sin\theta,$$
$$M_0^z = M_0\cos\theta, \tag{4}$$

where θ is the angle between the magnetization vector **M** and the symmetry axis **z**. The solution of the elasticity equations with allowance made for the Saint Venant compatibility conditions for the ferromagnetic spiral phase and relationships (4) makes it possible to obtain the equilibrium strain tensor U_{ik}^0. The components of this tensor are given in the Appendix [formulas (A2)]. Substitution of expressions (4) and (A2) into relationship (1) for the free energy, averaging of the energy at $qd \gg 1$, and minimization with respect to θ and q give the following equations for the equilibrium magnetization and the wave number of a spiral in the ferromagnetic spiral phase:

$$q = q_0 = (-\alpha_{\perp}/2\gamma)^{1/2},$$
$$M_0\cos\theta[\tilde{\beta}_1 + h_{me} + (\tilde{\beta}_2 - h_{me}/M_0^2)M_0^2\cos^2\theta \tag{5}$$
$$+ \alpha q^2 + \tilde{\Delta}] + H = 0,$$

where $\tilde{\Delta} = \gamma q^4$, $h_{me} = (\gamma_{11} - \gamma_{12})^2 M_0^2/(c_{11} - c_{12})$, and $\tilde{\beta}_1$ and $\tilde{\beta}_2$ are the anisotropy constants renormalized by the magnetostriction [9, 13].

3.2. The ultrasonic generation in the longitudinal spin wave phase. Now, we consider a magnet occupying the half-space $z > 0$ (this approximation is valid in the case when the acoustic wavelength is considerably less than the sample thickness and, in particular, under the aforementioned experimental conditions). We assume that a plane electromagnetic wave is incident normal to the magnet surface. Let the external magnetic field vector **H** be aligned along the hexagonal axis **c** of the sample (**H** || **k** || **c** || **z**).

The amplitude of the acoustic wave excited in the magnet can be determined by solving the system of elasticity, Landau–Lifshitz, and Maxwell coupled equations with the standard boundary conditions for the electric and magnetic field vectors, the stress tensor, and the magnetization [6], that is,

$$\dot{\mathbf{M}} = g[\mathbf{M}, \mathbf{H}^{\text{eff}}], \quad \rho\ddot{u}_i = \frac{\partial\sigma_{ik}}{\partial x_k},$$
$$\text{curl}\mathbf{H} = \frac{4\pi}{c}\sigma\mathbf{E}, \quad \text{curl}\mathbf{E} = -\frac{1}{c}\frac{\partial\mathbf{B}}{\partial t}, \tag{6}$$
$$\text{div}\mathbf{B} = 0, \quad \text{div}\mathbf{E} = 0.$$

Here, $\mathbf{B} = \mathbf{H} + 4\pi\mathbf{M}$ is the magnetic induction, **E** is the electric field strength, $\mathbf{H}^{\text{eff}} = -\frac{\partial F}{\partial\mathbf{M}} + \frac{\partial}{\partial x}\frac{\partial F}{\partial(\partial\mathbf{M}/\partial x_i)}$ is the effective magnetic field, ρ is the metal density, **u** is the displacement vector, g is the gyromagnetic ratio, c is the velocity of light in free space, and σ is the electrical conductivity. The terms responsible only for the magnetoelastic mechanism of sound generation are retained in Eqs. (6). This mechanism of electromagnetic–acoustic transformation dominates in magnetic fields as strong as 100 kOe [6].

We will analyze small deviations of the magnetization, elastic displacements, and electromagnetic field from the equilibrium values determined by relationships (2) and (3). For this purpose, all the variables are represented in the form

$$F = F_0(z) + f, \quad f = e^{ikz}\sum_{n=-\infty}^{n=+\infty} f_n e^{iqnz}, \tag{7}$$

where F_0 stands for the equilibrium values and f are small deviations from the equilibrium values. By substituting formulas (7) into the system of coupled equations (6) and eliminating the electric field strength **E**, we obtain an infinite set of equations (linearized in the vicinity of the equilibrium values) for the Fourier components f_n of coupled waves in the longitudinal spin wave phase. Within the approximation that the zeroth harmonics f_0 in the derived infinite set of equations have the largest amplitudes [9], the linearized system of equations (6) takes the form

$$(\omega^2 - \omega_t^2)u_0^{\pm} + \frac{ik\gamma_{44}M_0^z}{\rho}m_0^{\pm} = 0,$$
$$(k^2 - k_e^2)h_0^{\pm} - 4\pi i\delta^2 m_0^{\pm} = 0, \tag{8}$$
$$(\omega \mp \omega_1)m_0^{\pm} - 2igk\gamma_{44}(M_1^z)^2 u_0^{\pm} + M_0^z g h_0^{\pm} = 0.$$

Here, $m^{\pm}$, $h^{\pm}$, and $u^{\pm}$ are the circular components; ω is the frequency of the electromagnetic wave incident on the metal; $\omega_t = S_t k$ and $S_t = \sqrt{c_{44}/\rho}$ are the frequency and velocity of the transverse sound, respectively; $k_e^2 =$

$2i/\delta^2 = 4\pi i\sigma\omega/c^2$; δ is the skin depth in the metal; $\omega_1 = gM_0(L(k) + \beta_1 + 6(\tilde{b} + b_{me})M_1^2)$; and

$$b_{me} = \frac{2\tilde{\gamma}_3}{c_{33}}(\gamma_{33} - \gamma_3) + \frac{2(c_{33}\tilde{\gamma}_1 - c_{13}\tilde{\gamma}_3)}{3c_{33}\Delta}$$

$$\times\left[c_{33}\left(3\gamma_{11} + \gamma_{12} - 4\gamma_{13} + \gamma_1 - 3\frac{c_{13}}{c_{33}}\gamma_3\right) + 4c_{13}\tilde{\gamma}_3\right].$$

Note that only the transverse sound can be excited in the geometry under consideration [6].

It is assumed that the frequency of excited waves is considerably less than the frequency of uniform magnetization precession ($\omega \ll \omega_1$) and the spatial dispersion of spin waves is insignificant. Consequently, from Eqs. (8), we obtain the dispersion relation for coupled electromagnetic, spin, and elastic waves:

$$(1 - \zeta_t)k^4 = [(\mu - \zeta_t)k_e^2 + k_t^2]k^2 + \mu k_e^2 k_t^2 = 0, \quad (9)$$

where $k_t^2 = \omega^2/S_t^2$, $\chi = gM_0/\omega_1$ is the dynamic magnetic susceptibility, $\mu = 1 + 4\pi\chi$, and $\zeta_t = \chi\gamma_{44}^2 M_1^2/\rho S_t^2$ is the dynamic parameter of magnetoelastic interaction.

The dispersion equation (9) has the following solutions:

$$\begin{aligned} k_1^2 &= \frac{\mu}{\mu - \zeta_t}k_t^2, \quad k_2^2 = \frac{\mu - \zeta_t}{1 - \zeta_1}k_e^2, \quad k_e \gg k_t, \\ k_1^2 &= \frac{1}{1 - \zeta_t}k_t^2, \quad k_2^2 = \mu k_e^2, \quad k_e \ll k_t. \end{aligned} \quad (10)$$

Here, k_1 and k_2 are the wave numbers of the quasi-elastic and quasi-electromagnetic waves, respectively.

Under the assumption that the zeroth harmonics f_0 have the largest amplitudes, the linearized system of boundary conditions can be written as follows:

$$\begin{aligned} &i\gamma_{44}M_0(m_1^\pm + m_2^\pm) - c_{44}(k_1 u_1^\pm + k_2 u_2^\pm) = 0, \\ &\left(1 - \frac{ick_1}{4\pi\sigma}\right)h_1^\pm + \left(1 - \frac{ick_2}{4\pi\sigma}\right)h_2^\pm = 2h_0^\pm, \end{aligned} \quad (11)$$

where $h_0^\pm$ are the circular amplitudes of the incident electromagnetic wave. Subscripts 1 and 2 refer to the waves propagating in the metal and correspond to those in the solutions of the dispersion equation (10). It should be noted that the boundary condition for magnetization in the system of equations (11) is absent, because the dynamics of the magnet is considered within the approximation according to which the inhomogeneous exchange is disregarded in the energy density (1) [6, 9].

In the approximation $k_e \gg k_t$, which is usually satisfied under experimental conditions, the simultaneous solution of the systems of equations (8) and (11) enables us to derive the amplitude of the excited sound:

$$u_0^\pm = \left(\frac{c}{S_t}\right)^2 \frac{\gamma_{44}M_0\chi\mu^{1/2}}{2\pi\sigma\rho S_t(\mu - \zeta_t)^{3/2}}h_0^\pm. \quad (12)$$

The coefficient of the transformation of electromagnetic waves into acoustic waves (the EMAT efficiency) η is defined as the ratio between the acoustic and electromagnetic energy fluxes at the magnet boundary [6]. In the case under consideration, this coefficient is given by the formula

$$\eta = \left(\frac{c}{S_t}\right)^3 \frac{\gamma_{44}^2 M_0^2 \omega^2 \chi^2 \mu}{2\pi\rho\sigma^2 S_t^2(\mu - \zeta_t)^3}. \quad (13)$$

3.3. The sound generation in the ferromagnetic spiral phase. Let us examine small deviations of the displacement, magnetization, and electric and magnetic field vectors from the equilibrium values [relationships (4) and (5)]. In the case when the waves propagate along the **z** (spiral) axis and the fundamental harmonics have the largest amplitudes, the linearized system of equations (6) for the Fourier components of the above vectors takes the form [13]

$$m^\pm(k)\left[\cos\theta\left(\omega_2(k) + \frac{1}{2}\omega_{me4}\sin^2\theta\right) \mp \omega\right]$$

$$+ ig\gamma_{44}M_0^2 k\left(\cos^2\theta - \frac{1}{2}\sin^2\theta\right)u^\pm(k)$$

$$- gM_0\cos\theta h^\pm(k) = 0, \quad (14)$$

$$(\omega^2 - S_t^2 k^2)u^\pm(k) - \frac{ik}{\rho}\gamma_{44}M_0\cos\theta m^\pm(k) = 0,$$

$$(\omega^2 - \nu^2 k^2)h^\pm(k) + 4\pi\omega^2 m^\pm(k) = 0.$$

Here, we introduced the following designations: $\mathbf{h}^\pm(\mathbf{k})$, $\mathbf{m}^\pm(\mathbf{k})$, and $\mathbf{u}^\pm(\mathbf{k})$ are the circular components of the Fourier vectors **h**, **m**, and **u**, respectively; $\nu = c\sqrt{\omega/4\pi i\sigma}$; $\omega_2(k) = \omega_{20} + gM_0L_\perp(k)$; $\omega_{20} = \omega_{me4}\cos^2\theta$; $\omega_{me4} = g\gamma_{44}^2 M_0^3/c_{44}$; $L_\perp(k)$ is the eigenvalue of the differential operator $\hat{L}_\perp = -\alpha_\perp q^2 - \gamma q^4 - \alpha_\perp\frac{\partial^2}{\partial z^2} + \gamma\frac{\partial^4}{\partial z^4}$; $\omega_1(k) = \omega_{10} - \omega_{20} + gM_0\sin^2\theta L_\perp(k)$; $\omega_{10} = gM[h_{me4} - \sin^2\theta(\tilde{\beta}_1 + (\tilde{\beta}_2 + 2\beta_2)M_0^2\cos^2\theta + h_{me}\sin^2\theta)]$; and $h_{me4} = \omega_{me4}/gM_0$.

The dispersion relation of system (14) is defined by expression (9). The solution of this dispersion equation within the approximation $\omega_2 \gg \omega$ (the given approximation, as a rule, is valid in the frequency range used in experimental investigations of the electromagnetic–acoustic transformation in metals) is represented by expressions (10), where $\zeta_t = \gamma_{44}^2 M_0^2 \chi \cos\theta(\sin^2\theta/2 - \cos^2\theta)/\rho S_t^2$, $\mu = 1 + 4\pi\chi\cos\theta$, and $\chi = gM_0/[(\omega_2(k) + \omega_{me4}\sin^2\theta/2)\cos\theta]$. By ignoring the spatial dispersion of spin waves, the linearized system of boundary conditions is determined by formulas (11) in which the component M_0 should be replaced by $M_0\cos\theta$.

The simultaneous solution of the systems of equations (14) and (11) at $ck_i/4\pi\sigma \ll 1$ permits us to determine the amplitude of the generated elastic transverse wave in the case when the skin depth in the metal is substantially less than the incident electromagnetic wavelength; that is,

$$u_2^{\pm} = \left(\frac{c}{S_t}\right)^2 \frac{\gamma_{44} M_0 \chi \mu^{1/2} \cos^2\theta}{2\pi\sigma\rho S_t(\mu - \zeta_t)^{3/2}} h_0^{\pm}. \tag{15}$$

From this formula, we obtain the following relationship for the EMAT efficiency in the ferromagnetic spiral phase:

$$\eta = \left(\frac{c}{S_t}\right)^3 \frac{\gamma_{44}^2 \omega^2 M_0^2 \chi^2 \mu \cos^4\theta}{2\pi\sigma^2\rho S_t^2(\mu - \zeta_t)^3}. \tag{16}$$

4. RESULTS AND DISCUSSION

Let us dwell once again on the expression for the EMAT efficiency in the case of sound generation in the longitudinal spin wave phase. Taking into account that the inequality $\mu \gg \zeta_t$ is almost universally satisfied [6] and using expression (3) for M_0^z, formula (13) for the EMAT efficiency in the longitudinal spin wave phase can be rewritten in the form

$$\eta = \left(\frac{c}{S_t}\right)^3 \frac{\gamma_{44}^2 H^2 \omega^2 \chi_s^2 \chi_d^2}{2\pi\rho\sigma^2 S_t^2(1 + 4\pi\chi_d)^2}, \tag{17}$$

where χ_s and χ_d are the static and dynamic susceptibilities of the ferromagnetic metal, respectively. The static susceptibility is determined from expression (3) as the proportionality coefficient between M_0^z and H; that is,

$$\chi_s = (a - \beta_1 - 2\gamma q_0^4)^{-1}. \tag{18}$$

The dynamic susceptibility relates the alternating magnetization and the alternating magnetic field and, according to relationships (3), (8), and (9), can be expressed by the formula

$$\chi_d = (-a + 2\beta_1 + 2\gamma q_0^4 + 6\tilde{b}_{me} M_1^2)^{-1}. \tag{19}$$

The experimental dependence of the EMAT efficiency in the longitudinal spin wave phase of erbium (Fig. 1) can be explained in terms of the theoretical relationship (17) and expressions (18) and (19). As follows from relationship (17), the EMAT efficiency peak at the Néel point $T_{\mathrm{N1}} = 87$ K can be associated with the maximum of the static susceptibility χ_s [expression (18)]. This maximum, as a rule, is observed in magnetically ordered crystals upon transition from the paramagnetic state to the ordered state [14]. The small height of the generation efficiency peak in the vicinity of T_{N1} can be due to the small anisotropic magnetostriction constant γ_{44} in this temperature range [6].

The transition from the longitudinal spin wave phase to the cycloidal phase at $T = T_{\mathrm{N2}} = 54$ K is attended by a sharp increase in the dynamic susceptibility (19). This is caused by the fact that the frequency of the quasi-spin mode $\omega_1 = gM_0\chi_d^{-1}$ decreases upon the longitudinal spin wave $\longrightarrow$ cycloidal phase transition. According to relationship (19) (see also [1]), at this phase transition point, the frequency ω_1 takes the minimum value ($\omega_1 = 6gM_0\tilde{b}_{me}M_1^2$) determined by the magnetoelastic coupling and the dynamic susceptibility has a maximum. As follows from expression (17), this can be responsible for the second peak in the experimental dependence of the EMAT efficiency for erbium at $T = T_{\mathrm{N2}}$. Moreover, in accordance with expression (17), the EMAT efficiency depends on the external magnetic field and should increase with an increase in its strength. This is actually observed in the experimental dependence (Fig. 1).

It should be noted that the temperatures of the paramagnet–longitudinal spin wave (T_{N1}) and longitudinal spin wave–cycloidal phase (T_{N2}) transitions only slightly depend on the magnetic field (see the *H*–*T* phase diagrams in [3, 4]). Consequently, the EMAT efficiency peaks at $H = 10$ and 20 kOe in Fig. 1 are observed virtually at the same temperatures.

The next intense EMAT efficiency peak at $T \approx 47$ K in the cycloidal phase in the field $H = 10$ kOe, according to the *H*–*T* phase diagrams obtained in [3, 4], can be explained by the specific features of the static and dynamic susceptibilities in the range of transition either from the commensurate phase with a wave number of 2/7 to the commensurate phase with a wave number of 3/11 [3] or from the commensurate phase with a wave number of 2/7 to the incommensurate phase [4].

In the ferromagnetic spiral phase at $T < T_{\mathrm{C}}$, the magnetization M_0 entering into formula (16) for the EMAT efficiency can be treated as nearly constant (equal to the saturation magnetization at $T \longrightarrow 0$) and independent of the external magnetic field. In this case, the specific features in the EMAT efficiency in the ferromagnetic spiral phase are likely associated with the characteristic properties of the dynamic susceptibility and the equilibrium angle θ between the resultant vector of the magnetization along the hexagonal axis and the external magnetic field vector.

Formula (16) for the EMAT efficiency at $\mu \gg \zeta_t$ can be represented in the form

$$\eta = \left(\frac{c}{S_t}\right)^3 \frac{\gamma_{44}^2 \omega^2 M_0^2 \chi_d^2 \cos^2\theta}{2\pi\rho\sigma^2 S_t^2(1 + 4\pi\chi_d)^2}. \tag{20}$$

Here, the dynamic magnetic susceptibility χ_d at $\omega_2(k) \gg \omega$ (as was noted above, this inequality is well satisfied in the range of ultrasonic frequencies), according to relationships (5) and (14), can be written as follows:

$$\chi_d = \left[h_{me4}\left(1 - \frac{1}{2}\sin^2\theta\right) + 2\gamma q_0^4\right]^{-1}. \qquad (21)$$

The transition from the ferromagnetic spiral phase to the cycloidal phase at $T = T_C$ leads to a decrease in the wave number q_0 [1]. As a result, the susceptibility χ_d sharply increases at the transition point, which manifests itself in an increase in the EMAT efficiency in the experimental dependence (Fig. 1). According to the *H*–*T* phase diagrams [3, 4], the transition from the ferromagnetic spiral phase to the cycloidal phase is accompanied by the appearance of a small peak in the EMAT efficiency at $T \approx 27$ K in the field $H = 10$ kOe and a peak in the EMAT efficiency at $T \approx 45$ K in the field $H = 20$ kOe.

It can be seen from Fig. 1 that the ferromagnetic spiral phase is characterized by one more EMAT efficiency peak in the field $H = 10$ kOe and, at the minimum, two more EMAT efficiency peaks in the field $H = 20$ kOe. The peak in the field $H = 10$ kOe is observed at the temperature $T = 20$ K. Analysis of the phase diagrams obtained in [3, 4] (despite their certain disagreement) suggests that this peak can be associated with the specific features in the characteristics of erbium in the range of the transition between the commensurate phase with a wave number of 5/21 and the incommensurate phase within the ferromagnetic spiral phase. In the field $H = 20$ kOe, the first peak at the temperature $T \approx 38$ K is very weakly pronounced and can be explained by the specific feature in the susceptibility upon the transition from the incommensurate phase to the commensurate phase with a wave number of 1/4 within the ferromagnetic spiral phase [3, 4]. Similarly, the second peak at the temperature $T \approx 27$ K can be due to the specific feature in the susceptibility upon the transition from the commensurate phase with a wave number of 1/4 to the commensurate phase with a wave number of 5/21 within the ferromagnetic spiral phase [3, 4].

Note that an increase in the external magnetic field results in a decrease in the equilibrium angle θ between the magnetization and the field. Consequently, an increase in the magnetic field strength can lead to an increase in the EMAT efficiency over the entire temperature range $T \le T_C$ by virtue of the presence of the multiplier $\cos^2\theta$ in relationship (20). This is also observed in the experimental dependence (Fig. 1).

5. CONCLUSIONS

Thus, the comparison of the experimental data on the EMAT efficiency for the Er rare-earth metal (Fig. 1) and the theoretical expressions describing the EMAT efficiency in the longitudinal spin wave and ferromagnetic spiral phases [relationships (17) and (20)] allowed us to make the following inferences.

Analysis of relationships (17) and (20) provides a qualitative explanation of the EMAT efficiency peaks observed in the experiment (Fig. 1) in the range of paramagnet–longitudinal spin wave, longitudinal spin wave–cycloid, and cycloid–ferromagnetic spiral phase transitions. These peaks are associated with the specific features in the static and dynamic susceptibilities of erbium in the vicinity of the above transitions. Unfortunately, a quantitative comparison of the experimental and theoretical results cannot be performed because of the large number of unknown parameters entering into relationships (17) and (20). A quantitative comparison calls for complex experimental measurements of these parameters at different temperatures and magnetic fields. To the best of our knowledge, similar experiments with erbium crystals have not been performed to date. Moreover, quantitative comparison is complicated by the fact that finite samples are usually used in experiments, whereas the theory is constructed for semi-infinite single crystals. However, as was shown in [6], the theory developed for semi-infinite crystals offers a qualitative explanation for all the main regularities of the electromagnetic–acoustic transformation in ferromagnetic metals. As follows from analyzing relationships (17) and (20) and Fig. 1, a similar statement is true for the electromagnetic–acoustic transformation in erbium single crystals.

The other EMAT efficiency peaks observed in the experiment can be associated with the specific features in the characteristics of erbium in the range of transitions either between two commensurate phases or between commensurate and incommensurate phases within the cycloidal and ferromagnetic spiral phases. In the present work, the phenomenological theory of the electromagnetic–acoustic transformation was developed in the continuum approximation. This theory cannot describe the commensurability effects and, correspondingly, the phase transitions between different commensurate and incommensurate phases in the cycloidal and ferromagnetic spiral phases [1]. In order to describe these transitions and the electromagnetic–acoustic transformation in the presence of commensurability effects, it is necessary to construct the microscopic theory of electromagnetic generation of ultrasound in rare-earth metals, which is a special problem. This problem remains unsolved because of its complexity. However, the comparison between the temperature dependences of the EMAT efficiency at different magnetic fields (Fig. 1) and the *H*–*T* phase diagram of erbium [3, 4] allowed us to draw the conclusion that the commensurability effects in the cycloidal and ferromagnetic spiral phases can actually be responsible for the other EMAT efficiency peaks.

ACKNOWLEDGMENTS

This work was supported in part by the Ministry of Education of the Russian Federation, project no. E00-3.4-536.

APPENDIX

The equilibrium strain tensor in the longitudinal spin wave phase has the form

$$\begin{gathered} U_{ik}^0 = 0 \quad (i \neq k), \\ U_{zz}^0 = -\frac{\gamma_{33}-\gamma_{31}}{c_{33}}M_z^2 - \frac{2c_{13}}{c_{33}}U_{xx}^0 - \frac{\gamma_1}{2c_{33}}M_z^2, \qquad \text{(A1)} \\ U_{xx}^0 = U_{yy}^0 = -\frac{c_{33}}{\Delta}\left(\tilde{\gamma}_1 - \frac{c_{13}}{c_{33}}\tilde{\gamma}_3\right)\sum_n M_n^z M_{-n}^z, \end{gathered}$$

where $\tilde{\gamma}_1 = \gamma_{13} - \gamma_{12} + \gamma_1/2$, $\tilde{\gamma}_3 = \gamma_{33} - \gamma_{31} + \gamma_3/2$, and $\Delta = c_{33}(c_{11} + c_{12}) - 2c_{13}^2$.

The equilibrium strain tensor in the ferromagnetic spiral phase at $qd \gg 1$ can be represented as follows:

$$\begin{gathered} U_{xx}^0 = U_{yy}^0 = -\frac{c_{33}}{2\Delta}(\gamma_{11}-\gamma_{12})M_0^2\sin^2\theta \\ -\frac{1}{\Delta}[c_{33}(\gamma_{13}-\gamma_{12}) - c_{13}(\gamma_{33}-\gamma_{31})]M_0^2\cos^2\theta, \\ U_{zz}^0 = -\frac{2c_{13}}{c_{33}}U_{xx}^0 - \frac{1}{c_{33}}(\gamma_{33}-\gamma_{31})M_0^2\cos^2\theta, \qquad \text{(A2)} \\ U_{xz}^0 = -\frac{\gamma_{44}}{4c_{44}}M_0^2\sin 2\theta\cos qz, \\ U_{yz}^0 = -\frac{\gamma_{44}}{4c_{44}}M_0^2\sin 2\theta\sin qz, \quad U_{xy}^0 = 0. \end{gathered}$$

REFERENCES

1. Yu. A. Izyumov, *Neutron Diffraction by Long-Period Structures* (Énergoatomizdat, Moscow, 1987).
2. R. A. Cowley and J. Jensen, J. Phys.: Condens. Matter **4**, 9673 (1992).
3. D. F. McMorrow, D. A. Jahan, R. A. Cowley, *et al.*, J. Phys.: Condens. Matter **4**, 8599 (1992).
4. H. Lin and M. F. Collins, Phys. Rev. B **45**, 12873 (1992).
5. D. Gibbs, J. Bohr, J. D. Axe, *et al.*, Phys. Rev. B **34**, 8182 (1986).
6. A. N. Vasil'ev and V. D. Buchel'nikov, Usp. Fiz. Nauk **162** (3), 89 (1992) [Sov. Phys. Usp. **35**, 192 (1992)].
7. A. V. Andrianov, A. N. Vasil'ev, Yu. P. Gaĭdukov, *et al.*, Fiz. Met. Metalloved. **64**, 1036 (1987).
8. A. V. Andrianov, V. D. Buchel'nikov, A. N. Vasil'ev, *et al.*, Zh. Éksp. Teor. Fiz. **97**, 1674 (1990) [Sov. Phys. JETP **70**, 944 (1990)].
9. V. D. Buchel'nikov, I. V. Bychkov, and V. G. Shavrov, Zh. Éksp. Teor. Fiz. **105**, 739 (1994) [JETP **78**, 396 (1994)].
10. C. M. Lim, S. Dixon, C. Edwards, and S. B. Palmer, J. Phys. D **31**, 1362 (1998).
11. C. M. Lim, C. Edwards, S. Dixon, and S. B. Palmer, J. Magn. Magn. Mater. **234**, 387 (2001).
12. V. D. Buchel'nikov and V. G. Shavrov, Fiz. Tverd. Tela (Leningrad) **31** (5), 81 (1989) [Sov. Phys. Solid State **31**, 765 (1989)].
13. V. D. Buchelnikov, I. V. Bychkov, and V. G. Shavrov, J. Magn. Magn. Mater. **118**, 169 (1993).
14. A. S. Borovik-Romanov, in *Advances of Science: Antiferromagnetism and Ferrites* (Akad. Nauk SSSR, Moscow, 1962).

Translated by O. Borovik-Romanova

Physics of the Solid State, Vol. 44, No. 11, 2002, pp. 2124–2129. Translated from Fizika Tverdogo Tela, Vol. 44, No. 11, 2002, pp. 2029–2034.
Original Russian Text Copyright © 2002 by Shvachko, Starichenko, Shmatov, Gobov.

MAGNETISM AND FERROELECTRICITY

Width of the Ferromagnetic Resonance Line in an Anisotropic Magnet in Misoriented Resonance and Scanning Magnetic Fields

Yu. N. Shvachko, D. V. Starichenko, G. A. Shmatov, and Yu. V. Gobov

Institute of Metal Physics, Ural Division, Russian Academy of Sciences,
ul. S. Kovalevskoĭ 18, Yekaterinburg, 620219 Russia
e-mail: Yurii.Shvachko@imp.uran.ru

Received February 11, 2002

Abstract—The dependence of the width ΔH_β of the ferromagnetic resonance (FMR) line in anisotropic magnets on the angle of misorientation β between the static (resonance) and scanning magnetic fields was investigated both experimentally and theoretically. The change in the linewidth is due to the dependence of the equilibrium orientation of the magnetization vector on the direction of the magnetic field upon the passage through the resonance. Using iron garnet films as an example, it was shown that under such a misorientation (a nonzero angle β) the linewidth is smallest. It was also shown that a two-dimensional representation of FMR spectra, in contrast to one-dimensional angular dependences of the resonance parameters, contains full information on the spectral characteristics of the film, including noncollinear field configurations. *© 2002 MAIK “Nauka/Interperiodica”.*

1. INTRODUCTION

The width of the line of ferromagnetic resonance (FMR) measured in the process of scanning of an external magnetic field H is determined as a range of fields

$$\Delta H_{pp} = H_{p+} - H_{p-} \qquad (1)$$

whose initial and final points, H_{p+} and H_{p-}, respectively, correspond to the positions of the maximum and minimum of the first derivative dP/dH of the signal of absorption of the high-frequency field $P(H)$ (the point of the maximum slope). In this case, the magnitude of the resonance field H_R, determined as the point of passage of the dP/dH signal through zero, always lies in the range of values $H_{p+} < H_R < H_{p-}$. In the traditional process of measuring an FMR linewidth, the directions of the scanning field $\mathbf{h}_{sw}$ and resonance field $\mathbf{H}_R$ are coincident. In other words, the signal is detected due to a change in only the amplitude of the external field in the vicinity of the resonance value. In this method of measurement of the linewidth, the orientation of the magnetic field with respect to the anisotropy axes remains unaltered in the process of measurement.

It is known that the linewidth ΔH_{pp} determined by this method is independent of the angle φ that specifies the orientation of the resonance magnetic field relative to the anisotropy axes. This function $\Delta H_{pp}(\varphi)$ is nonmonotonic; it has local maxima and minima whose number and positions are determined by the type of anisotropy and the magnitude of the corresponding constants [1].

The physical cause of the change in the linewidth ΔH_{pp} in films of anisotropic ferromagnets is the change in the orientation of the equilibrium magnetization $\mathbf{M}$ during the registration of the absorption line, as was shown in [2] and [3]. The calculations performed in these works showed that the width of the FMR line ΔH_{pp} increased with the deviation of the magnetic field from the anisotropy axis (directed along the normal to the film). The linewidth reaches maximum values in the vicinity of angles φ corresponding to the ranges of the fastest variation of the function $H_R(\varphi)$. The increase in the linewidth obtained in the above-cited works is related to the fact that they were concerned with a special case of orientation of the magnetic and scanning fields, namely, the fields were collinear. We may suppose that in the case of misorientated resonance and scanning fields the above mechanism of the linewidth variation will lead not only to a broadening but also, at certain angles, to a narrowing of the FMR line.

In this paper, we analyze the width of the FMR line ΔH_β measured at a certain angle β to the static field H_R rather than along this field. In this case, the amplitude of the scanning field changes in the range $[-h_{sw}, +h_{sw}]$ along a new direction and the resulting field $H = H_R + h_{sw}$ changes in both magnitude and direction. It follows from an analysis of the experimental dependence of the FMR linewidth ΔH_β in the mixed iron garnet on the misorientation angle β and on the direction of the magnetic field (φ) that the line width ΔH_β proves to be smaller than the conventionally measured value ΔH_{pp}. It was shown experimentally and substantiated theoretically that a two-dimensional representation of the signal $P(H, \varphi)$ of FMR absorption contains full information on all possible values of ΔH_β and, thus, permits one to determine an optimum configuration of the fields and the smallest value of the linewidth.

2. EXPERIMENTAL

As an object of investigation, we used a film of mixed iron garnet of composition $(Y_{1.15}Eu_{0.5}Bi_{0.5}Ca_{0.85})(Fe_{4.15}Si_{0.85})(O_{12})$ 2.92 μm thick grown by liquid-phase epitaxy. The values of the uniaxial anisotropy constant and quality factor were $K = 1.696 \times 10^4$ erg/cm^3 and $Q = 4.3$, respectively. The film composition was controlled by the weight ratio of the components in the initial charge. As a substrate, we used a gallium gadolinium garnet sample 0.5 mm thick with a surface (111) on which a thin film of yttrium iron garnet (YIG) 0.2 μm thick was applied. The narrow line of YIG was not observed in the FMR spectra of the sample. The application of an YIG layer ensures a higher time and temperature stability of the two-layer system and suppresses the formation of hard bubble domains. As is known, it is precisely those films with an easily modified composition that are the basis of magnetic electronics [4]. Therefore, obtaining additional information on the resonance characteristics under the conditions of noncollinear magnetic fields is of great importance. The problems of the interaction of modes in magnetically coupled two-layered systems and the techniques of measuring magnetic parameters from FMR data have been discussed in detail earlier in [5, 6].

A sample (1 × 0.5 mm) was mounted on a vertical stock at the antinodal point of the magnetic component of the microwave field of a TE_{102} resonator. The FMR spectra were recorded using a standard CW homodyne EPR spectrometer in the X range (9.45 GHz). The derivative of the FMR signal dP/dH was recorded at power levels $p < 2$ mW every 5° in the range of $\varphi = 0°$–$360°$. All measurements were performed at room temperature.

The geometry of the experiment is shown in Fig. 1. The axis of the sample rotation perpendicular to the figure plane coincides with the OX axis, and the direction of the normal to the film coincides with the OZ axis. As the film is rotated, the angle φ between the field direction $\mathbf{H}_R$ and the OZ axis changes. Upon analyzing the FMR spectra under misorientation conditions, a configuration is assumed in which the direction of scanning of the field $\mathbf{h}_{sw}$ makes an angle β with the direction $\mathbf{H}_R$. The magnetization vector lags behind the direction of the external field, which is characterized by the angle θ. It is shown in the work that in the two-dimensional representation of the spectra, we can always determine a variety of points corresponding to the FMR signal under conditions of misoriented fields with an arbitrary angle β.

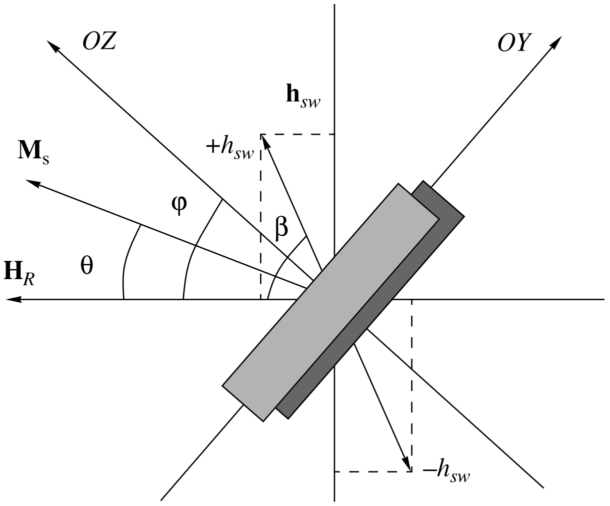

Fig. 1. Geometry of the experiment (for details, see the main text). The rotation of the film occurs about the OX axis. The vector $\mathbf{h}_{sw}$ directed at an angle β to the field $\mathbf{H} = \mathbf{H}_R$ corresponds to the effective scanning field under misorientation conditions (in the figure, corresponding parallel and perpendicular projections of $\mathbf{h}_{sw}$ are indicated).

In the process of measurements, each spectrum was integrated ($dP/dH \longrightarrow P(H)$) and was plotted in the form of a set of experimental points in a cylindrical coordinate system ($\rho, \varphi, Z) \longrightarrow (H, \varphi, P)$. Then, for each set of points with a fixed parameter H = const, we performed a procedure of smoothing of the dependence of P on the angle φ and subsequent approximation of the entire set of data in the form of a single surface $P(H, \varphi)$. Based on realistic spectra, we used a Lorentzian shape of the line when approximating the field dependence. As a result, the experimental set of 75000 points was described by a single surface in a relatively compact form. The general appearance of the surface for $(Y_{1.15}Eu_{0.5}Bi_{0.5}Ca_{0.85})(Fe_{4.15}Si_{0.85})(O_{12})$ is represented in Fig. 2.

Note that in the general case (complex spectra, anisotropies of various types, multilayered objects), the procedure of the choice of a single surface may prove to be inefficient because of a significant complexity. In this case, it appears to be more expedient to deal with an original set of data in the form of a 3D grid (a three-dimensional representation of a discrete set of data) and to perform the approximation using a smooth surface in the vicinities of singular points.

Note also that the method of recording in which a double scanning of the external field is performed for each fixed value of the azimuthal angle may also prove inefficient for the 3D representation of angular dependences. A fundamental advantage may be given by a method in which the sample rotates about the OX axis in such a way that the sample is rotated by 360° in a single elementary interval (step) of sweeping of the magnetic field. In this case, a large number of points at var-

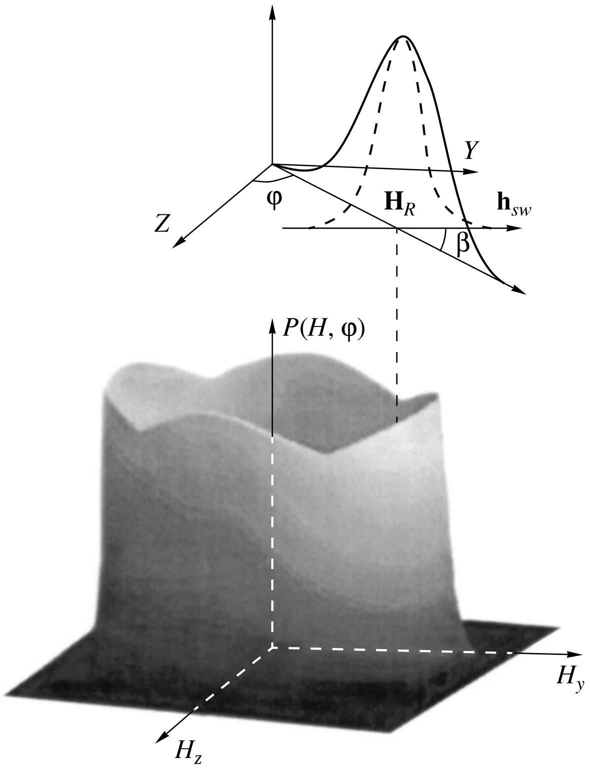

Fig. 2. Representation of the experimental angular dependence of the FMR spectrum $P(H, \varphi)$ for $(Y_{1.15}Eu_{0.5}Bi_{0.5}Ca_{0.85})(Fe_{4.15}Si_{0.85})(O_{12})$ in the form of an approximated surface in cylindrical coordinates (H, φ, P). The conventional absorption signal is a section of the surface along the radius vector $\mathbf{H}_R$. The FMR signal under misoriented conditions corresponds to a section in the vicinity of $\mathbf{H} = \mathbf{H}_R$ along the field $\mathbf{h}_{sw}$.

ious angles could be recorded in the course of a single act of sweeping with a field. The duration of the sweeping, which is determined by the inertia properties of the magnetic system, is usually $T = 3$–10 min, which means that the duration of an elementary step is $\Delta T \approx 0.2$ s. At the same time, it can easily be ensured that the sample is rotated at rates $\Omega \leq 1\ \mathrm{s}^{-1}$, so that during a rotation of the sample by 360° only a single scanning with the field is required at each sweeping step. If the condition

$$\Omega \ll (\tau)^{-1} \ll 2\pi f_{\mathrm{mod}} \qquad (2)$$

is fulfilled, where τ is the time of reading (with an analog–digital converter) and f_{mod} is the frequency of modulation of the field, the admissible number of values (angles) is $N \sim 1/\Omega\tau$. As a result, the total time of the experiment at $\Omega^{-1} \leq \Delta T$ does not exceed the duration of the recording of a single spectrum. At $\Omega^{-1} = 1$ s, the time of an experiment increases by a factor of $\Omega\Delta T = 5$ to be 15 min.

It can easily be shown that, upon successive variation of the angle between the normal to the surface of the sample and the plane *YOZ*, this procedure yields full information on the resonance properties of a magnet in spherical coordinates in the experiment with a single scanning of the magnetic field. In turn, the passage from the $1D$ spectra to a three-dimensional “portrait” permits one to pass to a qualitatively new analysis of the resonance properties of magnets from the viewpoint of the topological features of the corresponding equipotential surfaces and their sections.

From the methodological viewpoint, the $P(H, \varphi)$ surface shown in Fig. 2 represents a special case (section) of a $3D$ portrait. In turn, the case of a misoriented resonance and scanning fields, as can easily be shown, represents the intersection of this surface with a vertical plane that passes at an angle β to the plane $(H_R(\varphi), OX)$. In the general case, this plane can be inclined to the *YOZ* plane. In this case, the resultant curve represents an FMR spectrum under conditions of a noncollinear configuration. At fixed values of (H_R, φ), the points of the new spectrum $P(h, \beta)$ can be determined numerically by changing the coordinates into $P(H', \varphi')$ according to the following rule (Fig. 2):

$$H'^2 = H_R^2 + h_{sw}^2 + 2H_R h_{sw}\cos\beta, \qquad (3)$$

$$\varphi' = \varphi - \arcsin(h_{sw}\sin\beta). \qquad (4)$$

It is seen that for anisotropic magnets, the dependence of the linewidth ΔH_β on the angle β is nonmonotonic, exhibiting a local minimum with smallest values at certain angles φ that are different for different magnets.

3. PRINCIPAL EQUATIONS

In this section, we present a model that permits one to calculate the ΔH_β dependences and compare the experimental data with the results of calculation. It is known that in films of mixed iron garnets, the contribution to the angular dependence of H_R comes from both uniaxial (growth-related) and cubic (crystallographic) magnetic anisotropies. The applicability of the model of a uniaxial ferromagnet to samples with a cubic anisotropy is based on the fact that the constant of cubic anisotropy in the sample at hand was smaller by an order of magnitude than that of uniaxial anisotropy.

The dependence of the resonance field H_R on the angle φ that characterizes its orientation relative to the anisotropy axis is known to be determined from the equation for the natural frequency of uniform vibrations of magnetization [7]. In the model of a uniaxial ferromagnet, the magnitude of the resonance field is found from the equation

$$\left(\frac{\omega_R}{\gamma}\right)^2 = [H_R\cos(\theta-\varphi) + H_A\cos^2\theta] \times [H_R\cos(\theta-\varphi) + H_A\cos(2\theta)], \qquad (5)$$

where ω_R is the resonance frequency, γ is the gyromagnetic ratio, θ is the angle of the equilibrium orientation of the magnetization vector **M** in the field $\mathbf{H}_R$ reckoned from the anisotropy axis, $H_A = 2K/M - 4\pi M$ is the effective field of anisotropy, K is the uniaxial anisotropy constant, and M is the saturation magnetization. The angle θ is found by minimizing the free energy of the system, which, in the case of a uniaxial ferromagnet, leads to the relations

$$\begin{gathered} H_A\sin2\theta + 2H_R\sin(\theta-\varphi) = 0, \\ H_A\cos2\theta + 2H_R\cos(\theta-\varphi) > 0. \end{gathered} \tag{6}$$

Thus, at a given angle φ of the orientation of the magnetic field and the parameters of the problem (ω_R, K, M, γ), we can find H_R and θ can be found from Eqs. (5) and (6).

The method of the calculation of the linewidth ΔH_β is described in [8], where, using the example of a uniaxial ferromagnet, the following expression was obtained for the width of the FMR line measured at an arbitrary angle β to the direction of the resonance field:

$$\Delta H_\beta = F_\beta \Delta H_{pp}, \tag{7}$$

where

$$F_\beta = (\cos\beta + G\sin\beta)^{-1}, \tag{8}$$

$$\begin{gathered} G = \frac{1}{H_R}\frac{dH_R}{d\varphi} = \tan(\varphi-\theta) + \{\sin(\theta-\varphi) \\ + h\sin2\theta[1+\sin\varphi(2\sin\varphi - h\sin^3\theta)^{-1}]\} \\ \times[\cos(\theta-\varphi) + h\cos2\theta]^{-1} \end{gathered} \tag{9}$$

($h = H_A/H_R$). Thus, the linewidth ΔH_β is expressed through the known quantity ΔH_{pp} and the function F_β depending on the angles β and φ and on the ratio H_A/H_R. In this case, the equilibrium angle of the magnetization θ and the magnitude of the resonance field H_R entering into Eq. (8) can be found from the set of equations (5) and (6).

The method of calculating ΔH_{pp} was described in [3], where it was shown that the fields $H_{p+}(\varphi)$ and $H_{p-}(\varphi)$ entering into the definition of the linewidth $\Delta H_{pp}(\varphi)$ (Eq. (1)) can be found from the set of equations (5) and (6), in which one should substitute the frequencies

$$\omega_{p+} = (1-\alpha)\omega_R, \quad \omega_{p-} = (1+\alpha)\omega_R \tag{10}$$

for the resonance frequency ω_R (α is the damping parameter). In other words, the linewidth ΔH_{pp} is found by doubly solving the set of equations (5), (6) with respect to the fields H_{p+} and H_{p-}. For the angles $0 < \varphi < \pi/2$, this set of equations can be solved only numerically. However, for two directions ($\varphi = 0, \pi/2$), as was shown in [8], we can obtain analytical expressions for the linewidth ΔH_{pp}. Namely, at $\varphi = 0$ (the resonance field parallel to the anisotropy axis), we have

$$\Delta H_\parallel \equiv \Delta H_{pp}(0) = H_{p-} - H_{p+} = 2\alpha\frac{\omega_R}{\gamma}. \tag{11}$$

If $\varphi = \pi/2$ (the resonance field perpendicular to the anisotropy axis), we obtain

$$\begin{aligned} \Delta H_\perp &\equiv \Delta H_{pp}(\pi/2) \\ &= H_{p-} - H_{p+} = 2\alpha\frac{\omega_R}{\gamma}\left(1+\frac{h_A^2}{4}\right)^{-1/2}. \end{aligned} \tag{12}$$

Here, $h_A = H_A/(\omega_R/\gamma)$ is the normalized anisotropy field. It follows from Eq. (12) that if the magnetic field is perpendicular to the anisotropy axis, then, irrespective of the sign of the effective field H_A, the linewidth decreases as compared to the isotropic case.

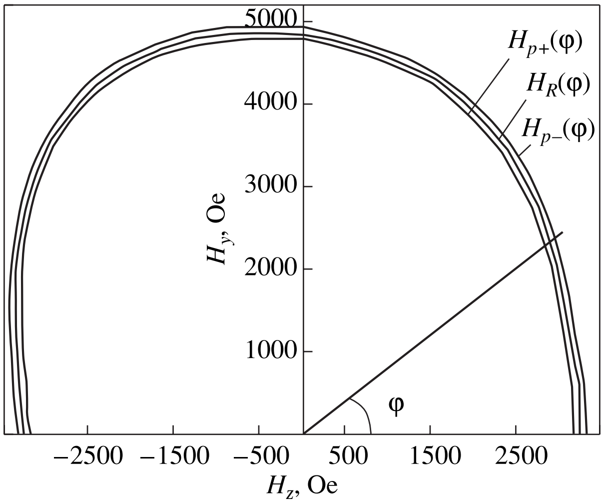

Fig. 3. Experimental angular dependences of three parameters of the FMR spectrum for $(Y_{1.15}Eu_{0.5}Bi_{0.5}Ca_{0.85})(Fe_{4.15}Si_{0.85})(O_{12})$ in polar coordinates (H, φ): maximum $H_{p+}(\varphi)$, minimum $H_{p-}(\varphi)$, and the values of the resonance field $H_R(\varphi)$ corresponding to the first derivative of the absorption signal dP/dH in the angular range $0° \le \varphi \le 180°$ (the angle φ is shown in Fig. 1).

4. DISCUSSION

In the case of a single FMR line of a Lorentzian shape, the analysis of the $P(H, \varphi)$ dependences is significantly simplified. Figure 3 displays experimentally obtained angular dependences of the three fields $H_{p+}(\varphi)$, $H_R(\varphi)$, and $H_{p-}(\varphi)$ in the range $0° \le \varphi \le 180°$. In this figure, the angle φ is a parameter and the coordinate axes correspond to the projections of the external field onto the axes OZ and OY, respectively. These curves also contain information on the angular dependence of the linewidth $\Delta H_{pp}(\varphi)$; namely, the linewidth

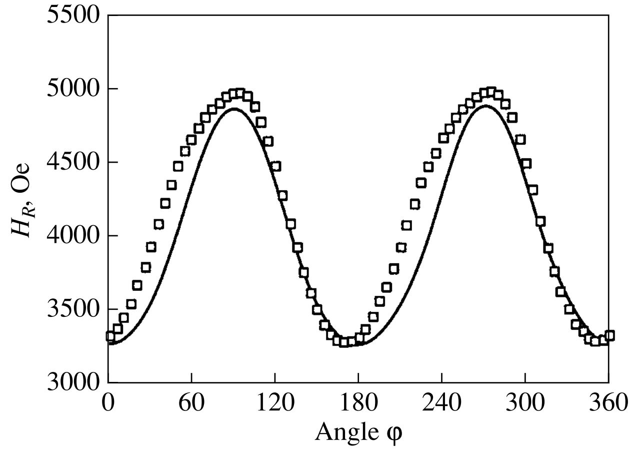

Fig. 4. Experimental (points) and theoretical (line) dependences of the resonance field $H_R(\varphi)$. The magnitudes of the parameters of the model are as follows: $f_R = \omega_R/2\pi = 9.5$ GHz, $\omega_R/\gamma = 4.31$ kOe, $M = 25$ G, and $H_A = 1.04$ kOe.

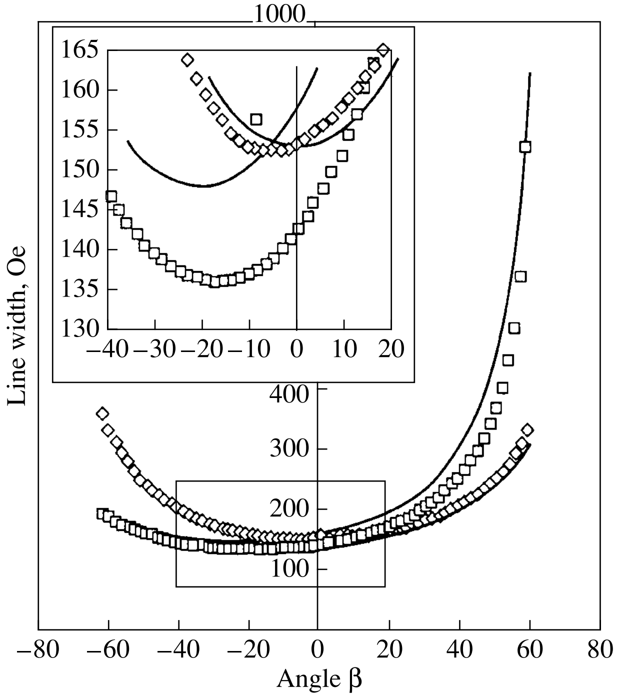

Fig. 5. Variation of the FMR linewidth as a function of the misorientation angle between the resonance and scanning fields at $\alpha = 0.018$. Other parameters: $\varphi = 60°$ (squares, experiment); $\varphi = 90°$ (rhombi, experiment); lines show the corresponding calculated dependences.

at a fixed φ is numerically equal to the distance between the first and third curves along the position vector $\mathbf{H}_R(\varphi)$. The slight asymmetry of the curves in quadrants I and II is due to the deviation of the easy axis from the normal to the surface and to the contribution from cubic anisotropy.

Figure 4 compares the experimental data with the $H_R(\varphi)$ dependence calculated according to Eqs. (5) and (6). As the parameters of the theory, we also used experimentally measured quantities (for the numerical values of the parameters, see the caption to Fig. 4). As might be expected, the model of the uniaxial ferromagnet satisfactorily describes experimental data in the case of a small constant of cubic anisotropy.

Figure 5 displays the experimentally obtained data (points) and the results calculated in accordance with the above model (lines) for the dependences of the linewidth on the misorientation angle β between the resonance and scanning fields. When comparing them, we should take into account that the error of the experimental measurement of the width of the FMR line is about 5%. In the case of a single symmetrical line, there is no need to construct sections of the surface for each (φ, β) set (Fig. 2), since the magnitudes of ΔH_β coincide with the distance $[H_{p-}(\varphi_1) + H_{p+}(\varphi_2)]$ intercepted by a straight line passing through the point $H_R(\varphi)$ and the origin at an angle β to the radius vector (Fig. 3). For more complex spectra, this simplification is invalid and we should perform the procedure of intersecting the surface described above. The width of the FMR line observed experimentally along the resonance field varied from 133 to 152 Oe.

In Fig. 5, both the theoretical and experimental curves are given for two directions of the magnetic field with respect to the anisotropy axis. Cases 1 and 2 correspond to the angles $\varphi = 60°$ and $90°$. It is seen from the figure that if $\varphi = 90°$ (the resonance field lies in the film plane), then the minimum width of the FMR line is observed at $\beta = 0$; i.e., the minimum width corresponds to the linewidth traditionally measured along the resonance field. However, as follows from the experiment and calculations, when the resonance field deviates by 30° from the film plane ($\varphi = 60°$), the minimum linewidth is observed at the misorientation angle $\beta = 20°$. Note that although the minimum linewidth for the $(Y_{1.15}Eu_{0.5}Bi_{0.5}Ca_{0.85})(Fe_{4.15}Si_{0.85})(O_{12})$ film at hand decreases insignificantly (by 10%), a significant fact is that the minimum linewidth is observed upon misorientations between the resonance and scanning fields as small as 20°. The latter means that we can select such a geometry of the resonance and scanning fields for the fields to be misoriented up to angles close to 90° but the linewidth to increase only insignificantly. This fact is, in particular, important from the applied viewpoint, since it offers additional opportunities, e.g., for the development of devices of microwave electronics based on FMR of spin waves.

5. CONCLUSION

Thus, in this paper, we established, using the example of an iron garnet film, that the minimum width of the FMR line in anisotropic magnets is realized in the case of a noncollinear configuration of the resonance and scanning magnetic fields. Information on the optimum configuration (on the angles φ and β) is contained in the two-dimensional representation of the FMR spectra in the form of a $P(H, \varphi)$ surface. The determination of this configuration reduces to seeking the section of this surface that yields a line with the smallest width. Such an analysis can be useful for the investigation of the interaction of modes in two-layer and multilayer magnetic films. Note that the passage from 1*D* spectra to a three-dimensional portrait permits us to go to a qualitatively new analysis of resonance properties of magnets from the viewpoint of topological features of the corresponding equipotential surfaces and their sections.

In addition, the results obtained permit us to suggest a new method of controlling the width of the FMR line in anisotropic magnets, which consists in variation of the orientation of the scanning field with respect to the resonance field. Such a variation can be sufficiently simply realized by applying, in the presence of a constant resonance field, an additional (scanning) magnetic field at a certain angle with respect to the resonance field. This method of controlling the width of the FMR line is of practical importance. For example, in the devices of microwave electronics, the resonance field is most frequently created with dc magnets, whereas the controlling (scanning) field is produced with coils. In such a situation, it is sometimes technologically convenient if the resonance and controlling fields are misoriented, but in such a way that the linewidth does not increase significantly. In particular, this permits one to additionally miniaturize the devices of microwave electronics.

ACKNOWLEDGMENTS

We are grateful to A.V. Kobelev for fruitful discussions. The work was supported in part by the Russian Foundation for Basic Research, project no. 00-15-96745.

REFERENCES

1. G. V. Skrotskiĭ and L. V. Kurbatov, in *Ferromagnetic Resonance* (Fizmatgiz, Moscow, 1961), p. 25.
2. F. G. Bar'yakhtar, V. L. Dorman, and N. M. Kovtun, Fiz. Tverd. Tela (Leningrad) **26** (12), 3646 (1984) [Sov. Phys. Solid State **26**, 2192 (1984)].
3. A. M. Zyuzin, Fiz. Tverd. Tela (Leningrad) **31** (7), 109 (1989) [Sov. Phys. Solid State **31**, 1161 (1989)].
4. A. H. Eschenfelder, *Magnetic Bubble Technology* (Springer, Berlin, 1980; Mir, Moscow, 1983).
5. A. V. Kobelev, V. P. Gogin, V. A. Matveev, *et al.*, Zh. Tekh. Fiz. **59** (2), 95 (1989) [Sov. Phys. Tech. Phys. **34**, 185 (1989)].
6. A. V. Kobelev, M. V. Perepelkina, A. A. Romanyukha, *et al.*, Zh. Tekh. Fiz. **60** (5), 117 (1990) [Sov. Phys. Tech. Phys. **35**, 605 (1990)].
7. A. G. Gurevich and G. A. Melkov, *Magnetic Oscillations and Waves* (Nauka, Moscow, 1994), p. 55.
8. G. A. Shmatov and Yu. L. Gobov, Fiz. Met. Metalloved. **88** (4), 16 (1999).

Translated by S. Gorin

Physics of the Solid State, Vol. 44, No. 11, 2002, pp. 2130–2144. Translated from Fizika Tverdogo Tela, Vol. 44, No. 11, 2002, pp. 2035–2048.
Original Russian Text Copyright © 2002 by Golovenchits, Sanina, Levin, Shepelev, Smolin.

MAGNETISM AND FERROELECTRICITY

Thermal Vibrations and the Structure of Quasi-Two-Dimensional R_2CuO$_4$ Crystals (R = La, Pr, Nd, Sm, Eu, and Gd)

E. I. Golovenchits[1], V. A. Sanina[1], A. A. Levin[2, 3], Yu. F. Shepelev[2], and Yu. I. Smolin[2]

[1] *Ioffe Physicotechnical Institute, Russian Academy of Sciences, Politekhnicheskaya ul. 26, St. Petersburg, 194021 Russia*
e-mail: E.Golovenchits@pop.ioffe.rssi.ru
[2] *Grebenshchikov Institute of Silicate Chemistry, Russian Academy of Sciences,*
ul. Odoevskogo 24/2, St. Petersburg, 199155 Russia
[3] *Institute of Crystallography and Solid-State Physics, Technical University, Dresden, D-1062 Germany*

Received January 18, 2002

Abstract—Thermal vibrations of ions in R_2CuO$_4$ crystals (R = La, Pr, Nd, Sm, Eu, Gd) were studied by x-ray diffractometry. A comparative analysis of thermal displacements of the copper and rare-earth ions permitted a conclusion as to the main interactions responsible for the structural state of the CuO$_2$ sheets and of a crystal as a whole. The structural properties were found to correlate with the magnitude of the ionic radius and with the ground state of the rare-earth ions. © *2002 MAIK “Nauka/Interperiodica”.*

1. INTRODUCTION

Thermal vibrations of ions in a crystal are determined by the symmetry and strength of the local crystal-field potential. This permits one to obtain information on the local potential by studying the spatial distribution of thermal ion displacements using diffraction methods. Our previous communications [1, 2] reported on an investigation of thermal vibrations of the Cu^{2+} and rare-earth (RE) ions in R_2CuO$_4$ crystals (R = La, Eu, Pr, Gd). Main attention was focused on the temperature dependence of the probability density function (PDF), which characterizes the spatial distribution of equally probable displacements of ions relative to their equilibrium positions. We succeeded in following the temperature-induced local structural distortions and structural phase transitions in the crystals under study.

The purpose of this study was to compare the PDFs of the Cu^{2+} and RE ions at a fixed temperature for a broader class of R_2CuO$_4$ crystals (R = La, Pr, Nd, Sm, Eu, Gd) and to follow the influence of the RE ions on the properties of the CuO$_2$ sheets and on the crystal structure as a whole. To do this, we studied, in addition to data obtained earlier, thermal vibrations in Nd$_2$CuO$_4$ and Sm$_2$CuO$_4$ crystals (at temperatures of 296 and 373 K). The analysis of the PDF for the Cu^{2+} and RE ions was carried out for the whole class of R_2CuO$_4$ crystals (R = La, Pr, Nd, Sm, Eu, Gd) at room temperature, taking into account the earlier data reported in [1, 2].

The structure of the La$_2$CuO$_4$ and R_2CuO$_4$ crystals with RE ions (R = Pr, Nd, Sm, Eu, Gd) is presented in Fig. 1. The R_2CuO$_4$ crystals (R = Pr, Nd, Sm, Eu) have T' structure (space group $I4/mmm$) at all temperatures. La$_2$CuO$_4$ and Gd$_2$CuO$_4$ undergo phase transitions from the high-temperature tetragonal to the low-temperature orthorhombic phase (see [3] and [4], respectively). A common feature in the structure of the La$_2$CuO$_4$ and R_2CuO$_4$ crystals with RE ions is its quasi-2D character. The ions are arranged in layers perpendicular to the c axis. Layers of R^{3+} and O^{2-} ions are sandwiched between the CuO$_2$ planes. The distances between the CuO$_2$ sheets and the layers containing copper and RE

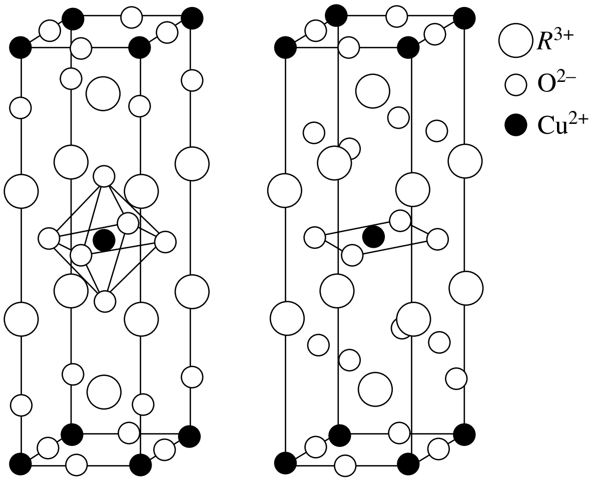

T
(a)

T'
(b)

Fig. 1. Crystal structure of (a) La$_2$CuO$_4$ and (b) R_2CuO$_4$ (R = Pr, Nd, Sm, Eu, Gd).

1063-7834/02/4411-2130$22.00 © 2002 MAIK “Nauka/Interperiodica”

ions exceed by far those between the in-plane ions. We are interested primarily in the properties of CuO_2 layers separated at a distance of $c/2$. The nearest environment of Cu^{2+} ions in La_2CuO_4 differs from that in R_2CuO_4 with RE ions. In La_2CuO_4, we have octahedra of O^{2-} ions (coordination number $Z = 6$), and in R_2CuO_4 with RE ions, we have squares of oxygen ions ($Z = 4$). The structural properties of the crystals under study are determined by in-plane interactions in the CuO_2 sheets and the layers containing RE ions, as well as by interlayer coupling (primarily between the Cu^{2+} and R^{3+} ions). We study here the main interactions responsible for the structural properties of the crystals and their dependence on the properties of the RE ions.

The cubic crystal-field potential is usually ~1 eV. The tetragonal distortions of the cubic lattice are related to a change in this potential by about ~0.1 eV. The anomalously strong 2D Heisenberg exchange interaction between the Cu^{2+} ion spins (exchange constant $J \sim 0.13$–0.15 eV [5]) and the spin–orbit (SO) coupling of Cu^{2+} ions with a constant $\lambda \sim 0.06$–0.08 eV [6] are practically of the same magnitude in the crystals under study. As a result, Cu^{2+} ions in the R_2CuO_4 crystals with RE ions are involved in a number of interactions of similar magnitude, which determine various, including structural, properties of the crystals.

As shown in [1, 2], the character of the PDF and, hence, the symmetries of the local crystal-field potential of the Cu^{2+} and RE ions in R_2CuO_4 crystals (R = La, Pr, Eu, Gd) are different. However, local distortions in CuO_2 layers were found to be dominant in all these crystals in the temperature interval 140–400 K. As follows from the present study, distortions in these layers are also dominant in Nd_2CuO_4. Only in Sm_2CuO_4 at room temperature do Jahn–Teller distortions for the Sm^{3+} ions dominate and is the character of the copper ion PDF determined primarily by the Sm^{3+}–Cu^{2+} interaction.

Thermal vibrations in Pr_2CuO_4 at room temperature were probed using neutron scattering [7]. A comparison of the measurements carried out on Pr_2CuO_4 and CuO crystals suggests [7] that the dynamic behavior of copper ions in Pr_2CuO_4 is a result of interaction mainly with the nearest neighbor oxygen atoms. At the same time, Raman scattering measurements performed on a number of R_2CuO_4 crystals (R = Pr, Nd, Sm, Gd), also at room temperature, suggest that the RE ions have a substantial effect on phonon spectra. It has been pointed out that the part played by the Cu–R coupling increases with decreasing RE ionic radius [8].

Gd_2CuO_4 occupies a special place among the R_2CuO_4 crystals with RE ions. This crystal undergoes a structural phase transition to the low-temperature orthorhombic phase ($T < 650$ K) [4]. The orthorhombic distortions in the CuO_2 layers originate from the oxygen OI ions rotating about the copper ions [4].

A study of the spin and lattice dynamics in R_2CuO_4 crystals (Pr, Sm, Eu), carried out in the millimeter range at low temperatures, revealed jumps in the microwave power absorption which were assigned to structural phase transitions [9]. A structural phase transition in Eu_2CuO_4 at $T \approx 150$ K was also observed to occur using other techniques [10–12]. The properties of the low-temperature phases and the transition points in R_2CuO_4 (Pr, Sm, Eu) were different for different crystals and are most likely determined by the RE ions.

Our present data show that the structural properties of the CuO_2 layers and of the crystal as a whole for R_2CuO_4 crystals with RE ions depend on the RE ions present in the crystals.

2. EXPERIMENTAL RESULTS

We carried out a complete x-ray diffraction characterization of the Sm_2CuO_4 and Nd_2CuO_4 crystals at temperatures of 296 and 373 K. The measurements were performed on single crystals grown by the spontaneous-crystallization method described in [2]. The crystals were stoichiometric in composition and dielectric.

The samples used for the diffractometric studies were rectangular prisms measuring 0.17 × 0.18 × 0.11 mm (Sm_2CuO_4) and 0.12 × 0.11 × 0.11 mm (Nd_2CuO_4). All measurements were taken on the same samples and in the same setup.

A preliminary diffractometric investigation showed the Sm_2CuO_4 and Nd_2CuO_4 crystals to have tetragonal symmetry (space group $I4/mmm$). The x-ray reflection intensities were measured up to the value $\sin\Theta/\lambda = 1.075$ Å^{-1} on an automated three-circle, single-crystal diffractometer in the normal-inclination, layer-by-layer ω scanning mode by properly rotating the crystal about the a axis. The MoK_α radiation used ($\lambda = 0.71069$ Å) was passed through a graphite monochromator.

The crystal structures were refined by least-squares techniques in the block-matrix approximation, basically, by the scheme employed in [1, 2]. The parameters of the cation temperature factors were refined in the fourth-order anharmonic approximation. The data thus obtained were used to construct the ion probability density functions, which are Fourier transforms of the corresponding temperature factors. To reduce the regions of negative values of the PDF which form when refining anharmonic parameters by least-squares techniques, we employed the Gram–Charlier model of the temperature factor [13]:

$$T(\mathbf{h}) = T_{\mathrm{harm}}(\mathbf{h})[1 + (2\pi i)^3/3!c_{pqr}\mathbf{h}_p\mathbf{h}_q\mathbf{h}_r + (2\pi i)^4/4!d_{pqrs}\mathbf{h}_p\mathbf{h}_q\mathbf{h}_r\mathbf{h}_s]. \tag{1}$$

Here, $T_{\mathrm{harm}}(\mathbf{h}) = \exp(-\beta_{pq}\mathbf{h}_p\mathbf{h}_q)$; β_{pq} are anisotropic harmonic temperature parameters; c_{pqr} and d_{pqrs} are the

Table 1. Details of the experiment and structural parameters of R_2CuO$_4$ single crystals at room temperature

Parameter	La$_2$CuO$_4$[a]	Pr$_2$CuO$_4$	Nd$_2$CuO$_4$	Sm$_2$CuO$_4$	Eu$_2$CuO$_4$	Gd$_2$CuO$_4$
Space group	*Abma*	*I*4/*mmm*	*I*4/*mmm*	*I*4/*mmm*	*I*4/*mmm*	*I*4/*mmm*
a, Å	5.397(3)	3.953(2)	3.944(1)	3.921(1)	3.897(3)	3.895(1)
b, Å	5.365(3)	*a*	*a*	*a*	*a*	*a*
c, Å	13.165(2)	12.232(3)	12.147(2)	11.994(2)	11.905(2)	11.8952(6)
N_{refl} ($I > 3\sigma(I)$)[b]	640	250	198	170	285	250
R, %[c]	3.23	2.79	1.79	2.09	4.00	2.79
R_W, %[d]	3.34	2.24	2.37	2.27	4.19	2.95
μ, cm^{-1}[e]	275.3(3)	304.3(1)	324.9(3)	370.6(3)	400.8(4)	423.3(1)
r_{ext}, Å[f]	1835(14)	3288(15)	2082(17)	5564(44)	7868(49)	2897(35)

Note: [a] La$_2$CuO$_4$ is twinned pseudomerohedrally along the (110) planes. Extinctions of the twin-domain reflections satisfy the *Abma* and *Bmab* space groups. Least-squares refinement yields for the twinning coefficient $K_{\text{tw}} = 0.68(2)$, which corresponds to the 2 : 1 ratio for the components described by lattices *A* and *B*;

[b] N_{refl} is the number of independent nonzero reflections;

[c] *R* is the structural divergence factor;

[d] R_W is the weighting factor of divergence according to the Cruckshank scheme [14];

[e] μ is the absorption coefficient (for MoK_α). The absorption was taken into account by numerical integration over the crystal volume;

[f] r_{ext} is the least-squares value of the extinction parameter. The extinction was taken into account using the method of Becker and Coppens [15] in isotropic approximation for crystals with $r_{\text{ext}} \ll \lambda g$ and a Lorentzian mosaic-block distribution.

Table 2. Refined room-temperature parameters for Cu^{2+}(0, 0, 0) ions in R_2CuO$_4$ crystals (R = La, Pr, Nd, Sm, Eu, Gd)

Parameter	La	Pr	Nd	Sm	Eu	Gd
B_{eq}, Å^2	0.67(1)	0.439(6)	0.43(2)	0.48(1)	0.42(1)	0.45(1)
U_{11}, Å	0.085(1)	0.0861(3)	0.055(1)	0.075(1)	0.072(2)	0.072(1)
U_{22}, Å	0.088(2)	U_{11}	U_{11}	U_{11}	U_{11}	U_{11}
U_{33}, Å	0.101(1)	0.079(1)	0.100(4)	0.084(4)	0.075(2)	0.075(2)
U_{13}, Å	0.006(30)	0	0	0	0	0
$d_{1111} \times 10^9$	154(49)	130(148)	–172(141)	1065(794)	–19(305)	305(262)
$d_{2222} \times 10^9$	–686(69)	d_{1111}	d_{1111}	d_{1111}	d_{1111}	d_{1111}
$d_{3333} \times 10^9$	–0.4(7)	0.3(10)	39(14)	–5(2)	–5(2)	–7(21)
$d_{1113} \times 10^9$	2(8)	0	0	0	0	0
$d_{1333} \times 10^9$	1(1)	0	0	0	0	0
$d_{1122} \times 10^9$	73(18)	325(71)	82(63)	–424(129)	–321(163)	649(132)
$d_{1133} \times 10^9$	13(3)	–8(8)	–41(17)	–17(19)	69(16)	58(16)
$d_{2233} \times 10^9$	–23(4)	d_{1133}	d_{1133}	d_{1133}	d_{1133}	d_{1133}
$d_{1223} \times 10^9$	–1(7)	0	0	0	0	0

Note: U_{ii} are RMS temperature-induced atomic displacements (harmonic part of the temperature factor); $U_{ij} = \text{sgn}(\beta_{ij})sqrt(\beta_{ij}/(2\pi)^2\mathbf{a}_i\mathbf{a}_j)$; d_{pqrs} are fourth-order anharmonic temperature parameters; B_{eq} is the equivalent isotropic temperature factor; $B_{\text{eq}} = 4/3\Sigma\beta_{ij}\mathbf{a}_i\mathbf{a}_j$, where β_{ij} are anisotropic temperature factors.

anharmonic temperature parameters of the third and fourth order, respectively; and **h** is the scattering vector with components (h_1, h_2, h_3) = (h, k, l).

The same method was applied to refine the room-temperature structural parameters of the La$_2$CuO$_4$ and Eu$_2$CuO$_4$ crystals studied by us earlier [1] by using the Edgeworth anharmonic approximation of the cation temperature factors [13]. The cation PDFs obtained in both models of the anharmonic temperature factor are qualitatively similar.

The experimental and main structural parameters of the crystals studied are listed in Tables 1–5. Figures 2 and 3 display the PDFs of the Cu^{2+} ions in R_2CuO$_4$ crystals (R = La, Pr, Nd, Sm, Eu, Gd) calculated for room

Table 3. Refined room-temperature parameters for R^{3+} ions (x/a, 0, z/c) in R_2CuO_4 crystals (R = La, Pr, Nd, Sm, Eu, Gd)

Parameter	La	Pr	Nd	Sm	Eu	Gd
x/a	0.00227(4)	0	0	0	0	0
z/c	0.36136(1)	0.35132(2)	0.35149(4)	0.35057(3)	0.35009(3)	0.34922(3)
B_{eq}, Å^2	0.718(4)	0.522(2)	0.556(7)	0.494(3)	0.389(4)	0.478(3)
U_{11}, Å	0.0938(5)	0.0861(3)	0.0578(4)	0.0850(4)	0.0758(6)	0.0832(4)
U_{22}, Å	0.1126(6)	U_{11}	U_{11}	U_{11}	U_{11}	U_{11}
U_{33}, Å	0.0761(6)	0.0707(4)	0.1201(13)	0.0658(7)	0.0575(10)	0.0655(7)
U_{13}, Å	0.057(13)	0	0	0	0	0
$c_{111} \times 10^8$	14(13)	0	0	0	0	0
$c_{333} \times 10^8$	–2(5)	–0.7(8)	–20(6)	–2.4(15)	–2(1)	–1.4(14)
$c_{122} \times 10^8$	–5(10)	0	0	0	0	0
$c_{113} \times 10^8$	8(4)	–19(10)	6(12)	–1(160)	–19(16)	–25(16)
$c_{133} \times 10^8$	1(1)	0	0	0	0	0
$c_{223} \times 10^8$	1(5)	c_{113}	c_{113}	c_{113}	c_{113}	c_{113}
$d_{1111} \times 10^9$	–309(7)	786(49)	–139(47)	887(242)	491(95)	765(78)
$d_{2222} \times 10^9$	–1410(26)	d_{1111}	d_{1111}	d_{1111}	d_{1111}	d_{1111}
$d_{3333} \times 10^9$	–0.2(2)	1.5(3)	135(7)	–3.6(5)	1.6(6)	–3.4(5)
$d_{1113} \times 10^9$	–2(3)	0	0	0	0	0
$d_{1333} \times 10^9$	0.5(5)	0	0	0	0	0
$d_{1122} \times 10^9$	363(6)	–513(24)	67(22)	–363(62)	–632(47)	–673(36)
$d_{1133} \times 10^9$	16(1)	–12(2)	–47(7)	–14(5)	13(5)	36(4)
$d_{2233} \times 10^9$	–15(1)	d_{1133}	d_{1133}	d_{1133}	d_{1133}	d_{1133}
$d_{1223} \times 10^9$	1(3)	0	0	0	0	0

Note: Notation for the quantities B_{eq}, U_{ii}, U_{ij}, and d_{pqrs} is the same as in Table 2; c_{pqr} are third-order anharmonic temperature parameters.

Table 4. Refined cation parameters for Nd_2CuO_4 (space group $I4/mmm$, a = 3.950(1) Å, c = 12.153(1) Å, N_{refl} = 178, R = 1.87%, R_W = 2.82%) and Sm_2CuO_4 (space group $I4/mmm$, a = 3.926(1) Å, c = 12.014(1) Å, N_{refl} = 168, R = 2.37%, R_W = 2.44%) at 373 K

Parameter	Nd_2CuO_4		Sm_2CuO_4	
	Nd	Cu	Sm	Cu
z/c	0.35079(7)	0	0.35055(2)	0
B_{eq}, Å^2	2.33(2)	2.31(5)	0.666(3)	0.65(1)
U_{11}, Å	0.0588(6)	0.047(2)	0.0969(4)	0.087(1)
U_{22}, Å	U_{11}	U_{11}	U_{11}	U_{11}
U_{33}, Å	0.2854(12)	0.289(3)	0.0807(6)	0.097(2)
$c_{333} \times 10^8$	–25(19)	0	38(14)	79(359)
$c_{113} \times 10^8$	31(25)	0	–124(166)	–1(160)
$c_{223} \times 10^8$	c_{113}	0	c_{113}	0
$d_{1111} \times 10^9$	–132(79)	–86(210)	564(105)	79(359)
$d_{2222} \times 10^9$	d_{1111}	d_{1111}	d_{1111}	d_{1111}
$d_{3333} \times 10^9$	49(17)	–34(48)	–0.6(5)	–10(2)
$d_{1122} \times 10^9$	69(33)	44(97)	–74(28)	–49(97)
$d_{1133} \times 10^9$	–43(15)	–22(47)	–12(4)	19(16)
$d_{2233} \times 10^9$	d_{1133}	d_{1133}	d_{1133}	d_{1133}

Note: Notation for the quantities B_{eq}, U_{ii}, U_{ij}, c_{pqr}, and d_{pqrs} is the same as in Tables 2 and 3.

Table 5. Room-temperature distances between ions (Å) in R_2CuO_4 crystals (R = La, Nd, Sm, Eu)

Parameter	La_2CuO_4	Nd_2CuO_4	Sm_2CuO_4	Eu_2CuO_4
R–O2	2.323(4)	2.3256(5) × 4	2.3019(5) × 4	2.284(1) × 4
R–O1	2.620(3) × 2	2.6726(5) × 4	2.6563(8) × 4	2.642(1) × 4
R–O1'	2.654(3) × 2	–	–	–
R–O2'	2.684(6)	–	–	–
R–O2''	2.752(2) × 2	–	–	–
R–O2'''	2.850(6)	–	–	–
Cu–O1	1.9028(8) × 4	1.9720(5) × 4	1.9605(5) × 4	1.948(1) × 4
Cu–O2	2.437(4) × 2	–	–	–

temperature. Figures 4 and 5 show the room-temperature PDFs of the R^{3+} ions calculated for the same crystals. Figures 6 and 7 present the PDFs of the Cu^{2+} and R^{3+} ions calculated for Nd_2CuO_4 and Sm_2CuO_4, respectively, for T = 373 K. We note that the ion PDFs in the (100) and (010) planes of R_2CuO_4 crystals (R = Pr, Nd, Sm, Eu, Gd), whose structure is described by the space symmetry group *I*4/*mmm*, are equivalent. At the same time, for La_2CuO_4 (space group *Abma*), the PDFs in the (100) and (010) planes are different. Because the (100) cut of the PDF is in this case more informative, it is the (100) PDFs that are presented in the figures.

As seen from Figs. 2–7, while PDFs for R_2CuO_4 crystals with different RE ions differ substantially, we observe, however, a certain pattern in the PDF variation which correlates with the increase in atomic number and decrease in radius of the RE ion.

As an illustration of two limiting cases, let us consider the PDFs of Cu^{2+} ions for La_2CuO_4 and Eu_2CuO_4. In La_2CuO_4, one observes a two-well potential with splitting along the *a* and *b* axes in the CuO_2 layer and a minimum of the PDF at the special ion position. We believe the Jahn–Teller vibronic interaction, which gives rise to the cooperative Jahn–Teller effect (CJTE) of copper ions [1], to dominate here. Eu_2CuO_4 exhibits a singly connected PDF with the maximum value at the special position. In this case, the orbit–orbit interaction mediated by 2D spin fluctuations is dominant [1].

Let us formulate the main criteria underlying the analysis of the data presented here for all R_2CuO_4 crystals.

First of all, the actual type of the PDF is important, namely, whether the PDF is multiply or singly connected. We believe that multiply connected PDFs, corresponding to double- or multiwell crystal-field potentials, form as a result of vibronic CJTE for the corresponding ions. In the case of a singly connected PDF with the maximum value (accepted as 100%) at the equilibrium ion position, there is no vibronic CJTE. The equilibrium position of an ion in the lattice corresponds to the center of the square panels in Figs. 2–7.

The density of the spatial distribution of PDF lines relative to its maximum value is a measure of the steepness of the local potential. For multiply connected PDFs, the value of the PDF at the center of a panel (field) characterizes the depth of the wells produced by the CJTE of the corresponding ions. Angular symmetry in the PDF distribution provides information on the directions of extremal ion displacements in thermal vibrations.

PDFs are constructed taking into account both the harmonic and anharmonic contributions to thermal ion vibrations (Tables 2–4). Large anharmonic contributions are indicated by the flat regions in the PDFs [13]. To find the effect of the RE properties, as well as of interactions between the copper and RE ions, on the structural states of a crystal, a comparative analysis is carried out of the PDF patterns for the copper and RE ions.

Consider the main features of the room-temperature Cu^{2+} PDF in the series of crystals studied by us.

In Eu_2CuO_4 and Gd_2CuO_4, one observes singly connected PDFs with the maximum value at the field center, which implies the absence of vibronic CJTE. By contrast, R_2CuO_4 crystals (R = La, Nd, Pr, Sm) exhibit multiply connected PDFs, which indicates the presence of vibronic CJTE for the Cu^{2+} ions.

In La_2CuO_4, Pr_2CuO_4, and Nd_2CuO_4, the crystal-field potential in the presence of vibronic CJTE splits in the (001) plane along the [100], [010], and [110] directions, respectively. In Sm_2CuO_4, this splitting occurs along the *c* axis ([001] direction).

In crystals with multiply connected PDFs, the deepest wells are observed in La_2CuO_4 and Nd_2CuO_4, with close-to-zero PDF values at the field centers. In the Pr_2CuO_4 and Sm_2CuO_4 crystals, the well depth is considerably smaller. In the latter crystal, a practically flat crystal-field potential is observed near the field center (Figs. 2, 3).

As also can be seen from Figs. 2–7, the symmetry of the PDFs in the (001) planes, corresponding to the CuO_2 sheets, and in the (100) and (010) planes, charac-

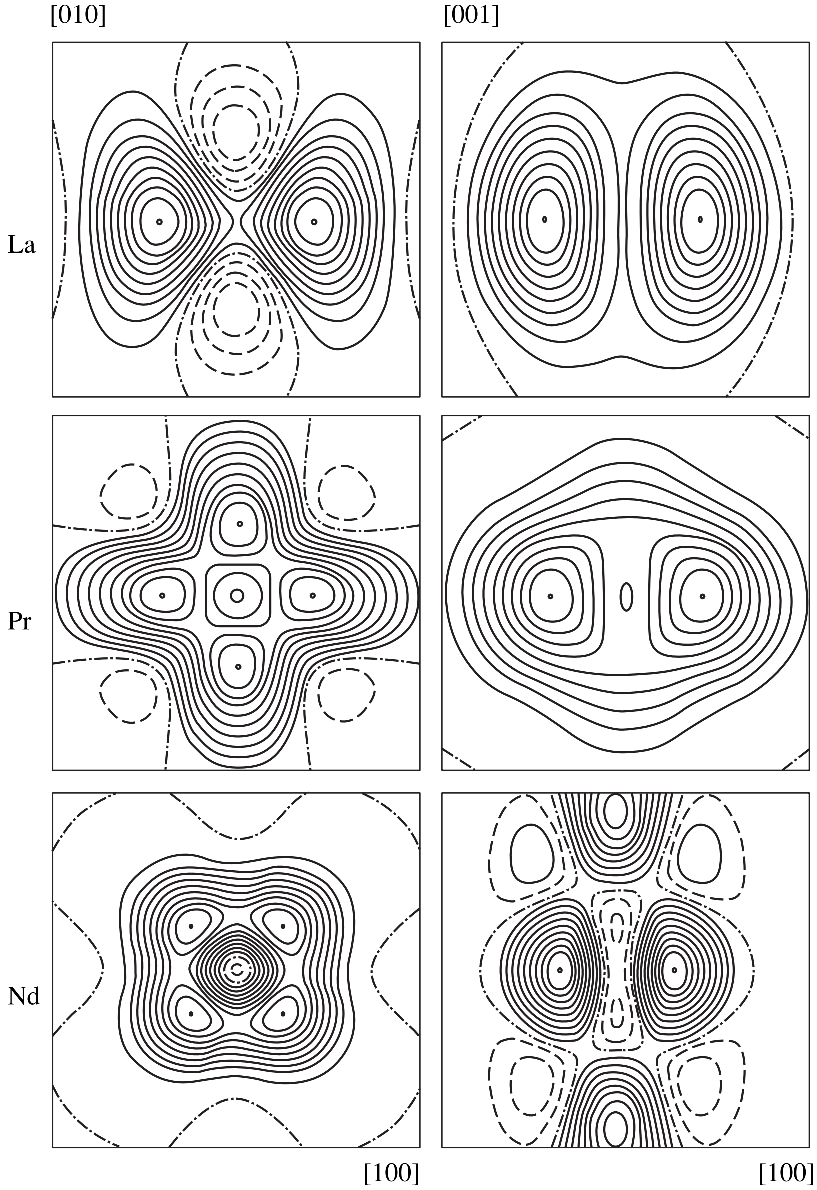

Fig. 2. Room-temperature PDF of Cu^{2+} ions for La_2CuO_4 (La), Pr_2CuO_4 (Pr), and Nd_2CuO_4 (Nd) calculated for the (001) and (010) planes. Field span 0.48 × 0.48 Å. PDF isolines drawn in steps of 10% of the maximum value. Dot specifies 100% PDF. Dot-and-dash line corresponds to PDF = 0. Dashed lines identify negative values of PDF. Field centers correspond to equilibrium lattice ion positions in the lattice.

terizing copper ions off the CuO_2 sheets, is substantially different.

In R_2CuO_4 crystals (R = Sm, Eu, Gd), the probability density function in the (001) planes for small ion thermal-vibration amplitudes (PDF > 50%) has a practically isotropic pattern, which implies a harmonic character of the thermal vibrations. In the case of large PDF > 50% (large thermal vibration amplitudes), flat PDF regions characteristic of an anharmonic component of thermal vibrations appear and the PDF distribution acquires a square anisotropy. In Nd_2CuO_4 and Pr_2CuO_4 crystals, one can see manifestations of a vibronic CJTE in the (001) plane, while the square anisotropy in the PDF distribution is retained. The PDF patterns in the (100) and (010) planes for R_2CuO_4 crystals with different RE ions differ more strongly than in the (001) plane. Copper ions in La_2CuO_4, Nd_2CuO_4, and Sm_2CuO_4 exhibit the largest thermal displacement along the c axis. In Sm_2CuO_4, the 100% value point of the PDF is shifted along the c axis from the equilibrium ion position. In Nd_2CuO_4, one sees only residual indications of a vibronic CJTE along the c axis, which possibly occurs at a lower temperature, as is the case with Pr_2CuO_4 (see [2]).

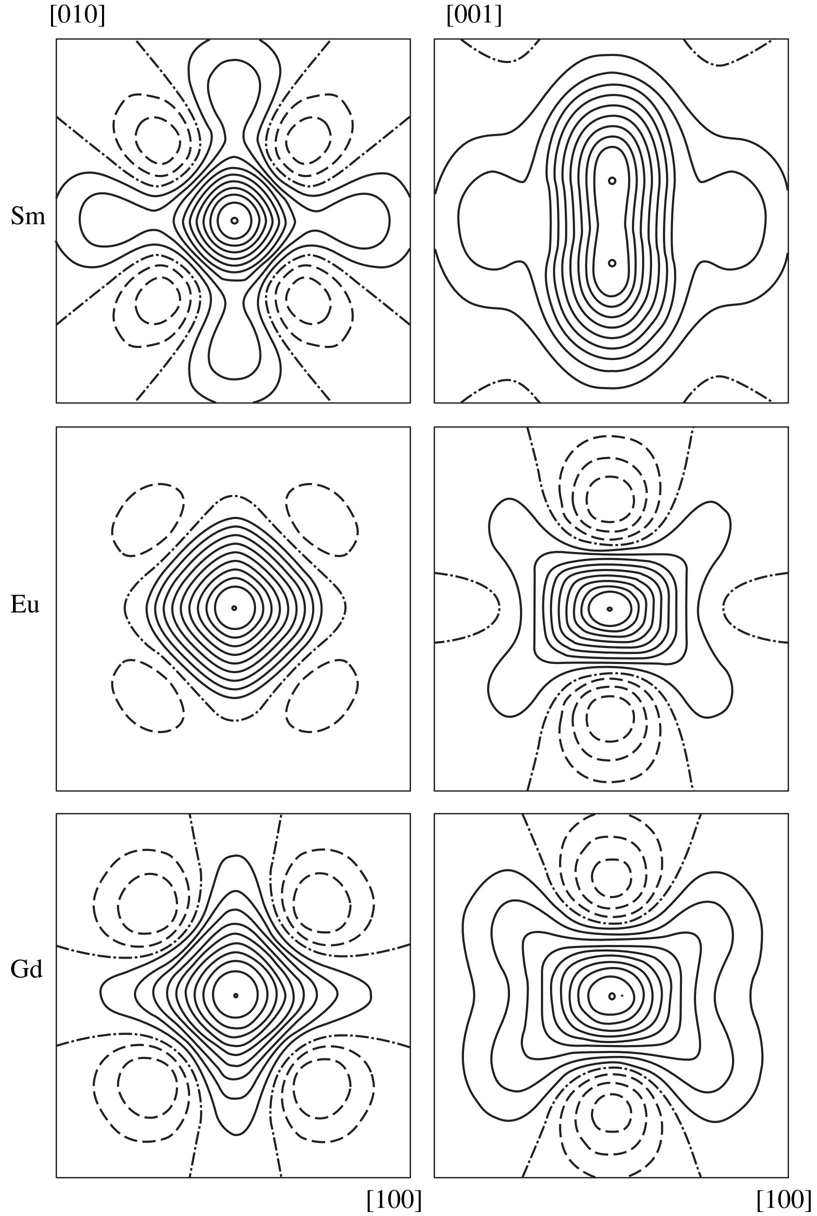

Fig. 3. Room-temperature PDF of Cu^{2+} ions for Sm_2CuO_4 (Sm), Eu_2CuO_4 (Eu), and Gd_2CuO_4 (Gd). For other explanatory notes, see Fig. 2.

Almost all the crystals studied exhibit flat PDF regions, indicating a large anharmonic component of thermal vibrations of the copper ions (see also Table 2). Note that the anharmonic contribution to thermal copper-ion vibrations is most prominent in crystals with weak CJTE manifestations. Also, anharmonic contributions manifest themselves more strongly in the (100) and (010) than the (001) plane.

As follows from the pattern of the angular PDF distribution, the nonsplit, centered part of the local potential has cubic symmetry ($Z = 8$) in all R_2CuO_4 crystals with RE ions.

Let us turn now to the experimental features of the PDF distribution of RE ions. As seen from Figs. 4 and 5, crystals with the Pr^{3+}, Eu^{3+}, and Gd^{3+} ions at room temperature exhibit singly connected PDFs and those with La^{3+}, Nd^{3+}, and Sm^{3+} ions exhibit multiply connected PDFs. Note that, in contrast to the copper ions, the PDF of the RE ions is singly connected but asymmetric relative to the [001] direction (see Table 5). This deviation from symmetry is also most likely a manifestation of the CJTE.

A comparison of the copper and RE PDFs shows them to have the same pattern for almost all crystals, with the exception of Pr_2CuO_4.

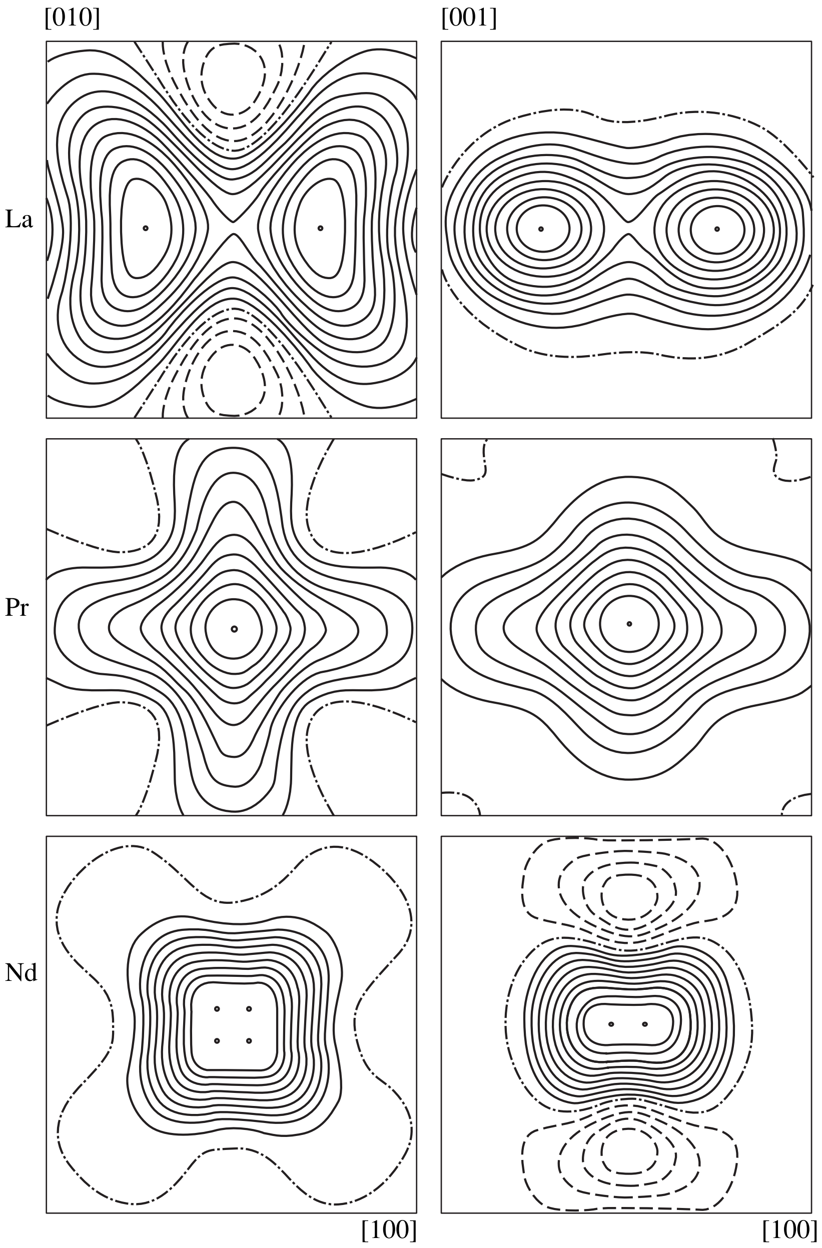

Fig. 4. Room-temperature PDF of R^{3+} ions for La_2CuO_4 (La), Pr_2CuO_4 (Pr), and Nd_2CuO_4 (Nd). For other explanatory notes, see Fig. 2.

As seen from Fig. 4, Nd^{3+} ions are characterized by flat potentials in the (001) plane with weakly pronounced shallow wells which are shifted along the [110] diagonals. Comparison of the PDFs of the copper and Nd^{3+} ions in Nd_2CuO_4 makes it possible to conclude that the CJTE-induced distortion of the local crystal-field potential for the copper ions is considerably larger than that for Nd^{3+}.

The Sm^{3+} ions in the (100) plane [as well as in the equivalent (010) plane] in Sm_2CuO_4 exhibit a vibronic CJTE, with wells that are asymmetric in depth and shifted along the [001] direction with respect to the equilibrium ion positions. The isoline that envelopes both wells and is closest to the equilibrium position corresponds to a PDF value of 40%. Thus, unlike Nd_2CuO_4, the degree of local crystal-field distortion for the Sm^{3+} ions in Sm_2CuO_4 is larger than that for the copper ions. We note that only in Sm_2CuO_4 is there a double-well potential with splitting along the *c* axis of the crystal for both the copper and RE ions.

In crystals with dominant vibronic Jahn–Teller distortion of the Cu^{2+} ions, this distortion is observed in

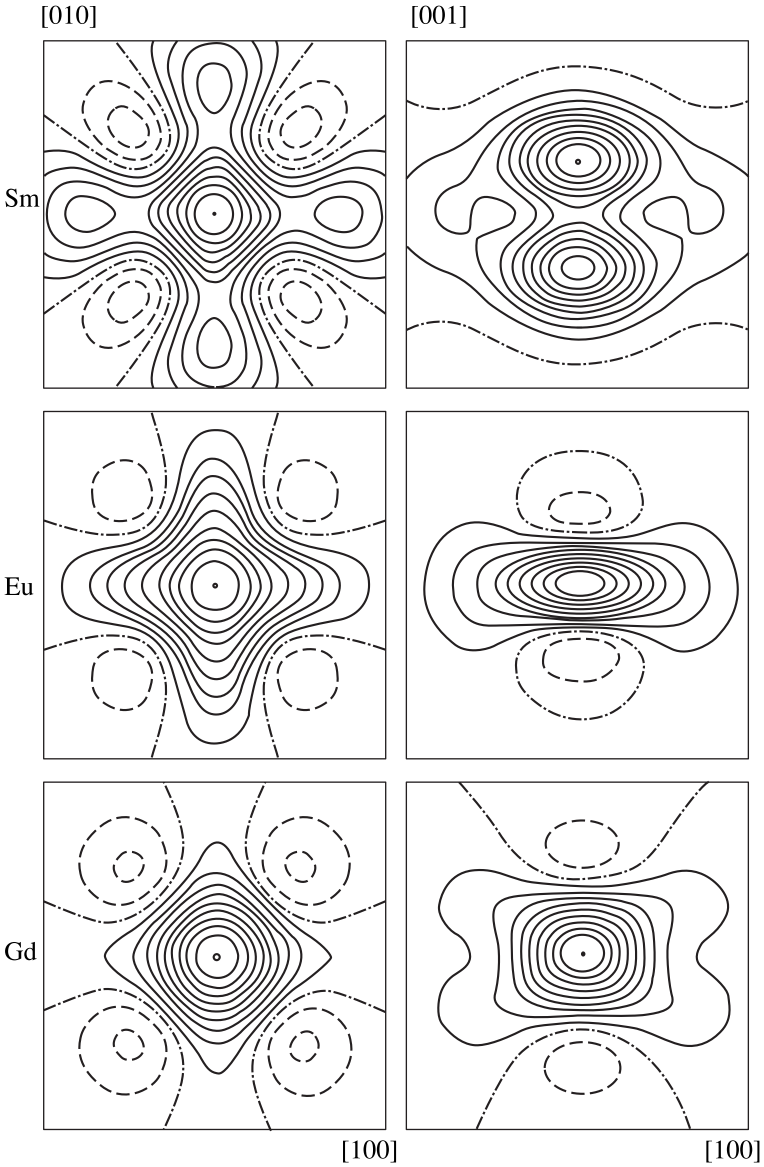

Fig. 5. Room-temperature PDF of R^{3+} ions for Sm_2CuO_4 (Sm), Eu_2CuO_4 (Eu), and Gd_2CuO_4 (Gd). For other explanatory notes, see Fig. 2.

the (001) planes. At the same time, in Sm_2CuO_4, the dominant vibronic distortion of the Sm^{3+} ions occurs along the [001] direction, with no vibronic CJTE present for the Cu^{2+} ions in the (001) plane.

In Gd_2CuO_4, there is no CJTE for the Gd^{3+} ions and the PDF distributions for the copper and RE ions are similar. In Eu_2CuO_4, the PDF of Eu^{3+} ions is singly connected but asymmetric relative to the [001] direction; this pattern results from the CJTE. No indication of the CJTE for the copper ions is seen, however.

For the RE ions, as well as for Cu^{2+}, there are large anharmonic contributions, i.e., flat PDF regions and large third- and fourth-order anharmonicity parameters (see Table 3).

3. ANALYSIS OF EXPERIMENTAL DATA

One can thus conclude that the structural properties of the CuO_2 layers in R_2CuO_4 crystals with RE ions differ substantially, depending on the actual type of the RE ion, more specifically, on its ionic radius and the character of the ground state.

The absence of apical oxygen ions in the nearest environment of the copper ions in R_2CuO_4 crystals with RE ions should enhance the effect of the latter on the properties of the CuO_2 sheets and the crystal structure

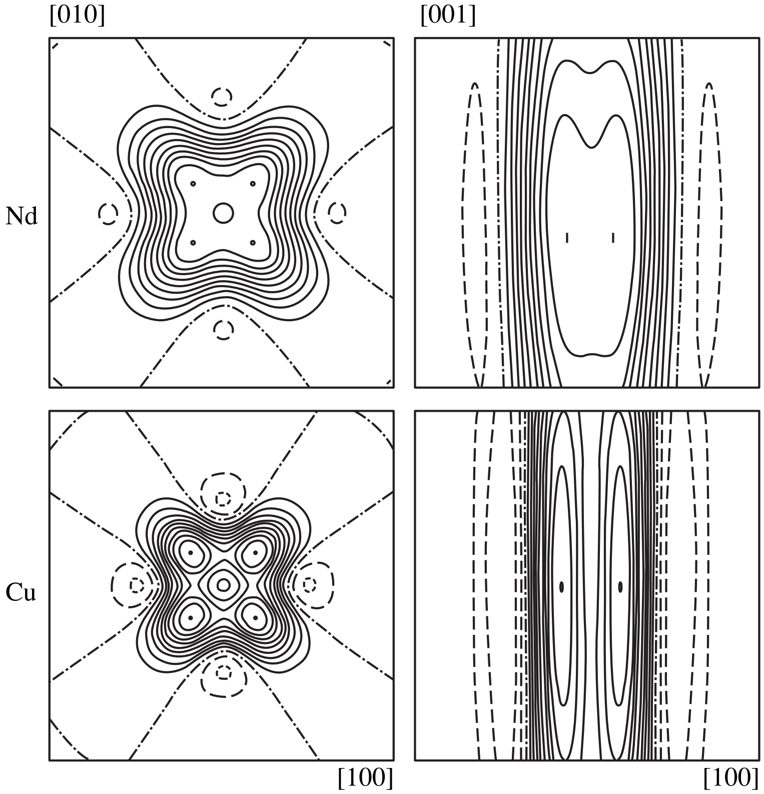

Fig. 6. PDF of Cu^{2+} and Nd^{3+} ions for Nd_2CuO_4 calculated for 373 K. For other explanatory notes, see Fig. 2.

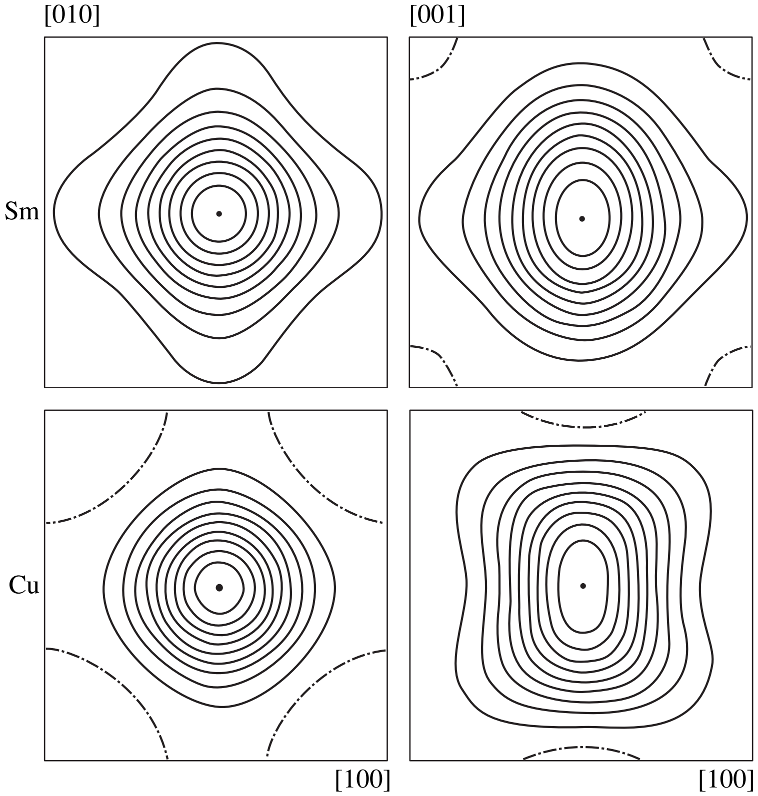

Fig. 7. PDF of Cu^{2+} and Sm^{3+} ions for Sm_2CuO_4 calculated for 373 K. For other explanatory notes, see Fig. 2.

as a whole compared with La_2CuO_4 (in which the apical oxygen ions in the Cu–O layers screen the effect of the RE ions on them). As a result, in La_2CuO_4, the local crystal-field potential of the copper ions is determined by the nearest neighbors in the 2D CuO_2 sheet, whereas in R_2CuO_4 crystals with RE ions, the effective local potential of the Cu^{2+} ions does not derive from them alone. To the field of the 2D plane square lattice in the CuO_2 sheet (the first coordination shell) is admixed to the crystal field of the next coordination shells and, primarily, of the RE ions, because the R^{3+} ions are closest to the Cu^{2+} ions in the c direction (see Fig. 1).

Let us turn now to an analysis of the intralayer interactions, which determine the structural properties of crystals. These are, first of all, the Jahn–Teller interactions in the CuO_2 sheets and in layers with RE ions. R_2CuO_4 crystals with RE ions contain Jahn–Teller ions of two types, namely, Cu^{2+} and R^{3+} [16, 17]. As follows from our results, the dominant lattice distortions existing in the crystals under study, which actually determine the crystal structure as a whole, are those caused by the Jahn–Teller effect of either the copper or RE ions. In Sm_2CuO_4, the Jahn–Teller RE ion interactions are dominant, whereas in the Nd_2CuO_4 and Pr_2CuO_4 crystals, the Jahn–Teller interaction of copper ions predominates. In this case, the intralayer Cu^{2+}–R^{3+} coupling plays, on the whole, an important role in governing the crystal structure.

Note that the vibronic CJTE for Cu^{2+} ions is observed in R_2CuO_4 crystals with the maximum possible RE ionic radii (R = Pr, Nd). By contrast, in crystals with smaller ionic radii (R = Sm, Gd, Eu), the vibronic CJTE for the Cu^{2+} ions is substantially weaker or is altogether absent.

Let us consider the situation in the CuO_2 sheets in more detail. The character of the Cu^{2+} orbital ground state and, accordingly, the character of the Jahn–Teller effect are known to be determined by the type of nearest environment in the cubic-lattice approximation [6, 16]. In R_2CuO_4 crystals with RE ions, the nearest environment of the copper ions derives from the contribution of two crystal-field components with different symmetries, namely, of the oxygen ion squares in the CuO_2 sheets (Cu–4OI) and of the cubic RE environment (Cu–8R). As is well known, the orbital ground state of Cu^{2+} ions in an oxygen ion square is a $d_{(x^2-y^2)}$ singlet. The cubic arrangement of R^{3+} ions around the Cu^{2+} ion corresponds to an orbital ground state of Cu^{2+} in the form of an e_g doublet [18].

Splitting of the e_g doublet in the tetragonal lattice produces a vibronic CJTE for copper ions [6, 16]. We believe, however, that the structural states of the CuO_2 sheets and of the crystals as a whole are also determined by the excited orbital states of the t_{2g} triplet. As already mentioned, in R_2CuO_4 crystals, a number of interactions comparable in strength to the splitting $\Delta = (e_g - t_{2g}) \sim 0.1$ eV in the cubic lattice are observed, which makes admixture of excited states to the ground state possible. The t_{2g} triplet in the tetragonal lattice splits into a d_{xy} singlet and a $d_{xz,\,yz}$ tetragonal doublet. The character of this splitting depends on the relative magnitude of the vibronic and SO couplings. If the former coupling dominates, the lower state is the d_{xy} singlet, and if the latter interaction is stronger, the $d_{xz,\,yz}$ tetragonal doublet is in a lower position [6, 16].

If the SO interaction in R_2CuO_4 crystals with RE ions is strong, the tetragonal doublet is admixed to the orbital ground singlet $d_{(x^2-y^2)}$ for the copper ions. Under these conditions, the orbit–orbit coupling through 2D spin fluctuations can give rise to a CJTE of spin origin. A CJTE of this type was assumed to be responsible for the 2D orbital glass state revealed in Eu_2CuO_4 for $T > 150$ K [11]. No strong lattice distortions occurred, but correlated spin and orbital states formed. We believe that the existence of a singly connected PDF in Eu_2CuO_4 for $T > 150$ K is due to Jahn–Teller stabilization through a CJTE of spin origin. A singly connected PDF is observed in Gd_2CuO_4, while the Pr_2CuO_4 and Nd_2CuO_4 crystals exhibit an admixture of centered PDF to the split PDF induced by vibronic CJTE. It appears only natural to assign the nonsplit, centered PDF of the copper ions to a contribution of orbit–orbit coupling through spin fluctuations.

The multiply connected copper-ion PDFs observed in R_2CuO_4 crystals (R = Nd, Pr) are evidence of a dominant contribution of vibronic Jahn–Teller interactions for the Cu^{2+} ions in CuO_2 sheets.

Thus, in the CuO_2 layers of R_2CuO_4 crystals with RE ions, there are two different interactions bringing about Jahn–Teller lattice stabilization, namely, vibronic (phonon-mediated orbit–orbit coupling) and orbit–orbit coupling mediated by 2D spin fluctuations. As already mentioned, the character of the Jahn–Teller stabilization is different for these two interactions. Their coexistence may produce nonuniform structural states, and variation of the relative strength of the interactions with temperature may give rise to structural phase transitions.

In the cases where the Jahn–Teller RE interaction in R_2CuO_4 crystals is dominant, a distortion of the cubic symmetry in the RE environment plays a primary role. Interaction between the copper and RE ions should also change the structural state of the Cu^{2+} ions. It is this situation that is apparently realized in Sm_2CuO_4.

Let us consider some characteristic features of the structural states of specific R_2CuO_4 crystals with RE ions in more detail.

3.1. La_2CuO_4

Atomic number $Z(\mathrm{La}) = 57$; ionic radius $r(\mathrm{La}^{3+}) = 1.032$ Å [19].

The La^{3+} ion is nonmagnetic. As mentioned above, for temperatures $T < 650$ K, La_2CuO_4 has a *T*-type orthorhombically distorted structure, with the nearest environment of the Cu^{2+} ions being oxygen octahedra in the CuO_2 sheets.

As seen from Fig. 2, the copper ion PDFs have a pattern typical of crystals with a vibronic CJTE. The crystal field has a double-well potential with a splitting in the (001) plane (in the CuO_2 layer) and a close-to-zero field-center PDF. The copper ion displacement in thermal vibrations is maximum along the *c* axis, which indicates that the nearest environment of the ion is an octahedron extended along the *c* axis.

3.2. Pr_2CuO_4

$Z(\mathrm{Pr}) = 59$; $r(\mathrm{Pr}^{3+}) = 0.99$ Å [19].

The ground state of the Pr^{3+} ion is $^3H_4$ ($S = 1$, $L = 5$, $J = 4$). The orbital and spin ground singlet is separated energywise from the excited orbital doublet by ~18 meV [20].

Vibronic Jahn–Teller distortions in the CuO_2 layers are dominant for copper ions at room temperature. Such distortions are not observed for the Pr^{3+} ions. As already mentioned, Pr_2CuO_4 is the only R_2CuO_4 crystal with RE ions in which there are no obvious correlations in PDF shape between the copper and RE ions.

The Pr^{3+} ion has the maximum ionic radius in R_2CuO_4 crystals with tetragonal *T*' structure. The lattice accommodating the slightly larger La^{3+} ion has *T* structure. The displacements of the Pr^{3+} ions in a lattice of *T*' symmetry are apparently constrained. As a result, the Coulomb repulsion between the Pr^{3+} and Cu^{2+} ions gives rise to a relatively larger copper-ion displacement in the CuO_2 layer; i.e., the Coulomb repulsion efficiently enhances the vibronic Jahn–Teller interaction between the copper ions. Nevertheless, near the field center, there is also a centered part of the copper ion PDF in the (001) plane; we associate this part with the contribution of the orbit–orbit coupling through spin fluctuations to the Jahn–Teller stabilization.

Thus, although the vibronic interaction of copper ions in the CuO_2 sheets is dominant in Pr_2CuO_4, the properties of the Pr^{3+} ion (in this case, its ionic radius) and the R^{3+}–Cu^{2+} interaction noticeably affect the crystal structure.

3.3. Nd_2CuO_4

$Z(\mathrm{Nd}) = 60$; $r(\mathrm{Nd}) = 0.983$ Å [19].

The Nd^{3+} ground state is $^4I_{9/2}$ ($S = 3/2$, $L = 2$). The orbital ground doublet is crystal-field split by 0.5 meV. The first excited orbital doublet is spaced energywise from the ground state by 16 meV [20].

The Nd_2CuO_4 crystal at room temperature exhibits a dynamic vibronic CJTE for both the copper and neodymium ions; however, the distortion of the local crystal field for copper ions is larger than that for Nd^{3+}. In other words, vibronic interactions for the Cu^{2+} ions dominate in Nd_2CuO_4. One readily sees a correlation between the copper ion and Nd^{3+} states. We believe this correlation to be due to Cu^{2+}–Nd^{3+} coupling giving rise to correlated ion displacements. The ionic radius of Nd^{3+} is smaller than that of Pr^{3+}; this accounts for the higher mobility of the former ion in the lattice.

The (001) plane displays a centered part of the copper ion PDF near the equilibrium position, which we assign to a contribution of the orbit–orbit interaction through spin fluctuations to the Jahn–Teller stabilization. Note that the relative contribution of the centered nonsplit potential in Nd_2CuO_4 is larger than that in Pr_2CuO_4.

Thus, the crystal structure of Nd_2CuO_4 is a result of three types of interactions, namely, the intralayer vibronic Jahn–Teller and SO coupling of copper ions and the Cu^{2+}–Nd^{3+} interlayer interaction. At room temperature, the Jahn–Teller vibronic interaction for the copper ions is dominant.

As seen from Figs. 2 and 6, an increase in temperature enhances copper-ion displacements along the [001] directions and decreases the contribution of singly connected PDFs in the (001) plane; i.e., it enhances the role of the in-plane vibronic Jahn–Teller coupling. The symmetry of the effective nearest environment of copper ions in Nd_2CuO_4 approaches ever more that of an octahedron extended along the [001] direction, making the PDF distribution pattern similar to that of La_2CuO_4.

3.4. Sm_2CuO_4

$Z(\mathrm{Sm}) = 62$; $r(\mathrm{Sm}^{3+}) = 0.958$ Å [19].

As already mentioned, the structure of Sm_2CuO_4 is dominated by the CJTE for the RE ions and the interaction between the copper and RE ions. The ionic radius of Sm^{3+} is slightly smaller than that of Nd^{3+} but is larger than those of europium and gadolinium.

The ground multiplet of the Sm^{3+} ion is $^6H_{5/2}$ ($S = 5/2$, $L = 5$, $J = 5/2$). Crystal field splitting makes the orbital singlet and Kramers doublet the ground state. The distance to the nearest excited orbital doublet is ~18 meV [21].

At room temperature, the Sm^{3+} ion is seen to undergo equilibrium-position displacement along the [001] direction from the field center (Fig. 5), which is a consequence of static CJTE for the Sm^{3+} ions. The local Jahn–Teller distortions for the Sm^{3+} ions are larger than those for the copper ions. The PDFs for the copper and samarium ions are similar. The off-plane displacement of the Cu^{2+} ions from the CuO_2 sheets along the c axis is most likely due to the Sm^{3+}–Cu^{2+} interaction. Note that the pattern of the Cu^{2+} displacement along the c axis corresponds to the case of dynamic CJTE (Cu^{2+} displacements up and down with respect to the layer are equally probable). At the same time, copper ions do not exhibit any manifestation of the vibronic CJTE in the (001) plane at room temperature. One sees, however, PDFs extended along the a and b axes, which can give rise to switching, at a low temperature, of the dominant type of interaction from the vibronic for RE ions to the vibronic for copper ions in the CuO_2 layer and, thus, can lead to a structural phase transition.

As seen from Fig. 7, the pattern of PDF distribution of copper and samarium ions in Sm_2CuO_4 obtained at $T = 373$ K changes qualitatively compared to that for room temperature. At $T = 373$ K, no vibronic CJTE is observed either for the Sm^{3+} or the Cu^{2+} ions. In the interval 300–373 K, Sm_2CuO_4 apparently undergoes a structural phase transition manifest in a transformation of the PDF from the doubly to singly connected pattern (compare Figs. 3, 4, 7). The situation becomes similar to that observed in Eu_2CuO_4 for $T > 150$ K (in the tetragonal phase) [1]. It may be assumed that orbit–orbit coupling through 2D spin fluctuations in the CuO_2 layers becomes dominant in Sm_2CuO_4 for $T > 296$ K.

Note that below the Néel temperature ($T_N \sim 250$–290 K), all R_2CuO_4 crystals with RE ions support long-range 3D antiferromagnetic order. If for $T < T_N$ the crystal is in a uniform 3D antiferromagnetic state, then 2D spin fluctuations with large correlation lengths are formed in CuO_2 sheets for temperatures $T > T_N$. If, however, the 3D antiferromagnetic state is nonuniform, 2D spin fluctuations also persist for $T < T_N$. The existence of well-developed 2D spin fluctuations with large correlation lengths can enhance the part played by a CJTE of spin origin. It is possible that Sm_2CuO_4, in contrast to Eu_2CuO_4, supports a uniform magnetic and a structural state for $T < T_N$. At the same time, in Pr_2CuO_4 and Nd_2CuO_4, which do not suffer noticeable changes in their structural properties (in the shape of the PDF) near the Néel temperature, a nonuniform 3D antiferromagnetic state most likely exists for $T < T_N$. The possibility of existence of well-developed 2D spin fluctuations in Pr_2CuO_4 for $T < T_N$ is also corroborated by spin dynamics studies [22, 23] and by the presence of centered, nonsplit PDFs of copper ions in CuO_2 sheets for $T < T_N$ [2].

3.5. *Gd_2CuO_4*

$Z(\mathrm{Gd}) = 60$; $r(\mathrm{Gd}^{3+}) = 0.938$ Å [19].

Unlike other RE ions, Gd^{3+} is not a Jahn–Teller ion, because its ground state is $^8S_{7/2}$. A nonzero orbital moment appears in the next term spaced from the ground state by ~2 eV. Gd^{3+} ions have the smallest ionic radius among the RE ions in R_2CuO_4 crystals. A T'-type lattice does not form for RE ions with smaller ionic radii. For temperatures $T < 600$ K, Gd_2CuO_4 exhibits orthorhombic distortions in the CuO_2 sheets caused by the O^{2-} (OI) ions rotating about the undisplaced Cu^{2+} ions [4, 8].

The shape of the copper-ion PDF suggests that the vibronic JT interaction is weak and does not affect the structural state of the crystal significantly. There is a similarity in the spatial PDF distribution between the copper and gadolinium ions. The PDF symmetry in the (100) and (010) planes reflects a $Z = 8$ coordination of the nearest environment of ions, which is in agreement, for the Gd^{3+} ions, with the actual nearest environment of OI and OII ions and indicates, for the Cu^{2+} ions, that the Gd^{3+}–Cu^{2+} interaction plays a dominant role in the formation of the crystal-field potential. There is a substantial anharmonic contribution to the PDF in the same planes, which usually reflects structural instability of the lattice, i.e., closeness to a displacive phase transition [24].

In the (001) plane, a square PDF symmetry is observed, which is a sign of a predominant contribution of the Cu–OI coupling to the potential formation in the CuO_2 sheets. As already pointed out, in this layer, one observes orthorhombic distortions associated with the OI ions turning with respect to the undisplaced copper ions.

One may thus assume that the Gd^{3+}–Cu^{2+} Coulomb repulsion and the Cu–OI coupling in the CuO_2 sheets are of the same order of magnitude in Gd_2CuO_4. Also, the Gd^{3+}–Cu^{2+} interaction in the (100) and (010) planes, combined with a strong anharmonicity, results in the RE and copper ion thermal displacements being correlated; this, possibly, gives rise to stabilization of the nearly unstable lattice.

As mentioned above, we associate the presence of nonsplit centered PDFs of the Cu^{2+} Jahn–Teller ions with a CJTE of spin origin. In Gd_2CuO_4, however, orthorhombic distortions in the CuO_2 sheets should bring about splitting of the $d_{xz,\,yz}$ tetragonal doublet and predominance of the vibronic Jahn–Teller interaction for the copper ions. If the structural state of the crystals were to be uniform and have orthorhombic symmetry, the PDFs would be split, reflecting the predominantly vibronic character of the Jahn–Teller lattice stabilization, which is at odds with the observed PDF distribution pattern. It may be conjectured that Gd_2CuO_4 supports a nonuniform structural state with a strong anharmonicity and that effects characteristic of both the tetragonal [23] and orthorhombic symmetry [4, 8, 22] are observed. Possible coexistence of the tetragonal and orthorhombic phases was reported recently in a study of weak ferromagnetism and Raman spectra [25].

3.6. Eu_2CuO_4

Z(Eu) = 63; r(Eu^{3+}) = 0.947 Å [19].

The ground state of the Eu^{3+} ion $^7F_0$ ($S = 3$, $L = 3$, $J = 0$) is singlet and nonmagnetic. However, the first excited multiplet of the Eu^{3+} ion ($^7F_1$), which is magnetic and degenerate (triplet), lies low in energy, 0.03 eV away from the ground-state multiplet [1]. Structural studies of Eu_2CuO_4 showed static CJTE of the Eu^{3+} ions ($^7F_1$) to form for temperatures $T > 350$ K when there is a noticeable thermal population of the $^7F_1$ excited triplet state [1].

Eu_2CuO_4 is reported [9–11] to undergo a structural phase transition at $T \approx 150$ K. For $T < 150$ K, orthorhombic distortions form in the CuO_2 layers that are similar to those observed in Gd_2CuO_4. For $T > 150$ K, these distortions disappear, restoring the square in-plane symmetry and tetragonal symmetry throughout the crystal [9]. However, the structural state is nonuniform and an orbital glass state is observed [11].

We believe that the phase transition at $T \approx 150$ K may be driven by a change in the character of the Cu^{2+}–Eu^{3+}($^7F_1$) interaction compared with Cu^{2+}–Eu^{3+}($^7F_0$). For $T \geq 150$ K, the displacement of the Jahn–Teller ions Eu^{3+}($^7F_1$) from the central positions may be assumed to be more probable than rotation of the oxygen ions OI in the CuO_2 layers. As a result, for $T < 150$ K, Eu_2CuO_4 acquires a structural state similar to that in Gd_2CuO_4. The difference is that Eu_2CuO_4 retains tetragonal symmetry throughout the crystal, with orthorhombic distortions present only in local regions. The state persisting in the temperature interval $150 < T < 350$ K is characterized by a singly connected, centered PDF for the copper ions, and we believe that the interactions in the CuO_2 sheets are dominated by orbit–orbit coupling through 2D antiferromagnetic spin fluctuations with large correlation lengths [11]. Nonuniform magnetic and structural states allowing the existence of 2D antiferromagnetic fluctuations form in Eu_2CuO_4 for $T > 150$ K as a result of simultaneously occurring structural and magnetic phase transitions (i.e., considerably below $T_N \approx 250$ K) [9, 12]. In this case, the role of the Cu^{2+}–Eu^{3+}($^7F_1$) interaction can be enhanced by its long-range character if it is mediated by 2D spin correlations in the CuO_2 layer.

4. CONCLUSION

Thus, our analysis of experimental data shows that the character of structural distortions occurring at room temperature in the CuO_2 sheets of R_2CuO_4 crystals with RE ions and the type of the dominant interaction are determined by the RE properties (ionic radius and the ground state). In all R_2CuO_4 crystals with RE ions, the part played by the Cu^{2+}–R^{3+} coupling is important and the main factor accounting for the structural features is the absence of RE ion screening for the copper ions.

The larger the RE ionic radius, the more significant the part played by the vibronic Jahn–Teller interactions for the copper ions in crystal structure formation. The copper ion displacements resulting from the CJTE in the CuO_2 layers efficiently increase the distance to the nearest positively charged RE ions. Correlated displacement of the Cu^{2+}–R^{3+} ions brings about stabilization of a T'-type tetragonal structure. In the cases where the RE ions are not of the Jahn–Teller type [Eu^{3+}($^7F_1$) and Gd^{3+}] and at the same time have minimum ionic radii, the Cu^{2+}–R^{3+} interaction gives rise to a strong anharmonicity characteristic of lattice states close to instability.

ACKNOWLEDGMENTS

This study was supported by the Russian Foundation for Basic Research (project no. 02-02-16140a) and, partially, by the “Basic Research” Foundation, Presidium RAS (project “Quantum Macrophysics”), and RBRF “Scientific Schools” grant (project no. 00-15-96757).

REFERENCES

1. E. I. Golovenchits, V. A. Sanina, A. A. Levin, *et al.*, Fiz. Tverd. Tela (St. Petersburg) **39** (9), 1600 (1997) [Phys. Solid State **39**, 1425 (1997)].
2. A. A. Levin, Yu. I. Smolin, Yu. F. Shepelev, *et al.*, Fiz. Tverd. Tela (St. Petersburg) **42** (1), 147 (2000) [Phys. Solid State **42**, 153 (2000)].
3. L. A. Muradyan, R. A. Tamazyan, A. M. Kevorkov, *et al.*, Kristallografiya **35**, 861 (1990) [Sov. Phys. Crystallogr. **35**, 506 (1990)].
4. M. Braden, W. Paulus, A. Cousson, *et al.*, Europhys. Lett. **25**, 625 (1994).
5. S. Chakravarty, B. Halperin, and D. Nelson, Phys. Rev. B **39**, 2344 (1989).
6. A. Abragam and B. Bleaney, *Electron Paramagnetic Resonance of Transition Ions* (Clarendon, Oxford, 1970; Mir, Moscow, 1972), Vol. 2.
7. P. P. Parshin, M. G. Zemlyanov, A. S. Ivanov, *et al.*, Fiz. Tverd. Tela (St. Petersburg) **41** (7), 1149 (1999) [Phys. Solid State **41**, 1046 (1999)].
8. M. Udagawa, Y. Nagaoka, N. Ogita, *et al.*, Phys. Rev. B **49**, 585 (1994).
9. E. I. Golovenchits and V. A. Sanina, Pis’ma Zh. Éksp. Teor. Fiz. **74** (1), 22 (2001) [JETP Lett. **74**, 20 (2001)].
10. V. P. Plakhty, A. B. Stratilatov, and S. Beloglazov, Solid State Commun. **103** (12), 683 (1997).
11. A. V. Babinskiĭ, S. L. Ginzburg, E. I. Golovenchits, and V. A. Sanina, Pis’ma Zh. Éksp. Teor. Fiz. **57** (5), 289 (1993) [JETP Lett. **57**, 299 (1993)].
12. E. I. Golovenchits, S. L. Ginzburg, V. A. Sanina, and A. V. Babinskiĭ, Zh. Éksp. Teor. Fiz. **107**, 1641 (1995) [JETP **80**, 915 (1995)].

13. V. G. Tsirel'son, Itogi Nauki Tekh., Ser.: Kristallokhim. **27**, 3 (1993).
14. D. W. J. Cruckshank, in *Computing Methods in Crystallography*, Ed. by J. S. Rollett (Pergamon, Oxford, 1965), p. 112.
15. P. J. C. Becker and P. Coppens, Acta Crystallogr., Sect. A **30**, 129 (1974).
16. K. I. Kugel' and D. I. Khomskiĭ, Usp. Fiz. Nauk **136** (4), 621 (1982) [Sov. Phys. Usp. **25**, 231 (1982)].
17. G. A. Gehring and K. A. Gehring, Rep. Prog. Phys. **38**, 1 (1975).
18. I. B. Bersuker, *Electronic Structure and Properties of Coordination Compounds* (Khimiya, Leningrad, 1986).
19. R. D. Shannon, Acta Crystallogr. A **32**, 751 (1976).
20. A. T. Boothroyd, S. M. Doyle, D. M. K. Paul, and R. Osborn, Phys. Rev. B **45** (17), 10075 (1992).
21. R. Sachidanandam, T. Yidirim, A. B. Harris, *et al.*, Phys. Rev. B **56** (1), 260 (1997).
22. E. I. Golovenchits and V. A. Sanina, Fiz. Tverd. Tela (St. Petersburg) **41**, 1437 (1999) [Phys. Solid State **41**, 1315 (1999)].
23. E. I. Golovenchits and V. A. Sanina, Physica B (Amsterdam) **284–288**, 1369 (2000).
24. B. A. Strukov and A. P. Levanyuk, *Physical Principles of Ferroelectric Phenomena in Crystals* (Nauka, Moscow, 1995).
25. Z. Fisk, P. G. Pagliuso, J. A. Sanjurjo, *et al.*, Physica B (Amsterdam) **305** (1), 48 (2001).

Translated by G. Skrebtsov

Physics of the Solid State, Vol. 44, No. 11, 2002, pp. 2145–2150. Translated from Fizika Tverdogo Tela, Vol. 44, No. 11, 2002, pp. 2049–2054.
Original Russian Text Copyright © 2002 by Shur, Rumyantsev, Nikolaeva, Shishkin, Baturin.

MAGNETISM AND FERROELECTRICITY

Kinetic Approach for Describing the Fatigue Effect in Ferroelectrics

V. Ya. Shur, E. L. Rumyantsev, E. V. Nikolaeva, E. I. Shishkin, and I. S. Baturin
Institute of Physics and Applied Mathematics, Ural State University, Yekaterinburg, 620083 Russia
e-mail: vladimir.shur@usu.ru

Received February 15, 2002

Abstract—A new kinetic approach is proposed for explaining the fatigue effect in ferroelectrics. A self-consistent variation in the area and geometry of the switching region of a sample upon a cyclic switching accompanied by the formation and growth of kinetically frozen domains is considered. It is assumed that fatigue is due to self-organized formation of a spatially inhomogeneous internal bias field due to retardation of bulk screening of the depolarization field. Variations in the switching charge and in the amplitude of switching current, which are calculated with the help of computer simulation of domain kinetics upon cyclic switching, are in good agreement with experimental data obtained for thin lead zirconate–titanate (PZT) thin films. *© 2002 MAIK "Nauka/Interperiodica".*

1. INTRODUCTION

A decrease in the switching charge as a result of long-time cyclic switching of polarization in thin ferroelectric films, which is known as the fatigue effect, remains a key problem, whose solution is essential for wide practical application of nonvolatile storage devices based on such films [1–16]. Recently, several alternative mechanisms have been proposed for explaining the fatigue effect in films. In accordance with the bulk-locking mechanism, charged domain walls in a film subjected to cyclic switching are fixed (pinning effect) by charge carriers localized at traps [9, 10]. It should be noted that this mechanism was proposed for the first time by Kudzin *et al.* [16] for explaining fatigue effects in barium titanate single crystals. According to another mechanism (interface scenario), fatigue is associated with the slowing down of domain growth, which is due to suppression of nucleation (seed termination) at the film–electrode interface [5, 6]. The role of oxygen vacancy redistribution in an electric field has also been discussed extensively [14]. In [12], it is proposed that fatigue can be explained by the growth of a nonferroelectric passive surface layer upon cyclic switching. It should be noted that, in all contemporary models, the relation between the fatigue effect and the domain-structure kinetics upon cyclic switching is disregarded while considering fatigue in thin films. At the same time, recent direct observations of the domain structure of thin films with the help of scanning-probe microscopy proved that the fatigue effect is accompanied by the formation of a complex-shaped region being switched and by the appearance and growth of regions with a frozen orientation of polarization ("frozen domains") [8, 17].

In this study, we propose an approach to describing the evolution of switched regions during cycling switching, which is based on the decisive role of retardation in the bulk screening of the depolarization field. For cyclic switching, this retardation leads to the self-organized formation of a spatially nonuniform internal bias field suppressing the formation of new domains and slowing down the switching. As a result, the switching cannot be completed in the regions with the maximum value of the internal bias field, which corresponds to the formation of kinetically frozen domains. The main predictions of the proposed model (the existence of an additional stage of formation (of a rejuvenation stage) preceding the fatigue stage and a change in the geometry of the switched region upon cycling switching) are in good agreement with the results of experimental investigations in thin films.

2. MODEL

It is well known that, after switching of polarization in a ferroelectric capacitor, external screening (charge redistribution on the electrodes accompanied by switching current) rapidly compensates the depolarization field E_{dep}. However, there is no complete field compensation in the bulk, since a nonpolar surface layer (dielectric gap) exists in ferroelectrics [18, 19]. After termination of external screening, the field E_{dep} is compensated only partly and a residual depolarization field $E_{\text{rd}} = E_{\text{dep}} - E_{\text{ex.scr}}$ is preserved in the bulk [19, 20]. The compensation of E_{rd} due to slow processes of bulk screening leads to the formation of an internal bias field E_b. This field is responsible for the unipolarity of the switching process, which is manifested in a shift of a hysteresis loop upon a quite rapid (as compared to the

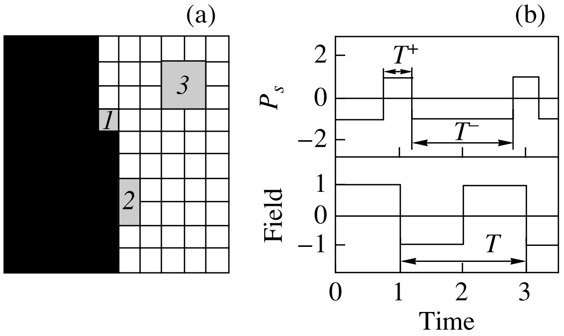

Fig. 1. (a) Three types of nuclei considered in simulation: (*1*) a nucleus at the end of a step, (*2*) a nucleus on a domain wall, and (*3*) an isolated nucleus. (b) Diagram showing variations in the relative local value of spontaneous polarization and in the relative value of the external field during a simulated switching cycle.

bulk screening) cyclic switching in an alternating field [20, 21]. It has been shown, using lead germanite single crystals as an example, that the field E_b is spatially nonuniform [22] and varies upon a long-time cyclic switching [19–23]. Bulk screening can be regarded as a result of competition between three groups of mechanisms: (1) orientation of defect dipoles [24–26], (2) redistribution of bulk charge carriers [18, 19], and (3) injection of charge carriers from electrodes through a dielectric gap [6, 27].

We take into account the fact that the domain kinetics during cyclic switching are a self-organized process, since the spatial distribution of E_b is determined by the preceding evolution of domains and determines, in turn, their subsequent kinetics. Earlier, we demonstrated experimentally that the field E_b is virtually uniform over the entire switched region in the case of long-time cyclic switching with asymmetric ($T_{\text{pos}} \neq T_{\text{neg}}$) rectangular pulses if the switching time is much shorter than the period of the switching field ($t_s \ll T$). In this case, the mean value of E_b is determined by the asymmetry of pulses $c \sim (T_{\text{pos}} - T_{\text{neg}})(T_{\text{pos}} + T_{\text{neg}})^{-1}$ [28]. It follows that in the case of slow switching ($t_s \leq T$), the internal bias field E_b becomes spatially nonuniform even when symmetric pulses are used, since different regions in the sample are in states with opposite directions of polarization for different periods of time. During long-time switching, the local value of E_b relaxes to a value determined by the relative difference in the residence times of a given part of the sample in the states with opposite directions of polarization, $(T^+ - T^-)/T$ (Fig. 1b). In this case, the magnitude and sign of the internal bias field $E_b(x, y)$ are spatially inhomogeneous and the distribution function $f(E_b)$ varies upon cyclic switching. The computer simulation of the domain kinetics carried out by us revealed that the variation of $f(E_b)$ upon cyclic switching leads to the appearance and growth of unswitched regions (kinetically frozen domains) [29, 30].

3. COMPUTER SIMULATION

The domain kinetics for cyclic polarization switching in a thin plate (film) of a uniaxial ferroelectric under the action of rectangular field pulses were simulated on a two-dimensional (2D) matrix. We used the classical model of polarization switching, in which the domain structure kinetics involve the formation of new domains and their subsequent growth (nucleation and growth model) [31, 32]. We assumed that both processes are controlled by nucleation. The formation of nuclei of three different types was considered (Fig. 1a).

(i) Formation of nuclei at the ends of the existing steps leads to step growth.

(ii) Nucleation at a domain wall leads to the formation of new steps.

(iii) The appearance of isolated nuclei leads to the formation of new domains.

The probability p_k of formation of nuclei of a specific type in a given element of the matrix (i, j) during the Nth switching cycle is determined by the local field $E_{\text{loc}}(i, j, N)$:

$$p_k(i, j, N) \sim \exp\{-E_{\text{ac},k}/[E_{\text{loc}}(i, j, N) - E_{\text{th},k}]\}, \quad (1)$$

where $E_{\text{ac},k}$ and $E_{\text{th},k}$ are the activation field and the threshold field, respectively [19].

It is well known that the nucleation probability at a domain wall is much higher than that at a distance from the wall, since $E_{\text{ac},1} < E_{\text{ac},2} < E_{\text{ac},3}$ [19]. Consequently, an increase in the length of a domain wall facilitates polarization switching.

The local field $E_{\text{loc}}(i, j, N)$ is the sum of the uniform external field E_{ex}, the residual depolarization field E_{rd}, and the spatial nonuniform internal bias field $E_b(i, j, N)$ formed by the end of the preceding switching cycle:

$$E_{\text{loc}}(i, j, N) = E_{\text{ex}} + E_{\text{rd}} + E_b(i, j, N). \quad (2)$$

In experiments on fatigue, bulk screening proceeds, as a rule, quite slowly, and $\tau \gg T$. In this case, $E_b(i, j, N)$ tends to compensate the sum of the external and the residual depolarization field averaged over a switching cycle, $\langle E_{\text{ex}} + E_{\text{rd}} \rangle$. For symmetric pulses of rectangular shape, we have $\langle E_{\text{ex}} \rangle = 0$ at any point, while $\langle E_{\text{rd}} \rangle$ is spatially nonuniform: $\langle E_{\text{rd}} \rangle = E_{\text{rd}}(T^+ - T^-)/T$, where T^+ and T^- are the times for which the spontaneous polarization at a given point is directed along one of the two opposite directions, respectively, during a switching cycle (Fig. 1b). It should be noted that the local values of T^+ and T^- for each cycle depend on the domain kinetics in the entire sample (since the probability of switching at a given point is determined by the state of its surroundings) and, hence, can be determined only as a result of simulation of the domain kinetics in the entire matrix. In our analysis, we did not aim at choosing a preferred screening mechanism from those described above and characterized the kinetics of screening only by a time constant τ.

The domain structure kinetics in each switching cycle were simulated by taking into account the field $E_b(i, j, N)$ formed by the end of the preceding cycle. The calculated local values of T^+ and T^- were used for recalculating the spatial distribution of E_b for the next switching cycle in accordance with the relation

$$\begin{aligned} E_b(i, j, N) &= E_b(i, j, N-1)\exp(-T/\tau) \\ &+ E_{\mathrm{rd}}[1-\exp(-T/\tau)]\Delta T(i, j, N)/T. \end{aligned} \tag{3}$$

Assuming the condition $T \ll \tau$ to be satisfied, we used the simplified relation

$$\begin{aligned} E_b(i, j, N) &= E_b(i, j, N-1)(1-T/\tau) \\ &- \langle E_{\mathrm{rd}}(i, j, N-1)\rangle T/\tau. \end{aligned} \tag{4}$$

Obviously, the results of simulation must depend to a considerable extent on the spatial distribution of E_b prior to the first switching cycle. In the course of simulation, we considered two versions of the initial state: an idealized version with a uniform zero internal bias field (without bulk screening) $E_b(i, j, 1) = 0$ and a realistic version with a completely screened polydomain initial state $E_b(i, j, 1) = -E_{\mathrm{rd}}(i, j)$. The latter version corresponds to the spatial distribution observed after prolonged holding of the domain structure in a static state. In this case, the fields E_b in domains with opposite orientations are equal in magnitude but opposite in sign.

3.1. Initial State with Zero Internal Bias Field

The evolution of the domain structure (a set of consecutive domain configurations each of which corresponds to a single switching cycle) at various stages of fatigue process, which is obtained for the initial state with zero internal bias field, is presented in Fig. 2. It can be seen that complete switching occurs during the first cycle (Fig. 2a), while after a long-time cyclic switching, polarization reversal occurs predominantly in narrow regions separating kinetically frozen domains of different polarities (Fig. 2b). Such a change in the geometry of the switching region leads to a qualitative change in the type of domain kinetics. In the initial state, switching is mainly due to a 2D growth of individual domains (Fig. 2a), while the appearance of frozen domains leads to an increase in the contribution from 1D motion of domain walls. After a long-time cyclic switching, the domain kinetics are mainly determined by a reversible parallel displacement of domain walls (Fig. 2b). It is important to note that a similar change in the geometry of the switching region was also detected by directly observing domain kinetics in PZT films using scanning-probe microscopy [8].

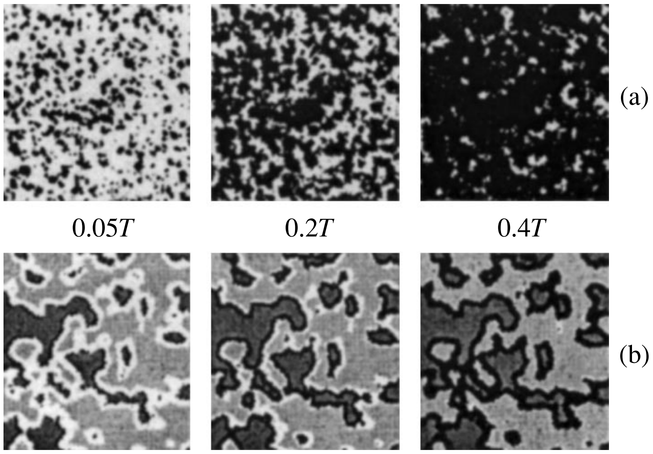

Fig. 2. Sequence of instantaneous domain configurations forming during a switching cycle, found with the help of computer simulation (a) during the first switching and (b) after a long-time cyclic switching. Switched domains of opposite polarities are shown by black and white, while frozen domains of various polarity are shown by light-gray or dark-gray color. The initial state corresponds to zero internal bias field.

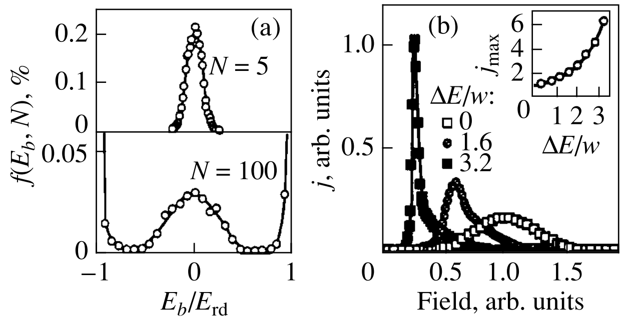

Fig. 3. Computer simulation (initial state with zero internal bias field): (a) distribution functions of the internal bias field for various values of N approximated by a Gaussian; and (b) switching current caused by a triangular pulse for $N = 50$: $\Delta E/w = 0$ corresponds to the Preisach theory, and $\Delta E/w \neq 0$, to a modified approach [25], where ΔE is the difference between the threshold fields required for the formation of an isolated seed and for domain growth, respectively. The inset shows the dependence of $j_{\max}$ on $1/w$ fitted by formula (5).

The spatially nonuniform field E_b formed after the completion of the Nth cycle was characterized by the instantaneous value of the distribution function $f(E_b, N)$ of the internal bias field:

$$f(E_b, N) = L^{-2}\sum\delta[E_b - E_b(i, j, N)]. \tag{5}$$

The distribution functions $f(E_b, N)$ obtained as a result of simulation are closely fitted by a Gaussian

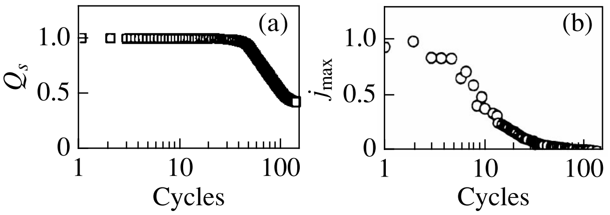

Fig. 4. Decrease (a) in the relative values of switched charge and (b) in the maximum value of switching current as a result of the cyclic switching process obtained by simulation. The initial state corresponds to zero internal bias field.

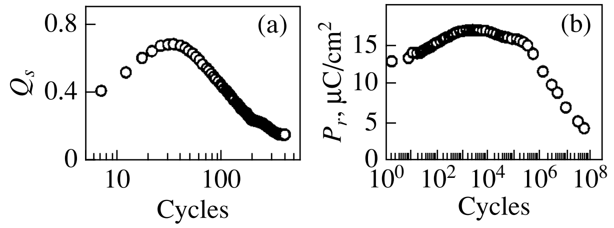

Fig. 5. Rejuvenation and fatigue stages: (a) simulation of switching from a completely screened polydomain initial state; and (b) experimental results for thin PZT films.

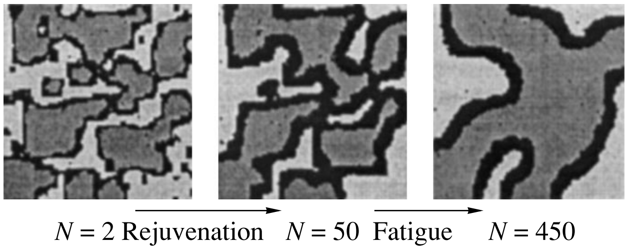

Fig. 6. Variation of switching region upon cyclic switching obtained as a result of simulation. Switching from a completely screened polydomain initial state. Dark field corresponds to the switching region, while light-gray and dark-gray fields correspond to frozen domains of different polarities.

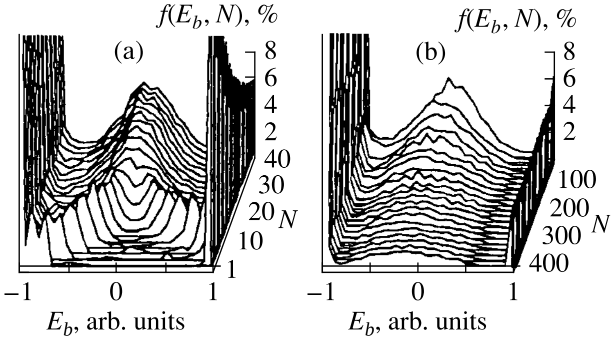

Fig. 7. Evolution of the distribution function of E_b obtained as a result of simulation in (a) the rejuvenation and (b) fatigue stages. The switching starts from a completely screened polydomain initial state.

(Fig. 3a). The initially narrow distribution function spreads in the course of cyclic switching (variance w increases significantly). The formation and growth of two peaks of the distribution function at $E_b = \pm E_{\mathrm{rd}}$ correspond to the formation and increase in the area of kinetically frozen domains (Fig. 3a).

According to the Preisach theory, the distribution function for the internal bias field determines the dependence of switching charge and current on the applied voltage during testing with triangular pulses [33, 34]. The spread of $f(E_b, N)$ upon cyclic switching decreases the switching charge, since polarization switching is terminated in the regions in which the local field E_{loc} becomes smaller than the threshold field E_{th}. In our modification [35] of the Preisach approach, we took into account the above-mentioned fact that the threshold fields required for the formation of a single nucleus and for domain growth (nucleation at a domain wall) differ significantly. It is shown that the dependence of the maximum value of switching current $j_{\max}$ on the variance w of the distribution function, which is found in our model with the help of computer simulation, can be fitted by the formula (Fig. 3) [35]

$$j_{\max}(1/w) = j_{\max}(0) + J[\exp(a/w) - 1], \qquad (6)$$

where J and a are constants.

It is important to note that the maximum value of the switching current, $j_{\max}$, decreases in the fatigue process to a considerably greater extent than the switched charge does (Fig. 4).

3.2. Completely Screened Polydomain Initial State

A simulation of cyclic switching from a polydomain completely screened state revealed an initial increase in the switching charge. This feature enabled us to single out an additional rejuvenation stage preceding the fatigue stage (Fig. 5a). It can be seen that the geometries of the switching region in the rejuvenation and fatigue stages are qualitatively different (Fig. 6). In the course of rejuvenation, the width of the switching region increases considerably and its connectivity changes. After the completion of rejuvenation, this region has the form of a connected labyrinth structure. At the fatigue stage, a self-consistent smoothing and simplification of the labyrinth structure is observed. The stimulation revealed that frozen domains of the same polarity are predominantly formed and grow (unipolar fatigue). The sign of unipolarity is determined by the geometry of the initial domain structure. This ten-

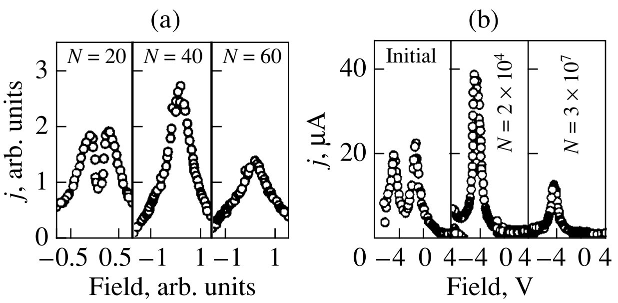

Fig. 8. Variation of the shape of switching current at the rejuvenation and fatigue stages: (a) simulation of switching from a completely screened polydomain initial state and (b) experimental results for thin PZT films.

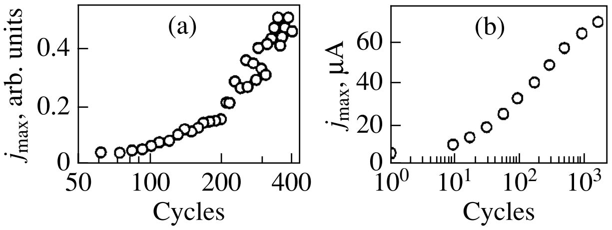

Fig. 9. Increase in the maximum value of switching current at the rejuvenation stage (a) obtained as a result of simulation, and (b) experimental data on cyclic switching in thin PZT films.

dency is in good agreement with the reported experimental results [13].

The evolution of the internal-bias-field distribution function in this case differs qualitatively from that in the case of a zero initial internal bias field considered above. Two peaks corresponding to initial domains of opposite signs spread and merge into a single broad peak during rejuvenation (Fig. 7a). The subsequent behavior of this peak repeats the variation of $f(E_b, N)$ described earlier (Fig. 7b). At the rejuvenation stage, the switching current is the sum of two contributions corresponding to switching in the regions differing in the sign of the internal bias field (Fig. 8a).

4. EXPERIMENT

The rejuvenation and fatigue were studied in lead zirconate–titanate $Pb(Zr_{0.2}Ti_{0.8})O_3$ films 100–200 nm thick. The films were deposited by sol–gel method on $Pt/Ti/SiO_2/Si/$ substrates [11]. The upper platinum electrode was used for applying rectangular bipolar pulses with 100% filling (without a pause between the pulses). The amplitude of pulses U_{cyc} was 5–8 V, and the frequency f_{cyc} was chosen in the interval from 10 Hz to 1 MHz. Hysteresis loops and switching currents were measured by applying triangular pulses (f_m = 10–100 Hz, U_m = 5–7 V) following a certain number of switching cycles with rectangular pulses. Cyclic switching and measurements were carried out at room temperature using an automated measuring complex [29].

The measured variations in switching charge (Fig. 5b) and in current (Fig. 8b) upon cyclic switching in PZT films confirm the existence of the rejuvenation stage, which is manifested most clearly in the increase in j_{max} (Fig. 9). The experimental data on the evolution of the shape of the current during cyclic switching is in qualitative agreement with the predictions of computer simulation (Figs. 5a, 8a). It should be noted that, in order to reduce the computer time required for simulation, the value of the time constant τ characterizing the kinetics of screening was chosen to be much smaller than its experimental value, which leads to the observed discrepancy between the theoretical and experimental values of N, for which the magnitude of the switched charge decreases to half the initial value (endurance).

5. CONCLUSION

Thus, the proposed model of self-consistent evolution of the local internal bias field enabled us to describe the variations in the geometry of the switching region during cyclic switching and to predict the existence of the rejuvenation stage. With the help of computer simulation, we observed a correlation between the variations in the internal-bias-field distribution function and in the shape of switching current upon cyclic switching. The established correlation makes it possible to extract important information concerning the fatigue kinetics from measurements of the switching current. The good agreement between the results of simulation and the experimental data obtained for thin PZT films confirm the applicability of the proposed approach.

ACKNOWLEDGMENTS

The authors are grateful to T. Schneller and R. Gerhardt for providing thin-film samples and to O. Lohse for consultations on measurements.

This study was partially supported by the Russian Foundation for Basic Research (grant no. 01-02-17443), the program "Russian Universities: Fundamental Studies," the program "University Studies in Priority Trends of Science and Technology: Electronics" (grant no. 03-03-29), and the American Foundation for Civil Studies and Development of Independent States of the Former Soviet Union (grant no. REC-005).

REFERENCES

1. H. M. Duiker, P. D. Beale, J. F. Scott, *et al.*, J. Appl. Phys. **68**, 5783 (1990).
2. C. J. Brennan, Integr. Ferroelectr. **2**, 73 (1992).
3. J. Lee, S. Esayan, A. Safari, and R. Ramesh, Appl. Phys. Lett. **65**, 254 (1994).

4. G. Arlt and U. Robels, Integr. Ferroelectr. **3**, 343 (1993).
5. E. Colla, D. Taylor, A. Tagantsev, and N. Setter, Appl. Phys. Lett. **72**, 2478 (1998).
6. I. Stolichnov, A. Tagantsev, E. Colla, and N. Setter, Appl. Phys. Lett. **73**, 1361 (1998).
7. V. Shur, S. Makarov, N. Ponomarev, *et al.*, J. Korean Phys. Soc. **32**, S1714 (1998).
8. E. Colla, S. Hong, D. Taylor, *et al.*, Appl. Phys. Lett. **72**, 2763 (1998).
9. W. Warren, D. Dimos, B. Tutler, *et al.*, Appl. Phys. Lett. **65**, 1018 (1994).
10. V. V. Lemanov and V. K. Yarmarkin, Fiz. Tverd. Tela (St. Petersburg) **38**, 2482 (1996) [Phys. Solid State **38**, 1363 (1996)].
11. M. Grossmann, D. Boten, O. Lohse, *et al.*, Appl. Phys. Lett. **77**, 1894 (2000).
12. A. M. Bratkovsky and A. P. Levanyuk, Phys. Rev. Lett. **84**, 3177 (2000).
13. A. Kholkin, E. Colla, A. Tagantsev, *et al.*, Appl. Phys. Lett. **68**, 2577 (1996).
14. J. F. Scott and M. Dawber, Appl. Phys. Lett. **76**, 3801 (2000).
15. R. Ramesh, W. K. Chan, B. Wilkens, *et al.*, Integr. Ferroelectr. **1**, 1 (1992).
16. A. Yu. Kudzin, T. V. Panchenko, and S. P. Yudin, Fiz. Tverd. Tela (Leningrad) **16**, 2437 (1974) [Sov. Phys. Solid State **16**, 1589 (1974)].
17. A. Gruverman, O. Auciello, and H. Tokumoto, Appl. Phys. Lett. **69**, 3191 (1996).
18. V. M. Fridkin, *Photoferroelectrics* (Nauka, Moscow, 1976; Springer, Berlin, 1979).
19. V. Ya. Shur, *Ferroelectric Thin Films: Synthesis and Basic Properties* (Gordon and Breach, New York, 1996), Vol. 10, Chap. 6.
20. V. Ya. Shur, Yu. A. Popov, and N. V. Korovina, Fiz. Tverd. Tela (Leningrad) **26**, 781 (1984) [Sov. Phys. Solid State **26**, 471 (1984)].
21. V. Ya. Shur, Phase Transit. **65**, 49 (1998).
22. V. Ya. Shur, Yu. A. Popov, and G. B. Soldatov, Fiz. Tverd. Tela (Leningrad) **25**, 265 (1983) [Sov. Phys. Solid State **25**, 148 (1983)].
23. V. Ya. Shur and E. L. Rumyantsev, Ferroelectrics **191**, 319 (1997).
24. V. A. Yurin, Izv. Akad. Nauk SSSR, Ser. Fiz. **24**, 1329 (1960).
25. U. Robels and G. Arlt, J. Appl. Phys. **73**, 3454 (1993).
26. P. Lambeck and G. Jonker, J. Phys. Chem. Solids **47**, 453 (1986).
27. I. Stolichnov, A. Tagantsev, N. Setter, *et al.*, Appl. Phys. Lett. **74**, 3552 (1999).
28. V. Ya. Shur, Author's Abstract of Doctoral Dissertation (UPI, Sverdlovsk, 1990).
29. V. Ya. Shur, E. L. Rumyantsev, E. V. Nikolaeva, *et al.*, Integr. Ferroelectr. **33**, 117 (2001).
30. V. Ya. Shur, E. L. Rumyantsev, E. V. Nikolaeva, *et al.*, J. Appl. Phys. **90**, 6312 (2001).
31. R. C. Miller and G. Weinreich, Phys. Rev. **117**, 1460 (1960).
32. M. Hayashi, J. Phys. Soc. Jpn. **33**, 616 (1972).
33. G. Robert, D. Damjanovic, and N. Setter, Appl. Phys. Lett. **77**, 4413 (2000).
34. A. Bartic, D. Wouters, H. Maes, *et al.*, J. Appl. Phys. **89**, 3420 (2001).
35. V. Ya. Shur, E. L. Rumyantsev, E. V. Nikolaeva, *et al.*, J. Appl. Phys. (in press).

Translated by N. Wadhwa

Physics of the Solid State, Vol. 44, No. 11, 2002, pp. 2151–2156. Translated from Fizika Tverdogo Tela, Vol. 44, No. 11, 2002, pp. 2055–2060.
Original Russian Text Copyright © 2002 by Shur, Nikolaeva, Shishkin, Kozhevnikov, Chernykh.

MAGNETISM AND FERROELECTRICITY

Kinetics of Domain Structure and Switching Currents in Single Crystals of Congruent and Stoichiometric Lithium Tantalate

V. Ya. Shur, E. V. Nikolaeva, E. I. Shishkin, V. L. Kozhevnikov, and A. P. Chernykh
Institute of Physics and Applied Mathematics, Ural State University, Yekaterinburg, 620083 Russia
e-mail: vladimir.shur@usu.ru

Received February 15, 2002

Abstract—A comparative analysis of polarization-switching kinetics in single crystals of congruent and stoichiometric lithium tantalate $LiTaO_3$ is carried out by recording a sequence of instantaneous domain configurations (optical visualization of the evolution of the domain-structure) and the switching current simultaneously. A new mechanism of fast kinetics of domains in congruent lithium titanate due to the growth of steps formed during domain coalescence is discovered experimentally and studied with the help of computer simulation. Additional information on the domain kinetics in stoichiometric lithium tantalate is obtained on the basis of statistical analysis of the noise component of a switching current. A model is proposed for description of the jerky motion of domain walls. *© 2002 MAIK “Nauka/Interperiodica”.*

1. INTRODUCTION

Recently, a new class of periodically polarized nonlinear optical materials has been used extensively for creating coherent radiation sources and frequency converters using the quasi-phase matching effect [1, 2]. Lithium tantalate $LiTaO_3$ is one of the most important representatives of this new class, since it is characterized by high values of electrooptical and nonlinear optical coefficients. A periodic domain structure can be created by applying an electric field to a system of periodic electrodes [3–5] deposited by photolithography. In recent years, attempts have been made to use stoichiometric lithium tantalate (SLT) with a much lower concentration of defects instead of congruent lithium tantalate (CLT) for manufacturing nonlinear optics devices. It was shown that making use of SLT not only considerably reduces photorefraction and qualitatively changes the domain shape but also decreases the coercive field by an order of magnitude [6]. However, the kinetics of domain structure in the case of polarization switching in SLT have not been studied comprehensively as yet. An integrated study of switching processes, including a comparison of the results obtained simultaneously by using direct and indirect methods, is of special interest. It has been proved recently for CLT that the domain kinetics can be observed with the help of an optical microscope directly during switching [7]. In this study, we report on the results of measurements of switching current and direct observation of evolution of the domain structure in CLT and SLT and analyze the mechanisms determining the domain kinetics.

2. EXPERIMENT

The experiments were performed on monocrystalline samples of commercial CLT (Crystal Technology, CA) and on lithium tantalate samples with a close-to-stoichiometric composition (SLT), which were grown by using the Czochralski method with a double crucible at the National Institute of Materials Science, Tsukuba, Japan [8]. The concentration of lithium vacancies was about 2% in CLT and 0.3% in SLT samples. The samples under investigation were in the form of monodomain plates having a size of 6 × 5 mm and cut perpendicularly to the polar axis. The thickness was 0.2 mm for CLT samples and 0.9 mm for SLT samples. Switching was carried out by rectangular field pulses using transparent electrodes having a diameter of 1 mm and made of liquid electrolyte (aqueous solution of LiCl). In addition, SLT samples were investigated using $In_2O_3{:}Sn$ (ITO) transparent electrodes of diameter 2.5 mm, deposited by reactive sputtering. All measurements were made at room temperature.

The evolution of the domain structure during switching in the entire switching region of a sample (for electrodes of diameter 1 mm) was observed directly with the help of a polarizing microscope in transmitted light. The sequence of instantaneous images was recorded by a video camera with a frequency of 25 frames per second. The switching current was recorded simultaneously by using traditional methods. In this way, a unique possibility of establishing a correspondence between the switching current and domain kinetics was realized. Subsequent computer processing of images was used for a quantitative analysis. Our

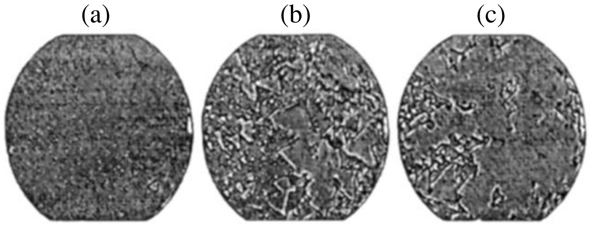

Fig. 1. Optical observation of domain-structure evolution during switching under the action of a rectangular field pulse in CLT (a) 0.3, (b) 0.9, and (c) 1.5 s from the instant of field application. The diameter of the switching region is 1 mm, $E = 190$ kV/cm.

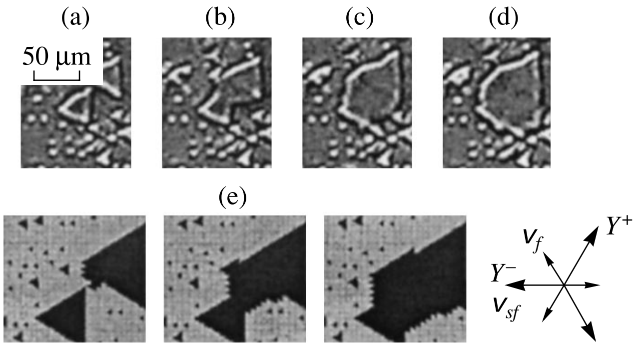

Fig. 2. Fast motion of a domain wall in the Y^+ direction and the formation of a superfast zigzag domain wall moving in the Y^- directions in CLT (a) 0.7, (b) 0.8, (c) 0.9, and (d) 1 s from the instant of field application. $E = 190$ kV/cm. (e) The results of simulation of domain kinetics.

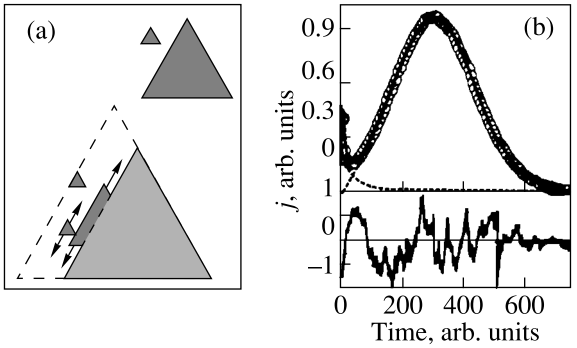

Fig. 3. (a) Diagram of domain growth (dashed lines indicate the final position of the domain wall). (b) Switching current and its noise component obtained as a result of simulation [fitting by Eq. (1)].

measurements proved that CLT and SLT differ quantitatively, not only in the shape of domains, but also in the domain-structure kinetics and, hence, in the shape of the switching current.

3. DOMAIN KINETICS IN CONGRUENT LITHIUM TANTALATE

The domain-structure switching in CLT has made it possible for the first time to experimentally observe a new domain wall motion mechanism, which was proposed by us earlier for explaining the domain kinetics in lead germanate [9, 10].

The switching from the single-domain state in CLT upon the application of a field (in the form of a rectangular pulse) begins with the almost instantaneous (as compared to the switching time) formation of a large number of small domains with a density attaining 1000 mm^{-2} (Fig. 1a). Subsequently, domain formation ceases completely and switching is carried out only due to domain growth. The following two mechanisms of domain growth can be singled out: (i) extremely slow growth of individual domains (at a rate v_s) and (ii) fast motion of domain walls (DWs) after coalescence of domains with considerable anisotropy (a difference in the velocities in the Y^+ and Y^- directions) (Figs. 1b, 1c). The fast motion of a DW (at a velocity v_f) in the three Y^+ directions is the result of formation of steps on the DW due to the coalescence of the moving wall with single isolated domains, followed by the growth of steps (Fig. 2). In addition, superfast zigzag DWs with a high concentration of steps are formed as a result of coalescence of large-size domains (Figs. 2c, 2d), which leads to an anomalously fast motion (at velocity v_{sf}) of DWs in the Y^- directions. Typical values of velocity of DWs, obtained as a result of statistical analysis of a sequence of instantaneous images for switching in a field of 190 kV/cm, were $v_s \sim 1$ μm/s, $v_f \sim 20$–60 μm/s, and $v_{sf} \sim 130$ μm/s. It can be seen that for such a relation of velocities, the switching process is determined not by the growth of individual domains due to nucleation at the walls [10–12] but by the growth of steps formed as a result of coalescence of domains. It should be noted that the mechanism under consideration differs qualitatively from the Kolmogorov–Avrami model [13, 14] used conventionally for analysis of switching currents and based on the study of the growth of individual domains.

Computer simulation of the switching process in CLT was carried out in accordance with the proposed mechanism. The only parameter of the model is the density of randomly distributed seeds formed on the first simulation step. Only the switching due to the growth of the steps formed during domain coalescence was simulated (Fig. 3a). The growth of individual domains was disregarded. The obtained domain configurations and the form of the switching current (Fig. 3b) qualitatively agree with the experimental results (Figs. 2, 4), which confirms the applicability of the proposed mechanism of domain evolution. A detailed discussion of the results of simulation will be given in a separate publication.

4. SWITCHING CURRENT IN CONGRUENT LITHIUM TANTALATE

In the switching mechanism under investigation, an elementary act of domain-structure rearrangement (coalescence of domains or rapid growth of steps) is accompanied by the generation of an elementary pulse of switching current. In CLT, the high initial concentration of isolated domains leads to a large number of simultaneous events. While measuring the switching current, elementary pulses over the entire switching region are added; for this reason, a smooth current pulse with an insignificant noise component is usually observed (Fig. 4a).

In order to quantitatively compare the switching current and the domain-structure kinetics in the course of computer processing of the domain-structure images, we calculated the "optical switching current" proportional to the change $\Delta S(t)$ of the switching-region area between two consecutive instantaneous domain configurations (Fig. 4b). It can be seen from Fig. 4 that the optical current obtained for the entire switching region is similar to the switching current measured simultaneously according to the conventional method. The time resolution for the optical current is relatively small; however, the application of this method makes it possible to determine the optical switching current for any part of the switching region, which provides a unique possibility to attribute the features of the switching current to specific processes of domain-structure rearrangement.

Our detailed analysis of instantaneous domain configurations made it possible to separate three mechanisms of domain evolution, which we used for choosing an adequate mathematical description of the form of the switching current. The switching current was approximated by the sum of two current components:

$$j(t) = j_1(t) + j_2(t) = At^{-\gamma} - 2P_S dq/dt. \qquad (1)$$

The first current component, $j_1(t)$, corresponds to coalescence of the initial small individual domains. For a low initial concentration of domains (in a weak field), only partial switching is observed, which terminates with the formation of individual domains with a considerable size dispersion. Traditionally, the first component of the switching current is not considered, since it is attributed to the "dielectric contribution" associated with the recharging of the ferroelectric capacitor.

The second current component, $j_2(t)$, is observed only for a high density of nuclei (in a strong field). Its time dependence has two stages, which can be approximately described by the Kolmogorov–Avrami formula modified by us [15] (this formula is normally used for analysis of experimental currents) with a transition of growth dimensionality from 2D to 1D (geometrical catastrophe), $\alpha(2D) \longrightarrow \beta(1D)$:

$$q(t) = k_1 \exp[-(t/t_{01})^3], \quad t < t_{cat}, \qquad (2)$$

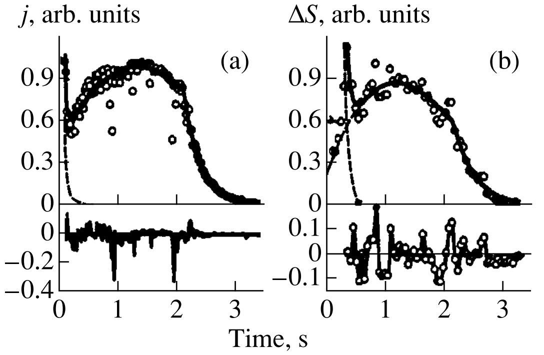

Fig. 4. (a) Traditional and (b) optical switching currents and their noise components in CLT [fitting by Eq. (1)]. $E = 190$ kV/cm.

$$q(t) = k_2 \exp[-(t - t_{cat})/t_{02}], \quad t > t_{cat}, \qquad (3)$$

where k_1 and k_2 are the fractions of area, t_{01} and t_{02} are time constants, and t_{cat} is the catastrophe time.

Such an analysis makes it possible to determine the effective velocity of lateral motion and the nucleation rate. Alternative methods of the analysis of the current shape for the switching mechanism under investigation will be discussed in a separate publication.

Analysis of an image clearly shows that the formation and growth of domains [α(2D) process] dominates at the first stage (Fig. 1b), while coalescence of domains due to annihilation of domain walls [β(1D) process] mainly occurs at the second stage (Fig. 1c).

It should be noted that the method of analysis described above can be applied to extract information on the domain kinetics from the results of measurement of the conventional switching current, without direct optical observations of the domain kinetics in the course of switching.

The jerky rearrangement of the domain structure leads to a considerably nonmonotonic switching current and to the emergence of a noise component (Barkhausen noise). This component can be found by subtracting the approximating curve from the switching current (Fig. 4). Elementary acts of domain-structure rearrangement leading to individual jumps were singled out from an analysis of instantaneous domain configurations.

5. DOMAIN-STRUCTURE KINETICS IN STOICHIOMETRIC LITHIUM TANTALATE

Domain kinetics in SLT were studied in the case of switching under the action of a field and in the case of spontaneous reversal of polarization after the removal of the field [4, 16]. It can be seen from Figs. 1 and 5 that the shapes of domains in CLT and SLT differ qualitatively. Single domains in SLT have the shape of hexagonal prisms and pyramids (for nonthrough domains), as

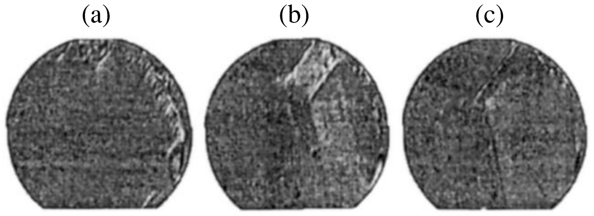

Fig. 5. Optical observation of domain-structure evolution during switching in a dc field in SLT with liquid electrodes (a) 2.4, (b) 4.44, and (c) 10.32 s from the instant of field application. The diameter of the switching region is 1 mm, E = 32 kV/cm.

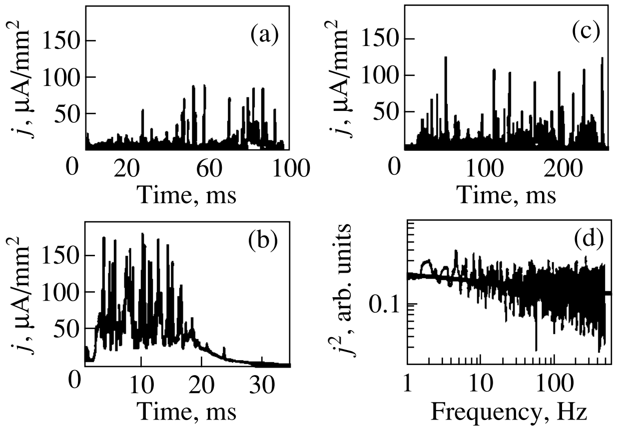

Fig. 6. Switching currents in SLT with (a, b) liquid and (c, d) ITO electrodes. E, kV/cm: (a, c) 20 and (b) 33. (d) The Fourier spectrum of switching current (E = 25 kV/cm).

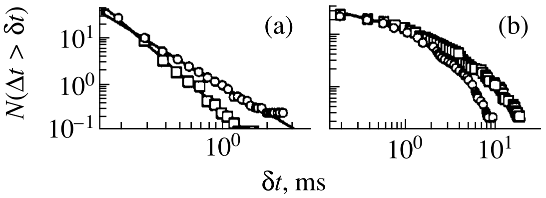

Fig. 7. Analysis of switching currents in SLT with liquid electrodes: cumulative distribution functions of (a) current pulse duration and (b) rest time. Fitting (a) by a power-law dependence and (b) by Eq. (4). Squares and circles correspond to polarization switching with the field switched on and off, respectively. E = 20 kV/cm, liquid electrodes.

is the case with switching in lithium niobate with the help of liquid electrodes [17, 18], in contrast to the triangular prisms and pyramids observed in CLT [17, 18].

Domain kinetics in CLT and SLT also differ considerably. After the application of a field, several hexagonal domains are formed in SLT under the edges of an electrode (Fig. 5a). The subsequent kinetics of the domain structure are determined by jerky motion of a small number of domain walls oriented strictly along preferred crystallographic directions (Figs. 5b, 5c). The DWs stop and, after a certain "rest time," rapidly jump to a new static position. As a result, the switching current is a sequence of individual short current pulses (Fig. 6) corresponding to the jumps of DWs. The average time between pulses (rest time) decreases with increasing applied field (Figs. 6a, 6b). In contrast to congruent lithium niobate [19], the evolution of domains in SLT is independent of the type of electrodes used (cf. Figs. 6a, 6c).

6. ANALYSIS OF BARKHAUSEN NOISE IN STOICHIOMETRIC LITHIUM TANTALATE

It is obvious that classical methods cannot be used for an analysis of switching currents in SLT (as in the case of lithium niobate) [9, 15, 20–22]; for this reason, we applied statistical methods developed for the analysis of noise.

An analysis of the frequency spectrum proved that the Fourier spectrum of switching current in SLT (Fig. 6d) is continuous and contains no well-defined harmonics. The spectrum can be approximated by a power-law dependence with an exponent close to 0.1.

A statistical analysis of switching currents by using a modified Korcak method [23] made it possible to determine the cumulative distribution functions for the duration of individual current pulses (Fig. 7a) and for the rest time (Fig. 7b). The distribution function for current-pulse duration demonstrates the power-law-dependence with exponents 2.8 and 2.0 for polarization switching with the field switched on and off, respectively. It should be noted that such behavior, which is invariant to scaling, is typical of self-organized processes [24].

The power-law dependence for the rest time, corresponding to a self-organized behavior, is observed only in a narrow time interval. For this reason, we approximated the experimental data by a formula taking into account the finite scaling range (upper cutoff) [25]:

$$N(\delta t) = B\delta t^{-\alpha}\exp(-\delta t/\xi), \qquad (4)$$

where δt is a time interval, α is the scaling exponent, and ξ is the fractal correlation time.

As a result of the approximation, we determined the scaling exponent $\alpha = 0.33$ and the fractal correlation time $\xi = 5$ ms.

With the help of the *R/S* analysis of switching current [24], we determined the value of the Hurst exponent $H = 0.70 \pm 0.05$ (Fig. 8a), which is direct evidence of the persistence of domain-wall motion with a long correlation time. It is well known that persistent stochastic processes are characterized by the preservation of tendencies with low noise, as compared to Brownian

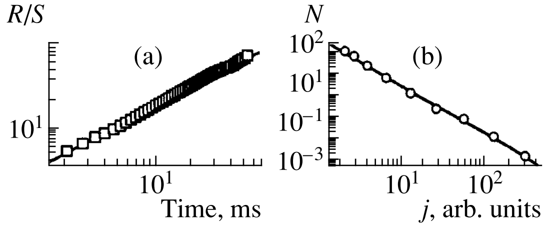

Fig. 8. Analysis of switching currents in SLT: (a) *R*/*S* analysis and (b) distribution function for current-pulse amplitudes. *E*, kV/cm: (a) 20 and (b) 24. Fitting by a power-law dependence.

(random) processes [24]. The distribution function for the current-pulse amplitudes demonstrates a power-law dependence with an exponent 2.3 over the entire range investigated (Fig. 8b).

In order to explain the obtained results, a mechanism of jerky motion of a DW was proposed. It is well known [26, 27] that the velocity of a planar DW decreases after its displacement from the initial position. This slowing down is associated with a decrease in the local field at the wall under the action of a residual depolarization field (partly compensated by a fast external screening) created by bound charges in the region behind the moving wall [10]. For switching in fields exceeding the threshold value insignificantly, this effect leads to a halt of the DW after its displacement [27, 28]. Obviously, defects (which locally enhance the threshold field) may play the role of pinning centers in this case.

The pinning force and the distance between the centers determine the power law of the distribution functions for the duration of current pulses and their amplitudes with close values of exponents. A similar power-law dependence was also obtained from an analysis of Barkhausen pulses emerging during the motion of a DW in magnets [29].

A domain wall can continue its motion only if the local field exceeds its local threshold value. This can be realized during DW rest due to bulk screening of the residual depolarization field as a result of simultaneous operation of the following three competing mechanisms: (i) redistribution of volume charges [10, 30], (ii) reorientation of dipole defects [31, 32], and (iii) injection of a charge from electrodes through the dielectric gap [33]. According to estimates, the rest time for a single planar DW must be considerably shorter than the time constant of bulk screening. In addition, the experimentally determined rest time must decrease due to the fact that several DWs move simultaneously and independently in the sample. This conclusion is confirmed by the relation between the value of the fractal correlation time obtained by us (5 ms) and the experimentally determined time constant of bulk screening in SLT (40 ms) [34].

7. CONCLUSION

Thus, we have carried out a detailed analysis of the switching kinetics by comparing the sequences of instantaneous domain configurations with switching current, which allowed us to find for CLT a new mechanism of fast domain kinetics associated with the coalescence of domains in ferroelectrics. It is shown that important information on the domain kinetics in SLT can be extracted from a statistical analysis of the noise component of the switching current. The proposed model of jerky motion of a domain wall is also applicable to lithium niobate. The mechanisms responsible for the observed differences will be considered in a separate publication.

ACKNOWLEDGMENTS

The authors are grateful to Prof. K. Kitamura and Dr. K. Terabe for providing the samples of stoichiometric lithium tantalate.

This study was partially supported by the Russian Foundation for Basic Research (grant no. 01-02-17443), the program “Russian Universities: Fundamental Studies” (grant no. 5563), the program “University Studies in Priority Trends of Science and Technology: Electronics” (grant no. 03-02-29), and the American Foundation of Civil Studies and Development of Independent States of the Former Soviet Union (grant no. REC-005).

REFERENCES

1. R. L. Byer, J. Nonlinear Opt. Phys. Mater. **6**, 549 (1997).
2. G. Rosenman, A. Skliar, and A. Arie, Ferroelectr. Rev. **1**, 263 (1999).
3. M. Yamada, M. Saitoh, and H. Ooki, Appl. Phys. Lett. **69**, 3659 (1996).
4. R. G. Batchko, V. Ya. Shur, M. M. Fejer, and R. L. Byer, Appl. Phys. Lett. **75**, 1673 (1999).
5. V. Ya. Shur, E. L. Rumyantsev, R. G. Bachko, *et al.*, Fiz. Tverd. Tela (St. Petersburg) **41**, 1831 (1999) [Phys. Solid State **41**, 1681 (1999)].
6. K. Kitamura, Y. Furukawa, K. Niwa, *et al.*, Appl. Phys. Lett. **73**, 3073 (1998).
7. V. Gopalan and T. E. Mitchell, J. Appl. Phys. **85**, 2304 (1999).
8. Y. Furukawa, K. Kitamura, E. Suzuki, and K. Niwa, J. Cryst. Growth **197**, 889 (1999).
9. V. Ya. Shur, A. L. Gruverman, V. V. Letuchev, *et al.*, Ferroelectrics **98**, 29 (1989).
10. V. Ya. Shur, in *Ferroelectrics Thin Films: Synthesis and Basic Properties* (Gordon and Breach, New York, 1996), Vol. 10, Chap. 6.
11. R. C. Miller and G. Weinreich, Phys. Rev. **117**, 1460 (1960).
12. E. Fatuzzo and W. J. Merz, *Ferroelectricity* (North-Holland, Amsterdam, 1967).
13. A. N. Kolmogorov, Izv. Akad. Nauk SSSR, Ser Mat. **3**, 355 (1937).

14. M. Avrami, J. Chem. Phys. **7**, 1103 (1939); **8**, 212 (1940); **9**, 177 (1941).
15. V. Ya. Shur, E. L. Rumyantsev, and S. D. Makarov, J. Appl. Phys. **84**, 445 (1998).
16. V. Ya. Shur, E. L. Rumyantsev, E. V. Nikolaeva, *et al.*, Appl. Phys. Lett. **76**, 143 (2000).
17. S. Kim, V. Gopalan, and B. Steiner, Appl. Phys. Lett. **77**, 2051 (2000).
18. V. Ya. Shur, E. L. Rumyantsev, E. V. Nikolaeva, *et al.*, Proc. SPIE **3992**, 143 (2000).
19. V. Ya. Shur, E. L. Rumyantsev, E. V. Nikolaeva, and E. I. Shishkin, Appl. Phys. Lett. **77**, 3636 (2000).
20. V. Ya. Shur, E. L. Rumyantsev, and S. D. Makarov, Fiz. Tverd. Tela (St. Petersburg) **37**, 1687 (1995) [Phys. Solid State **37**, 917 (1995)].
21. V. Ya. Shur, S. D. Makarov, N. Yu. Ponomarev, *et al.*, Fiz. Tverd. Tela (St. Petersburg) **38**, 1889 (1996) [Phys. Solid State **38**, 1044 (1996)].
22. V. Ya. Shur, E. L. Rumyantsev, S. A. Makarov, *et al.*, Integr. Ferroelectr. **27**, 179 (1999).
23. J. Russ, *Fractal Surfaces* (Plenum, New York, 1994).
24. J. Feder, *Fractals* (Plenum, New York, 1988; Mir, Moscow, 1991).
25. A. Hasmy, M. Foret, J. Pelous, and R. Jullien, Phys. Rev. B **48**, 9345 (1993).
26. M. Drougard and R. Landauer, J. Appl. Phys. **30**, 1663 (1959).
27. V. Ya. Shur, E. L. Rumyantsev, V. P. Kuminov, *et al.*, Fiz. Tverd. Tela (St. Petersburg) **41**, 126 (1999) [Phys. Solid State **41**, 112 (1999)].
28. V. Ya. Shur, A. L. Gruverman, V. P. Kuminov, and N. A. Tonkachyova, Ferroelectrics **111**, 197 (1990).
29. B. Alessandro, C. Beatrice, G. Bertotti, and A. Montorsi, J. Appl. Phys. **68**, 2908 (1990).
30. V. M. Fridkin, *Photoferroelectrics* (Nauka, Moscow, 1976; Springer, Berlin, 1979).
31. U. Robels and G. Arlt, J. Appl. Phys. **73**, 3454 (1993).
32. P. Lambeck and G. Jonker, J. Phys. Chem. Solids **47**, 453 (1986).
33. I. Stolichnov, A. Tagantsev, N. Setter, *et al.*, Appl. Phys. Lett. **74**, 3552 (1999).
34. V. Ya. Shur, E. V. Nikolaeva, E. I. Shishkin, *et al.*, Appl. Phys. Lett. (in press).

Translated by N. Wadhwa

Physics of the Solid State, Vol. 44, No. 11, 2002, pp. 2157–2164. Translated from Fizika Tverdogo Tela, Vol. 44, No. 11, 2002, pp. 2061–2068.
Original Russian Text Copyright © 2002 by Yu. Boĭkov, Erts, Claeson, A. Boĭkov.

MAGNETISM AND FERROELECTRICITY

Dielectric Response of $Ba_{0.75}Sr_{0.25}TiO_3$ Epitaxial Films to Electric Field and Temperature

Yu. A. Boĭkov*, D. Erts, T. Claeson**, and A. Yu. Boĭkov*****

** Ioffe Physicotechnical Institute, Russian Academy of Sciences,*
Politekhnicheskaya ul. 26, St. Petersburg, 194021 Russia

*** Chalmers Technical University, Göteborg, S-41296 Sweden*

**** St. Petersburg State University, Universitetskiĭ pr. 2, St. Petersburg, Petrodvorets, 198094 Russia*

Received January 15, 2002; in final form, February 18, 2002

Abstract—The structure and dielectric parameters of the intermediate ferroelectric layer in the $(001)SrRuO_3 \parallel (100)Ba_{0.75}Sr_{0.25}TiO_3 \parallel (001)SrRO_3$ heterostructure grown by laser ablation on $(001)La_{0.294}Sr_{0.706}Al_{0.647}Ta_{0.353}O_3$ were studied. Tensile mechanical stresses accounted for the polar axis in the ferroelectric, being oriented predominantly parallel to the substrate plane. The remanent polarization in the $Ba_{0.75}Sr_{0.25}TiO_3$ layer increased approximately linearly with decreasing temperature in the interval 320–200 K. The real part of the dielectric permittivity of the intermediate ferroelectric layer reached a maximum $\varepsilon'/\varepsilon_0 = 4400$ at $T_M \approx 285$ K ($f = 100$ kHz). The narrow peak in the temperature dependence of the dielectric loss tangent for the $Ba_{0.75}Sr_{0.25}TiO_3$ ferroelectric layer, observed for $T < T_M$, shifted toward lower temperatures with decreasing frequency and increasing bias voltage applied to the electrodes. © *2002 MAIK “Nauka/Interperiodica”.*

1. INTRODUCTION

For the device potential of ferroelectric films to be realizable in microelectronics and microwave technology, they should be employed as an integral part of a multilayer heterostructure grown on the corresponding substrate and including interlayers of metals, conducting oxides, or superconductors.

In the large family of perovskite-like ferroelectrics, the $Ba_xSr_{1-x}TiO_3$ solid solutions are among the most likely candidates for application in storage cells [1], tunable microwave devices [2], IR detector sensors [3], etc. The possibility of using physical techniques of film preparation (laser ablation, magnetron sputtering, molecular-beam epitaxy, etc.) to grow multilayer heterostructures, including films of ferroelectrics and metals (superconductors), has been demonstrated in a number of publications [4, 5].

In the case of metallic electrodes (Pt, Au, etc.), the Shottky barrier forming near the electrode/ferroelectric interface favors suppression of leakage currents in a plane-parallel capacitor structure [5]. However, the real part of the dielectric permittivity ε' of the intermediate ferroelectric layer becomes noticeably reduced [6] and its temperature dependence cannot be fitted to the Curie–Weiss relation. While replacing the metal electrodes with electrodes made from an oxide having metallic conductivity [$SrRuO_3$ (SRO), $La_{0.5}Sr_{0.5}CoO_3$, etc.) strongly enhances the response of ε' to temperature and electric field, dielectric losses are also increased in this case.

The mechanisms responsible for the substantial differences in the temperature and field dependences of both the real and imaginary (ε'') parts of the dielectric permittivity $\varepsilon = \varepsilon' - i\varepsilon''$ between ferroelectric films and single crystals remain unclear. Our knowledge of the temperature dependences of the remanent polarization and coercive field for *c*- and *a*-oriented $Ba_xSr_{1-x}TiO_3$ films (with the polar axis perpendicular and parallel to the substrate plane, respectively) is far from complete.

This communication reports on a study of the response of ε' and dielectric loss tangent $\tan\delta$ of $(100)Ba_{0.75}Sr_{0.25}TiO_3$ (BSTO) epitaxial films to variations in temperature, electric field, and frequency. Estimates of the activation energy and of the characteristic relaxation time of the process governing the value of $\tan\delta$ at temperatures below the phase transition point are presented.

2. EXPERIMENT

The laser ablation method (COMPex 100, KrF, $\lambda = 248$ nm, $\tau = 30$ ns) was employed to grow SRO/BSTO/SRO trilayer heterostructures on a (001)LSATO substrate $[(LaAlO_3)_{0.3} + (Sr_2AlTaO_6)_{0.7}]$. Consecutive SRO ⟶ BSTO ⟶ SRO ablation of the original ceramic targets was conducted at a laser radiation density on their surface of 1.5 J/cm^2 and an oxygen pressure of 0.4 mbar. The deposited layers of the metal oxide and the intermediate ferroelectric layer were saturated by oxygen in the course of cooling of the SRO/BSTO/SRO heterostructure (760°C ⟶ 20°C,

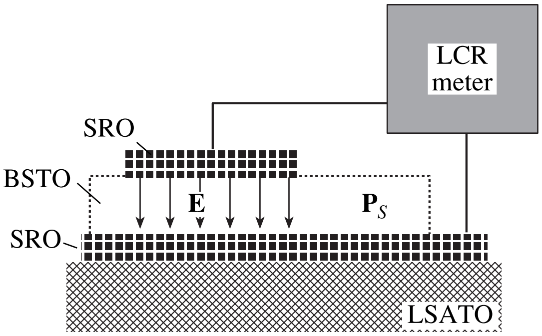

Fig. 1. Sketch of a plane-parallel capacitor SRO/BSTO/SRO heterostructure formed by photolithography and ion milling. The spontaneous polarization vector $\mathbf{P}_S$ in the BSTO layer is oriented predominantly parallel to the substrate plane.

20°C/min) in an oxygen environment (1 atm). The technology for growing the SRO/(Ba,Sr)TiO_3/SRO heterostructures is described in more detail in [7, 8].

The microstructure and phase composition of the heterostructures thus grown were studied by x-ray diffraction (CuK_α radiation, $\omega/2\theta$ and ϕ scans, rocking curves). To determine the lattice unit cell parameters of the BSTO layer in the direction parallel to the substrate plane ($a_\parallel$) and along the normal to its surface ($a_\perp$), diffractograms were measured in the geometry where the plane containing the incident and reflected X-ray beams was orthogonal to either (001) or (101)LSATO. To estimate the effective grain size and strain distribution in the ferroelectric layer, the first four peaks in a $(00n)\omega/2\theta$ x-ray scan were measured using high-precision x-ray optics [7].

The surface morphology of the BSTO layer grown on SRO/LSATO was studied with an atomic-force microscope (Nanoscope-IIIa, tapping mode). The data on the surface morphology of the SRO layer grown on LSATO can be found in [9].

The preparation of contact pads on the top SRO layer and of auxiliary holes in the intermediate ferroelectric layer is outlined in [10].

The capacitance C and $\tan\delta$ of the plane-parallel SRO/BSTO/SRO capacitors formed (Fig. 1) were measured with an hp 4263A LCR meter in the frequency interval 1–100 kHz, both with a bias voltage $V_b = \pm 2.5$ V applied to the electrodes and without it. The real and imaginary parts of the dielectric permittivity of the BSTO layer were calculated from the relations $\varepsilon' = Cd/S$ and $\varepsilon'' = \varepsilon' \tan\delta$, where $d = 700$ nm is the ferroelectric layer thickness and $S = 200 \times 200\ \mu\mathrm{m}^2$ is the area of the upper contact in the capacitor heterostructure; the bottom electrode was common for all the capacitors grown on the chip.

3. EXPERIMENTAL RESULTS AND DISCUSSION

An SRO layer grown epitaxially at condensation temperatures of 700–800°C on the LSATO surface has a smooth surface [9] with rare growth steps whose height is a multiple of the metal-oxide unit cell parameter. Because the temperature coefficients of linear thermal expansion of strontium ruthenate ($\beta_{\mathrm{SRO}} = 11 \times 10^{-6}\ \mathrm{K}^{-1}$ for the orthorhombic phase at $T = 300$–650 K [11]) and of the substrate ($\beta_{\mathrm{LSATO}} = 10 \times 10^{-6}\ \mathrm{K}^{-1}$ according to the specification of Crystec, which provided the substrates) are similar, the character of mechanical strains in a SRO film grown on LSATO is determined by the lattice misfit of the two crystals [$m = (a_L - a_S)/a_S \approx +2\%$, where a_L is the lattice parameter of the film and a_S is that of the substrate]. An SRO layer grown on (001)LSATO is acted upon by compressive mechanical stresses in the substrate plane.

The temperature coefficient of linear expansion of BSTO ($\beta_0 \approx 12.5 \times 10^{-6}\ \mathrm{K}^{-1}$) is considerably larger than those of LSATO and SRO. As a result, at temperatures close to that of the phase transition ($T_{\mathrm{C}} = 340$ K for bulk samples [12]), a BSTO layer grown on SRO/LSATO is subject to tensile mechanical stresses in the substrate plane. The mechanical strains generated in the heterostructure due to the BSTO and SRO lattice misfit become partially relieved during the formation of the ferroelectric layer. The tensile mechanical stresses acting in the substrate plane favor the in-plane orientation of the polar axis of the BSTO ferroelectric layer (parallel to the substrate plane).

Let us analyze first the x-ray diffractograms obtained for the grown SRO/BSTO/SRO heterostructures and the data on the free-surface morphology of the BSTO layer and, after this, the dielectric parameters of this layer.

3.1. The Structure of the BSTO Layer and the Morphology of Its Free Surface

The x-ray diffractograms obtained did not contain peaks indicating the presence of macroinclusions of secondary phases in the grown SRO/BSTO/SRO heterostructures (Fig. 2 and inset to Fig. 3). The preferred orientation of the ferroelectric layer and the oxide electrodes in the SRO/BSTO/SRO heterostructure was (001)[010]SRO ‖ (100)[010]BSTO ‖ (001)[010]SRO ‖ (001)[010]LSATO.

The parameter $a_\perp = 3.981$ Å, calculated for the BSTO layer from the x-ray data ($T = 300$ K), was substantially smaller than $a_\parallel = 3.992$ Å. This suggests that the polar axis in the grown ferroelectric layer is oriented predominantly parallel to the substrate plane (*a*-oriented layer). The FWHM of the rocking curve for the (200)BSTO x-ray peak of the SRO/BSTO/SRO heterostructure was 0.23° [inset (a) in Fig. 3]. The FWHM obtained for the BSTO layer is in accord with the typical values reported in the literature for $(Ba,Sr)TiO_3$ epitaxial layers with the polar axis parallel to the substrate plane. The slight increase in the FWHM of the ferroelectric layer in the SRO/BSTO/SRO compared to that of the rocking curve measured for a precisely *c*-oriented $Ba_{0.25}Sr_{0.75}TiO_3$ film in the SRO/$Ba_{0.25}Sr_{0.75}TiO_3$/SRO heterostructure [7] should be attributed to the presence of grains whose polar axis is orthogonal to the substrate plane in the bulk of the BSTO layer. The effective lattice parameter for the BSTO layer in the SRO/BSTO/SRO heterostructure, $a_{\text{eff}} = (a_\perp^2 a_\parallel)^{1/3} \approx 3.98$ Å, was larger than the corresponding parameter for stoichiometric bulk samples ($a \approx 3.97$ Å) [13]. This signals a high density of oxygen vacancies in the intermediate ferroelectric layer.

Figure 3 presents the FWHM Ø of the (*n*00) peaks plotted vs. θ for an x-ray (001)ω/2θ scan. The Ø vs. θ dependence can be written as [14]

$$\varnothing = 0.9\lambda_0(d_0\cos\theta) + 2\tan\theta\partial a/a, \qquad (1)$$

where $\lambda_0 = 1.54056$ Å is the x-ray wavelength, d_0 is the sample grain size, *a* is the lattice parameter, and ∂a is the lattice parameter distortion associated with nonuniform lattice strains. The slope of the straight line in Fig. 3 was used to determine $2\partial a/a \approx 1.2 \times 10^{-3}$, the value characterizing the average strain in the BSTO layer. The intercept of the same line on the ordinate axis provided an estimate of the grain size in the BSTO layer, $d_0 = 35$ nm. The values obtained in this way for $\partial a/a$ and d_0 for the BSTO layer in the SRO/BSTO/SRO heterostructure agree well, on the whole, with the corresponding literature figures for the $SrTiO_3$ [15] and $Ba_{0.25}Sr_{0.75}TiO_3$ [7] epitaxial films. The lattice parameter distortion in the BSTO layer may be caused by offstoichiometry, the presence of structural defects (grain boundaries, stacking faults, dislocations, etc.) in its volume, and mechanical stresses.

Data on the morphology of the free surface of a film are useful when analyzing the mechanisms governing its growth. These data are particularly important in the case of thin multicomponent oxide layers grown on the surface of auxiliary (buffer or electrode) layers with a high density of structural defects. Figure 4a presents an atomic-force microscope (AFM) image of the (100)BSTO || (001)SRO || (001)LSATO free surface obtained in height mode. One can clearly see grains of size d_1 = 150–200 nm (dimensions in the substrate plane) whose interfaces are decorated by characteristic grooves. The formation of grooves on the free film surface at the points where it crosses the grain boundaries results from free-energy minimization in the growing film–substrate system. The character of the grooves is determined to a considerable extent by the relative magnitude of the free energy of the free surface and of that of the grain boundaries (the ions present in the region of grain boundaries and in the surface layer have excess free energy compared to the ions in the grain bulk). As follows from the x-ray data [ϕ scan of the (111)BSTO peak], the azimuthal misorientation of grains in the ferroelectric layer did not exceed 0.4°. Because grain boundaries can substantially affect the parameters of films of the perovskite-like oxides, it appears appropriate to mention at least the main mech-

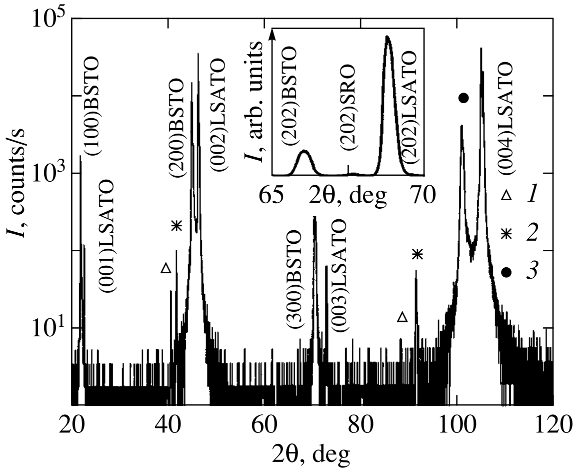

Fig. 2. Diffractogram (CuK_α, ω/2θ) obtained for a SRO/BSTO/SRO heterostructure in the geometry where the incident and reflected x-ray beams were in a plane normal to (001)LSATO. (*1, 2*) CuK_β x-ray peaks from the ferroelectric layer and the substrate, respectively, and (*3*) (400)BSTO. Inset shows a fragment of the diffractogram measured on the same heterostructure in the geometry where the incident and reflected x-ray beams were in a plane normal to (101)LSATO.

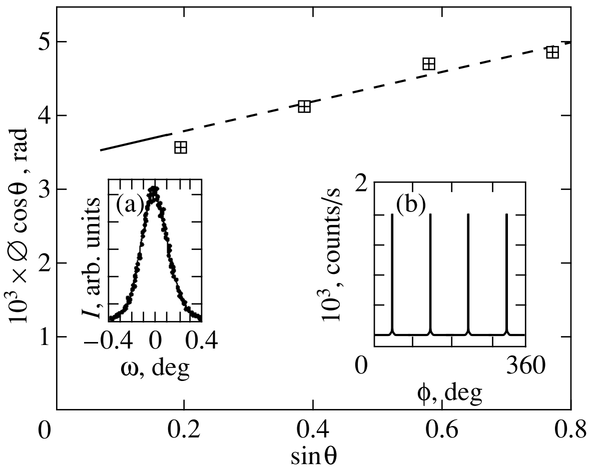

Fig. 3. FWHM of x-ray peaks Ø obtained in a (00*n*)ω/2θ scan plotted as a function of θ for the BSTO layer in the SRO/BSTO/SRO heterostructure. Inset *a* shows a rocking curve for the (200)BSTO peak, and inset *b*, a ϕ scan for the (111)BSTO x-ray peak from the same heterostructure.

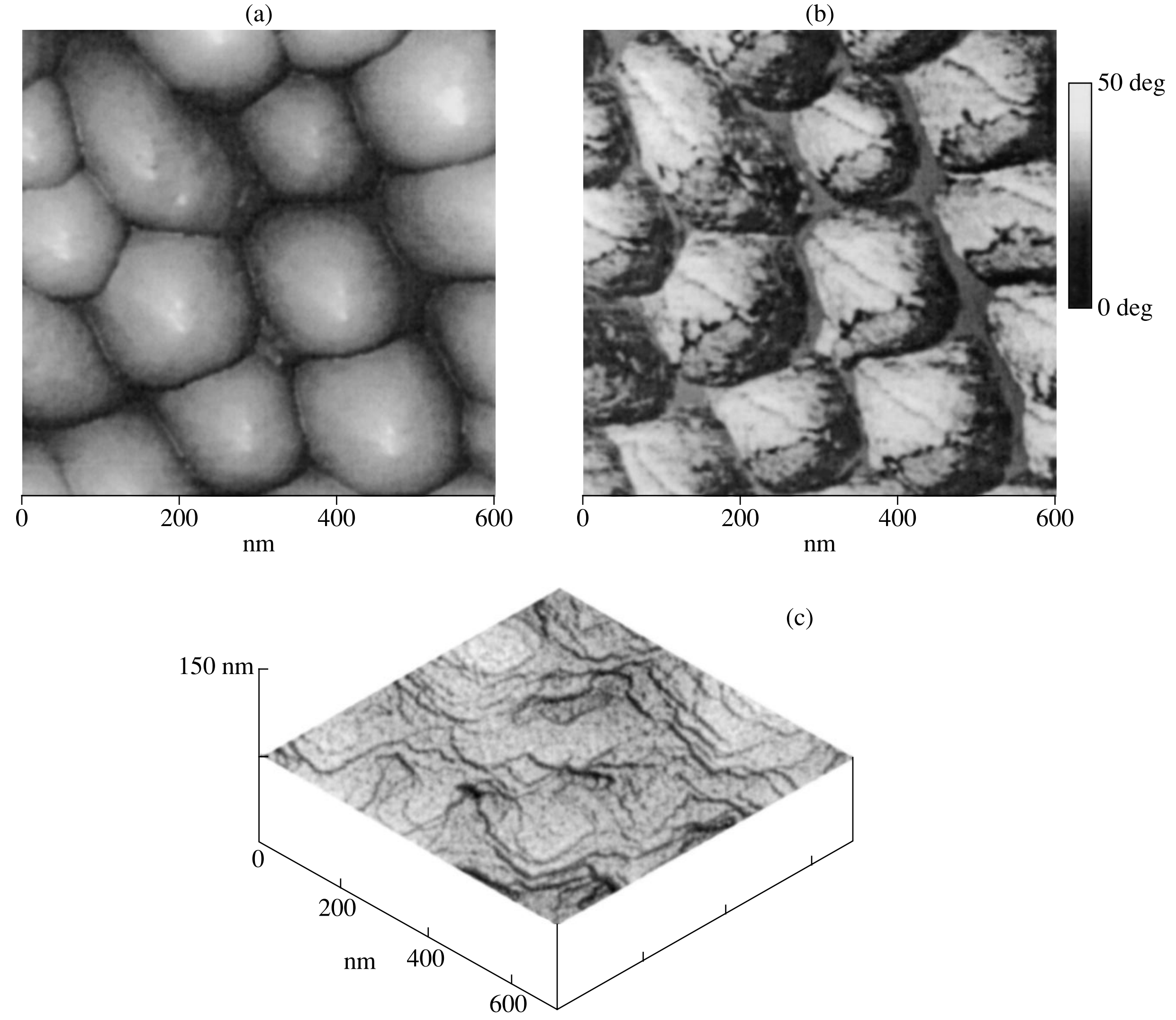

Fig. 4. (a) AFM image of the free surface of a 700-nm-thick BSTO layer obtained in height mode (top view). The ferroelectric layer was grown on (001)SRO || (001)LSATO. (b) AFM image of the same part of the ferroelectric layer obtained in phase mode (top view). (c) Image of the free surface of a 700-nm-thick $SrTiO_3$ layer grown on (001)SRO || (001)LSATO obtained in height mode (viewed at 45°).

anisms responsible for their formation. One of the reasons for grain formation in a BSTO layer is lattice misfit with the substrate [in our case, with (001)SRO || (001)LSATO]. Minimization of the energy of elastic mechanical stresses in the nucleus–substrate system can produce a certain azimuthal misorientation of stable islands forming in the initial growth stage of a ferroelectric layer. This accounts for the formation of a polycrystalline layer with grains separated by small-angle boundaries. The small-angle grain boundaries are seen clearly in high-resolution electron-microscopy images of cross sections of multilayer heterostructures containing layers of perovskite-like oxides [4].

Grain boundaries can also form in a ferroelectric film in the case where the nuclei of the condensing material are deposited on the substrate in a coherent manner. Grain boundaries can originate here due to the phase adsorbed on the surface of the growing layer being off-stoichiometric or as a result of the low mobility of the particles of this phase. The excess components segregate at the outer boundaries of the growing islands. As a result, the grown film is made up of grains of the given composition, with interlayers of an off-stoichiometric phase. The density of such interlayers in the layer volume can be reduced by appropriate heat treatment in an oxygen environment [16].

The pronounced difference between the effective grain sizes derived from x-ray measurements and from images of the BSTO layer free surface can be accounted for by the grains growing with increasing layer thickness or by the presence of a fine structure of block interfaces within a grain, which is not resolved when viewing the film free surface in height mode.

In contrast to the height mode, the AFM images obtained in the phase mode contain information on variations in the nanoscale mechanical characteristics of the sample surface layer. The image obtained in the phase mode (Fig. 4b, $T = 300$ K) of the same part of the BSTO layer that is shown in Fig. 4a resolves clearly not only the small-angle crystallographic boundaries but also characteristic features within the grains in the form of sharp boundaries where the signal changes its phase. Azimuthal orientation of these intragrain boundaries is predominantly along the directions making an angle of 45° with [001] and [010]BSTO. At room temperature, the grown BSTO layer (or at least a sizable part of its volume) was in the ferroelectric phase. One of the reasons for the appearance of the above features in the phase-mode images of the free surface of the BSTO film can be the formation of 90° walls between ferroelectric domains in its volume. Phase-mode AFM images of $Ba_{0.25}Sr_{0.75}TiO_3$ epitaxial films [7], which were in paraelectric phase at 300 K, did not reveal any features indicating a complex structure of crystallographic grains. The atomic-force microscope was used successfully in the height mode to study the domain structure of PZT films [17].

To find the extent to which the granular character of a grown BSTO layer can be accounted for by off-stoichiometry of the adsorbed phase and by the lattice misfit between BSTO and SRO/LSATO, we grew a 700-nm thick $SrTiO_3$ epitaxial layer on the (001)SRO ‖ (001)LSATO surface under the same technological conditions. Strontium titanate is a better lattice match to SRO and LSATO ($m < 0.7\%$). The mechanisms that can give rise to a BSTO layer becoming off-stoichiometric but that do not operate in STO were considered in [18]. The FWHM of the rocking curve of the (200)STO reflection from the SRO/STO/SRO heterostructure is smaller by about a factor of three [9] than the corresponding figures for the BSTO layer. Figure 4c shows an image of the free surface of a 700-nm thick STO layer grown on SRO/LSATO. On the free STO surface, we clearly see resolved growth steps whose height is a multiple of the strontium titanate lattice parameter. No grooves decorating grain boundaries on the free STO layer surface were found. This, however, cannot be considered proof of the absence of grain boundaries in the strontium titanate layer but rather indicates that the azimuthal misorientation of grains and the density of grain boundaries in its volume are smaller than those in BSTO/SRO/LSATO.

3.2. Dielectric Parameters of the BSTO Layer

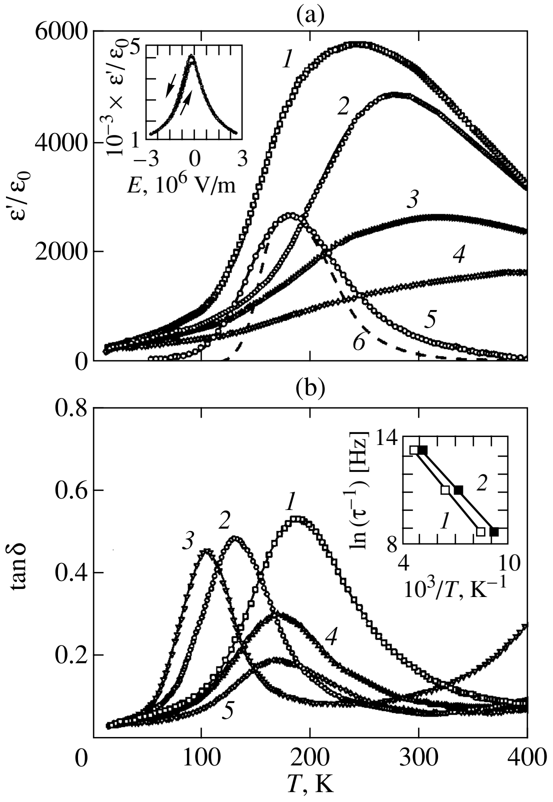

Fig. 5. (a) Temperature dependences of the real part of dielectric permittivity $\varepsilon'/\varepsilon_0$ (curves *1–4*) and of $\Delta\varepsilon'/\varepsilon_0$ (curves *5*, *6*) obtained for the BSTO layer in the SRO/BSTO/SRO heterostructure. f (kHz): (*1*) 10 and (*2–4*) 100; V_b (V): (*1*, *2*) 0, (*3*) +1, and (*4*) +2.5; (*5*, *6*) experiment and calculation made using Eq. (7), respectively. Inset shows the $\varepsilon'/\varepsilon_0(E)$ dependence measured for a BSTO layer at $T = 295$ K and $f = 100$ kHz. (b) Temperature dependences of $\tan\delta$ measured on the BSTO layer at different frequencies and bias voltages applied to the electrodes. f (kHz): (*1*, *4*, *5*) 100, (*2*) 10, and (*3*) 1. V_b (V): (*1–3*) 0, (*4*) +1, and (*5*) +2.5. Inset shows Arrhenius plots for the relaxation time $\tau^{-1}(1/T)$ in the BSTO layer obtained at V_b (V): (*1*) 0 and (*2*) +2.5.

The temperature dependence of ε' measured at 100 kHz for the BSTO layer had a clearly pronounced maximum at a temperature $T_M \approx 280$–290 K (Fig. 5a). As in the case of bulk BSTO crystals, the maximum in the $\varepsilon'(T)$ curve shifted toward higher temperatures when a bias voltage was applied to the electrodes (curves *3*, *4* in Fig. 5a). At temperatures below T_M, ε' exhibited a noticeable frequency dispersion. As f decreased, the real part of the dielectric permittivity increased, with the difference $\Delta\varepsilon' = \varepsilon'(10\text{ kHz}) - \varepsilon'(100\text{ kHz})$ passing through a sharp peak at $T \approx 185$ K (Fig. 5a). For $T > T_M$, the difference $\Delta\varepsilon'$ decreased monotonically with increasing temperature. When f was lowered from 10 to 1 kHz, the peak in the $\Delta\varepsilon'(T)$ curve shifted toward lower temperatures by about 30 K. Taking into account the fact that the real part of dielectric permittivity of epitaxial layers of the (Ba,Sr)TiO_3 solid solutions in the paraelectric phase is virtually frequency-independent [7, 19], it seems natural to attribute the presence of the peak in the $\Delta\varepsilon(T)$ relation to dielectric relaxation of the ferroelectric phase. At temperatures below T_C, a BSTO film is divided into ferroelectric domains. Ferroelectric domains in an *a*-oriented BSTO layer are separated by 90° domain walls. The displacement of ferroelectric domain walls by an electromagnetic wave propagating in a BSTO layer is accompanied by redistribution of the electrons, canceling the polarization charge. Incomplete compensation of the polarization charge at the points where domain walls cross the grains accounts for the generation of an internal electric depolarization field, which acts directly on ε' and $\tan\delta$ [19]. The dielectric relaxation time τ_D associated with charge redistribution in the BSTO layer can be written as [20]

$$\tau_D = \varepsilon'\rho, \quad (2)$$

where ρ is the electrical resistivity.

The electrical resistivity of the $(Ba,Sr)TiO_3$ intermediate layer in an epitaxial heterostructure with electrodes of conducting oxides is, as a rule, substantially lower than that of the corresponding single crystals. One of the main reasons accounting for the substantial conductivity of epitaxial ferroelectric layers is the high concentration of oxygen vacancies in their volume. The conductivity of oxygen-deficient BSTO films is determined to a considerable extent by the intensity of electron promotion from donor centers into the conduction band [18]. Under these conditions, the carrier concentration in the ferroelectric layer depends exponentially on the temperature and electric field (the Poole–Frenkel emission [21]) and the temperature dependence of ρ follows the relation

$$\rho \sim \exp[(\varphi_L - \beta E^{1/2})/k_B T], \quad (3)$$

where φ_L is the energy gap between the donor level and the conduction band edge, k_B is the Boltzmann constant, $\beta = (e^3/\pi\varepsilon_{hf}\varepsilon_0)^{1/2}$, e is the electronic charge, ε_{hf} is the high-frequency dielectric permittivity, and ε_0 is the dielectric permittivity of the vacuum. From the temperature dependence of the conductivity determined for oxygen-deficient STO single crystals and BSTO epitaxial films, the value of φ_L was found to be ~0.1 eV [9, 18]. For $E = V_b/d > 2 \times 10^7$ V/m, ions can also contribute to the conductivity of the ferroelectric layer [22].

Recalling Eqs. (2) and (3), the dielectric relaxation time associated with electron redistribution in the domain wall region in the BSTO layer can be written as

$$\tau = \tau_0 \exp(\varphi_0/k_B T), \quad (4)$$

where τ_0 is the attempt time and $\varphi_0 \sim (\varphi_L - \beta E^{1/2})$ is the activation energy.

To make a comprehensive analysis of the extent to which the relaxation process affects the dynamics of dielectric permittivity, we used $\varepsilon'(T)$ and $\tan\delta(T)$ dependences measured at different frequencies. It seems natural to assign the sharp peak in the temperature dependence of $\tan\delta$ to resonance in the interaction of domain walls with the electromagnetic wave, when its frequency approaches τ^{-1}. When the frequency was lowered, the peak in the $\tan\delta(T)$ dependence for the BSTO layer shifted toward lower temperatures (Fig. 5b), which is in full agreement with the temperature dependence of τ [see Eq. (4)].

Within the Debye model, the contribution of the relaxation process to dielectric permittivity ε_r can be written in the form [23]

$$\varepsilon_r = \varepsilon_\infty + (\varepsilon_S - \varepsilon_\infty)/(1 - i\omega\tau), \quad (5)$$

where ε_S and ε_∞ are the relaxation contributions to the dielectric permittivity at low and high frequencies, respectively, and $\omega = 2\pi f$. For BSTO, we have $\varepsilon_S \gg \varepsilon_\infty$ [24]. It follows from Eq. (5) that

$$\varepsilon'' \sim \omega\tau/(1 + \omega^2\tau^2). \quad (6)$$

According to Eq. (6), ε'' should be maximum at $\omega\tau = 1$. To estimate τ_0 and φ_0, we made use of the temperature dependence of the reciprocal relaxation time. The values of τ^{-1} at different temperatures were derived from the position of the maximum in the measured $\varepsilon''(T)$ plots. The $\ln(\tau^{-1}) \sim 1/T$ dependences for the BSTO layer at $E = 0$ are plotted in the inset to Fig. 5b (curve *1*). The Arrhenius plot yielded the following values: $\tau_0(E = 0) = 5 \times 10^{-9}$ s and $\varphi_0(E = 0) = 105$ meV.

The maximum in the $\tan\delta(T)$ curve for the BSTO layer shifted toward lower temperatures when a bias voltage was applied to the metal-oxide electrodes (curves *4*, *5* in Fig. 5b). In accordance with Eq. (3), the height of the barrier governing the intensity of electron promotion into the conduction band from donor centers decreased in an electric field, which was accompanied by a decrease in τ. The relation $\ln(\tau^{-1}) \sim 1/T$ obtained at $E = 3.5 \times 10^6$ V/m for the BSTO layer in the SRO/BSTO/SRO heterostructure is plotted in the inset to Fig. 5b (curve *2*). When biased at $E = 3.5 \times 10^6$ V/m, the activation energy φ_0 decreased by about 12% to 93 meV, while the attempt time did not change: $\tau_0(E = 3.5 \times 10^6 \text{ V/m}) = \tau_0(E = 0) = 5 \times 10^{-9}$ s.

According to [21], $\beta = 5.1 \times 10^{-24}$ J m$^{1/2}$ V$^{-1/2}$ for bulk STO crystals. With such a coefficient β, the activation energy should have decreased in a field $E = 3.5 \times 10^6$ V/m by about 50%. Since there are no grounds to suspect a sharp increase in the high-frequency dielectric permittivity of the BSTO layer compared with the corresponding figures available for bulk single crystals, the relatively weak response of φ_0 to an external electric field in the BSTO layer should be apparently attributed

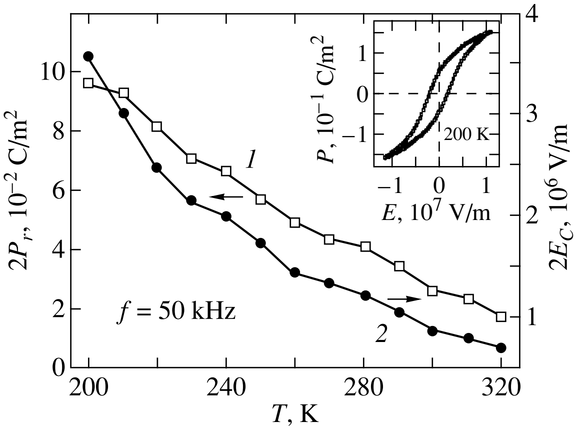

Fig. 6. Remanent polarization P_r and coercive field E_C plotted as a function of temperature for the BSTO layer in the SRO/BSTO/SRO heterostructure. Inset shows the field dependence of the polarization $P(E)$ measured on the same layer at T = 200 K.

to the electric fields in the bulk of crystal grains and at grain boundaries being substantially different.

We used the values of τ_0 and φ_0 thus obtained to approximate the measured temperature dependence of $\Delta\varepsilon'(T) = \varepsilon'(10\text{ kHz}) - \varepsilon'(100\text{ kHz})$ for the BSTO layer (Fig. 5a). It follows from Eq. (5) that

$$\Delta\varepsilon'(T) = (\varepsilon_S - \varepsilon_\infty) \times(\omega_2^2 - \omega_1^2)\tau^2/(1+\omega_1^2\tau^2)(1+\omega_2^2\tau^2), \tag{7}$$

where $\omega_1/2\pi$ = 10 kHz and $\omega_2/2\pi$ = 100 kHz. The experimental $\Delta\varepsilon'(T)$ relation can be fitted quite well by Eq. (7) for $(\varepsilon_S - \varepsilon_\infty)/\varepsilon_0 \approx 3300$.

The $\varepsilon'(T = 295\text{ K})$ curve (inset to Fig. 5a) exhibits a weak hysteresis, signaling the presence of a ferroelectric phase in the bulk of the BSTO layer. At T = 295 K, the dependence of ε' of the BSTO layer on electric field was virtually symmetrical with respect to the E = 0 point. In contrast to a c-oriented $Ba_{0.25}Sr_{0.75}TiO_3$ film [7], the electronic processes occurring at the SRO/BSTO interface do not noticeably affect the dynamics of BSTO dielectric permittivity. At T = 300 K, ε' of the ferroelectric layer in the SRO/BSTO/SRO heterostructure decreased by about a factor of three when a bias voltage ±2.5 V was applied to the electrodes.

The field dependence of polarization $P(E)$ measured at $T < 320$ K exhibited distinct hysteresis loops. For $T < 300$ K, the hysteresis loops were practically symmetrical with respect to the E = 0 point (inset to Fig. 6) and remained unchanged with the frequency varied from 10 to 50 kHz. The temperature dependences of the remanent polarization P_r and coercive field E_C for the BSTO layer are displayed in Fig. 6. For $200 < T < 320$ K, P_r increased approximately linearly with decreasing temperature. For $T < 200$ K, the growth of P_r with decreasing temperature became less steep. The coercive field increased with decreasing temperature in the interval 320–200 K without a visible sign of saturation.

Thus, the polar axis orientation in the BSTO layer is determined to a considerable extent by the actual type of mechanical strains due to the lattice misfit and a difference in the thermal expansion coefficient between the layer and the substrate. For $T < T_C$, relaxation of ferroelectric domain walls in the BSTO layer accounts for the substantial frequency dependence of dielectric permittivity. For E = 0, the characteristic time τ_0 and the activation energy φ_0 describing domain wall relaxation in the BSTO layer are 10^{-9} s and 105 meV, respectively, so that φ_0 decreases by about 12% when a bias voltage of ±2.5 V is applied to the electrodes.

ACKNOWLEDGMENTS

This study was carried out under the aegis of scientific cooperation between the Russian and the Swedish Royal Academies of Sciences and was partially supported by the Ministry of Science of the Russian Federation, project no. 4B19.

REFERENCES

1. C. S. Hwang, Mater. Sci. Eng. B **56**, 178 (1998).
2. J. P. Hong and J. S. Lee, Appl. Phys. Lett. **68**, 3034 (1996).
3. J.-G. Cheng, X.-J. Meng, J. Tang, *et al.*, Appl. Phys. Lett. **75**, 3402 (1999).
4. Yu. A. Boikov, Z. G. Ivanov, A. N. Kiselev, *et al.*, J. Appl. Phys. **78**, 4591 (1995).
5. B. Nagaraj, T. Sawhney, S. Perusse, *et al.*, Appl. Phys. Lett. **74**, 3194 (1999).
6. L. J. Sinnamon, R. M. Bowman, and J. M. Gregg, Appl. Phys. Lett. **78**, 1724 (2001).
7. Yu. A. Boĭkov and T. Claeson, Fiz. Tverd. Tela (St. Petersburg) **43**, 2170 (2001) [Phys. Solid State **43**, 2267 (2001)].
8. B. M. Gol'tsman, Yu. A. Boĭkov, and V. A. Danilov, Fiz. Tverd. Tela (St. Petersburg) **43**, 874 (2001) [Phys. Solid State **43**, 908 (2001)].
9. Yu. A. Boikov and T. Claeson, Physica C (Amsterdam) **336**, 300 (2000).
10. Yu. A. Boĭkov and T. Claeson, Fiz. Tverd. Tela (St. Petersburg) **43**, 323 (2001) [Phys. Solid State **43**, 337 (2001)].
11. J.-P. Maria, H. L. McKinstry, and S. Trolier-McKinstry, Appl. Phys. Lett. **76**, 3382 (2000).
12. A. D. Hilton and B. W. Rickkets, J. Phys. D **29**, 1321 (1996).
13. A. von Hippel, Rev. Mod. Phys. **22**, 221 (1950).

14. E. D. Specht, R. E. Clausing, and L. Heatherly, J. Mater. Res. **5**, 3251 (1999).
15. D. Fuchs, M. Adam, P. Schweiss, *et al.*, J. Appl. Phys. **88**, 1844 (2000).
16. Yu. A. Boĭkov, T. Claeson, and A. Yu. Boĭkov, Zh. Tekh. Fiz. **71** (10), 54 (2001) [Tech. Phys. **46**, 1260 (2001)].
17. A. Seifert, F. F. Lange, and L. S. Speck, J. Mater. Res. **16**, 680 (1995).
18. Yu. A. Boikov and T. Claeson, Supercond. Sci. Technol. **12**, 654 (1999).
19. Yu. A. Boikov and T. Claeson, Appl. Phys. Lett. **79**, 2052 (2001).
20. N. P. Bogoroditskiĭ, Yu. M. Volokobinskiĭ, A. A. Vorob'ev, and B. M. Tareev, *Theory of Dielectrics* (Moscow, 1965).
21. J. R. Yeargan and H. L. Taylor, J. Appl. Phys. **39**, 5600 (1968).
22. J.-H. Lee, R. Mohammedali, J. H. Han, *et al.*, Appl. Phys. Lett. **75**, 1455 (1999).
23. C. Kittel, *Introduction to Solid State Physics* (Wiley, New York, 1966, 3rd ed.), p. 392.
24. W. Kleemann and H. Schremmer, Phys. Rev. B **40**, 7428 (1989).

Translated by G. Skrebtsov

Physics of the Solid State, Vol. 44, No. 11, 2002, pp. 2165–2170. Translated from Fizika Tverdogo Tela, Vol. 44, No. 11, 2002, pp. 2069–2074.
Original Russian Text Copyright © 2002 by Shmyt'ko, Afonikova, Torgashev.

MAGNETISM AND FERROELECTRICITY

Anomalous States of the Crystal Structure of $(Rb_{0.1}(NH_4)_{0.9})_2SO_4$ Solid Solutions in the Temperature Range 4.2–300 K

I. M. Shmyt'ko*, N. S. Afonikova*, and V. I. Torgashev**

** Institute of Solid-State Physics, Russian Academy of Sciences, Chernogolovka, Moscow oblast, 142432 Russia*

*** Research Institute of Physics, Rostov State University, pr. Stachki 194, Rostov-on-Don, 344090 Russia*

Received February 25, 2002

Abstract—Crystals of $(Rb_{0.1}(NH_4)_{0.9})_2SO_4$ solid solutions are studied using x-ray diffractometry. It is revealed that the temperature dependence of the lattice parameter a exhibits an anomalous behavior, namely, the "invar effect" at temperatures above the ferroelectric phase transition point T_c and an anomalous increase in the temperature range from T_c to the liquid-helium temperature. An anomalous increase in the lattice parameter a and an increase in the intensity of Bragg reflections with a decrease in the temperature are interpreted within the model of the coexistence of two sublattices hypothetically responsible for the ferroelectric phase transition. A series of superstructure reflections observed along the basis axes corresponds to a sublattice formed in the matrix of the host structure. Analysis of the ratio between the lattice parameters of these structures allows the inference that, in the temperature range 4.2–300 K, the structure of the crystal under investigation can be considered an incommensurate single-crystal composite. © *2002 MAIK "Nauka/Interperiodica".*

1. INTRODUCTION

It is known that crystals belonging to the structural family of rubidium ammonium sulfates of the general formula $(Rb_x(NH_4)_{(1-x)})_2SO_4$ form a continuous series of solid solutions [1]. Crystals of the rubidium-free ammonium sulfate $(NH_4)_2SO_4$ undergo a first-order ferroelectric phase transition with a change in the symmetry from *Pnam* to $Pna2_1$ at a temperature of 223 K. A decrease in the temperature brings about reversal of the spontaneous polarization of these crystals [2]. In the $(Rb_x(NH_4)_{(1-x)})_2SO_4$ system, the ferroelectric phases are retained up to compositions with $x = 0.6$–0.65 [1].

The origin of the ferroelectric phase transition in crystals of this family has been discussed in the framework of different models, such as the order–disorder model [3], improper ferroelectrics [4], coupled oscillators [5], coupled oscillators–relaxors [6], and the model of two ferroelectric nonequivalent sublattices [7]. As is evident from the aforementioned approaches, the mechanism of the ferroelectric phase transition under investigation is rather complicated and, until presently, has not been clearly understood [8].

The compounds under consideration belong to a very interesting class, namely, the class of orientational glasses, in which the subsystem of multipole moments is efficiently frozen with a decrease in the temperature. These compounds exhibit a disorder intermediate between the disorders observed in crystals and conventional "canonical" glasses [9–12].

In the present work, we performed an x-ray diffraction investigation of the real structure of $(Rb_{0.1}(NH_4)_{0.9})_2SO_4$ solid solutions. In our opinion, this investigation is necessary for correct interpretation of the temperature behavior of the physical properties of these compounds and elucidation of the nature and mechanisms of the phase transitions involved.

2. SAMPLE PREPARATION AND EXPERIMENTAL TECHNIQUE

The experiments were carried out using single-crystal samples with a rubidium content $x = 0.1$. According to the phase diagram, these crystals at temperatures below 223 K belong to ferroelectrics [1]. The choice of this composition was made for the following reasons: (i) the low content of rubidium in the solid solution and, consequently, the possible manifestation of the properties of the rubidium-free ammonium sulfate $(NH_4)_2SO_4$, on the one hand, and (ii) the presence of substitutional atoms that would provide a manifestation of the structural features typical of the entire series of compositions $0 < x < 0.6$ containing low-temperature ferroelectric phases, on the other hand.

The quality of the studied samples was controlled using traditional rolling-crystal and Laue methods. The determination of the crystal symmetry and precision measurements of the unit cell parameters were performed on a Rigaku AFC6S four-circle diffractometer (MoK_α radiation) at temperatures above and below T_c (300 and 203 K, respectively). The low-temperature measurements were carried out using a Strimer cryostat (Rigaku). For x-ray diffraction analysis, samples were prepared in the form of balls ~0.25–0.35 mm in diameter. The space groups were determined prior to and after the transformation and coincided with those available in the literature, namely, *Pnam* and $Pna2_1$, respectively. The results of the solution of the atomic structure at these temperatures will be published in a separate paper.

Lattice parameters of $(Rb_{0.1}(NH_4)_{0.9})_2SO_4$ crystals

T, K	Space group	*a*, Å (Δ*a*)	*b*, Å (Δ*b*)	*c*, Å (Δ*c*)	α, deg (Δα)	β, deg (Δβ)	γ, deg (Δγ)
300	*Pnma*	7.8081	5.9862	10.5525	90.003	90.038	89.994
		(0.0010)	(0.0008)	(0.0016)	(0.012)	(0.010)	(0.011)
203	$Pna2_1$	7.8161	5.9564	10.5206	90.024	89.985	89.978
		(0.0018)	(0.0012)	(0.0012)	(0.012)	(0.013)	(0.018)

The temperature measurements of the lattice parameters were performed on a Siemens D500 x-ray diffractometer with the use of a helium cryostat designed at the Institute of Solid-State Physics, Russian Academy of Sciences. The diffractometer was modified using special programs with the aim of recording reciprocal lattice maps of the single-crystal sections.

3. RESULTS AND DISCUSSION

The measured characteristics of the crystal structure of $(Rb_{0.1}(NH_4)_{0.9})_2SO_4$ solid solutions are presented in the table. The angular distribution of substructure elements of the samples (ω scan mode) did not exceed 0.3°. Analysis of the rocking x-ray patterns revealed additional (superstructure) reflections lying off the main layer lines. The superstructure reflections observed were identified using the reciprocal lattice cross sections along the basis axes. Figure 1 shows the characteristic (**b***–**a***) plane sections of the reciprocal space with the aforementioned superstructure reflections at room temperature. It can be seen that the superstructure reflections are located along the **b*** direction not only for the (0 *k* 0) reflections but for the (*h k* 0) reflections as well. The distance from these reflections to the main reflection changes with variations in the order of the reflection in accordance with the coexistence of two lattices with the following parameters: 10.5525 Å for Bragg reflections and 9.2593 Å for satellite reflections. Similar sections were obtained for the (**b***–**c***) plane of the reciprocal space. An examination of these sections revealed that the (0 *k l*) superstructure reflections are also located along the **b*** direction. In the reciprocal space, the obtained sections correspond to two interpenetrating lattices in which the projections of all the points onto the (**a***–**c***) plane virtually coincide, thus retaining the motif of the initial structure, whereas the points along the **b*** direction are spaced at progressively larger intervals with distance away from the origin of the coordinates.[1]

Reasoning from the results obtained, we can propose three models of the crystal structure under investigation. According to the first model, the crystal structure is formed by layers of new phase precipitates whose lattice spacing differs from the lattice spacing of the matrix along the **b*** direction. It should be noted that these phase precipitates are unrelated to enrichment or depletion of particular regions of the crystal with rubidium atoms in the case when these atoms are statistically distributed over the (NH_4) positions. As follows from analyzing the reciprocal lattice maps depicted in Fig. 1, the lattice parameter b_{ph} of the possible phase precipitates is less than the lattice parameter b_m of the matrix ($b^*_{ph} > b^*_m$). This ratio between the lattice parameters of the new phase precipitates and the matrix should correspond to an enrichment of the new-phase regions with rubidium atoms in accordance with the concentration dependence of the lattice parameter *b*(*x*) obtained in [1]. However, the lattice parameter *b* of the possible phase precipitates proves to be equal to 9.2593 Å, whereas this parameter even for pure Rb_2SO_4 must be no less than 10.44 Å. Moreover, within the framework of the concentration model, a change in the lattice parameter *b* should be attended by variations in the lattice parameters *a* and *c*, which is in contradiction with the experiment. The lattice parameters *a* and *c* of the new phase precipitates observed are assumed to be nearly identical to those of the matrix. This inference stems from the fact that, in the case of the (*h k* 0) reflections (see, for example, the reciprocal lattice map in the vicinity of the (1 6 0) point in Fig. 1d), the satellite reflections (–*h k* 0), (0 *k l*), and (0 *k* –*l*) are located, accurate to within the scan step, along the **a*** (**c***) direction at the same distance in the reciprocal space as the main reflection. Furthermore, the absence of the satellite reflection for the Bragg reflection (0 4 0) and the presence of the satellite reflections for the Bragg reflections (0 2 0) and (0 6 0) suggest a structural dissimilarity between the possible phase precipitates and the matrix. For a statistical distribution of rubidium atoms, each Bragg reflection should be accompanied by the satellite reflections.

The model of phase precipitates is consistent with the experiment under the assumption that, in particular regions of the crystal, the rubidium atoms occupy regular positions in the unit cell (for example, a certain layer along the **b** direction) instead of being statistically distributed over the (NH_4) positions. This structure can be

---

[1] It is quite possible that the points of both sublattices also do not coincide in the (**a***–**c***) plane. This assumption is based on the reciprocal lattice map in the vicinity of the (1 0 0 0) point (Fig. 1e), which contains a very weak diffuse reflection in addition to the strong Bragg reflection. Similar superstructure reflections are also observed for higher orders of reflection along the **c** direction. The difference between the parameters *a* and *c* of the satellite lattices and the relevant Bragg lattices is so small that they can be considered to be nearly identical in the (**a***–**c***) plane.

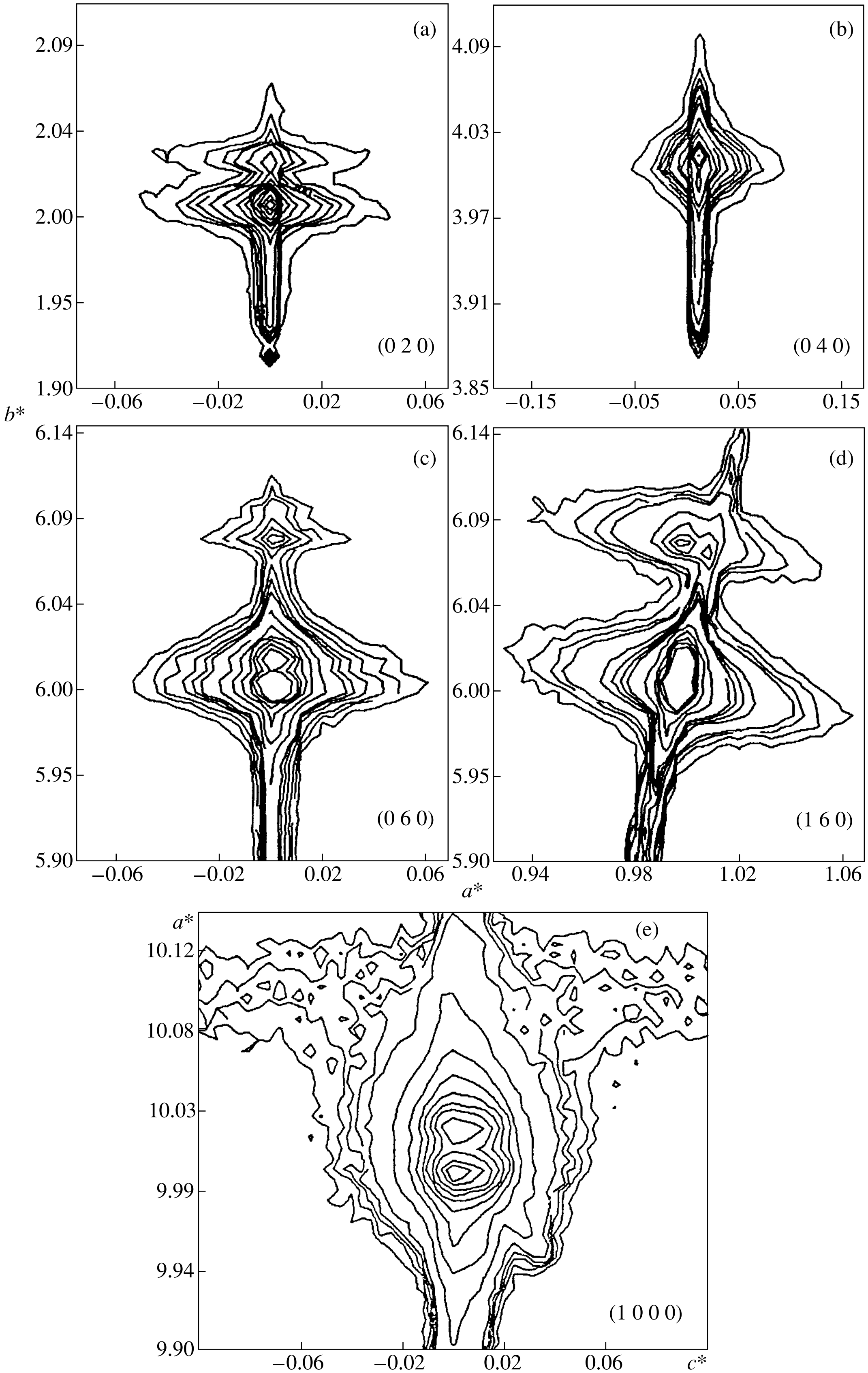

Fig. 1. Reciprocal lattice maps in the vicinity of the (a) (0 2 0), (b) (0 4 0), (c) (0 6 0), (d) (1 6 0), and (e) (1 0 0 0) points for $(Rb_{0.1}(NH_4)_{0.9})_2SO_4$ crystals.

considered a polytype structure with a layer packing of Rb and (NH_4). In this case, the absence of certain superstructure reflections and a considerable change in the lattice parameter along the direction of layer packing become possible. For this distribution of rubidium atoms, the lattice parameters in the (**a**–**c**) plane remain unchanged. The verification of the above model calls for investigation of $(Rb_x(NH_4)_{(1-x)})_2SO_4$ compounds of other compositions for which, in the case under consideration, the positions of the satellite reflections will change with variations in the rubidium content.

The second model describes a crystal structure with substitutional modulations such that, in the reciprocal space, the distance from the satellite reflection to the main reflection can change with variations in the order of reflection and, moreover, the satellite reflections can arise on only one side of the main reflection [13]. In this model, the (NH_4) tetrahedron changing its orientation with respect to the (SO_4) tetrahedron can serve as a substitutional element and the rubidium atoms can be statistically distributed over the (NH_4) positions. The choice of the (NH_4) tetrahedron as an ordering element corresponds to an extremely low intensity of superstructure reflections. In order to verify the validity of the second model, it is necessary to examine rubidium-free ammonium sulfate crystals of the composition $(NH_4)_2SO_4$, which, in this case, are also characterized by substitutional modulations.

According to the third model, the structure of the crystal under investigation is treated as an incommensurate single-crystal composite in which two weakly interacting and interpenetrating nonequivalent (host and guest) substructures coexist in such a way that their lattice parameters coincide in one of the basal planes and are incommensurate along the direction perpendicular to this plane [14–20]. In this case, it would appear reasonable that the guest substructure is formed by (NH_4) groups, which, owing to the low reflection power, are responsible for lower intensities of the satellite reflections from the guest lattice sites as compared to those of the host substructure containing (SO_4) groups. Therefore, the structures described above become possible for rubidium-free ammonium sulfate, as is the case with substitutional modulations.

Finally, the assumption that the additional reflections are associated with the degradation of the surface layer of the sample should be rejected. Judging from the depth of the diffracting layer (~5–50 μm) and the intensity ratio of the additional and main reflections (1/500), the disturbed surface layer does not exceed 100–1000 Å. This layer should be easily polished. However, the additional reflections were observed even after deep mechanical polishing. This indicates a volume distribution of the phase precipitates over the matrix.

Analysis of the results obtained permits us to choose the most appropriate model. In actual fact, the main lattice must be a multiple of the superstructure lattice in both the polytype model and the model of substitutional modulations. For an incommensurate single-crystal composite, the ratio between the lattice parameters of the substructures must have an irrational value. In this case, the multiplicity or the irrationality can be estimated using the ratio $a_{\text{sat}}/(a_{\text{Bragg}} - a_{\text{sat}})$, which follows from the coincidence (or noncoincidence) of the sites in both lattices within N periods: $a_{\text{sat}}(N + 1) = a_{\text{Bragg}}N$. This ratio must have an integral value for the first two models and an irrational value for incommensurate structures. From the aforementioned parameters, we obtain $N = 7.36877513\ldots$. Therefore, the most appropriate model is an incommensurate single-crystal composite.

In order to obtain additional information on the crystal structure of $(Rb_{0.1}(NH_4)_{0.9})_2SO_4$ solid solutions, we measured the temperature dependences of the lattice parameters (Fig. 2). As can be seen from Fig. 2a, the lattice parameter a exhibits an anomalous behavior, namely, a decrease in the temperature from T_c to 4.2 K is accompanied by an increase in the lattice parameter a. To account for the anomalous behavior of the lattice parameter a, it is necessary to elucidate the physical nature of the changes observed in the lattice parameters with variations in the temperature. It should be noted that the changes in the lattice parameters are associated primarily with the anharmonicity of atomic vibrations in local potential wells. It is evident that, in the general case, changes in the temperature (or, what amounts to the same, changes in the energy of atomic vibrations) should be attended by variations in the amplitude of atomic vibrations and, consequently, in the mean interatomic distances and lattice parameters. Within this interpretation, there must be no expansion of the crystal lattice with a decrease in the temperature.

A different situation can arise when atoms are not independent of one another but form coupled nonequivalent sublattices. As the temperature decreases, these sublattices can expand not through anharmonicity of atomic vibrations but through other interactions, for example, due to a dipole–dipole interaction of their constituent structural elements (in our case, for example, due to an interaction of dipole moments of (SO_4) and (NH_4) distorted tetrahedra). In the case under consideration, the mechanism of the anomalous increase in the lattice parameter a can be determined from the changes observed in the intensity of reflections due to variations in the temperature. For anharmonicity of atomic vibrations, the increase in the lattice parameters with variations in the temperature should lead to a decrease in the diffracted intensity at the expense of the Debye–Waller factor. In the case when the lattice parameter a increases as a result of displacement of the sublattices, the diffracted intensity either can decrease with a decrease in the temperature or can increase with temperature variations in the structure factor of the reflection involved. In general, upon transformation of

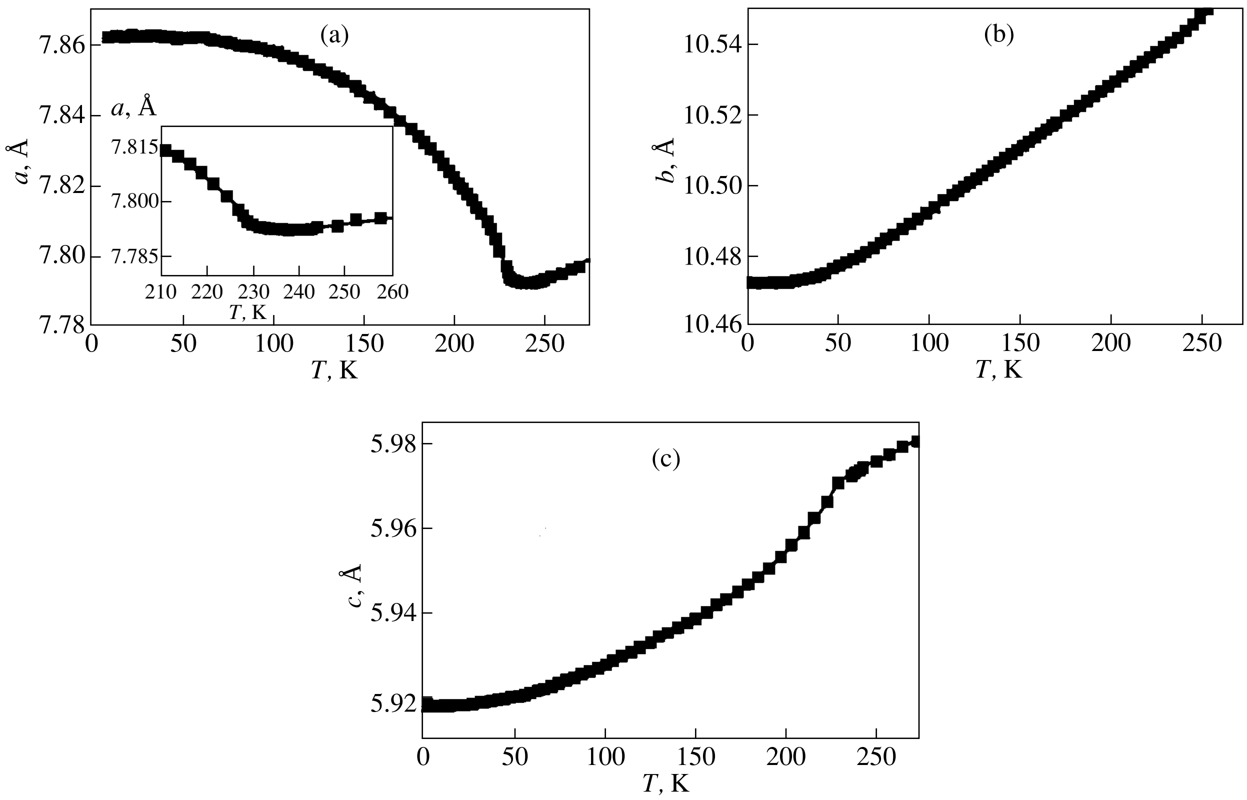

Fig. 2. Temperature dependences of the lattice parameters (a) *a*, (b) *b*, and (c) *c* for $(Rb_{0.1}(NH_4)_{0.9})_2SO_4$ crystals.

the sublattices, the intensity of reflections increases or decreases depending on the temperature range. We observed only an increase in the integrated intensity of the (*h* 0 0) reflection with a decrease in the temperature. This is indirect evidence that nonequivalent sublattices coexist in the studied structures. In this respect, the observed increase in the lattice parameter *a* and the increase in the integrated intensity of the (*h* 0 0) reflection with a decrease in the temperature count in favor of the model of the coexistence of two nonequivalent sublattices, especially from the standpoint of the elucidation of the mechanism of the ferroelectric phase transition [7].

Apart from the anomalous increase at temperatures below T_c, the lattice parameter *a* exhibits an “invar effect” with a change in the temperature above T_c (see inset in Fig. 2a). It is known that the invar effect can be observed in the temperature range of the existence of incommensurately modulated phases. However, we failed to reveal superstructure reflections that would be symmetric with respect to the Bragg reflections and, moreover, would be located at regular intervals with variations in the order of reflection (wave vectors ±**k**) along the basis axes (by analogy with the known directions for isomorphic compounds [21, 22]). No equidistant reflections along the basis axes were observed until the intensity ratio of the superstructure reflection to the main reflection became equal to 1/1000. The latter circumstance suggests that the modulation, if it exists, exhibits a complex nature in these crystals.

The temperature dependence of the unit cell volume (Fig. 3) provides additional information on the origin of the ferroelectric phase transition. It can be seen from Fig. 3 that, below T_c, the unit cell volume first smoothly increases with a decrease in the temperature and then decreases. Note that the bulk thermal expansion coefficient of the studied sample substantially changes in the vicinity of T_c. An increase in the unit cell volume with

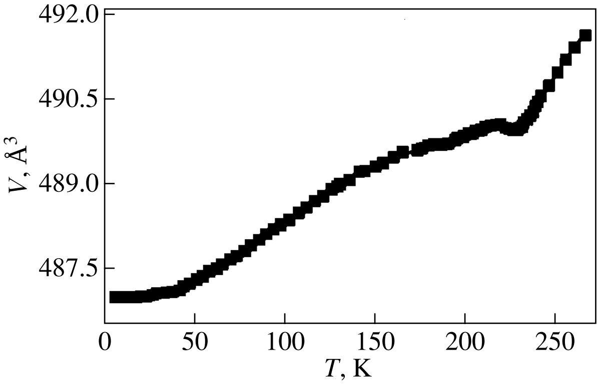

Fig. 3. Temperature dependence of the unit cell volume for $(Rb_{0.1}(NH_4)_{0.9})_2SO_4$ crystals.

a decrease in the temperature of the crystal indicates a radical transformation of the crystal structure upon the ferroelectric phase transition. A considerable decrease in the bulk thermal expansion coefficient at temperatures below T_c suggests that, after the ferroelectric phase transition, the lattice atoms reside in potential wells with a smaller anharmonicity coefficient.

4. CONCLUSIONS

Thus, the results obtained in our investigation clearly demonstrated that crystals of $(Rb_{0.1}(NH_4)_{0.9})_2SO_4$ solid solutions are characterized by structural states of complex nature. This manifests itself in the following phenomena: (i) a decrease in the temperature leads to an anomalous increase in the lattice parameters and the unit cell volume, (ii) the temperature dependence of the lattice parameters exhibits an invar effect at temperatures above the ferroelectric phase transition point T_c, and (iii) a set of superstructure reflections indicates the presence of an incommensurate sublattice in the host structure. The observed increase in the integrated intensity of scattering with a decrease in the temperature and an anomalous increase in the lattice parameter below T_c are indirect evidence in favor of the model of the coexistence of two ferroelectric sublattices. However, the available data are still insufficient to interpret definitively the structural state of a crystal composed of two nonequivalent incommensurate substructures. In particular, the role played by rubidium atoms in the formation of superstructure reflections and, consequently, the anomalous structural states of these crystals are not clearly understood. In our opinion, a complete understanding of the nature of the observed anomalous states of the crystal structure calls for detailed investigation into the structure of crystals of the other compositions, specifically of rubidium-free ammonium disulfide crystals.

ACKNOWLEDGMENTS

This work was supported by the Russian Foundation for Basic Research, project no. 99-02-18238.

REFERENCES

1. K. Ohi, J. Osaka, and H. Uno, J. Phys. Soc. Jpn. **44**, 529 (1978).
2. N. G. Unruh, Solid State Commun. **8**, 1915 (1970).
3. D. E. O'Reily and T. Tsang, J. Chem. Phys. **46**, 1301 (1967).
4. T. Ikeda, K. Fudjibayashi, T. Nada, and J. Kobayashi, Phys. Status Solidi A **16**, 279 (1973).
5. A. Sawada, Y. Tagagi, and Y. Ishibashi, J. Phys. Soc. Jpn. **34**, 748 (1973).
6. J. Petzelt, J. Grigas, and I. Myerova, Ferroelectrics **6**, 225 (1974).
7. A. Sawada, S. Ohya, Y. Ishibashi, and Y. Takagi, J. Phys. Soc. Jpn. **38**, 1408 (1975).
8. G. V. Kozlov, S. P. Lebedev, and A. A. Volkov, J. Phys. C **21**, 4883 (1988).
9. E. Courtens, Ferroelectrics **72**, 229 (1987).
10. U. T. Hochli, K. Knorr, and A. Loidl, Adv. Phys. **39**, 405 (1990).
11. P. Simon, Ferroelectrics **135**, 169 (1992).
12. D. DeSousa Meneses, G. Hauret, and P. Simon, Phys. Rev. B **51**, 2669 (1995).
13. A. Guinier, *Theorie et Technique de la Radiocristallographie* (Dunod, Paris, 1956; Fizmatgiz, Moscow, 1961).
14. D. Brown, B. D. Cotforth, C. G. Davides, *et al.*, Can. J. Chem. **52**, 791 (1974).
15. J. M. Hastling, J. P. Pouget, G. Shirane, *et al.*, Phys. Rev. Lett. **39**, 1484 (1977).
16. A. J. Schultz, J. M. Williams, N. D. Miro, *et al.*, Inorg. Chem. **17**, 646 (1978).
17. Sander van Smaalen, Cryst. Rev. **4**, 79 (1995).
18. R. J. Nelmes, D. R. Allan, M. T. McMahon, and S. A. Belmonte, Phys. Rev. Lett. **83**, 4081 (1999).
19. M. I. McMahon, T. Bovornratanaraks, D. R. Allan, *et al.*, Phys. Rev. B **61** (5), 3135 (2000).
20. V. Heine, Nature **403**, 836 (2000).
21. H. Dohata and S. Kawada, J. Phys. Soc. Jpn. **57**, 4284 (1988).
22. A. Kunishige and H. Mashiyama, J. Phys. Soc. Jpn. **56**, 3189 (1988).

Translated by O. Borovik-Romanova

Physics of the Solid State, Vol. 44, No. 11, 2002, pp. 2171–2174. Translated from Fizika Tverdogo Tela, Vol. 44, No. 11, 2002, pp. 2075–2078.
Original Russian Text Copyright © 2002 by Malygin.

Mechanism of Homogenization of the Martensite State of Crystals with a Shape Memory Effect

G. A. Malygin
Ioffe Physicotechnical Institute, Russian Academy of Sciences,
Politekhnicheskaya ul. 26, St. Petersburg, 194021 Russia
e-mail: malygin.ga@pop.ioffe.rssi.ru

Received February 20, 2002

Abstract—The mechanism of homogenization of the martensite state of crystals with a shape memory effect under mechanical stresses applied to a crystal is theoretically analyzed in the framework of the thermodynamic approach and the theory of smeared martensite transitions. The homogenization of the martensite state of the crystal is considered for two variants of martensite that differ in all parameters (the temperature and the heat of transformation, spontaneous strains, etc.) and for many variants of martensite that differ from one another in the orientation of the habit planes. *© 2002 MAIK “Nauka/Interperiodica”.*

1. INTRODUCTION

Experimental investigations have revealed several variants of martensite in the course of martensite transformation of crystals with a shape memory effect [1, 2]. Different martensites either can have the same crystal lattice and differ only in the orientation of the habit planes or can exhibit different crystal structures. This multivariance takes place when the martensite transformation is initiated by variations in the temperature. Owing to the isotropic nature of the thermodynamic forces involved, the martensite transformation, as a rule, leads to the formation of a system of self-accommodated (twinned) martensite layers in the crystal.

Under external mechanical stresses or internal stresses arising in the crystal, the isotropy of the crystal and the multivariance and self-accommodation of the martensite state disappear. When the stresses are sufficiently strong, there occurs a complete or partial homogenization of the martensite state due to “freezing-out” of the martensites unfavorably oriented with respect to the acting mechanical force [1, 2]. At present, this phenomenon has been understood qualitatively. However, in a quantitative sense, the physical mechanism of homogenization remains poorly investigated.

In this work, the homogenization mechanism was analyzed in terms of the recently developed phenomenological theory of smeared martensite transitions [3, 4], which is based on a thermodynamic approach to first-order phase transitions, among them martensite transformations in alloys with a shape memory effect. This theory describes the phase equilibrium in a crystal as a function of temperature and different forces acting on the crystal, including mechanical forces.

Earlier [3, 4], I developed the theory describing the phase equilibrium in a crystal with one variant of martensite. In Section 2 of the present paper, the phase equilibrium in a crystal and the homogenization of the martensite state are considered in the framework of the theory of smeared martensite transitions as applied to the crystal with two variants of martensite. In Section 3, a similar analysis is performed for a larger but finite number of martensite variants.

2. TWO VARIANTS OF MARTENSITE

Within the thermodynamic approach, the phase equilibrium in a crystal undergoing a structural transformation is determined by the minimum (minima) of the free energy $\Delta F = \Delta U - T\Delta S$, where T is the temperature, ΔU is the change in the internal energy of the crystal upon the structural transition, and ΔS is the change in the entropy of the crystal. Let us assume that particles (atoms) in the crystal exist in three states with concentrations (relative volume fractions) φ_1, φ_2, and φ_3, where φ_3 is the volume fraction of particles in the ground state. Since the number of atoms in the crystal during the transformation remains unchanged, we can write the condition

$$\varphi_1 + \varphi_2 + \varphi_3 = 1. \tag{1}$$

For the given system of particles, the free energy can be represented in the form

$$\begin{aligned}\Delta F = {} & U_1\varphi_1 + U_2\varphi_2 + U_3\varphi_3 + U_{\rm int}(\varphi_1, \varphi_2, \varphi_3)\\ & + kT[\varphi_1\ln\varphi_1 + \varphi_2\ln\varphi_2 + \varphi_3\ln\varphi_3].\end{aligned} \tag{2}$$

Here, U_1, U_2, and U_3 are the internal energies of particles in states *1*, *2*, and *3*, respectively, and $U_{\rm int}(\varphi)$ is the energy of interaction between particles in different states. The last term in the right-hand side of Eq. (2) is the change in the entropy of the crystal due to mixing of the particle states, and k is the Boltzmann constant. Since our concern here is with the martensite embryos

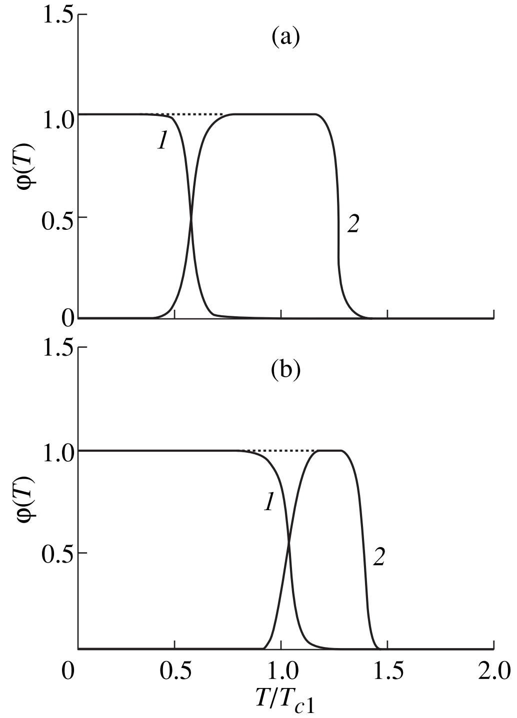

Fig. 1. Temperature dependences of the volume fraction of (*1*) martensite **1** and (*2*) martensite **2** according to formulas (4) and (6a)–(6c): (a) in the absence of stresses and (b) in the presence of stresses. The dotted lines correspond to the total amount of martensite in the crystal.

whose sizes exceed the critical embryo size, in what follows, we will disregard the interaction energy of particles in different states $U_{\text{int}}(\varphi)$, i.e., the surface energy [3, 4].

According to condition (1), two concentrations are independent, namely, φ_1 and φ_2. In order to determine their thermodynamically equilibrium values, we have two conditions,

$$\frac{\partial \Delta F}{\partial \varphi_1} = 0, \quad \frac{\partial \Delta F}{\partial \varphi_2} = 0. \tag{3}$$

Substituting potential (2) into these equations and taking into account the particle balance equation (1), we obtain the following expressions for equilibrium concentrations:

$$\varphi_1 = \varphi_3 \exp(-\Delta U_1/kT), \quad \varphi_2 = \varphi_3 \exp(-\Delta U_2/kT),$$
$$\varphi_3 = \frac{1}{1 + \exp(-\Delta U_1/kT) + \exp(-\Delta U_2/kT)}, \tag{4}$$

where $\Delta U_1 = U_1 - U_3$ and $\Delta U_2 = U_2 - U_3$ are the changes in the particle energies upon the transitions from the ground state to new structural states *1* and *2*, respectively. Since the transition to a new state occurs in portions of volume ω (where ω is the elementary volume of transformation), we have $\Delta U_{1,2} = \omega_{1,2}\Delta u_{1,2}$. Here, Δu is the change in the density of the internal energy of the crystal upon the structural transition:

$$\Delta u_{1,2} = q_{1,2}\frac{T - T_{c1,2}}{T_{c1,2}} - \xi_{ik}^{(1,2)}\tau_{ik} - \xi_0^{(1,2)}P, \tag{5}$$

where q is the heat of transformation; T_c is the critical (characteristic) temperature of transformation; ξ_{ik} and ξ_0 are the shear strain and the dilatation of the lattice upon its structural transformation, respectively; τ_{ik} is the shear stress applied to the crystal; and P is the uniform pressure.

It is assumed that the two variants of martensite differ from each other in all parameters (ω, q, T_c, ξ_{ik}, ξ_0). For simplicity, we assume that the shear strain tensor and stress tensor have only one nonzero component, namely, $\xi_{ik}^{(1,2)} \equiv \xi_{1,2}$ and $\tau_{ik} \equiv \tau$. As a result, in expressions (4), we obtain

$$\frac{\Delta U_1}{kT} = B_1\left(T/T_{c1} - 1 - m_1\sigma/\tau_1 - P/P_1 \pm \frac{\tau_{f1}}{\tau_1}\right), \tag{6a}$$

$$\frac{\Delta U_2}{kT} = B_2\left(T/T_{c2} - 1 - m_2\sigma/\tau_2 - P/P_2 \pm \frac{\tau_{f2}}{\tau_2}\right), \tag{6b}$$

$$B_1 = \omega_1 q_1/kT, \quad B_2 = \omega_2 q_2/kT,$$
$$\tau_{1,2} = q_{1,2}/\xi_{1,2}, \quad P_{1,2} = q_{1,2}/\xi_0^{(1,2)}, \tag{6c}$$

where m_1 and m_2 are the orientational factors of the habit planes during the structural transformation of the lattice with respect to the mechanical stress σ applied to the crystal and $\pm\tau_f$ is the stress of dry friction in the course of the interaction between the interphase boundaries and defects in the crystal during the direct and reverse martensite transitions.

Figure 1a displays the temperature dependences of the volume fractions of martensites **1** and **2** according to expressions (4) and (6a)–(6c) in the absence of the stress ($\sigma = 0$) and the uniform pressure ($P = 0$) at the following parameters: $B_2 = 0.8B_1$, $B_1 = 100$, $T_{c2} = 1.25T_{c1}$, and $\tau_{f1} = \tau_{f2} = 0$. It can be seen that, at these parameters, there exist two temperature regions of the homogenization of the martensite state of the crystal: (i) $T < 0.5T_{c1}$, in which martensite **1** dominates, and (ii) $0.6T_{c1} < T < 1.3T_{c1}$, in which martensite **2** dominates. In the intermediate temperature range $0.5T_{c1} < T < 0.6T_{c1}$, there exists a mixed martensite state. The dotted line in Fig. 1a corresponds to the total amount of martensite in the crystal.

Let us now consider the change in the martensite state of the crystal under mechanical stresses. Figure 1b shows the volume fractions of martensites **1** and **2** according to formulas (4) and (6a)–(6c) at the external stress $\sigma = 0.5\tau_1$ and $m_1 = 0.5$, $m_2\tau_1/\tau_2 = 0.2$, and $P = 0$. It can be seen that, under the applied stress, the temperature range of existence of martensite **2** becomes narrower, whereas the temperature range of existence of martensite **1** broadens. This results in the homogenization of the martensite in the temperature range $0.5T_{c1} < T < 0.6T_{c1}$, in which a mixed state is observed in the absence of stresses. An increase in the stress to $\sigma = \tau_1$ leads to the complete disappearance of martensite **2**. It is evident that the uniform pressure P, when applied to the crystal in the presence of nonzero lattice dilatations $\xi_0^{(1,2)}$, should also affect the ratios of the martensite volume fractions in certain temperature ranges.

The martensite transformation in the crystal is accompanied by its macrodeformation (transformation plasticity), depending on the amount of martensite in the crystal, the spontaneous strains ξ_{ik}, and the orientational factors m. In the example considered above, the strain arising in the crystal due to the formation of the two types of martensite (martensites **1** and **2**) is determined as $\varepsilon(T, \sigma) = \varepsilon^{(1)}(T, \sigma) + \varepsilon^{(3)}(T, \sigma)$. Here,

$$\varepsilon^{(1)}(T, \sigma) = m_1\xi_1[\varphi_1(T, m_1\sigma) - \varphi_1(T, -m_1\sigma)], \quad (7a)$$

$$\varepsilon^{(2)}(T, \sigma) = m_2\xi_2[\varphi_2(T, m_2\sigma) - \varphi_2(T, -m_2\sigma)]. \quad (7b)$$

In the absence of external stresses, martensites **1** and **2** reside in a twinned state. The martensite variants in a twinned pair differ from each other in that their orientational factors are opposite in sign ($\pm m_1$ and $\pm m_2$, respectively). Consequently, we obtain $\varepsilon^{(1)}(T) = \varepsilon^{(2)}(T) = 0$; i.e., the strain of the crystal is absent. The application of stresses leads to partial or complete detwinning of the martensites and a nonzero strain of the crystal.

Figure 2a shows the temperature dependences of $\varepsilon^{(1)}$ and $\varepsilon^{(2)}$ according to expressions (7a) and (7b) at the above parameters, $\sigma = 0.5\tau_1$, and $\varepsilon_2 = m_2\xi_2 = 0.5\varepsilon_1$, where $\varepsilon_1 = m_1\xi_1$. The solid curve indicates the temperature dependence of the total strain of transformation ε. It can be seen that this curve has a two-step shape due to the formation of two variants of martensite with a decrease in the temperature. Similar step curves of transformation are observed, for example, in crystals of titanium nickelide TiNi [2]. The steps correspond to the formation of martensite of types R and $B19$, respectively. The reverse martensite transition is characterized by a hysteresis of the transformation due to the dry friction stress τ_f. Figure 2b depicts the curves of the direct and reverse martensite transformations at the friction stresses $\tau_{f1}/\tau_1 = \pm 0.1$ and $\tau_{f2}/\tau_2 = \pm 5 \times 10^{-2}$.

The existence of two variants of martensite is responsible for the step shape of hyperelastic strain curves of the crystal [2]. Figure 3 depicts the hyperelastic strain curves according to expressions (7a) and (7b) at the temperature $T = 1.3T_{c1}$ for loading and unloading of the crystal. The dotted line corresponds to the hyperelastic strain in the absence of a hysteresis of the transformation.

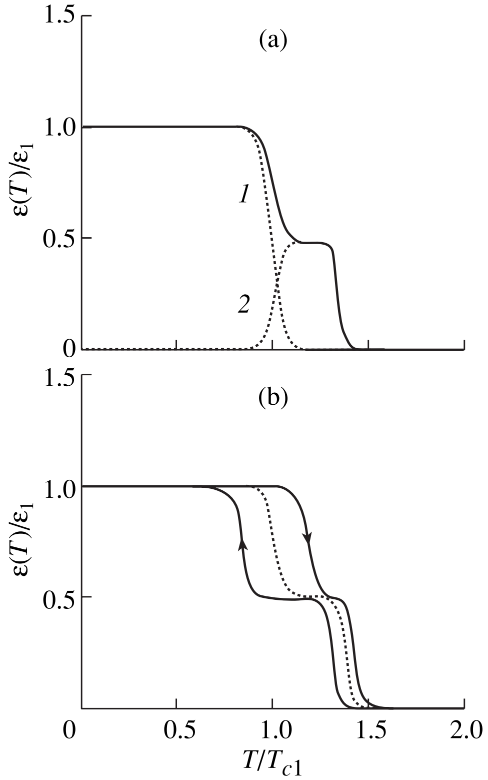

Fig. 2. Temperature dependences of (a) the partial strains upon transformation of (*1*) martensite **1** and (*2*) martensite **2** (the solid line indicates the total strain of transformation) and (b) the total strain of the direct and reverse martensite transformations in the absence (dotted line) and in the presence (solid lines) of the hysteresis of the transformation.

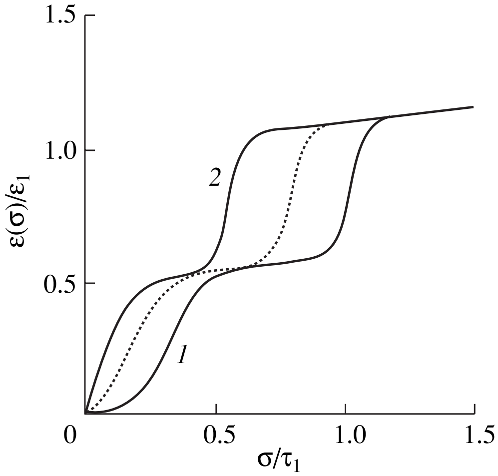

Fig. 3. Hyperelastic strain curves for two variants of martensite in the absence (dotted line) and in the presence (solid lines) of the hysteresis of the transformations: (*1*) loading and (*2*) unloading.

3. MANY VARIANTS OF MARTENSITE

The obvious generalization of expressions (4) to the case of N variants of martensite (instead of two variants) can be represented by the following relationships:

$$\varphi_n = \varphi_N \exp(-\Delta U_n/kT),$$

$$\varphi_N = \frac{1}{1 + \sum_{n=1}^{N} \exp(-\Delta U_n/kT)}, \tag{8a}$$

$$\varphi = \sum_{n=1}^{N} \varphi_n = \frac{\sum_{n=1}^{N} \exp(-\Delta U_n/kT)}{1 + \sum_{n=1}^{N} \exp(-\Delta U_n/kT)}, \tag{8b}$$

$$\Delta U_n = U_n - U_N.$$

As an illustration, we consider a conventional structural transformation—a transition from a face-centered cubic lattice to a hexagonal close-packed lattice. Theoretically, there can exist 24 variants of martensite upon this transition. These variants differ from each other in both the orientation of the habit planes (four octahedral planes) and the direction of their displacements (six directions in each octahedral plane, including displacements of the opposite sign). All the parameters are identical except for the orientational factors m. Consequently, taking into account the designations of formulas (6a)–(6c), using expressions (8a) and (8b), and assuming that $P = 0$, we obtain

$$\varphi_n(T, \sigma) = \frac{\exp[-B(T/T_c - 1 - m_n\sigma/\tau_1)]}{1 + \exp[-B(T/T_c - 1)] \sum_{n=1}^{N} \exp(m_n B\sigma/\tau_1)}, \tag{9a}$$

$$\varphi(T, \sigma) = \frac{\exp[-B(T/T_c - 1)] \sum_{n=1}^{N} \exp(m_n B\sigma/\tau_1)}{1 + \exp[-B(T/T_c - 1)] \sum_{n=1}^{N} \exp(m_n B\sigma/\tau_1)}. \tag{9b}$$

It follows from the above expressions that, in the case when the stress σ is absent, the volume fractions of martensites φ_n are identical and the temperature dependence of the sum of fractions of all the martensite variants can be represented by the relationship

$$\varphi(T) = \frac{N\exp[-B(T/T_c - 1)]}{1 + N\exp[-B(T/T_c - 1)]}. \tag{10}$$

In the presence of external stresses, the volume fraction of each martensite depends on the particular orientational factor m, i.e., on the orientation of the crystal with respect to the applied stress. For example, under uniaxial tension or compression of the crystal in the [111] direction, the shear stress in the (111) octahedral plane is equal to zero, whereas the orientational factors in the other three octahedral planes are nonzero. Note that, in each of these planes, there exists one variant with the maximum orientational factor $m = 0.416$. According to formulas (9a) and (9b), this means that application of a sufficiently strong stress to the crystal should suppress all martensite variants, except for the three variants with maximum orientational factors. For less symmetric directions of loading of the crystal, a variant whose orientational factor is maximum in this scheme of loading has a good chance of surviving.

4. CONCLUSION

Thus, the theory of smeared martensite transitions offers an adequate quantitative description of the homogenization of the martensite state of a crystal subjected to mechanical stresses over the entire temperature range of the transformation.

REFERENCES

1. T. Saburi and C. M. Waymen, Acta Metall. **28** (1), 1 (1980).
2. V. N. Khachin, V. G. Pushin, and V. V. Kondrat'ev, *Titanium Nickelide: The Structure and Properties* (Nauka, Moscow, 1992).
3. G. A. Malygin, Fiz. Tverd. Tela (St. Petersburg) **36** (5), 1489 (1994) [Phys. Solid State **36**, 815 (1994)].
4. G. A. Malygin, Usp. Fiz. Nauk **171** (2), 187 (2001).

Translated by O. Moskalev

Physics of the Solid State, Vol. 44, No. 11, 2002, pp. 2175–2180. Translated from Fizika Tverdogo Tela, Vol. 44, No. 11, 2002, pp. 2079–2083.

Perturbation Methods in the Kinetics of Nanocluster Growth

P. V. Gordon, S. A. Kukushkin, and A. V. Osipov

Institute for Problems of Mechanical Engineering, Russian Academy of Sciences,
Bol'shoĭ pr. 61, Vasil'evskiĭ ostrov, St. Petersburg, 199178 Russia
e-mail: oav@math.ipme.ru

Received January 21, 2002

Abstract—The rigorous perturbation theory of the evolution of a small-sized cluster is developed in the framework of the density functional method. The solution of the general equation for relaxation of the order parameter field is derived in the form of a power series of the metastability parameter (an analog of supersaturation or supercooling) and the curvature. The profile of the cluster density and the cluster growth rate are determined in an analytical form. The surface tension and the Tolman parameter are calculated. The results obtained are applied to a van der Waals three-dimensional gas and a two-dimensional lattice gas. It is shown that the theoretical results are in good agreement with experimental data. *© 2002 MAIK "Nauka/Interperiodica".*

1. INTRODUCTION

Over the last six decades, first-order phase transitions have attracted the particular attention of many researchers [1–3]. At present, there exist two principal approaches to the description of the kinetics of first-order phase transitions. According to the first (classical) approach, a phase transition is treated as a fluctuation nucleation and the growth of a new phase in the size space [1]. Within this approach, the growth of individual nuclei is described by an appropriate microscopic equation, for example, the diffusion equation or the heat conduction equation [3]. The second approach is based on the so-called density functional theory. In the framework of the second approach, the growth of individual nuclei is regarded as a relaxation of the order parameter field [4–6]. In the case of first-order phase transitions, the order parameter is a local density of the material and the effective Hamiltonian represents a grand thermodynamic potential. The second approach is considered to be more general because it can offer an adequate description of the nucleation and growth of a new phase even when the first approach is inapplicable, for example, due to a small size of nuclei. In this respect, the density functional method becomes especially efficient when applied to the description of the evolution of nanometer-sized clusters and islands, i.e., the so-called quantum dots, which are widely used in modern optoelectronics. The disadvantage of the density functional method is that, within this approach, no analytical solution describing either the cluster growth or the evaporation of clusters has hitherto been obtained for real thermodynamic potentials. There are only a few results obtained from numerical simulations [7–9].

The purpose of the present work was to derive a general analytical solution to the relaxation equation with a grand thermodynamic potential of the general form that would allow first-order phase transitions. This solution was represented in the form of a convergent series in terms of the ε difference in the chemical potentials of the initial and equilibrium phases, which was used as the small parameter of the theory. In other words, we developed a rigorous theory of perturbations of the general equation for relaxation of the order parameter. Within this approach, we uniquely determined the surface tension and the Tolman parameter (the correction to the surface tension for the curvature in the case of small sizes). The results obtained were applied to the van der Waals three-dimensional gas and the two-dimensional lattice gas (which provides the growth of a wetting layer for quantum dots [10]). It was shown that the proposed model is in good agreement with the experimental data.

2. THE EQUATION FOR RELAXATION OF THE ORDER PARAMETER

According to the general kinetic theory, the most probable path of the evolution of a thermodynamic system can be described by the Markov master equation [5]. For a slowly varying order parameter, this equation can be simplified. Specifically, if the system is described by only one order parameter ρ, this equation takes the form

$$\frac{\partial\rho(\mathbf{r}, t)}{\partial t} = -\frac{1}{t_\rho}\frac{\delta H}{\delta\rho} + \tilde{h}. \qquad (1)$$

Here, H is the dimensionless effective Hamiltonian of the system, t is the time, $\mathbf{r}$ specifies the coordinates of a point of the medium, the dimensionless field ρ is the density of the material at each point (ρ is conveniently expressed in terms of the critical density ρ_c), t_ρ is the characteristic time of variation in ρ, and $\tilde{h}$ is the external force simulating a thermal ensemble. Generally speaking, this equation describes the relaxation of the field of the nonpersistent order parameter ρ [4].

In the case of first-order phase transitions, the effective Hamiltonian is equal to a grand thermodynamic potential (because the variable of the description is the chemical potential rather than the number of particles) expressed in terms of k_BT_c, where k_B is the Boltzmann constant and T_c is the critical temperature. The inhomogeneous part of the grand thermodynamic potential represents a complex nonlocal density functional. However, when the density field slowly varies in the space (as is the case with first-order phase transitions), the inhomogeneous part is significantly simplified and becomes local. In this approximation, we obtain

$$H = \int_V \left[F - \mu\rho + \frac{\lambda^2}{2}(\nabla\rho)^2\right]d\mathbf{r} + H_0, \tag{2}$$

where *F* is the free energy density of the homogeneous medium (expressed in terms of k_BT_c), $d\mathbf{r}$ is the elementary volume, H_0 stands for the contributions of all the remaining degrees of freedom, λ is the typical scale of spatial variation in ρ, and μ is the chemical potential.

The quantities λ and t_ρ can be determined by comparing the results obtained in the framework of the classical theory and the density functional theory. Specifically, in the case when $\rho(r, t)$ is represented by the expression derived below, an unambiguous correspondence between these theories can be achieved only under the condition

$$\lambda = \sqrt[3]{\frac{m}{\rho_c}}, \tag{3}$$

where *m* is the mass of one molecule and ρ_c is the critical density. The characteristic time t_ρ can be determined by making the cluster growth rate obtained in terms of the density functional theory equal to the corresponding result of the classical microscopic theory. In particular, when applied to the free-molecular growth of a spherical drop, the perturbation theory developed below gives

$$t_\rho = \frac{2\sqrt{3k_BT_m}}{\sigma_0 V}\left(\frac{m}{\rho_c}\right)^{2/3}, \tag{4}$$

where *V* is the volume per molecule in a liquid and σ_0 is the surface tension coefficient for a planar interface between the vapor and the liquid.

The chemical potential μ can be represented as the sum $\mu_e + \varepsilon$, where μ_e is the equilibrium chemical potential and $\varepsilon = \mu - \mu_e$ is the difference in chemical potentials (expressed in terms of k_BT_c) between the initial and equilibrium phases. The second term of the sum is often referred to as the metastability parameter. This parameter is an analog of supersaturation or supercooling. In order for a liquid drop to nucleate from a supersaturated vapor, the metastability parameter must be equal to $(T/T_c)\ln(p/p_e)$ [1], where *p* is the supersaturation vapor pressure and p_e is the equilibrium pressure. Within this theory, ε is considered to be so small that the system resides in a metastable state (well away from the spinodal). It is assumed that the external forces maintain a constant value of ε. Moreover, we will deal only with a temperature range in which thermal fluctuations of the order parameter are negligible compared to the density of the denser phase. For a van der Waals system, this range satisfies the condition $0 < T/T_c < 0.8$. According to the classification of metastable states [11], we consider only a nonfluctuating region. As a result, the equation of the evolution without regard for thermal fluctuations $\tilde{h}$ can be written in the form

$$t_\rho\frac{\partial\rho(\mathbf{r}, t)}{\partial t} = \lambda^2\Delta\rho - [\mu(\rho, T) - \mu_e(T)] + \varepsilon, \tag{5}$$

where $\mu(\rho, T) = \partial F/\partial\rho$ is the chemical potential per particle of the material with density ρ and temperature *T*. Let us assume that, in this case, the time is measured in terms of t_ρ and the length is expressed in terms of λ. For spherical symmetry, we obtain the relationship

$$\begin{aligned}\frac{\partial\rho(r, t)}{\partial t} &= \frac{\partial^2\rho(r, t)}{\partial r^2}\\ &+ \frac{d-1}{r}\frac{\partial\rho(r, t)}{\partial r} - \Omega_e'(\rho) + \varepsilon.\end{aligned} \tag{6}$$

Here, *d* is the space dimension (*d* = 3 for a drop and *d* = 2 for a disk-shaped island in the growth of thin films) and Ω_e is the grand thermodynamic potential, which is defined at the equilibrium chemical potential μ_e (μ_e can be found from phase equilibrium equations) as follows:

$$\begin{aligned}\Omega_e &= \int_0^\rho [\mu(\xi, T) - \mu_e(t)]d\xi + \Omega_0\\ &= F(\rho, T) - \mu_e\rho + \Omega_0.\end{aligned} \tag{7}$$

At temperatures below the critical point, the dependence of Ω_e on ρ exhibits two isolated minima at ρ_G and ρ_L, which correspond to the gaseous and liquid states. The constant of integration Ω_0 is chosen in such a way that these minima become zero.

Specifically, in the case of a van der Waals three-dimensional gas, which is an important example of systems undergoing a first-order phase transition, we have

$$F(\rho, T) = T\rho\ln\frac{\rho}{1-\rho/3} - \frac{9}{8}\rho^2, \tag{8}$$

$$\mu(\rho, T) = T\rho\ln\frac{\rho}{1-\rho/3} + \frac{T}{1-\rho/3} - \frac{9}{4}\rho. \tag{9}$$

Here, the temperature and the density are expressed in critical units. For a two-dimensional lattice gas [6], we can write the following expressions:

$$F(\rho, T) = \frac{a}{2}\{T[(2-\rho)\ln(2-\rho) + \rho\ln\rho] + \rho(2-\rho)\}, \tag{10}$$

$$\mu(\rho, T) = \frac{a}{2}T\ln\frac{\rho}{2-\rho} + a(1-\rho). \tag{11}$$

Figure 1 shows the dependence of Ω_e on ρ for the van der Waals three-dimensional gas at $T = 0.8T_c$. It is evident that relationship (6) is a typical Ginzburg–Landau equation which is frequently used in the density functional theory for first-order phase transitions.

Below, we will derive an analytical solution to the evolution equation (6) with allowance made for the fact that ε is the small parameter.

3. THE PERTURBATION THEORY

Before proceeding to an analytical solution of the evolution equation (6), we consider a simpler equation for arbitrary grand thermodynamic potentials $\Omega_e(\rho)$ with two minima at ρ_L and ρ_G [in this case, $\Omega_e(\rho_L) = \Omega_e(\rho_G) = 0$], that is,

$$\frac{\partial\rho}{\partial t} = \frac{\partial^2\rho}{\partial r^2} - \Omega_e'(\rho) + \varepsilon. \tag{12}$$

We seek an analytical solution to this equation in the following form:

$$\rho(r, t) = \sum_{k=0}^{\infty}\varepsilon^k\rho_k(\theta), \tag{13}$$

$$\theta = r - R(\tau, \varepsilon), \quad R(\tau, \varepsilon) = \sum_{k=0}^{\infty}\varepsilon^k R_k(\tau), \tag{14}$$

where $\tau = \varepsilon t$ is the so-called "slow time." By substituting expressions (13) and (14) into Eq. (12) and equating terms with identical exponents ε^k, we obtain the following recurrent system of equations:

$$\rho_0'' - \Omega_e'(\rho_0) = 0 \tag{15}$$

for ε^0 and

$$\rho_k'' - \Omega_e''(\rho_0)\rho_k = F_k(\rho_{k-1}, \rho_{k-2}, \ldots, \rho_0), \quad k \geq 1 \tag{16}$$

for ε^k. Here, F_k are the known functions determined from expressions (12)–(14). Specifically, at $k = 1$, we have

$$F_1(\rho_0, \tau) = -\frac{dR_0}{d\tau}\rho_0' - 1. \tag{17}$$

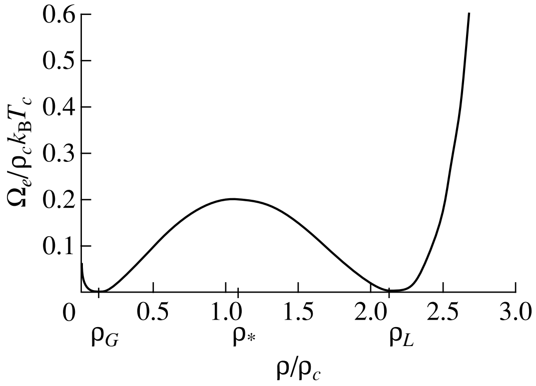

Fig. 1. Dependence of the grand thermodynamic potential on the density for the van der Waals three-dimensional gas at $T = 0.7T_c$.

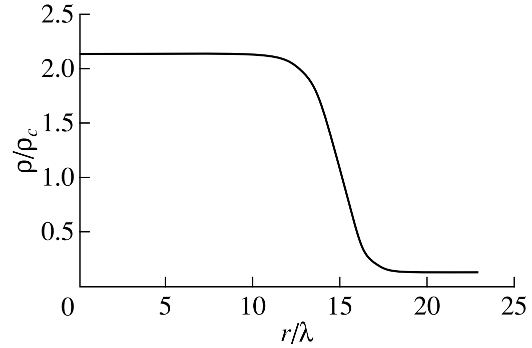

Fig. 2. Density profile for a liquid cluster in the van der Waals three-dimensional gas at $T = 0.7T_c$.

Equation (15) has an obvious solution,

$$\rho_0 = f(\theta), \quad \eta\int_{\rho_*}^{f}\frac{d\rho}{\sqrt{2\Omega_e(\rho)}} = r, \tag{18}$$

where ρ_* is the point at a maximum of the grand thermodynamic potential Ω between the minima at ρ_L and ρ_G (Fig. 1), $\eta = \pm1$ (sign "–" corresponds to a nucleus of the liquid phase *L*, and sign "+" corresponds to a nucleus of the gas phase *G*). Figure 2 depicts the density profile $f(r)$ for a liquid cluster in the van der Waals three-dimensional gas at $T = 0.7T_c$. According to the rigorous perturbation theory [12], the power series defined by expression (13) converges at any values of *r* and *t* (i.e., it is a uniformly convergent series) provided the growth law $R_k(\tau)$ is chosen in such a way that the inequalities $\rho_{k+1}/\rho_k < \infty$ and $k \geq 0$ hold at any values of θ and τ. Essentially, this is the renormalization method in the rigorous perturbation theory [12]. In particular, the zeroth-order approximation ρ_0 is uniformly suitable provided R_0 is chosen such that the condition $\rho_1/\rho_0 < \infty$ is universally satisfied. Equation (16) is linear with respect to ρ (to within the *k*th correction) and can be solved using the following method. For definiteness, we consider an equation for ρ_1, that is,

$$\rho_1'' - \Omega_e''(\rho_0)\rho_1 = F_1(\rho_0). \tag{19}$$

The solution to this equation will be sought in the form

$$\rho_1 = z(\theta)\rho_0'(\theta). \tag{20}$$

Substitution of expression (20) into Eq. (19) gives

$$z''\rho_0' + 2z'\rho_0'' = F_1. \tag{21}$$

Equation (21) can be simplified by multiplying the left-hand and right-hand sides of this equation by ρ_0'; that is,

$$(z''\rho_0'^2)' = F_1\rho_0'. \tag{22}$$

As a consequence, we obtain

$$\rho_1 = \rho_0'\int\limits_0^{\theta_0}\frac{d\theta_1}{\rho_0'^2}\int\limits_{-\infty}^{\theta_1}F_1\rho_0'd\theta_2. \tag{23}$$

It follows from relationship (18) that the quantity $1/\rho_0'^2$ takes on exponentially large values; therefore, the necessary condition for convergence of the exterior integral in expression (23) has the form

$$\int\limits_{-\infty}^{\infty}F_1\rho_0'd\theta = 0. \tag{24}$$

This is an important result of the present work. Only when condition (24) is met can inequality $\rho_1/\rho_0 < \infty$ be satisfied and can the zeroth-order approximation in the form of a traveling wave $\rho_0(r - R(t))$ have physical meaning. By substituting relationship (17) into expression (24), we found the cluster growth law in the following form:

$$\frac{dR_0}{d\tau} = \frac{\rho_L - \rho_G}{\sigma_0}, \tag{25}$$

where

$$\sigma_0 = \int\limits_{-\infty}^{\infty}\rho_0'^2 d\theta = \int\limits_{\rho_G}^{\rho_L}\sqrt{2\Omega_e(\rho)}d\rho. \tag{26}$$

Thus, within the framework of the perturbation theory, the fulfillment of the uniform convergence condition for the power series (14) of the metastability parameter leads to the cluster growth law (25) and the surface tension coefficient (26). It is obvious that formula (26) is in complete agreement with the results obtained in terms of the stationary perturbation theory [13].

Now, we turn to the analysis of the initial equation (6). The term $[(d-1)/r](\partial\rho/\partial r)$ can be treated as a small perturbation of the antikink-type solution (13) for the new small parameter $1/R$ (the curvature of the studied cluster) because we have

$$\frac{1}{r}\rho_0' = \frac{1}{R}\rho_0' + O\left(\frac{1}{R^2}\right). \tag{27}$$

The asymptotic construction of the zeroth-order approximation with respect to ε has precisely the same form; however, in this case, the function F_1 is more complicated; that is,

$$F_1 = -\frac{dR_0}{d\tau}\rho_0' - \frac{d-1}{\varepsilon R}\rho_0' - 1. \tag{28}$$

Substitution of relationship (28) into expression (24) gives the growth law for clusters of the new phase. Consequently, to the zeroth order in ε and to the first order in $1/R$, we have

$$\rho(r, t) = f(r - R(t)) + O(\varepsilon) + O\left(\frac{1}{R^2}\right), \tag{29}$$

$$\frac{dR}{dt} = (d-1)\left(\frac{1}{R_c} - \frac{1}{R}\right) + O(\varepsilon^2) + O\left(\frac{1}{R^2}\right), \tag{30}$$

$$R_c = \frac{(d-1)\sigma_0}{(\rho_L - \rho_G)\varepsilon}. \tag{31}$$

It is evident that R_c plays the role of a radius of a critical nucleus.

In general, the method described above can be used to determine higher orders of the approximation both in ε and in the curvature $1/R$. It should be noted that, in this case, the surface tension depends on $1/R$. The inclusion of this dependence is particularly important for small-sized nanoclusters. We leave out the mathematical treatment and write the final expressions to the first order in ε and to the second order in $1/R$:

$$\begin{aligned}\rho &= f(r - R(t)) - \rho_0'(\theta)\int\limits_0^{\theta}\frac{d\theta_1}{\rho_0'^2(\theta_1)}\int\limits_{-\infty}^{\theta_1}\rho_0'^2(\theta_2)\\ &\times\left[\varepsilon\left(\frac{\rho_L - \rho_G}{\sigma_0} + \frac{1}{\rho_0'(\theta_2)}\right) - \frac{(d-1)(\delta + \theta_2)}{R^2}\right]d\theta_2 \\ &+ O(\varepsilon^2) + O\left(\frac{\varepsilon}{R^2}\right) + O\left(\frac{1}{R^3}\right),\end{aligned} \tag{32}$$

$$\begin{aligned}\frac{dR}{dt} &= (d-1)\left(\frac{1}{R_c} - \frac{1}{R}\right) + \frac{(d-1)\delta}{R^2} \\ &+ O(\varepsilon^3) + O\left(\frac{\varepsilon}{R^2}\right) + O\left(\frac{1}{R^3}\right),\end{aligned} \tag{33}$$

$$R_c = \frac{(d-1)\sigma(R)}{(\rho_L - \rho_G)\varepsilon}, \tag{34}$$

$$\sigma(R) = \sigma_0 \frac{R}{R + (d-1)\delta} + O\left(\frac{1}{R^2}\right), \qquad (35)$$

$$\delta = \frac{\int_{-\infty}^{\infty} \theta(-\rho_0')d\theta}{\rho_L - \rho_G} - \frac{\int_{-\infty}^{\infty} \theta \rho_0'^2 d\theta}{\sigma_0}. \qquad (36)$$

It is obvious that δ plays the role of a correction to the surface tension for the curvature; i.e., δ is the Tolman parameter. We see little reason for refining expressions (32)–(36) by calculating new corrections, because the initial Ginzburg–Landau equation is valid to the second order in $1/R$. In the case of bubbles (gas nuclei in a liquid), the correction to the surface tension for the curvature changes sign:

$$\sigma(R) = \sigma_0 \frac{R + (d-1)\delta}{R} + O\left(\frac{1}{R^2}\right). \qquad (37)$$

The important advantage of the above approach is that the quantities λ and t_ρ can be uniquely determined by identifying expressions (32)–(36) with the appropriate relationships derived in the framework of the classical thermodynamic theory; furthermore, σ_0 can be identified with the surface tension of a planar interface, δ can be identified with the Tolman parameter, etc. In particular, the free energy of formation of a liquid cluster from a supersaturated vapor in the three-dimensional case ($d = 3$) can be determined from the relationship

$$F = \int_0^{\infty} 4\pi r^2 \left[\frac{\rho'^2}{2} + \Omega_e(\rho) - \varepsilon(\rho - \rho_G)\right] dr + \text{const.} \qquad (38)$$

By using relationship (32) and integrating to a required accuracy, after changing over to a dimensional form with the use of formula (4), we obtain

$$F(R) = 4\pi\sigma(R)R^2 - \frac{4\pi R^3}{3} \frac{\rho_L - \rho_G}{m} \varepsilon + \text{const.} \qquad (39)$$

Expression (39) completely coincides with the classical formula for the energy of formation of a nucleus. This confirms the validity of formula (4).

The temperature dependences of the surface tension (in a dimension form) calculated according to expressions (8), (10), and (26) for the van der Waals three-dimensional gas and the two-dimensional lattice gas are displayed in Fig. 3. This figure also shows experimental values of the surface tension for four gases, namely, methane, neon, argon, and krypton [14]. As is clearly seen, the theoretical results obtained above for the surface tension of the van der Waals gases are in excellent agreement with experimental data. Figure 4 depicts the temperature dependence of the Tolman parameter for the van der Waals three-dimensional gas (since the thermodynamic potential of the lattice gas is a symmetric function with respect to $\rho - \rho_*$, the Tolman parameter for this system is equal to zero). It can easily be shown that, in the temperature range $0.5 < T/T_c < 1$, the Tolman parameter is of the order of $\delta \sim 0.1\sqrt[3]{\rho_c/m} \sim 0.5 \times 10^{-10}$ m. This will suffice to have a pronounced effect on the nucleation [15].

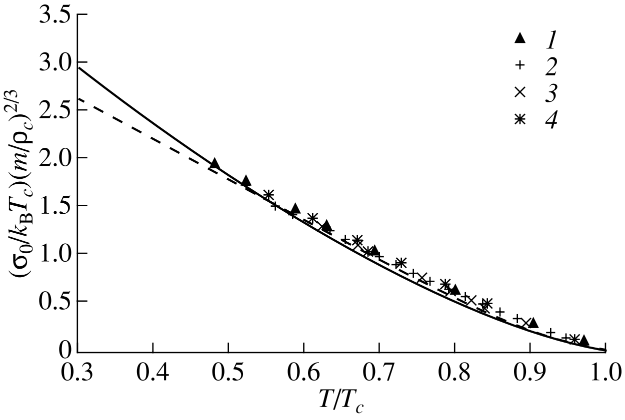

Fig. 3. Temperature dependences of the surface tension of the planar interface for the van der Waals three-dimensional gas (solid line) and the two-dimensional lattice gas (dashed line). Points are the experimental data taken from [14]: (*1*) CH_4, (*2*) Ne, (*3*) Ar, and (*4*) Kr.

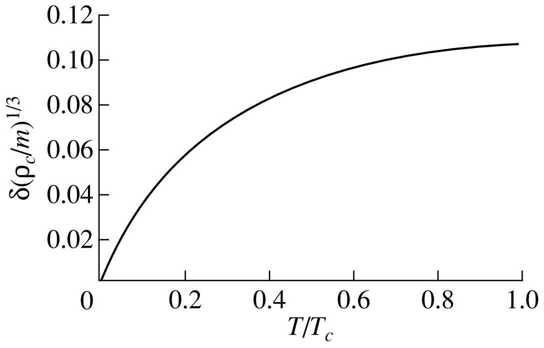

Fig. 4. Temperature dependence of the Tolman parameter for the van der Waals three-dimensional gas.

4. CONCLUSIONS

Thus, we developed a rigorous perturbation theory for the evolution of nanoclusters of a new phase for an arbitrary grand thermodynamic potential that allows first-order phase transitions. The solution of the general equation for relaxation of the order parameter was derived in the form of a uniformly convergent series of the metastability parameter. It was demonstrated that the fulfillment of the uniform convergence condition for this series uniquely determines the evolution law for nanoclusters and, consequently, the coefficient of their surface tension. The analytical results obtained are in good agreement with experimental data.

ACKNOWLEDGMENTS

This work was supported by the Russian Foundation for Basic Research (project nos. 02-02-17216 and 02-03-32471), the Russian Federal Center “Integration” (project no. A0151), and the Complex Program (project no. 19).

REFERENCES

1. D. Kashchiev, *Nucleation: Basic Theory with Applications* (Butterworths–Heinemann, Oxford, 2000).
2. *Nucleation Theory and Applications*, Ed. by J. W. P. Schmelzer, G. Ropke, and V. B. Priezzhev (Joint Inst. for Nuclear Research, Dubna, 1999).
3. S. A. Kukushkin and A. V. Osipov, Usp. Fiz. Nauk **168** (10), 1083 (1998) [Phys. Usp. **41**, 983 (1998)].
4. D. W. Oxtoby and R. J. Evans, Chem. Phys. **89** (10), 7521 (1998).
5. C. Varea and A. Robledo, J. Chem. Phys. **75** (10), 5080 (1981).
6. A. V. Osipov, J. Phys. D **28** (8), 1670 (1995).
7. Yu. E. Kuzovlev, T. K. Soboleva, and A. E. Filippov, Zh. Éksp. Teor. Fiz. **103** (5), 1742 (1993) [JETP **76**, 858 (1993)].
8. Y. C. Shen and D. W. Oxtoby, J. Phys. Chem. **105** (8), 6517 (1996).
9. A. Laaksonen, J. Phys. Chem. **106** (10), 7268 (1997).
10. N. N. Ledentsov, V. M. Ustinov, V. A. Shchukin, *et al.*, Fiz. Tekh. Poluprovodn. (St. Petersburg) **32** (4), 385 (1998) [Semiconductors **32**, 343 (1998)].
11. V. G. Boĭko, Kh.-Ĭ. Mogel’, V. M. Sysoev, and A. V. Chalyĭ, Usp. Fiz. Nauk **161** (2), 77 (1991) [Sov. Phys. Usp. **34**, 141 (1991)].
12. A. H. Nayfeh, *Perturbation Methods* (Wiley, New York, 1973).
13. M. P. A. Fisher and M. Wortis, Phys. Rev. B **29** (11), 6252 (1984).
14. B. D. Summ, in *Handbook of Physical Quantities*, Ed. by I. S. Grigoriev and E. Z. Meilikhov (Énergoatomizdat, Moscow, 1991; CRC Press, Boca Raton, 1997).
15. E. N. Brodskaya, J. C. Eriksson, A. Laaksonen, and A I. Rusanov, J. Colloid Interface Sci. **180** (1), 86 (1996).

Translated by O. Borovik-Romanova

Physics of the Solid State, Vol. 44, No. 11, 2002, pp. 2181–2195. Translated from Fizika Tverdogo Tela, Vol. 44, No. 11, 2002, pp. 2084–2096.
Original Russian Text Copyright © 2002 by Lang, Korovin, Contreras-Solorio, Pavlov.

LOW-DIMENSIONAL SYSTEMS AND SURFACE PHYSICS

A Manifestation of the Magnetopolaron Effect in Reflection and Absorption of Light by a Three-Level System in a Quantum Well

I. G. Lang[1], L. I. Korovin[1], D. A. Contreras-Solorio[2], and S. T. Pavlov[2, 3]
[1] *Ioffe Physicotechnical Institute, Russian Academy of Sciences, Politekhnicheskaya ul. 26, St. Petersburg, 194021 Russia*
[2] *Escuela de Fisica de la UAZ, Apartado Postal c-580, 98060 Zacatecas, Mexico*
[3] *Lebedev Institute of Physics, Russian Academy of Sciences, Leninskiĭ pr. 53, Moscow, 117924 Russia*
e-mail: ilang@dor.ioffe.rssi.ru
e-mail: pavlov@ahabon.reduas.mx

Received February 8, 2002

Abstract—The absorption and reflection of light by a quantum well are investigated in the case of two closely spaced levels of electronic excitations in the well. The dependences of the dimensionless absorptance $\mathcal{A}$ and reflectance $\mathcal{R}$ on the frequency ω_l of the exciting light are calculated. The overall sequence of processes involving absorption and reemission of photons is taken into account. This is beyond the scope of the perturbation theory for the photon–electron coupling constant. It is shown that the perturbation theory is inapplicable when the reciprocal radiative lifetimes of excitations are comparable to the reciprocal nonradiative lifetimes. In this case, the nontrivial dependences $\mathcal{A}(\omega_l)$ and $\mathcal{R}(\omega_l)$ are obtained. The total reflection and the total transparency points are determined. The relationships derived are used to analyze the special case of two excitation levels that are formed in the quantum well in a strong magnetic field H normal to its plane due to the Johnson–Larsen magnetopolaron effect. The reciprocal radiative lifetimes of electron–hole pairs are calculated far from and in the vicinity of the magnetophonon resonance. It is found that these lifetimes are proportional to H in the range far from the resonance and depend strongly on the difference $H–H_{\text{res}}$ in the vicinity of the resonance. The dependences of the coefficients $\mathcal{A}$ and $\mathcal{R}$ on the magnetic field H at different frequencies of the exciting light are deduced. © *2002 MAIK "Nauka/Interperiodica".*

1. INTRODUCTION

The role of the electron–phonon interaction in the formation of a polaron state in magnetic fields sharply enhances when the following resonance condition is satisfied:

$$\omega_{LO} = j\Omega, \quad j = 1, 2, 3, \ldots, \tag{1}$$

where ω_{LO} is the frequency of longitudinal optical (LO) phonons,

$$\Omega = |e|H/(cm_{e(h)}) \tag{2}$$

is the cyclotron frequency, e is the elementary charge, and $m_{e(h)}$ is the effective electron (hole) mass. In this case, the resonant coupling between electron levels clearly manifests itself. The fulfillment of condition (1) leads to the intersection of the magnetic-field dependences of the energy terms for the electron–phonon system. The formation of the polaron states results in divergence of the energy levels at the intersection points. The divergence of the terms was first revealed by Johnson and Larsen [1] in the interband magnetooptical absorption in massive InSb.

The polaron states are formed in three-dimensional and quasi-two-dimensional systems. In systems of both types, these states play an important role in the formation of the frequency dependence of magnetooptical effects, such as reflection, interband absorption, cyclotron resonance, and Raman light scattering (see, for example, reviews [2–4]). The difference between the systems manifests itself in the energy spectrum of an electron (hole), which is represented by Landau one-dimensional bands in the three-dimensional system and discrete levels in the quasi-two-dimensional system. This difference leads to a different divergence of the energy levels of the electron–phonon system: the divergence is of the order of $\alpha^{2/3}\hbar\omega_{LO}$ in the three-dimensional case [5] and $\alpha^{1/2}\hbar\omega_{LO}$ in the quasi-two-dimensional case [6–9], where α is the dimensionless constant of the electron–phonon coupling [10].

A single quantum well is considered as a quasi-two-dimensional system. The well is assumed to be ideal, and the inhomogeneous broadening of levels is ignored. The dimensionless reflectance $\mathcal{R}$ and absorptance $\mathcal{A}$ of the light are calculated as the ratio between the reflected or absorbed light flux and the incident flux. The quantum well has a finite depth. Moreover, the quantum well is characterized by the discrete energy levels of electron–hole pairs and a continuous spectrum. We are interested in the optical effects caused by the resonance between the exciting light of frequency

ω_l and the discrete energy levels of electron–hole pairs or magnetopolarons. For magnetic fields H and frequencies ω_l far from those corresponding to the magnetopolaron resonance, the quantum well is treated as a two-level system (one energy level corresponds to the ground state of the crystal, and the other energy level is associated with the electron–hole pair). Under conditions close to the magnetopolaron resonance, the well is regarded as a three-level system (the ground energy and two polaron levels).

The absorption and reflection of light in quasi-two-dimensional systems have been investigated repeatedly. The absorption is traditionally calculated within the perturbation theory to the lowest order in the interaction of light with the electronic system [11–13]. The expression for the absorptance involves the multiplier $\Delta_{\gamma_\rho}(\hbar\omega_l - E_\rho)$, where E_ρ is the electronic excitation energy reckoned from the ground-state energy,

$$\Delta_\gamma(E) = \frac{1}{\pi}\frac{\hbar\gamma/2}{E^2 + (\hbar\gamma/2)^2} \tag{3}$$

is the function transforming into the Dirac delta function at $\gamma \longrightarrow 0$, and γ_ρ is the reciprocal nonradiative lifetime of the level ρ. This relationship is rather contradictory. Actually, we obtain $\Delta_\gamma(E) \longrightarrow \infty$ at $E = 0$ and $\gamma \longrightarrow 0$, whereas the dimensionless absorptance $\mathcal{A}$ cannot exceed unity. The contradiction can be resolved when going beyond the scope of the perturbation theory in the photon–electron coupling constant, i.e., by summing the contributions of all the orders in this constant. Summation of the contributions means inclusion of the overall sequence of processes involving the absorption and reemission of a photon $\hbar\omega_l$. The new theory includes the notion of the radiative lifetime $\gamma_{r\rho}^{-1}$ of electronic excitation, which was introduced by Andreani *et al.* [14] as applied to excitons in quantum wells at $H = 0$.

Initially, the new approach was used to describe the light reflection from quantum wells at frequencies ω_l close to those corresponding to exciton energies [12, 14–16]. More recently, Kavokin *et al.* [17, 18] constructed the consistent theory for absorption. It was demonstrated that, in the case of absorption, the results obtained using the perturbation theory are applicable when the following condition is satisfied:

$$\gamma_{r\rho} \ll \gamma_\rho. \tag{4}$$

The new theory should work well, especially, when applied to an analysis of the specific features of reflection and absorption of light by ideal quantum wells in a strong magnetic field, because the reciprocal nonradiative lifetimes γ_ρ for discrete levels of electron–hole pairs in strong magnetic fields are very small and condition (4) can be violated. We will calculate the coefficients $\mathcal{R}$ and $\mathcal{A}$ for the normal incidence of light on the quantum well in the presence of a strong magnetic field perpendicular to the well plane with due regard for the magnetopolaron effects.

This paper is organized as follows. In Section 2, we derive the relationships for the electric fields to the right and the left of the quantum well under normal irradiation by exciting light in the case of a multilevel system. The formulas for the coefficients of reflection and absorption of light by the quantum well are deduced in Section 3. The reciprocal radiative lifetimes of the electron–hole pair and two magnetopolaron states in the quantum well in a strong magnetic field are calculated in Sections 4 and 5. In Section 6, we determine the broadening associated with the nonradiative lifetimes of the magnetopolaron states. The results of numerical calculations of the reflectance and absorptance are given in Section 7.

In Sections 2 and 3, we only disregard the inhomogeneous broadening of levels, without any other approximations. This broadening can be reduced to a minimum in the quantum well with a high perfection of boundaries. In these sections, we consider the case of two excited discrete levels of the electronic system in the quantum well. The locations of the levels are assumed to be arbitrary, and the levels are characterized by the nonradiative [$\gamma_{1(2)}$] and radiative [$\gamma_{r1(2)}$] reciprocal lifetimes. This pair of levels can exist in an exciton in the absence of a magnetic field or in a magnetopolaron in a quantizing magnetic field in the quantum well. No assumptions regarding the smallness of the exciton effect and a weak influence of longitudinal optical phonons on the magnetopolaron spectrum are made in Sections 2 and 3. In our earlier work [19], we showed that neither exciton effect nor phonon dispersion can transform the magnetopolaron levels into energy bands if the equality $\mathbf{K}_\perp = 0$ is satisfied (where $\hbar\mathbf{K}_\perp$ is the projection of the quasi-momentum of the magnetopolaron onto the *xy* plane of the quantum well). It is assumed that the light creates magnetopolarons with $\mathbf{K}_\perp = 0$, because we consider only the normal incidence of light on the quantum well plane. At $\mathbf{K}_\perp = 0$, the exciton effect and the phonon dispersion result only in a shift of the magnetopolaron energy levels and in an additive addition to the nonradiative broadening of the levels. In Sections 4–7, for the purpose of obtaining qualitative results and simplifying calculations, we assume that the Coulomb attraction between the electron and the hole, the phonon dispersion, and the nonparabolicity of the bands of the crystal have a weak effect. These assumptions hold true in the case of strong magnetic fields and narrow quantum wells. Indeed, according to Lerner and Lozovik [20], the exciton effect can be disregarded under the conditions

$$a_{\text{exc}}^2 \gg a_H^2, \quad a_{\text{exc}} \gg d. \tag{5}$$

Here,

$$a_{\text{exc}} = \hbar^2\varepsilon_0/(\mu e^2) \tag{6}$$

is the Wannier–Mott exciton radius in the absence of a magnetic field, ε_0 is the static permittivity, μ =

$m_e m_h/(m_e + m_h)$ is the reduced effective mass, $a_H = (c\hbar/|e|H)^{1/2}$ is the magnetic length, and d is the quantum well width. For GaAs, we have [21]

$$a_{\rm exc} = 146\ \text{Å}, \quad a_H^{\rm res} = 57.2\ \text{Å}, \tag{7}$$

where $a_H^{\rm res}$ corresponds to the magnetic field $H_{\rm res}$ derived from condition (1) at $j = 1$. From formulas (7), we obtain $(a_H^{\rm res}/a_{\rm exc})^2 \simeq 0.154$. Therefore, the first inequality (5) is satisfied and the second inequality imposes a limitation on the quantum well width.

In Sections 4–6, we use the results of our earlier work [22], in which we developed the theory of magnetopolarons. As in [22], we assume that the frequencies of confined and interface phonons [23] involved in the formation of the magnetopolaron coincide with ω_{LO}. The approximation according to which the interaction with confined phonons is replaced by the interaction with bulk phonons and the interaction with interface phonons is ignored is used only in Section 6 in order to estimate the nonradiative broadening γ_p of the polaron levels. This approximation is applicable for wide quantum wells [24]. The nonradiative broadening γ_p with allowance made for the confined and interface phonons was calculated in our previous work [25]. Hereafter, we will use the magnetopolaron classification proposed in [24]. The specific calculations are performed for the polaron A, in which the electron–phonon interaction binds two adjacent Landau levels (with $n = 0$ and 1) belonging to the same quantum-well level. The obtained results, as in [22, 24], are valid when the polaron splitting is small compared to the difference between the energies of the adjacent quantum-well levels. Since the level spacing decreases with an increase in d, this condition places an upper limit on the permissible well widths (see numerical estimates in [24]). In the present work, we examine the irradiation of the quantum well in a strong magnetic field by monochromatic light. Note that, in [26], we proposed a technique for detecting and examining the magnetopolaron effect with the use of irradiation of the quantum well by light pulses and recording of transmitted and reflected pulses.

2. ELECTRIC FIELDS TO THE RIGHT AND THE LEFT OF A QUANTUM WELL

Let us assume that an electromagnetic wave (or a superposition of waves that corresponds to a time-limited light pulse) is incident on a single quantum well normally to its plane from the left and the electric field of this wave has the form

$$E_{0,\alpha}(z,t) = (1/2\pi) \times \int_{-\infty}^{\infty} d\omega \exp[-i\omega(t - zn/c)]\mathscr{E}_{0,\alpha}(\omega) + \text{c.c.}, \tag{8}$$

where n is the refractive index of the barrier.[1] We introduce the designation

$$\mathscr{E}_{0\alpha}(\omega) = 2\pi E_0 e_{l\alpha}\mathscr{D}_0(\omega), \tag{9}$$

where E_0 is the scalar amplitude; $\mathbf{e}_l$ is the polarization vector of the exciting light; and $\mathscr{D}_0(\omega)$ is the frequency function, which, upon excitation by monochromatic light with the frequency ω_l, can be represented by the expression

$$\mathscr{D}_0(\omega) = \delta(\omega - \omega_l). \tag{10}$$

Now, we assume the incident wave to have a circular polarization; that is,

$$\mathbf{e}_l = (1/\sqrt{2})(\mathbf{e}_x \pm i\mathbf{e}_y), \tag{11}$$

where $\mathbf{e}_x$ and $\mathbf{e}_y$ are the unit vectors along the x and y axes, respectively.

In the quantum well, the states of the electronic system are excited by the incident electromagnetic wave. The energy of the excited states will be characterized by a set of indices ρ. For example, upon normal incidence of the wave in a strong magnetic field, the set of indices ρ for electron–hole pairs involves l_e, l_h, and $n_e = n_h$, where l_e (l_h) are the quantum numbers of the quantum confinement of electrons (holes) and n_e (n_h) are the Landau quantum numbers of electrons (holes). In the case of an infinitely deep quantum well, we have $l_e = l_h$. The state with the set ρ is characterized by the energy $\hbar\omega_\rho$ reckoned from the ground-state energy and the radiative ($\gamma_{r\rho}$) and nonradiative (γ_ρ) reciprocal lifetimes. Now, we analyze the quantum well with width $d \ll c/\omega_l n$. In this case, the electric fields $E_{L(R)}(z, t)$ on the left (right) of the quantum well are given by the relationship [27]

$$\mathbf{E}_{L(R)}(z,t) = \mathbf{E}_0(z,t) + \Delta\mathbf{E}_{L(R)}(z,t), \tag{12}$$

$$\Delta E_{\alpha L(R)}(z,t) = E_0 e_{l\alpha} \times \int_{-\infty}^{\infty} d\omega \exp[-i\omega(t \pm zn/c)]\mathscr{D}(\omega) + \text{c.c.}, \tag{13}$$

where the upper (lower) sign corresponds to the subscript L (R). The frequency distribution is defined as follows:[2]

$$\mathscr{D}(\omega) = -4\pi\chi(\omega)\mathscr{D}_0(\omega)/[1 + 4\pi\chi(\omega)], \tag{14}$$

---

[1] It is possible to omit the complex conjugate and to replace the term $\mathscr{E}_{0\alpha}(\omega)$ by $\mathscr{E}_{0\alpha}(\omega) = \mathscr{E}_{0\alpha}(\omega) + \mathscr{E}^*_{0\alpha}(-\omega) = 2\pi E_0[e_{l\alpha}D_0(\omega) + e^*_{l\alpha}D^*_0(-\omega)]$.

[2] Expression (15) is written taking into account that either of two circular polarizations corresponds to the excitation of one of two types of electron–hole pairs with identical energies from the ground state [see formula (78)].

$$\chi(\omega) = (i/4\pi)\sum_{\rho}(\gamma_{r\rho}/2)$$
$$\times[(\omega-\omega_{\rho}+i\gamma_{\rho}/2)^{-1}+(\omega+\omega_{\rho}+i\gamma_{\rho}/2)^{-1}]. \tag{15}$$

Relationships (12)–(15) describe the electric fields on both sides of the quantum well and, hence, the energy fluxes of the transmitted and reflected light for the multilevel system. The second term in the square brackets on the right-hand side of relationship (15) is nonresonant but is required to fulfill the relationship

$$\chi^*(\omega) = \chi(-\omega). \tag{16}$$

In real quantum wells with a finite depth in a strong magnetic field, there always exist discrete energy levels (or at least one discrete level). Moreover, there exists a continuous spectrum in addition to the discrete spectrum. Therefore, the index ρ on the right-hand side of relationship (15) takes both discrete and continuous values. In a strong magnetic field, proper allowance must sometimes be made for a large number of levels (see [28, 29]). For a two-level system, it is assumed that the influence of all the levels, except for the level that is at resonance with the frequency ω_l, can be ignored.

The reflectance and absorptance for the two-level system corresponding to one exciton level in the quantum well at $H = 0$ were calculated in [14–18]. The following relationships were derived for the electric fields:

$$E_{\alpha L} = E_0 e_{l\alpha}$$
$$\times\left\{e^{-i\omega_l(t-zn/c)}-\frac{i\gamma_r}{2(\omega_l-\omega+i\Gamma/2)}e^{-i\omega_l(t+zn/c)}\right\}+\text{c.c.}, \tag{17}$$

$$E_{\alpha R} = E_0 e_{l\alpha} e^{-i\omega_l(t-zn/c)}$$
$$\times\left\{1-\frac{i\gamma_r}{2(\omega_l-\omega+i\Gamma/2)}\right\}+\text{c.c.}, \tag{18}$$

$$\Gamma = \gamma+\gamma_r. \tag{19}$$

Formulas (17) and (18) can be obtained from expressions (10) and (12)–(15) by retaining one term in the sum over ρ on the right-hand side of relationship (15) using the designations

$$\omega_\rho = \omega, \quad \gamma_{r\rho} = \gamma_r, \quad \gamma_\rho = \gamma, \tag{20}$$

and omitting the nonresonant term in the square brackets.

The three-level system involves the ground level of the electronic system in the quantum well and two levels characterized by the energies $\hbar\omega_{1(2)}$ and the radiative $[\gamma_{r1(2)}]$ and nonradiative $[\gamma_{1(2)}]$ reciprocal lifetimes. The calculation of the electric fields for the three-level system is somewhat more complicated, because it is necessary to solve the quadratic equation [see Eq. (23)]. By using relationships (10) and (12)–(15) and rejecting the nonresonant term on the right-hand side of expression (15), we obtain

$$E_{\alpha L}(z,t) = E_0 e_{l\alpha}\Bigg\{\exp(-i\omega_l(t-zn/c))$$
$$-i\exp(-i\omega_l(t+zn/c))\left[\frac{\bar{\gamma}_{r1}/2}{\omega_l-\Omega_1+iG_1/2}\right. \tag{21}$$
$$\left.+\frac{\bar{\gamma}_{r2}/2}{\omega_l-\Omega_2+iG_2/2}\right]\Bigg\}+\text{c.c.},$$

$$E_{\alpha R}(z,t) = E_0 e_{l\alpha}\exp(-i\omega_l(t-zn/c))$$
$$\times\left\{1-i\left[\frac{\bar{\gamma}_{r1}/2}{\omega_l-\Omega_1+iG_1/2}+\frac{\bar{\gamma}_{r2}/2}{\omega_l-\Omega_2+iG_2/2}\right]\right\}+\text{c.c.} \tag{22}$$

The quantities $O_{1,2} = \Omega_{1,2} - iG_{1,2}/2$ (G and Ω are real quantities by definition) obey the equation

$$(O-\omega_1+i\gamma_1/2)(O-\omega_2+i\gamma_2/2)$$
$$+i(\gamma_{r1}/2)(O-\omega_2+i\gamma_2/2) \tag{23}$$
$$+i(\gamma_{r2}/2)(O-\omega_1+i\gamma_1/2) = 0$$

and are given by the formula

$$(\Omega-iG/2)_{1,2}$$
$$= [\tilde{\omega}_1+\tilde{\omega}_2\pm\sqrt{(\tilde{\omega}_1-\tilde{\omega}_2)^2-\gamma_{r1}\gamma_{r2}}]/2 \tag{24}$$

(the plus and minus signs refer to subscripts 1 and 2, respectively), where

$$\tilde{\omega}_{1(2)} = \omega_{1(2)}-i\Gamma_{1(2)}/2, \quad \Gamma_{1(2)} = \gamma_{1(2)}+\gamma_{r1(2)}. \tag{25}$$

In general, the relationship under the radicand in formula (24) is a complex-valued expression. Moreover, we used the designations

$$\bar{\gamma}_{r1} = \gamma_{r1}+\Delta\gamma, \quad \bar{\gamma}_{r2} = \gamma_{r2}-\Delta\gamma, \tag{26}$$

$$\Delta\gamma = \frac{\gamma_{r1}[\Omega_2-\omega_2-i(G_2-\gamma_2)/2]+\gamma_{r2}[\Omega_1-\omega_1-i(G_1-\gamma_1)/2]}{\Omega_1-\Omega_2+i(G_2-G_1)/2}. \tag{27}$$

A comparison of relationships (21) and (22) with the corresponding expressions (17) and (18) for the two-level system shows that the summation of the contributions from levels 1 and 2 is not a simple summation but is accompanied by the replacement

$$\omega_{1(2)} \longrightarrow \Omega_{1(2)}, \quad \Gamma_{1(2)} \longrightarrow G_{1(2)}, \quad \gamma_{r1(2)} \longrightarrow \bar{\gamma}_{r1(2)}. \tag{28}$$

The calculation of the electric fields for a four-level system is even more difficult because it requires the solution of a cubic equation, etc. At present, the problem for an arbitrary number ρ of levels has defied exact solution. However, at $\gamma_{r\rho} \ll \gamma_\rho$, the perturbation theory for the interaction of light with the electronic system in the quantum well is applicable and, hence, the term $4\pi\chi(\omega)$ in the denominator on the right-hand side of relationship (14) can be rejected. As a result, we obtain the solution for any number ρ of levels in the form

$$E^M_{\alpha L}(z, t) = E_0 e_{l\alpha}\left\{e^{-i\omega_l(t - zn/c)} - ie^{-i\omega_l(t + zn/c)} \times \sum_\rho \frac{\gamma_{r\rho}/2}{\omega_l - \omega_\rho + i\gamma_\rho/2}\right\} + \text{c.c.}, \tag{29}$$

$$E^M_{\alpha R}(z, t) = E_0 e_{l\alpha} e^{-i\omega_l(t - zn/c)} \times \left[1 - i\sum_\rho \frac{\gamma_{r\rho}/2}{\omega_l - \omega_\rho + i\gamma_\rho/2}\right] + \text{c.c.} \tag{30}$$

3. REFLECTANCE AND ABSORPTANCE OF LIGHT

With knowledge of the relationships for the electric fields to the left and the right of the quantum well, it is possible to calculate the reflectance and absorptance of light. Let us introduce the Poynting vector $\mathbf{S}_{L(R)}$ on the left (right) of the quantum well. The vector $\mathbf{S}_L$ can be written in the form

$$\mathbf{S}_L = \mathbf{S}_0 + \Delta\mathbf{S}_L, \tag{31}$$

where

$$\mathbf{S}_0 = (c/2\pi)E_0^2\mathbf{e}_z \tag{32}$$

is the flux of the exciting light and $\Delta\mathbf{S}_L$ is the flux of the reflected light directed along the vector $-\mathbf{e}_z$. The reflectance of light is defined by the ratio

$$\mathcal{R} = |\Delta\mathbf{S}_L|/|\mathbf{S}_0|, \tag{33}$$

the dimensionless absorptance is represented by the formula

$$\mathcal{A} = |\mathbf{S}_L - \mathbf{S}_R|/|\mathbf{S}_0|, \tag{34}$$

and the transmittance of light is given by the expression

$$\mathcal{T} = 1 - \mathcal{R} - \mathcal{A} = |\mathbf{S}_R|/|\mathbf{S}_0|. \tag{35}$$

With the use of relationships (17) and (18) for the two-level system, we obtain

$$\mathcal{R} = (\gamma_r/2)^2/[(\omega_l - \omega)^2 + (\Gamma/2)^2], \tag{36}$$

$$\mathcal{A} = (\gamma\gamma_r/2)/[(\omega_l - \omega)^2 + (\Gamma/2)^2] \tag{37}$$

(see [14–18]). From formula (37), it follows that, at $\gamma = 0$, the absorption of light by the electronic system in the quantum well is absent [17, 18].

Let us consider two limiting cases: $\gamma_r \ll \gamma$ and $\gamma_r \gg \gamma$. At $\gamma_r \ll \gamma$, the perturbation theory is applicable to the lowest order in the interaction of light with electrons. The absorptance and reflectance appear to be quantities of the second and fourth order in the interaction, respectively. From relationships (36) and (37), we have

$$\mathcal{R} \simeq (\pi\hbar/2)(\gamma_r^2/\gamma)\Delta_\gamma[\hbar(\omega_l - \omega)], \tag{38}$$

$$\mathcal{A} \simeq \pi\hbar\gamma_r\Delta_\gamma[\hbar(\omega_l - \omega)]. \tag{39}$$

Here, $\Delta_\gamma(E)$ is the function defined by formula (3). At $\gamma_r \ll \gamma$, the following inequalities are satisfied:

$$\mathcal{A} \ll 1, \quad \mathcal{R} \ll \mathcal{A}. \tag{40}$$

For $\gamma_r \gg \gamma$, the quantity Γ in relationships (36) and (37) is approximately replaced by γ_r. As a result, at resonance, we have $\mathcal{R}(\omega_l = \omega) \simeq 1$; i.e., the total reflection takes place and $\mathcal{A} \ll 1$. Consequently, the absorptance is small in both limiting cases. The maximum absorptance $\mathcal{A}(\omega_l = \omega) = 1/2$ is observed at $\gamma_r = \gamma$.

For the three-level system with the use of expressions (21), (22), (33), and (34), we obtain

$$\mathcal{R} = \frac{1}{4Z}\left\{[\gamma_{r1}(\omega_l - \omega_2) + \gamma_{r2}(\omega_l - \omega_1)]^2 + \frac{1}{4}(\gamma_{r1}\gamma_2 + \gamma_{r2}\gamma_1)^2\right\}, \tag{41}$$

$$\mathcal{A} = \frac{1}{2Z}\left\{\gamma_{r1}\gamma_1\left[(\omega_l - \omega_2)^2 + \frac{\gamma_2^2}{4}\right] + \gamma_{r2}\gamma_2\left[(\omega_l - \omega_1)^2 + \frac{\gamma_1^2}{4}\right]\right\}, \tag{42}$$

where

$$Z = \left[(\omega_l - \Omega_1)^2 + \frac{G_1^2}{4}\right]\left[(\omega_l - \Omega_2)^2 + \frac{G_2^2}{4}\right]. \tag{43}$$

It follows from formula (42) that the absorptance of light for the three-level system is equal to zero under the condition

$$\gamma_1 = \gamma_2 = 0. \tag{44}$$

With due regard for Eq. (23), the quantity Z can be rearranged to the form

$$Z = \left[(\omega_l-\omega_1)(\omega_l-\omega_2) - \frac{\gamma_{r1}\gamma_2+\gamma_{r2}\gamma_1+\gamma_1\gamma_2}{4}\right]^2 + \frac{1}{4}[(\omega_l-\omega_1)\Gamma_2+(\omega_l-\omega_2)\Gamma_1]^2. \tag{45}$$

Next, we derive the simplified expressions for the coefficients $\mathcal{R}$ and $\mathcal{A}$ in different limiting cases. Relationships (41) and (42) are conveniently used sometimes with formula (43) and sometimes with formula (45). The first limiting case corresponds to the inequalities

$$\gamma_{r1(2)} \ll \gamma_{1(2)}, \tag{46}$$

when the perturbation theory for the interaction of light with the electronic system can be applied. Under condition (46) and by setting $\Omega_{1(2)} \simeq \omega_{1(2)}$ and $G_{1(2)} = \gamma_{1(2)}$ in formula (43), we obtain the relationships

$$\mathcal{R} \simeq \frac{(\gamma_{r1}/2)^2}{(\omega_l-\omega_1)^2+(\gamma_1/2)^2} + \frac{(\gamma_{r2}/2)^2}{(\omega_l-\omega_2)^2+(\gamma_2/2)^2} + \frac{\gamma_{r1}\gamma_{r2}}{2} \times \frac{(\omega_l-\omega_1)(\omega_l-\omega_2)+\gamma_1\gamma_2/4}{[(\omega_l-\omega_1)^2+(\gamma_1/2)^2][(\omega_l-\omega_2)^2+(\gamma_2/2)^2]}, \tag{47}$$

$$\mathcal{A} \simeq \frac{\gamma_{r1}\gamma_1/2}{(\omega_l-\omega_1)^2+(\gamma_1/2)^2} + \frac{\gamma_{r2}\gamma_2/2}{(\omega_l-\omega_2)^2+(\gamma_2/2)^2}. \tag{48}$$

According to relationship (48), the absorptance $\mathcal{A}$ is the sum of contributions (39) from levels 1 and 2, because the absorptance under condition (46) is linear in the constants γ_{r1} and γ_{r2}. According to formula (47), the reflectance $\mathcal{R}$ is quadratic in the constants γ_{r1} and γ_{r2} and, hence, includes the interference contribution in addition to the contributions from the individual levels.

By generalizing relationship (48) to an arbitrary number of levels under condition (4), we obtain

$$\mathcal{A}^M \simeq \frac{1}{2}\sum_{\rho} \frac{\gamma_{r\rho}\gamma_\rho}{(\omega_l-\omega_\rho)^2+(\gamma_\rho/2)^2}. \tag{49}$$

The next limiting case is opposite to that considered above; i.e., it is described by the inequality

$$\gamma_{r1(2)} \gg \gamma_{1(2)}. \tag{50}$$

Setting $\gamma_1 = \gamma_2 = 0$ on the right-hand sides of relationships (41) and (42), we obtain $\mathcal{A} = 0$ and

$$\mathcal{R} = \frac{[(\gamma_{r1}+\gamma_{r2})/2]^2(\omega_l-\omega_0)^2}{(\omega_l-\omega_1)^2(\omega_l-\omega_2)^2+[(\gamma_{r1}+\gamma_{r2})/2]^2(\omega_l-\omega_0)^2}, \tag{51}$$

$$\omega_0 = (\omega_1\gamma_{r2}+\omega_2\gamma_{r1})/(\gamma_{r1}+\gamma_{r2}). \tag{52}$$

As follows from relationship (51), the reflectance for the three-level system is characterized by the specific properties when the reciprocal radiative times are predominant. At any constants γ_{r1} and γ_{r2}, the reflectance is equal to zero at the point $\omega_l = \omega_0$ and unity at the points $\omega_l = \omega_1$ and $\omega_l = \omega_2$. Assume that $\gamma_{r1} = \gamma_{r2} = \gamma_r$. Then, we have $\mathcal{R} = 0$ at $\omega_l = (\omega_1 + \omega_2)/2$. At $\gamma_r \gg \omega_1 - \omega_2$, the reflectance at the point $\omega_l = (\omega_1 + \omega_2)/2$ exhibits a narrow minimum with $\mathcal{R} = 0$. The half-width at half-minimum is equal to $(\omega_1 - \omega_2)^2/(2^{3/2}\gamma_r)$.

Figure 1a shows the functions $\mathcal{R}(\omega_l)$ under the conditions

$$\gamma_1 = \gamma_2 = \gamma, \quad \gamma_{r1} = \gamma_{r2} = \gamma_r, \quad \gamma \ll \gamma_r. \tag{53}$$

Figure 1b depicts the dependences $\mathcal{A}(\omega_l)$ under the same conditions (53). At fixed values of γ, an increase in γ_r leads to changes in the curves $\mathcal{A}(\omega_l)$. Curves *1–6* are constructed for the following values of $\hbar\gamma_r$: 0.002, 0.005, 0.008, 0.04, 0.125, and 0.5.[3] Two maxima are observed in curve *1* (at $\hbar\gamma_r = 0.002$). The other curves have only one maximum. Curve *5* ($\hbar\gamma_r = 0.125$) exhibits the most pronounced maximum with $\mathcal{A}_{\max} = 0.5$. The absorptance $\mathcal{A}_0$ that corresponds to the central point $\omega_l = (\omega_1 + \omega_2)/2$ and coincides with $\mathcal{A}_{\max}$ in curves *2–5* can be described by the exact formula

$$\mathcal{A}_0 = \frac{4\gamma_r\gamma[(\omega_1-\omega_2)^2+\gamma^2]}{[(\omega_1-\omega_2)^2+2\gamma_r\gamma+\gamma^2]^2}, \tag{54}$$

which can be easily deduced from expression (42) by setting $\omega_l = (\omega_1 + \omega_2)/2$. The absorptance $\mathcal{A}_0$ is maximum at

$$\gamma_{r0} = \frac{(\omega_1-\omega_2)^2+\gamma^2}{2\gamma}. \tag{55}$$

Substitution of $\hbar(\omega_1 - \omega_2) = 0.005$ and $\hbar\gamma = 0.0001$ (these values correspond to Fig. 1b) into formula (55) gives $\hbar\gamma_{r0} = 0.125$ and $\mathcal{A}_{\max} = \mathcal{A}_0 = 0.5$ (curve *5* in Fig. 1b).

---

[3] All the parameters and frequencies in Figs. 1 and 2 are given in arbitrary units, because relationships (47) and (48) include only the ratios of these quantities.

The next limiting case is specified by the smallness of the reciprocal lifetimes $\gamma_{1(2)}$ and $\gamma_{r1(2)}$ as compared to $\omega_1 - \omega_2$. Assume that the following conditions are met:

$$\gamma_{1(2)} \ll \omega_1 - \omega_2, \quad \gamma_{r1(2)} \ll \omega_1 - \omega_2. \qquad (56)$$

Note that the ratio between the nonradiative and radiative reciprocal lifetimes $\gamma_{1(2)}$ and $\gamma_{r1(2)}$ can be arbitrary. Cosequently, when the frequency ω_l is close to resonance with one of the levels, for example, $\omega_l \simeq \omega_1$, from relationships (41) and (42), we obtain

$$\mathcal{R} \simeq \frac{\gamma_1^2/4}{(\omega_l - \omega_1)^2 + (\Gamma_1/2)^2},$$
$$\mathcal{A} \simeq \frac{\gamma_{r1}\gamma_1/2}{(\omega_l - \omega_1)^2 + (\Gamma_1/2)^2}. \qquad (57)$$

These formulas coincide with expressions (36) and (37) for the two-level system.

Finally, we examine the case of merging levels. Under the conditions

$$\gamma_1 = \gamma_2 = \gamma, \quad \omega_1 = \omega_2 = \omega,$$
$$\gamma_{r1} = \gamma_{r2} = \gamma_r, \qquad (58)$$

from relationships (41) and (42), we have

$$\mathcal{R} \simeq \frac{\gamma_r^2}{(\omega_l - \omega)^2 + (\gamma_r + \gamma/2)^2}, \qquad (59)$$

$$\mathcal{A} \simeq \frac{\gamma_r\gamma}{(\omega_l - \omega)^2 + (\gamma_r + \gamma/2)^2}. \qquad (60)$$

Analysis of these expressions demonstrates that the formulas for the two-level system with twice the reciprocal lifetime γ_r are valid in the case of the doubly degenerate excited level.

4. CALCULATION OF THE RADIATIVE LIFETIME FOR AN ELECTRON–HOLE PAIR IN A QUANTUM WELL IN A STRONG MAGNETIC FIELD

The reciprocal radiative lifetime γ_r of the electron–hole pair in a strong magnetic field can be calculated from the following formula of the perturbation theory in the second order:

$$\gamma_{r\eta} = \frac{2\pi}{\hbar}\sum_s |\langle s|U|\eta\rangle|^2 \delta(\hbar\omega_s - E_\eta). \qquad (61)$$

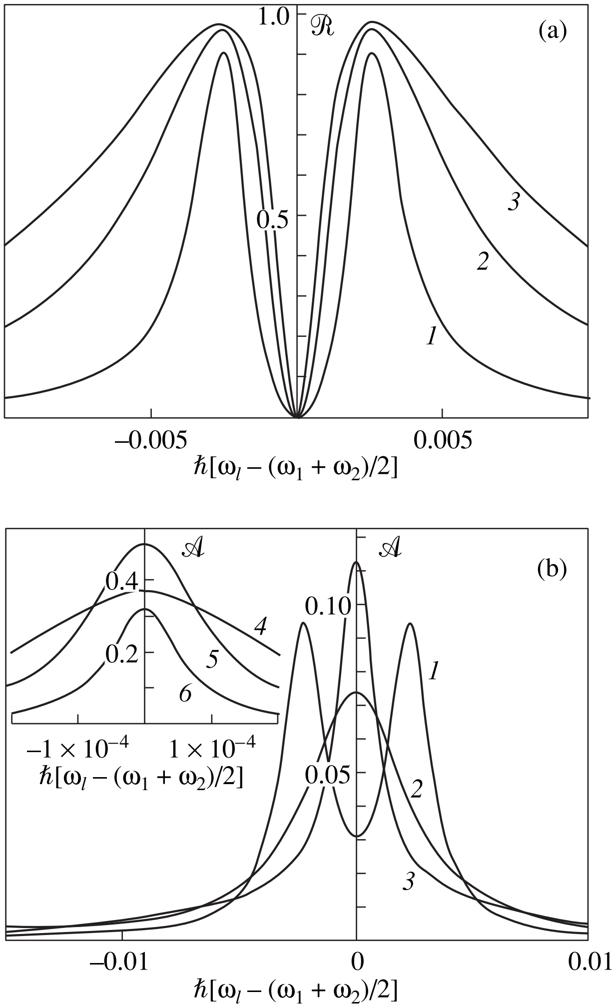

Fig. 1. Dependences of the dimensionless (a) reflectance $\mathcal{R}$ and (b) absorptance $\mathcal{A}$ of light on the light frequency ω_l for a three-level system at $\gamma \ll \gamma_r$ (where $\gamma_r = \gamma_{r1} = \gamma_{r2}$ is the radiative broadening of the levels and $\gamma = \gamma_1 = \gamma_2$ is the nonradiative broadening of the levels). $\hbar(\omega_1 - \omega_2) = 0.005$; $\hbar\gamma = 0.0001$; and $\hbar\gamma_r$ = (*1*) 0.002, (*2*) 0.005, and (*3*) 0.008. The inset shows the dependences $\mathcal{A}(\omega_l)$ at $\hbar\gamma_r$ = (*4*) 0.04, (*5*) 0.125, and (*6*) 0.5.

Here, $|\eta\rangle$ and $|s\rangle$ are the wave functions in the second quantization representation. The function $|\eta\rangle$ of the initial state corresponds to the presence of one pair with the set of indices η, and function $|s\rangle$ of the final state corresponds to the presence of one photon with the set of indices s. The interaction U can be written in the form

$$U = -\frac{1}{c}\int d\mathbf{r}\mathbf{A}(\mathbf{r})\mathbf{j}(\mathbf{r}). \qquad (62)$$

Here,

$$\mathbf{A}(\mathbf{r}) = \sqrt{\frac{2\pi\hbar}{V_0}}\frac{c}{n}\sum_s \omega_s^{-1/2}(c_s\mathbf{e}_s e^{i\boldsymbol{\kappa}\mathbf{r}} + c_s^+\mathbf{e}_s^* e^{-i\boldsymbol{\kappa}\mathbf{r}}) \qquad (63)$$

is the vector potential, the set of indices s consists of the wave vector $\boldsymbol{\kappa}$ and the polarization index i (which takes two values); c_s^+ and c_s are the creation and annihilation operators for the photon s, respectively; $\mathbf{e}_s$ and $\hbar\omega_s$ are the polarization vector and the energy of the photon, respectively; and V_0 is the normalization volume. The current density operator can be represented by the expression

$$\mathbf{j}(\mathbf{r}) = \frac{e}{m_0}\sum_{\xi}[\mathbf{p}_{cv}F^*_{\xi}(\mathbf{r})a^+_{\xi} + \mathbf{p}^*_{cv}F_{\xi}(\mathbf{r})a_{\xi}]. \qquad (64)$$

Here, m_0 is the mass of the free electron, a^+_{ξ} and a_{ξ} are the creation and annihilation operators for the electron–hole pair in the state ξ;

$$F_{\xi}(\mathbf{r}) = \Psi_{\xi}(\mathbf{r}_e = \mathbf{r}_h = \mathbf{r}), \qquad (65)$$

$\Psi_{\xi}(\mathbf{r}_e, \mathbf{r}_h)$ is the slowly varying part of the electron–hole pair wave function (in the effective-mass approximation) dependent on the radius vectors $\mathbf{r}_e$ and $\mathbf{r}_h$ of the electron and hole, and $\mathbf{p}_{cv}$ is the interband matrix element of the momentum operator.

Let us determine the wave functions $\Psi_{\xi}(\mathbf{r}_e, \mathbf{r}_h)$. The symbol ξ designates the set of indices characterizing the state of the electron–hole pair, that is,

$$\xi \longrightarrow c, v, n_e, n_h, \mathbf{K}_{\perp}, l_e, l_h. \qquad (66)$$

The subscripts c and v indicate the conduction and valence bands, respectively (which, in principle, can be degenerate). By introducing the coordinates

$$\mathbf{r}_{\perp} = \mathbf{r}_{e\perp} - \mathbf{r}_{h\perp}, \quad \mathbf{R}_{\perp} = (m_h\mathbf{r}_{h\perp} + m_e\mathbf{r}_{e\perp})/M$$

for the relative and cooperative motion of the electron and hole in the xy plane, we obtain [30–33]

$$\begin{aligned}\Psi_{\xi}(\mathbf{r}_e, \mathbf{r}_h) &= \frac{1}{\sqrt{2\pi a_H^2 L_x L_y}}\exp\left[i(K_x X + K_y Y) - i\frac{yX}{a_H^2}\right]\\ &\times \exp\left[i\frac{m_e - m_h}{2M}(-\mathbf{K}_{\perp}\mathbf{r}_{\perp} + a_H^2 K_x K_y) + \frac{xy}{a_H^2}\right] \qquad (67)\\ &\times \mathcal{K}_{n_e, n_h}\left(\frac{\mathbf{r}_{\perp} - \mathbf{r}_{\perp 0}}{a_H}\right)\varphi_{cl_e}(z_e)\varphi_{vl_h}(z_h),\end{aligned}$$

where $\hbar\mathbf{K}_{\perp}$ is the quasi-momentum of the electron–hole pair in the xy plane, $M = m_e + m_h$, L_x and L_y are the normalization lengths, and $\mathbf{r}_{\perp 0} = a_H^2\mathbf{H} \times \mathbf{K}_{\perp}/H$. The function $\mathcal{K}_{n, m}$ is defined by the relationship [31]

$$\begin{aligned}\mathcal{K}_{n, m}(\mathbf{p}) &= \sqrt{\min(n!, m!)/\max(n!, m!)}\, i^{|n-m|}\\ &\times \exp(-p^2/4)(p/\sqrt{2})^{|n-m|} \qquad (68)\\ &\times \exp[i(\phi - \pi/2)(n - m)]L^{|n-m|}_{\min(n, m)}(p^2/2),\end{aligned}$$

where $p = \sqrt{p_x^2 + p_y^2}$, $\phi = \arctan(p_y/p_x)$, and $L^n_m(x)$ is the associated Laguerre polynomial. The form of the real functions $\varphi_{c(v)l}(z)$ corresponding to the quantum number l of quantum confinement for the quantum well with a finite depth is given in [22]. In formula (67), we used the gauge of the vector potential $\mathbf{A} = \mathbf{A}(0, xH, 0)$. In our earlier work [32], we demonstrated that functions (67) are the eigenfunctions of the momentum operator $\hat{\mathbf{P}}_{\perp}$ of the electron–hole pair in the xy plane and correspond to the eigenvalues of $\hbar\mathbf{K}_{\perp}$. The operator $\hat{\mathbf{P}}_{\perp}$ was determined in [34]. The energies of the states of functions (67) are as follows:

$$\begin{aligned}E_{\xi} &= \hbar\omega_{\xi} = E_g + \varepsilon^e_{le} + \varepsilon^h_{lh}\\ &+ \hbar\Omega_e(n_e + 1/2) + \hbar\Omega_h(n_h + 1/2),\end{aligned} \qquad (69)$$

where E_g is the band gap and $\Omega_{e(h)} = |e|H/m_{e(h)}$. Now, the reciprocal radiative lifetime $\gamma_{r\xi}$ of the electron–hole pair with the set of indices ξ can be calculated with the use of formulas (61)–(69). By assuming that the x axis is aligned along $\mathbf{K}_{\perp}$, we find (for more details, see [25])

$$\begin{aligned}\gamma_{r\xi} &= [2e^2\Omega_0/(\hbar^2 cnm_0\omega_{\xi})]B_{n_e, n_h}(K_{\perp})\\ &\times \left|R_{l_e, l_h}(\sqrt{(\omega_{\xi}n/c)^2 - K_{\perp}^2})\right|^2 F_{\xi}(K_{\perp}), \qquad (70)\\ K_{\perp} &< \omega_{\xi}n/c, \quad \gamma_{r\xi} = 0, \quad K_{\perp} > \omega_{\xi}n/c,\end{aligned}$$

where $\Omega_0 = |e|H/m_0c$ is the cyclotron frequency corresponding to the mass m_0 of the free electron,

$$\begin{aligned}B_{n, m}(K_{\perp}) &= \left|\mathcal{K}_{n, m}\left(-\frac{\mathbf{r}_{\perp 0}}{a_H}\right)\right|^2 = \frac{\min(n!, m!)}{\max(n!, m!)}\\ &\times \exp\left(-\frac{a_H^2K_{\perp}^2}{2}\right)\left(\frac{a_H^2K_{\perp}^2}{2}\right)^{|n-m|}\left[L^{|n-m|}_{\min(n, m)}\left(\frac{a_H^2K_{\perp}^2}{2}\right)\right]^2, \qquad (71)\end{aligned}$$

$$R_{l_e, l_h}(k) = \int_{-\infty}^{\infty} dz e^{-ikz}\varphi_{cl_e}(z)\varphi_{vl_h}(z),$$

$$\begin{aligned}F_{\xi}(K_{\perp}) &= \frac{\sqrt{(\omega_{\xi}n/c)^2 - K_{\perp}^2}}{\omega_{\xi}n/c}|p_{cvx}|^2\\ &+ \frac{\omega_{\xi}n/c}{\sqrt{(\omega_{\xi}n/c)^2 - K_{\perp}^2}}|p_{cvy}|^2 + \frac{K_{\perp}^2|p_{cvz}|^2}{(\omega_{\xi}n/c)\sqrt{(\omega_{\xi}n/c)^2 - K_{\perp}^2}}.\end{aligned} \qquad (72)$$

A comparison of relationship (70) with the results obtained in [14] for the exciton level in the quantum well at $H = 0$ shows that the dependences on $\mathbf{p}_{cv}$ for both cases coincide with each other and $\gamma_{r\xi} = 0$ at $K_{\perp} > \omega_{\xi}n/c$.

The right-hand side of relationship (70) involves the multipliers Ω_0 and $B_{n_e, n_h}(K_{\perp})$ associated with the magnetic field. The multiplier $\left|R_{l_e, l_h}(\sqrt{(\omega_{\xi}n/c)^2 - K_{\perp}^2})\right|^2$ is absent in the expressions deduced in [14], because these authors considered the quantum wells with $d \ll c/n\omega_l$, whereas we did not impose this limitation in the derivation of relationship (70). For narrow wells ($d \ll \lambda$), we have

$$R_{l_e,\,l_h}\left(\sqrt{(\omega_\xi n/c)^2 - K_\perp^2}\right) \simeq \pi_{l_e,\,l_h} = \int_{-\infty}^{\infty} dz\,\varphi_{cl_e}(z)\varphi_{vl_h}(z). \quad (73)$$

In the case of infinitely deep quantum wells, we obtain

$$\pi_{l_e,\,l_h} = \delta_{l_e,\,l_h}. \quad (74)$$

For the quantum well with $d \simeq c/n\omega_l$, the multiplier $\left|R_{l_e,\,l_h}\left(\sqrt{(\omega_\xi n/c)^2 - K_\perp^2}\right)\right|^2$ depends on the quantum well width, namely, decreases with an increase in d. As a result, the reciprocal lifetime $\gamma_{r\xi}$ also decreases. In the limiting case $d \gg \lambda$, we obtain $\gamma_{r\xi} \longrightarrow 0$, as should be expected when changing over to the bulk crystal [12].

For normal incidence of light on the quantum well, it is sufficient to determine the reciprocal lifetimes described by formula (70) at $K_\perp = 0$. Since the equality $B_{n_e,\,n_h}(0) = \delta_{n_e,\,n_h}$ is satisfied, we calculate the reciprocal lifetime $\gamma_{r\xi_0}$ for the set of indices

$$\xi_0 \longrightarrow c,\ v,\ n_e = n_h, \quad \mathbf{K}_\perp = 0,\ l_e,\ l_h. \quad (75)$$

With the use of expression (70), we find

$$\gamma_{r\xi_0} = \frac{2e^2\Omega_0}{\hbar cn}\left|R_{l_e,\,l_h}(\omega_{\xi_0} n/c)\right|^2 \frac{|p_{cvx}|^2 + |p_{cvy}|^2}{m_0\hbar\omega_{\xi_0}}, \quad (76)$$

$$\hbar\omega_{\xi_0} = E_g + \varepsilon^c_{l_e} + \varepsilon^h_{l_h} + \hbar\Omega_\mu(n_e + 1/2),$$
$$\Omega_\mu = \frac{|e|H}{\mu c}, \quad \mu = \frac{m_e m_h}{M}. \quad (77)$$

It follows from formula (76) that the reciprocal radiative lifetime of the electron–hole pair is proportional to the magnetic field H when the energy $\hbar\omega_{\xi_0}$ weakly depends on the field H ($E_{\xi_0} \simeq \tilde{E}_g$, where $\tilde{E}_g = E_g + \varepsilon^e_{l_e} + \varepsilon^h_{l_h}$).

Now, we calculate the reciprocal lifetime $\gamma_{r\xi_0}$ for the band model of GaAs. The conduction band is doubly degenerate (with respect to the spin), and the subscript c can take two values: $c = 1$ or 2. The valence band (of heavy holes) is also doubly degenerate: $v = 1$ or 2. There exist pairs of two sorts denoted by the indices I and II such that $c = 1$ and $v = 1$ in pairs of sort I and $c = 2$ and $v = 2$ in pairs of sort II. The electron–hole pairs of these sorts differ in the interband matrix elements $\mathbf{p}_{cv}$, which can be written in the following form:

$$\mathbf{p}^{\mathrm{I}}_{cv} = \frac{1}{\sqrt{2}}p_{cv}(\mathbf{e}_x - i\mathbf{e}_y),$$
$$\mathbf{p}^{\mathrm{II}}_{cv} = \frac{1}{\sqrt{2}}p_{cv}(\mathbf{e}_x + i\mathbf{e}_y). \quad (78)$$

Within the proposed model, the wave functions $\varphi_{cl_e}(z)$ and $\varphi_{vl_h}(z)$ do not depend on the subscripts c and v. With the use of the circular polarizations (11), each polarization (the left-hand or right-hand polarization with respect to the z axis) is rigidly associated with a particular sort (I or II) of electron–hole pairs, because the interaction of the pair with light is proportional to the quantity $\mathbf{e}_s\mathbf{p}_{cv}$. From formula (76) for model (78), we find the reciprocal radiative time of pairs of any sort, that is,[4]

$$\gamma_{r\xi_0} = \frac{2e^2\Omega_0}{\hbar cn}\left|R_{l_e,\,l_h}(\omega_{\xi_0} n/c)\right|^2 \frac{p^2_{cv}}{m_0\hbar\omega_{\xi_0}}. \quad (79)$$

In the case of narrow quantum wells ($d \ll \lambda$), we use approximation (73) and have

$$\gamma_{r\xi_0} \simeq \frac{2e^2\Omega_0}{\hbar cn}\pi^2_{l_e,\,l_h}\frac{p^2_{cv}}{m_0\hbar\omega_{\xi_0}}. \quad (80)$$

By using the parameters taken from [21] for GaAs and approximation (74) and also setting $\hbar\omega_{\xi_0} \simeq E_g$, we obtain the numerical estimate for the reciprocal radiative time in the form

$$\hbar\gamma_r \simeq 5.35 \times 10^{-5}(H/H_{\mathrm{res}})\ \mathrm{eV}, \quad (81)$$

where H_{res} corresponds to polaron A, i.e., is given by the formula $H_{\mathrm{res}} = m_e c\omega_{LO}/|e|$.

5. RECIPROCAL RADIATIVE LIFETIMES OF THE MAGNETOPOLARON

Now, let us calculate the radiative lifetime of the system composed of a magnetopolaron and a hole. As an example, we choose polaron A in combination with the hole described by the quantum number l_h of the quantum confinement and the Landau quantum number $n_h = 1$. In the vicinity of the resonance $\omega_{LO} = \Omega_e$, the energy level of the electron–hole pair is split into two energy terms. Either energy term is characterized by the reciprocal radiative lifetime γ_{ra} or γ_{rb} according to the designations proposed in [22] (the subscripts a and b refer to the higher and lower terms of the magnetopolaron). The reciprocal radiative lifetimes γ_{ra} and γ_{rb} can

---

[4] The relationship derived in [28] coincides with expression (79) at $n = 1$.

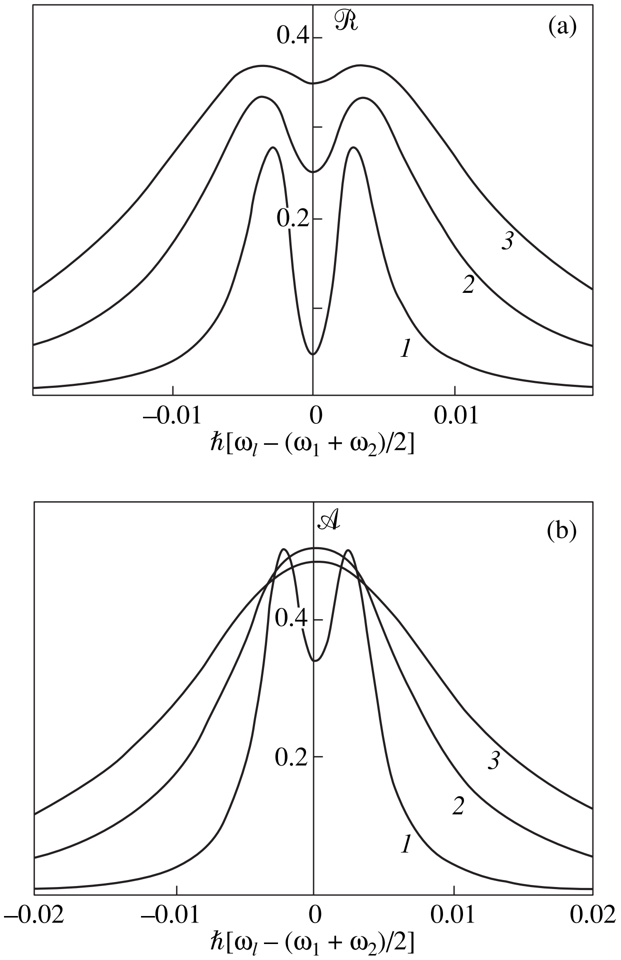

Fig. 2. Dependences of the dimensionless (a) reflectance ℛ and (b) absorptance 𝒜 of light on the light frequency ω_l for a three-level system at $\gamma = \gamma_r$. $\hbar(\omega_1 - \omega_2) = 0.005$ and $\hbar\gamma_r$ = (*1*) 0.002, (*2*) 0.005, and (*3*) 0.008.

be calculated using formula (61). The initial state is characterized by the set of indices

$$\eta \longrightarrow c,\ v,\ p,\ \mathbf{K}_\perp,\ l_e,\ l_h, \tag{82}$$

where the index p is equal to a or b and $\hbar\mathbf{K}_\perp$ is the quasi-momentum (lying in the xy plane) of the system. The wave functions of the system with indices (82) were calculated in our previous works [22, 25]. The corresponding energies can be written in the form

$$E_\eta = \hbar\omega_\eta = E_g + \varepsilon^e_{l_e} + \varepsilon^h_{l_h} + (3/2)\hbar\Omega_h + E_p, \tag{83}$$

where E_p is the polaron energy measured from the level $\varepsilon^e_{l_e}$. According to [22], the polaron energy is defined by the relationship

$$\begin{gathered} E_p = \hbar\Omega_e + \hbar\omega_{LO}/2 \pm \sqrt{(\lambda/2)^2 + A^2}, \\ \lambda = \hbar(\Omega_e - \omega_{LO}), \end{gathered} \tag{84}$$

where the upper (lower) sign corresponds to the term $p = a$ ($p = b$). At resonance, we have $\Omega_e = \omega_{LO}$ and

$$\begin{gathered} E_p^{\text{res}} = (3/2)\hbar\omega_{LO} \pm \sqrt{A^2}, \\ \Delta E = E_a^{\text{res}} + E_b^{\text{res}} = 2\sqrt{A^2}. \end{gathered} \tag{85}$$

For the reciprocal radiative lifetimes, we obtain

$$\begin{gathered} \gamma_{r\eta} = [2Q_{0p}e^2\Omega_0/(\hbar^2 cnm_0\omega_\eta)]B_{11}(K_\perp) \\ \times \left|R_{l_e,\,l_h}\left(\sqrt{(\omega_\eta n/c)^2 - K_\perp^2}\right)\right|^2 F_\eta(K_\perp), \\ K_\perp < \omega_\eta n/c, \\ \gamma_{r\eta} = 0, \quad K_\perp > \omega_\eta n/c, \end{gathered} \tag{86}$$

$$Q_{0p} = (1/2)\left(1 \pm \lambda/\sqrt{\lambda^2 + 4A^2}\right). \tag{87}$$

Compared to expression (70), formula (86) includes an additional multiplier Q_{0p}, which strongly depends on the deviation λ of the cyclotron frequency Ω_e from the resonance frequency ω_{LO}, i.e., on the magnetic field strength H. The reason for this strong dependence is as follows. In [22], we demonstrated that the wave function of the magnetopolaron is a linear combination of two functions of the electron–phonon system, one of which corresponds to the electron with the Landau quantum number $n = 1$ and phonon vacuum and the other function is associated with the electron with the quantum number $n = 0$ and one phonon with the frequency ω_{LO}. The coefficients Q_{0p} and Q_{1p} are the probabilities of finding the system in these states (the index 0 indicates the absence of phonons, and the index 1 indicates the presence of one phonon). The coefficient Q_{0p} is defined by formula (87), and the coefficient Q_{1p} can be represented by the expression

$$Q_{1p} = 1 - Q_{0p} = (1/2)\left(1 \mp \lambda/\sqrt{\lambda^2 + 4A^2}\right). \tag{88}$$

At resonance, we have $\Omega_e = \omega_{LO}$ and $Q_{0p}^{\text{res}} = Q_{1p}^{\text{res}} = 1/2$. The presence of the multiplier Q_{0p} in relationship (86) can be explained by the fact that only one of two excitations (whose superposition comprises the magnetopolaron–hole system), namely, the excitation with the indices $n_e = n_h = 1$ and $N = 0$, can undergo light annihilation. The light annihilation of the other excitation with the indices $n_e = 0$, $n_h = 1$, and $N = 1$ is impossible. It follows from expressions (86) and (87) that, at $\lambda = 0$ (i.e., at true resonance), the reciprocal radiative lifetimes γ_{ra} and γ_{rb} are equal to each other and involve an additional multiplier 1/2 as compared to those of the electron–hole pair with the indices $n_e = n_h = 1$. At $\mathbf{K}_\perp = 0$, we introduce the set of indices $\eta_0 \longrightarrow c,\ v,\ p,\ \mathbf{K}_\perp = 0,\ l_e$, and l_h. In this case, the formulas derived for the reciprocal lifetimes $\gamma_{r\eta_0}$ differ from relationships (76), (79), and (80) only in the replacement of the indices ξ_0 by the indices η_0 and the presence of the multiplier Q_{0p}.

The replacement of ω_{ξ_0} by ω_{η_0} is of no significance because we approximately have $\omega_{\xi_0} \simeq \omega_{\eta_0} \simeq \tilde{E}_g/\hbar$, where $\tilde{E}_g = E_g + \varepsilon_{l_e} + \varepsilon_{l_h}$. As a result, instead of expression (80), we obtain

$$\gamma_{r\eta_0} \simeq \frac{2Q_{0p}e^2}{\hbar c}\frac{\Omega_0 p_{cv}^2}{nm_0\hbar\omega_{\eta_0}}\pi^2_{l_e, l_h}. \tag{89}$$

The strong dependence of the reciprocal radiative lifetime on the index p and the magnetic field H is determined by the multiplier Q_{0p}. The dependences of the reciprocal radiative lifetimes γ_{ra} and γ_{rb} on the field H in the vicinity of the resonance are plotted in Fig. 3.

6. NONRADIATIVE LIFETIMES OF THE MAGNETOPOLARON

We will not calculate the reciprocal nonradiative lifetimes of the electron–hole pair in a quantum well in a strong magnetic field far from the magnetopolaron resonance because the nature of the processes responsible for these times remains unclear. One-phonon processes are forbidden by the energy conservation law. Possibly, two-phonon processes with the participation of acoustic phonons make the main contribution. However, in the vicinity of the magnetophonon resonance, there arises a contribution to the reciprocal lifetimes γ_p ($p = a$ and b) due to the finite lifetimes of the longitudinal optical phonons comprising the magnetopolaron. This contribution will be calculated in this section. In this way, the lower limit of the quantities γ_p ($p = a$ and b) can be determined in the vicinity of the resonance.

In the quantum well, the phonon with the set of indices ν is characterized by the reciprocal nonradiative lifetime γ_ν governed by the phonon–phonon interaction, for example, by the decay of one longitudinal optical phonon into two acoustic phonons. First, we derive the relationship for the reciprocal lifetime γ_ν. This lifetime can be written in the form

$$\gamma_\nu = \frac{2\pi}{\hbar}\sum_f |\langle f|\mathcal{H}_{pp}|i\rangle|^2\delta(E_i - E_f), \tag{90}$$

where $\mathcal{H}_{pp}$ is the phonon–phonon interaction, $|i\rangle = b_\nu^+|0\rangle$ is the initial state corresponding to one phonon with the set of indices ν and the energy $E_i = \hbar\omega_{LO}$, $|f\rangle = a_\tau^+|0\rangle$ is the final state of the phonon system with the set of indices τ and the energy $E_f = E_\tau$, and a_τ^+ is the phonon operator corresponding, for example, to the creation of two acoustic phonons. In our earlier work [25], we calculated the reciprocal lifetimes γ_ν and γ_p for the model proposed in [22], according to which confined and interface phonons with the same frequency ω_{LO} without dispersion participate in the formation of the polaron in the quantum well. In the present work, we use an even simpler model in which the interaction of electrons with confined phonons can be approximated by the Fröhlich interaction with bulk phonons and the interaction with interface phonons is disregarded. In [24], we demonstrated that the interaction of electrons with bulk phonons can be used for sufficiently wide quantum wells.

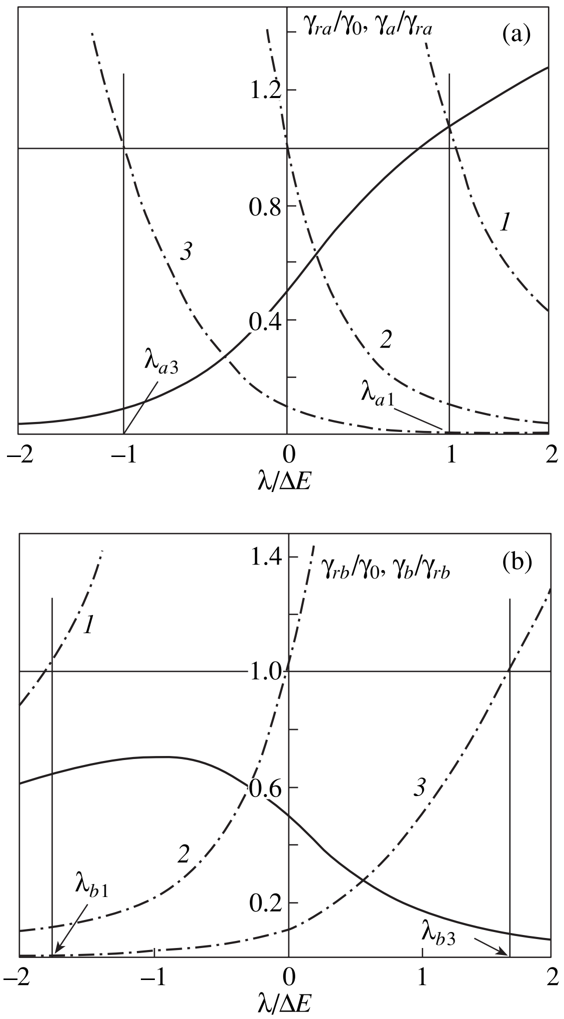

Fig. 3. Magnetic-field dependences of the radiative and nonradiative broadening of the excited level of the system consisting of polaron $\mathcal{A}$ and the hole with the quantum numbers $n_h = 1$ and l in the quantum well at $p =$ (a) a and (b) b. $\Delta E/\hbar\omega_{LO} = 0.18$ (this is characteristic of GaAs [24]). Solid lines correspond to γ_{rp}/γ_0, and dashed lines represent γ_p/γ_{rp} at $\bar{\gamma}_{LO}/\gamma_0 =$ (*1*) 10, (*2*) 1, and (*3*) 0.1.

In the case of bulk longitudinal optical phonons, the set of indices ν reduces to the three-dimensional wave vector $\mathbf{q}$. The final phonon state is characterized by the resultant three-dimensional wave vector $\mathbf{q}'$ and other indices φ. For example, when the phonon decays into two acoustic phonons, we have $\mathbf{q}' = \mathbf{q}_1 + \mathbf{q}_2$.

The matrix element in formula (90) can be defined by the expression

$$\left\langle 0\left|a_\tau \mathcal{H}_{pp} b_\nu^+\right|0\right\rangle = \delta_{\mathbf{q},\mathbf{q}'} W(\mathbf{q},\varphi). \qquad (91)$$

Then, formula (90) can be rearranged to give

$$\gamma_\nu = \gamma_{\mathbf{q}} = 2\pi/\hbar \sum_{\varphi} |W(\mathbf{q},\varphi)|^2 \delta(\hbar\omega_{LO} - E_{\mathbf{q},\varphi}), \qquad (92)$$

where $E_{\mathbf{q},\varphi}$ is the energy of the final phonon state represented, for example, by two bulk acoustic phonons. In the framework of the same model, the reciprocal nonradiative lifetime of the polaron can be deduced in the following form [25]:

$$\gamma_p = \frac{2\pi}{\hbar}\frac{Q_{1p}}{A^2}\sum_{\mathbf{q},\varphi}|U(\mathbf{q})|^2|W(\mathbf{q},\varphi)|^2 \times \delta(\lambda/2 \pm \sqrt{(\lambda/2)^2 + A^2} + \hbar\omega_{LO} - E_{\mathbf{q},\varphi}). \qquad (93)$$

Here, the upper (lower) sign corresponds to the polaron state $p = a$ ($p = b$), the quantity Q_{1p} is given by relationship (88), and the function $U(\mathbf{q})$ was derived in [22] in the form

$$U(\mathbf{q}) = \mathcal{M}(q_z)\mathcal{C}_{\mathbf{q}}\mathcal{K}^*_{10}(\mathbf{q}_\perp), \qquad (94)$$

where

$$\mathcal{M}(q_z) = \int_{-\infty}^{\infty} dz[\varphi_l(z)]^2 e^{iq_z z},$$

$$\mathcal{C}_{\mathbf{q}} = -(i\hbar\omega_{LO}/ql)(4\pi\alpha l^3/V_0)^{1/2},$$

$$l = [\hbar/(2m_e\omega_{LO})]^{1/2}, \quad \alpha = e^2(\varepsilon_\infty^{-1} - \varepsilon_0^{-1})/(2\hbar\omega_{LO} l),$$

ε_0 (ε_∞) is the static (high-frequency) permittivity, $\mathcal{K}_{10}$ ($\mathbf{q}_\perp$) is defined by expression (68), and

$$A^2 = \sum_{\mathbf{q}} |U(\mathbf{q})|^2. \qquad (95)$$

In formulas (93)–(95), we used the designations given in [22]. From a comparison of relationships (92) and (93), we find that, in the vicinity of the polaron resonance, i.e., under the condition

$$\left|\lambda/2 \pm \sqrt{(\lambda/2)^2 + A^2}\right| \ll \hbar\omega_{LO}, \qquad (96)$$

the reciprocal time γ_p is expressed through $\gamma_{\mathbf{q}}$. As a result, we obtain

$$\gamma_p = Q_{1p}\bar{\gamma}_{LO}, \qquad (97)$$

$$\bar{\gamma}_{LO} = \sum_{\mathbf{q}} \gamma_{\mathbf{q}} |U(\mathbf{q})|^2 \Big/ \sum_{\mathbf{q}} |U(\mathbf{q})|^2. \qquad (98)$$

Owing to the multiplier Q_{1p} in expression (97), the reciprocal lifetime γ_p strongly depends on the quantity $\lambda = \hbar(\Omega_e - \omega_{LO})$ describing the deviation of the magnetic field from the resonance $\Omega_e = \omega_{LO}$. At resonance, we have

$$\gamma_p = (1/2)\bar{\gamma}_{LO} \qquad (99)$$

for both terms $p = a$ and b.

Now, we analyze the results obtained with the use of relationship (93) far from the resonance $\Omega_e = \omega_{LO}$. It is seen from Fig. 3 that, under the condition $|\lambda| \gg |A|$, the term a at $\lambda > 0$ and the term b at $\lambda < 0$ transform into the electron level with the indices $n = 1$ and l. In this case, according to formula (88), we have $Q_{1p} \simeq A^2/\lambda^2$. As a result, from expression (93), we obtain

$$\gamma_p \simeq \frac{2\pi}{\hbar}\frac{A^2}{\lambda^2}\sum_{\mathbf{q},\varphi}\frac{|U(\mathbf{q})|^2}{A^2}|W(\mathbf{q},\varphi)|^2\delta(\hbar\Omega_e - E_{\mathbf{q},\varphi}). \qquad (100)$$

This quantity cannot be expressed through $\bar{\gamma}_{LO}$ but, compared to it, includes the small multiplier A^2/λ^2. It is worth noting that the argument of the δ function in formula (100) corresponds to the transition from the electron level $n = 1$ to the level $n = 0$ with the emission, for example, of two acoustic phonons. The quantity γ_p [formula (100)] is determined to the second order in the interaction of electrons with longitudinal optical phonons and to the second order in the phonon–phonon interaction. This quantity is one of the contributions to the reciprocal nonradiative lifetime of the electron–hole pair far from the magnetophonon resonance. Two other branches of the terms, namely, a at $\lambda < 0$ and b at $\lambda > 0$ ($|\lambda| \gg |A|$), correspond to the state of an electron at the level $n = 0$, l + one longitudinal optical phonon. For these branches, we have $Q_{1p} \simeq 1$ and

$$\gamma_p \simeq \bar{\gamma}_{LO}, \qquad (101)$$

as should be observed for the state including the longitudinal optical phonon. Therefore, formula (93) correctly describes the limiting cases at $|\lambda| \gg |A|$.

Thus, the reciprocal nonradiative lifetime γ_p of the electron–hole pair sharply increases in the vicinity of the intersection between the electronic terms and reaches half the reciprocal lifetime of the longitudinal optical phonon. At resonance $\Omega_e = \omega_{LO}$, the reciprocal nonradiative lifetime for each term is no less than $\bar{\gamma}_{LO}/2$.

7. RESULTS OF NUMERICAL CALCULATIONS

Figures 1 and 2 depict the dependences of the reflectance $\mathcal{R}(\omega_l)$ and absorptance $\mathcal{A}(\omega_l)$ for the three-level system at different ratios between the parameters $\gamma_{r1(2)}$, $\gamma_{1(2)}$, and $\omega_1 - \omega_2$. These results should be used in the case of any two excited, rather closely spaced levels in the quantum well. At $\gamma_{r1(2)} \ll \omega_1 - \omega_2$ and $\gamma_{1(2)} \ll \omega_1 - \omega_2$, the results for two two-level systems are applicable.

The dependences $\mathcal{R}(\omega_l)$ and $\mathcal{A}(\omega_l)$ for the three-level system at $\gamma_{r1} = \gamma_{r2} = \gamma_r$, $\gamma_1 = \gamma_2 = \gamma$, and $\gamma_r \gg \gamma$ are depicted in Fig. 1. Curves *1* are obtained at $\gamma_r < \omega_1 - \omega_2$. Curves *2* are constructed at $\gamma_r = \omega_1 - \omega_2$. Curve *3* in Fig. 1a and curves *3–6* in Fig. 1b are plotted at $\gamma_r > \omega_1 - \omega_2$. Curves *1* correspond to the dependences for two two-level systems. The other curves exhibit a specific behavior. In particular, the reflectance $\mathcal{R}(\omega_0)$ at the point $\omega_l = \omega_0$ in all three curves in Fig. 1a is close to zero.

As for two-level systems, the reflectance and absorptance at $\gamma_{r1(2)} \ll \gamma_{1(2)}$ are considerably less than unity and $\mathcal{R}(\omega_l) \ll \mathcal{A}(\omega_l)$. At $\gamma_{r1(2)} \gg \gamma_{1(2)}$, the absorptance reaches values close to unity.

Figure 2 shows the dependences $\mathcal{R}(\omega_l)$ and $\mathcal{A}(\omega_l)$ for the three-level system at $\gamma_{r1} = \gamma_{r2} = \gamma_r$, $\gamma_1 = \gamma_2 = \gamma$, and $\gamma_r = \gamma$. Curves *1* are obtained at $\gamma_r < \omega_1 - \omega_2$, curves *2* are constructed at $\gamma_r = \omega_1 - \omega_2$, and curves *3* are plotted at $\gamma_r > \omega_1 - \omega_2$. It can be seen that the absorptance reaches a maximum but never exceeds 0.5.

Below, the formulas obtained for the coefficients $\mathcal{A}(\omega_l)$ and $\mathcal{R}(\omega_l)$ in the case of the three-level system in the quantum well will be used for the system comprised of a magnetopolaron and a hole with the indices $n_h = 1$ and $l_h = l$. The energy levels of this system are determined by expressions (83) and (84). If the energy of the system is reckoned from the level

$$E_0 = E_g + \varepsilon_l^e + \varepsilon_l^b + (3/2)(1 + m_e/m_h)\hbar\omega_{LO},$$

relationship (83) is conveniently rewritten in the form

$$\frac{\mathcal{E}_p}{\Delta E} = \frac{\lambda}{\Delta E}\left(1 + \frac{3}{2}\frac{m_e}{m_h}\right) \pm \frac{1}{2}\sqrt{1 + \left(\frac{\lambda}{\Delta E}\right)^2}, \qquad (102)$$

where $\lambda = \hbar(\Omega_e - \omega_{LO})$, ΔE is the splitting of the terms at $\lambda = 0$, and the upper (lower) sign corresponds to the term $p = a$ ($p = b$). With the use of relationships (89) and (87), we obtain

$$\frac{\gamma_{rp}}{\gamma_0} = \frac{1}{2}\left(1 + \frac{\lambda/\Delta E}{\hbar\omega_{LO}/\Delta E}\right)\left[1 \pm \frac{\lambda/\Delta E}{\sqrt{1 + (\lambda/\Delta E)^2}}\right], \qquad (103)$$

where the constant γ_0 is the reciprocal radiative lifetime of the electron–hole pair with the indices $n_e = n_h = 1$ and $l_e = l_h = l$ at $\lambda = 0$ without regard for the polaron effect. The multiplier in the parentheses describes the dependence of the quantity Ω_0 entering into the expression for γ_{rp} on the magnetic field. By using relationships (89) and (97), the ratio between the nonradiative and radiative reciprocal lifetimes can be estimated as

$$\frac{\gamma_p}{\gamma_{rp}} = \frac{\bar{\gamma}_{LO}/\gamma_0}{1 + (\lambda/\hbar\omega_{LO})}\frac{\sqrt{1 + (\lambda/\Delta E)^2} \mp (\lambda/\Delta E)}{\sqrt{1 + (\lambda/\Delta E)^2} \pm (\lambda/\Delta E)}. \qquad (104)$$

When plotting Figs. 3 and 4, we used the following parameters for GaAs: $m_e/m_h = 0.2$ and $\Delta E/\hbar\omega_{LO} = 0.18$.[5] According to the formulas derived in Section 4, we obtain the relationship

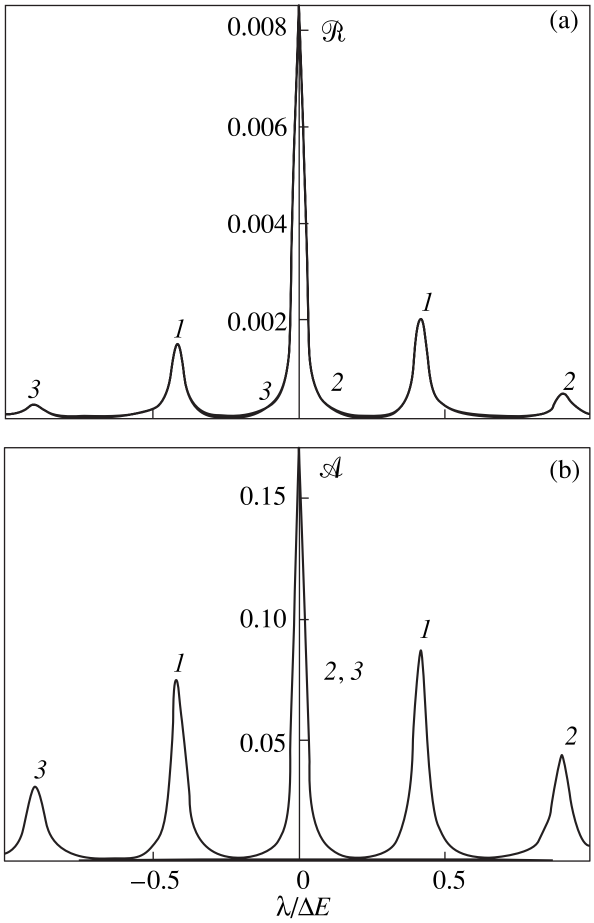

Fig. 4. Dependences of the dimensionless (a) reflectance $\mathcal{R}$ and (b) absorptance $\mathcal{A}$ on the magnetic field in the vicinity of the resonance for polaron $\mathcal{A}$. $m_e/m_h = 0.2$, $\hbar\omega_{LO} = 0.036$ eV, $\Delta E = 6.65 \times 10^{-3}$ eV [24], $\hbar\gamma_0 = 5.35 \times 10^{-5}$ eV, $\bar{\gamma}_{LO}/\gamma_0 = 10$. (*1*) $\hbar\omega_l = E_0$, (*2*) $\hbar\omega_l = E_0 + \Delta E/2$, and (*3*) $\hbar\omega_l = E_0 - \Delta E/2$. E_0 is determined in Section 7. The given parameters correspond to GaAs.

$$\gamma_0 = \frac{2e^2\omega_{LO}m_e}{\hbar cnm_0}\frac{p_{cv}^2}{m_0E_g}\pi_{ll}^2, \qquad (105)$$

which, with the use of the parameters taken from [21], gives the estimate

$$\hbar\gamma_0 \simeq 5.35 \times 10^{-5}\ \text{eV}. \qquad (106)$$

Thus, the reciprocal lifetime γ_{rp} can be estimated (as was done above), whereas the reciprocal lifetime γ_p

---

[5] According to [24], the splitting of the terms is estimated to be $\Delta E \simeq 6.65 \times 10^{-3}$ eV for polaron *A* in the quantum well 300 Å thick in GaAs. Since $\hbar\omega_{LO} = 0.0367$ eV, we obtain the ratio $\Delta E/\hbar\omega_{LO} \simeq 0.181$.

remains unknown.[6] For this reason, Figs. 3 and 4 present the results obtained at different ratios $\bar{\gamma}_{LO}/\gamma_0$.

Figure 3 shows the dependences of the reciprocal radiative lifetime γ_{rp} and the ratio γ_p/γ_{rp} on the magnetic field in the vicinity of the magnetophonon resonance. The dependences for the terms *a* and *b* are plotted in Figs. 3a and 3b, respectively. The dependences of the ratio γ_p/γ_{rp} on $\lambda/\Delta E$ are constructed for three parameters $\bar{\gamma}_{LO}/\gamma_0$. As can be seen from Fig. 3, the reciprocal lifetimes γ_{rp} and γ_p in the range of the magnetophonon resonance very strongly depend on the magnetic field.

The magnetopolaron effect is observed in the range approximately from $\lambda/\Delta E = -2$ to $\lambda/\Delta E = 2$. The term *a* at $\lambda/\Delta E > 2$ and the term *b* at $\lambda/\Delta E < -2$ transform into the energy level of the electron–hole pair with the quantum numbers of the electron and hole $n_e = n_h = 1$ and $l_e = l_h = l$. The term *b* at $\lambda/\Delta E > 2$ and the term *a* at $\lambda/\Delta E < -2$ transform into the energy level of the system composed of an electron–hole pair (with the quantum numbers $n_e = 0$, $n_h = 1$, and $l_e = l_h = l$) and one phonon. This state involves the longitudinal optical phonon and weakly interacts with the exciting light outside the range of the magnetophonon resonance.

The energy splitting ΔE is very large in the case of polaron *A*. Therefore, the conditions $\gamma_{rp} \ll \omega_1 - \omega_2$ and $\gamma_p \ll \omega_1 - \omega_2$ are satisfied and the coefficients $\mathcal{R}$ and $\mathcal{A}$ can be calculated in the approximation of two two-level systems [see formulas (36) and (37) in Section 3]. The expressions derived for the three-level system in Section 3 should be used for the small splittings ΔE, which can be observed for weakly coupled polarons [24, 25].

In the range of the magnetopolaron effect, the functions $\mathcal{R}(\omega_l)$ and $\mathcal{A}(\omega_l)$ should have two maxima at a constant magnetic field *H*. At ω_l = const, two maxima should be observed in the functions $\mathcal{R}(H)$ and $\mathcal{A}(H)$.

The coefficients $\mathcal{R}(\omega_l)$ and $\mathcal{A}(\omega_l)$ depend on the ratio $\bar{\gamma}_{LO}/\gamma_0$. In the range of the ratios $\lambda/\Delta E$ (i.e., the fields *H*) at which $\gamma_p/\gamma_{rp} \gg 1$, the absorptance is substantially less than unity but exceeds the reflectance. For curves *1* plotted in Fig. 3 at the ratio $\bar{\gamma}_{LO}/\gamma_0 = 10$, this range for both terms (*a* and *b*) covers almost the entire magnetic field range in which the polaron effect is pronounced. Actually, in this case, we have $\gamma_a/\gamma_{ra} = 1$ at $\lambda_{a1}/\Delta E = 1.24$ and $\gamma_b/\gamma_{rb} = 1$ at $\lambda_{b1}/\Delta E = -1.82$. In the vicinity of the points λ_{a1} and λ_{b1}, the absorption by the terms *a* and *b* reaches a maximum ($\mathcal{A} = 1/2$ and $\mathcal{R} = 1/4$ at a maximum). In the ranges $\lambda \gg \lambda_{a1}$ and $\lambda \ll \lambda_{b1}$, the polaron effect is of no significance. The second maxima in the curves $\mathcal{R}(\omega_l)$ and $\mathcal{A}(\omega_l)$ disappear. The results obtained are similar to those for the pair with the indices $n_e = n_h = 1$ and $l_e = l_h = l$ far from the polaron resonance. In this range, we have $\gamma_p/\gamma_{rp} \ll 1$ and the reflectance is larger than the absorptance.

In the other limiting case $\bar{\gamma}_{LO}/\gamma_0 = 0.1$ (curve *3*), the inequality $\gamma_p/\gamma_{rp} \ll 1$ is satisfied virtually over the entire range of the magnetophonon resonance. This range involves the resonance point $\lambda = 0$. The absorptance is appreciably less than the reflectance, which is as large as $\mathcal{R} = 1$ at the points of both maxima in the curve $\mathcal{R}(\omega_l)$. At $\lambda_{a3}/\Delta E = -1.24$ and $\lambda_{b3}/\Delta E = 1.68$, the radiative and nonradiative reciprocal lifetimes become equal to each other, which corresponds to the maximum absorptance. The term *a* does not interact with the light to the left of the point λ_{a3}, as judged from the very small values of γ_{ra}. The same holds true for the term *b* to the right of the point λ_{b3}. Curves *2* in Fig. 3 correspond to the intermediate case $\bar{\gamma}_{LO}/\gamma_0 = 1$. The maximum absorptance is observed at the resonance point $\lambda = 0$. For the term *a*, the condition $\gamma_a/\gamma_{ra} < 1$ is fulfilled at $\lambda > 0$ and the condition $\gamma_a/\gamma_{ra} > 1$ is met at $\lambda < 0$. The opposite situation occurs for the term *b*. The reflectance is predominant at $\gamma_p/\gamma_{rp} < 1$, and the absorptance is dominant at $\gamma_p/\gamma_{rp} > 1$.

The calculated dependences $\mathcal{R}(H)$ and $\mathcal{A}(H)$ in the vicinity of the magnetophonon resonance are displayed in Fig. 4. Curves *1*–*3* are constructed at three different frequencies ω_l with the use of the parameters for GaAs at the ratio $\bar{\gamma}_{LO}/\gamma_0 = 10$.

8. CONCLUSIONS

The main results obtained in the present work can be summarized as follows. The reflection and absorption of light by a quantum well was analyzed in the case of three-level electronic systems. The relationships for the dimensionless reflectance and absorptance were derived upon normal incidence of light on the quantum well plane. The calculations were performed with due regard for the radiative lifetimes of two excited levels in the electronic system. The radiative lifetime of the electron–hole pair in the quantum well in a strong magnetic field was calculated far from the magnetophonon resonance at an arbitrary wave vector $\mathbf{K}_\perp$ of the pair in the quantum well plane. The radiative lifetime of the system composed of a magnetopolaron and a hole in the valence band was determined. The expressions for the contributions associated with finite lifetimes of longitudinal optical phonons to the nonradiative lifetimes of the polaron states were deduced. It was found that the radiative and nonradiative lifetimes of the polarons very strongly depend on the magnetic field *H* in the vicinity of the magnetophonon resonance. The functions $\mathcal{A}(H)$ and $\mathcal{R}(H)$ were determined taking into account the magnetopolaron effect.

---

[6] In principle, the quantity γ_{rp} can be estimated from the line width of one-phonon scattering in bulk GaAs.

ACKNOWLEDGMENTS

We are grateful to V.M. Bañuelos for his cooperation and A. D'Amore for critical remarks.

This work was supported by the Russian Foundation for Basic Research (project no. 00-02-16904) and the International Scientific and Technical Program "Physics of Solid-State Nanostructures" (project no. 97-1099). S.T. Pavlov acknowledges the support and hospitality of Zacatecas University and the Consejo Nacional de Ciencia y Tecnologĭa (CONACyT). D.A. Contreras-Solorio acknowledges the support of the CONACyT (27736-E).

REFERENCES

1. E. J. Johnson and D. M. Larsen, Phys. Rev. Lett. **16** (15), 655 (1966).
2. A. Petrou and B. D. McCombe, in *Landau Level Spectroscopy*, Ed. by G. Landwer and E. I. Rashba (North-Holland, Amsterdam, 1991), Modern Problems in Condensed Matter Sciences, Vol. 27.2.
3. R. J. Nicholas, D. J. Barnes, D. R. Leadley, *et al.*, in *Spectroscopy of Semiconductors Microstructures*, Ed. by G. Fasol, A. Fasolino, and P. Lugli (Plenum, New York, 1990), NATO ASI Ser., Ser. B: Phys., Vol. 206, p. 451.
4. P. J. Nicholas, in *Handbook of Semiconductors*, Ed. by M. Balkanski (North-Holland, Amsterdam, 1994, 2nd ed.), Vol. 2.
5. L. I. Korovin and S. T. Pavlov, Zh. Éksp. Teor. Fiz. **53** (5), 1708 (1967) [Sov. Phys. JETP **26**, 979 (1968)]; Pis'ma Zh. Éksp. Teor. Fiz. **6** (2), 525 (1967) [JETP Lett. **6**, 50 (1967)].
6. L. I. Korovin, S. T. Pavlov, and B. É. Éshpulatov, Fiz. Tverd. Tela (Leningrad) **20** (12), 3594 (1978) [Sov. Phys. Solid State **20**, 2077 (1978)].
7. S. Das Sarma and I. Madhukar, Phys. Rev. B **22**, 2823 (1980).
8. S. Das Sarma, Phys. Rev. Lett. **53**, 859 (1984); **52**, 1570 (1984).
9. G. Q. Hai, T. M. Peeters, and J. T. Devreese, Phys. Rev. B **47** (16), 10358 (1993).
10. H. Fröhlich, Adv. Phys. **3** (2), 325 (1954).
11. L. I. Korovin and B. É. Éshpulatov, Fiz. Tverd. Tela (Leningrad) **21** (12), 3703 (1979) [Sov. Phys. Solid State **21**, 2137 (1979)].
12. L. C. Andreani, in *Confined Electrons and Photons*, Ed. by E. Burstein and C. Weisbuch (Plenum, New York, 1995), p. 57.
13. L. I. Korovin, I. G. Lang, and S. T. Pavlov, Pis'ma Zh. Éksp. Teor. Fiz. **65** (7), 511 (1997) [JETP Lett. **65**, 532 (1997)].
14. L. C. Andreani, F. Tassone, and F. Bassani, Solid State Commun. **77** (11), 641 (1991).
15. E. L. Ivchenko, Fiz. Tverd. Tela (Leningrad) **33** (8), 2388 (1991) [Sov. Phys. Solid State **33**, 1344 (1991)].
16. F. Tassone, F. Bassani, and L. C. Andreani, Phys. Rev. B **45** (11), 6023 (1992).
17. A. V. Kavokin, M. R. Vladimirova, L. C. Andreani, and G. Panzarini, in *Proceedings of the International Symposium "Nanostructures: Physics and Technology 97," Ioffe Physicotechnical Institute, Russian Academy of Sciences, St. Petersburg, 1997*, p. 31.
18. L. C. Andreani, G. Panzarini, A. V. Kavokin, and M. R. Vladimirova, Phys. Rev. B **57** (8), 4670 (1998).
19. L. I. Korovin, I. G. Lang, and S. T. Pavlov, Zh. Éksp. Teor. Fiz. **118** (2), 388 (2000) [JETP **91**, 338 (2000)].
20. I. V. Lerner and Yu. E. Lozovik, Zh. Éksp. Teor. Fiz. **78** (3), 1167 (1980) [Sov. Phys. JETP **51**, 588 (1980)].
21. A. Garsia-Cristobal, A. Cantarero, and C. Trallero-Giner, Phys. Rev. B **49**, 13430 (1994).
22. I. G. Lang, V. I. Belitsky, A. Cantarero, *et al.*, Phys. Rev. B **54** (24), 17768 (1996).
23. N. Mori and T. Ando, Phys. Rev. B **40** (9), 6175 (1989).
24. L. I. Korovin, I. G. Lang, and S. T. Pavlov, Zh. Éksp. Teor. Fiz. **115** (1), 187 (1999) [JETP **88**, 105 (1999)].
25. I. G. Lang, L. I. Korovin, A. Cantarero, and S. T. Pavlov, cond-mat/0001248.
26. D. A. Contreras-Solorio, S. T. Pavlov, L. I. Korovin, and I. G. Lang, Phys. Rev. B **62** (24), 16815 (2000); cond-mat/0002229.
27. I. G. Lang and V. I. Belitsky, Solid State Commun. **107** (10), 577 (1998).
28. I. G. Lang and V. I. Belitsky, Phys. Lett. A **245** (3–4), 329 (1998).
29. I. G. Lang, L. I. Korovin, D. A. Contreras-Solorio, and S. T. Pavlov, Fiz. Tverd. Tela (St. Petersburg) **43** (6), 1117 (2001) [Phys. Solid State **43**, 1159 (2001)]; cond-mat/0004178.
30. A. G. Zhilich and S. G. Monozon, *Magnetoabsorption and Electroabsorption of Light in Semiconductors* (Leningr. Gos. Univ., Leningrad, 1984), p. 204.
31. V. I. Belitsky, M. Cardona, I. G. Lang, and S. T. Pavlov, Phys. Rev. B **46** (24), 15767 (1992).
32. I. G. Lang, S. T. Pavlov, and A. V. Prokhorov, Zh. Éksp. Teor. Fiz. **106** (1), 244 (1994) [JETP **79**, 133 (1994)].
33. I. G. Lang, A. V. Prokhorov, V. I. Belitsky, *et al.*, J. Phys.: Condens. Matter **8**, 6769 (1996).

Translated by O. Borovik-Romanova

Physics of the Solid State, Vol. 44, No. 11, 2002, pp. 2196–2199. Translated from Fizika Tverdogo Tela, Vol. 44, No. 11, 2002, pp. 2097–2100.
Original Russian Text Copyright © 2002 by Meĭlanov, Abramova, Gadzhialiev, Dzhabrailov.

LOW-DIMENSIONAL SYSTEMS AND SURFACE PHYSICS

Specific Features of Chemisorption on a Size-Quantized Film in an External Quantizing Magnetic Field

R. P. Meĭlanov, B. A. Abramova, M. M. Gadzhialiev, and V. V. Dzhabrailov
Institute of Geothermal Problems, Dagestan Scientific Center, Russian Academy of Sciences,
pr. Kalinina 39a, Makhachkala, 367030 Russia
e-mail: lan_rus@dgu.ru

Received November 22, 2001; in final form, February 18, 2002

Abstract—The energy of an electron of an adatom chemisorbed on a size-quantized film is investigated as a function of the external quantizing magnetic field. Consideration is given to the cases when the external magnetic field is directed parallel and transverse to the film surface. It is demonstrated that, as the magnetic field increases, the energy of chemisorption jumpwise decreases. © *2002 MAIK “Nauka/Interperiodica”.*

1. The specific features of chemisorption on size-quantized films were investigated in [1–3]. It has been demonstrated that the chemisorption energy is an oscillating function of the film thickness due to specific features of the energy spectrum and the density of states of the electrons of a thin film. The chemical bonding between an atom and the surface of a crystal has been studied within the Anderson–Newns approach with the use of model Hamiltonians [4–6]. According to the Anderson–Newns model, the renormalized energy of an electron of an adatom can be represented by the relationship $E_{a,s} = \varepsilon_a + U\langle n_s\rangle$. Here, ε_a is the energy of an electron of an isolated atom; U is the potential of the intraatomic Coulomb repulsion; and $\langle n_s\rangle$ is the perturbation of the electron density of the atom due to the interaction with the substrate, which is determined by the expression $\langle n_s\rangle = \int_{-\infty}^{\infty} d\omega/\pi \overset{<}{g}_s(\omega)$, where $\overset{<}{g}_s$ is the correlation function of the electron of the adatom and s is the spin quantum number. The energy attenuation at the electron energy level of the adatom can be written in the form $\Delta \approx |V|^2\rho$, where $\rho(W)$ is the density of states of the electrons of the substrate (W is the conduction band width of the electrons of the film) and V is the potential of hybridization of the seed electron energy states of the adatom and the substrate.

At present, different versions of the Anderson–Newns method with the use of model Hamiltonians enjoy wide application. In particular, the charge exchange in the course of interaction of atomic particles with the surface of a crystal was investigated in the framework of a nonstationary model developed in [7–11]. The distribution of the electron density in a monoatomic adsorbed layer was examined in [12]. The derivation of quantum kinetic equations for a “crystal + adatom” system on the microscopic level and the generalization of the Anderson–Newns model within the Kadanoff–Baym formalism are presented in [13, 14].

In the present work, based on the results obtained in [14], we analyzed the influence of an external magnetic field on the energy of an electron of an adatom chemisorbed on a thin film. We considered two cases: (i) the external quantizing magnetic field is directed transversely to the film surface, and (ii) the external quantizing magnetic field is aligned parallel to the film surface.

2. The equations of motion for the Green's functions of an “adatom + thin film” electronic subsystem in the stationary case have the form [14]

$$\begin{gathered}
[\omega - \varepsilon_{\lambda s}(\omega)]\overset{<}{g}_{\lambda s,\lambda' s'}(\omega) - \sum_{\lambda'' s''}\{\overset{<}{\sigma}_{\lambda s,\lambda'' s'}(\omega) g^{A}_{\lambda'' s'',\lambda' s'}(\omega) \\
+ \sigma^{R}_{\lambda s,\lambda'' s''}(\omega)\overset{<}{g}_{\lambda'' s'',\lambda' s'}(\omega)\} = 0, \\
[\omega - \varepsilon_{\lambda s}(\omega)] g^{R,A}_{\lambda s,\lambda' s'}(\omega) \\
- \sum_{\lambda'' s''}\{\sigma^{R,A}_{\lambda s,\lambda'' s''}(\omega) g^{R,A}_{\lambda'' s'',\lambda' s'}(\omega)\} = \delta_{\lambda\lambda'}\delta_{ss'}.
\end{gathered} \tag{1}$$

Here, λ stands for the quantum numbers characterizing the motion of electrons of an adatom, $\varepsilon_{\lambda,s}(\omega)$ is the energy of the adatom, $\overset{<}{g}_s$ is the correlation function of an electron of the adatom, $g^{R,A}$ are the retarded and advanced Green's functions of the electron of the adatom, $\sigma^{R,A}$ are the corresponding mass operators, and $\overset{<}{\sigma}$ is the generalized collision integral. The mass operator consists of two parts: $\sigma^{R,A} = \sigma_0^{R,A} + \sigma_a^{R,A}$, where σ_0 is the mass operator of an isolated atom and σ_a is the contribution to the mass operator of the electron of the adatom due to the interaction with a thin film. This contribution has the form

$$\overset{<}{\sigma}{}^{(R,A)}_{a,\lambda s,\lambda' s'}(\omega) = \sum_{\substack{i\mathbf{k}s''\\ i'\mathbf{k}'s'''}} V_{\lambda s,\, i\mathbf{k}s''}(\omega)\overset{<}{G}{}^{(R,A)}_{i\mathbf{k}s'';\, i'\mathbf{k}'s'''}(\omega)V_{i'\mathbf{k}'s''',\, \lambda' s'}(\omega), \qquad (2)$$

where G is the Green's function of an electron of the film and i, $\mathbf{k}$ is the set of quantum numbers describing the motion of the electron in the film.

The equations of motion for the Green's function of an electron of the film are similar to Eqs. (1) and (2) with appropriate substitution for the set of quantum numbers describing the motion of the electron.

The system of equations (1) and (2), together with the equations of motion for the Green's functions of the electrons of the film, describes the general case with allowance made for all possible interactions of adatoms with one another and with the substrate. Let us consider the case when the interaction between adatoms is absent. Moreover, we assume that an adatom has a single energy level (in what follows, we will drop the index λ). The correlation function of an electron of the adatom, according to relationships (1), takes the following form (we assume that σ_0 is taken into account in the determination of the energy of the electron of the atom in the absence of the interaction with the film):

$$\overset{<}{g}_s(\omega) = g^R_s(\omega)\overset{<}{\sigma}_{a,s}(\omega)g^A_s(\omega). \qquad (3)$$

Under the assumption that the hybridization potential is constant, it can easily be shown that $\overset{<}{\sigma}(\omega)$ satisfies the following expression:

$$\overset{<}{\sigma}_{a,s}(\omega) = |V|^2\sum_{i\mathbf{k}}\overset{<}{G}_{i\mathbf{k}s}(\omega). \qquad (4)$$

For the correlation function of the electron of the film, we obtain

$$\overset{<}{G}_{i\mathbf{k}s}(\omega) = f(\omega)A_{i\mathbf{k}s}(\omega), \qquad (5)$$

where $f(\omega)$ is the Fermi–Dirac distribution function and $A_{i\mathbf{k}s}$ is the spectral function,

$$A_{i\mathbf{k}s}(\omega) = \frac{\Gamma_{i\mathbf{k}s}(\omega)}{(\omega - \varepsilon_{i\mathbf{k}s}(\omega) - \mathrm{Re}\Sigma_{i\mathbf{k}s}(\omega))^2 + \Gamma^2_{i\mathbf{k}s}(\omega)}.$$

Here, Γ is the attenuation of single-particle states and $\mathrm{Re}\Sigma$ is the renormalization of single-particle states due to the interaction (the Coulomb and crystal potentials). The self-consistent energy of the electrons of the substrate can be determined according to the expression

$$E_{i\mathbf{k}s} = \varepsilon_{i\mathbf{k}s}(\omega = E_{i\mathbf{k}s}) + \mathrm{Re}\Sigma_{i\mathbf{k}s}(\omega = E_{i\mathbf{k}s}).$$

Then, we obtain the expression for the spectral function:

$$A_{i\mathbf{k}s}(\omega) = z_{i\mathbf{k}s}\frac{\Gamma_{i\mathbf{k}s}(\omega)}{(\omega - E_{i\mathbf{k}s})^2 + z^2_{i\mathbf{k}s}\Gamma^2_{i\mathbf{k}s}(\omega)}, \qquad (6)$$

where

$$z^{-1}_{i\mathbf{k}s} = 1 - \frac{\partial}{\partial\omega}(\varepsilon_{i\mathbf{k}s}(\omega) + \mathrm{Re}\Sigma_{i\mathbf{k}s}(\omega))_{\omega = E_{i\mathbf{k}s}}$$

is the renormalization constant. From expressions (1)–(6), we obtain the correlation function of the electron of the adatom in the following form:

$$\overset{<}{g}_s(\omega) = |V|^2 f(\omega)a_s(\omega), \qquad (7)$$

where the spectral function of the electron of the adatom has the form

$$a_s(\omega) = \frac{\sum_{i\mathbf{k}}A_{i\mathbf{k}s}(\omega)}{[\omega - \varepsilon_{as}(\omega) - \Lambda_{as}(\omega)]^2 + |V|^4\left(\sum_{i\mathbf{k}}A_{i\mathbf{k}s}(\omega)\right)^2}. \qquad (8)$$

Here,

$$\Lambda_{as}(\omega) = |V|^2\sum_{i\mathbf{k}}\frac{\omega - \varepsilon_{i\mathbf{k}s}(\omega) - \mathrm{Re}\Sigma_{i\mathbf{k}s}(\omega)}{(\omega - \varepsilon_{i\mathbf{k}s}(\omega) - \mathrm{Re}\Sigma_{i\mathbf{k}s}(\omega))^2 + \Gamma^2_{i\mathbf{k}s}(\omega)}.$$

When analyzing the expressions for the electron energy of the adatom, the self-consistent energy is introduced according to the definition $E_{as} = (\varepsilon_{as}(\omega) + \Lambda_{as}(\omega))|_{\omega = E_{as}}$, which, in turn, can be parametrized in the usual manner: $E_{as} = \varepsilon_a + U\langle n_{-s}\rangle$.

Further consideration depends on the concrete expression for the electronic spectrum of the thin film. This problem is considered in [1–3] in the absence of an external magnetic field. Here, we analyze the case when an external magnetic field is present.

3. Let us consider the case when the external magnetic field is directed parallel to the film surface. The OZ axis is perpendicular to the film surface. The magnetic field is assumed to be such that the magnetic length $l_B = (h/eB)^{-1/2}$ (h is the Planck constant, e is the elementary charge, and B is the magnetic field induction) is of the same order of magnitude as the film thickness L. Under the assumption that the film potential can be approximated by the expression $V(z) = m\omega_0^2 z^2/2$, we

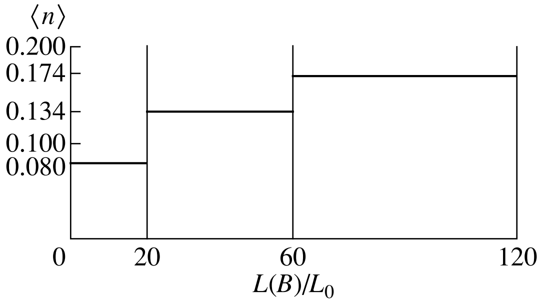

Fig. 1. Dependence of ⟨*n*⟩ on the dimensionless thickness $L(B)/L_0$ of the film in a constant magnetic field. $B = 4 \times 10^3$ T, $L_0 = 10^{-7}$ cm.

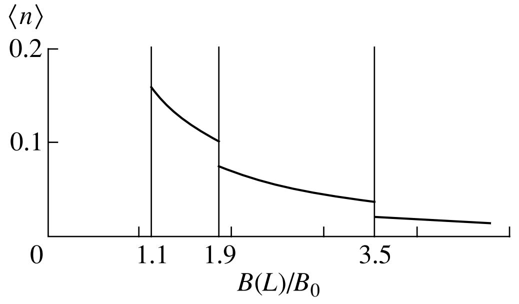

Fig. 2. Dependence of ⟨*n*⟩ on the dimensionless magnetic field $B(L)/B_0$ at a constant thickness *L* of the film. $B_0 = 4 \times 10^3$ T, $L = 25L_0$, $L_0 = 10^{-7}$ cm.

can exactly solve the Schrödinger equation and obtain the following expression for the electron energy:

$$E_{p_x,\,p_y,\,n,\,\sigma} = \frac{p_x^2}{2m} + \frac{\omega_0^2}{\tilde{\omega}^2}\frac{p_y^2}{2m} + \tilde{\omega}\left(n + \frac{1}{2}\right),$$

where $\tilde{\omega} = (\omega_c^2 + \omega_0^2)^{1/2}$ and $n = 0, 1, 2, \ldots$ ($\omega_c = eB/m$ is the cyclotron frequency).

Consequently, the spectral function takes the form

$$A_\sigma(\omega) = \frac{z_\Pi m L_x L_y}{\pi h}\frac{\tilde{\omega}}{\omega_0}\sum_{n=1}^{n_F}\left\{\arctan\left(\frac{\omega - \tilde{\omega}\left(n + \frac{1}{2}\right)}{z_\Pi \Gamma_s}\right) + \frac{\pi}{2}\right\},$$

$$z_\Pi \equiv z_{i\mathbf{k}s}.$$

Finally, in the approximation $\Gamma_s \longrightarrow 0$, $\langle n_s \rangle$ can be represented by the following expression:

$$\langle n_s \rangle = \frac{z_a}{\pi}\sum_{n=1}^{n_F}\left[\arctan\left(\frac{\tilde{\omega}\left(n + \frac{3}{2}\right) - \varepsilon_a - U\langle n_{-s}\rangle}{n\rho_\parallel}\right) - \arctan\left(\frac{\tilde{\omega}\left(n + \frac{1}{2}\right) - \varepsilon_a - U\langle n_{-s}\rangle}{n\rho_\parallel}\right)\right], \qquad (9)$$

where

$$\rho_\parallel = z_a z_\Pi |V|^2 \frac{\tilde{\omega}}{\omega_0}\frac{mL_xL_y}{\hbar^2},$$

$$z_a^{-1} = 1 - [\varepsilon_{as}(\omega) + \Lambda_{as}(\omega)]_{\omega = E_{as}}$$

is the renormalization constant of the adatom, and n_F is the number of discrete energy states below the Fermi level.

For numerical calculations, it is necessary to establish a relationship between the chemical potential, the film thickness, and the magnetic field. Within the above approximation ($\Gamma_s \longrightarrow 0$), the number of electrons in the film can be determined from the expression

$$N = \frac{mL_xL_y}{\pi h^2}\frac{\tilde{\omega}}{\omega_0}(n_F + 1)\left[\mu - \frac{\tilde{\omega}}{2}(n_F + 1)\right], \qquad (10)$$

where μ is the chemical potential. The condition of filling of the *n*th discrete state has the form $\mu(n) = \tilde{\omega}(n + 1/2)$. From expression (10), we determine the chemical potential μ and, then, obtain the following condition:

$$\tilde{\omega}^2 = \frac{2\pi h^2 N}{mL_xL_y}\frac{\omega_0}{n(n+1)}. \qquad (11)$$

According to formula (11), we can determine the film thickness L_n at which the *n*th energy level is filled in a constant magnetic field *B*: $L_n(B) = L_0(1 + B^2/B_0^2)n(n + 1)$, where $L_0 = (N/V_0)^{-1/3}$, V_0 is the volume of the system, and $B_0 = 2\pi h/eL_0^2 = 4.12 \times 10^3$ T. It is assumed that $\omega_0 = 2\pi h/mL_0^2$. In the case when the film thickness *L* is constant, the magnetic field B_n corresponding to filling of the *n*th energy level is determined by the relationship $B_n^2(L)/B_0^2 + 1 = (L/L_0)/n(n + 1)$. As the film thickness increases and becomes equal to L_n the number of discrete states below the Fermi level also increases and reaches *n*. The reverse situation is observed with an increase in the magnetic field: when the magnetic field reaches B_n, the number of filled discrete energy states decreases by unity.

Figure 1 presents the results of the numerical calculation of $\langle n_s \rangle$ as a function of the film thickness in a constant magnetic field. It is evident that the value of $\langle n_s \rangle$ remains constant until the next discrete energy level is filled. This is due to the approximation used for the film potential. Upon filling of the next energy level, $\langle n_s \rangle$ jumpwise increases, thus exhibiting an oscillating dependence on the film thickness; consequently, there appears an oscillating dependence of the chemisorption energy of an adatom on the film thickness. Figure 2 depicts the dependence of $\langle n_s \rangle$ on the magnetic field at a specified thickness of the film. It can be seen that, as the magnetic field increases, the value of $\langle n_s \rangle$ continuously decreases and jumps when the number of filled discrete energy levels decreases. Thus, an increase in the quantizing magnetic field is accompanied by a decrease in the chemisorption energy.

4. Let us now consider the case when the magnetic field is directed transversely to the film surface. The energy spectrum is totally quantized and has the form $E_{ni} = \omega_c\left(n + \frac{1}{2}\right) + \varepsilon_i$. Here, ε_i is the energy corresponding to the motion of an electron across the film. The spectral function of the adatom electron has the form

$$a_s(\omega) = |V|^2 \rho_\perp \times \sum_{n,\, i} \frac{\delta\left(\omega - \omega_c\left(n + \frac{1}{2}\right) - \varepsilon_i\right)}{(\omega - E_a)^2 + \left|V^4\right| \rho_\perp^2 \left[\sum_{n'i'} \frac{\Gamma_{n,\, i}}{\left(\omega - \omega_c\left(n + \frac{1}{2}\right) - \varepsilon_i\right)^2 + \Gamma^2_{n',\, i'}}\right]^2}.$$

Here, $\rho_\perp = z_a z_\Pi \frac{m\omega_c L_x L_y}{2\hbar\pi}$.

In this case, $\langle n_s \rangle$ takes the following form:

$$\langle n_s \rangle = |V|^2 z_a \rho_\perp \sum_{n,\, i}^{n_\mathrm{F}} \left\{ \left[\omega_c\left(n + \frac{1}{2}\right) + \varepsilon_i - \varepsilon_a - U\langle n_{-\sigma}\rangle\right]^2 + |V|^2 \rho_\perp^2 \frac{|V|^2}{\Gamma^2_{n,\, i}} \right\}^{-1}. \quad (12)$$

When deriving expression (12), we disregarded the quantities of the order of magnitude $\approx(\Gamma_{n,\, i}/\omega_c)^2 \ll 1$. The calculations demonstrate that, qualitatively, the dependences of $\langle n_s \rangle$ on the film thickness and the magnetic field, in this case, remain unchanged.

5. The experimental observation of the aforementioned effects under changes in the external magnetic field and film thickness will make it possible to determine the specific features of the energy characteristics of an adatom and the electronic subsystem of the film. The decrease in the energy of interaction between the adatom and the substrate in an external magnetic field is of interest from the viewpoint of controlled changes in the surface properties of thin films. The condition of observation of oscillations in a magnetic field has the form $\tilde{\omega} \gg T, h/\tau$ (T is the absolute temperature and τ is the relaxation time). Note that this condition is less stringent than that for bulk samples: $\omega_c \gg T, h/\tau$.

REFERENCES

1. R. P. Meĭlanov, Fiz. Tverd. Tela (Leningrad) **31** (7), 270 (1989) [Sov. Phys. Solid State **31**, 1254 (1989)].
2. R. P. Meĭlanov, Fiz. Tverd. Tela (Leningrad) **32** (9), 2839 (1990) [Sov. Phys. Solid State **32**, 1649 (1990)].
3. R. P. Meĭlanov, Poverkhnost, No. 3, 52 (1999).
4. P. W. Anderson, Phys. Rev. **124** (1), 419 (1961).
5. D. M. Newns, Phys. Rev. **178** (3), 1123 (1969).
6. T. L. Einstein, J. A. Hertz, and J. R. Schrieffer, in *Theory of Chemisorption*, Ed. by J. R. Smith (Springer-Verlag, Berlin, 1980; Mir, Moscow, 1983).
7. Y. Muda and D. M. Newns, Phys. Rev. B **37** (12), 7048 (1988).
8. D. C. Langreth and P. Nordlander, Phys. Rev. B **43** (4), 2541 (1991).
9. H. Shao, D. C. Langreth, and P. Nordlander, Phys. Rev. B **49** (19), 13929 (1994).
10. M. Yu. Gusev, D. V. Klushin, S. V. Shavrov, and I. F. Urazgil'din, Zh. Éksp. Teor. Fiz. **109** (2), 562 (1996) [JETP **82**, 299 (1996)].
11. S. Yu. Davydov, Fiz. Tverd. Tela (St. Petersburg) **42** (7), 1331 (2000) [Phys. Solid State **42**, 1370 (2000)].
12. S. Yu. Davydov, Fiz. Tverd. Tela (St. Petersburg) **41** (9), 1543 (1999) [Phys. Solid State **41**, 1413 (1999)].
13. R. P. Meĭlanov, Poverkhnost, No. 12, 28 (1990).
14. R. P. Meĭlanov, Poverkhnost, No. 6, 37 (1994).

Translated by O. Moskalev

Physics of the Solid State, Vol. 44, No. 11, 2002, pp. 2200–2203. Translated from Fizika Tverdogo Tela, Vol. 44, No. 11, 2002, pp. 2101–2105.
Original Russian Text Copyright © 2002 by Makarov, Sherman.

Low-Frequency Dispersion of the Negative Dielectric Permittivity in C_{70} Films

V. V. Makarov and A. B. Sherman

Ioffe Physicotechnical Institute, Russian Academy of Sciences, Politekhnicheskaya ul. 26, St. Petersburg, 194021 Russia
e-mail: mak@pop.ioffe.rssi.ru

Received November 2, 2001

Abstract—Measurements performed at frequencies of 0.1–10 kHz on films of C_{70} fullerite revealed a negative dielectric permittivity $\varepsilon' < -1000$. The largest drop in ε' occurred in the temperature interval 170–270 K and was accompanied by frequency dispersion. The negative sign of the dielectric permittivity and its low-frequency dispersion are accounted for by the Lorentz correction to the local field acting on the conduction electrons. This correction originates from the polarization of the electrons bound to impurity centers. *© 2002 MAIK "Nauka/Interperiodica".*

1. INTRODUCTION

C_{70} fullerite is a semiconductor with a band gap of 1.7–1.8 eV [1, 2]. Thermopower measurements made after heat treatment at 200°C in vacuum showed C_{70} films to have *n*-type conduction [1]. The nature of the donor centers remains unclear. The electrical conductivity σ and its activation energy E depend strongly on the oxygen content in the C_{70} samples. Exposure to air leads to an increase in E from 0.52 to 0.71 eV and a decrease in σ at room temperature from 10^{-9} to $10^{-12}\ \Omega^{-1}\ \text{cm}^{-1}$ [2]. This suggests that oxygen creates compensation centers in C_{70} which capture electrons from the donor centers and, thus, lower the Fermi level.

The low-frequency dielectric permittivity ε' of C_{70} measured at low temperatures has a constant positive value of about 4; above 300 K, this permittivity increases to 20, which is accompanied by frequency dispersion [3]. This growth is believed [3] to be caused by the intrinsic dipole relaxation of C_{70}. Moreover, a weak anomaly of ε' was observed near 300 K, which has been associated [3] with a structural phase transition. The effect of oxygen on the dielectric permittivity of C_{70} has not been studied. That this effect may be quite strong is shown by measurements performed on samples of C_{60} fullerite, which is close in electrical properties to C_{70}. For instance, ε' of C_{60} measured at 100 Hz can vary by up to a factor of five depending on the exposure time in air at room temperature [4]. Here, we also note that all of the above data were obtained on samples that were subjected to ambient air after their preparation. At the same time, annealing in vacuum was shown not to restore completely the properties of samples that underwent oxidation [5]. This is particularly valid in the case of C_{70}, where this is believed [2] to be the reason why no one has succeeded in reaching values of E less than 0.5 eV, whereas in C_{60}, $E = 0.2$ eV was achieved by vacuum annealing. Therefore, the only way in which one can study a fullerite with a low oxygen concentration lies in making measurements immediately after the preparation of a sample, without taking it out of the vacuum chamber (i.e., *in situ*). Indeed, the measurements of the conductivity of C_{60} carried out in this way showed E to be less by about one half and σ to be higher by several orders of magnitude in comparison with the results obtained after exposure to air [5]. We have not succeeded in finding any mention on *in situ* measurements of ε' in fullerites or of σ in C_{70}.

The purpose of this study was to investigate the dielectric permittivity and electrical conductivity of C_{70} fullerite films that were not subjected to ambient air. The low-frequency (0.1–10 kHz) measurements performed in this investigation revealed frequency-dependent negative dielectric permittivity (Fig. 1a).

2. EXPERIMENT

The films used in our experiment were prepared in vacuum at 10^{-5} Torr. The measurements were conducted *in situ* in the vacuum chamber immediately after deposition of C_{70} on a mica substrate. The 99%-pure C_{70} powder was produced by the company MER. The characteristic sublimation temperature was 750 K. Prior to this deposition, planar interdigitated electrodes were deposited on the substrate. The substrate temperature during the film deposition was 470 K. X-ray structural characterization performed at 300 K showed that the films were single phase and had an hcp structure and cell parameters $a = 10.593$ Å and $c = 17.262$ Å. The ac electric field strength between the electrodes was 20 V/cm. The measurements were carried out in the temperature region 100–500 K with a rate of temperature variation of 2 K/min.

The dielectric permittivity ε' and the electrical conductivity σ of the film were calculated using the technique proposed in [6]. The film capacitance was found by subtracting the capacitance of the substrate (measured before the film deposition) from the total capacitance measured after the deposition.

As already mentioned, the most interesting finding made in the measurements was the discovery of a high negative dielectric permittivity and of its frequency dispersion in the low-frequency range (Fig. 1a). At low temperatures, ε' is positive, but as the temperature is increased, a fast drop in ε' is observed, accompanied by a reversal of its sign and frequency dispersion. As the temperature is increased further, ε' saturates and the dispersion disappears. In this stage, ε' becomes less than -10^3.

The temperature and frequency dependences of σ of the C_{70} film (Fig. 1b) exhibit a typically semiconductor character. At low temperatures, σ is only weakly temperature-dependent and grows proportionally to $\omega^{0.9}$ (ω is the circular frequency): $\sigma_{LT} = 9 \times 10^{-10}\omega^{0.9}$. This behavior of σ is characteristic of impurity conduction [7]. In the high-temperature domain, σ is frequency-independent and, hence, coincides with the dc conductivity σ_c: $\sigma_{HT} = \sigma_c = e_0^2 n\tau_e/m^*$, where e_0 is the electronic charge, τ_e is the electron mean free time, and m^* is the effective electron mass. The conduction electron concentration n in the free-electron model for parabolic bands is given by the relation $n = (1/4)\pi^{-1.5}(2\hbar^{-2}m^*kT)^{3/2}\exp(-E/kT)$, where E is the activation energy, which, as derived from the slope of the $\log\sigma(1000/T)$ plot, is 0.33 eV. The room-temperature conductivity is 1.5×10^{-2} S/m. Thus, E measured *in situ* in films is indeed substantially smaller than E measured [2] after exposure to air and the conductivity is several orders of magnitude higher. The total electrical conductivity is the sum $\sigma = \sigma_{LT} + \sigma_{HT}$.

Now, one can find the temperature dependence of the mean free time. This quantity was found to scale with temperature as $\tau_e = 2.88 \times 10^{-13}T^{-3/2}$. Such a dependence is typical of electron scattering from optical phonons.

The oxidation of films substantially affects the magnitude and sign of their dielectric permittivity and the character of its temperature dependence. Figure 2 displays temperature dependences of the dielectric permittivity of a film measured after its exposure to air at different pressures for 12 h. As the air pressure in the chamber increases, ε' of the film decreases in absolute value. After air is admitted to atmospheric pressure, ε' becomes positive, as was observed earlier with the C_{70} fullerite acted upon by air [3].

As the film undergoes oxidation, its high-temperature conductivity decreases and the activation energy increases. As a result, the boundary of high-temperature conductivity shifts toward higher temperatures.

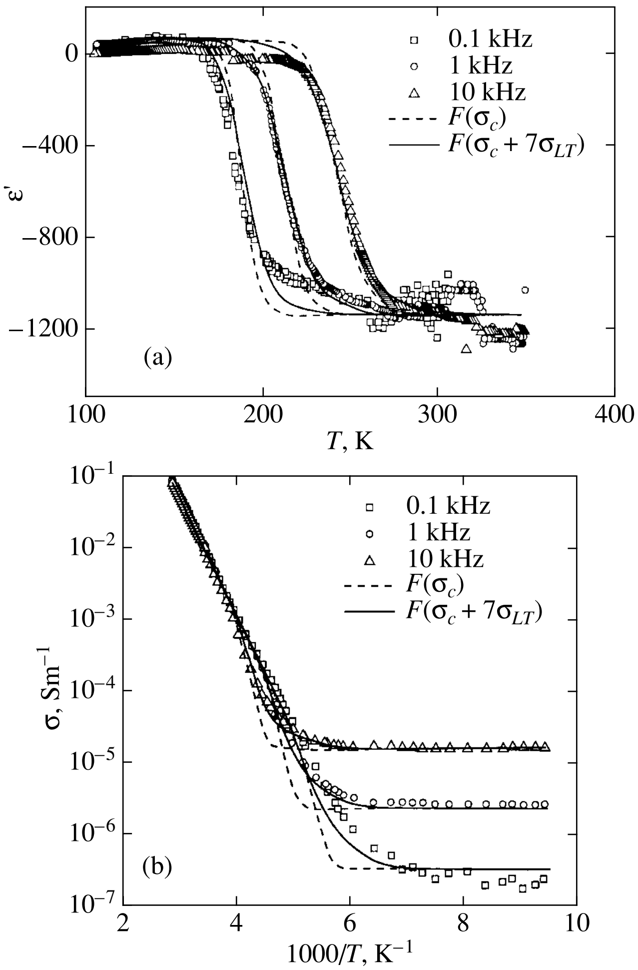

Fig. 1. (a) Dielectric permittivity ε' and (b) electrical conductivity σ of a C_{70} film measured at the three frequencies specified in the graphs. The lines are plots of the calculations made for different dependences of the Lorentz factor F on conductivity.

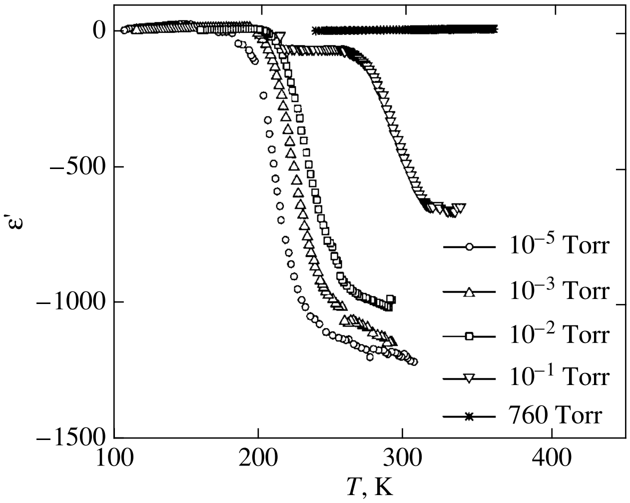

Fig. 2. Dielectric permittivity ε' of a C_{70} film measured at 1 kHz after its successive exposure to air at different pressures.

3. DISCUSSION

Let us consider the conditions conducive to the onset of a negative dielectric permittivity. The relative complex dielectric permittivity ε^* is given by the Drude–Lorentz relation

$$\varepsilon^* = \varepsilon_\infty + \frac{Ne^2/(\varepsilon_0 m)}{\omega_0^2 - \omega_F^2 - \omega^2 + i\omega/\tau}, \tag{1}$$

where ε_∞ is the relative dielectric permittivity for $\omega \longrightarrow \infty$, N is the concentration of charge carriers contributing to $\varepsilon^* - \varepsilon_\infty$, e is the charge of a carrier, m is the carrier mass, ε_0 is the absolute dielectric permittivity of vacuum, ω_0 is the circular resonance frequency characterizing the elastic restoring force, and τ is the relaxation (decay) time. The term $\omega_F^2 = Fe^2N/(\varepsilon_0 m)$ is the Lorentz correction characterizing the local field enhancement caused by charge polarization; F is the Lorentz factor depending on the symmetry of the local environment and the extent of carrier wave function localization. For localized charges in the case of local spherical symmetry, we have $F = 1/3$, and for free electrons, we have $F = 0$, i.e., $\omega_F = 0$ [8].

Equation (1) permits one to find the real part of dielectric permittivity ε' and the electrical conductivity $\sigma = \varepsilon''\varepsilon_0\omega$, where ε'' is the imaginary part of ε^*:

$$\varepsilon' = \varepsilon_\infty + \frac{e^2N}{\varepsilon_0 m}\frac{\omega_{\text{eff}}^2}{\omega_{\text{eff}}^4 + \omega^2/\tau^2}, \tag{2a}$$

$$\sigma = \frac{e^2N}{m\tau}\frac{\omega^2}{\omega_{\text{eff}}^4 + \omega^2/\tau^2}, \tag{2b}$$

where $\omega_{\text{eff}}^2 = \omega_0^2 - \omega_F^2 - \omega^2$. The necessary condition for the onset of negative ε' is given by the inequality $\omega^2 > \omega_0^2 - \omega_F^2$.

Let us see how this condition can be satisfied in our experiment.

As follows from a comparison of the $\varepsilon'(T)$ and $\sigma(T)$ plots (Fig. 1), within the temperature region where one observes the largest drop and dispersion of ε', σ is determined primarily by the conduction electrons. This suggests that the behavior of ε' is likewise related to the inertia of free electrons. In this case, the quantities e, N, m, and τ in Eqs. (2) should be replaced by the corresponding quantities for the conduction electrons, i.e., e_0, n, m^*, and τ_e. At high temperatures, where one can neglect ε_∞, Eqs. (2a) and (2b) yield

$$\frac{\varepsilon'\varepsilon_0}{\sigma_{HT}} = \tau_e\frac{\omega_{\text{eff}}^2}{\omega^2}. \tag{3}$$

In the case of free electrons, as already mentioned, ω_0 and ω_F are zero and $\omega_{\text{eff}}^2 = -\omega^2$. Then, as follows from Eq. (3), $-\varepsilon'$ and σ_{HT} should depend on temperature in approximately the same way and be frequency-independent. Because, as follows from experiment, this is not the case, we assume that $\omega_F \neq 0$. In view of the fact that the effect of the Lorentz correction on ε' becomes significant for $\omega_F^2 > \omega^2$, we replace ω_{eff} with ω_F; in this case, we find the following expression relating ε' to σ:

$$\varepsilon' = -\frac{F}{\varepsilon_0^2}\frac{\sigma_c\sigma_{HT}}{\omega^2}. \tag{4}$$

As pointed out earlier, at high temperatures, we have $\sigma_{HT} = \sigma_c$. Therefore, Eq. (4) takes the form

$$\varepsilon'_{HT} = -\frac{F\sigma_c^2}{\varepsilon_0^2\omega^2} = -(\varepsilon''_c)^2F. \tag{5}$$

As follows from Eq. (2b), for the equality $\sigma_{HT} = \sigma_c$ to hold, the condition $\omega_F^2 \ll \omega/\tau$ should be satisfied; this inequality can be recast in the form

$$\varepsilon''_c \ll 1/F. \tag{6}$$

This condition imposes certain constraints on the choice of the F factor.

In the region of ε' saturation (the high-temperature domain), according to Eq. (5), the following relation should be valid:

$$F = F_0(1/\varepsilon''_c)^2, \tag{7}$$

where $F_0 = \text{const}$ and we have $\varepsilon' = -F_0$. A comparison with experiment shows that $F_0 = 1.2 \times 10^3$.

As the temperature decreases, ε''_c drops; therefore, the product $F\varepsilon''_c \sim 1/\varepsilon''_c$ increases and condition (6) fails, to be replaced by the inverse inequality $\varepsilon''_c \gg 1/F$ (Fig. 3). The expression for ε' assumes the form $\varepsilon' = -(\varepsilon''_c)^2/F_0$; i.e., ε' depends on frequency, and its absolute value drops with decreasing temperature. The calculated values of ε' in the region of dispersion almost coincide with the experimental figures (Fig. 1a). Simultaneously, the relation $\sigma_{HT} = \sigma_c$ transforms to $\sigma_{HT} = \sigma_c^3/(\varepsilon_0\omega F_0)^2$, and as the temperature decreases, the calculated $\log\sigma\,(1000/T)$ plots deviate from a straight line toward smaller values, i.e., have a negative curvature. Negative curvature is indeed observed in the experimental plots. It is particularly pronounced below 250 K in the graph constructed for 10 kHz (Fig. 1b). The lesser curvature of the experimental graphs in comparison with that of the plots of Eq. (7) suggests that in actual fact F grows more slowly than proportional to $(1/\varepsilon''_c)^2$.

That the growth of F with decreasing temperature must be limited is obvious, because the Lorentz factor can in no case be larger than unity. The constraint on the values of F will appear in a natural way with decreasing

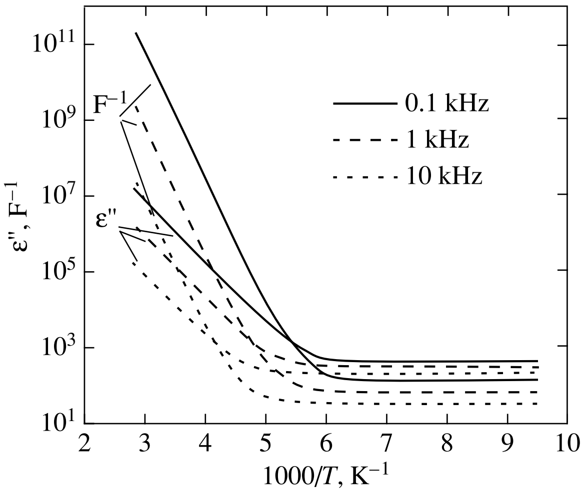

Fig. 3. Temperature behavior of ε" and of the Lorentz factor *F*.

temperature if we replace ε''_c in Eq. (7) with ε", i.e., if we replace the high-temperature conductivity $\sigma_{HT} = \sigma_c$ by the total conductivity $\sigma = \sigma_c + \sigma_{LT}$. In this case, as one approaches the region of impurity conduction, the growth of *F* will slow, subsequently stopping altogether.

The replacement of σ_c by σ does indeed reduce the negative curvature somewhat, but this decrease is obviously too small to reconcile the results with experiment. To enhance the effect of the termσ_{LT}, we multiply it by a coefficient $k > 1$:

$$F = F_0(\varepsilon_0\omega)^2/(\sigma_c + k\sigma_{LT})^2. \qquad (8)$$

The best fit of the experimental curves with the calculations is obtained for $k = 7$ (Fig. 1b). At the same time, the agreement of the calculated with experimental curves for ε' is also improved (Fig. 1a). All this means that in reality the effect of impurity conductivity on the Lorentz factor in the transition region is considerably stronger than in the case when only the contribution of the impurity conductivity to the total conductivity is taken into account.

4. CONCLUSION

Thus, the temperature and frequency dependences of the negative dielectric permittivity of C_{70} and of the conductivity are fitted very well by the Drude–Lorentz model, which assumes the conduction electrons to be charge carriers. These electrons cannot, however, be considered as completely free and, in order to correctly describe the results of an experiment, one should introduce the Lorentz correction. At low temperatures, the value of the Lorentz factor is determined by the impurity conductivity, which drops with increasing temperature because of the increasing conductivity in the conduction band. In the temperature region where negative permittivity is observed, the Lorentz factor is negligible, 10^{-2}–10^{-11} (Fig. 3).

Oxidation of a sample reduces the absolute value of ε' and, hence, the coefficient F_0. Simultaneously, the conductivity activation energy increases and the conductivity itself decreases. This means that oxygen creates in C_{70} compensating impurity centers capturing electrons from the donors, a circumstance which lowers the Fermi level and increases the electron activation energy. Thus, the decrease in F_0 observed during C_{70} oxidation correlates with the decrease in the electron concentration at the donor centers. One may, therefore, expect that it is the polarization of these electrons that is responsible for the weak polarization of the conduction electrons and for the Lorentz correction.

As C_{70} is oxidized still further, the positive lattice permittivity begins to dominate and the total dielectric permittivity becomes positive. This provides an answer to the question of why negative ε' was not observed in [3], where well-oxidized C_{70} fullerite samples were measured. In the present study, the dielectric permittivity of fullerites was measured for the first time on nonoxidized samples (*in situ*).

ACKNOWLEDGMENTS

The authors are indebted to N.F. Kartenko for the x-ray characterization of the films, to Yu.A. Stotskiĭ for upgrading the experimental equipment, and to V.V. Lemanov for useful discussions.

The support of the Russian State Program “Fullerenes and Atomic Clusters” (project no. 3-2-98) and program “Low-Dimensional Quantum Structures” of the Presidium of the Russian Academy of Sciences is gratefully acknowledged.

REFERENCES

1. D. Han, H. Habuchi, and S. Nitta, Phys. Rev. B **57** (7), 3773 (1998).
2. H. Habuchi, S. Nitta, D. Han, and S. Nanomura, J. Appl. Phys. **87** (12), 8580 (2000).
3. P. Mondal, P. Lunkenheimer, and A. Loidl, Z. Phys. B **99**, 527 (1996).
4. B. Pevzner, A. F. Hebard, and M. S. Dresselhaus, Phys. Rev. B **55** (24), 16439 (1997).
5. T. Asakava, M. Sasaki, T. Shiraishi, and H. Koinuma, Jpn. J. Appl. Phys. **34** (4), 1958 (1995).
6. O. G. Vendik, S. P. Zubko, and M. A. Nikolskiĭ, Zh. Tekh. Fiz. **69** (4), 1 (1999) [Tech. Phys. **44**, 349 (1999)].
7. M. Pollak and T. H. Geballe, Phys. Rev. **122** (6), 1742 (1961).
8. J. C. Slater, *Quantum Theory of Molecules and Solids*, Vol. 3: *Insulators, Semiconductors, and Metals* (McGraw-Hill, New York, 1967; Mir, Moscow, 1969).

Translated by G. Skrebtsov

Physics of the Solid State, Vol. 44, No. 11, 2002, pp. 2204–2209. Translated from Fizika Tverdogo Tela, Vol. 44, No. 11, 2002, pp. 2106–2111.
Original Russian Text Copyright © 2002 by Razbirin, Starukhin, Chugreev, Zgoda, Smirnov, Grushko, Kolesnik, Coheur, Liévin, Colin.

Absorption Line Spectrum of the $C_{60}Cl_{24}$ Halofullerene

B. S. Razbirin*, A. N. Starukhin*, A. V. Chugreev*, A. S. Zgoda*, V. P. Smirnov,
Yu. S. Grushko***, S. G. Kolesnik***, P.-F. Coheur****,
J. Liévin****, and R. Colin******

** Ioffe Physicotechnical Institute, Russian Academy of Sciences, Politekhnicheskaya ul. 26, St. Petersburg, 194021 Russia*
e-mail: b.razbirin@pop.ioffe.rssi.ru
*** St. Petersburg State Institute of Fine Mechanics and Optics, ul. Sablinskaya 14, St. Petersburg, 197101 Russia*
**** Konstantinov Institute of Nuclear Physics, Russian Academy of Sciences, Gatchina, Leningrad oblast, 188350 Russia*
***** Université Libre de Bruxelles, Brussels, 1050 Belgium*

Received December 29, 2001

Abstract—Optical spectra of the $C_{60}Cl_{24}$ halofullerene in the crystalline state, as well as of $C_{60}Cl_{24}$ matrix-isolated molecules, were studied. In both cases, a rich line structure was revealed in absorption spectra in the energy region 1.5–3.0 eV. An energy diagram of the electronic levels of the molecule which are responsible for the observed optical transitions is proposed. The parameters of the geometrical structure of the $C_{60}Cl_{24}$ molecule were calculated under the assumption of its having T_h symmetry. These data were used in a theoretical study of the embedment of the $C_{60}Cl_{24}$ molecule in a toluene crystal matrix, which leads to the formation of a fine spectral structure (an analog of the Shpol'skiĭ effect) observed experimentally in this study. *© 2002 MAIK “Nauka/Interperiodica”.*

1. INTRODUCTION

Halogenated fullerenes belong to the so-called synthones, typical intermediate links in the preparation of a number of fullerene derivatives that have application potential. Therefore, investigation of the physical properties and, in particular, the electronic structure of halofullerenes by optical methods is currently a problem of primary interest. Combining fluorine, chlorine, or bromine with C_{60} produces stable halofullerene molecules with different stoichiometries [1–3] with the formation of strong covalent bonds, whereas the iodofullerenes exhibit weak van der Waals bonds of molecular iodine with the carbon cage.

Under normal conditions, the halofullerenes are molecular crystals. At the same time, they can be dissolved in a number of organic solvents with their molecular structure being conserved, which permits a comparative study of their optical spectra both in the crystalline state (in fullerites) and in the molecular state, in the form of a frozen gas of matrix-isolated molecules. This communication presents the results of a study of optical electronic spectra made on the least studied fullerene, $C_{60}Cl_{24}$, in both the crystalline and molecular states. It is first established that, in contrast to other halofullerenes, $C_{60}Cl_{24}$ has a distinct line structure in the near-IR and visible regions of the spectrum. We also briefly describe the method used to synthesize $C_{60}Cl_{24}$ and the results obtained in a theoretical investigation of the geometrical structure of this molecule (assuming it to have T_h symmetry).

2. PREPARATION OF $C_{60}Cl_{24}$

$C_{60}Cl_{24}$ was synthesized by chlorinating crystalline C_{60} in a chlorine environment under heating. The C_{60} fullerene was isolated from fullerene-containing soot prepared from spectroscopically pure graphite rods by the standard electric-arc technique of Krätschmer [4]. The isolation and purification were achieved by selective recrystallization, followed by flash chromatography on activated carbon and vacuum annealing. The purity of the C_{60} thus obtained, as derived from high-performance liquid chromatography (HPLC) data obtained on a C18-silica gel stationary-phase column, was 99.9%+. The chlorine was produced by oxidizing HCl in a concentrated solution of chromic acid under heating, dried successively over $CaCl_2$ and P_2O_5, and purified of oxygen by passing over porous charcoal at 750°C. The C_{60} was heated in the dark at 310°C in a chlorine flow of 15 ml/min, with the sample weight controlled periodically. It was found that the weight of the reaction product increased, to approach asymptotically the value corresponding to the $C_{60}Cl_{24}$ formula. We succeeded in reaching the maximum chlorine content in the molecule, which corresponded to an atomic carbon/chlorine ratio of 60 : 23.97 (Fig. 1). These data suggest that the original product obtained under the given conditions of preparation had no molecules containing more than 24 chlorine atoms.

The product was a fine-grained, yellowish-brown powder well soluble in organic solvents.

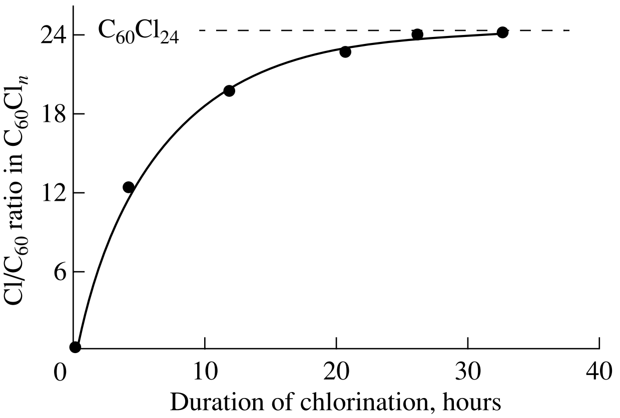

Fig. 1. Mass of the reaction product plotted as a function of the reaction time.

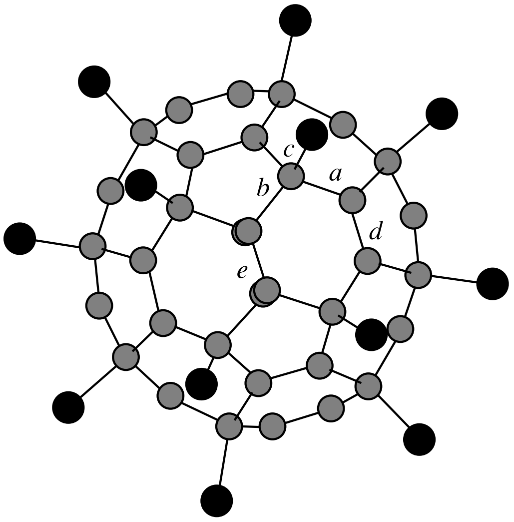

Fig. 2. Geometric structure of the $C_{60}Cl_{24}$ molecule.

3. THE GEOMETRIC STRUCTURE OF THE $C_{60}Cl_{24}$ MOLECULE

The lines seen in vibrational spectra of the $C_{60}Cl_{24}$ halofullerene are either Raman-or IR-active [5], which means that the molecule has inversion symmetry. Thus, there are grounds to believe that the symmetry of the $C_{60}Cl_{24}$ molecule is T_h, similar to that of $C_{60}Br_{24}$. In this structure, all the chlorine atoms are equivalent.

We calculated the geometric structure of the $C_{60}Cl_{24}$ molecule using universal force field (UFF) parameterization [6]. Then, the $C_{60}Cl_{24}$ geometry was optimized at the Hartree–Fock semiempirical AM1 (Austin Model 1) quantum-chemical level with the use of the Gaussian 98 code [7].

This molecule has C–C bonds of five types, 72 of which are single and the remaining 18 of which are double (Fig. 2). Table 1 lists the results of the calculations for $C_{60}Cl_{24}$ and compares them with the figures obtained for $C_{60}Br_{24}$ by us by using the same method and with experimental data from [1]. The single C–C bonds in the $C_{60}Cl_{24}$ molecule are longer than those in $C_{60}Br_{24}$, and the double bonds are somewhat shorter. The calculated length of the C–Cl bond (1.7507 Å) is noticeably less than that of the corresponding C–Br bond in $C_{60}Br_{24}$. An AM1 analysis of the populations of the molecular orbitals shows the electron density in the $C_{60}Cl_{24}$ molecule to be shifted toward the chlorine atoms. Each chlorine atom donates to the fullerene cage an average charge of +0.0055 $|e|$, and this charge is distributed primarily over the carbon atoms with sp^2-hybridized orbitals. In contrast to $C_{60}Br_{24}$, where all carbon atoms have an excess positive charge as a result of the strongly shifted electron density, the carbon atoms with sp^3- and sp^2-hybridized orbitals in $C_{60}Cl_{24}$ are short of positive charge or have an excess of it, respectively.

4. OPTICAL SPECTRA OF $C_{60}Cl_{24}$

Spectroscopic studies were carried out on a DFS-12 double-monochromator-based setup with a reverse dispersion of 0.5 nm/mm. Spectra were measured with an FÉU-79 PM tube in the photon counting mode. A $C_{60}Cl_{24}$ polycrystalline sample was a layer of powdery material 100–200 μm thick sandwiched between two glass plates. The samples of matrix-isolated molecules were prepared by freezing the fullerene solution in an organic solvent placed in a glass ampoule.

Figure 3 displays a transmission spectrum of polycrystalline $C_{60}Cl_{24}$ measured at $T = 80$ K. The spectrum is seen to consist of a large number of absorption lines of different widths, the widths increasing toward shorter wavelengths. The observed spectrum can be

Table 1. Geometrical structure and charge distribution in halofullerene molecules, obtained by quantum chemical calculations

	$C_{60}Cl_{24}$	$C_{60}Br_{24}$
C–C bond length, Å		
a	1.4876	1.4828
b	1.5272	1.5235
c	1.5231	1.5187
d	1.3537	1.3559
e	1.3351	1.3367
C–X bond length, Å		
	1.7507	1.9425
Charge distribution		
Average charge per halogen atom	+0.005488$\|e\|$	+0.09325$\|e\|$
Total charge transferred to carbon cage	+0.1317$\|e\|$	+2.238$\|e\|$

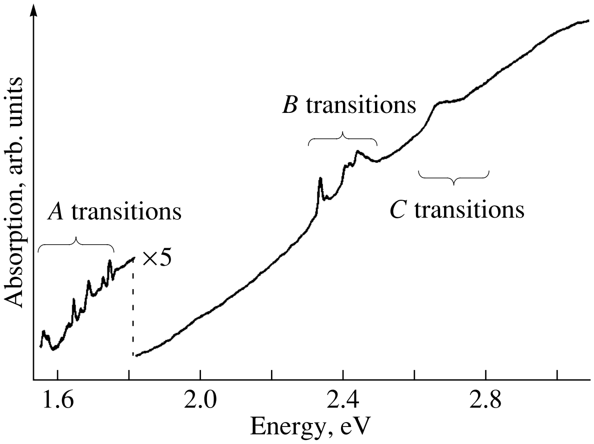

Fig. 3. Absorption spectrum of $C_{60}Cl_{24}$ crystalline powder. $T = 80$ K.

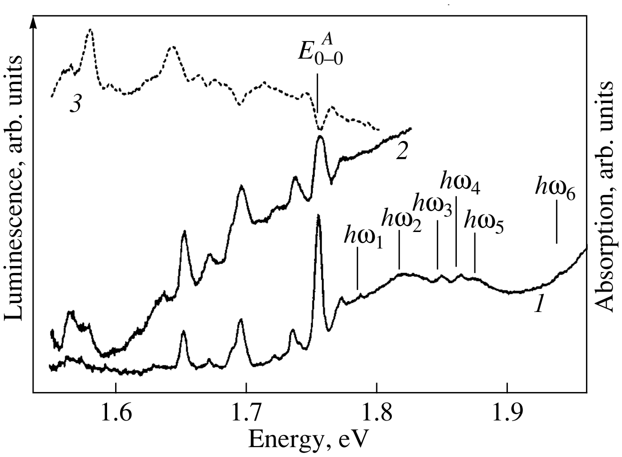

Fig. 4. Spectra of (*1*, *2*) absorption and (*3*) luminescence of (*2*) $C_{60}Cl_{24}$ crystalline powder and of (*1*, *3*) matrix-isolated $C_{60}Cl_{24}$ molecules in a matrix of 1,2,4-chlorobenzene. The dips in the luminescence spectrum observed in the interval 1.69–1.76 eV are caused by reabsorption of the radiation. $T = 80$ K.

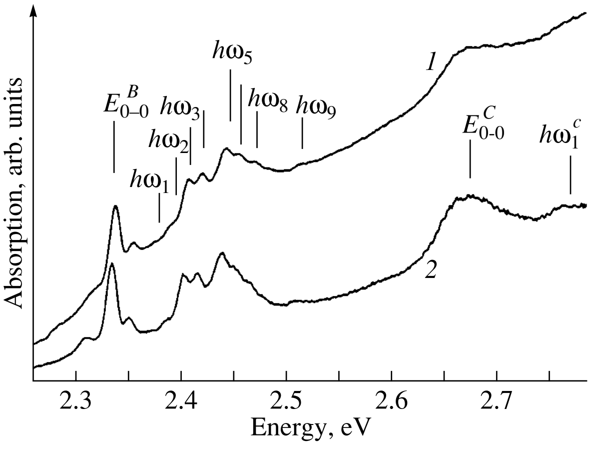

Fig. 5. Fragment of the absorption spectrum of (*1*) crystalline powder and (*2*) matrix-isolated molecules of $C_{60}Cl_{24}$ in bromobenzene. $T = 80$ K.

divided, in a first approximation, into three groups of lines. We denote them by *A*, *B*, and *C*. The long-wavelength group (*A*) is characterized by the smallest linewidth (the FWHM is ≈10 meV) and is confined to the energy interval 1.5–1.8 eV. The second group (*B*) is observed in the energy interval 2.3–2.5 eV. The line halfwidth is ≈20 meV. The third group (*C*) consists of two bands of halfwidth ≈50 meV. Within each group, one can isolate lines due to purely electronic transitions, as well as lines associated with their vibrational replicas. Table 2 lists the energies of all the line series observed (*A*, *B*, *C*) and their tentative assignment. The table specifies the energies of the purely electronic transitions (E_{0-0}) and of the corresponding vibrational quanta. We note that the line peaking at 1.817 eV is broader and apparently associated with more than one vibrational mode with energy in the interval 50–80 meV.

The $C_{60}Cl_{24}$ luminescence is extremely weak, which implies that a considerable role is played by nonradiative processes. At $T = 80$ K, we succeeded in observing only three weak emission lines in the interval 1.55–1.66 eV, which approximately coincide energywise with the corresponding absorption lines (Fig. 4).

Our study of $C_{60}Cl_{24}$ in frozen organic solvents performed at $T = 80$ K showed that the spectra of matrix-isolated molecules virtually do not differ from those of the $C_{60}Cl_{24}$ crystalline powder (Fig. 4). The only differences that are observed are a slight line narrowing and some intensity redistribution between them. All this indicates a clearly pronounced molecular character of the $C_{60}Cl_{24}$ crystal. Figures 4 and 5 illustrate in more detail the spectra of groups *A* and *B*. We note that the intensity of the long-wavelength line group *A* is approximately one-fifth that of the short-wavelength lines *B* and *C*. This suggests that type-*A* transitions occur with a lower probability.

Theoretical calculations of electronic energy levels of the $C_{60}Cl_{24}$ molecule are not found in the literature. Therefore, we propose a variant of the electronic level diagram of the molecule in the region of the HOMO–LUMO transitions which is based only on an analysis of our experimental data (Fig. 6). In accordance with this diagram, the line group *A* corresponds to transitions between levels *2* and *3*; line group *B*, to the 1 ⟶ 3 transitions; and line group *C*, to the 1 ⟶ 4 transitions. The 2 ⟶ 4 transitions are manifest extremely weakly in the spectrum, only in the form of barely seen features in the absorption spectrum in the interval 1.8–1.9 eV. The large linewidth observed in the 1 ⟶ 4 transitions is possibly associated with short electron lifetimes on level *4* because of a fast excitation conversion to level *3* accompanied by the emission of a vibrational quantum of the molecule with $\hbar\omega \approx 0.33$ eV (264 cm^{-1}). Approximately the same vibrational quanta ($\hbar\omega \approx 31$ and 37 meV) were observed by us in the vibronic absorption spectrum, as well as in the Raman spectrum ($\hbar\omega \approx$ 34 meV). The characteristic conversion time should be

Table 2. Energy positions of the lines observed in the absorption spectra of $C_{60}Cl_{24}$ at T = 80 K

Transitions *A*				Transitions *B*			
No.	*E*, eV	assignment	$\hbar\omega_i$, meV	No.	*E*, eV	assignment	$\hbar\omega_i$, meV
1	1.522	E_{0-0}		1	2.313	E_{0-0}	
2	1.538			2	2.340	E^*_{0-0}	
3	1.549			3	2.357	E_{0-0}	
4	1.566			4	2.377	$E^*_{0-0} + \hbar\omega_1$	37
5	1.579			5	2.392	$E^*_{0-0} + \hbar\omega_2$	52
6	1.614			6	2.409	$E^*_{0-0} + \hbar\omega_3$	69
7	1.632			7	2.422	$E^*_{0-0} + \hbar\omega_4$	82
8	1.650	E_{0-0}		8	2.444	$E^*_{0-0} + \hbar\omega_5$	104
9	1.669			9	2.456	$E^*_{0-0} + \hbar\omega_6$	116
10	1.693	E_{0-0}		10	2.471	$E^*_{0-0} + \hbar\omega_7$	131
11	1.734			11	2.485	$E^*_{0-0} + \hbar\omega_8$	145
12	1.753	E^*_{0-0}		12	2.514	$E^*_{0-0} + \hbar\omega_9$	174
13	1.761	E_{0-0}					
14	1.784	$E^*_{0-0} + \hbar\omega_1$	31	Transitions *C*			
15	1.817	$E^*_{0-0} + \hbar\omega_2$	64				
16	1.846	$E^*_{0-0} + \hbar\omega_3$	93	1	2.67	E^*_{0-0}	
17	1.861	$E^*_{0-0} + \hbar\omega_4$	108	2	2.77	$E^*_{0-0} + \hbar\omega_1$	100
18	1.873	$E^*_{0-0} + \hbar\omega_5$	120				
19	1.939	$E^*_{0-0} + \hbar\omega_6$	186				
20	1.979						

on the order of 0.1 ps, which is in reasonable agreement with current ideas on the relaxation processes occurring in molecules and crystals. We believe each of the levels of this diagram to have a complex structure, which may account for the presence of several E_{0-0} lines in the type-*A* and *B* transitions at T = 80 K.

The width of the lines of groups *A* (10 meV) and *B* (20 meV) is due to inhomogeneous broadening, as well as to interaction with acoustic vibrations of the $C_{60}Cl_{24}$ lattice or of the matrix. In certain cases, the broadening associated with the latter effect can be eliminated by properly choosing the corresponding matrix producing an optical counterpart of the Mössbauer effect [8, 9]. In this case, spectra of a number of fullerene molecules (C_{70}, C_{60}, and some derivatives) reveal a fine line structure corresponding to pure electronic transitions [10]. This is similar to the Shpol'skiĭ effect, which was observed in aromatic molecules embedded in frozen solutions in organic solvents (*n*-paraffines) [11].

In the $C_{60}Cl_{24}$–toluene crystal matrix system, in samples cooled to a temperature of 2 K, we succeeded in observing the formation of a fine structure in the lines A^*_{0-0} (E = 1.753 eV) and B^*_{0-0} (E = 2.340 eV), as well as a vibrational satellite structure in the B^*_{0-0} line (Fig. 7). The linewidth of the fine structure of line *A* is 1 meV, and that of line *B* is 2 meV. This structure disappears as the temperature is raised to ≈30 K. There is no fine structure in the $C_{60}Cl_{24}$–glass matrix system. We believe that this structure of the $C_{60}Cl_{24}$ spectrum originates from the Shpol'skiĭ effect.

It appears logical to assume that the fine structure in the A^*_{0-0} and B^*_{0-0} lines is associated with the molecule occupying several inequivalent sites in the matrix. In connection with this, we carried out a theoretical study of the structure of the $C_{60}Cl_{24}$ centers in a toluene matrix.

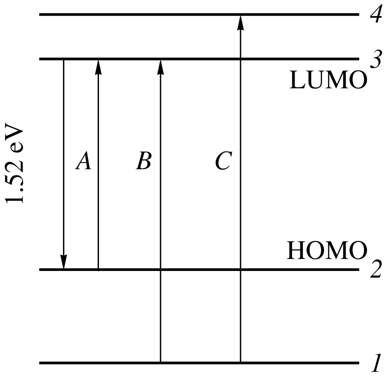

Fig. 6. Electronic-level diagram of the $C_{60}Cl_{24}$ molecule accounting for the experimental spectra.

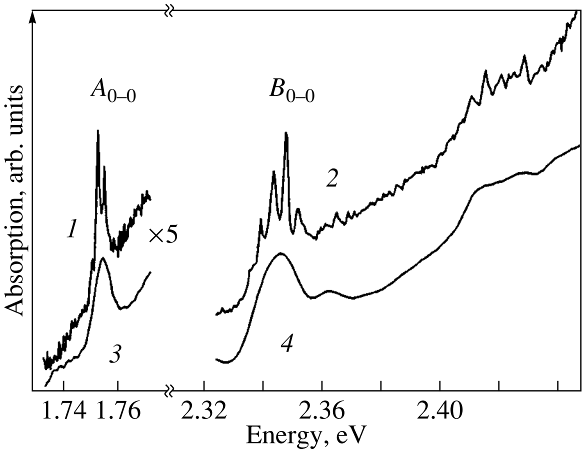

Fig. 7. (*1, 2*) Fine structure of absorption lines *A* and *B* of the $C_{60}Cl_{24}$ molecule in the crystal matrix of toluene. (*3, 4*) The spectrum of the molecule in the glassy toluene matrix does not have a fine structure. $T = 80$ K.

The geometry of the $C_{60}Cl_{24}$ molecule was chosen in accordance with the T_h symmetry and the parameters determined in this work and in [12]. The nonvalent interactions between the $C_{60}Cl_{24}$ molecule and the molecules of crystalline toluene were simulated by the interatomic potentials taken from [13]. The interatomic interaction in [13] had the form of the Lennard–Jones potential with parameters chosen [13] such as to obtain a good fit between the calculated and experimental data for several model substances. The toluene crystal matrix was simulated by a 60-molecule fragment of it. The matrix represents a high-temperature modification of the toluene crystal lattice, which has, according to [14], monoclinic symmetry $P2_1/C(C_{2h}^5)$.

The position, dimensions, and shape of the crystal-matrix cavity for a $C_{60}Cl_{24}$ molecule were determined by the following technique. The linear dimensions of the cavity (for the $C_{60}Cl_{24}$ molecule in toluene) cannot be less than ~14.6 Å, because otherwise the repulsive (positive) part of the energy with which fullerene atoms interact with atoms of the crystal matrix would become too high for the incorporation of the fullerene molecule into the cavity of the crystal matrix to be energetically favorable. However, the smaller the number of toluene molecules that have to be removed to create the cavity, the more energetically favorable its formation. Therefore, in order to determine the position, dimensions, and shape of the cavity, we scanned the irreducible part of the primitive cell of the toluene crystal by a sphere of radius 7.3 Å and found, for each position of the sphere's center, the number of crystal molecules that have at least one atom located within the sphere (it is the removal of such atoms that produces a cavity for the $C_{60}Cl_{24}$ molecule); thereafter, we chose the variants of the cavity that require removal of the smallest number of toluene molecules from the crystal. Finally, we established that the most energetically preferable are cavities centered at a common point with the coordinates $\mathbf{r}_c = 0.636\mathbf{a} + 0.227\mathbf{b} + 0.477\mathbf{c}$ and at equivalent points; these cavities are obtained by removing 17 toluene molecules (the primitive cell of the crystal contains eight molecules). In such a cavity, we found several deep energy minima (corresponding to different positions of the $C_{60}Cl_{24}$ molecule in the matrix); it is with these minima that one should apparently identify experimental points in the optical spectra.

The existence of a comparatively small number of possible energetically favorable positions of the molecule incorporated into the toluene crystal matrix correlates with the small number of lines due to purely electronic transitions that are observed in the spectrum of this system. Taking into account the relaxation of the crystal matrix molecules around the embedded $C_{60}Cl_{24}$ molecule should permit a more detailed comparison of the theoretical and experimental results.

ACKNOWLEDGMENTS

The authors are indebted to J. Cornil for performing some calculations.

This paper was partially supported by the Russian Foundation for Basic Research, project no. 00-03-33016; the Ministry of Education of the Russian Federation (RF), grant no. E00-5.0-338 (V.P.S.); the Ministry of Science and Technology of the RF the (program "Fullerenes and Atomic Clusters"); and INTAS, grant nos. 97-11894 and YSF 00-59 (A.V.Ch.).

REFERENCES

1. F. N. Tebbe, R. L. Harlow, D. B. Chase, *et al.*, Science **256**, 822 (1992).
2. P. R. Birkett, H. W. Kroto, R. Taylor, *et al.*, Chem. Phys. Lett. **205**, 399 (1993).

3. A. V. Eletskiĭ and B. M. Smirnov, Usp. Fiz. Nauk **165**, 977 (1995) [Phys. Usp. **38**, 935 (1995)].
4. W. Kraetschmer, K. Fostiropoulos, and D. R. Huffman, Chem. Phys. Lett. **170**, 167 (1990).
5. M. F. Limonov, Yu. E. Kitaev, A. V. Chugreev, *et al.*, Phys. Rev. B **57** (13), 7586 (1998).
6. A. K. Rappé, C. J. Casewit, K. S. Colwell, *et al.*, J. Am. Chem. Soc. **114**, 10024 (1992).
7. M. J. Frisch, G. W. Trucks, H. B. Schlegel, *et al.*, Gaussian 98 (Revision A.1) (Gaussuan Inc., Pittsburgh, 1998).
8. E. D. Trifonov, Dokl. Akad. Nauk SSSR **147**, 826 (1962) [Sov. Phys. Dokl. **7**, 1105 (1963)].
9. E. F. Gross, S. A. Permogorov, and B. S. Razbirin, Dokl. Akad. Nauk SSSR **147**, 338 (1962) [Sov. Phys. Dokl. **7**, 1012 (1963)]; Dokl. Akad. Nauk SSSR **154**, 1306 (1964) [Sov. Phys. Dokl. **9**, 164 (1964)].
10. B. S. Razbirin, A. N. Starukhin, A. V. Chugreev, *et al.*, Pis'ma Zh. Éksp. Teor. Fiz. **60**, 435 (1994) [JETP Lett. **60**, 451 (1994)]; B. S. Razbirin, A. N. Starukhin, A. V. Chugreev, *et al.*, Fiz. Tverd. Tela (St. Petersburg) **38**, 943 (1996) [Phys. Solid State **38**, 522 (1996)].
11. É. V. Shpol'skiĭ, Usp. Fiz. Nauk **77**, 321 (1962) [Sov. Phys. Usp. **5**, 522 (1962)].
12. O. E. Kvyatkovskiĭ, M. G. Shelyapina, B. F. Shchegolev, *et al.*, Fiz. Tverd. Tela (St. Petersburg) **44**, 557 (2002) [Phys. Solid State **44**, 585 (2002)].
13. T. V. Timofeeva, N. Yu. Chernikova, and P. M. Zorkiĭ, Usp. Khim. **49**, 966 (1980).
14. M. Anderson, L. Bosto, J. Bruneaux-Poulle, and R. Fourme, J. Chim. Phys. Phys. Chim. Biol. **74**, 68 (1977).

Translated by G. Skrebtsov